SYNTHESIS, CHARACTERIZATION AND CHARGE TRANSPORT PROPERTIES OF BODIPY, AZA-BODIPY, AND AZA-DIPYRROMETHENE COMPLEXES OF GROUP 13 AND FIRST-ROW TRANSITION METALS

A Dissertation Presented for the

Doctor of Philosophy

Degree

The University of Tennessee, Knoxville

Tayo Morris Oyelowo

August 2026

Copyright © 2026 by Tayo Morris Oyelowo.

All rights reserved.

DEDICATION

I dedicate this thesis to my parents, whose sacrifices, unconditional love, unwavering support, and endless encouragement have made this journey possible. Their strength, belief in me, and countless sacrifices have been the foundation of every achievement in my life. This work reflects their love and dedication, and I will forever be grateful to them.

ACKNOWLEDGEMENTS

First and foremost, I would like to express my deepest gratitude to God, and my parents for their immeasurable love, sacrifices, encouragement, and unwavering support throughout my academic journey. Their belief in me has been the foundation upon which all of my achievements stand. I am forever grateful for the values they instilled in me and for always encouraging me to pursue excellence.

I would also like to sincerely thank my advisor, Professor Victor N. Nemykin, for his exceptional mentorship, scientific insight, patience, and continuous guidance throughout my PhD studies. His depth of knowledge, creativity, and passion for science have profoundly influenced my growth as a researcher and scientist. Working under his supervision has been an incredible privilege, and I genuinely consider him one of the most brilliant scientists I have ever known. I am deeply grateful for the opportunities, encouragement, and intellectual freedom he provided during my doctoral training.

I would like to extend my sincere appreciation to my dissertation committee members: Dr. Ziling Xue, Dr. Joshua Baccile, and Dr. Timothy Bender, for their valuable feedback, thoughtful discussions, and support throughout this work. Their insights and suggestions greatly contributed to the development and completion of this dissertation.

Finally, I would like to thank my colleagues in Nemykin Group, collaborators, friends, and everyone who contributed directly or indirectly to this research journey. Your support and encouragement made this experience both meaningful and rewarding.

This study was supported in part by University of Tennessee Knoxville, National Science Foundation and the generous computing time offered by the University of Minnesota Supercomputing Institute.

ABSTRACT

This dissertation investigates the design, synthesis, characterization, magnetic behavior, photophysical and electronic properties of aza-dipyrromethene-based molecular systems exhibiting diradicaloid behavior, redox activity, and charge-transport functionality. The work focuses on BODIPY, aza-BODIPY, Group 13 aza-dipyrromethene complexes, first-row transition-metal complexes, and related panchromatic chromophores as platforms for advanced molecular materials with tunable magnetic, optical, and electronic properties.

My first project (chapter II) centered on the synthesis and characterization of the first aza-BODIPY diradicaloids bearing 4-(2,6-di-tert-butyl)phenoxyl radicals at the 1,7-positions of the chromophore. Spectroscopic, electrochemical, magnetic, and computational studies revealed predominantly closed-shell singlet ground states with thermally accessible open-shell singlet and triplet states. Variable-temperature nuclear proton magnetic resonance (^{1}H NMR), electron paramagnetic resonance (EPR), and SQUID magnetometry studies demonstrated solvent-dependent diradical character, while transient absorption spectroscopy revealed ultrafast excited-state deactivation associated with open-shell behavior. In subsequent studies (Chapter III) we extended the approach of introducing diracaloid to a series of strongly fluorescent dyes of boron, aluminum, gallium, and indium N_2O_2-bis(phenolate) aza-dipyrromethene. Oxidation generated stable diradicaloid species with strong near-infrared absorption, while computational and spectroscopic magnetic studies established how the Group 13 centers influence spin delocalization, redox properties, and singlet–triplet energy gaps. Chapter IV examines homoleptic Co(II), Ni(II), Cu(II), and Zn(II) complexes of phenol-substituted aza-dipyrromethene ligands. Oxidized quinone/bis(diradicaloid) species exhibited panchromatic

absorption, ligand-centered spin delocalization, and accessible magnetic states. Charge-transport measurements revealed modest electron mobilities and unusually high hole mobilities approaching 10^{-3} cm^2 V^{-1} s^{-1}, highlighting their potential as hole-transport materials. Chapter V introduces highly conjugated BODIPY systems designed to achieve broad visible-to-near-infrared absorption through controlled redox transformations. Spectroelectrochemical and computational investigations established the formation of stable mixed-valence (radical-anion) species, dianionic, and diradicaloid states with intense low-energy optical transitions and enhanced electronic communication across the chromophore framework.

This project establishes aza-dipyrromethene and dipyrromethene-based systems as versatile molecular platforms for tuning spin states, redox activity, optical absorption, and charge transport, providing important design principles for future applications in spintronics, optoelectronics, photovoltaics, and quantum information technologies.

TABLE OF CONTENTS

CHAPTER I: INTRODUCTION……... 1

1.1 Open-Shell Organic Molecules 2

1.2 Diradicals 2

1.2.1 Diradicaloids 4

1.2.2 Classification of Diradicals 8

1.3 Biradicals versus Diradicals 9

1.4 Bis(diradicals) and Tetraradicals 11

1.5 Applications of Diradicals 12

1.6 Previous Works on BODIPY-Based Diradicals and Diradicaloids 13

1.7 Scope of Dissertation 17

References 18

CHAPTER II: Exploring aza-BODIPY Diradicaloids with 4-(2,6-Ditert-butyl)Phenoxy Radicals Located in 1,7-Positions of the Aza-BODIPY Core 41

2.1 Abstract 42

2.2 Introduction 43

2.3 Results and Discussion 45

2.3.1 Synthesis and Characterization of aza-BODIPY diradicaloids 2.9 and 2.10 with 4-(2,6-di-tert-butyl)phenoxy radicals located in 1,7-positions of the aza-BODIPY core.... 45

2.3.2 Photophysical Studies 47

2.3.2 Absorption and Emission Studies 47

2.3.2 Transient Absorption Studies 49

2.3.3 Electrochemical and Spectroelectrochemistry 51
2.3.4 Magnetic Studies 56
2.3.4.1 Variable Temperature Proton NMR 56
2.3.4.2 Variable Temprature EPR 59
2.3.4.3 Variable Temprature SQUID Magnetometry 62
2.3.5 X-Ray Crystallography Studies 63
2.3.2 DFT and TDDFT Calculations 66
2.4 Conclusion 74
2.5 Experimental 75
2.5.1 General Materials and Methods 75
2.5.2 Synthesis of 2.1 79
2.5.3 Synthesis of 2.2 79
2.5.4 Synthesis of 2.3 80
2.5.5 Synthesis of 2.4 80
2.5.6 Synthesis of 2.5 81
2.5.7 Synthesis of 2.6 82
2.5.8 Synthesis of 2.7 82
2.5.9 Synthesis of 2.8 83
2.5.10 Synthesis of 2.9 84
2.5.11 Synthesis of 2.10 84
References 86
Appendix 104

CHAPTER III: DESIGN OF STABLE DIRADICALOIDS BASED ON GROUP 13 DYES OF N2O2-BIS(PHENOLATE) AZA-DIPYRROMETHENE AND AZA-BODIPY 126
3.1 Abstract 127
3.2 Introduction 128
3.3 Results and Discussion 130
3.3.1 Synthesis and Characterization of Diradicaloids (3.5a – 3.5d) Based on N_2O_2-Bisphenolate-aza-BODIPY (3.4a), N_2O_2-Bisphenolate-aza-ALDIPY (3.4b), N_2O_2-Bisphenolate-aza-GADIPY (3.4c), N_2O_2-Bisphenolate-aza-INDIPY (3.4d) 130
3.3.2 Absorption and Emission Studies 132
3.3.2 Electrochemical and Spectroelectrochemical Studies 135
3.3.2 Magnetic Studies 143
3.3.4.1 Variable Tempearture NMR 143
3.3.4.2 Variable Tempearture EPR 145
3.3.4.3 Variable Tempearture SQUID Magnetometry 147
3.3.5 X-Ray Crystallographic Studies 148
3.3.6 DFT and TDDFT Calculations 151
3.4 Conclusion 158
3.5 Experimental 158
3.5.1 General Materials and Methods 158
3.5.2 Synthesis of 3.1 163
3.5.3 Synthesis of 3.2 163
3.5.4 Synthesis of 3.3 163

3.5.5 Synthesis of 3.4a 164
3.5.6 Synthesis of 3.5a 165
3.5.7 Synthesis of 3.4b 163
3.5.8 Synthesis of 3.5b 166
3.5.9 Synthesis of 3.4c 166
3.6.10 Synthesis of 3.5c 167
3.5.11 Synthesis of 3.4d 168
3.5.12 Synthesis of 3.5d 168
References 170
Appendix 185
CHAPTER IV: SYNTHESIS, SPIN DELOCALIZATION, AND CHARGE TRANSPORT PROPERTIES OF PHENOL-SUBSTITUTED AZA-DIPYRROMETHENE COMPLEXES OF COBALT, NICKEL, COPPER, ZINC AND THEIR OXIDIZED FORMS 200
4.1 Abstract 201
4.2 Introduction 202
4.3 Results and Discussion 205
4.3.1 Synthesis of Homoleptic Complexes of Co(II), Ni(II), Cu(II), and Zn(II) supported by Aza-Dipyrromethene Ligand Bearing Phenolic Substituents at the 1,7-Positions (4.1a – 4.1d) and their Oxidized Forms (4.2a – 4.2d) 205
4.3.2 Absorption and Emission Studies 207
4.3.3 Electrochemical and Spectroelectrochemical Studies 209
4.3.4 Magnetic Studies 216

4.3.4.1 Magnetic Studies of Co(II) Complex 4.1a 216
4.3.4.2 Magnetic Studies of Ni(II) Complex 4.2b 217
4.3.4.3 Magnetic Studies of Cu(II) Complexes 4.1c and 4.2c 218
4.3.4.3 Magnetic Studies of Zn(II) Complexe 4.2d 220
4.3.5 X-Ray Crystallographic Studies 222
4.3.6 Charge Transport Properties 225
4.3.7 DFT and TDDFT Calculations 229
4.4 Conclusions 236
4.5 Experimental 236
4.5.1 General Materials and Methods 236
4.5.2 Synthesis of 4.1a 241
4.5.3 Synthesis of 4.1b 241
4.5.4 Synthesis of 4.1c 242
4.5.5 Synthesis of 4.1d 242
4.5.6 Synthesis of 4.2a 242
4.5.7 Synthesis of 4.2b 243
4.5.8 Synthesis of 4.2c 244
4.5.9 Synthesis of 4.2d 244
References 246
Appendix 263

CHAPTER V: TRYING TO CRACK THE SHELL: INVESTIGATING THE MAGNETIC PROPERTIES AND ELECTRONIC STRUCTURES OF REDOX-ACTIVE ESTER-SUBSTITUTED BODIPY-BENZOQUINONE DIRADICALOID 275
5.1 Abstract 276
5.2 Introduction 277
5.3 Results and Discussion 280
5.3.1 Synthesis and Characterization of BODIPY 5.2 and 5.3 280
5.3.2 Photophysical Studies 281
5.3.3 Electrochemical and Spectroelectrochemical Studies 283
5.3.4 Magnetic Studies 288
5.3.4.1 Variable Temperature NMR and EPR Spectroscopic Studies 288
5.3.5 X-Ray Diffraction Experiments and Related Studies 289
5.3.6 Quantum Chemical Calculations 293
5.4 Conclusions 301
5.5 Experimental 302
5.5.1 General Materials and Methods 302
5.5.2 Synthesis of 5.7 306
5.5.3 Synthesis of 5.8 306
5.5.4 Synthesis of 5.9 307
5.5.5 Reduction of dye 5.8 to BODIPY 5.7 308
References 309
Appendix 324

CHAPTER VI: CONCLUSIONS AND OUTLOOK 333

6.1 Conclusions 334

6.1 Future Outlook 336

VITA 337

LIST OF TABLES

Table 2.1. Selected photophysical properties of the target aza-BODIPYs. 49

Table 2.2. Fitting parameters for compounds studied (Fit time slice at 510 nm) Parallel Fitting 50

Table 2.3. Redox properties of the aza-BODIPYs..... 53

Table 2.3. Redox properties of the aza-BODIPYs..... 53

Table 2.4. Selected bond distances observed in the variable-temperature XRD experiments for **2.9**..... 65

Table 2.5. DFT-predicted relative energies (kcal/mol), spin densities at oxygen atoms, and diradical character coefficients for **2.9CS**, **2.9OS**, and **2.9TS**……..…69

Table 2.6a. Major TDDFT-Predicted Excited States of 2.7. 120

Table 2.6b. Major TDDFT-predicted Excited States of $[2.12]^{2-}$..... 120

Table 2.6c. Major TDDFT-Predicted Excited States of 2.9(CS)…..... 120

Table 2.6d. Major TDDFT-Predicted Excited States of 2.9(OS) using wB97X_MO6.. 121

Table 2.6e. Major TDDFT-Predicted Excited States of 2.9(OS) using CAM_B3LYP.. 121

Table 2.6f. Major TDDFT-Predicted Excited States of 2.9(TS)..... 122

Table 2.6g. Major TDDFT-Predicted Excited States of $[2.11]^{\cdot-}$. 123

Table 3.1. Photophysical Properties of 3.4a – 3.4d in MeOH and DMSO, 3.5a – 3.5d in DCM……...133

Table 3.2. Redox potentials (V) of the target compounds…….…..134

Table 3.3. The experimental singlet–triplet energy gap (ΔE_{S-T}) and calculated diradical character (y_0) using the TPSSh exchange correlation functional…….150

Table 3.4. Spin Distribution in Open-Shell Singlet 4b(OS) and Open-shell Triplet 4b(TS) States……...….151

Table 3.5a. Major TDDFT-Predicted Excited States of 3.4a ……...…...193

Table 3.5b. Major TDDFT-Predicted Excited States of 3.5a(CS) ……..…....193

Table 3.5c. Major TDDFT-Predicted Excited States of 3.5a(OS) …….……...….194

Table 3.5d. Major TDDFT-Predicted Excited States of 3.5a(TS) ……...…..195

Table 3.5e. Major TDDFT-Predicted Excited States of $[3.6a]^{-}$ ...……..196

Table 3.5f. Major TDDFT-Predicted Excited States of $[3.7a]^{2-}$……...…...197

Table 4.1. Summary of UV-Vis spectra of 4.1a – 4.1d and 4.2a – 4.2d in THF (sh = shoulder)……..207

Table 4.2. Electrochemical Complexes 4.2a – 4.2d. Potentials are in volts vs Fc/Fc^{+} for dry DCM/0.1 M TBAP solutions……...209

Table 4.3. Selected bond length of Ni(II) 4.1b and Zn(II) 4.1d complexes……....221

Table 4.4. Selected angles and torsion of Ni(II) 4.1b and Zn(II) 4.1d complexes……..222

Table 4.5. Summary of average electron and hole mobility in diodes using the SCLC method……225

Table 4.6. Major TDDFT-predicted excited states contributions for complex 4.1d using TPSSh exchange correlation functional……....233

Table 5.1. Photophysical properties of BODIPYs 5.2, 5.3 and 5.6 in DCM at room temperature……..280

Table 5.2a. Major TDDFT-Predicted Excited States of BODIPY 5.7…...…….326

Table 5.2b. Major TDDFT-Predicted Excited States of BODIPY 5.8(CS)…...…….326

Table 5.2c. Major TDDFT-Predicted Excited States of BODIPY 5.8(TS)…...……..327

Table 5.2d. Major TDDFT-Predicted Excited States of BODIPY 5.8(OS)…...…….....328

Table 5.2e. Major TDDFT-Predicted Excited States of Mixed Valent Radiacal Anion $[5.10]^{\cdot -}$

…...…….……329

Table 5.2f. Major TDDFT-Predicted Excited States of Dianin $[5.11]^{2-}$…...…….....330

LIST OF FIGURES

Figure 1.1. Zeeman splitting of electrons in triplet diradicals in the solid state……...…..3

Figure 1.2. Chemical structures of Gomberg radical, Schlenk diradical, Thiele, Chichibabin, and Müller diradical(oids)……..5

Figure 1.3. (a) Classical carbon-centered organic diradicaloid of Chichibabin's hydrocarbon and its two characteristic resonance structures. (b) Diradical character (y_0) of organic diradicaloids. (c) Target nitrogen-centered diradicaloid…….....8

Figure 1.4. Schematic description of electron coupling in biradical versus diradical with Zeeman's splitting of electrons in applied magnetic field…….……....10

Figure 1.5. Possible forms of tetraradical created by connection of two diradicals (σ = short-range coupling, λ = long-range coupling; $|\sigma| \geq |\lambda|$)…….....12

Figure 1.6. Schematic illustration of the electronic applications of organic diradicaloids……....13

Figure 1.7. The structures of *p*-QDM, *m*-QDM, and their bridged BODIPY dimers BD-1 and BD-2. Ar = 4-*tert*-butylphenyl…….……...15

Figure 2.1. Normalized UV-Vis and fluorescent spectra of 2.7, 2.8, 2.9 and 2.10 in DCM…....48

Figure 2.2. Excited state absorption following excitation at 531 nm. Fitted time constants and the wavelengths of the probe and full ΔOD spectra (**4a** = **2.7, 5a** = **2.9, 5b** = **2.10**)……...50

Figure 2.3. CV and DPV data on 2.8 in DCM/0.1M TBAP system…….52

Figure 2.4. UV/Vis/NIR absorption change of 2.7 and 2.8 upon electrochemical oxidation (DCM) using TBAP as electrolyte in a spectroelectrochmical setup. Arrows show spectra changes with increasing positive potential……....53

Figure 2.5. Cyclic voltammograms of 2.9 and 2.10 in dry DCM…….54

Figure 2.6. Cyclic voltammograms of 2.9 and 2.10 in dry DMF……..……..….54

Figure 2.7. UV/Vis/NIR absorption change of aza-BODIPY 2.9 upon electrochemical Reduction (1^{st} and 2^{nd}) in a spectroelectrochmical setup (DMF) using TBAP as electrolyte. Arrows show spectra changes with increasing negative potential……....…..55

Figure 2.8. UV/Vis/NIR absorption change of 5b upon electrochemical Reduction (1^{st} and 2^{nd}) in a spectroelectrochmical setup (DCM) using TBAP as electrolyte. Arrows show spectra changes with increasing negative potential (5a = 2.9 & 5b = 2.10)……..……...55

Figure 2.9. Variable-temperature ^{1}H NMR spectrum of 2.9 in THF…….57

Figure 2.10. Variable-temperature ^{1}H NMR spectrum of 2.9 in DCM…….....….57

Figure 2.11. Variable-temperature ^{1}H NMR spectrum of 2.9 in DMF……..58

Figure 2.12. Variable-temperature ^{1}H NMR spectrum of 2.10 in DMF……58

Figure 2.13: Variable-temperature ^{1}H NMR spectrum of 2.10 in DCM……...59

Figure 2.14. Variable-temperature EPR spectra of 2.9 in a solid state (left) and DCM/toluene solution (right)……...…....60

Figure 2.15. Variable-temperature EPR spectra of 2.10 in a solid state (left) and DCM/toluene solution (right)……...……60

Figure 2.16. Variable-temperature EPR spectra of 2.9 (left) and 2.10 (right) in THF……..61

Figure 2.17. Variable-temperature EPR spectra of 2.9 (left) and 2.10 (right) in DMF……61

Figure 2.18. SQUID measurements from 0-300K in polycarbonate capsules of: (a) 2.9 at 3000 Oe (b) 2.9 at 5000 Oe (c) 2.10 at 3000 Oe (d) 2.10 at 5000 Oe……....62

Figure 2.19. X-ray crystal structures of 2.5 (left) and 2.9 (right) with schematic representation below……..64

Figure 2.20. DFT-predicted energy diagram for the frontier MOs in aza-BODIPYs 2.7, 2.9(CS), 2.9(OS)-α, 2.9(OS)-β, 2.9(TS)-α, 2.9(TS)-β, 2.11-α, 2.11-β and 2.13……..……68

Figure 2.21. DFT-predicted (M06 exchange-correlation functional) total spin density for 2.9(OS) (left), and HOMO/LUMO pairs for 2.9(CS), 2.9(OS), and 2.9(TS)……..…….68

Figure 2.22. Experimental versus TDDFT-predicted (M06 exchange-correlation functional) UV-Vis spectra of 2.7, 2.9, $[2.11]^{-\cdot}$, and $[2.13]^{2-}$…….……70

Figure 2.23. DFT-predicted compositions of frontier orbitals for aza-BODIPYs 2.7 and 2.9(CS).…….....72

Figure 2.24. DFT-predicted compositions of frontier orbitals for aza-BODIPY Dianion $[2.13]^{2-}$. …….....72

Figure 2.25. DFT-predicted compositions of frontier orbitals for aza-BODIPY Mixed Valence Species $[2.11]^{-\cdot}$……..…….73

Figure 2.26. DFT-predicted compositions of frontier orbitals for aza-BODIPY Diradical 2.9 in singlet 2.9(OS) and triplet 2.9(TS) State……..……73

Figure 2.27. ^{1}H NMR spectra of compound 2.1 in $CDCl_3$……..…….....104

Figure 2.28. ^{13}C NMR spectra of compound 2.1 in $CDCl_3$…….....104

Figure 2.29. ^{1}H NMR spectra of compound 2.2 in $CDCl_3$…….....105

Figure 2.30. ^{13}C NMR spectra of compound 2.2 in $CDCl_3$…….....105

Figure 2.31. ^{1}H NMR spectra of compound 2.3 in $CDCl_3$…….....106

Figure 2.32. ^{13}C NMR spectra of compound 2.3 in $CDCl_3$…….....106

Figure 2.33. ^{1}H NMR spectra of compound 2.4 in $CDCl_3$…….....107

Figure 2.34. ^{13}C NMR spectra of compound 2.4 in $CDCl_3$…….....107

Figure 2.35. ^{1}H NMR spectra of compound 2.5in $CDCl_3$…….....108

Figure 2.36. ^{13}C NMR spectra of compound 2.5 in $CDCl_3$…….....108

Figure 2.37. ^{1}H NMR spectra of compound 2.6 in $CDCl_3$…….....109

Figure 2.38. ^{13}C NMR spectra of compound 2.6 in $CDCl_3$…….....109

Figure 2.39. ^{1}H NMR spectra of compound 2.7 in $CDCl_3$…….....110

Figure 2.40. ^{13}C NMR spectra of compound 2.7 in $CDCl_3$…….....110

Figure 2.41. ^{11}B NMR spectra of compound 2.7 in $BF_3.EtO_2$…….....111

Figure 2.42. ^{19}F NMR spectra of compound 2.7 in $BF_3.EtO_2$…….....111

Figure 2.43. ^{1}H NMR spectra of compound 2.8 in $CDCl_3$…….....112

Figure 2.44. ^{13}C NMR spectra of compound 2.8 in $CDCl_3$…….112

Figure 2.45. ^{1}H NMR spectra of compound 2.9 in $CDCl_3$…….....113

Figure 2.46. ^{13}C NMR spectra of compound 2.9 in $CDCl_3$……..…..113

Figure 2.47. ^{1}H NMR spectra of compound 2.10 in $CDCl_3$…….....114

Figure 2.48. ^{13}C NMR spectra of compound 2.10 in $CDCl_3$……...114

Figure 2.49. Mass spectrum (MALDI) of compound 2.3…….....115

Figure 2.50. Mass spectrum (MALDI) of compound 2.4…….....115

Figure 2.51. Mass spectrum (MALDI) of compound 2.5…….....116

Figure 2.52. Mass spectrum (MALDI) of compound 2.6…….....116

Figure 2.53. Mass spectrum (MALDI) of compound 2.7…….....117

Figure 2.54. Mass spectrum (MALDI) of compound 2.8…….....117

Figure 2.55. Mass spectrum (MALDI) of compound 2.9…….....118

Figure 2.56. Mass spectrum (MALDI) of compound 2.10……..118

Figure 2.57. IR Spectrum of 2.7 in solid state…….119

Figure 2.58. IR Spectrum of 2.9 in solid state…….119

Figure 3.1. Normalized UV-vis-NIR absorption spectra (CH_3OH) of 3.4a – 3.4d (black solid line), as well as fluorescence spectra (CH_3OH) of 3.4a – 3.4d (red dashed line). Also shown are the absorption spectra (CH_2Cl_2) of diradical molecules 3.5a – 3.5d (blue solid line)…….132

Figure 3.2. Cyclic voltammogram (blue curve) of 3.4a in DCM and 3.4b - 3.4d in DMF/0.1M TBAP system……...……135

Figure 3.3. Cyclic voltammogram (blue curve), diffrential pulse voltammogram (red & black curve) of 3.4a - 3.4d in DCM/0.1M TBAP system…….……....136

Figure 3.4. UV/vis/NIR absorption spectral changes of (a) 3.4a to 3.5b, (b) 3.4b to 3.5b (c) 3.4c to 3.5c and (d) 3.4d to 3.5d ($c \approx 4$ mM in THF, rt, 0.3 M TBAP (^{n}Bu$_4$N)[ClO_4] upon electrochemical oxidation in a spectroelectrochemical setup. Arrows indicate spectral changes with increasing positive potential…….…..…….138

Figure 3.5. UV/vis/NIR absorption spectral changes of 3.4a – 3.4d in THF upon titration with TBAOH (^{n}Bu$_4$NOH) for 3.4a and TBAF (^{n}Bu$_4$NF) solution for 3.4b – 3.4d to form dianion $[3.7a]^{2-}$ - $[3.7d]^{2-}$…….……..139

Figure 3.6. UV-vis-NIR spectroscopic changes observed upon gradual oxidation of the $3.7a^{2-}$ to mixed valent $[3.6a]^{-\cdot}$ (a) and $[3.6a]^{-\cdot}$ to 3.5a (b) the spectroelectrochemical experiment in THF/0.3 M (nBu$_4$N)[PF_6] system……....139

Figure 3.7. UV-vis-NIR absorption spectroscopic changes of $[3.7b]^{2-}$ to $[3.6b]^{-\cdot}$ (a), $[3.6b]^{-\cdot}$ to 3.5b (b), $[3.7c]^{2-}$to $[3.6c]^{-\cdot}$ (c), $[3.6c]^{-\cdot}$ to 3.5c (d), $[3.7d]^{2-}$ to $[3.6d]^{-\cdot}$ (e), and $[3.6d]^{-\cdot}$ to 3.5d (f,

THF, rt, 0.3 M (^{n}Bu$_4$N)[PF$_6$]) upon electrochemical oxidation in a spectroelectrochemical setup. Arrows indicate spectroscopic changes with increasing positive potential……...……..140

Figure 3.8. Variable Temperature 1H NMR of 3.5a in CD_2Cl_2 ……..141

Figure 3.9. Variable Temperature 1H NMR of 3.5b in CD_2Cl_2 ……..…142

Figure 3.10. Variable Temperature 1H NMR of 3.5c in CD_2Cl_2 ……142

Figure 3.11. Variable Temperature 1H NMR of 3.5d in CD_2Cl_2 ……143

Figure 3.12. Variable Temperature EPR of 3.5a - 3.5d with KBr in the solid state……....144

Figure 3.13. χ_MT vs T curve (blue line) in the SQUID measurement for the powder of 3.5a – 3.5d. The fitting obtained by the Bleany-Bowers equation (red line)……..…...145

Figure 3.14. Molecular structure of 3.4a. Ellipsoids are drawn to a 50% probability level……146

Figure 3.15. Molecular structure of 3.4c with Pyridine. Ellipsoids are drawn to 50% probability level……...……...148

Figure 3.16. Molecular structure of 3.4c dimer. Ellipsoids are drawn to 50% probability level. THF molecules are eliminated from view “a” for clarity……....148

Figure 3.17. (a) Spin density distribution of open-shell singlet state 3.5a(OS). (b) Spin density distribution of open-shell triplet state 3.5a(TS)……..…151

Figure 3.18. DFT-predicted energy diagram for the frontier MOs 3.4a, 3.5a(CS), 3.5a(OS)-α, 3.5a(OS)-β, 3.5a(TS)-α, 3.5a(TS)-β, $[3.6a]^{-\cdot}$-α, $[3.6a]^{-\cdot}$-β and $[3.7a]^{2-}$……152

Figure 3.19. (a) Experimental versus TDDFT-predicted (M06 exchange-correlation functional) UV-vis spectra of 3.4a, $[3.6a]^{-\cdot}$, $[3.7]^{2-}$, 3.5a(CS), 3.5a(OS), and 3.5a(TS)…….153

Figure 3.20. DFT-predicted frontier molecular orbitals for 3.5a(CS), 3.5a(OS), and 3.5a(TS)..155

Figure 3.21. DFT-predicted compositions of frontier orbitals for 3.4a, $[3.6a]^{-\cdot}(\alpha)$, $[3.6a]^{-\cdot}(\beta)$, $[3.7a]^{2-}$. Abbreviation: "aza-DIPY" = aza-BODIPY……..……..155

Figure 3.22. DFT-predicted compositions of frontier orbitals for 3.5a(CS), 3.5a(OS)-α, 3.5a(OS)-β, 3.5a(TS)-α, and 3.5a(TS)-β Abbreviation: "aza-DIPY" = aza-BODIPY……..……..156

Figure 3.23. ^{1}H NMR spectrum of compound 3.3 in $CDCl_3$…….....183

Figure 3.24. ^{13}C NMR spectrum of compound 3.3 in $CDCl_3$……..183

Figure 3.25. ^{1}H NMR spectrum of compound 3.4a in $CDCl_3$…….....184

Figure 3.26. ^{13}C NMR spectrum of compound 3.4a in $CDCl_3$……....184

Figure 3.27. ^{1}H NMR spectrum of compound 3.4b in DMSO-d_6……..……..185

Figure 3.28. ^{13}C NMR spectrum of compound 3.4b in DMSO-d_6……..185

Figure 3.29. ^{1}H NMR spectrum of compound 3.4c in DMSO-d_6……..…….....186

Figure 3.30. ^{13}C NMR spectrum of compound 3.4c in DMSO-d_6……..186

Figure 3.31. ^{1}H NMR spectrum of compound 3.4d in DMSO-d_6….....187

Figure 3.32. ^{13}C NMR spectrum of compound 3.4d in DMSO-d_6……..187

Figure 3.33. ^{1}H NMR spectrum of compound 3.5a in $CDCl_3$…….188

Figure 3.34. ^{13}C NMR spectrum of compound 3.5a in $CDCl_3$……188

Figure 3.35. Mass spectrum of compound of compound 3.4c…….189

Figure 3.36. Mass spectrum of compound of compound 3.4c…….189

Figure 3.37. Mass spectrum of compound of compound 3.4c…….190

Figure 3.38. Mass spectrum of compound of compound 3.4d…….190

Figure 3.39. Mass spectrum of compound of compound 3.5a…….191

Figure 3.40. Mass spectrum of compound of compound 3.5b…….191

Figure 3.41. Mass spectrum of compound of compound 3.5c…….192

Figure 3.42. Mass spectrum of compound of compound 3.5d…….192

Figure 4.1. Normalized UV/vis/NIR absorption spectra (THF) of complexes 4.1a – 4.1d (blue solid line), as well as the absorption spectra (THF) of bis(diradicaloid) complexes 4.2a – 4.2d (red solid line)…….……...……..206

Figure 4.2. Cyclic voltammogram and differential pulse voltammogram of (a) Co(II) complex 4.2a, (b) Ni(II) complex 4.2b, (c) Cu(II) complex 4.2c, (d) Zn(II) complex 4.2d in DCM / 0.1 M TBAP as supporting electrolyte; scan rate of 50 mV/s for CV……...….210

Figure 4.3. UV-vis-NIR absorption spectroscopic changes of 4.1a to 4.2a (a), 4.1b to 4.2b (b), 4.1d to 4.2d THF/0.3 M (NBu_4)[PF_6]) at room temperature upon oxidation….....….210

Figure 4.4. UV/vis/NIR absorption spectral changes during deprotonation and dehydrogenation of (a) Co(II) 4.1a, (b) Ni(II) 4.1b, (c) Cu(II) 4.1c, and (d) Zn(II) 4.1d in THF upon titration with TBAF (NBu_4)[F] solution…….....……..212

Figure 4.5. UV-vis-NIR absorption spectroscopic changes of $[4.4a]^{4-}$ to $[4.3a]^{2-\cdot}$ (a), $[4.3a]^{2-\cdot}$ to 4.2a (b), $[4.4b]^{4-}$ to $[4.3b]^{2-\cdot}$ (c), $[4.3b]^{2-\cdot}$ to 4.2b (d), $[4.4d]^{4-}$ to $[4.3d]^{2-\cdot}$ (e), and $[4.4d]^{2-\cdot}$ to 4.2d (f), $[4.4c]^{2-\cdot}$ to 4.2c (g). THF/0.3 M ((NBu_4)[PF_6]), room temperature, upon electrochemical oxidation in a spectroelectrochemical setup. Arrows indicate spectroscopic changes with increasing positive potential……...…213

Figure 4.6. Variable Temperature EPR spectra of complex 4.1a in solid state……...…214

Figure 4.7. VT EPR spectra of complex 4.2b in solid state. (b) IT versus temperature plot of complex 4.2b in solid state…….…..215

Figure 4.8. $\chi_M T$ versus temperature plot of complex 4.2c at 1000 Oe……...….216

Figure 4.9. (a) Variable temperature EPR of complex 4.1c in solid state at X-band. (b) Variable temperature EPR of complex 4.1c in THF at X-band……...…...217
Figure 4.10. Variable temperature EPR of complex 4.2c in solid state at X-band. (b) Variable temperature EPR of complex 4.2c in THF at X-band……...…...217
Figure 4.11. (a) $\chi_M T$ versus temperature plot of complex 4.2d at 1000 Oe (b) $\chi_M T$ versus temperature plot of complex 4.2d at 1 Tesla…….……...219
Figure 4.12. (a) Variable Temperature EPR spectra of complex 4.2d in solid state, (b) Bleany-Bowers fitting of IT vs Temperature curve of VT EPR of 4.2d in solid state…….…219
Figure 4.13. Molecular structure of 4.1b (left) and 4.1d (right). Thermal ellipsoids are drawn to 50% probability level. Hydrogen atoms except O-H groups are omitted for clarity…….……..221
Figure 4.14. (a) dihedral angle between the two ligands in complex 4.1b, and (b) dihedral angle between the two ligands in complex 4.1d (c) intramolecular π–π stacking distances in 4.1b. (d) intramolecular π–π stacking distances in 4.1b…….....222
Figure 4.15. Electron and hole mobilities in diodes using the SCLC method…….……224
Figure 4.16. Electron mobility of (a) complex 4.2a, (b) complex 4.2c, (c) complex 4.2b, and (d) complex 4.2d: (left) plot of the double logarithm relationship between J and absolute V. The data highlighted in yellow shows the SCLC region which fits to the Mott-Gurney law. (right) $J^{1/2}$ characteristics shown versus V for electron mobility……..225
Figure 4.17. Hole mobility of (a) complex 4.2a, (b) complex 4.2c, (c) complex 4.2b, and (d) complex 4.2d: (left) plot of the double logarithm relationship between J and absolute V. The data highlighted in yellow shows the SCLC region which fits to the Mott-Gurney law. (right) $J^{1/2}$ characteristics shown versus V for electron mobility…….…….226

Figure 4.18. Calculated energy levels and HOMO-LUMO energy gaps of complexes 4.1a – 4.1d……...……228

Figure 4.19. Calculated percentage contribution (α-spin only) of different segments of complexes 4.1a (Co), 4.1b (Ni), 4.1c (Cu), and 4.1d (Zn)……..……..…..229

Figure 4.20. Calculated percentage contribution (β-spin only) of different segments of complexes 4.1a (Co), 4.1b (Ni), 4.1c (Cu)…….…….……...230

Figure 4.21. Experimental versus TDDFT-predicted (TPSSH exchange-correlation functional) UV-vis spectra of 4.1d…….……...…….232

Figure 4.22. ^{1}H NMR of compound 4.1a in THF-d_8…….....261

Figure 4.23. ^{1}H NMR of compound 4.1b in THF-d_8…….……..…….....261

Figure 4.24. ^{1}H NMR of compound 4.1d in THF-d_8…….……..…….....262

Figure 4.25. ^{13}C NMR of compound 4.1d in THF-d_8…….....262

Figure 4.26. ^{1}H NMR of compound 4.2b in $CDCl_3$……..….....263

Figure 4.27. ^{13}C NMR of compound 4.2b in $CDCl_3$…….....263

Figure 4.28. ^{1}H NMR of compound 4.2d in $CDCl_3$…….....264

Figure 4.29. ^{13}C NMR of compound 4.2d in $CDCl_3$…….……..…….....264

Figure 4.30. Mass spectrum of complex 4.1a (MALDI)…….……265

Figure 4.31. Mass spectrum of complex 4.1b (MALDI)…….……266

Figure 4.32. Mass spectrum of complex 4.1c (ESI)…….……..…….....267

Figure 4.33. Mass spectrum of complex 4.1d (MALDI)…….……268

Figure 4.34. Mass spectrum of complex 4.2a (MALDI)…….……269

Figure 4.35. Mass spectrum of complex 4.2b (MALDI)…….……270

Figure 4.36. Mass spectrum of complex 4.2c (ESI)…….....271

Figure 4.37. Mass spectrum of complex 4.2d (MALDI)…….……272

Figure 5.1. Representative examples of BODIPYs and aza-BODIPYs related to this work..…277

Figure 5.2. Normalized UV-Vis-NIR absorption (black) and emission (blue) spectra of BODIPY 5.7, and absorption spectrum (red) of BODIPY 5.8 in DCM…….….280

Figure 5.3. Changes in the UV-Vis-NIR absorption spectra of BODIPY 5.8 in the methanol/DCM system resulting in formation of dimer 5.9 at room temperature (right)……...280

Figure 5.4. Cyclic voltammogram of BODIPY 5.2 (blue curve, left) and BODIPY 5.3 (red curve, right) in DCM/0.1M TBAP system……...….282

Figure 5.5. UV-vis-NIR spectral changes observed for BODIPY 5.2 in DCM upon titration with TBAF solution to form dianion $[5.5]^{2-}$…….283

Figure 5.6. UV-vis-NIR spectral changes observed upon gradual oxidation of the $[5.5]^{2-}$ to $[5.4]^{-\cdot}$ (left) and $[5.4]^{-\cdot}$ to 5.3 (right) the spectroelectrochemical experiment in DCM/0.3 M TBAP system……...……...285

Figure 5.7. IVCT region band deconvolution analysis of mixed valent radical anion $[5.4]^{-\cdot}$…….……285

Figure 5.8. Variable temperature ^{1}H NMR spectra of styryl and aromatic region for BODIPY 5.8 (500 MHz, DCM-d_2)…….……...…...….287

Figure 5.9. X-ray crystallographic structure of BODIPY 5.3 (left), BODIPY 5.6 (center), and side view of BODIPY 5.6 (right) excluding distal phenyl groups. All hydrogen atoms except phenolic hydrogens are omitted for clarity……..……....288

Figure 5.10. (a) Spin density distribution of open-shell singlet state 5.3(OS) and open-shell triplet state 8(TS). Blue and green surfaces indicate α and β spin densities. (b) Highest occupied and lowest unoccupied molecular orbitals of BODIPY 5.3 in closed-shell singlet state 5.3(CS). (c) broken symmetry orbitals α-HOMO and α-LUMO of BODIPY 8 in open-shell singlet state 8(OS). (c) α-HOMO and α-LUMO of BODIPY 5.3 in open-shell triplet state 5.3(TS)…….....292

Figure 5.11. Calculated energy levels and HOMO-LUMO energy gaps of 5.2, $[5.5]^{2-}$, $[5.4]^{-\cdot}$, 5.3(CS), 5.3(OS), and 5.3(TS)……..…...294

Figure 5.12. (a) Experimental versus TDDFT-predicted (TPSSH exchange-correlation functional) UV-vis spectra of 5.2, $[5.5]^{2-}$, $[5.4]^{-\cdot}$, 5.3(CS), 5.3(OS), and 5.3(TS)……..….294

Figure 5.13. DFT-predicted percentage compositions of frontier orbitals for 5.2, $[5.5]^{2-}$, $[5.4]^{-\cdot}$……..…….……...……296

Figure 5.14. DFT-predicted percentage compositions of frontier orbitals for 5.3(CS), 5.3(OS), 5.3(TS)…….……...…….298

Figure 5.15. ^{1}H NMR of BODIPY 5.7 in $CDCl_3$ at 298 K……..322

Figure 5.16. ^{13}C NMR of BODIPY 5.7 in $CDCl_3$ at 298 K…….322

Figure 5.17. ^{1}H NMR of BODIPY 5.8 in $CDCl_3$ at 220 K……..323

Figure 5.18. ^{13}C NMR of BODIPY 5.8 in $CDCl_3$ at 298 K…….323

Figure 5.19. ^{1}H NMR of BODIPY 5.9 in CD_2Cl_2 at 220 K…….324

Figure 5.20. Mass spectrum of BODIPY 5.7 (ESI)…….324

Figure 5.21. Mass spectrum of BODIPY 5.8 (ESI)…….325

Figure 5.22. Mass spectrum of BODIPY 5.9 (ESI)…….325

LIST OF SCHEMES

Scheme 1.1. Chemical structures of oligo-*para*-phenyl quinones (1), and a boron dipyrromethene (BODIPY)-bridged bisphenoxyl diradicaloid (2) in closed-shell quinoidal and open-shell diradical resonance forms……..……16

Scheme 2.1. Synthesis of diradicaloids 2.9 and 2.10. Reagents and conditions: (i) HCl(g), EtOH; (ii) CH_3NO_2, DBU; (iii) NH_4OAc, BuOH; (iv) BF_3*Et_2O, DIPEA; and (v) PbO. ……..46

Scheme 3.1. The synthesis of compounds 3.4a - 3.4d and 3.5a - 3.5d……130

Scheme 3.2. Formation of dianions $[3.7a]^{2-}$ - $[3.7a]^{2-}$ and mixed-valence radical anion $[3.6a]^{-\cdot}$ - $[3.6a]^{-\cdot}$, and diradicals 3.5a - 3.5d……..…..137

Scheme 4.1. Synthetic scheme yielding homoleptic complexes 4.1a - 4.1d and 4.2a - 4.2d…...204

Scheme 4.2. Formation of tetraanions $[4.4a - 4.4d]^{4-}$, mixed valence radical anion $[4.3a - 4.3d]^{2-\cdot}$, and bis(diradicaloids) 4.2a - 4.2d…….....212

Scheme 5.1. Synthetic pathways to BODIPY 5.3. Reagents and conditions: (i) acetic acid, piperidine, toluene, reflux 48 hours (ii) DDQ, DCM, RT, 15 min……..278

Scheme 5.2. Formation of dianion $[5.5]^{2-}$ and mixed-valent radical-anion $[5.4]^{-\cdot}$ from benzoquinonemethide BODIPY 5.3……282

Scheme 5.3. Synthetic pathways to dimer 5.6. Reagents and conditions: (i) DCM-MeOH, RT, 24 h; (ii) Zn, HOAc, RT, 5 min……289

LIST OF ABBREVIATIONS

DCM – dichloromethane

DMF – dimethylformamide

Aza-BODIPY – aza-boron-dipyrromethene

BODIPY – boron-dipyrromethene

NIR – near infrared

CV – cyclic voltammetry

DPV – differential pulse voltammetry

HRMS – high resolution mass spectrometry

MALDI – matrix-assisted laser desorption/ionization

ESI – electrospray ionization

TBAP – tetrabutylammonium perchlorate

TBAF – tetrabutylammonium fluoride

$TFAPF_6$ – tetrabutylammonium-hexafluorophosphate

NMR – nuclear magnetic resonance

EPR – Electron paramagnetic resonance

SQUID – superconductor quantum interference device

SCLC – space charge limited current

UV-Vis – ultraviolet-visible

IVCT – intervalence charge transfer

DFT – density functional theory

TDDFT – time dependent density functional theory

NPA – Natural Population Analysis

MO – molecular orbital

HOMO – highest occupied molecular orbital

LUMO – lowest unoccupied molecular orbital

MLCT – metal to ligand charge transfer

DIPEA – diisopropylethylamine

DBU – 1,8-diazabicyclo[5.4.0]undec-7-ene

CHAPTER I: INTRODUCTION

1.1 Open-Shell Organic Molecules

Open-shell organic compounds occupy a unique position at the intersection of physical organic chemistry, materials science, and molecular electronics.[1–4] They are characterized by the presence of one or more unpaired electron(s).[5–8] Among these species, biradical and diradical molecules containing two unpaired electrons distributed over distinct or partially overlapping molecular orbitals have attracted sustained attention due to their unusual electronic structures and the diverse properties that emerge from spin–spin interactions.[9–16] Unlike conventional closed-shell molecules, diradicals and biradicals can access multiple spin states, typically singlet and triplet, whose relative energies are exquisitely sensitive to molecular structure, conjugation, and the surrounding environment.[12,17–19] This sensitivity offers both challenges and opportunities: while the inherent reactivity of open-shell systems complicates their kinetic and thermodynamic stabilization,[1,20–22] controlled access to diradical character enables the rational design of molecules with tailored magnetic, optical, and electronic functionalities.[21,23–25]

1.2 Diradicals

In the simplest description, a diradical is defined as a molecular system possessing two electrons occupying nearly degenerate frontier molecular orbitals.[26–28] Depending on the extent of orbital overlap and electron-electron exchange interactions,[26,29] these two electrons may couple to give either a singlet (antiparallel spins) or a triplet (parallel spins) electronic state.[11,26] When the singlet and triplet states are well separated in energy, the molecule can often be described as a classical diradical.[26,29,30] Electron paramagnetic resonance is one of the most important

spectroscopic techniques used to understand magnetic ground state of diradical molecules.[26] A diradical with a triplet ground state will show three resonance absorption peaks in rigid solid state, two of which are spin-allowed ($\Delta m_s = +1$), while the one with lowest energy is spin disallowed ($\Delta m_s = +2$) as shown in Figure 1.1.[26]

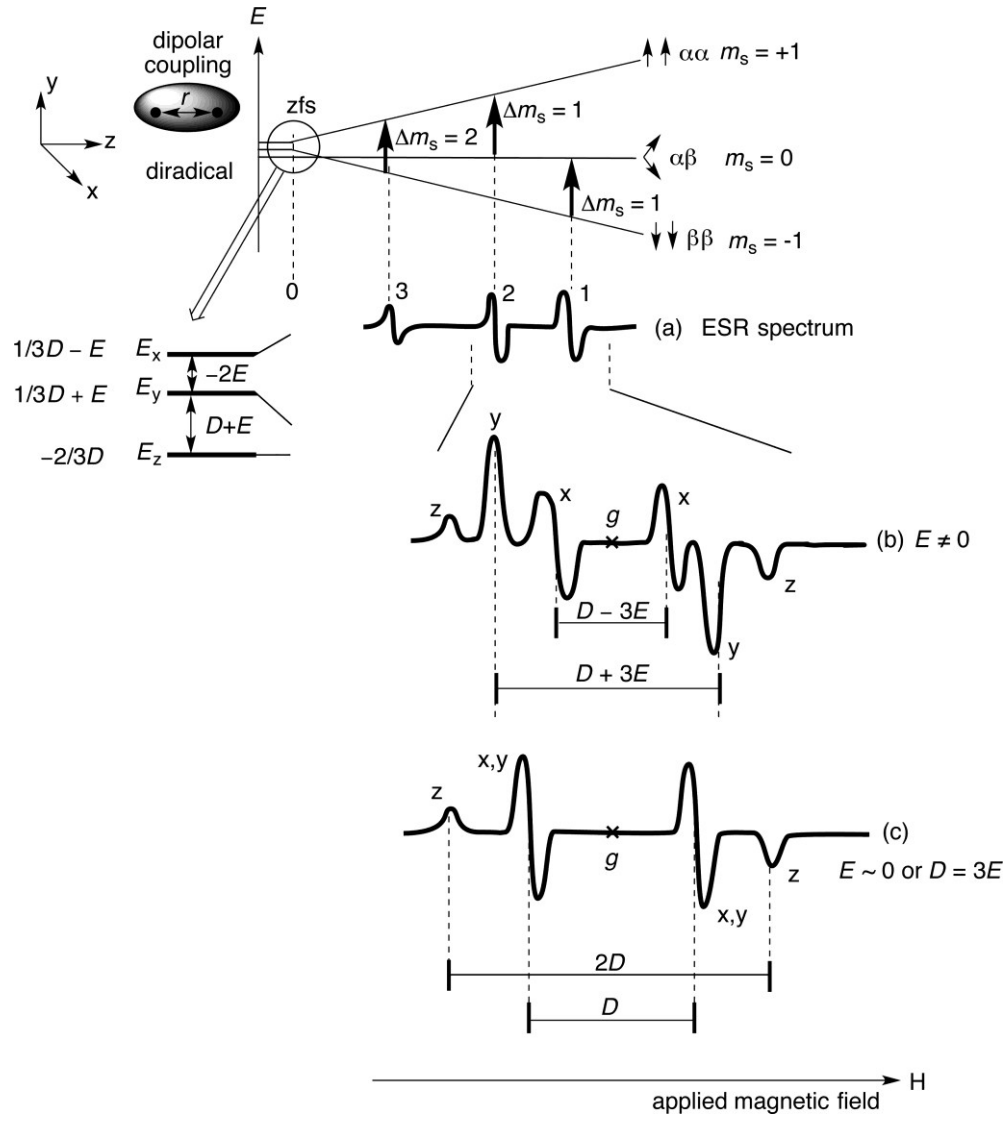


Figure 1.1: Zeeman's splitting of electrons in triplet diradicals in the solid state.[26]

However, many experimentally accessible systems fall into the broader category of diradicaloid,[31] in which closed-shell and open-shell resonance structures coexist and contribute simultaneously to the ground-state electronic structure.[17,27,32,33] The degree of open-shell character in such systems is commonly quantified by the diradical character parameter (y_0),[27,31,34] which provides a continuum description between purely closed-shell ($y_0 \approx 0$) and ideal diradical ($y_0 \approx 1$) limits.[31] The balance between closed-shell and open-shell contributions is governed by several interrelated factors, including the extent of π-conjugation,[33,35,36] aromatic stabilization or quinoidal distortion,[35,37] substituent effects,[38] and the spatial distribution of frontier molecular orbitals.[31,39] As a result, diradical behavior cannot be predicted solely from simple structural motifs but instead requires a combined experimental and theoretical approach.[18,27,40,41] Experimental and theoretical techniques such as variable-temperature NMR spectroscopy,[42,43] electron paramagnetic resonance (EPR),[44,45] SQUID magnetometry,[46] and modern quantum chemical calculations[18,27,31,41] have therefore become indispensable tools for probing diradical systems and quantifying diradical character.[31]

1.2.1 Diradicaloids

In many π-conjugated systems of practical interest, the electronic structure cannot be adequately described as either purely closed-shell or purely open-shell.[17,27] Historically, the conceptual foundations of diradical and diradicaloid chemistry can be traced back to Thiele's quinoidal hydrocarbons at the beginning of the 20th century,[47] followed by Chichibabin's hydrocarbon,[48] which provided one of the earliest experimentally accessible examples of a molecule exhibiting equilibrium between closed-

shell and open-shell electronic structures.[18,31,47–52] These pioneering systems laid the groundwork for modern diradicaloid chemistry, in which advances in molecular design, spectroscopy, and quantum chemical methods have enabled the stabilization and systematic study of molecules with well-defined and tunable diradical character.[18,33,49,50,52,53] Diradicaloids typically possess two frontier molecular orbitals that are nearly degenerate in energy, leading to partial occupation of both orbitals and significant static electron correlation.[27,30,54–56]

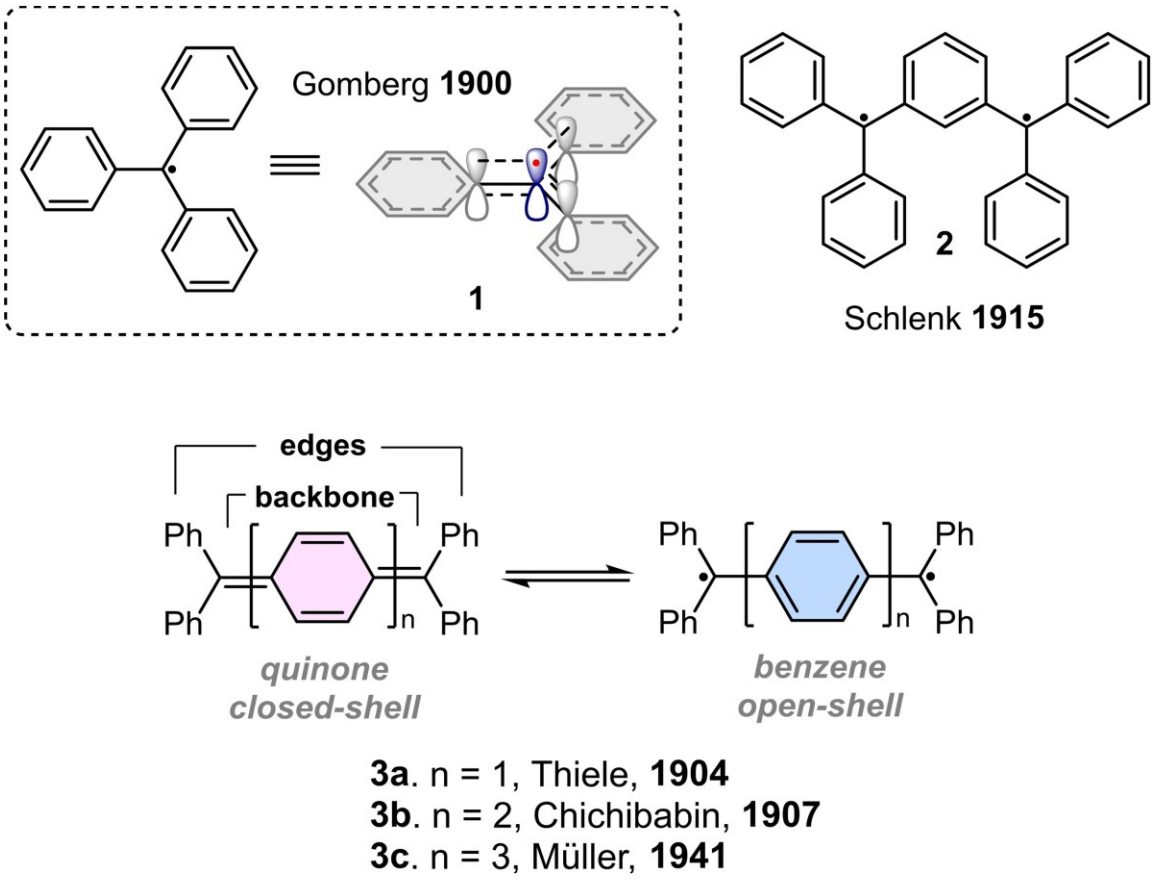


Figure 1.2: Chemical structures of Gomberg radical, Schlenk diradical, Thiele, Chichibabin, and Müller diradical(oids).[5]

From a chemical perspective, diradicaloids can be viewed as molecules with weakened or partially broken π-bonds,[11] often arising from quinoidal distortion,[35] extension of π-conjugation,[11,57] or incorporation of heteroatoms that perturb aromatic stabilization.[11,27] From a physical perspective, they correspond to systems in an intermediate electron-correlation regime, lying between weakly correlated closed-shell molecules and strongly correlated pure diradicals.[11,17,27] As a result, diradicaloids frequently exhibit open-shell singlet ground states with thermally accessible triplet excited states,[58–60] giving rise to temperature-dependent magnetic and spectroscopic behavior.[52,61–64] The concept of diradicaloids is particularly valuable because it provides a quantitative framework for correlating molecular structure with observable properties such as singlet–triplet energy gaps,[29] magnetic susceptibility,[65] optical absorption, and nonlinear optical response.[66–69] Many stable organic and organometallic systems reported in recent years including extended quinodimethanes,[14,70] quinoidal oligomers,[20,71–74] nanographenes,[75,76] macrocycles like porphyrins,[77,78] BODIPYs[79,80] and heteroatom-centered radical systems[6] are best understood within this diradicaloid paradigm.[46,62,81–86] The extent of open-shell character in a diradicaloid is commonly quantified by the diradical character parameter, y (or y_0), which varies continuously between 0 and 1.[68] A value of $y = 0$ corresponds to an ideal closed-shell system, whereas $y = 1$ represents a pure diradical molecule.[27] Intermediate values ($0 < y < 1$) indicate partial diradical character and define the diradicaloid regime.[75,76,87–91] Within a natural orbital framework, the diradical character can be expressed in terms of the occupation numbers of the

frontier natural orbitals as described by Yamaguchi equation.[93] For singlet diradicaloids described by a two-electron–two-orbital model, y_0 is commonly defined as:

$$y_0 = 1 - \frac{2T_0}{1 + T_0^2}$$

$$T_0 = \frac{n_{HONO} - n_{LUNO}}{2}$$

where n_{LUNO} is the occupation number of the lowest unoccupied natural orbital (LUNO) and n_{HONO} is the occupation number of the highest occupied natural orbital.[93] In this formulation, an ideal closed-shell system has $n_{HONO} = 2$ and $n_{LUNO} = 0$, yielding $y_0 = 0$, whereas a classical diradical has $n_{HONO} = n_{LUNO} = 1$, giving $y_0 = 1$. These definitions provide a chemically intuitive measure of bond weakening and electron correlation, directly linking molecular electronic structure to experimentally accessible observables.[11,27,75,76,88,91]

Because experimental determination of natural orbital occupations is not straightforward, diradical character is typically estimated using high-level quantum chemical methods such as unrestricted hartree fork,[93,94] multireference approaches,[95] broken-symmetry density functional theory,[96] or spin-flip methodologies.[97] When combined with experimental probes including variable-temperature ^{1}H NMR, EPR spectroscopy, SQUID magnetometry, and optical spectroscopy, the diradical character parameter serves as a powerful descriptor for understanding and predicting the behavior of diradicaloid systems.[9,11,27,54,89,98]

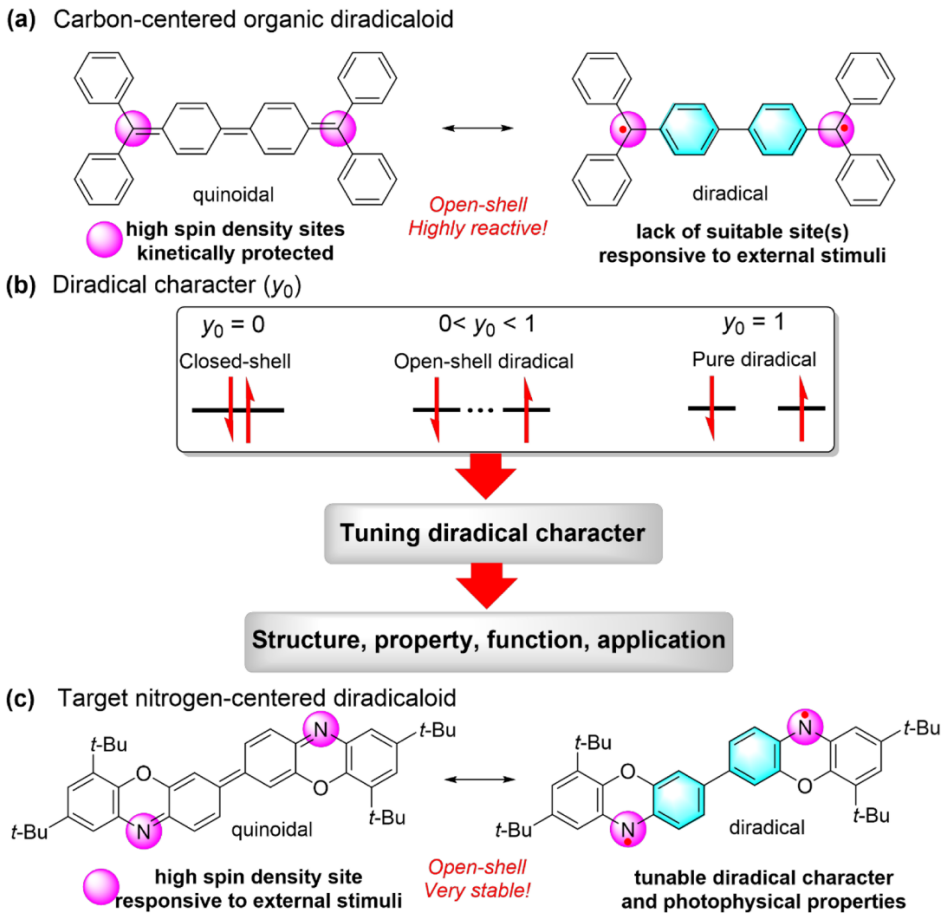


Figure 1.3: (a) Classical carbon-centered organic diradicaloid of Chichibabin's hydrocarbon and its two characteristic resonance structures. (b) Diradical character (y_0) of organic diradicaloids. (c) Target nitrogen-centered diradicaloid.[6]

1.2.3 Classification of Diradicaloids

Diradical(oids) can be broadly classified based on their electronic structure and bonding topology.[26] Non-Kekulé diradical(oids) lack a classical closed-shell resonance structure and inherently possess unpaired electrons,[99,100] as exemplified by systems such as m-xylylene[59] and certain triangulene derivatives.[60,101] These species typically exhibit pronounced open-shell character but are often highly reactive and difficult to isolate under ambient conditions.[59,60,99,101–105] In contrast, Kekulé diradicals can be represented

by both closed-shell and open-shell resonance forms.[100,106,107] Quinodimethane and quinoidal frameworks fall into this category, where the competition between aromatic stabilization and bond-length alternation plays a central role in determining the ground-state spin configuration.[60,100] Within this class, substituent effects, heteroatom incorporation, and extension of π-conjugation have been widely exploited to modulate singlet-triplet gaps ($\Delta E_{S\text{-}T}$) and enhance kinetic stability.[100,106–109] Another important distinction arises from the nature of the radical centers themselves. Carbon-centered diradicals have historically dominated the field, but their limited stability has motivated growing interest in heteroatom-centered diradicals, particularly those based on oxygen and nitrogen.[11,110] Oxygen-centered phenoxyl and quinone-type radicals, for example, benefit from effective spin delocalization and resonance stabilization,[111] allowing access to persistent diradical and diradicaloid species that can be studied under laboratory conditions.[12,72,74,111]

1.3 Biradicals versus Diradicals

The terms biradical and diradical are often used interchangeably in the literature; however, they originate from subtly different conceptual frameworks and convey distinct physical meanings.[22] According to the IUPAC definition, a biradical refers to a molecular species containing two unpaired electrons that act independently or nearly independently of each other, with negligible electron-electron exchange interaction between the two radical centers.[112] In such systems, the two spins behave essentially as isolated doublet radicals within the same molecular framework, typically due to large spatial separation or minimal orbital overlap.[22,112,113]

In contrast, the term diradical is used when the two unpaired electrons interact sufficiently to give rise to well-defined singlet (S = 0) and triplet (S = 1) spin states separated by an exchange coupling constant (J).[22,26,31] In diradicals, the interaction between the two radical centers can either be through space, bond, or both leading to measurable singlet-triplet energy gaps and characteristic magnetic and spectroscopic signatures.[22,26,27]

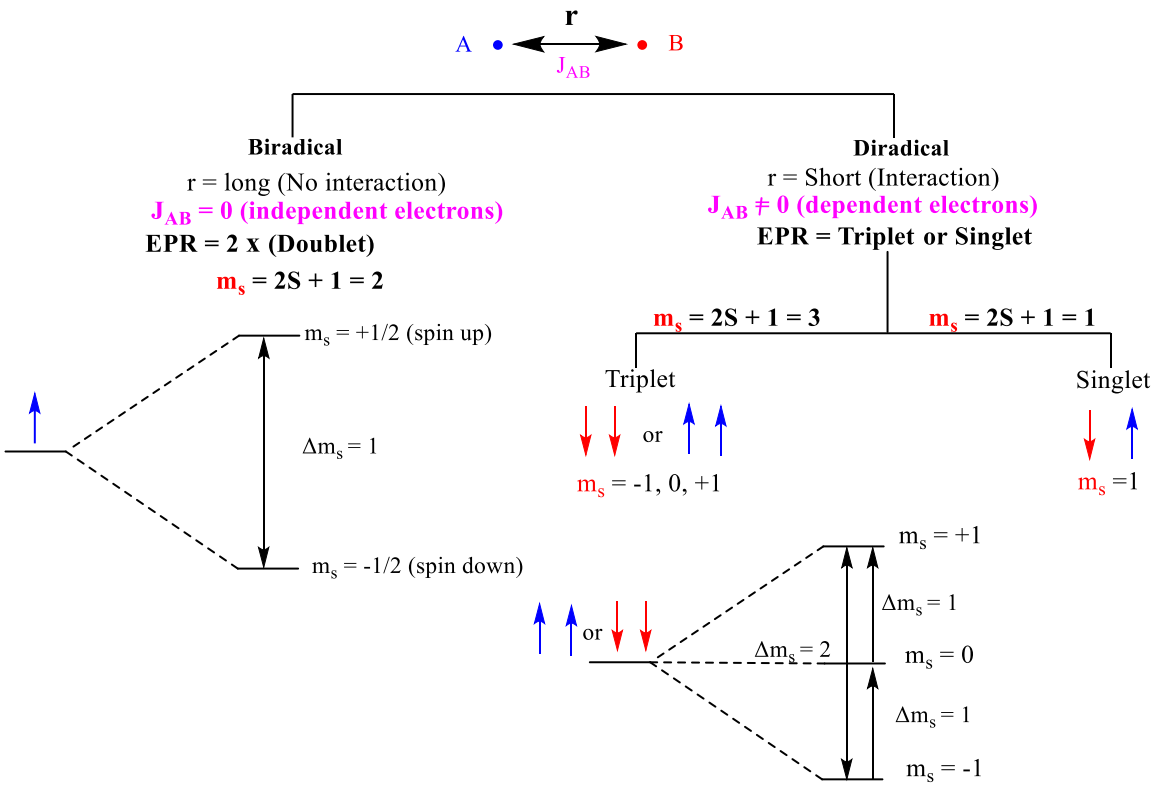


Figure 1.4: Schematic description of electron coupling in biradical versus diradical with Zeeman's splitting of electrons in applied magnetic field.

As a result, diradicals can exhibit either singlet or triplet ground states depending on the magnitude and sign of the exchange interaction.[26,29]

From an experimental standpoint, this distinction is significant. Biradicals often behave as two weakly coupled radicals and typically display EPR spectra resembling those of independent monoradicals,[22,29,113] whereas diradicals may be EPR silent in their singlet ground state and show temperature-dependent paramagnetism arising from thermal population of the triplet excited state.[27,114] Thus, the presence or absence of observable spin-spin coupling provides a practical criterion for differentiating between biradical and diradical behavior.[15,16,26,27]

Importantly, many π-conjugated systems discussed in modern materials chemistry including quinoidal hydrocarbons,[71] extended acenes,[14] iminiums,[115] diketopyrrolopyrroles,[15] and heteroatom-stabilized open-shell molecules do not fit neatly into the idealized biradical or diradical limits. Instead, they occupy an intermediate regime best described as diradicaloids,[27] where partial spin coupling and significant configuration mixing lead to open-shell singlet ground states with tunable diradical character.[22,27] In this context, biradicals and diradicals represent limiting cases within a broader continuum of two-electron open-shell electronic structures.

1.4 Bis(diradicals) and Tetraradicals

Beyond simple diradicals, molecular architectures containing multiple radical centers offer access to even richer electronic landscapes.[116–118] Bis(diradicals) and tetraradicals comprise four unpaired electrons that may interact cooperatively or independently depending on their spatial arrangement and electronic communication pathways.[11] Most of the reported tetraradical(oids) are formed by connecting two diradicaloids, hence terms like bis(diradicaloid) and dis-tetraradical.[11] These multiradical

systems are particularly intriguing because they can support multiple low-lying spin states, leading to complex magnetic behavior and enhanced spin multiplicity.[11,116–119] The design of bis(diradicals) and tetraradicals requires careful control over intramolecular coupling to prevent uncontrolled reactivity while preserving open-shell character.[11] Strategies such as rigid π-conjugated backbones, incorporation of quinoidal motifs, and the use of sterically demanding substituents have proven effective in stabilizing these systems.[1,120] When successful, multiradical compounds provide valuable platforms for exploring fundamental questions in spin coupling, as well as for developing advanced functional materials.[1,53,116–124]

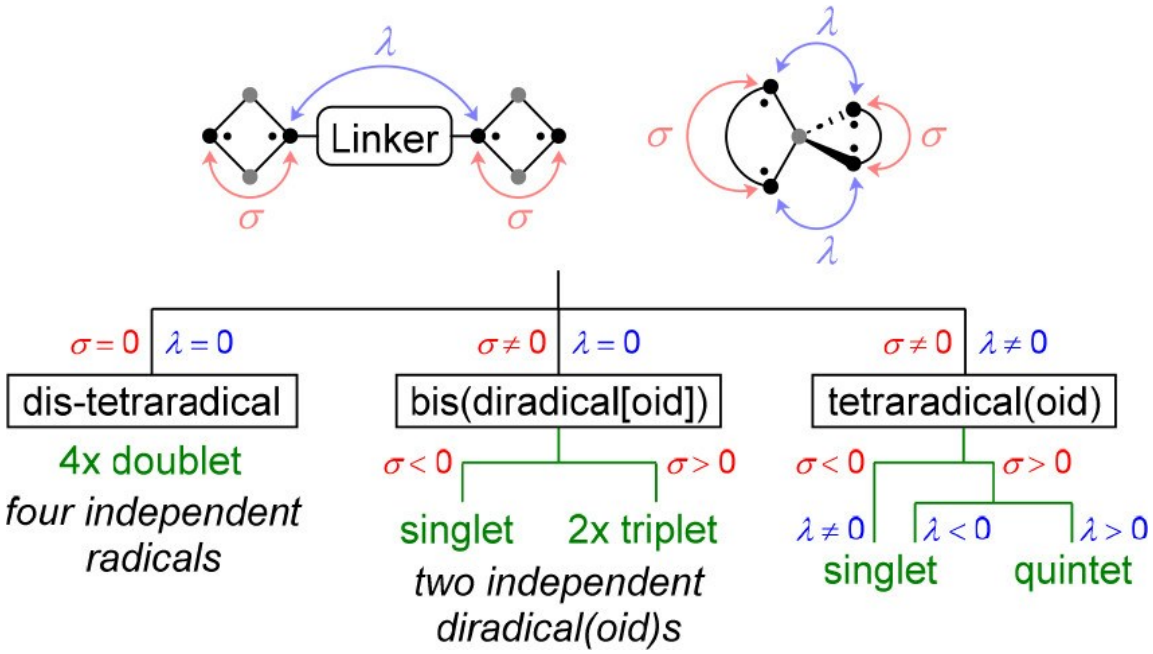


Figure 1.5: Possible forms of tetraradical created by connection of two diradicals (σ = short-range coupling, λ = long-range coupling; $|\sigma| \geq |\lambda|$).[11]

1.5 Applications of Diradicals

The unique electronic structures of diradicals and diradicaloids underpin a wide range of emerging applications.[1] In the field of molecular magnetism and spintronics,[7] weakly coupled spins and thermally accessible triplet states make diradicals attractive candidates for spin-based information storage and processing.[7,17,18,63,125,126] Similarly, the narrow energy gaps and strong near-infrared absorption often associated with diradical character are advantageous for optoelectronic devices,[7] including organic semiconductors,[127] photodetectors,[128] molecular qubit,[129] and non-linear optical materials.[7,42,63,76,125,128–132]

Diradicals have also gained attention in organic electronics due to their ability to facilitate charge transport without the need for external dopants.[20,21] The presence of partially occupied frontier orbitals can enhance carrier mobility and enable ambipolar or unusual charge-transport behavior.[133,134] In addition, redox-active diradical systems are increasingly explored in energy-related applications such as batteries[135] and thermoelectric materials,[21] where multielectron redox processes and spin effects can be leveraged for improved performance.[20,21,24,25,136]

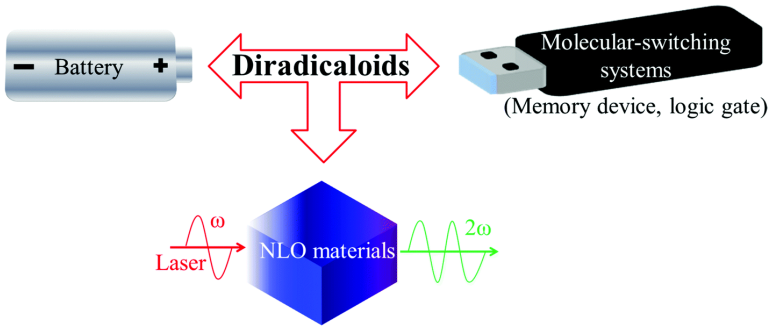


Figure 1.6: Schematic illustration of the electronic applications of organic diradicaloids.[62]

1.6 Previous Work on BODIPY-Based Diradicals and Diradicaloids

Boron dipyrromethene (BODIPY) dyes have attracted significant attention as promising platforms for the development of stable organic diradicaloids because of their strong electron-withdrawing BF_2 unit, excellent photostability, and tunable optical and electronic properties.[80,137–141] Conventional BODIPY chromophores generally absorb in the visible to short near-infrared (NIR) region;[79,80,141–143] however, incorporation of diradical character into the BODIPY framework has emerged as an effective strategy for reducing the HOMO–LUMO energy gap and extending absorption into the deep NIR region.[69,79,80,138,141]

A pioneering contribution in this area was reported by Ni and co-workers in 2016 through the synthesis of para- and meta-quinodimethane-bridged BODIPY dimers, BD-1 and BD-2.[69] These systems were designed by connecting two BODIPY units through para-quinodimethane (p-QDM) and meta-quinodimethane (m-QDM) bridges, thereby introducing moderate diradical character into the conjugated framework. Structural and computational studies revealed that BD-1 and BD-2 possessed diradical character values of 6.9% and 26.2%, respectively, with BD-2 exhibiting greater open-shell contribution due to the m-QDM bridge.[69] Both compounds showed excellent ambient stability despite their open-shell nature. Importantly, these diradicaloids displayed exceptionally intense NIR absorption bands at 1088 nm for BD-1 and 1136 nm for BD-2, together with very high molar extinction coefficients and large two-photon absorption (TPA) cross-sections. The increased diradical character in BD-2 resulted in a more red-shifted absorption, larger TPA response, shorter excited-state lifetime, and lower fluorescence quantum

yield.[69] Femtosecond transient absorption measurements further demonstrated ultrafast excited-state decay arising from rapid non-radiative relaxation associated with the small singlet–triplet energy gap. In addition, both compounds exhibited selective fluorescence turn-on responses toward hydroxyl radicals, demonstrating the potential application of BODIPY diradicaloids as responsive NIR materials.[69]

Subsequent work by Miao, Phan, and Wu in 2019 expanded the chemistry of BODIPY-based diradicaloids through the synthesis of a BODIPY-bridged bisphenoxyl diradicaloid containing two 2,6-di-tert-butylphenoxyl substituents attached directly to the α-positions of the BODIPY core.[79]

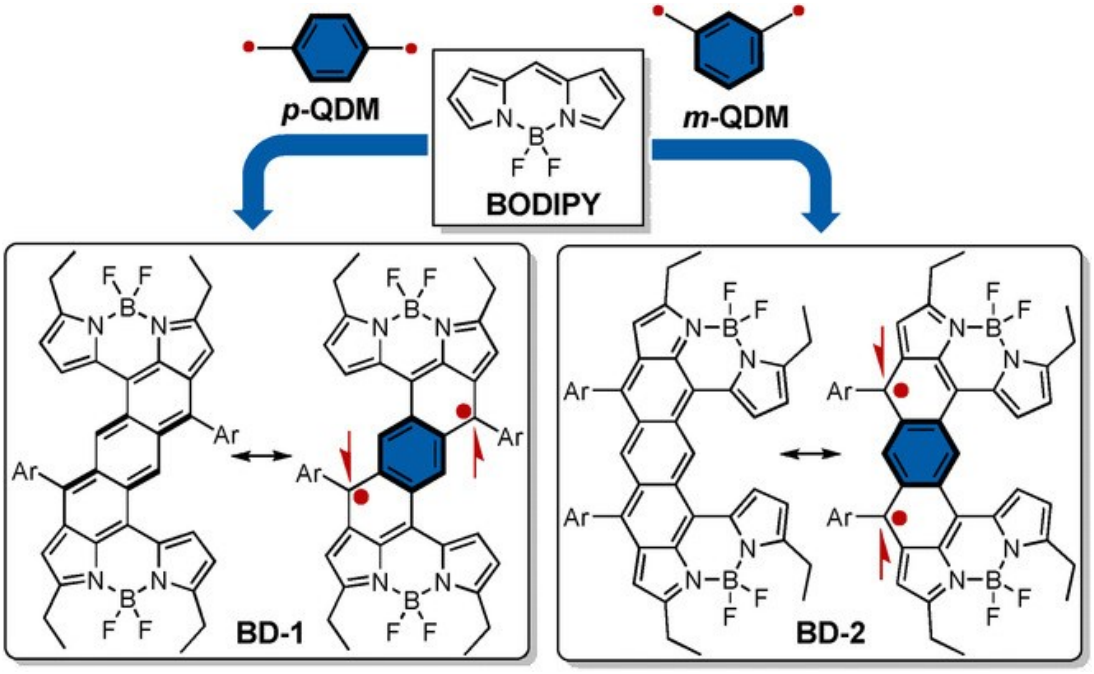
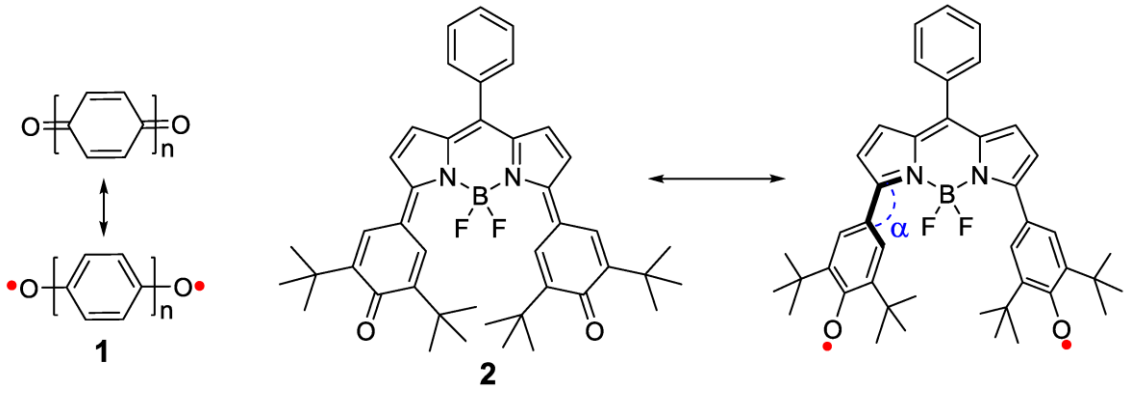


Figure 1.7: The structures of *p*-QDM, *m*-QDM, and their bridged BODIPY dimers **BD-1** and **BD-2**. Ar = 4-*tert*-butylphenyl.[69]

Unlike the quinodimethane-bridged systems, this molecule exhibited remarkable solvent-dependent diradical character. In non-polar solvents such as benzene and dichloromethane, the compound behaved predominantly as a closed-shell diamagnetic species, whereas in highly polar solvents such as DMF, broad ^{1}H NMR resonances and clear ESR signals indicated significant open-shell diradical character. Variable-temperature ESR analysis revealed a thermally accessible triplet state with a singlet–triplet energy gap of −6.40 kcal mol^{-1}.[79] Computational studies suggested that this unusual solvent dependence originated from conformational flexibility, where increased rotation of the phenoxyl units in polar solvents enhanced the diradical character.[79] The compound also displayed solvent-dependent NIR absorption and electrochemical behavior, further demonstrating the strong relationship between molecular conformation, environment, and open-shell electronic structure.[79]



Scheme 1.1: Chemical structures of oligo-*para*-phenyl quinones (**1**), and a boron dipyrromethene (BODIPY)-bridged bisphenoxyl diradicaloid (**2**) in closed-shell quinoidal and open-shell diradical resonance forms.[79]

These studies established important design principles for BODIPY-based diradicaloids. They demonstrated that moderate diradical character can effectively extend absorption into the NIR region while maintaining molecular stability, and that subtle structural and environmental factors strongly influence the magnetic, optical, and electrochemical properties of these systems. These pioneering investigations laid the foundation for the development of aza-BODIPY diradicaloids and related open-shell group 13 aza-DIPY systems explored in this dissertation.

1.7 Scope of This Dissertation

The work presented in this dissertation focuses on the rational design, synthesis, and comprehensive characterization of stable diradical and multiradical systems based on π-conjugated chromophoric frameworks of aza-BODIPY, aza-ALDIPY, aza-GADIPY, aza-INDIPY and aza-dipyrromethene complexes of group 1 transition metals. Important emphasis is placed on understanding how molecular structure, heteroatom incorporation, and redox activity influence ground state magnetic behavior, diradical character, spin state energetics, and functional photophysical properties of these compounds. By integrating experimental spectroscopy, electrochemistry, magnetometry, and quantum chemical calculations, this study aims to establish clear structure-property relationships that can guide the future development of diradical-based materials for advanced electronic, magnetic, optoelectronic and photovoltaic applications.

References

(1) Chen, Z. X.; Li, Y.; Huang, F. Persistent and Stable Organic Radicals: Design, Synthesis, and Applications. *Chem* **2021**, *7*, 288–332. https://doi.org/10.1016/j.chempr.2020.09.024.

(2) Baldwin, A. C.; Golden, D. M. Reactions of Methyl Radicals of Importance in Combustion Systems. *Chem. Phys. Lett.* **1978**, *55*, 350–352. https://doi.org/10.1016/0009-2614(78)87036-5.

(3) Tan, Y.; Hsu, S.-N.; Tahir, H.; Dou, L.; Savoie, B. M.; Boudouris, B. W. Electronic and Spintronic Open-Shell Macromolecules. *J. Am. Chem. Soc.* **2022**, *144*, 626–647. https://doi.org/10.1021/jacs.1c09815.

(4) Cong, L.; Chahal, M. K.; Osterloh, R.; Sankar, M.; Kadish, K. M. Synthesis, Electrochemistry, and Reversible Interconversion among Perhalogenated Hydroxyphenyl Ni(II) Porphyrins, Porphodimethenes, and Porpho-5,15-Bis-Paraquinone Methide. *Inorg. Chem.* **2019**, *58*, 14361–14376. https://doi.org/10.1021/acs.inorgchem.9b01642.

(5) Dzieszkowski, K.; Pawlicki, M. Open-Shell States in Dynamic Diradicaloids. *Chempluschem* **2025**, *90*, e202500033. https://doi.org/10.1002/cplu.202500033.

(6) Huang, B.; Kang, H.; Zhang, C.-W.; Zhao, X.-L.; Shi, X.; Yang, H.-B. Design of an Open-Shell Nitrogen-Centered Diradicaloid with Tunable Stimuli-Responsive Electronic Properties. *Commun. Chem.* **2022**, *5*, 127. https://doi.org/10.1038/s42004-022-00747-8.

(7) Yeo, H.; Debnath, S.; Krishnan, B. P.; Boudouris, B. W. Radical Polymers in Optoelectronic and Spintronic Applications. *RSC Appl. Polym.* **2024**, *2*, 7–25. https://doi.org/10.1039/D3LP00213F.

(8) Dong, S.; Li, Z. Recent Progress in Open-Shell Organic Conjugated Materials and Their Aggregated States. *J. Mater. Chem. C Mater.* **2022**, *10*, 2431–2449. https://doi.org/10.1039/D1TC04598A.

(9) Dai, D.; Zhan, Q.; Shi, T.; Wang, D.; Zheng, Y. Spin Characteristics in Conjugated Stable Diradicals. *Chem. Commun.* **2024**, *60*, 8997–9006. https://doi.org/10.1039/D4CC03067B.

(10) Mizuno, A.; Matsuoka, R.; Mibu, T.; Kusamoto, T. Luminescent Radicals. *Chem. Rev.* **2024**, *124*, 1034–1121. https://doi.org/10.1021/acs.chemrev.3c00613.

(11) Hinz, A.; Bresien, J.; Breher, F.; Schulz, A. Heteroatom-Based Diradical(Oid)s. *Chem. Rev.* **2023**, *123*, 10468–10526. https://doi.org/10.1021/acs.chemrev.3c00255.

(12) Zhang, H.; Miao, F.; Liu, X.; Wang, D.; Zheng, Y. Recent Advances of Stable Phenoxyl Diradicals. *Chem. Res. Chin. Univ.* **2023**, *39*, 170–175. https://doi.org/10.1007/s40242-023-3012-6.

(13) Ishigaki, Y.; Harimoto, T.; Shimajiri, T.; Suzuki, T. Carbon-Based Biradicals: Structural and Magnetic Switching. *Chem. Rev.* **2023**, *123*, 13952–13965. https://doi.org/10.1021/acs.chemrev.3c00376.

(14) Sun, Z.; Zeng, Z.; Wu, J. Zethrenes, Extended *p* -Quinodimethanes, and Periacenes with a Singlet Biradical Ground State. *Acc. Chem. Res.* **2014**, *47*, 2582–2591. https://doi.org/10.1021/ar5001692.

(15) Rausch, R.; Röhr, M. I. S.; Schmidt, D.; Krummenacher, I.; Braunschweig, H.; Würthner, F. Tuning Phenoxyl-Substituted Diketopyrrolopyrroles from Quinoidal to Biradical Ground States through (Hetero-)Aromatic Linkers. *Chem. Sci.* **2021**, *12*, 793–802. https://doi.org/10.1039/d0sc05475e.

(16) Doehnert, D.; Koutecky, J. Occupation Numbers of Natural Orbitals as a Criterion for Biradical Character. Different Kinds of Biradicals. *J. Am. Chem. Soc.* **1980**, *102*, 1789–1796. https://doi.org/10.1021/ja00526a005.

(17) Kubo, T. Closed-Shell and Open-Shell Dual Nature of Singlet Diradical Compounds. *Pure and Applied Chemistry* **2023**, *95*, 363–375. https://doi.org/10.1515/pac-2023-0114.

(18) Sun, Q.; Brédas, J.-L.; Li, H. Reliable Diradical Characterization via Precise Singlet–Triplet Gap Calculations: Application to Thiele, Chichibabin, and Müller Analogous Diradicals. *J. Chem. Theory Comput.* **2025**, *21*, 1194–1202. https://doi.org/10.1021/acs.jctc.4c01384.

(19) Zhu, Z.; Zhang, D.; Xiao, T.; Fang, Y.; Xiao, X.; Wang, X.; Jiang, S.; Zhao, D. Rational Design of an Air-Stable, High-Spin Diradical with Diazapyrene. *Angew. Chem.* **2023**, *135*, e202314900. https://doi.org/10.1002/ange.202314900.

(20) Yang, K.; Zhang, X.; Harbuzaru, A.; Wang, L.; Wang, Y.; Koh, C.; Guo, H.; Shi, Y.; Chen, J.; Sun, H.; Feng, K.; Ruiz Delgado, M. C.; Woo, H. Y.; Ortiz, R. P.; Guo, X. Stable Organic Diradicals Based on Fused Quinoidal Oligothiophene Imides with High Electrical Conductivity. *J. Am. Chem. Soc.* **2020**, *142*, 4329–4340. https://doi.org/10.1021/jacs.9b12683.

(21) Pal, S. K.; Itkis, M. E.; Tham, F. S.; Reed, R. W.; Oakley, R. T.; Haddon, R. C. Resonating Valence-Bond Ground State in a Phenalenyl-Based Neutral Radical Conductor. *Science.* **2005**, *309*, 281–284. https://doi.org/10.1126/science.1112446.

(22) Betkhoshvili, S.; Poater, J.; Moreira, I. de P. R.; Bofill, J. M. Leap from Diradicals to Tetraradicals by Topological Control of π-Conjugation. *J. Org. Chem.* **2024**, *89*, 14006–14020. https://doi.org/10.1021/acs.joc.4c01375.

(23) Kato, K.; Osuka, A. Platforms for Stable Carbon-Centered Radicals. *Angew. Chem.* **2019**, *131*, 9074–9082. https://doi.org/10.1002/ange.201900307.

(24) Rudebusch, G. E.; Zafra, J. L.; Jorner, K.; Fukuda, K.; Marshall, J. L.; Arrechea-Marcos, I.; Espejo, G. L.; Ponce Ortiz, R.; Gómez-García, C. J.; Zakharov, L. N.; Nakano, M.; Ottosson, H.; Casado, J.; Haley, M. M. Diindeno-Fusion of an Anthracene as a Design Strategy for Stable Organic Biradicals. *Nat. Chem.* **2016**, *8*, 753–759. https://doi.org/10.1038/nchem.2518.

(25) Oyaizu, K.; Nishide, H. Radical Polymers for Organic Electronic Devices: A Radical Departure from Conjugated Polymers? *Advanced Materials* **2009**, *21* (22), 2339–2344. https://doi.org/10.1002/adma.200803554.

(26) Abe, M. Diradicals. *Chem. Rev.* **2013**, *113*, 7011–7088. https://doi.org/10.1021/cr400056a.

(27) Wu, J. *Diradicaloids*; Jenny Stanford Publishing: New York, 2022. https://doi.org/10.1201/9781003277248.

(28) Yamada, S.; Shigemoto, I.; Kawakami, T.; Isobe, H.; Shoji, M.; Miyagawa, K.; Yamaguchi, K. Quantum Mechanical Approaches to Strongly Correlated Electron

Systems: Structure, Bonding, and Properties of Diradicals, Triradicals, and Polyradicals. *Chemistry (Easton).* **2025**, *7*, 38–69. https://doi.org/10.3390/chemistry7020038.

(29) Wang, X.-Q.; Song, C.; Lei, T. Open-Shell Oligomers and Polymers: Theory, Characterization Methods, Molecular Design, and Applications. *Chin. J. Polym. Sci.* **2024**, *42*, 417–436. https://doi.org/10.1007/s10118-024-3087-7.

(30) Orms, N.; Rehn, D. R.; Dreuw, A.; Krylov, A. I. Characterizing Bonding Patterns in Diradicals and Triradicals by Density-Based Wave Function Analysis: A Uniform Approach. *J. Chem. Theory Comput.* **2018**, *14*, 638–648. https://doi.org/10.1021/acs.jctc.7b01012.

(31) Y. Gopalakrishna, T.; Zeng, W.; Lu, X.; Wu, J. From Open-Shell Singlet Diradicaloids to Polyradicaloids. *Chem. Commun.* **2018**, *54*, 2186–2199. https://doi.org/10.1039/C7CC09949E.

(32) Salem, L.; Rowland, C. The Electronic Properties of Diradicals. *Angew. Chem. Int. Ed.* **1972**, *11*, 92–111. https://doi.org/10.1002/anie.197200921.

(33) Shen, L.; Gao, X.; Chang, Z.; Zhang, C.; Li, Y.; Lu, J.; Meng, Q.; Wu, Q. Sufficient Driving Force for Quinoidal Isoindigo-Based Diradicaloids with Tunable Diradical Characters. *Phys. Chem. Chem. Phys.* **2024**, *26*, 2529–2538. https://doi.org/10.1039/D3CP05199D.

(34) Ramos-Cordoba, E.; Salvador, P. Diradical Character from the Local Spin Analysis. *Phys. Chem. Chem. Phys.* **2014**, *16*, 9565. https://doi.org/10.1039/c4cp00939h.

(35) Kim, Y.; Kim, Y.-J.; Kim, Y.-A.; Jung, E.; Mok, Y.; Kim, K.; Hwang, H.; Park, J.-J.; Kim, M.-G.; Mathur, S.; Kim, D.-Y. Open-Shell and Closed-Shell Quinoid–

Aromatic Conjugated Polymers: Unusual Spin Magnetic and High Charge Transport Properties. *ACS Appl. Mater. Interfaces* **2021**, *13*, 2887–2898. https://doi.org/10.1021/acsami.0c15893.

(36) Anglada, J. M.; Poater, J.; Moreira, I. de P. R.; Bofill, J. M. Controlling the Diradical Character of Thiele Like Compounds. *J. Org. Chem.* **2023**, *88*, 8553–8562. https://doi.org/10.1021/acs.joc.3c00482.

(37) Betkhoshvili, S.; de P. R. Moreira, I.; Poater, J.; Bofill, J. M. Aromaticity-Induced Spin State Switching and High-Spin States in Non-Alternant Polyradicals. *J. Comput. Chem.* **2026**, *47*, e70366. https://doi.org/10.1002/jcc.70366.

(38) Wang, T.; Krylov, A. I. The Effect of Substituents on Electronic States' Ordering in *Meta* -Xylylene Diradicals: Qualitative Insights from Quantitative Studies. *J. Chem. Phys.* **2005**, *123*, 104304. https://doi.org/10.1063/1.2018645.

(39) Chen, Z.; Li, W.; Sabuj, M. A.; Li, Y.; Zhu, W.; Zeng, M.; Sarap, C. S.; Huda, M. M.; Qiao, X.; Peng, X.; Ma, D.; Ma, Y.; Rai, N.; Huang, F. Evolution of the Electronic Structure in Open-Shell Donor-Acceptor Organic Semiconductors. *Nat. Commun.* **2021**, *12*, 5889. https://doi.org/10.1038/s41467-021-26173-3.

(40) Flynn, C. R.; Michl, J. ..Pi., .Pi.-Biradicaloid Hydrocarbons. o-Xylylene. Photochemical Preparation from 1,4-Dihydrophthalazine in Rigid Glass, Electric Spectroscopy, and Calculations. *J. Am. Chem. Soc.* **1974**, *96*, 3280–3288. https://doi.org/10.1021/ja00817a042.

(41) Doehnert, D.; Koutecky, J. Occupation Numbers of Natural Orbitals as a Criterion for Biradical Character. Different Kinds of Biradicals. *J. Am. Chem. Soc.* **1980**, *102*, 1789–1796. https://doi.org/10.1021/ja00526a005.

(42) Wang, C.; Hao, H.; Tajima, K. *Essential Role of Triplet Diradical Character for Large Magnetoresistance in Quinoidal Organic Semiconductor with High Electron Mobility*.

(43) Vidal, E.; Warren, G. I.; Barker, J. E.; Haley, M. M. The Interplay of Antiaromaticity and Diradical Character in Diarenoindacenes and Diindenoarenes. *Chem. Sci.* **2025**, *16*, 19026–19047. https://doi.org/10.1039/D5SC05050B.

(44) Moons, H.; Goovaerts, E.; Gubskaya, V. P.; Nuretdinov, I. A.; Corvaja, C.; Franco, L. W-Band Transient EPR and Photoinduced Absorption on Spin-Labeled Fullerene Derivatives. *Phys. Chem. Chem. Phys.* **2011**, *13*, 3942. https://doi.org/10.1039/c0cp01902j.

(45) Asano, M. S.; Ishizuka, K.; Kaizu, Y. Spin-Multiplicity of a Moderately Coupled Triplet–Doublet Spin Pair in a Biphenylene-Linked Porphyrin Dimer. *Mol. Phys.* **2006**, *104*, 1609–1618. https://doi.org/10.1080/00268970600647789.

(46) Huang, B.; Kang, H.; Zhang, C.-W.; Zhao, X.-L.; Shi, X.; Yang, H.-B. Design of an Open-Shell Nitrogen-Centered Diradicaloid with Tunable Stimuli-Responsive Electronic Properties. *Commun. Chem.* **2022**, *5*, 127. https://doi.org/10.1038/s42004-022-00747-8.

(47) Thiele, J.; Balhorn, H. Ueber Einen Chinoïden Kohlenwasserstoff. *Berichte der deutschen chemischen Gesellschaft* **1904**, *37*, 1463–1470. https://doi.org/10.1002/cber.19040370245.

(48) Tschitschibabin, A. E. Über Einige Phenylierte Derivate Des p, P-Ditolyls. *Berichte der deutschen chemischen Gesellschaft* **1907**, *40*, 1810–1819. https://doi.org/10.1002/cber.19070400282.

(49) Punzi, A.; Dai, Y.; Dibenedetto, C. N.; Mesto, E.; Schingaro, E.; Ullrich, T.; Striccoli, M.; Guldi, D. M.; Negri, F.; Farinola, G. M.; Blasi, D. Dark State of the Thiele Hydrocarbon: Efficient Solvatochromic Emission from a Nonpolar Centrosymmetric Singlet Diradicaloid. *J. Am. Chem. Soc.* **2023**, *145*, 20229–20241. https://doi.org/10.1021/jacs.3c05251.

(50) Nishiuchi, T.; Aibara, S.; Sato, H.; Kubo, T. Synthesis of π-Extended Thiele's and Chichibabin's Hydrocarbons and Effect of the π-Congestion on Conformations and Electronic States. *J. Am. Chem. Soc.* **2022**, *144*, 7479–7488. https://doi.org/10.1021/jacs.2c02318.

(51) Ambhore, M. D.; Shukla, P.; Gonnade, R. G.; Anand, V. G. Tailoring Diradicaloid Properties of Expanded Isophlorinoids with Systematic Core-Modification. *Chemical Communications* **2022**, *58* (64), 8946–8949. https://doi.org/10.1039/D2CC02970G.

(52) Zeng, Z.; Shi, X.; Chi, C.; López Navarrete, J. T.; Casado, J.; Wu, J. Pro-Aromatic and Anti-Aromatic π-Conjugated Molecules: An Irresistible Wish to Be Diradicals. *Chem. Soc. Rev.* **2015**, *44*, 6578–6596. https://doi.org/10.1039/C5CS00051C.

(53) Zhao, Y.; Wang, W.; Zhang, L.; Wang, T.; He, L.; Sun, Q.; Zhao, Y.; Wang, X. An Olefin Radical Based Thiele's Hydrocarbon Derivative and Macrocyclic Tetraradical. *Angew. Chem. Int. Ed.* **2025**, *64*, e202500943. https://doi.org/10.1002/anie.202500943.

(54) Hu, X.; Wang, W.; Wang, D.; Zheng, Y. The Electronic Applications of Stable Diradicaloids: Present and Future. *J. Mater. Chem. C Mater.* **2018**, *6*, 11232–11242. https://doi.org/10.1039/C8TC04484H.

(55) Choppella, S.; Paramasivam, G.; Sambasivam, S.; Ravva, M. K. Understanding the Stability of π-Conjugated Diradicaloid Organic Molecules. *J. Electron. Mater.* **2023**, *52*, 1681–1690. https://doi.org/10.1007/s11664-022-10082-2.

(56) Kodama, T.; Hirao, Y.; Kubo, T. Synthesis and Properties of a Through-Space Interacting Diradicaloid. *Precision Chemistry* **2023**, *1*, 183–191. https://doi.org/10.1021/prechem.3c00024.

(57) Shi, X.; Burrezo, P. M.; Lee, S.; Zhang, W.; Zheng, B.; Dai, G.; Chang, J.; López Navarrete, J. T.; Huang, K.-W.; Kim, D.; Casado, J.; Chi, C. Antiaromatic Bisindeno-[n]Thienoacenes with Small Singlet Biradical Characters: Syntheses, Structures and Chain Length Dependent Physical Properties. *Chem. Sci.* **2014**, *5*, 4490–4503. https://doi.org/10.1039/C4SC01769B.

(58) Steffenfauseweh, H.; Rottschäfer, D.; Vishnevskiy, Y. V.; Neumann, B.; Stammler, H.; de Bruin, B.; Ghadwal, R. S. Non-Kekulé *Meta* -Quinodimethane Singlet Diradicals Based on Classical N-Heterocyclic Carbenes. *Chem. Eur. J.* **2024**, *30*, e202403029. https://doi.org/10.1002/chem.202403029.

(59) Olankitwanit, A.; Pink, M.; Rajca, S.; Rajca, A. Synthesis of Aza- *m* -Xylylene Diradicals with Large Singlet–Triplet Energy Gap and Statistical Analyses of Their EPR Spectra. *J. Am. Chem. Soc.* **2014**, *136*, 14277–14288. https://doi.org/10.1021/ja508119d.

(60) Valenta, L.; Mayländer, M.; Kappeler, P.; Blacque, O.; Šolomek, T.; Richert, S.; Juríček, M. Trimesityltriangulene: A Persistent Derivative of Clar's Hydrocarbon. *Chem. Commun.* **2022**, *58*, 3019–3022. https://doi.org/10.1039/D2CC00352J.

(61) Ni, Y.; Gopalakrishna, T. Y.; Wu, S.; Wu, J. A Stable All-Thiophene-Based Core-Modified [38]Octaphyrin Diradicaloid: Conformation and Aromaticity Switch at Different Oxidation States. *Angew. Chem. Int. Ed.* **2020**, *59*, 7414–7418. https://doi.org/10.1002/anie.202000188.

(62) Miao, F.; Phan, H.; Wu, J. A BODIPY-Bridged Bisphenoxyl Diradicaloid: Solvent-Dependent Diradical Character and Physical Properties. *Molecules* **2019**, *24*, 1446. https://doi.org/10.3390/molecules24081446.

(63) Hu, X.; Wang, W.; Wang, D.; Zheng, Y. The Electronic Applications of Stable Diradicaloids: Present and Future. *J. Mater. Chem. C Mater.* **2018**, *6*, 11232–11242. https://doi.org/10.1039/C8TC04484H.

(64) Dressler, J. J.; Teraoka, M.; Espejo, G. L.; Kishi, R.; Takamuku, S.; Gómez-García, C. J.; Zakharov, L. N.; Nakano, M.; Casado, J.; Haley, M. M. Thiophene and Its Sulfur Inhibit Indenoindenodibenzothiophene Diradicals from Low-Energy Lying Thermal Triplets. *Nat. Chem.* **2018**, *10*, 1134–1140. https://doi.org/10.1038/s41557-018-0133-5.

(65) Gallagher, N.; Zhang, H.; Junghoefer, T.; Giangrisostomi, E.; Ovsyannikov, R.; Pink, M.; Rajca, S.; Casu, M. B.; Rajca, A. Thermally and Magnetically Robust Triplet Ground State Diradical. *J. Am. Chem. Soc.* **2019**, *141*, 4764–4774. https://doi.org/10.1021/jacs.9b00558.

(66) Dressler, J. J.; Cárdenas Valdivia, A.; Kishi, R.; Rudebusch, G. E.; Ventura, A. M.; Chastain, B. E.; Gómez-García, C. J.; Zakharov, L. N.; Nakano, M.; Casado, J.; Haley, M. M. Diindenoanthracene Diradicaloids Enable Rational, Incremental Tuning of Their Singlet-Triplet Energy Gaps. *Chem* **2020**, *6*, 1353–1368. https://doi.org/10.1016/j.chempr.2020.02.010.

(67) Nakano, M.; Champagne, B. Theoretical Design of Open-Shell Singlet Molecular Systems for Nonlinear Optics. *J. Phys. Chem. Lett.* **2015**, *6*, 3236–3256. https://doi.org/10.1021/acs.jpclett.5b00956.

(68) Smith, T. L.; Zhang, Z.; Balandin, T. A.; Mahalingam, P.; Comstock, A. H.; Österholm, A. M.; Bowman, M. K.; Lockart, M. M.; Hu, G.; Azoulay, J. D. Modular Donor-Acceptor Diradicaloids Based on an Electron Deficient *N* -Heteroacene Acceptor. *Small* **2026**, *22*, e10228. https://doi.org/10.1002/smll.202510228.

(69) Ni, Y.; Lee, S.; Son, M.; Aratani, N.; Ishida, M.; Samanta, A.; Yamada, H.; Chang, Y.; Furuta, H.; Kim, D.; Wu, J. A Diradical Approach towards BODIPY-Based Dyes with Intense Near-Infrared Absorption around λ =1100 Nm. *Angew. Chem. Int. Ed.* **2016**, *55*, 2815–2819. https://doi.org/10.1002/anie.201511151.

(70) Zeng, Z.; Ishida, M.; Zafra, J. L.; Zhu, X.; Sung, Y. M.; Bao, N.; Webster, R. D.; Lee, B. S.; Li, R.-W.; Zeng, W.; Li, Y.; Chi, C.; Navarrete, J. T. L.; Ding, J.; Casado, J.;

Kim, D.; Wu, J. Pushing Extended *p* -Quinodimethanes to the Limit: Stable Tetracyano-Oligo(*N* -Annulated Perylene)Quinodimethanes with Tunable Ground States. *J. Am. Chem. Soc.* **2013**, *135*, 6363–6371. https://doi.org/10.1021/ja402467y.

(71) Casado, J. Para-Quinodimethanes: A Unified Review of the Quinoidal-Versus-Aromatic Competition and Its Implications. *Top. Curr. Chem.* **2017**, *375*, 73. https://doi.org/10.1007/s41061-017-0163-2.

(72) Intorp, S. N.; Hodecker, M.; Müller, M.; Tverskoy, O.; Rosenkranz, M.; Dmitrieva, E.; Popov, A. A.; Rominger, F.; Freudenberg, J.; Dreuw, A.; Bunz, U. H. F. Quinoidal Azaacenes: 99 % Diradical Character. *Angew. Chem. Int. Ed.* **2020**, *59*, 12396–12401. https://doi.org/10.1002/anie.201915977.

(73) Zeng, W.; Wu, J. Push–Pull Type Quinoidal Perylene Showing Solvent Polarity Dependent Diradical Character and Negative Solvatochromism. *Mater. Chem. Front.* **2019**, *3*, 2668–2672. https://doi.org/10.1039/C9QM00566H.

(74) Wang, K.; Zhan, Q.; Han, B.; Quintero, S. M.; Huang, W.; Ji, Y.; Miao, F.; Chen, H.; Casado, J.; Zheng, Y. The Smallest Oligothiophene Diradicals by Asymmetric Substitution of Quinoidal Cores. *J. Mater. Chem. C Mater.* **2022**, *10*, 12724–12730. https://doi.org/10.1039/D2TC02433K.

(75) Zeng, W.; Wu, J. Open-Shell Graphene Fragments. *Chem* **2021**, *7*, 358–386. https://doi.org/10.1016/j.chempr.2020.10.009.

(76) Yoneda, K.; Nakano, M.; Kishi, R.; Takahashi, H.; Shimizu, A.; Kubo, T.; Kamada, K.; Ohta, K.; Champagne, B.; Botek, E. Third-Order Nonlinear Optical Properties of Trigonal, Rhombic and Bow-Tie Graphene Nanoflakes with Strong

Structural Dependence of Diradical Character. *Chem. Phys. Lett.* **2009**, *480*, 278–283. https://doi.org/10.1016/j.cplett.2009.09.047.

(77) Shimizu, D.; Osuka, A. Porphyrinoids as a Platform of Stable Radicals. *Chem. Sci.* **2018**, *9*, 1408–1423. https://doi.org/10.1039/C7SC05210C.

(78) Wang, K.; Liu, P.; Zhang, F.; Xu, L.; Zhou, M.; Nakai, A.; Kato, K.; Furukawa, K.; Tanaka, T.; Osuka, A.; Song, J. A Robust Porphyrin-Stabilized Triplet Carbon Diradical. *Angew. Chem. Int. Ed.* **2021**, *60*, 7002–7006. https://doi.org/10.1002/anie.202015356.

(79) Miao, F.; Phan, H.; Wu, J. A BODIPY-Bridged Bisphenoxyl Diradicaloid: Solvent-Dependent Diradical Character and Physical Properties. *Molecules* **2019**, *24*, 1446. https://doi.org/10.3390/molecules24081446.

(80) Pachpatil, P. K.; Kanojia, S. V.; Ghosh, A.; Majumdar, A. G.; Wadawale, A.; Mohapatra, M.; Patro, B. S.; Ghanty, T. K.; Goswami, D. Stable, Triplet Ground State BODIPY-TEMPO Diradical as a Selective Turn on Fluorescence Sensor for Intracellular Labile Iron Pool. *Sens. Actuators B Chem.* **2022**, *370*, 132474. https://doi.org/10.1016/j.snb.2022.132474.

(81) Liu, Y.; Phan, H.; Herng, T. S.; Gopalakrishna, T. Y.; Ding, J.; Wu, J. Toward Benzobis(Thiadiazole)-based Diradicaloids. *Chem. Asian J.* **2017**, *12*, 2177–2182. https://doi.org/10.1002/asia.201700732.

(82) Wei, H.; Zhang, L.; Phan, H.; Huang, X.; Herng, T. S.; Zhou, J.; Zeng, W.; Ding, J.; Luo, S.; Wu, J.; Zeng, Z. A Stable *N* -Annulated Perylene-Bridged Bisphenoxyl

Diradicaloid and the Corresponding Boron Trifluoride Complex. *Chem. Eur. J.* **2017**, *23*, 9419–9424. https://doi.org/10.1002/chem.201701692.

(83) Shen, L.; Gao, X.; Chang, Z.; Zhang, C.; Li, Y.; Lu, J.; Meng, Q.; Wu, Q. Sufficient Driving Force for Quinoidal Isoindigo-Based Diradicaloids with Tunable Diradical Characters. *Phys. Chem. Chem. Phys.* **2024**, *26*, 2529–2538. https://doi.org/10.1039/D3CP05199D.

(84) Privado, M.; Moles Quintero, S.; Barrejón, M.; de La Cruz, P.; P. M., J. B.; Casanova, D.; Langa, F.; Casado, J. Dibenzoquinone Cyclopentadithiophene Diradicaloids Show Optical Transitions of Different Spin States and Anomalous Near-Infrared Emission. *Angew. Chem. Int. Ed.* **2025**, *64*. https://doi.org/10.1002/anie.202413988.

(85) Oyelowo, M.; Schaffner, J. W.; Jeaydi, T. I.; Blank, D. A.; Ziegler, C. J.; Nemykin, V. N. Introducing of an Unexplored Aza-BODIPY Diradicaloids with 4-(2,6-Di *Tert* -Butyl)Phenoxyl Radicals Located in 1,7-Positions of the Aza-BODIPY Core. *Inorg. Chem.* **2024**, *63*, 24008–24021. https://doi.org/10.1021/acs.inorgchem.4c04409.

(86) Boerner, L. J. K.; Dye, David. F.; Köpke, T.; Zaleski, J. M. Expansion and Contraction: Shaping the Porphyrin Boundary via Diradical Reactivity. *Coord. Chem. Rev.* **2013**, *257*, 599–620. https://doi.org/10.1016/j.ccr.2012.07.009.

(87) Petakova, V.; Nedyalkova, M.; Stoycheva, J.; Tadjer, A.; Romanova, J. The Interplay between Diradical Character and Stability in Organic Molecules. *Symmetry.* **2021**, *13*. https://doi.org/10.3390/sym13081448.

(88) Muhammad, S.; Nakano, M.; Al-Sehemi, A. G.; Kitagawa, Y.; Irfan, A.; Chaudhry, A. R.; Kishi, R.; Ito, S.; Yoneda, K.; Fukuda, K. Role of a Singlet Diradical Character in Carbon Nanomaterials: A Novel Hot Spot for Efficient Nonlinear Optical Materials. *Nanoscale* **2016**, *8*, 17998–18020. https://doi.org/10.1039/C6NR06097H.

(89) Kamada, K.; Ohta, K.; Shimizu, A.; Kubo, T.; Kishi, R.; Takahashi, H.; Botek, E.; Champagne, B.; Nakano, M. Singlet Diradical Character from Experiment. *J. Phys. Chem. Lett.* **2010**, *1*, 937–940. https://doi.org/10.1021/jz100155s.

(90) Minami, T.; Nakano, M. Diradical Character View of Singlet Fission. *J. Phys. Chem. Lett.* **2012**, *3*, 145–150. https://doi.org/10.1021/jz2015346.

(91) Nakano, M.; Kishi, R.; Nitta, T.; Kubo, T.; Nakasuji, K.; Kamada, K.; Ohta, K.; Champagne, B.; Botek, E.; Yamaguchi, K. Second Hyperpolarizability (γ) of Singlet Diradical System: Dependence of γ on the Diradical Character. *J. Phys. Chem. A* **2005**, *109*, 885–891. https://doi.org/10.1021/jp046322x.

(92) Yamanaka, S.; Kawakami, T.; Nagao, H.; Yamaguchi, K. Effective Exchange Integrals for Open-Shell Species by Density Functional Methods. *Chem. Phys. Lett.* **1994**, *231*, 25–33. https://doi.org/10.1016/0009-2614(94)01221-0.

(93) Yamaguchi, K.; Okumura, M.; Mori, W.; Maki, J.; Takada, K.; Noro, T.; Tanaka, K. Comparison between Spin Restricted and Unrestricted Post-Hartree—Fock Calculations of Effective Exchange Integrals in Ising and Heisenberg Models. *Chem. Phys. Lett.* **1993**, *210* , 201–210. https://doi.org/10.1016/0009-2614(93)89124-Z.

(94) Yamanaka, S.; Okumura, M.; Yamaguchi, K.; Hirao, K. CASPT2 and MR MP2 Calculations of Potential Curves and Effective Exchange Integrals for the Dimer of

Triplet Methylene. *Chem. Phys. Lett.* **1994**, *225*, 213–220. https://doi.org/10.1016/0009-2614(94)00599-0.

(95) Hirao, K. Multireference Møller—Plesset Perturbation Theory for High-Spin Open-Shell Systems. *Chem. Phys. Lett.* **1992**, *196*, 397–403. https://doi.org/10.1016/0009-2614(92)85710-R.

(96) Sherrill, D.; Lee, M. S.; Head-Gordon, M. *On the Performance of Density Functional Theory for Symmetry-Breaking Problems*; 1999; Vol. 302.

(97) Chen, Z.; Mendoza-Gomez, S.; Azar-Tanguay, J. E.; Ancajas, C. M. F.; Sirianni, D. A.; Parish, C. A. A Spin–Flip Study of the Diradical Isomers of Pyrrole, Furan, and Thiophene. *J. Chem. Phys.* **2024**, *161*, 154304. https://doi.org/10.1063/5.0233736.

(98) Shu, C.; Yang, Z.; Rajca, A. From Stable Radicals to Thermally Robust High-Spin Diradicals and Triradicals. *Chem. Rev.* **2023**, *123*, 11954–12003. https://doi.org/10.1021/acs.chemrev.3c00406.

(99) Weng, T.; Xu, Z.; Li, K.; Guo, Y.; Chen, X.; Li, Z.; Sun, Z. 1,1′-Biolympicenyl: A Stable Non-Kekulé Diradical with a Small Singlet and Triplet Energy Gap. *J. Am. Chem. Soc.* **2024**, *146*, 26454–26465. https://doi.org/10.1021/jacs.4c09627.

(100) Kuriakose, F.; Commodore, M.; Hu, C.; Fabiano, C. J.; Sen, D.; Li, R. R.; Bisht, S.; Üngör, Ö.; Lin, X.; Strouse, G. F.; DePrince, A. E.; Lazenby, R. A.; Mentink-Vigier, F.; Shatruk, M.; Alabugin, I. V. Design and Synthesis of Kekulè and Non-Kekulè Diradicaloids via the Radical Periannulation Strategy: The Power of Seven Clar's Sextets. *J. Am. Chem. Soc.* **2022**, *144*, 23448–23464. https://doi.org/10.1021/jacs.2c09637.

(101) Steffenfauseweh, H.; Rottschäfer, D.; Vishnevskiy, Y. V.; Neumann, B.; Stammler, H.; de Bruin, B.; Ghadwal, R. S. Non-Kekulé *Meta* -Quinodimethane Singlet Diradicals Based on Classical N-Heterocyclic Carbenes. *Chem. Eur. J.* **2024**, *30*, e202403029. https://doi.org/10.1002/chem.202403029.

(102) Gao, S.; Li, F. Neutral Stable Nitrogen-Centered Radicals: Structure, Properties, and Recent Functional Application Progress. *Adv. Funct. Mater.* **2023**, *33*, 2304291. https://doi.org/10.1002/adfm.202304291.

(103) Vidal, E.; Warren, G. I.; Barker, J. E.; Haley, M. M. The Interplay of Antiaromaticity and Diradical Character in Diarenoindacenes and Diindenoarenes. *Chem. Sci.* **2025**, *16*, 19026–19047. https://doi.org/10.1039/D5SC05050B.

(104) Arikawa, S.; Shimizu, A.; Shiomi, D.; Sato, K.; Takui, T.; Sotome, H.; Miyasaka, H.; Murai, M.; Yamaguchi, S.; Shintani, R. A Kinetically Stabilized Nitrogen-Doped Triangulene Cation: Stable and NIR Fluorescent Diradical Cation with Triplet Ground State. *Angew. Chem. Int. Ed.* **2023**, *62*, e202302714. https://doi.org/10.1002/anie.202302714.

(105) Steffenfauseweh, H.; Rottschäfer, D.; Vishnevskiy, Y. V.; Neumann, B.; Stammler, H.; de Bruin, B.; Ghadwal, R. S. Non-Kekulé *Meta* -Quinodimethane Singlet Diradicals Based on Classical N-Heterocyclic Carbenes. *Chem. Eur. J.* **2024**, *30*, e202403029. https://doi.org/10.1002/chem.202403029.

(106) Kundu, G.; Pramanik, D.; Dash, S. R.; Kumar, R.; Tothadi, S.; Ghosh, A.; Vanka, K.; Sen, S. S. A Kekulé Diradicaloid with a Naphthalene Spacer. *Organometallics* **2026**, *45*, 624–627. https://doi.org/10.1021/acs.organomet.5c00508.

(107) Jiang, Q.; Wang, L.; Wei, H.; Peng, Y.; Xu, G.; Li, Z.; Liu, P.; Hu, Z.; Niu, W.; Chen, Y.; Tang, H.; Zeng, W.; Li, G. A Kinetically Stabilized Dianthraceno[2,3- *a* :3′,2′- *h*]- *s* -Indacene: Stable Kekulé Diradical Polycyclic Hydrocarbon with Triplet Ground State. *Angew. Chem.* **2025**, *137*, e202422994. https://doi.org/10.1002/ange.202422994.

(108) Venkatareddy, V. K.; Kamble, A. V.; Rao, M. R. Modulation of Open-Shell Diradical Character of Imidazole Quinoidal Systems. *Org. Lett.* **2026**, *28*, 4055–4060. https://doi.org/10.1021/acs.orglett.6c00532.

(109) Shimizu, A. M-Quinodimethane-Based Fused-Ring Diradicals with Singlet and Triplet Ground States. *Chemistry (Easton).* **2025**, *7*, 40. https://doi.org/10.3390/chemistry7020040.

(110) Olivier, Y.; Sancho-García, J. Design Strategies for Diradical Boron/Nitrogen Doped Carbon-Based Materials. *Angew. Chem.* **2023**, *135*, e202305501. https://doi.org/10.1002/ange.202305501.

(111) Hicks, R. G. What's New in Stable Radical Chemistry? *Org. Biomol. Chem.* **2007**, *5*, 1321. https://doi.org/10.1039/b617142g.

(112) Moss, G. P.; Smith, P. A. S.; Tavernier, D. Glossary of Class Names of Organic Compounds and Reactivity Intermediates Based on Structure (IUPAC Recommendations 1995). *Pure Appl. Chem.* **1995**, *67*, 1307–1375. https://doi.org/10.1351/pac199567081307.

(113) Gschwind, D. T.; Bresien, J. Bond and Antibond Resonances: A Unified Framework for Singlet Biradical Character. *Chem. Eur. J.* **2026**, e70968. https://doi.org/10.1002/chem.70968.

(114) Shimizu, D.; Sotome, H.; Miyasaka, H.; Matsuda, K. Optically Distinguishable Electronic Spin-Isomers of a Stable Organic Diradical. *ACS Cent. Sci.* **2024**, 890–898. https://doi.org/10.1021/acscentsci.4c00284.

(115) Ji, W.; Zou, Y.; Guo, L.; Niu, W.; Jiao, T.; Phan, H.; Wu, J.; Li, G. Stable Iminium Singlet and Triplet Diradical(Oid)s with Intense NIR-II Absorptions. *Angew. Chem.* **2025**, *137*, e202512663. https://doi.org/10.1002/ange.202512663.

(116) Rassat, A. Magnetic Properties of Nitroxide Multiradicals. *Pure Appl. Chem.* **1990**, *62*, 223–227. https://doi.org/10.1351/pac199062020223.

(117) Straub, D.; Gross, M.; Arnold, M. E.; Zolg, J.; Kuehne, A. J. C. On the Photoluminescence in Triarylmethyl-Centered Mono-, Di-, and Multiradicals. *Beilstein J. Org. Chem.* **2025**, *21*, 964–998. https://doi.org/10.3762/bjoc.21.80.

(118) Plasser, F.; Pašalić, H.; Gerzabek, M. H.; Libisch, F.; Reiter, R.; Burgdörfer, J.; Müller, T.; Shepard, R.; Lischka, H. The Multiradical Character of One- and Two-Dimensional Graphene Nanoribbons. *Angew. Chem. Int. Ed.* **2013**, *52*, 2581–2584. https://doi.org/10.1002/anie.201207671.

(119) Casanova, D. How Much Tetraradical Character Is Present in the Si_6Ge_9 Cluster? *J. Comput. Chem.* **2014**, *35*, 944–949. https://doi.org/10.1002/jcc.23580.

(120) Hu, P.; Lee, S.; Herng, T. S.; Aratani, N.; Gonçalves, T. P.; Qi, Q.; Shi, X.; Yamada, H.; Huang, K.-W.; Ding, J.; Kim, D.; Wu, J. Toward Tetraradicaloid: The Effect of Fusion Mode on Radical Character and Chemical Reactivity. *J. Am. Chem. Soc.* **2016**, *138*, 1065–1077. https://doi.org/10.1021/jacs.5b12532.

(121) Bell, F.; Casanova, D.; Head-Gordon, M. Theoretical Study of Substituted PBPB Dimers: Structural Analysis, Tetraradical Character, and Excited States. *J. Am. Chem. Soc.* **2010**, *132*, 11314–11322. https://doi.org/10.1021/ja104772w.

(122) Pozo, I.; Bogani, L. A Perspective on Radicaloid Conjugated Polycyclic Hydrocarbons. *Trends Chem.* **2024**, *6*, 581–595. https://doi.org/10.1016/j.trechm.2024.08.005.

(123) Guo, J.; Li, Z.; Zhang, J.; Li, B.; Liang, Y.; Wang, Y.; Xie, S.; Phan, H.; Herng, T. S.; Ding, J.; Wu, J.; Tang, B. Z.; Zeng, Z. Stable Quadruple Helical Tetraradicaloid with Thermally Induced Intramolecular Magnetic Switching. *CCS Chemistry* **2022**, *4*, 95–103. https://doi.org/10.31635/ccschem.021.202000658.

(124) Rajca, A. Organic Diradicals and Polyradicals: From Spin Coupling to Magnetism? *Chem. Rev.* **1994**, *94*, 871–893. https://doi.org/10.1021/cr00028a002.

(125) Zhu, Y.; Zhu, Z.; Wang, S.; Peng, Q.; Abdurahman, A. Stable Luminescent Diradicals: The Emergence and Potential Applications. *Angew. Chem. Int. Ed.* **2025**, *64*. https://doi.org/10.1002/anie.202423470.

(126) Sun, Z.; Ye, Q.; Chi, C.; Wu, J. Low Band Gap Polycyclic Hydrocarbons: From Closed-Shell near Infrared Dyes and Semiconductors to Open-Shell Radicals. *Chem. Soc. Rev.* **2012**, *41*, 7857. https://doi.org/10.1039/c2cs35211g.

(127) Castellanos, S.; Gaidelis, V.; Jankauskas, V.; Grazulevicius, J. V.; Brillas, E.; López-Calahorra, F.; Juliá, L.; Velasco, D. Stable Radical Cores: A Key for Bipolar Charge Transport in Glass Forming Carbazole and Indole Derivatives. *Chem. Commun.* **2010**, *46*, 5130. https://doi.org/10.1039/c0cc00529k.

(128) Jeong, M.-K.; Lee, S. H.; Won, Y.; Ahn, J.; Kim, M. I.; Oh, J. H. Stable Open-Shell Conjugated Terpolymer with Extended NIR Absorption for Organic Photodetectors Detecting Beyond 1000 Nm. *ACS Appl. Mater. Interfaces* **2025**, *17*, 25591–25601. https://doi.org/10.1021/acsami.5c03911.

(129) Kopp, S. M.; Nakamura, S.; Phelan, B. T.; Poh, Y. R.; Tyndall, S. B.; Brown, P. J.; Huang, Y.; Yuen-Zhou, J.; Krzyaniak, M. D.; Wasielewski, M. R. Luminescent Organic Triplet Diradicals as Optically Addressable Molecular Qubits. *J. Am. Chem. Soc.* **2024**, *146*, 27935–27945. https://doi.org/10.1021/jacs.4c11116.

(130) Chen, S.; Zhu, Z.; Zhou, L.; Huang, H.; Abdurahman, A.; Qiao, X.; Ma, D. A Room-Temperature Diradical-Based High-Spin Qubit. *J. Phys. Chem. Lett.* **2025**, *16*, 9401–9407. https://doi.org/10.1021/acs.jpclett.5c02104.

(131) Nakano, M. Open-Shell-Character-Based Molecular Design Principles: Applications to Nonlinear Optics and Singlet Fission. *Chem. Rec.* **2017**, *17*, 27–62. https://doi.org/10.1002/tcr.201600094.

(132) Duggin, M.; Bissember, A. C.; Fuller, R. O. Applications of Verdazyl Radicals in Energy Storage, Molecular Electronics and Magnetism: Teaching Old Molecules New Tricks. *Chem. Asian J.* **2025**, *20*, e202401550. https://doi.org/10.1002/asia.202401550.

(133) Mori, S.; Moles Quintero, S.; Tabaka, N.; Kishi, R.; González Núñez, R.; Harbuzaru, A.; Ponce Ortiz, R.; Marín-Beloqui, J.; Suzuki, S.; Kitamura, C.; Gómez-García, C. J.; Dai, Y.; Negri, F.; Nakano, M.; Kato, S.; Casado, J. Medium Diradical Character, Small Hole and Electron Reorganization Energies and Ambipolar Transistors

in Difluorenoheteroles. *Angew. Chem.* **2022**, *134*, e202206680. https://doi.org/10.1002/ange.202206680.

(134) Zhang, C.; Zang, Y.; Gann, E.; McNeill, C. R.; Zhu, X.; Di, C.; Zhu, D. Two-Dimensional π-Expanded Quinoidal Terthiophenes Terminated with Dicyanomethylenes as n-Type Semiconductors for High-Performance Organic Thin-Film Transistors. *J. Am. Chem. Soc.* **2014**, *136*, 16176–16184. https://doi.org/10.1021/ja510003y.

(135) Oyaizu, K.; Nishide, H. Radical Polymers for Organic Electronic Devices: A Radical Departure from Conjugated Polymers? *Adv. Mater.* **2009**, *21*, 2339–2344. https://doi.org/10.1002/adma.200803554.

(136) Nakahara, K.; Oyaizu, K.; Nishide, H. Organic Radical Battery Approaching Practical Use. *Chem. Lett.* **2011**, *40*, 222–227. https://doi.org/10.1246/cl.2011.222.

(137) Kaur, M.; Janaagal, A.; Balsukuri, N.; Gupta, I. Evolution of Aza-BODIPY Dyes-A Hot Topic. *Coord. Chem. Rev.* **2024**, *498*, 215428. https://doi.org/10.1016/j.ccr.2023.215428.

(138) Gao, H.; Liu, H.; Jiang, L.; Gai, L.; Shen, Z. A Near-Infrared Benzoquinone-Coupled BODIPY: Synthesis, Spectroscopic and Electrochemical Properties. *J. Porphyr. Phthalocyanines* **2019**, *23*, 76–83. https://doi.org/10.1142/S1088424619500044.

(139) Zhang, D.; Liu, L.; Zhang, X.; Lu, J.; Jiang, X.-D. Rational Design of Photofunctional Dyes BODIPYs/Aza-BODIPYs and Applications for Photocatalysis, Photoelectric Conversion and Thermochromic Materials. *Res. Chem. Mater.* **2024**, *3*, 103–122. https://doi.org/10.1016/j.recm.2024.01.001.

(140) Su, J.; Zhu, L.; Dong, Z.; Liu, M.; Zhang, F.; Li, X.; Wang, S.; Chen, Z. Triphenylamine-Functionalized Aza-BODIPY Dyes: Synthesis, Characterization, and Their Application as Hole Transport Materials in Perovskite Solar Cells. *Org. Chem. Front.* **2024**, *11*, 7044–7052. https://doi.org/10.1039/D4QO01616E.

(141) Wei, H.; Feng, R.; Fang, Y.; Wang, L.; Chen, C.; Zhang, L.; Cui, H.; Wang, X. The Diradical-Dication Strategy for BODIPY- and Porphyrin-Based Dyes with Near-Infrared Absorption Maxima from 1070 to 2040 Nm. *Chem. Eur. J.* **2018**, *24*, 19341–19347. https://doi.org/10.1002/chem.201804449.

(142) Ivaniuk, K.; Pidluzhna, A.; Stakhira, P.; Baryshnikov, G. V.; Kovtun, Y. P.; Hotra, Z.; Minaev, B. F.; Ågren, H. BODIPY-Core 1,7-Diphenyl-Substituted Derivatives for Photovoltaics and OLED Applications. *Dyes Pigm.* **2020**, *175*, 108123. https://doi.org/10.1016/j.dyepig.2019.108123.

(143) Shamova, L. I.; Zatsikha, Y. V.; Nemykin, V. N. Synthesis Pathways for the Preparation of the BODIPY Analogues: Aza-BODIPYs, BOPHYs and Some Other Pyrrole-Based Acyclic Chromophores. *Dalton Trans.* **2021**, *50*, 1569–1593. https://doi.org/10.1039/D0DT03964K.

CHAPTER II: EXPLORING AZA-BODIPY DIRADICALOIDS WITH 4-(2,6-DITERT-BUTYL)PHENOXY RADICALS LOCATED IN 1,7-POSITIONS OF THE AZA-BODIPY CORE

A version of this chapter was originally published by Morris Oyelowo, Jacob W. Schaffner, Towhidi Illius Jeaydi, David A. Blank, Christopher J. Ziegler, and Victor Nemykin:

Oyelowo, M.; Schaffner, J. W.; Jeaydi, T. I.; Blank, D. A.; Ziegler, C. J.; Nemykin, V. N. Introducing of an Unexplored Aza-BODIPY Diradicaloids with 4-(2,6-Di *Tert* -Butyl)Phenoxyl Radicals Located in 1,7-Positions of the Aza-BODIPY Core. *Inorg Chem* **2024**, *63*, 24008–24021. https://doi.org/10.1021/acs.inorgchem.4c04409

In this research article, I was responsible for synthesizing all compounds studied. I performed characterization including variable temperature NMR, SQUID magnetometry, electrochemistry, spectroelectrochemistry, FT-IR, UV/Vis absorption and fluorescence emission. I also grew the crystals used for X-ray diffractions. Towhidi Illius jeaydi carried out variable temperature EPR experiment. Jacob W. Schaffner performed transient absorption experiments. Dr. Christopher Ziegler facilitated the variable temperature EPR and helped in proofreading the manuscript. Dr. David Blank facilitated and organized the transient absorption spectroscopy data. Dr. Viktor Nemykin helped with DFT and TDDFT calculations. He also assisted in writing and editing the manuscript.

2.1 Abstract

Two diradicaloid systems **2.9** and **2.10** that originated from the oxidation of a 1,7-(4-(2,6-di-*tert*-butyl)phenol)-substituted aza-BODIPY core were synthesized and characterized. The aza-BODIPY diradicaloids were characterized by a large array of experimental and computational methods. The diamagnetic closed-shell state was

postulated as the ground state in solution and a solid-state with the substantial thermal population originating from both open-shell diradical and open-shell triplet state observed at room temperature. Transient absorption spectroscopy indicates fast (~20 ps) excited state deactivation pathways associated with the target compounds' diradical character in solution at room temperature. Variable-temperature ^{1}H NMR spectra indicate the solvent dependency of the diradical character in **2.9** and **2.10**. The diradicaloids could be stepwise reduced to the mixed-valence radical-anion and dianion states upon consequent single-electron reductions. Similarly, deprotonated 1,7-(4-(2,6-di-*tert*-butyl)phenol)-substituted aza-BODIPYs can be oxidized to the diradicaloid form. Both mixed-valence and dianionic forms exhibit an intense absorption in the NIR region. Density Functional Theory (DFT) and time-dependent DFT (TDDFT) calculations were used to explain the transformations in the UV-Vis-NIR spectra of all target compounds.

2.2 Introduction

4,4-Difluoro-4-bora-3,4-diaza-s-indacene (BODIPY)[1-11] and meso-nitrogen atom substituted BODIPY (aza-BODIPY)[12-17] systems are very popular chromophores that have potential applications as photosensitizers for photodynamic therapy,[18-22] bioimaging agents,[23-27] photosensitizers for solar cells,[28-32] near-IR (NIR) laser agents,[33-37] and solid-state photoelectronic devices,[38-41] including photovoltaic systems,[42-44] organic field effect transistor (OFET),[45-49] and organic light-emitting diodes (OLEDs).[50-55] The ease of fine-tuning the photophysical, and redox properties of this group of compounds[4,5,12] can lead to new applications of this class of materials in spintronics and magnetic memory devices with high storage capacities and fast operation speeds.

Organic diradicaloids are a relatively new class of compounds that are thought to provide an alternative pathway for materials useful in spintronics and quantum computing applications.[56-65] A number of Kekule-[66-73] and non-Kekule-based[74-76] diradicaloids have been studied over the last decade. It was shown that the oxygen-centered diradicaloids are significantly more stable under ambient conditions compared to the majority of the carbon-centered diradicaloids. The orbital overlap between redox-active fragments and the overall type of the p-system of the chromophore determines whether diradicals exhibit triplet or singlet ground states, although there is still no general guideline developed for predicting such behavior.[56] When applied to the oxygen-centered diradicaloids, oligo-para-phenyl quinones can generally be described as closed-shell resonance structures (diamagnetic), as open-shell diradicals or a superposition of the two.[56] There are only a few Kekulean oxygen-centered species with high diradical character that are stable and persist under laboratory conditions.[56,77-81] The porphyrin-quinones are known to have diamagnetic ground states without any accessible diradical character.[82-84]

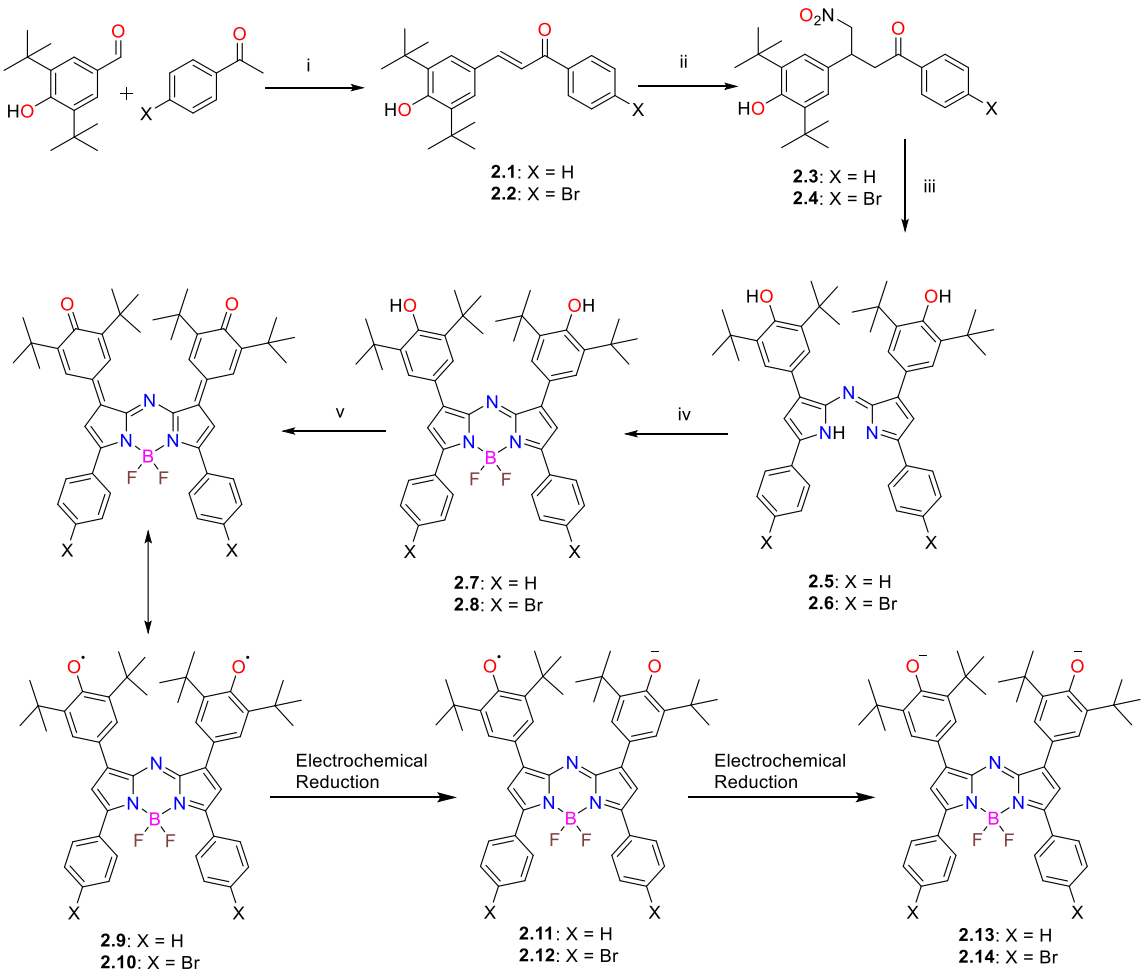
However, recently, Wu and co-workers reported a single BODIPY-quinone system with diradical properties.[85] In contrast, aza-BODIPYs with diradical character remain unknown. Thus, in this study, we report the first two aza-BODIPY-bridged para-quinoidal systems that demonstrate diradical character. Also, we demonstrated how polarity of solvent and phase (i.e. solid-phase versus solution) affects the singlet and triplet diradical character of these compounds.

2.3 Results and Discussion

2.3.1 Synthesis and characterization of aza-BODIPY diradicaloids 2.9 and 2.10 with 4-(2,6-di-tert-butyl)phenoxyl radicals located in 1,7-positions of the aza-BODIPY core

Compounds **2.9** and **2.10** were synthesized using a well-established synthetic pathway[12] as shown in Scheme 1. First, an aldol condensation of arylaldehydes and acetophenones in the presence of hydrogen chloride gas gave chalcones **2.1** and **2.2** in high yields. The chalcones **2.1** and **2.2** were nitromethylated under standard conditions to form compounds **2.3** and **2.4** in very high yields. The heterocyclization of the nitromethylated chalcones **2.3** and **2.4** with excess ammonium acetate in n-nutanol leads to the formation of aza-DIPYs **2.5** and **2.6** in 28-45% yield. The BF_2 fragment was then inserted into the aza-DIPYs **2.5** and **2.6** by using BF_3 etherate in the presence of sterically hindered organic amine in dichloromethane to give aza-BODIPYs **2.7** and **2.8**. column chromatography on silica gel using DCM/Hexane (1:2) eluent was required to obtain pure samples of **2.7** and **2.8.** Finally, the oxidation of the diphenol-aza-BODIPYs **2.7** and **2.8** to diradicaloids **2.9** and **2.10** was achieved quantitatively by using excess lead dioxide in dichloromethane. No further purification was required for diradicaloids **2.9** and **2.10** after filtering out the excess lead dioxide. Both aza-BODIPY derivatives **2.7** and **2.8** are stable in solutions. However, diradicaloids **2.9** and **2.10**, although stable for some time in solution, slowly decay over several weeks. We introduced two bromine atoms in the **2.2, 2.4, 2.6, 2.8** and **2.10** series to investigate the influence of the heavy-atom effect on the spectroscopic properties of compounds **2.8** and **2.10** in comparison with **2.7** and **2.9**. We wanted to see how these heavier bromine atoms will aid intersystem crossing and

influence their excited state spin. Compounds **2.7, 2.8, 2.9,** and **2.10** can be stored in vial for several weeks in both solid state and DCM solutions.



Scheme 2.1. Synthesis of diradicaloids **2.9** and **2.10**. Reagents and conditions: (i) HCl(g), EtOH; (ii) CH_3NO_2, DBU; (iii) NH_4OAc, BuOH; (iv) BF_3*Et_2O, DIPEA; and (v) PbO_2.

2.3.2 Photophysical Studies

2.3.2.1 Absorption and Emission Studies

The influence of the bromine atoms on the UV-Vis spectra of **2.8** and **2.10** as compared with the parent **2.7** and **2.9** is quite small (Figure 2.1). The UV-Vis spectra of **2.7** and **2.8** are typical for the tetraaryl-aza-BODIPYs[12] and are dominated by an intense low-energy band observed at 660-670 nm, which has a lower intensity 0-1 vibronic satellites at ~520 nm and several low-intensity transitions observed between 250 and 450 nm. This band shifts to the NIR region (~800 nm) with a significant reduction in intensity upon oxidation to **2.9** and **2.10**. The other band in **2.9** and **2.10** (observed at ~750 nm) is comparable in intensity with the low-energy transition band observed in these compounds and, according to the TDDFT calculations, belongs to a different excited state as discussed in the DFT/TDDFT section. In addition, prominent bands at ~555 and ~388 nm were also observed (Figure 2.1). The aza-BODIPYs **2.7** and **2.8** have reasonable fluorescent quantum yields of 23 and 19% respectively, which is lower than those in regular tetraaryl aza-BODIPYs.[11,17,100-102] Such fluorescence quantum yield reduction is expected for BODIPYs and aza-BODIPYs substituted with hydroxy or phenoxy fragments because of the presence of the potential low-energy charge-transfer transition(s) and/or proton-transfer processes in the excited states.[12] Interestingly, two bromine atoms in aza-BODIPY **2.8** do not significantly affect the fluorescence quantum yield in this compound compared to the parent aza-BODIPY **2.7**. The Stoke's shifts in **2.7** and **2.8** are close to 1,000 cm^{-1}, which are within the range (although at the upper border) expected for the aza-BODIPY dyes.[12] The excited state dynamics for **2.7** in DCM

and DMF are significantly shorter than those in regular aza-BODIPYs (a few ns), which can be attributed to the potential intra-molecular charge- or proton-transfer processes and can be responsible for the lower fluorescence quantum yields in these compounds.

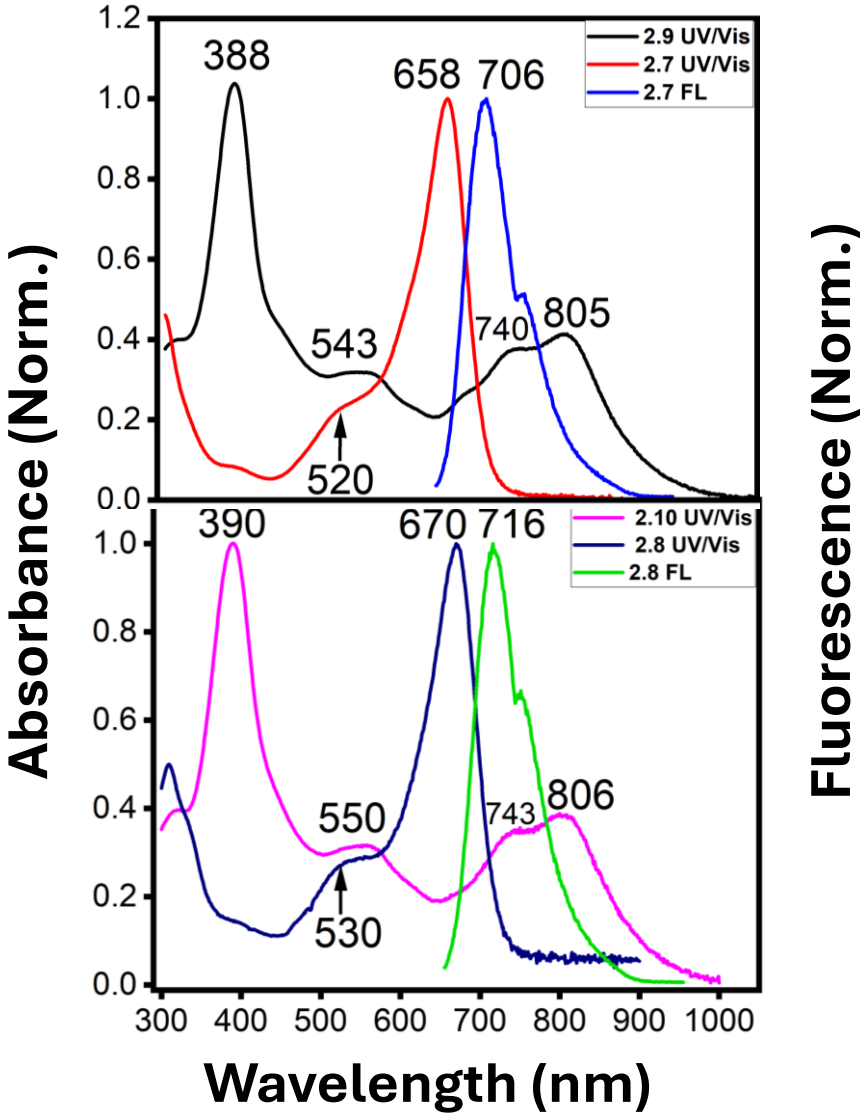


Figure 2.1: Normalized UV-Vis and fluorescent spectra of **2.7**, **2.8**, **2.9**, and **2.10** in DCM.

2.3.3.2 Transient Absorption Studies

Transient absorption spectra of **2.7**, **2.9**, and **2.10** were collected in both DCM and DMF. No significant differences between the two solvents were observed for the **2.7** and **2.8** as well as **2.9** and **2.10**, which is, apparently, indicative of the lack of the influence of a bromine atom at *para*-position of the phenyl substituent on the expected intersystem crossing process. The excited state lifetimes for **2.7** and **2.8** were found to be solvent-dependent (Tables 2.1& 2.2) and are significantly shorter than those in the regular aza-BODIPY and BODIPY compounds[12] probably because of the potential proton-transfer or intra-molecular charge-transfer processes in these compounds. The excited state lifetimes for diradicaloids **2.9** and **2.10** are two orders of magnitude shorter (Table 2.1, Table 2.2 & Figure 2.2) but fit well within known diradicals with thermally populated or ground-state paramagnetic character.[56] More interestingly, the excited state lifetimes in **2.9** and **2.0** are solvent-independent and heavy-atom free. An order of magnitude reduction of the excited states lifetimes in **2.9** and **2.10** at room temperature compared to those observed in aza-BODIPYs **2.7** and **2.8** is clearly indicative of the non-negligible diradical character in **2.9** and **2.10** in agreement with the other experiments discussed.

Table 2.1. Photophysical properties of the target aza-BODIPYs **2.7**, **2.8**, **2.9** and **2.10**

Compound	λ_{max} (abs), nm	ε (10^4 $M^{-1}cm^{-1}$)	λ_{em},nm	φ_f	Lifetime (τs)
2.7	658	7.02	706	0.19	3 ns
2.8	670	5.87	716	0.13	3 ns
2.9	388	7.55	-	-	20 ps
2.10	390	5.65	-	-	20 ps

Table 2.2. Fitting parameters for compounds studied (Fit time slice at 510 nm) Parallel Fitting: $A \xrightarrow{\tau 1} B$ $A \xrightarrow{\tau 2} C$

Compound	Solvent	τ_1	τ_1 weight	τ_2	τ_2 weight
2.7	DCM	321.80 ± 9.96	0.943 ± 0.004		
2.7	DMF	182.5 ± 14.02	0.186 ± 0.008	11.73± 0.99	0.160 ± 0.007
2.9	DCM	6.45 ± 0.19	1.000 ± 0.010		
2.9	DMF	0.40 ± 0.05	0.414 ± 0.026	5.22 ± 0.34	0.586 ± 0.020
2.10	DCM	5.29 ± 0.17	1.000 ± 0.032		
2.10	DMF	0.46 ± 0.04	0.585 ± 0.018	5.67 ± 0.28	0.415 ± 0.018

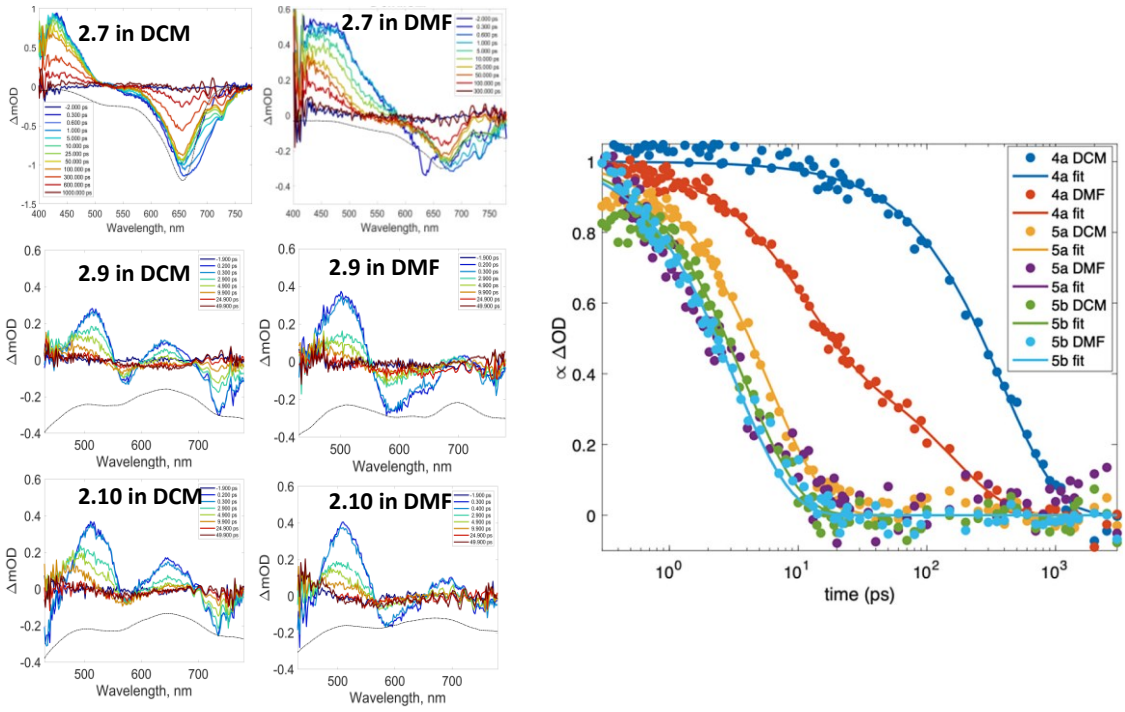


Figure 2.2: Excited state absorption following excitation at 531 nm. Fitted time constants and the wavelengths of the probe and full ΔOD spectra (**4a** = **2.7, 5a** = **2.9, 5b** = **2.10**)

2.3.3 Electrochemistry and Spectroelectrochemistry

The redox properties of compounds **2.7**, **2.9** and **2.10** were investigated using electro- (cyclic voltammetry, CV, and differential pulse voltammetry, DPV) and spectroelectrochemical methods. For BODIPY **2.7,** two oxidation and four reduction processes were observed in the electrochemical experiments (Figure 2.3 & Table 2.3).

The oxidation of **2.7** and **2.8** under spectroelectrochemical setups result in the formation of diradicaloids **2.9** and **2.10** and confirms its two-electron, two-proton nature (Figure 2.4). In particular, the disappearance of the aza-BODIPY transition at 659 (**2.7**) or 670 nm (**2.8**) and the appearance of lower intensity bands at 739 and 803 nm confirms the formation of **2.9** and **2.10** under spectroelectrochemical oxidation. Indeed, the final UV-vis spectra of **2.9** and **2.10** obtained during the oxidation of **2.7** and **2.8** under chemical and spectroelectrochemical oxidation conditions are identical.

The electrochemical experiments on diradicaloids **2.9** and **2.10** were conducted in relatively low-polarity DCM and polar DMF solvents. In both solvents, multiple reduction processes are observed for both compounds confirming the ease of formation of mixed radical-anion species and dianions. The first reduction process in DMF is shifted to a more negative potential for ~200 mV in both diradicaloids (Figures 2.5 and 2.6).

Taking into consideration the clearly reversible nature of the first and the second reduction processes in DMF and DCM, we conducted spectroelectrochemical stepwise two-electron reduction experiments on **2.9** and **2.10** (Figures 2.7 and 2.8). In both cases and in both solvents, nearly identical spectroscopic changes were observed during stepwise electrolysis. The first reduction process is associated with the growth of bands at

~950 and ~1550 nm. These bands disappear during the second reduction process, while intense bands at ~780 and ~1200 nm appear in the spectra. The first one-electron reduction process should generate monoradical species **[2.11]**$^{-\cdot}$ and **[2.12]**$^{-\cdot}$, which have one anionic and one radical terminal oxygen atom (Supporting Information Scheme S1). The low-energy band observed at ~1500 nm can be assigned as the inter-valence charge-transfer (IVCT) transition expected for the mixed-valence compounds and our TDDFT calculations is in agreement with this assignment. We conducted band deconvolution analysis of the NIR region (~1100-1700 nm) in the UV-Vis-NIR spectra of **[2.11]**$^{-\cdot}$ and **[2.12]**$^{-\cdot}$ and estimated H_{ab} value for these compounds as 374 and 336 cm^{-1}, respectively. These values are typical for class II (weakly coupled) mixed-valence compounds in the Robin-Day classification.[103] The second one-electron reduction process should form diamagnetic **[2.13]**$^{2-}$ and **[2.14]**$^{2-}$, which have two anionic terminal oxygen atoms and can be viewed as doubly deprotonated **2.7** and **2.8** compounds .

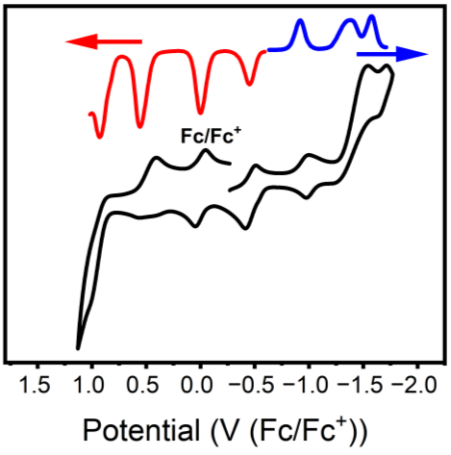


Figure 2.3**:** CV and DPV curves of **2.8** in DCM/0.1M TBAP electrolyte

Table 2.3 Redox properties of the aza-BODIPYs.[a]

Compound	Solvent	Ox_1, V	Ox_2, V	Red_1, V	Red_2, V	Red_3, V	Red_4, V
4a	DCM	0.53	0.88	-0.47	-0.95	-1.40	-1.69
4b	DCM	0.54	0.94	-0.45	-0.94	-1.41	-1.65
5a	DMF	-	-	-0.31	-0.90	-	-
	DCM	-	-	-0.51	-1.01	-	-
5b	DMF	-	-	-0.28	-0.88	-	-
	DCM	-	-	-0.48	-1.00	-	-

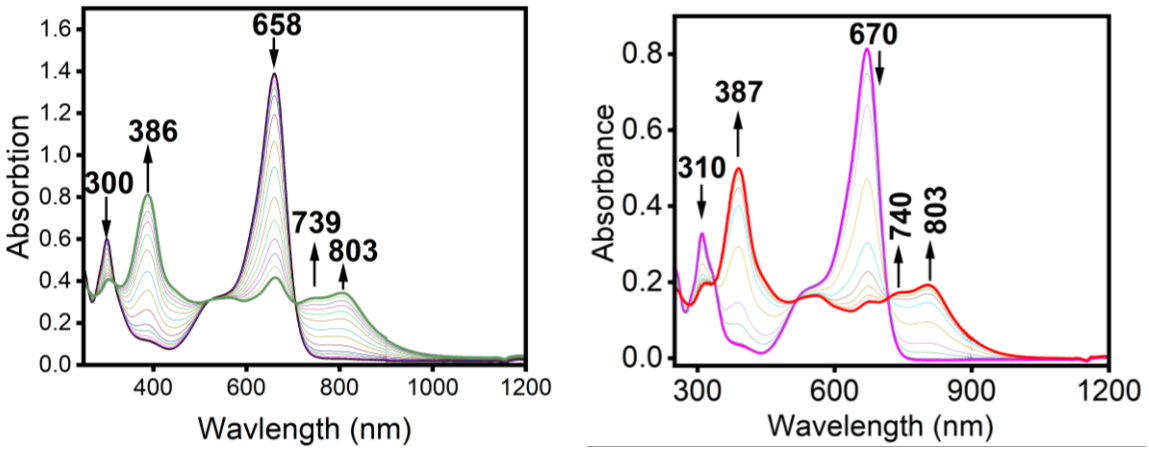


Figure 2.4: UV/Vis/NIR absorption change of **2.7** and **2.8** upon electrochemical oxidation (DCM) using TBAP as electrolyte in a spectroelectrochmical condition. Arrows show spectra changes with increasing positive potential.

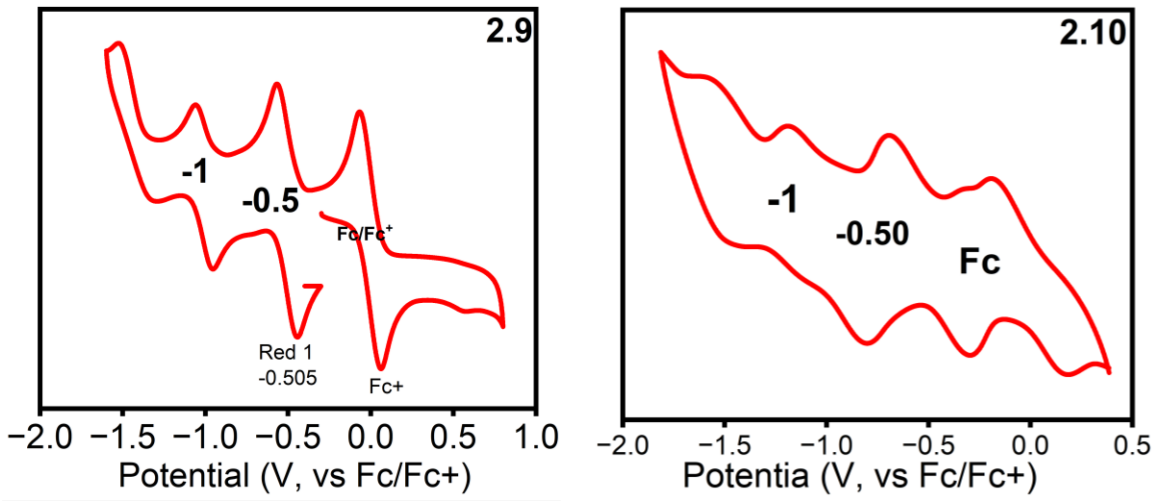


Figure 2.5: Cyclic voltammograms of **2.9** and **2.10** in dry DCM.

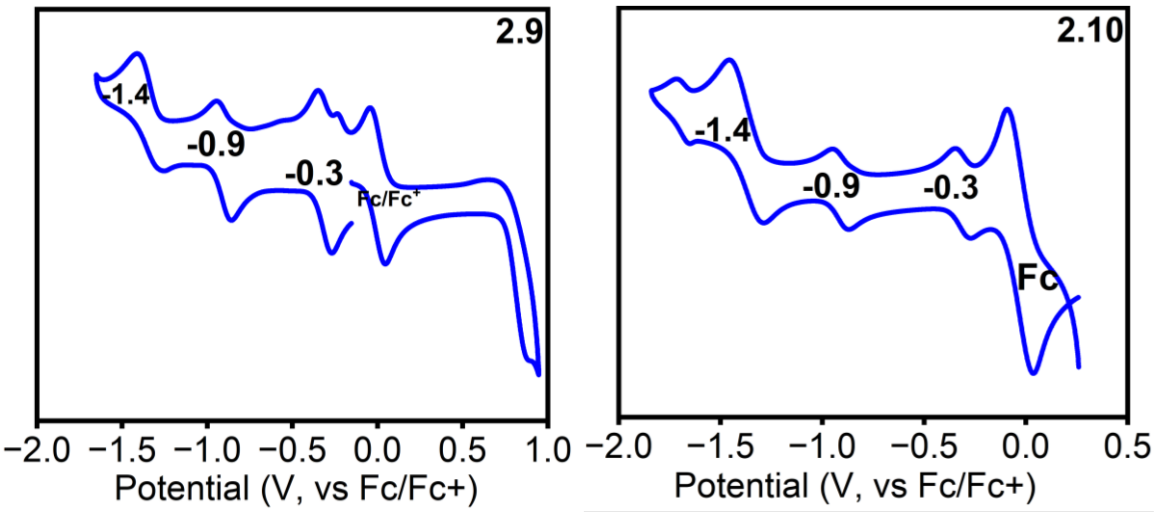


Figure 2.6: Cyclic voltammograms of **2.9** and **2.10** in dry DMF.

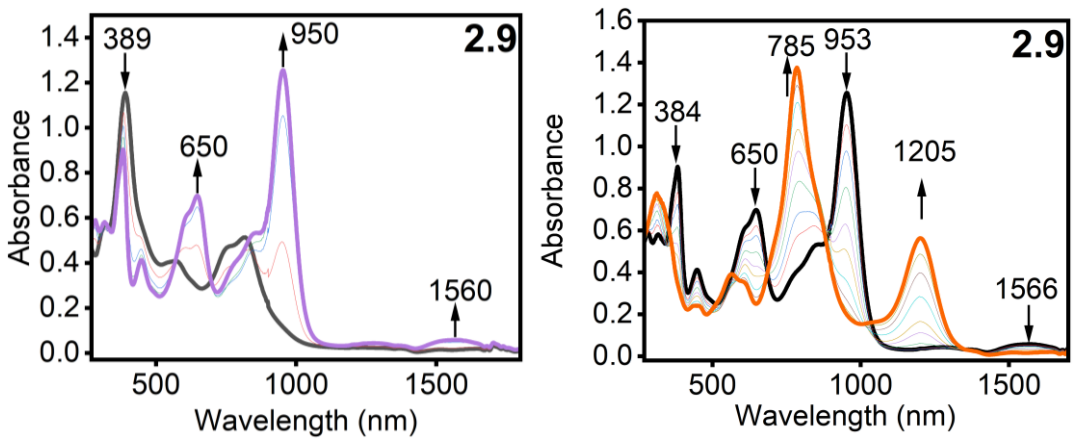


Figure 2.7**:** UV/Vis/NIR absorption change of aza-BODIPY **2.9** upon electrochemical Reduction (1st and 2nd) in a spectroelectrochmical setup (DMF) using TBAP as electrolyte. Arrows show spectra changes with increasing negative potential.

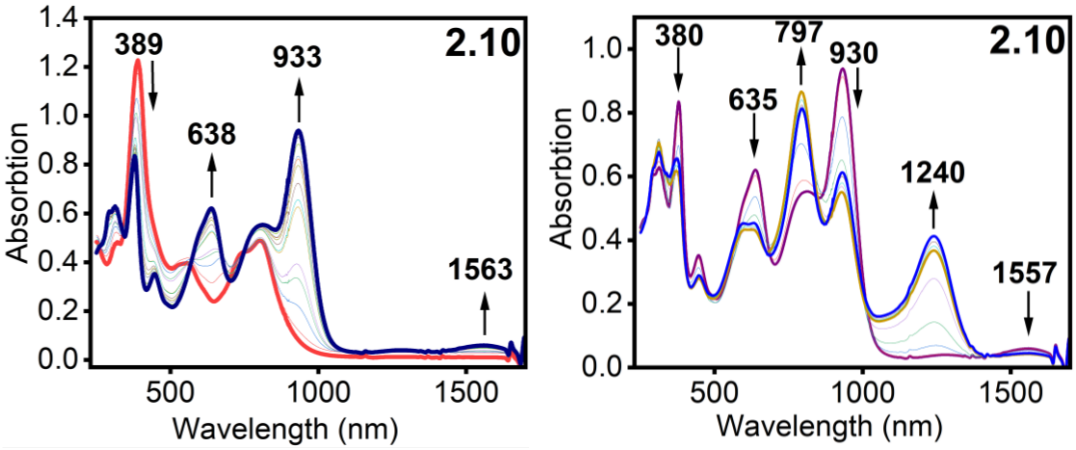


Figure 2.8**:** UV/Vis/NIR absorption change of aza-BODIPY **2.10** upon electrochemical Reduction (1st and 2nd) in a spectroelectrochmical setup (DCM) using TBAP as electrolyte. Arrows show spectra changes with increasing negative potential

2.3.4. Magnetic Studies

2.3.4.1 Variable Temperature Proton NMR

The variable-temperature ^{1}H NMR spectra of **2.9** and **2.10** were collected in DCM, THF, and DMF (Figures 2.9 – 2.13). In DCM and THF as the solvents, the initial broad signals associated with the pyrrolic and quinone *meta*-protons of both diradicaloids **2.9** and **2.10** become narrower with decreasing temperature. It should be noted that quinone *meta*-protons and *tert*-butyl groups in **2.9** and **2.10** are non-equivalent and give two different signals in their ^{1}H NMR spectra. Such behavior is clearly indicative of the rotational hindrance of the quinoidal fragments in **2.9** and **2.10**. In DCM and THF solvents, as temperature decreases the ^{1}H NMR signals of both diradicaloids become narrower and well-resolved. In the case of DMF solvent, the *meta*-protons signals of quinone fragments in diradicaloid **2.10** are significantly broader at room temperature but resolvable, while the same signals in **2.9** are not observable at room temperature until lower temperatures. Thus, ^{1}H NMR spectra of **2.9** and **2.10** are indicative of the presence of the paramagnetic spin density in these compounds. Since NMR linewidths reduce with decrease of the temperature in all solvents, one may suspect the diamagnetic ground state of compounds **2.9** and **2.10** in the solution. The observed spin density can be associated either with a thermally populated triplet excited state or a thermally populated open-shell diradicaloid state. More interestingly, NMR data in DMF suggest significantly stronger paramagnetism (i.e. the presence of the unpaired electron density at quinoidal fragments in **2.9** and **2.10**) in this solvent compared to THF and DCM. To the best of our

knowledge, this observation is the first report on the solvent-dependent diradicaloid character influenced by solvent polarity

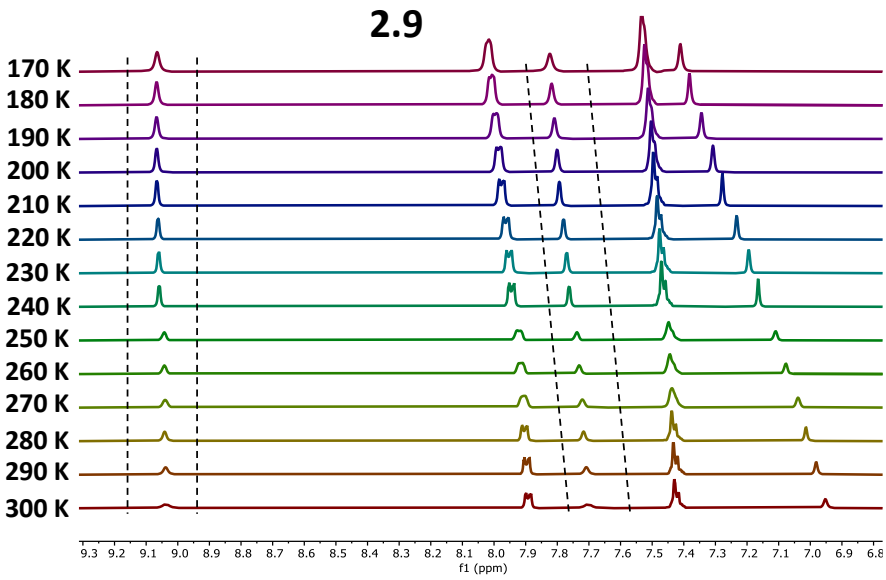


Figure 2.9: Variable-temperature ^{1}H NMR spectrum of **2.9** in THF

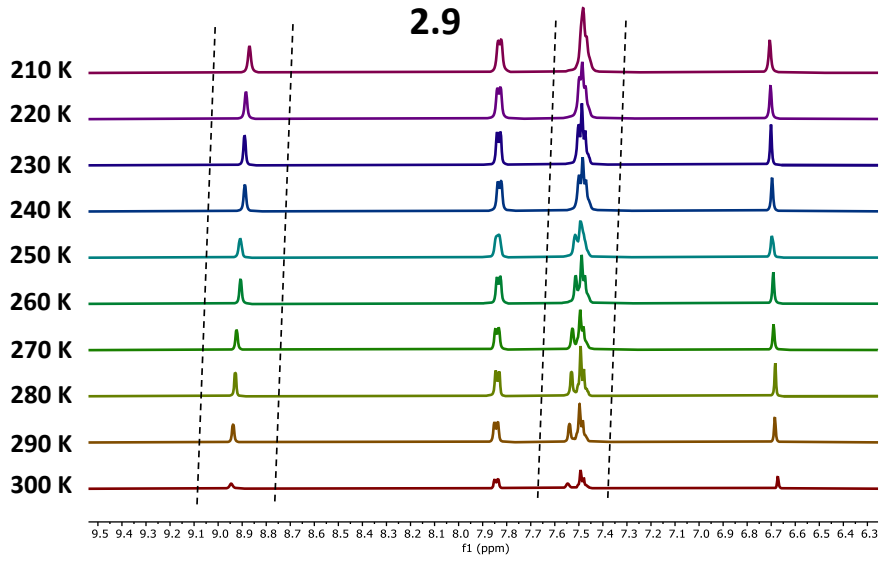


Figure 2.10: Variable-temperature ^{1}H NMR spectrum of **2.9** in DCM

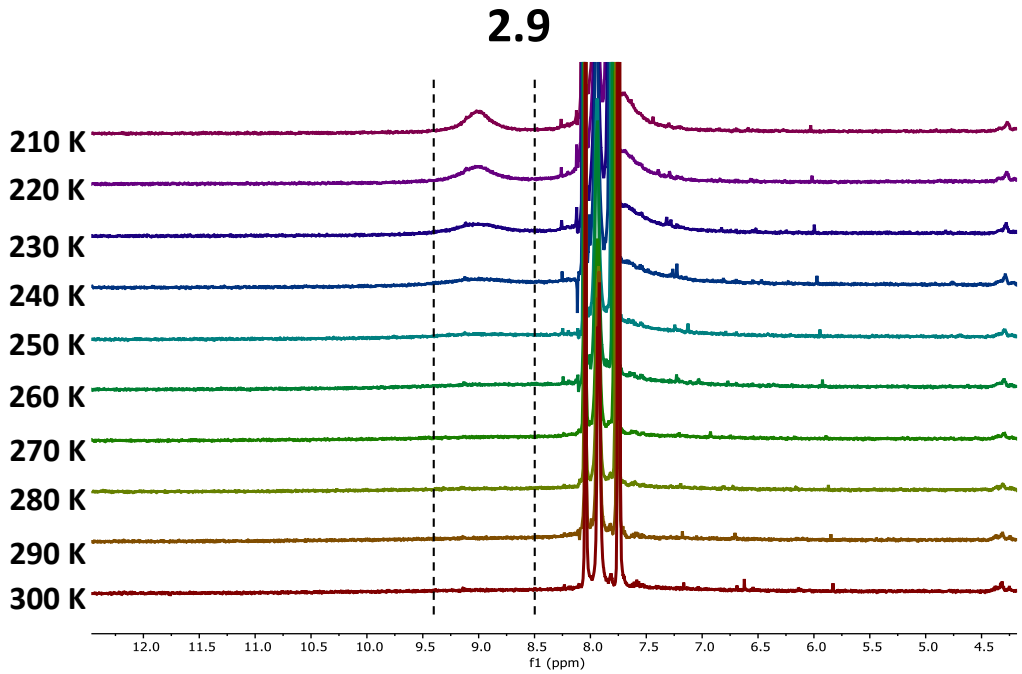


Figure 2.11: Variable-temperature ^{1}H NMR spectrum of **2.9** in DMF

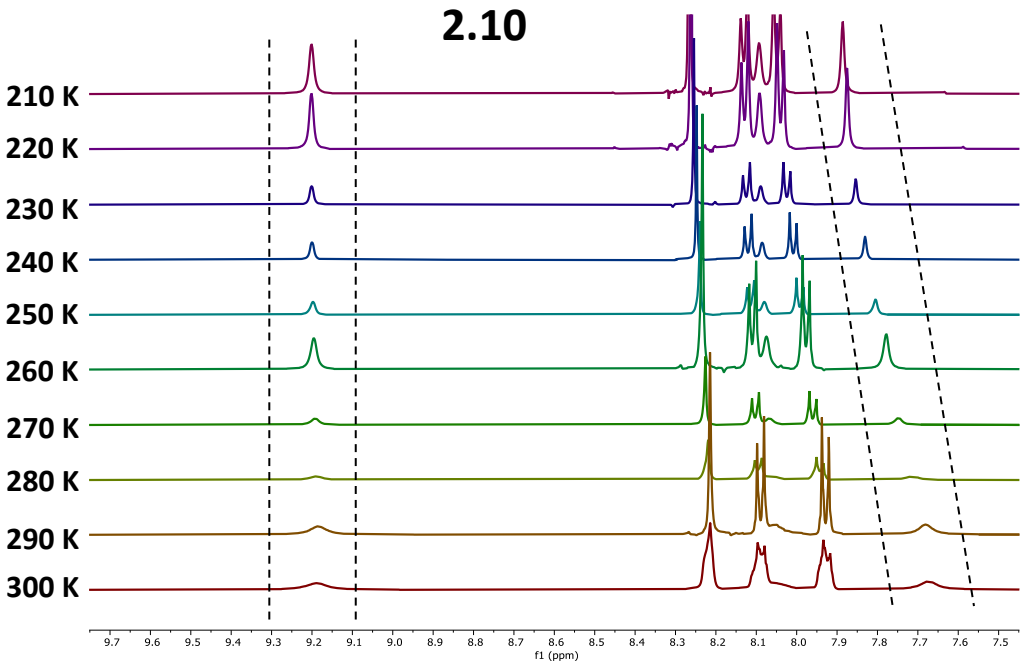


Figure 2.12: Variable-temperature ^{1}H NMR spectrum of **2.10** in DMF

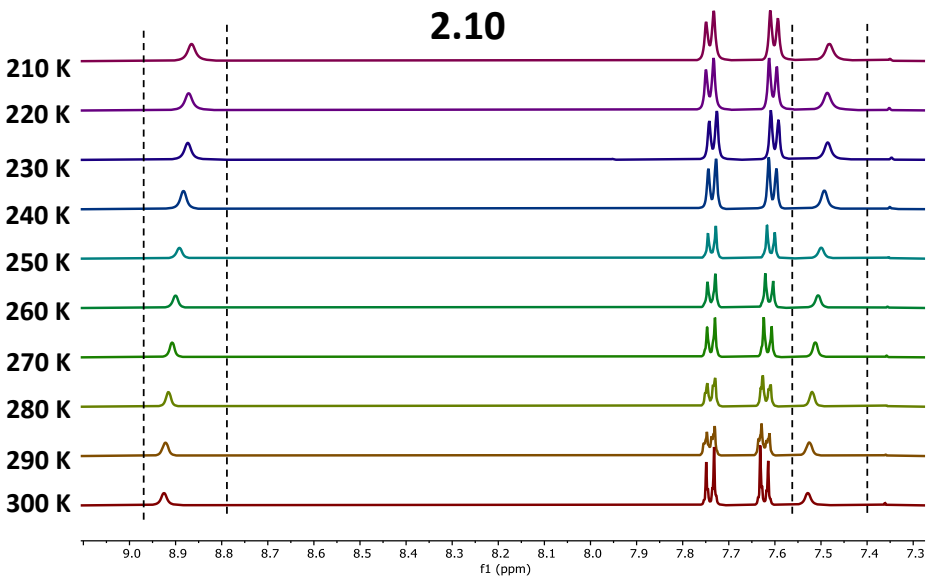


Figure 2.13: Variable-temperature ^{1}H NMR spectrum of **2.10** in DCM

2.3.3.2 Variable Temperature EPR

In agreement with the ^{1}H NMR data, we observed room-temperature isotropic EPR signals in **2.9** and **2.10** in DCM and the solid-state samples. The g-value of this isotropic signal is close to that of a free electron in both **2.9** and **2.10** (Figures 2.14 & 2.15). The intensity of this signal decreases with the decreasing temperature in both solid state and DCM/Toluene solution of **2.9**. Thus, both VT ^{1}H NMR and EPR data indicate a diamagnetic ground state with accessible triplet excited state in **2.9** and **2.10**. In more polar THF and DMF, no EPR signal was observed between room temperature and the freezing point of the solvent (Figure 2.16 & 2.17). This behavior is not surprising as both THF and DMF strongly absorb microwave irradiation in the liquid phase when the regular EPR cavity is used in the experiment.[104] The lack of $M_s \pm 2$ EPR signal in the EPR spectra at 2K for frozen DMF solutions of **2.9** and **2.10** (and the presence of the

isotropic signal at this temperature) is indicative of the diamagnetic ground state with open-shell diradicaloid singlet state being in close proximity.

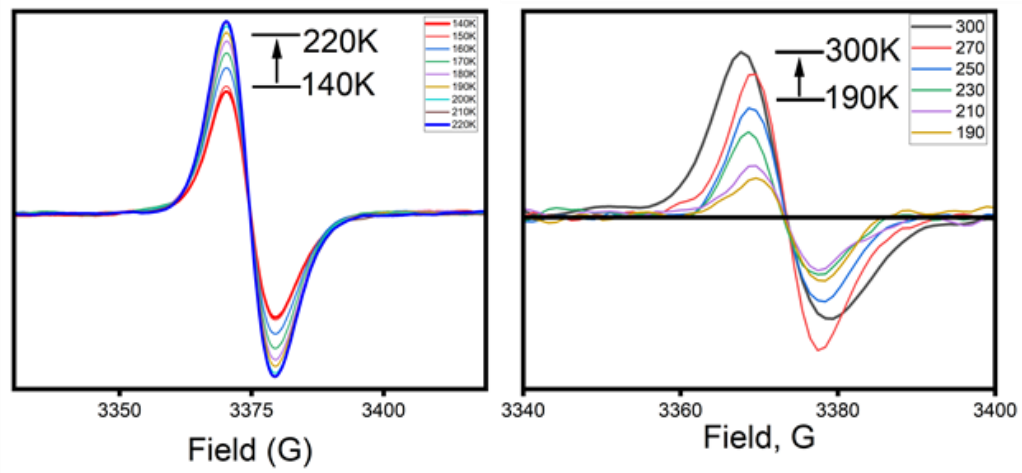


Figure 2.14: Variable-temperature EPR spectra of **2.9** in a solid state (left) and DCM/toluene solution (right).

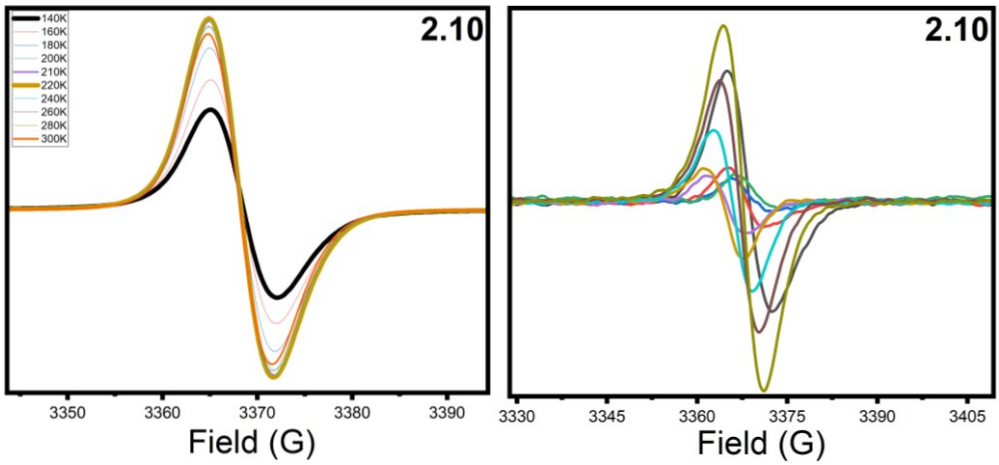


Figure 2.15: Variable-temperature EPR spectra of **2.10** in a solid state (left) and DCM/toluene solution (right).

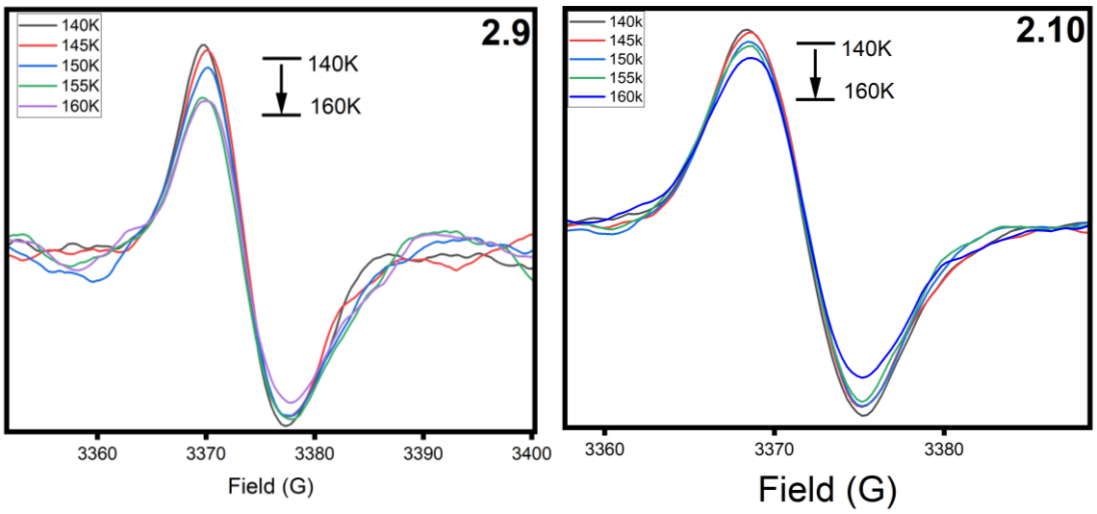


Figure 2.16: Variable-temperature EPR spectra of **2.9** (left) and **2.10** (right) in THF.

2.3.3.3 Variable Temperature SQUID Magnetometry

The magnetism on powdered samples of **2.9** and **2.10** was further probed by SQUID magnetometry measurement. We ensure the powder samples are tightly packed and well-sealed to avoid oxygen. The molecular susceptibility ($\chi_M T$) of both samples gradually increase linearly as temperature increases from 2 and 320 K (Figure 2.18), which is indicative of the thermal population of the triplet state or open-shell diradicaloid state, which agrees well with the EPR and ^{1}H NMR data. The magnetometry data fit well to the Bleaney-Bowers equation giving $\Delta E_{S\text{-}T}$ values of 1.107 kcal/mol for **2.9** and 1.1072 kcal/mol for **2.10**), which are virtually identical for both samples confirming that bromine atoms has little to no effect on the singlet-triplet energy gap or magnetism of **2.10**. Again, the values of the singlet-triplet gap have a reasonable magnitude of the interaction between two centers with partial radical character.[53]

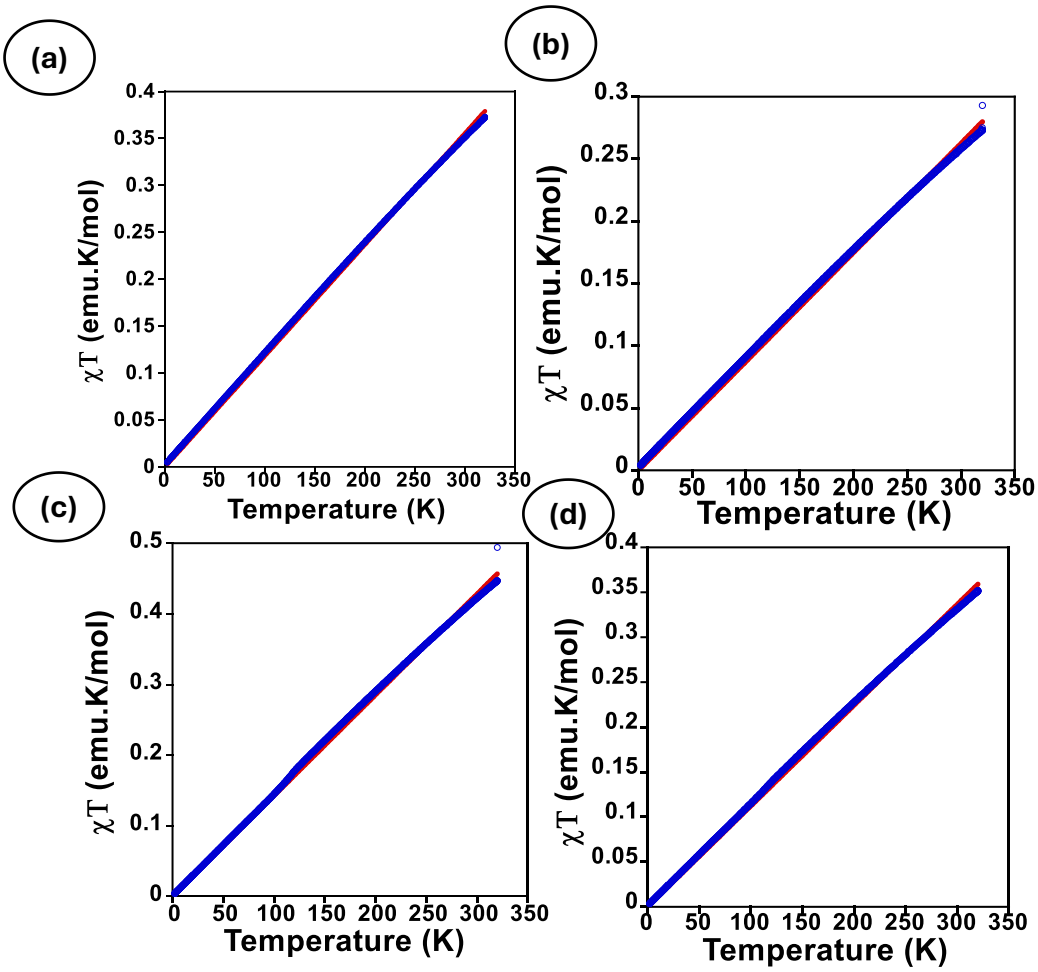


Figure 2.18: SQUID measurements from 0-300K in polycarbonate capsules of: (a) **2.9** at 3000 Oe (b) **2.9** at 5000 Oe **(c) 2.10** at 3000 Oe (d) **2.10** at 5000 Oe.

2.3.5. X-Ray Crystallographic Studies

The X-ray structures of **2.5** and **2.9** (as DMF solvate) were obtained and shown in Figure 7). The crystals of **2.5** were obtained from slow evaporation of *n*-butanol solution of compound **2.5**. Good crystals of **2.9** were obtained by slow evaporation of DMF solution of **2.9**. The structure of **2.9** was elucidated at room temperature as well as -50 ºC and -173 ºC. We focused on the temperature dependency for C=O and C=C bonds in

quinoidal fragments. First, similar to the recently published structure of BODIPY-quinone-based diradicaloid,[85] the torsion angles between two quinone fragments and the BODIPY core in **2.9** are slightly different at all three temperatures (Table 2.4). The C=O bond distances are slightly longer than those expected for classic carbonyl groups and quinones as well as those observed for the BODIPY analogue of **2.9**. However, they all have double-bond rather than single-bond character. The C-C bond distances in quinoidal fragment alternate; however, again, C=C bond distances are slightly longer than those expected for quinones. The C=C bond distance between two carbon atoms that connect quinoidal fragment with aza-BODIPY core in **2.9** (~1.4 Å) is significantly shorter than that in **2.5** (~1.47 Å). There were no systematic trends observed for C-C and C=C bond distances in **2.9** as a function of temperature (Table 2.4). We were expecting elongation of quinoidal C=O and C=C bond lengths as temperature increases from -173 °C to 25 °C, but that was not what we observed experimentally. However, observed bond distances imply some diradical character in this compound. In agreement with this assignment, a clear carbonyl C=O peak is present in the IR spectra of **2.9** (see appendix for Figure 2.58) confirming the diradicaloid nature of this compound in agreement with X-Ray, variable temperature NMR, EPR and SQUID magnetometry.

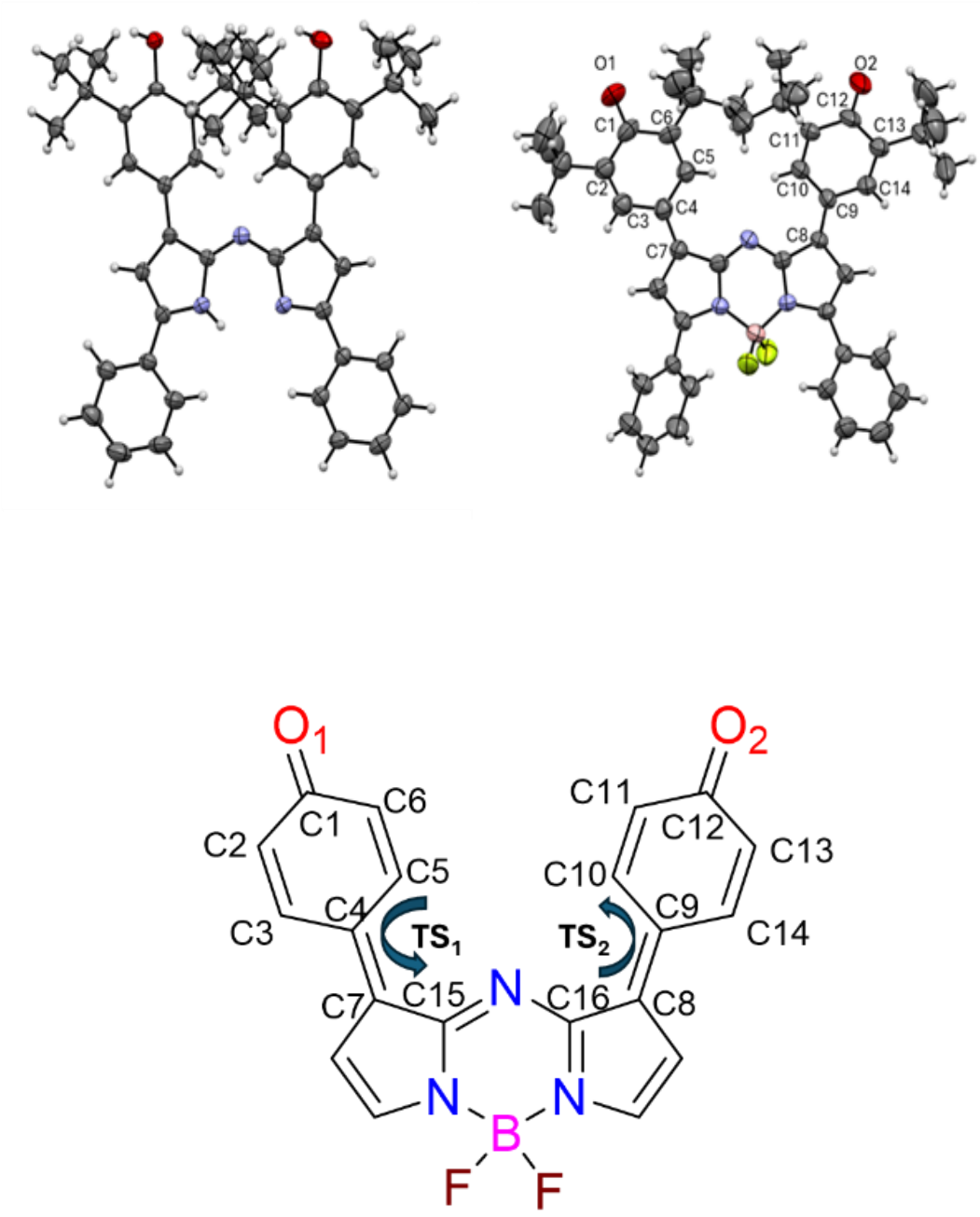


Figure 2.19: X-ray crystal structures of **2.5** (left) and **2.9** (right) with schematic representation below.

Table 2.4: Selected bond distances observed in the variable-temperature XRD experiments for **2.9**

Bond distance/T	25 °C	-50 °C	-173 °C
O1-C1	1.240(5)	1.231(4)	1.241(8)
O2-C12	1.232(4)	1.238(4)	1.250(8)
C1-C2	1.472(6)	1.482(5)	1.495(9)
C1-C6	1.480(5)	1.489(5)	1.484(9)
C2-C3	1.372(5)	1.339(5)	1.357(9)
C3-C4	1.452(5)	1.447(5)	1.439(9)
C4-C5	1.441(5)	1.445(5)	1.446(9)
C4-C7	1.393(5)	1.392(5)	1.391(9)
C5-C6	1.349(5)	1.351(5)	1.373(9)
C8-C9	1.392(5)	1.385(5)	1.399(9)
C9-C10	1.433(5)	1.432(5)	1.434(9)
C9-C14	1.440(5)	1.449(5)	1.444(9)
C10-C11	1.352(5)	1.355(5)	1.367(8)
C11-C12	1.483(5)	1.496(5)	1.486(9)
C12-C13	1.480(6)	1.479(5)	1.474(9)
C13-C14	1.348(5)	1.349(5)	1.355(9)
Torsion Angle TS1	8.55°	14.41°	9.27°
Torsion Angle TS2	14.51°	9.60°	14.36°

2.3.6. DFT and TDDFT calculations

Taking into consideration close similarities in spectroscopy between brominated and non-brominated series of compounds, we only conducted extensive DFT and TDDFT calculations on **2.7**, **2.9**, **[2.11]**$^{\bullet-}$, and **[2.13]**$^{2-}$. In the case of **2.7** and **[2.13]**$^{2-}$, only diamagnetic ground states were considered. Similarly, only the doublet ground state was considered for **[2.11]**$^{\bullet-}$. Three states were considered for **2.9**: (i) diamagnetic closed-shell singlet (**2.9CS**), (ii) open-shell singlet diradicaloid (**2.9OS**), and (iii) open-shell triplet (**2.9TS**).

The DFT-predicted energy diagrams are shown in Figure 2.20, selected frontier molecular orbitals (Figure 2.21), and percentage compositions (Figures 2.23 – 2.26). Independent of the used exchange-correlation functional, the triplet excited state was found to be several kcal/mol above the open- and closed-shell singlet states. Both the closed-shell singlet state and the open-shell diradical state in **2.9** were found in very close energies to each other (Table 2.5). Thus, within the expected energy errors for DFT calculations, the diamagnetic ground state in **2.9** and **2.10** was confirmed by the DFT calculations. The DFT calculation for open-shell singlet diradicaloid is indicative of a large delocalization of the spin density over the whole molecule with predicted spin density at the oxygen atoms ranging only between 0.06 and 0.22 e^- depending on the used exchange-correlation functional (Table 2.5 and Figure 2.21). The DFT-predicted diradical character (y_0) for **2.9OS** was calculated using procedures reported earlier[56,90,91] and values are summarized for all exchange-correlation functionals in Table 2.5. Again, a

clear diradicaloid nature can be seen for **2.9**, which is in agreement with the experimental data.

The HOMO and the LUMO in **2.7** and **[2.13]$^{2-}$** are typical for BODIPYs and aza-BODIPYs.[12] The HOMO has an ample contribution from the pyrrolic α- and β-carbon atoms, and the LUMO has a large contribution from the nitrogen atoms. Two-electron oxidation of **2.7** to **2.9** result is the electronic structure close to that discussed earlier for MB-DIPYs.[92-96] Indeed, the HOMO in open- and closed-shell singlets of **2.9** has a significant contribution from the nitrogen atoms, while the LUMO has a significant contribution from the pyrrolic α- and β-carbon atoms (Figures 2.21). More interesting, the HOMO-2 and HOMO-3 in **2.9OS** and **2.9CS** are localized on the quinone fragments, and the HOMO-4 and HOMO-5 are localized on the phenyl substituents, which opens a pathway for potential intra-ligand charge-transfer-like (ILCT) transitions in these systems. In contrast, the DFT-predicted HOMO and LUMO in **2.9TS** resemble those in normal aza-BODIPYs and BODIPYs (Figure 2.21).

TDDFT calculations for all compounds are in good agreement with the experimental data (Figure 2.22). In particular, they correctly predict the redshift of the most intense low-energy band in **2.9**, **[2.11]$^{-\cdot}$**, **[2.13]$^{2-}$** series, the energy of the intervalence charge transfer (IVCT) band in the mixed-valence **[2.11]$^{-\cdot}$**, and the red-shift as well as the significant drop in intensity of the aza-BODIPY's low-energy band upon oxidation of **2.7** to **2.9**. Interestingly, the TDDFT-predicted UV-Vis spectra for **2.9OS**, **2.9TS**, and **2.9CS** are fairly similar, which probably reflects their close energies and electronic structures. In the case of parent **2.7**, the lowest energy transition belongs to

almost pure HOMO → LUMO single-electron excitation and this is usual for BODIPY and aza-BODIPY systems.[12]

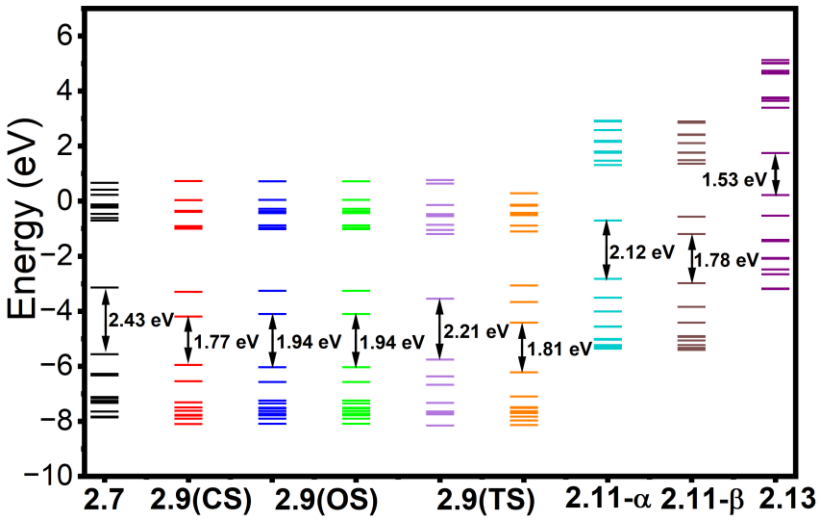


Figure 2.20: DFT-predicted energy diagram for the frontier MOs in aza-BODIPYs **2.7, 2.9(CS), 2.9(OS)-α, 2.9(OS)-β, 2.9(TS)-α**, **2.9(TS)-β, 2.11-α, 2.11-β** and **2.13**.

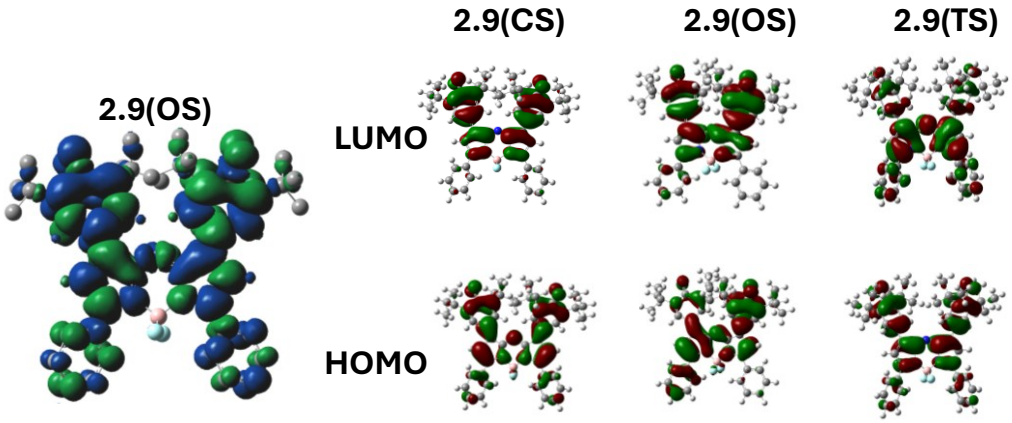


Figure 2.21: DFT-predicted (M06 exchange-correlation functional) total spin density for **2.9(OS)** (left), and HOMO/LUMO pairs for **2.9(CS), 2.9(OS),** and **2.9(TS)**.

Table 2.5. DFT-predicted relative energies (kcal/mol), spin densities at oxygen atoms, and diradical character coefficients for **2.9CS**, **2.9OS**, and **2.9TS**. ECF = exchange-correlation functional; b = spin density at the oxygen atoms provided in parentheses.

ECF[a]	**2.9CS**	**2.9OS**[b]	**2.9TS**[b]	y_0
TPSSh	0.005	0 (0.06)	4.99 (0.29)	0.054
M06	0.003	0 (0.03)	6.42 (0.27)	0.028
CAM-B3LYP	1.13	0 (0.21)	6.11 (0.31)	0.135
wB97X	1.76	0 (0.22)	7.97 (0.31)	0.185

The HOMO → LUMO single-electron excitation has small phenol → aza-BODIPY core intra-ligand charge transfer (ILCT) character, which might be responsible for the decreased fluorescence quantum yield and shorter than usual excited state lifetime in **2.7** and **2.8** (Figures 2.22 – 2.23, and see appendix for Tables 2.6). TDDFT calculations also predicted two unusual excited states around 500 nm (excited states 2 and 3, see appendix for Table 2.6). These are dominated by the HOMO-1 → LUMO and HOMO-2 → LUMO single-electron transitions, respectively, and have substantial phenol → aza-BODIPY core ILCT character. Deprotonation of the **2.7** and **2.8** increases the donor ability of the phenol fragments and thus, it was not surprising to see that the ILCT process contributes more to the first and second excited states of **[2.13]**$^{2-}$ (Figures 2.22 & 2.24 and see appendix for Tables 2.61). Indeed, these are dominated by the HOMO → LUMO and HOMO-1 → LUMO single-electron transitions that have a significant phenolate → aza-BODIPY core ILCT character.

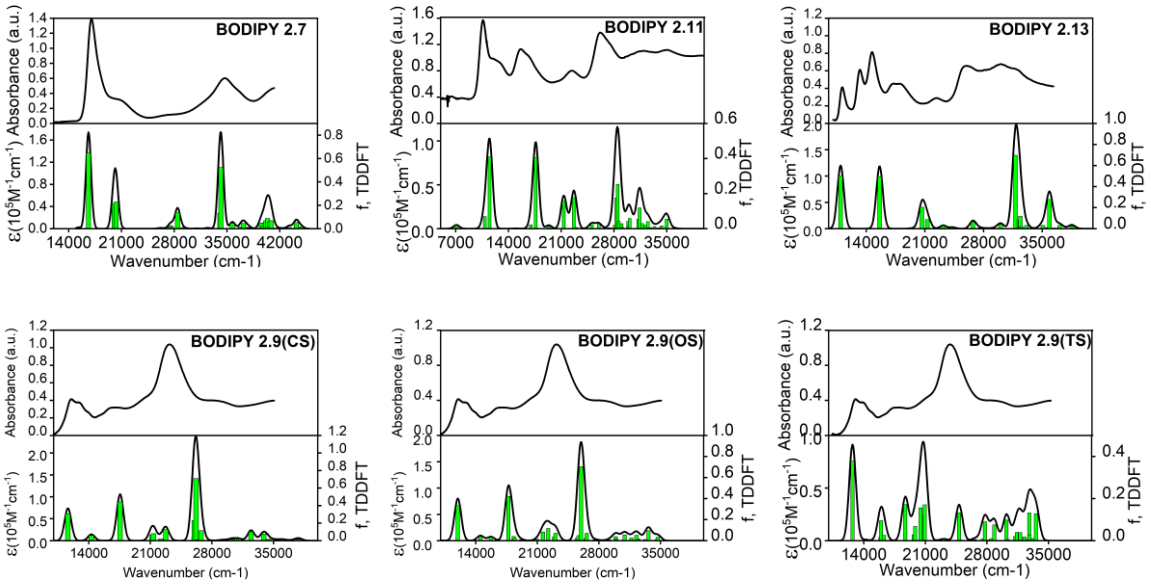


Figure 2.22: Experimental versus TDDFT-predicted (M06 exchange-correlation functional) UV-Vis spectra of **2.7**, **2.9**, **[2.11]**$^{-\cdot}$, and **[2.13]**$^{2-}$.

Single-electron reduction of either **2.9** or **2.10** leads to the formation of the mixed-valence **[2.11]**$^{-\cdot}$ or **[2.12]**$^{-\cdot}$ systems with characteristic IVCT band observed ~1550 nm. TDDFT calculations confirm that this excited state has substantial IVCT character (excited state 1 predicted at ~1400 nm (Figures 2.22 & 2.25). According to TDDFT calculations, in the low-energy region, the UV-Vis spectrum of **[2.11]**$^{-\cdot}$ is dominated by the excited states 3 (870 nm; f = 0.41) and 8 (568 nm; f = 0.40). Both excited states have substantial ILCT (phenoxy → aza-BODIPY core) character (Figures 2.22 and 2.25, see appendix for Table 2.6).

In the case of the lowest-energy **2.9OS** diradicaloid, TDDFT calculations predict that the UV-vis spectrum should be dominated by three excited states. The lowest energy excited state of high intensity (836 nm; f = 0.330) is dominated by the $HOMO_{\alpha,\beta}$ →

$LUMO_{\alpha,\beta}$ single-electron transitions and has a small ILCT contribution (Figures 2.22 and 2.26, see appendix for Table 2.6). The second excited state (excited state 8 predicted at 571 nm; $f = 0.374$) is dominated by the $HOMO_{\alpha,\beta} \rightarrow LUMO{+}1_{\alpha,\beta}$ (53%) and $HOMO{-}1_{\alpha,\beta} \rightarrow LUMO_{\alpha,\beta}$ (18%) single-electron transitions. The third one has a significantly more complex structure and was predicted at 387nm ($f = 0.603$) see Figure 2.22, and appendix for Table 2.6. In addition, there are two weaker transitions between 800 and 600 nm predicted by TDDFT calculations. The first one (predicted at 661 nm) is dominated by the $HOMO{-}1_{\alpha,\beta} \rightarrow LUMO_{\alpha,\beta}$ (73%) single-electron transitions. The second one (predicted at 647 nm) is dominated by the $HOMO_{\alpha,\beta} \rightarrow LUMO{+}1_{\alpha,\beta}$ (58%) and $HOMO{-}1_{\alpha,\beta} \rightarrow LUMO_{\alpha,\beta}$ (37%) single-electron transitions. For **2.9CS** species, TDDFT predicts very similar excited states to that of **2.9OS**. According to TDDFT data, the low-energy envelope (500-900 nm) should be dominated by two excited states. The first state (excited state 1, f = 0.306) is predicted at 860 nm and is pure HOMO → LUMO transition and the second one (excited state 5, $f = 0.4397$) is predicted at 570 nm and is dominated by the HOMO → LUMO+1 single-electron excitation. Two weak transitions were also predicted in this region. The first one (669 nm, $f = 0.06$) is dominated by the HOMO-1 → LUMO single-electron excitations and the second transition (622 nm, $f = 0.001$) is dominated by the HOMO-2 → LUMO single-electron excitations. Finally, similar to the TDDFT data on **2.9OS**, TDDFT calculations on **2.9CS** predict a very strong transition located at 382 nm ($f = 0.708$). This excited state is predominantly formed by the HOMO-11 → LUMO single-electron excitations. Overall, TDDFT predictions suggest that the low-energy region (600-900 nm) in the UV-Vis-NIR spectra

of **2.9** and **2.10** has two closely spaced bands originating from two different excited states.

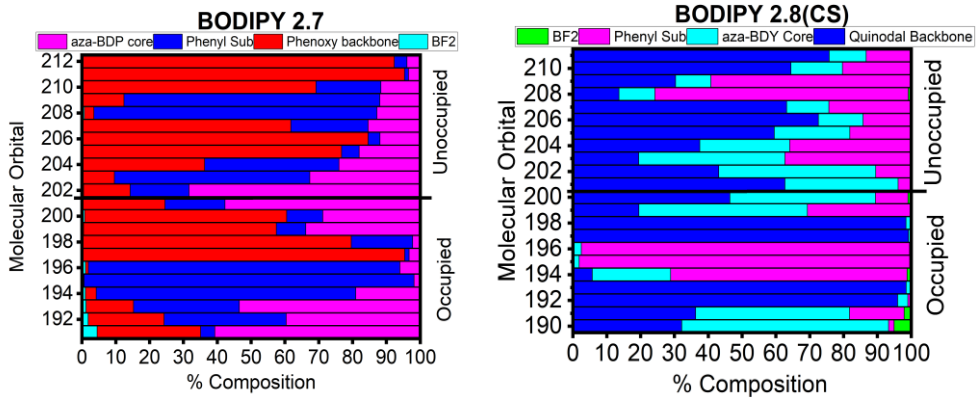


Figure 2.23: DFT-predicted compositions of frontier orbitals for aza-BODIPYs **2.7** and **2.9(CS)**. Abbreviation: "aza-BDP" = aza-BODIPY.

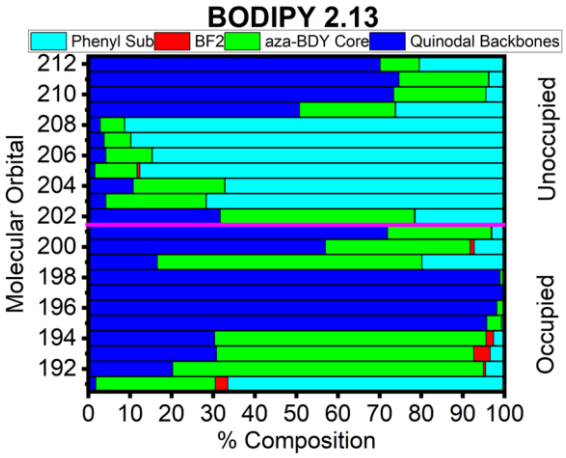


Figure 2.24: DFT-predicted compositions of frontier orbitals for aza-BODIPY Dianion $[\mathbf{2.13}]^{2-}$. Abbreviation: "aza-BDP" = aza-BODIPY.

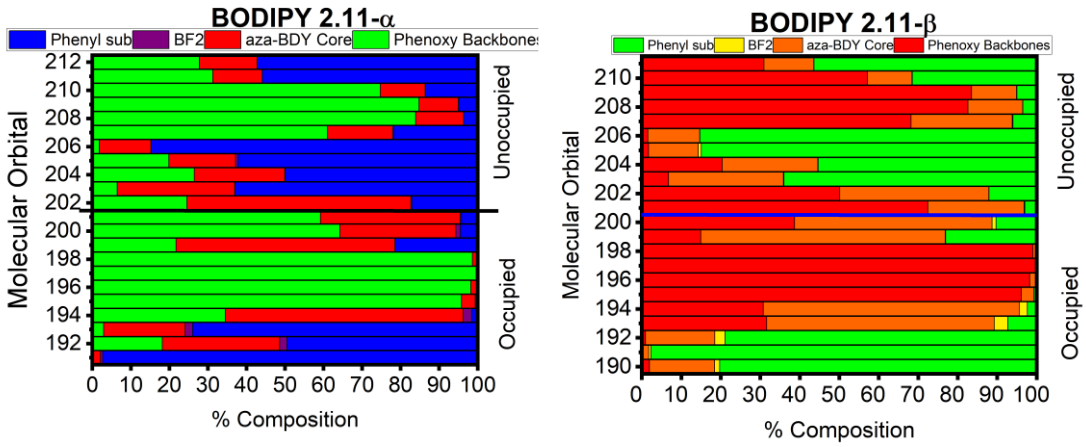


Figure 2.25: DFT-predicted compositions of frontier orbitals for aza-BODIPY Mixed Valence Species [**2.11**]$^{\cdot-}$. Abbreviation: "aza-BDP" = aza-BODIPY.

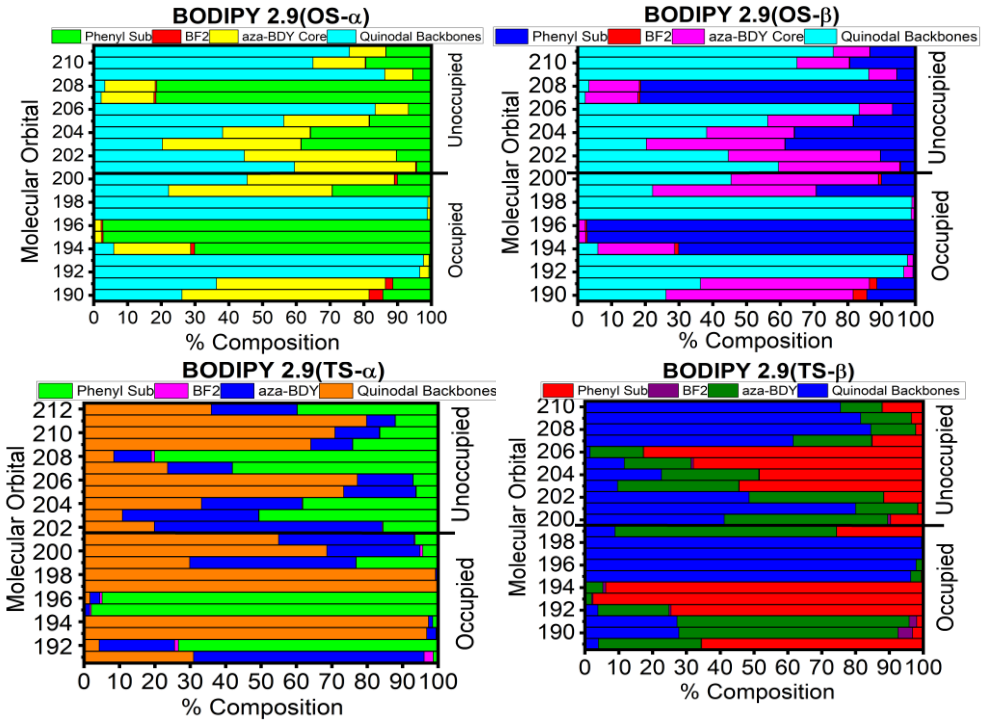


Figure 2.26: DFT-predicted compositions of frontier orbitals for aza-BODIPY Diradical **2.9** in singlet **2.9(OS)** and triplet **2.9(TS)** states. Abbreviation: "aza-BDP" = aza-BODIPY.

2.4 Conclusions

We report on the preparation and characterization of two diradicaloid systems (**2.9** and **2.10**) that originated from the oxidation of the 1,7-(4-(2,6-di-*tert*-butyl)phenol)-substituted aza-BODIPY cores **2.7** and **2.8**. The aza-BODIPY diradicaloids were characterized by a large array of experimental and computational methods. The diamagnetic closed-shell state was postulated as the ground state in solution and a solid state with the substantial thermal population originating from both open-shell diradical and open-shell triplet state observed at room temperature. Transient absorption spectroscopy indicates fast (~20 ps) excited state deactivation pathways associated with the target compounds' diradical character in solution at room temperature. The presence of two bromine atoms in **2.10** does not influence any photophysical properties in the phenolic or diradicaloid systems to a significant extent. The diradicaloids **2.9** and **2.10** could be stepwise reduced to the mixed-valence radical-anions $\mathbf{[2.11]}^{-\cdot}$ and $\mathbf{[2.12]}^{-\cdot}$, respectively, and dianion states $\mathbf{[2.13]}^{2-}$ and $\mathbf{[2.14]}^{2-}$ upon consequent single-electron reductions. Similarly, deprotonated 1,7-(4-(2,6-di-*tert*-butyl)phenol)-substituted aza-BODIPYs $\mathbf{[2.13]}^{2-}$ and $\mathbf{[2.14]}^{2-}$ can be oxidized to the diradicaloid forms **2.9** and **2.10** under spectroelectrochemical conditions. Both mixed-valence and dianionic forms have an intense absorption in the NIR region. Density Functional Theory (DFT) and time-dependent DFT (TDDFT) calculations were used to explain the transformations in the UV-Vis-NIR spectra of all target compounds.

2.5 Experimental

2.5.1 General Materials and Methods

All solvents were purchased from commercial sources and purified with the use of standard procedures. All glassware was rigorously dried overnight at 160 °C and cooled under vacuum prior to use. All reagents and starting materials were purchased from commercial vendors and used without further purification. Column chromatography was performed on silica gel (Dynamic Adsorbents, Inc, 63-200 μm). Deuterated solvents were purchased from Cambridge Isotope Laboratories and used as received.

Electrochemistry. Cyclic voltametric measurements were made using a three-electrode system consisting of a glassy carbon or platinum working electrode, a platinum auxiliary electrode, and either a saturated calomel reference electrode (SCE) separated from the bulk of the solution by a fritted solution-filled glass bridge of low porosity or an Ag/AgCl wire pseudo reference electrode. Ferrocene (Fc) was used as an internal standard for the studied complexes, and the reported potentials were corrected to the Fc/Fc^+ couple. For consistency, all potentials and figures in this work are reported vs the Fc/Fc^+ redox couple. All electrochemical experiments were conducted in either dichloromethane (DCM), *N*, *N*-dimethylformamide (DMF) and 0.1 M tetrabutylammonium perchlorate (TBAP) or 0.05 M tetrabutylammonium tetrakis (pentafluoro phenyl) borate (TFAB) system.

Spectroelectrochemistry. Spectroelectrochemical experiments were performed using either a Jasco V-770 UV–vis–NIR spectrophotometer in tandem with a CH Instruments electrochemical analyzer, which was operated using the bulk electrolysis mode or a

Hewlett-Packard model 8453 diode array paired with an EG&G PAR Model 173 potentiostat/galvanostat used to apply a controlled potential. The data were collected using a custom-made 1 mm cell, a platinum mesh working electrode, a platinum auxiliary electrode, and either a saturated calomel reference electrode (SCE) separated from the bulk of the solution by a fritted solution-filled glass bridge of low porosity or a Ag/AgCl wire pseudo reference electrode. Spectroelectrochemical solutions consisted of 0.1, 0.15, or 0.3 M solutions of either TBAP or TFAB in DCM and DMF.

NMR. NMR spectra were recorded on a 500 MHz Brucker III spectrometer. All chemical shifts (δ) are listed in parts per million (ppm) and are referenced to solvent. Spectra are referenced internally due to residual proton solvent resonances.

SQUID. Magnetic studies were carried out using 7-Tesla Quantum Design SQUID magnetometer at the applied magnetic fields H = 1000, 3000 and 5000 Oe and at temperature T = 2 – 320 K. The empty plastic capsule exhibited diamagnetism, and its magnetic moment was measured for correction. For both samples in powder form, primary correction for diamagnetism is implemented by point-by-point background subtraction, together with Pascal constants correction.

Single Crystal X-ray Crystallographic Analysis. Single crystals of **2.5** were obtained by slow cooling of a hot butanol solution. Single crystals of **2.9** were obtained by slow evaporation of the saturated DMF solution. Crystalline samples were mounted on a 150 mm MiTeGen Dual-Thickness MicroMount using Paratone N oil (Hampton). X-ray diffraction experiment on **2.5** was conducted at 150 K, while for **2.9** data were collected at 150, 223, and 298 K. In the case of the room-temperature experiment, the single crystal

was glued to the MiTeGen mesh using epoxy glue. Diffraction data was collected using a Bruker Smart Apex II single crystal diffractometer with a TRIUMPH monochromated Mo Kα radiation (λ = 0.71073 Å) source with a crystal-to-detector distance of 50 mm, using a series of θ and ω scans in 0.50° oscillations. The data was processed and corrected for Lorentz and polarization effects and an empirical absorption correction was applied, using the Bruker Apex II software suite. The structures were solved with ShelxS,[98] and subsequent refinements were performed using the SHELXTL crystallographic software package of Bruker-AXS.[99] The coordinates and anisotropic displacement parameters for the non-hydrogen atoms were refined. Hydrogen atoms were placed in idealized geometric positions and linked to their respective carbon atoms using a riding model during refinement. Platon SQUEEZE algorithm[100] was used to remove the electron density associated with the DMF solvent molecule for the room-temperature data set of **2.9** because of the severe disorder of DMF molecule at this temperature. Diagrams were prepared using MERCURY.[101] Additional crystallographic information can be found in CCDC 2388285 (**2.5**), 2388288 (**2.9**, 150 K), 2388287 (**2.9**, 223 K), and 2388286 (**2.9**, 298 K), respectively.

Determination of Fluorescence Quantum Yield. All fluorescence spectra were corrected for apparatus response. Quartz cuvettes with an optical path of 1 cm were used. The sample concentrations were chosen to obtain a maximum absorbance between 0.3 and 1.0 for UV spectra and between 0.05 and 0.1 at excitation wavelength for quantum yield measurements. Relative quantum yields were obtained by comparing the areas under the corrected emission spectrum. All measurements were performed in chloroform

and DCM at 298 K. "bismethoxy" AzaBODIPY (Φ = 0.36 in $CHCl_3$, λex = 670 nm). In all quantum yield determinations, correction for the solvent refractive index (η) was applied [$CHCl_3$: η = 1.4458, DCM: η = 1.442].

The following equation was used to calculate the quantum yield of the sample:

$$\Phi X = \Phi ref\ (Grad_X/Grad_{ref})\ (\eta_X^2/\eta_{ref}^2)$$

Of which indices X and ref stand for the studied compounds (**2.7** and **2.8**) and the reference compound, Φ is the quantum yield, Grad is the gradient of the linear graph between the integrated fluorescence intensity versus absorbance at the excitation wavelength, and η is the refraction index of the solvent in which the measure is performed

Computational Methods. All computations were performed using Gaussian 16 software[102] running under Windows or UNIX OS. Molecular orbital contributions were compiled from single-point calculations using the QMForge program.[103] In DFT calculations, the TPSSh[104,105] (10% of Hartree–Fock exchange) and M06[106] (27% of Hartree–Fock exchange) hybrid exchange correlation functionals as well as range-separated CAM-B3LYP[107] and wB97X[108] exchange-correlation functionals were used for geometry optimization. In all calculations, 6-311G(d) basis set was employed.[109] In the case of modeling compound **2.9**, three spin states were considered. In the first one (**2.9CS**), a molecule of **2.9** was treated as a closed-shell singlet. In the case of **2.9OS**, a molecule of **2.9** was treated as an open-shell diradicaloid. Stable = opt keyword was used to ensure the correct diradicaloid character of the initial guess and the final wave function. In the case of **2.9TS**, triplet state was used in calculations. Frequencies were

calculated for each geometry optimization to ensure the energy minimum. DFT calculations for **2.7**, **2.9CS**, **2.9OS**, and **2.9TS** converged to C_2 symmetry, which was used in the single-point and TDDFT calculations. In all TDDFT calculations, the lowest 40 excited states were calculated to cover experimentally observed transitions in the UV–visible region. Diradical character in 5OS was further probed using TPSSh, CAM-B3LYP, M06, and wB97X exchange-correlation functionals and the Natural Population Analysis (NPA) algorithm.

2.5.2 Synthesis of (E)-3-(3,5-di-tert-butyl-4-hydroxyphenyl)-1-phenylprop-2-en-1-one (2.1)

This chalcone was prepared as previously reported.[110] 3,5-di-tert-4-hydroxylbenzaldehyde (25 mmol, 5.86 g) and acetophenone (25 mmol, 3 g) were dissolved in 350 mL of absolute ethanol saturated with hydrogen chloride gas; the resultant solution was then stirred for two hours at room temperature and left overnight. Compound **2.1** crystallized and was filtered off as a yellowish green crystal. The product was recrystallized from ethanol (6.5 g, 80% yield). ^{1}H NMR ($CDCl_3$), 500 MHz): δ (ppm) 7.99-8.01 (d, J = 10 Hz, 2H), 7.76-7.79 (d, J = 15Hz, 1H), 7.49-7.59 (m, 5H), 7.33-7.36 (d, J = 15 Hz, 1H), 5.57 (S, 1 H), 1.48 (S, 18H). ^{13}C ($CDCl_3$, 500 MHz): δ (ppm) 30.2, 34.4, 119.3,125.97, 126.3, 128.45, 128.53, 132.4, 136.5, 138.8, 146.5, 156.56, 191.1.). ^{1}H NMR and ^{13}C NMR spectra are shown in Figures 2.27 – 2.28.

2.5.3 Synthesis of (E)-1-(4-bromophenyl)-3-(3,5-di-tert-butyl-4-hydroxyphenyl)-1-phenylprop-2-en-1-one (2.2)

This chalcone was prepared as previously reported.[110] 3,5-di-tert-4-hydroxylbenzaldehyde (25 mmol, 5.86 g) and 4-bromoacetophenone (25 mmol, 5 g) were dissolved in 350 mL of absolute ethanol saturated with hydrogen chloride gas; the resultant solution was then stirred for two hours at room temperature and left overnight. Compound **2.2** was obtained upon dilution with water. Purification was carried out by recrystallization from ethanol. (6.6 g, 80% yield). ^{1}H NMR ($CDCl_3$), 500 MHz): δ (ppm) 7.85-7.87 (d, *J* = 10 Hz, 2H), 7.75-7.78 (d, *J* = 15Hz, 1H), 7.63-7.65 (d, *J* = 10Hz, 2H), 7.48 (s, 2H), 7.27-7.30 (d, *J* = 15 Hz, 1H), 5.59 (S, 1 H), 1.48 (S, 18H). ^{13}C ($CDCl_3$, 500 MHz): δ (ppm) 30.1, 34.4, 118.7, 126.1, 127.4, 130, 131.8, 136.6, 137.5, 147.1, 156.8, 159.7, 189.9. MALDI-TOF-MS (HR): 415.1265. Calcd for $C_{23}H_{28}BrO_2$ ($[M+H]^+$): 415.1273. ^{1}H NMR and ^{13}C NMR spectra are shown in Figures 2.29 – 2.30.

2.5.4 Synthesis of 1-(3,5-di-tert-butyl-4-hydroxyphenyl)-4-nitro-3-phenylprop-2-en-1-one (2.3)

To a solution of compound **2.1** (4.16 mmol, 1.4 g) in nitromethane (20 mL), 1,8-diazabicyclo [5.4.0] undec-7-ene (DBU) (4.16mmol, 0.632g) was added. The resulting mixture was refluxed for 30 minutes. The resulting reddish-brown solution was cooled to room temperature and diluted with 2 mL 1% $HCl_{(aq)}$ and 30 mL of water. The product was extracted with chloroform and the organic layer was dried over $MgSO_4$ and evaporated to dryness, yielding 1.26 g (90%) of pure compound **2.3**. ^{1}H NMR ($CDCl_3$), 500 MHz): δ (ppm) 7.88 – 7.90 (d, *J* = 10 Hz, 2H), 7.55 – 7.58 (t, 1H), 7.43 – 7.46 (t,

2H), 7.01 (s, 2H), 5.15 (s, 1H), 4.79 – 4.82 (m, 1H), 4.66 – 4.70 (m, 1H), 4.10 -4.16 (m, 1H), 3.39 – 3.41 (m, 2H), 1.40 (s, 18H). ^{13}C (CDCl3, 500 MHz): δ (ppm) 30.4, 34.4, 39.5, 42.0, 79.8 123.6, 128.1, 128.7, 129.7, 133.4, 136.4, 153.2, 197.6. MALDI-TOF-MS (HR): 420.2141. Calcd for $C_{24}H_{31}NO_4Na$ ($[M+Na]^+$): 420.2151. ^{1}H NMR and ^{13}C NMR spectra are shown in Figures 2.31 – 2.32. Mass spectrum is shown in Figure 2.49.

2.5.5 Synthesis of 1-(4-bromophenyl)-3-(3,5-di-tert-butyl-4-hydroxyphenyl)-4-nitro-3-phenylbutan-1-one (2.4)

To a solution of compound **2.2** (4.74 mmol, 2 g) in nitromethane (20 mL), 1,8-diazabicyclo [5.4.0] undec-7-ene (DBU) (4.74 mmol, 0.72 g) was added. This mixture was then refluxed for 30 minutes. The resulting reddish-brown solution was cooled to room temperature and diluted with 2 mL 1% HCl and 30 mL of water. The product was extracted with chloroform and the organic layer was dried over $MgSO_4$ and evaporated to dryness, yielding 1.52 g (90%) of pure compound **2.4**. ^{1}H NMR ($CDCl_3$), 500 MHz): δ (ppm) 7.73 – 7.75 (d, J = 10 Hz, 2H), 7.57 – 7.59 (d, J = 10Hz, 2H), 6.99 (s, 2H), 5.16 (s, 1H), 4.76 – 4.80 (m, 1H), 4.65 – 4.69 (m, 1H), 4.07 -4.13 (m, 1H), 3.35 – 3.37 (m, 2H), 1.40 (s, 18H). ^{13}C ($CDCl_3$, 500 MHz): δ (ppm) 30.3, 34.4, 39.5, 42.0, 79.7 123.9, 128.6, 129.6, 132, 135.4 136.4, 153.3, 196.6. MALDI-TOF-MS (HR): 474.1260. Calcd for $C_{24}H_{29}BrNO_4$ ($[M-H]^-$): 474.1280. ^{1}H NMR and ^{13}C NMR spectra are shown in Figures 2.33 – 2.34. Mass spectrum is shown in Figure 2.50.

2.5.6 Synthesis of 2,6-di-tert-butyl-4-(2-((3-(3,5-di-tert-butyl-4-hydroxyphenyl)-5-phenyl-1H-pyrrol-2-yl)imino)-5-phenyl-2H-pyrrol-3-yl)phenol (2.5)

A mixture of compound **2.3** (3.062 mmol, 1.26 g) and ammonium acetate (50 equiv) was refluxed in n-butanol (100 mL) for 36 h. After cooling to room temperature, the solvent concentrated to 30 mL and the precipitate was filtered off, washed with ethanol, and dried to yield compound **2.5** as a purplish blue solid 0.36 g (28%). ^{1}H NMR ($CDCl_3$), 500 MHz): δ (ppm) 7.95 – 7.97 (d, *J* = 10Hz, 4H), 7.51 – 7.54 (t, 4H), 7.48 (s, 4 H), 7.43 – 7.46 (t, 2H), 7.01 (s, 2H), 5.25 (s, 2H), 1.32 (s, 36H) (NH not observed). ^{13}C ($CDCl_3$, 500 MHz): δ (ppm) 30.4, 34.2, 114.0, 125.6, 126.5, 126.9, 129.1, 129.7. 132.7, 135.2, 145.2, 149.6, 154.1, 154.6. UV/vis (CH_2Cl_2, λ_{max}[nm] (ε, 10^4 $M^{-1}cm^{-1}$)): 592 (3.45). ESI-TOF-MS (HR): 706.4341. Calcd for $C_{48}H_{56}N_3O_2$ ($[M+H]^+$): 706.4373. ^{1}H NMR and ^{13}C NMR spectra are shown in Figures 2.35 – 2.36. Mass spectrum is shown in Figure 2.51.

2.5.7 Synthesis of 4-(5-(4-bromophenyl)-2-((5-(4-bromophenyl)-3-(3,5-di-tert-butyl-4-hydroxyphenyl)-1H-pyrrol-2-yl)imino)-2H-pyrrol-3-yl)-2,6-di-tert-butylphenol (2.6)

A mixture of compound **2.4** (3.062 mmol, 1.46 g) and ammonium acetate (50 equivalent) was refluxed in n-butanol (100 mL) for 36 h. After cooling to room temperature, the solvent was concentrated to 30 mL and the precipitate was filtered off, washed with ethanol, and dried to yield compound **2.6** as a purplish blue solid 0.43 g (28%). ^{1}H NMR ($CDCl_3$), 500 MHz): δ (ppm) 7.78 – 7.80 (d, *J* = 10Hz, 4H), 7.64 – 7.66 (d, *J* = 10 Hz, 4H), 7.45 (s, 4 H), 6.96 (s, 2H), 5.27 (s, 2H), 1.31 (s, 36H) (NH not observed). ^{13}C ($CDCl_3$, 500 MHz): δ (ppm) 30.4, 34.3, 114.0, 124.03, 125.4, 126.9,

127.8, 131.5, 132.3. 135.2, 145.6, 149.7, 153.7, 154.2. UV/vis (CH_2Cl_2, λ_{max}[nm] (ε, 10^4 $M^{-1}cm^{-1}$)): 600 (6.84). MALDI-TOF-MS (HR): 886.2376. Calcd for $C_{48}H_{53}Br_2N_3O_2Na$ ($[M+Na]^+$): 886.2388. ^1H NMR and ^{13}C NMR spectra are shown in Figures 2.37 – 2.38. Mass spectrum is shown in Figure 2.52.

2.5.8 Synthesis of BF_2 Chelate of 2,6-di-tert-butyl-4-(2-((3-(3,5-di-tert-butyl-4-hydroxyphenyl)-5-phenyl-1H-pyrrol-2-yl)imino)-5-phenyl-2H-pyrrol-3-yl)phenol (2.7)

A solution of compound **2.5** (0.26 mmol, 0.184 g) was prepared in dry DCM (50 mL), treated with N,N-diisopropylethylamine (DIPEA) (1.28 mmol, 0.22 mL) and $BF_3.Et_2O$ (1.80 mmol, 0.22 mL), and stirred at room temperature for 24 hours under a nitrogen atmosphere. Then, the reaction mixture was washed with 50 mL of water, and the organic layer was dried over sodium sulfate and evaporated to dryness. Column chromatography on silica gel eluting with methylene chloride/hexane (1:1) gave the product as a blue solid (0.14 g, 62%). ^1H NMR ($CDCl_3$), 500 MHz): δ (ppm) 8.01 – 8.03 (m, 4H), 7.60 (s, 4H), 7.45- 7.49 (m, 6H). 6.80 (s, 2H), 5.45 (s, 2H), 1.38 (s, 36H). ^{13}C (CDCl3, 500 MHz): δ (ppm) 30.4, 34.4, 118.5, 124.6, 127, 128.5, 129.4, 130.4, 132.1, 136.0, 145.9, 146.7, 155.4, 158.4. UV/vis (CH_2Cl_2, λ_{max}[nm] (ε, 10^4 $M^{-1}cm^{-1}$)): 658 (7.02). Fluorescence ($CHCl_3$, λ_{em}[nm] (λ_{ex}[nm], Φ_F)): 706 (638, 0.29). ESI-TOF-MS (HR): 754.4341. Calcd for $C_{48}H_{55}BF_2N_3O_2$ ($[M+H]^+$): 754.4363. ^1H NMR, ^{13}C NMR, ^{11}B NMR, and ^{19}F NMR spectra are shown in Figures 2.39 – 2.42. Mass spectrum is shown in Figure 2.53. FTIR spectrum is shown in Figure 2.57.

2.5.9 Synthesis of BF_2 Chelate of 4-(5-(4-bromophenyl)-2-((5-(4-bromophenyl)-3-(3,5-di-tert-butyl-4-hydroxyphenyl)-1H-pyrrol-2-yl)imino)-2H-pyrrol-3-yl)-2,6-di-tert-butylphenol (2.8)

A solution of compound **2.6** (0.26 mmol, 0.225 g) was prepared in dry DCM (50 ml), treated with DIPEA (1.28 mmol, 0.22 ml) and $BF_3.Et_2O$ (1.80 mmol, 0.22 ml), and stirred at room temperature for 24 hours under a nitrogen atmosphere. Then, the reaction mixture was washed with 50 mL of water, and the organic layer was dried over sodium sulfate and evaporated to dryness. Column chromatography on silica gel eluting with methylene chloride/hexane (1:1) gave the product as a blue solid (0.16 g, 62%). ^{1}H NMR ($CDCl_3$), 500 MHz): δ (ppm) 7.88 – 7.90 (d, *J* = 10Hz, 4H), 7.59- 7.61 (m, 8H). 6.78 (s, 2H), 5.48 (s, 2H), 1.37 (s, 36H). ^{13}C ($CDCl_3$, 500 MHz): δ (ppm) 30.4, 34.4, 118.2, 124.4, 125.4, 127, 130.85, 130.92, 131.8, 136.1, 146.1, 147.1, 155.6, 157.1. UV/vis (CH_2Cl_2, λ_{max}[nm] (ε, 10^4 $M^{-1}cm^{-1}$)): 670 (4.90). Fluorescence ($CHCl_3$, λ_{em}[nm] (λ_{ex}[nm], Φ_F)): 716 (650, 0.23). MALDI-TOF-MS (HR): 911.2482. Calcd for $C_{48}H_{52}BBr_2F_2N_3O_2$ ($[M]^+$): 911.2480. ^{1}H NMR and ^{13}C NMR spectra are shown in Figures 2.43 – 2.44. Mass spectrum is shown in Figure 2.54.

2.5.10 Synthesis of 4,4'-(5,5-difluoro-3,7-diphenyl-1H-4λ⁴,5λ⁴-dipyrrolo[1,2-c:2',1'-f][1,3,5,2]triazaborinine-1,9(5H)-diylidene)bis(2,6-di-tert-butylcyclohexa-2,5-dien-1-one) (2.9)

Dry DCM was added into a mixture of compound **2.7** (75 mg, 0.1 mmol) and lead(II) oxide under argon (0.718 g, 3 mmol), and the reaction mixture was stirred at room temperature for half an hour with a color change from deep blue to greenish brown.

The reaction was monitored by TLC. Once the reaction was finished, the solid lead(II) oxide was filtered off. The filtrate was dried via rotary evaporator, and then the final product was obtained as a black solid (73.5 mg, 99%) without further purification. ^{1}H NMR (THF-d_8), 500 MHz): δ (ppm) 9.00 (s, 2H), 7.84 – 7.86 (m, 4H), 7.66 (s, 2H), 7.36 – 7.40 (m, 6H), 6.91 (s, 2H), 1.32-1.37 (d, 36H). ^{13}C ($CDCl_3$, 500 MHz): δ (ppm) 29.5, 36.32, 110, 128.2, 128.8, 129.2, 130, 131.8, 140.4, 141.1, 151.9, 152.7, 161.6, 186. UV/vis (CH_2Cl_2, λ_{max}[nm] (ε, 10^4 $M^{-1}cm^{-1}$)): 387 (7.2), 805 (3.52). ESI-TOF-MS (HR): 752.4176. Calcd for $C_{48}H_{53}N_3O_2$ ($[M+H]^+$): 752.4107. ^{1}H NMR and ^{13}C NMR spectra are shown in Figures 2.45 – 2.46. Mass spectrum is shown in Figure 2.55. FTIR spectrum is shown in Figure 2.58.

2.5.11 Synthesis of 4,4'-(3,7-bis(4-bromophenyl)-5,5-difluoro-1H-4λ⁴,5λ⁴-dipyrrolo[1,2-c:2',1'-f][1,3,5,2]triazaborinine-1,9(5H)-diylidene)bis(2,6-di-tert-butylcyclohexa-2,5-dien-1-one) (2.10)

Compound **2.8** (91 mg, 0.1 mmol) and lead (II) oxide (0.718 g, 3 mmol) were added in dry DCM under an argon atmosphere, and the reaction mixture was stirred at room temperature for half an hour with a color change from deep blue to greenish brown. The reaction was monitored via TLC. Once the reaction was finished, the solid lead (II) oxide was filtered off. The filtrate was dried via rotary evaporator, and then the final product was obtained as a black solid (90 mg, 99%) without further purification. ^{1}H NMR (DMF-d_7 300K), 500 MHz): δ (ppm) 8.97 (s, 2H), 7.89 – 7.90 (d, 4H), 7.86 (s, 2H), 7.80 – 7.82 (d, 4H), 7.65 (s, 2H), 1.28-1.32 (d, 36H). ^{13}C ($CDCl_3$, 500 MHz): δ (ppm) 28.7, 35.4, 109.4, 123.7, 128.2, 129.7, 130, 130.7, 140, 150.5, 151.4, 152.1, 160.8, 185.8.

UV/vis (CH_2Cl_2, λ_{max}[nm] (ε, 10^4 $M^{-1}cm^{-1}$)): 389 (7.0), 807 (3.2). MALDI-TOF-MS (HR): 909.2349. Calcd for $C_{48}H_{50}BBr_2F_2N_3O_2$ ($[M]^+$): 909.2324. ^1H NMR and ^{13}C NMR spectra are shown in Figures 2.47 – 2.48. Mass spectrum is shown in Figure 2.56.

References

(1) Li, Y.; Jiang, M.; Yan, M.; Ye, J.; Li, Y.; Dehaen, W.; Yin, S. "Near-infrared boron-dipyrrin (BODIPY) nanomaterials: Molecular design and anti-tumor therapeutics." *Coord. Chem. Rev.* **2024**, *506*, 215718.

(2) Ma, D.; Bian, H.; Gu, M.; Wang, L.; Chen, X.; Peng, X. "Recent advances in the design and applications of near-infrared II responsive small molecule phototherapeutic agents." *Coord. Chem. Rev.* **2024**, *505*, 215677.

(3) Li, H.; Wang, J.; Jiao, L.; Hao, E. "BODIPY-based photocages: rational design and their biomedical application." *Chem. Commun.* **2024**, *60*, 5770-5789.

(4) Kovtun, O. M.; Zatsikha, Y. V.; Kovtun, Y. P. "New approaches to the modification of chemical structure and photophysical properties of BODIPY dyes." *Chem. Heterocyclic Comp.* **2023**, *59*, 357-367.

(5) Gapare, R. L.; Thompson, A. "Substitution at boron in BODIPYs." *Chem. Commun.* **2022**, *58*, 7351-7359.

(6) Zatsikha, Y. V.; Prasannan, D.; Scharge, B.; Herbert, D. E.; Gerasimchuk, N. N.; Zeller, M.; Nemykin, V. N. "Use of unprecedented intramolecular 1, 3-dipolar cycloaddition reaction in meso-nitrile oxide-containing BODIPYs as a new pathway for the preparation of fused NIR platforms." *Chem. Eur. J.* **2024**, *30*, e202401210.

(7) Zatsikha, Y. V.; Blesener, T. S.; King, A. J.; Healy, A. T.; Goff, P. C.; Didukh, N. O.; Blank, D. A.; Kovtun, Y. P.; Nemykin, V. N. "Fully conjugated pyrene-BODIPY and pyrene-BODIPY-ferrocene dyads and triads: synthesis,

characterization, and selective noncovalent interactions with nanocarbon materials." *J. Phys. Chem. B* **2021**, *125*, 360-371.

(8) Zatsikha, Y. V.; Didukh, N. O.; Swedin, R. K.; Yakubovskyi, V. P.; Blesener, T. S.; Healy, A. T.; Herbert, D. E.; Blank, D. A.; Nemykin, V. N.; Kovtun, Y. P. "Preparation of viscosity-sensitive isoxazoline/isoxazolyl-based molecular rotors and directly linked BODIPY-fulleroisoxazoline from the stable meso-(nitrile oxide)-substituted BODIPY." *Org. Lett.* **2019**, *21*, 5713-5718.

(9) Didukh, N. O.; Yakubovskyi, V. P.; Zatsikha, Y. V.; Rohde, G. T.; Nemykin, V. N.; Kovtun, Y. P. "Flexible BODIPY platform that offers an unexpected regioselective heterocyclization reaction toward preparation of 2-pyridone[a]-fused BODIPYs." *J. Org. Chem.* **2019**, *84*, 2133-2147.

(10) Nemykin, V. N.; Blesener, T. S.; Ziegler, C. J. "Photophysics, redox processes, and electronic structures of ferrocenyl-containing BODIPYs, aza-BODIPYs, BOPHYs, transition-metal dipyrromethenes and aza-dipyrromethenes." *Makrogeterotsikly* **2017**, *10*, 9-26.

(11) Didukh, N. O.; Zatsikha, Y. V.; Rohde, G. T.; Blesener, T. S.; Yakubovskyi, V. P.; Kovtun, Y. P.; Nemykin, V. N. "NIR absorbing diferrocene-containing meso-cyano-BODIPY with a UV-Vis-NIR spectrum remarkably close to that of magnesium tetracyanotetraferrocenyltetraazaporphyrin." *Chem. Commun.* **2016**, *52*, 11563-11566.

(12) Shamova, L. I.; Zatsikha, Y. V.; Nemykin, V. N. “Synthesis pathways for the preparation of the BODIPY analogues: aza-BODIPYs, BOPHYs and some other pyrrole-based acyclic chromophores.” *Dalton Trans.* **2021**, *50*, 1569-1593.

(13) Wang, J.; Yu, C.; Hao, E.; Jiao, L. “Conformationally restricted and ring-fused aza-BODIPYs as promising near infrared absorbing and emitting dyes.” *Coord. Chem. Rev.* **2022**, *470*, 214709.

(14) Kaur, M.; Janaagal, A.; Balsukuri, N.; Gupta, I. “Evolution of aza-BODIPY dyes-A hot topic.” *Coord. Chem. Rev.* **2024**, *498*, 215428.

(15) Zatsikha, Y. V.; Blesener, T. S.; Goff, P. C.; Healy, A. T.; Swedin, R. K.; Herbert, D. E.; Rohde, G. T.; Chanawanno, K.; Ziegler, C. J.; Belosludov, R. V.; Blank, D. A.; Nemykin, V. N. “1,7-dipyrene-containing aza-BODIPYs: Are pyrene groups effective as ligands to promote and direct complex formation with common nanocarbon materials?” *J. Phys. Chem. C* **2018**, *122*, 27893-27916.

(16) Zatsikha, Y. V.; Holstrom, C. D.; Chanawanno, K.; Osinski, A. J.; Ziegler, C. J.; Nemykin, V. N. “Observation of the strong electronic coupling in near-infrared-absorbing tetraferrocene aza-dipyrromethene and aza-BODIPY with direct ferrocene-α- and ferrocene-β-pyrrole bonds: toward molecular machinery with four-bit information storage capacity.” *Inorg. Chem.* **2017**, *56*, 991-1000.

(17) Maligaspe, E.; Pundsack, T. J.; Albert, L. M.; Zatsikha, Y. V.; Solntsev, P. V.; Blank, D. A.; Nemykin, V. N. “Synthesis and Charge-transfer dynamics in a ferrocene-containing organoboryl aza-BODIPY donor-acceptor triad with boron as the hub.” *Inorg. Chem.* **2015**, *54*, 4167-4174.

(18) Wang, J.; Gong, Q.; Jiao, L.; Hao, E. “Research advances in BODIPY-assembled supramolecular photosensitizers for photodynamic therapy.” *Coord. Chem. Rev.* **2023**, *496*, 215367.

(19) Mahanta, C. S.; Ravichandiran, V.; Swain, S. P. “Recent developments in the design of new water-soluble boron dipyrromethenes and their applications: An updated review.” *ACS Appl. Bio Mater.* **2023**, *6*, 2995-3018.

(20) Vargas-Zuniga, G. I.; Kim, H. S.; Li, M.; Sessler, J. L.; Kim, J. S. “Pyrrole-based photosensitizers for photodynamic therapy - a Thomas Dougherty award (for excellence in PDT) paper.” *J. Porphyrins Phthalocyanines* **2021**, *25*, 773-793.

(21) Wang, J.; Gong, Q.; Wang, L.; Hao, E.; Jiao, L. “The main strategies for tuning BODIPY fluorophores into photosensitizers.” *J. Porphyrins Phthalocyanines* **2020**, *24*, 603-635.

(22) Kamkaew, A.; Lim, S. H.; Lee, H. B.; Kiew, L. V.; Chung, L. Y.; Burgess, K. “BODIPY dyes in photodynamic therapy.” *Chem. Soc. Rev.* **2013**, *42*, 77-88.

(23) Carmo, C.; Almeida, J. M. S.; Araujo, J.; Brett, C. M. A.; Botelho, M. F.; Cordova, A.; Laranjo, M.; Sobral, A. J. F. N. “Exploring the impact of meso-position fluorination on BODIPYs: Synthesis, electrochemical Insights, and potential therapeutic applications in breast cancer.” *Dyes Pigments* **2024**, *229*, 112263.

(24) Saladin, L.; Breton, V.; Le Berruyer, V.; Nazac, P.; Lequeu, T.; Didier, P. ; Danglot, L.; Collot, M. “Targeted photoconvertible BODIPYs based on directed

photooxidation-induced conversion for applications in photoconversion and live super-resolution imaging." *J. Am. Chem. Soc.* **2024**, *146*, 17456-17473.

(25) Reese, A. E.; de Moliner, F.; Mendive-Tapia, L.; Benson, S.; Kuru, E.; Bridge, T.; Richards, J.; Rittichier, J.; Kitamura, T.; Sachdeva, A.; et al "Inserting "OFF-to-ON" BODIPY tags into cytokines: A fluorogenic interleukin IL-33 for real-time imaging of immune cells." *ACS Central Sci.* **2024**, *10*, 143-154.

(26) Zhang, Y.; Zheng, Y.; Tomassini, A.; Singh, A. K.; Raymo, F. M. "Photoactivatable BODIPYs for live-cell PALM." *Molecules* **2023**, *28*, 2447.

(27) Gao, Y.; Pan, Y.; Chi, Y.; He, Y.; Chen, H.; Nemykin, V. N. "A "reactive" turn-on fluorescence probe for hypochlorous acid and its bioimaging application." *Spectrochim. Acta, A* **2019**, *206*, 190-196.

(28) Yadav, I. S.; Misra, R. "Design, synthesis and functionalization of BODIPY dyes: applications in dye-sensitized solar cells (DSSCs) and photodynamic therapy (PDT)." *J. Mater. Chem. C* **2023**, *11*, 8688-8723.

(29) Knoll, S.; Zens, C.; Maisuradze, T.; Schmidt, H.; Kupfer, S.; Zedler, L.; Dietzek-Ivansic, B.; Streb, C. "Light-induced charge separation in covalently linked BODIPY-quinone-alkyne dyads." *Chem. Eur. J.* **2024**, *30*, e202303250.

(30) Ptaszek, M.; Meares, A.; Ansteatt, S. "Hydroporphyrin-BODIPY arrays." *J. Porphyrins Phthalocyanines* **2024**, *28*, 201-216.

(31) Klfout, H.; Stewart, A.; Elkhalifa, M.; He, H. "BODIPYs for dye-sensitized solar cells." *ACS Appl. Mater. Inter.* **2017**, *9*, 39873-39889.

(32) Bucher, L.; Desbois, N.; Harvey, P. D.; Sharma, G. D.; Gros, C. P. "Porphyrins and BODIPY as building blocks for efficient donor materials in bulk heterojunction solar cells." *Solar RRL* **2017**, *1*, 1-26.

(33) Wu, D.; Zhang, Z.; Li, X.; Zhou, J.; Cao, Y.; Qi, S.; Wang, L.; Liu, Z.; Yu, G. "Dynamically assembled nanomedicine based on host-guest molecular recognition for NIR laser-excited chemotherapy and phototheranostics." *Acta Biomater.* **2023**, *168*, 565-579.

(34) Chen, X.; Yu, B.; Wang, J.; Luo, Z.; Meng, H.; Xie, B.; Zhou, R.; Liu, S.; Zhao, Q. "A near-infrared organic photodetector based on an aza-BODIPY dye for a laser microphone system." *J. Mater. Chem. C* **2023**, *11*, 2267-2272.

(35) Song, S.; Xu, G.; Yang, N.; Shahzad, S. A.; Lv, J.; Shen, X.; Yu, C. "Aza-BODIPY nanoparticles for near-infrared triggered synergistic photothermal and photodynamic antibacterial therapy." *J. Mater. Sci.* **2022**, *57*, 21206-21218.

(36) Wu, Q.; Zhu, Y.; Fang, X.; Hao, X.; Jiao, L.; Hao, E.; Zhang, W. "Conjugated BODIPY Oligomers with controllable near-infrared absorptions as promising phototheranostic agents through excited-state intramolecular rotations." *ACS Appl. Mater. Inter.* **2020**, *12*, 47208-47219.

(37) Xu, Y.; Feng, T.; Yang, T.; Wei, H.; Yang, H.; Li, G.; Zhao, M.; Liu, S.; Huang, W.; Zhao, Q. "Utilizing intramolecular photoinduced electron transfer to enhance photothermal tumor treatment of aza-BODIPY-based near-infrared nanoparticles." *ACS Appl. Mater. Inter.* **2018**, *10*, 16299-16307.

(38) Pinjari, D.; Patil, Y.; Misra, R. “Near-infrared absorbing aza-BODIPY Dyes for optoelectronic applications.” *Chem. Asian J.* **2024**, 19, e202400167.

(39) Patil, Y.; Butenschon, H.; Misra, R. “Tetracyanobutadiene bridged push-pull chromophores: Development of new generation optoelectronic materials.” *Chem. Record* **2023**, *23*, e202200208.

(40) Squeo, B. M.; Ganzer, L.; Virgili, T.; Pasini, M. “BODIPY-based molecules, a platform for photonic and solar cells.” *Molecules* **2021**, *26*, 153.

(41) Poddar, M.; Misra, R. “Recent advances of BODIPY based derivatives for optoelectronic applications.” *Coord. Chem. Rev.* **2020**, *421*, 213462.

(42) Singh, S. P.; Gayathri, T. “Evolution of BODIPY dyes as potential sensitizers for dye-sensitized solar cells.” *Eur. J. Org. Chem.* **2014**, *2014*, 4689-4707.

(43) El-Khouly, M. E.; Fukuzumi, S.; D'Souza, F. “Photosynthetic antenna-reaction center mimicry by using boron dipyrromethene sensitizers.” *ChemPhysChem* **2014**, *15*, 30-47.

(44) Benniston, A. C.; Copley, G. “Lighting the way ahead with boron dipyrromethene (Bodipy) dyes.” *Phys. Chem. Chem. Phys.* **2009**, *11*, 4124-4131.

(45) Emilio de la Cerda-Pedro, J.; Hernandez-Ortiz, O. J.; Vazquez-Garcia, R. A.; Garcia-Baez, E. V.; Gomez-Aguilar, R.; Espinosa-Roa, A.; Farfan, N.; Padilla-Martinez, I. I. “Highly crystalline and fluorescent BODIPY-labelled phenyl-triazole-coumarins as n-type semiconducting materials for OFET devices.” *Heliyon* **2024**, *10*, e23517.

(46) Talalaev, F. S.; Frolova, L. A.; Bochkov, A. Y.; Babenko, S. D.; Gutsev, L. G.; Aldoshin, S. M.; Traven, V. F.; Troshin, P. A. "Efficient OFET-based optical memory and photodetectors using novel BODIPY dye." *J. Mater. Chem. C* **2023**, *11*, 742-749.

(47) Ozcan, E.; Ozdemir, M.; Ho, D.; Zorlu, Y.; Ozdemir, R.; Kim, C.; Usta, H.; Cosut, B. "A solution-processable meso-phenyl-BODIPY-based n-channel semiconductor with enhanced fluorescence emission." *ChemPlusChem* **2019**, *84*, 1423-1431.

(48) Huaulme, Q.; Sutter, A.; Fall, S.; Jacquemin, D.; Leveque, P.; Retailleau, P.; Ulrich, G.; Leclerc, N. "Versatile synthesis of α-fused BODIPY displaying intense absorption in the NIR region and high electron affinity." *J. Mater. Chem. C* **2018**, *6*, 9925-9931.

(49) Ozdemir, M.; Choi, D.; Zorlu, Y.; Cosut, B.; Kim, H.; Kim, C.; Usta, H. "A new rod-shaped BODIPY-acetylene molecule for solution-processed semiconducting microribbons in n-channel organic field-effect transistors." *New J. Chem.* **2017**, *41*, 6232-6240.

(50) Gawale, Y.; Palanisamy, P.; Lee, H. S.; Chandra, A.; Kim, H. U.; Ansari, R.; Chae, M. Y.; Kwon, J. H. "Structural optimization of BODIPY derivatives: Achieving stable and long-lived green emission in hyperfluorescent OLEDs." *ACS Appl. Mater. Inter.* **2024**, *16*, 22274-22281.

(51) Jiang, W.; Zhou, R.; Zhao, G.; Ma, D.; Chen, H.; Zhang, Z.; Tian, W.; Sun, Y. "Isomer engineering to adjusting full width at half maximum and

emission wavelength for efficient solution-processed red OLEDs." *Optical Mater.* **2023**, *136*, 113505.

(52) Liu, J.; Liu, J.; Li, H.; Bin, Z.; You, J. "Boron-dipyrromethene-based fluorescent emitters enable high-performance narrowband red organic light-emitting diodes." *Angew. Chem., Int. Ed.* **2023**, 62, e202306471.

(53) Ma, D.; Zhao, G.; Chen, H.; Zhou, R.; Zhang, G.; Tian, W.; Jiang, W.; Sun, Y. "Creation of BODIPYs-based red OLEDs with high color purity via modulating the energy gap and restricting rotation of substituents." *Dyes Pigments* **2022**, *203*, 110377.

(54) Jung, Y. H.; Karthik, D.; Lee, H.; Maeng, J. H.; Yang, K. J.; Hwang, S.; Kwon, J. H. "A new BODIPY material for pure color and long lifetime red hyperfluorescence organic light-emitting diode." *ACS Appl. Mater. Inter.* **2021**, *13*, 17882-17891.

(55) Ivaniuk, K.; Pidluzhna, A.; Stakhira, P.; Baryshnikov, G. V.; Kovtun, Y. P.; Hotra, Z.; Minaev, B. F.; Agren, H. "BODIPY-core 1,7-diphenyl-substituted derivatives for photovoltaics and OLED applications." *Dyes Pigments* **2020**, *175*, 108123.

(56) Diradicaloids, Wu, J. (Ed.), Jenny Stanford Publishing, **2022**, pp. 1-622.

(57) Zeng, Z.; Shi, X.; Chi, C.; Lopez Navarrete, J. T.; Casado, J.; Wu, J. "Pro-aromatic and anti-aromatic π-conjugated molecules: an irresistible wish to be diradicals." *Chem. Soc. Rev.* **2015**, *44*, 6578-6596.

(58) Olivier, Y.; Sancho-Garcia, J.-C. “Design strategies for diradical boron/nitrogen doped carbon-based materials.” *Angew. Chem., Int. Ed.* **2023**, *62*, e202305501.

(59) Moles Quintero, S.; Haley, M. M.; Kertesz, M.; Casado, J. “Polycyclic hydrocarbons from [4n]Annulenes: Correlation versus hybridization forces in the formation of diradicaloids.” *Angew. Chem., Int. Ed.* **2022**, *61*, e202209138.

(60) Kato, S.-I. “Phenanthrylene-alkynylene macrocycles, phenanthrene-fused dicyclopenta[b,g]naphthalene, as well as relevant diradicaloids and antiaromatic compounds.” *Adv. Phys. Org. Chem.* **2021**, *55*, 41-66.

(61) Dressler, J. J.; Haley, M. M. “Learning how to fine-tune diradical properties by structure refinement.” *J. Phys. Org. Chem.* **2020**, *33*, e4114.

(62) Stuyver, T.; Chen, B.; Zeng, T.; Geerlings, P.; De Proft, F.; Hoffmann, R. “Do diradicals behave like radicals?” *Chem. Rev.* **2019**, *119*, 11291-11351.

(63) Liu, C.; Ni, Y.; Lu, X.; Li, G.; Wu, J. “Global aromaticity in macrocyclic polyradicaloids: Hückel's rule or baird's rule?” *Acc. Chem. Res.* **2019**, *52*, 2309-2321.

(64) Kirk, M. L.; Shultz, D. A.; Marri, A. Reddy; van der Est, A. “Photoinduced magnetic exchange-jump promotes ground state biradical electron spin polarization.” *J. Am. Chem. Soc.* **2024**, *146*, 9285-9292.

(65) Miller, P. D.; Mengell, J.; Shultz, D. A.; Kirk, M. L. “Metal-ligand exchange coupling alters the open-shell ligand electronic structure in a bis(semiquinone) complex.” *Inorg. Chem.* **2024**, *63*, 6493-6499.

(66) Banachowicz, P.; Das, M.; Kruczala, K.; Siczek, M.; Sojka, Z.; Kijewska, M.; Pawlicki, M. “Breaking global diatropic current to tame diradicaloid character: Thiele's hydrocarbon under macrocyclic constraints.” *Angew. Chem., Int. Ed.* **2024**, *63*, e202400780.

(67) Maiti, A.; Elvers, B. J.; Bera, S.; Lindl, F.; Krummenacher, I.; Ghosh, P.; Braunschweig, H.; Yildiz, C. B.; Schulzke, C.; Jana, A. “Disclosing cyclic(alkyl)(amino)carbenes as one-electron reductants: synthesis of acyclic(amino)(aryl)carbene-based Kekule diradicaloids.” *Chem. Eur. J.* **2022**, *28*, e202104567.

(68) Yamamoto, K.; Quintero, S. M.; Jinnai, S.; Jeong, E.; Matsuo, K.; Suzuki, M.; Yamada, H.; Casado, J.; Ie, Y. “Cross-conjugated isothianaphthene quinoids: a versatile strategy for controlling electronic structures.” *J. Mater. Chem. C* **2022**, *10*, 4424-4433.

(69) Maiti, A.; Sobottka, S.; Chandra, S.; Jana, D.; Ravat, P.; Sarkar, B.; Jana, A. “Diamidocarbene-based Thiele and Tschitschibabin hydrocarbons: Carbonyl functionalized Kekulé diradicaloids.” *J. Org. Chem.* **2021**, *86*, 16464-16472.

(70) Maiti, A.; Chandra, S.; Sarkar, B.; Jana, A. “Acyclic diaminocarbene-based Thiele, Chichibabin, and Muller hydrocarbons.” *Chem. Sci.* **2020**, *11*, 11827-11833.

(71) Kundu, G.; De, S.; Tothadi, S.; Das, A.; Koley, D.; Sen, S. S. “Saturated N-heterocyclic carbene based Thiele's Hydrocarbon with a tetrafluorophenylene linker.” *Chem. Eur. J.* **2019**, *25*, 16533-16537.

(72) Hansmann, M. M.; Melaimi, M.; Munz, D.; Bertrand, G. “Modular approach to Kekule diradicaloids derived from cyclic (alkyl)(amino)carbenes.” *J. Am. Chem. Soc.* **2018**, *140*, 2546-2554.

(73) Rottschaefer, D.; Neumann, B.; Stammler, H.-G.; Andrada, D. M.; Ghadwal, R. S. “Kekule diradicaloids derived from a classical N-heterocyclic carbene.” *Chem. Sci.* **2018**, *9*, 4970-4976.

(74) Takamuku, S.; Nakano, M.; Kertesz, M. “Intramolecular pancake bonding in helical structures.” *Chem. Eur. J.* **2017**, *23*, 7474-7482.

(75) Mishra, S.; Melidonie, J.; Eimre, K.; Obermann, S.; Groning, O.; Pignedoli, C. A.; Ruffieux, P.; Feng, X.; Fasel, R. “On-surface synthesis of super-heptazethrene.” *Chem. Commun.* **2020**, *56*, 7467-7470.

(76) Maeda, T.; Oka, T.; Sakamaki, D.; Fujiwara, H.; Suzuki, N.; Yagi, S.; Konishi, T.; Kamada, K. “Unveiling a new aspect of oxocarbons: open-shell character of 4- and 5-membered oxocarbon derivatives showing near-infrared absorption.” *Chem. Sci.* **2023**, *14*, 1978-1985.

(77) Sugiura, S.; Kubo, T.; Haketa, Y.; Hori, Y.; Shigeta, Y.; Sakai, H.; Hasobe, T.; Maeda, H. “Deprotonation-induced and ion-pairing-modulated diradical properties of partially conjugated pyrrole-quinone conjunction.” *J. Am. Chem. Soc.* **2023**, *145*, 8122-8129.

(78) Li, G.; Phan, H.; Herng, T. S.; Gopalakrishna, T. Y.; Liu, C.; Zeng, W.; Ding, J.; Wu, J. “Toward stable superbenzoquinone diradicaloids.” *Angew. Chem., Int. Ed.* **2017**, *56*, 5012-5016.

(79) Matsuta, Y.; Sakamaki, D.; Kurata, R.; Ito, A.; Seki, S. “Modulation of open-shell characters of amine-inserted diphenoquinones via structural modification.” *Chem. Asian J.* **2017**, *12*, 1889-1894.

(80) Zhou, J.; Rieker, A. “Electrochemical and spectroscopic properties of a series of tert-butyl-substituted para-extended quinones.” *J. Chem. Soc., Perkin Trans. 2* **1997**, 931-938.

(81) Rebmann, A.; Zhou, J.; Schuler, P.; Stegmann, H. B.; Rieker, A. “Synthesis, EPR spectroscopy and voltammetry of a p-quaterphenyl biradical/quinone.” *J. Chem. Res., Synop.* **1996**, 318-319.

(82) Traylor, T. G.; Nolan, K. B.; Hildreth, R. “Polyvalent porphyrins. 1. Properties of tetrakis(3,5-di-tert-butyl-4-hydroxyphenyl)porphyrin (1-P) and its iron(III) and zinc(II) derivatives.” *J. Am. Chem. Soc.* **1983**, *105*, 6149-6151.

(83) Hill, J. P.; Hewitt, I. J.; Anson, C. E.; Powell, A. K.; McCarty, A. Lea; Karr, P. A.; Zandler, M. E.; D'Souza, F. “Highly nonplanar, electron deficient, N-substituted tetra-oxocyclohexadienylidene porphyrinogens: Structural, computational, and electrochemical investigations.” *J. Org. Chem.* **2004**, *69*, 5861-5869.

(84) Ding, Y.; Li, X.; Hill, J. P.; Ariga, K.; Agren, H.; Andreasson, J.; Zhu, W.; Tian, H.; Xie, Y. “Acid/Base switching of the tautomerism and conformation of a dioxoporphyrin for integrated binary subtraction.” *Chem. Eur. J.* **2014**, *20*, 12910-12916.

(85) Miao, F.; Phan, H.; Wu, J. "A BODIPY-bridged bisphenoxyl diradicaloid: solvent-dependent diradical character and physical properties." *Molecules* **2019**, *24*, 1446.

(86) Pivovarenko, V. G.; Klymchenko, A. S. Fluorescent probes based on charge and proton transfer for probing biomolecular environment. *Chem. Rec.* **2024**, *24*, e202300321. DOI: 10.1002/tcr.202300321

(87) Fontes, L. F. B.; Rocha, J.; Silva, A. M. S.; Guieu, S. Excited-state proton transfer in luminescent dyes: From theoretical insight to experimental evidence. *Chem.─Eur. J.* **2023**, *29*, e202301540 DOI: 10.1002/chem.202301540

(88) Kosower, E. M.; Huppert, D. Excited state electron and proton transfers. *Annu. Rev. Phys. Chem.* **1986**, *37*, 127– 156, DOI: 10.1146/annurev.pc.37.100186.001015.

(89) Robin, M. B.; Day, P. Mixed-valence chemistry: A survey and classification. *Adv. Inorg. Chem. Radiochem.* **1968**, *10*, 247– 422, DOI: 10.1016/S0065-2792(08)60179-X.

(90) *Electron paramagnetic resonance; A practitioner's toolkit*, Brustolon, M.; Giamello, E., Eds.; Wiley, 2009; p 539.

(91) Nakano, M. Open-shell-character-based molecular design principles: Applications to nonlinear optics and singlet fission. *Chem. Rec.* **2017**, *17*, 27– 62, DOI: 10.1002/tcr.201600094.

(92) Nakano, M.; Kishi, R.; Ohta, S.; Takahashi, H.; Kubo, T.; Kamada, K.; Ohta, K.; Botek, E.; Champagne, B. Relationship between third-order

nonlinear optical properties and magnetic interactions in open-shell systems: A new paradigm for nonlinear optics. *Phys. Rev. Lett.* **2007**, *99*, 033001 DOI: 10.1103/PhysRevLett.99.033001.

(93) Zatsikha, Y. V.; Shamova, L. I.; Blesener, T. S.; Kuzmin, I. A.; Germanov, Y. V.; Herbert, D. E.; Nemykin, V. N. Development of a class of easily scalable, electron-deficient, core-extended benzo-fused azadipyrromethene derivatives (″MB-DIPY″). *J. Org. Chem.* **2019**, *84*, 14540– 14557, DOI: 10.1021/acs.joc.9b02074.

(94) Zatsikha, Y. V.; Shamova, L. I.; Blesener, T. S.; Herbert, D. E.; Nemykin, V. N. Rigid, yet flexible: formation of unprecedented silver MB-DIPY dimers with orthogonal chromophore geometry. *Dalton Trans.* **2020**, *49*, 5034– 5038, DOI: 10.1039/D0DT00927J.

(95) Zatsikha, Y. V.; Shamova, L. I.; Schaffner, J. W.; Healy, A. T.; Blesener, T. S.; Cohen, G.; Wozniak, B.; Blank, D. A.; Nemykin, V. N. Probing electronic communication and excited-State dynamics in the unprecedented ferrocene-containing zinc MB-DIPY. *ACS Omega* **2020**, *5*, 28656– 28662, DOI: 10.1021/acsomega.0c03764.

(96) Zatsikha, Y. V.; Shamova, L. I.; Shepit, M.; Berry, S. M.; Thomas, F.; Herbert, D. E.; van Lierop, J.; Nemykin, V. N. Radical Complexes of nickel(II)/copper(II) and redox non-innocent MB-DIPY ligands: Unusual stability and strong near-infrared absorption at λmax ∼ 1300 nm. *Chem.─Eur. J.* **2022**, *28*, e202201181 DOI: 10.1002/chem.202201181.

(97) *KaleidaGraph, version 5.04* , 1986–2023; Synergy Software Inc..

(98) Sheldrick, G. M. A short history of *SHELX*. *Acta Crystallogr.* **2008**, *A64*, 112– 122, DOI: 10.1107/S0108767307043930.

(99) *Bruker-AXS APEX3 v2016.1–0*, Madison, Wisconsin, USA, 2016..

(100) Spek, A. L. Structure validation in chemical crystallography. *Acta Crystallogr.* **2009**, *D65*, 148– 155, DOI: 10.1107/S090744490804362X.

(101) Macrae, C. F.; Sovago, I.; Cottrell, S. J.; Galek, P. T. A.; McCabe, P.; Pidcock, E.; Platings, M.; Shields, G. P.; Stevens, J. S.; Towler, M.; Wood, P. A. Mercury 4.0: from visualization to analysis, design and prediction. *J. Appl. Crystallogr.* **2020**, *53*, 226– 235, DOI: 10.1107/S1600576719014092.

(102) Frisch, M. J.; Trucks, G. W.; Schlegel, H. B.; Scuseria, G. E.; Robb, M. A.; Cheeseman, J. R.; Scalmani, G.; Barone, V.; Petersson, G. A.; Nakatsuji, H.; Li, X.; Caricato, M.; Marenich, A. V.; Bloino, J.; Janesko, B. G.; Gomperts, R.; Mennucci, B.; Hratchian, H. P.; Ortiz, J. V.; Izmaylov, A. F.; Sonnenberg, J. L.; Williams-Young, D.; Ding, F.; Lipparini, F.; Egidi, F.; Goings, J.; Peng, B.; Petrone, A.; Henderson, T.; Ranasinghe, D.; Zakrzewski, V. G.; Gao, J.; Rega, N.; Zheng, G.; Liang, W.; Hada, M.; Ehara, M.; Toyota, K.; Fukuda, R.; Hasegawa, J.; Ishida, M.; Nakajima, T.; Honda, Y.; Kitao, O.; Nakai, H.; Vreven, T.; Throssell, K.; Montgomery, J. A., Jr.; Peralta, J. E.; Ogliaro, F.; Bearpark, M. J.; Heyd, J. J.; Brothers, E. N.; Kudin, K. N.; Staroverov, V. N.; Keith, T. A.; Kobayashi, R.; Normand, J.; Raghavachari, K.; Rendell, A. P.; Burant, J. C.; Iyengar, S. S.; Tomasi, J.; Cossi, M.; Millam, J. M.; Klene,

M.; Adamo, C.; Cammi, R.; Ochterski, J. W.; Martin, R. L.; Morokuma, K.; Farkas, O.; Foresman, J. B.; Fox, D. J. *Gaussian 16, Revision B.01*; Gaussian, Inc.: Wallingford CT, 2016.

(103) Tenderholt, A. L. *QMForge, version 2.1*; Standord University: Stanford, CA, 2011. https://qmforge.net/.

(104) Tao, J. M.; Perdew, J. P.; Staroverov, V. N.; Scuseria, G. E. Climbing the density functional ladder: Nonempirical meta-generalized gradient approximation designed for molecules and solids. *Phys. Rev. Lett.* **2003**, *91*, 146401/1– 146401/4, DOI: 10.1103/PhysRevLett.91.146401.

(105) Staroverov, V. N.; Scuseria, G. N.; Tao, J.; Perdew, J. P. Comparative assessment of a new nonempirical density functional: Molecules and hydrogen-bonded complexes. *J. Chem. Phys.* **2003**, *119*, 12129– 12137, DOI: 10.1063/1.1626543.

(106) Zhao, Y.; Truhlar, D. G. The M06 Suite of density functionals for main group thermochemistry, thermochemical kinetics, noncovalent interactions, excited states, and transition elements: Two new functionals and systematic testing of four M06 functionals and twelve other functionals. *Theor. Chem. Acc.* **2008**, *120*, 215– 241, DOI: 10.1007/s00214-007-0310-x.

(107) Becke, A. D. Density-functional thermochemistry. III. The role of exact exchange. *J. Chem. Phys.* **1993**, *98*, 5648– 5652, DOI: 10.1063/1.464913.

(108) Chai, J. D.; Head-Gordon, M. Long-range corrected hybrid density functionals with damped atom-atom dispersion corrections. *Phys. Chem. Chem. Phys.* **2008**, *10*, 6615– 6620, DOI: 10.1039/b810189b.

(109) McLean, A. D.; Chandler, G. S. Contracted Gaussian basis sets for molecular calculations. 1. Second row atoms, Z = 11–18. *J. Chem. Phys.* **1980**, *72*, 5639– 5648, DOI: 10.1063/1.438980.

(110) Herdan, J. M.; Dinoiu, V.; Meghea, A.; Schiketanz, A.; Gheorghiu, M. D.; Balaban, A. T. Synthesis and EPR spectra of persistent aroxyls. Part 5. AROXYLS derived from chalcone and derivatives. *Rev. Roumaine Chim.* **1990**, *35*, 1017– 1024

Appendix

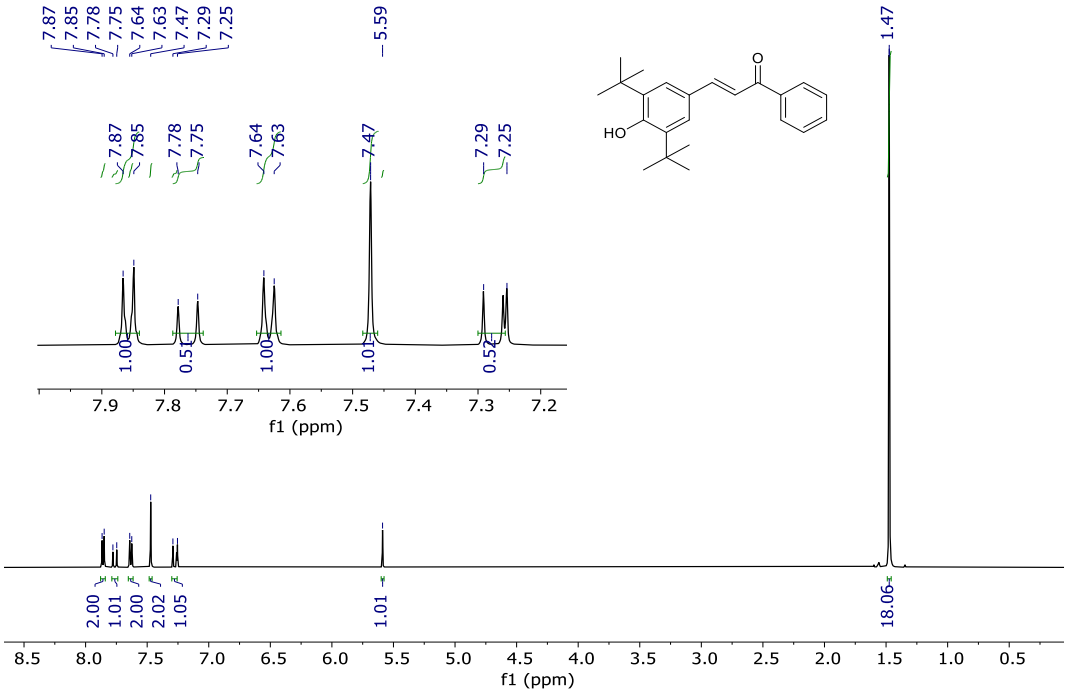


Figure 2.27: ^{1}H NMR spectrum of compound **2.1** in $CDCl_3$.

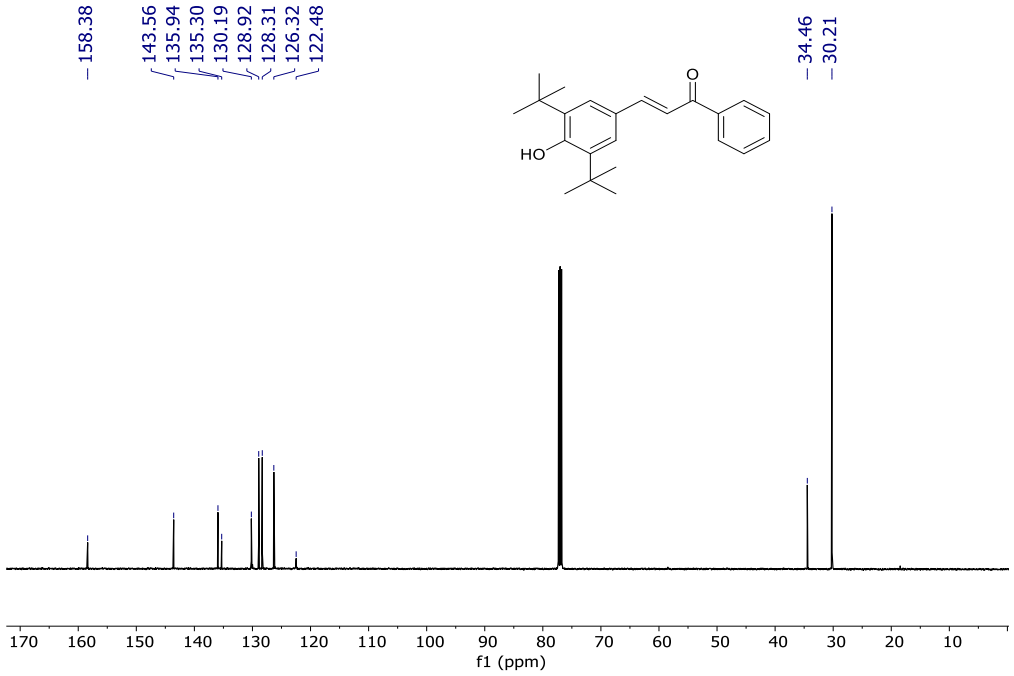


Figure 2.28: ^{13}C NMR spectra of compound **2.1** in $CDCl_3$.

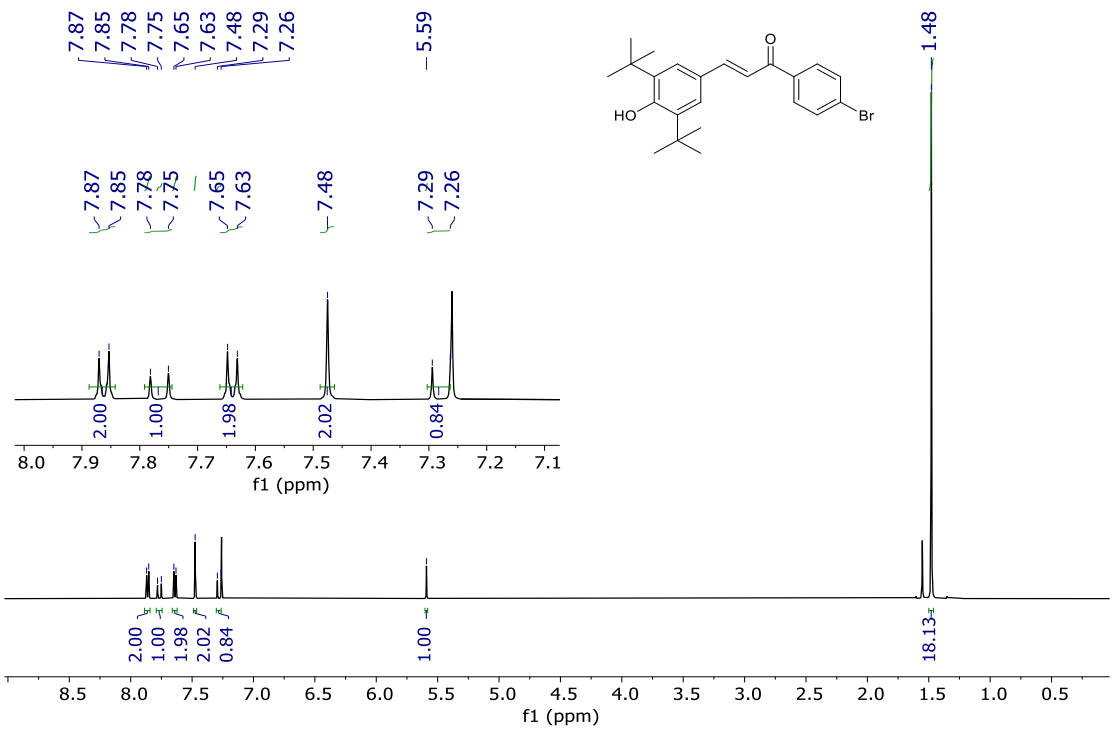


Figure 2.29: ^{1}H NMR spectrum of compound **2.2** in $CDCl_3$.

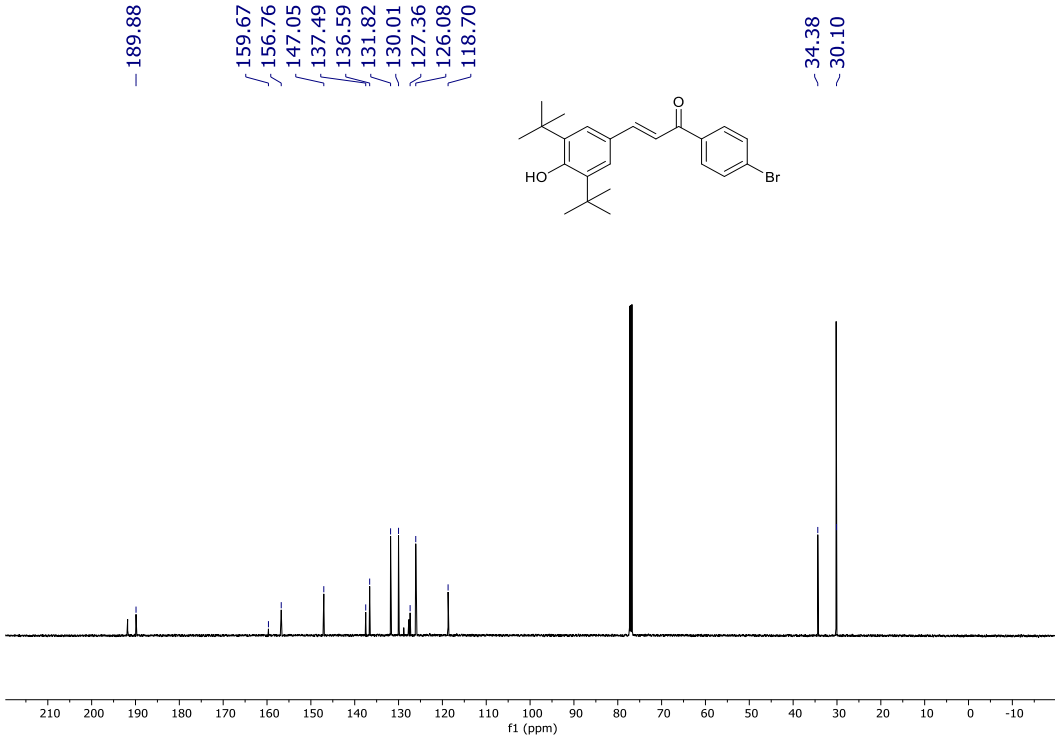


Figure 2.30: ^{13}C NMR spectra of compound **2.2** in $CDCl_3$.

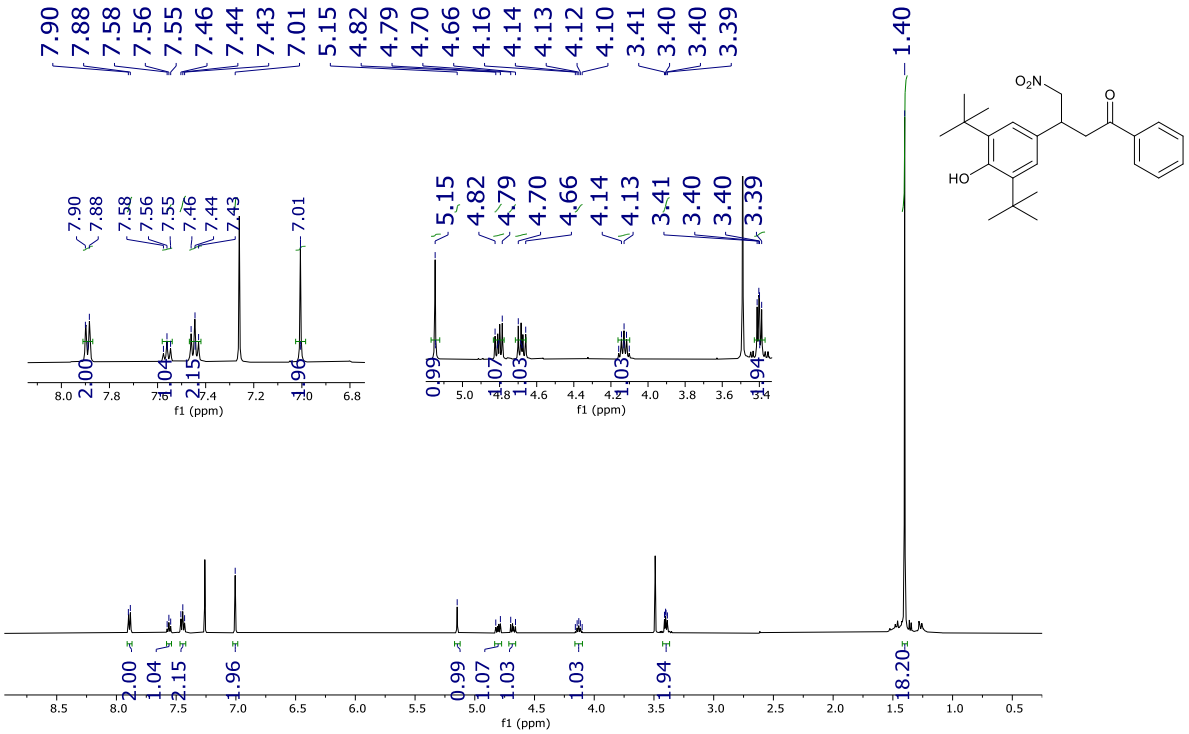


Figure 2.31: ^{1}H NMR spectra of compound **2.3** in $CDCl_3$.

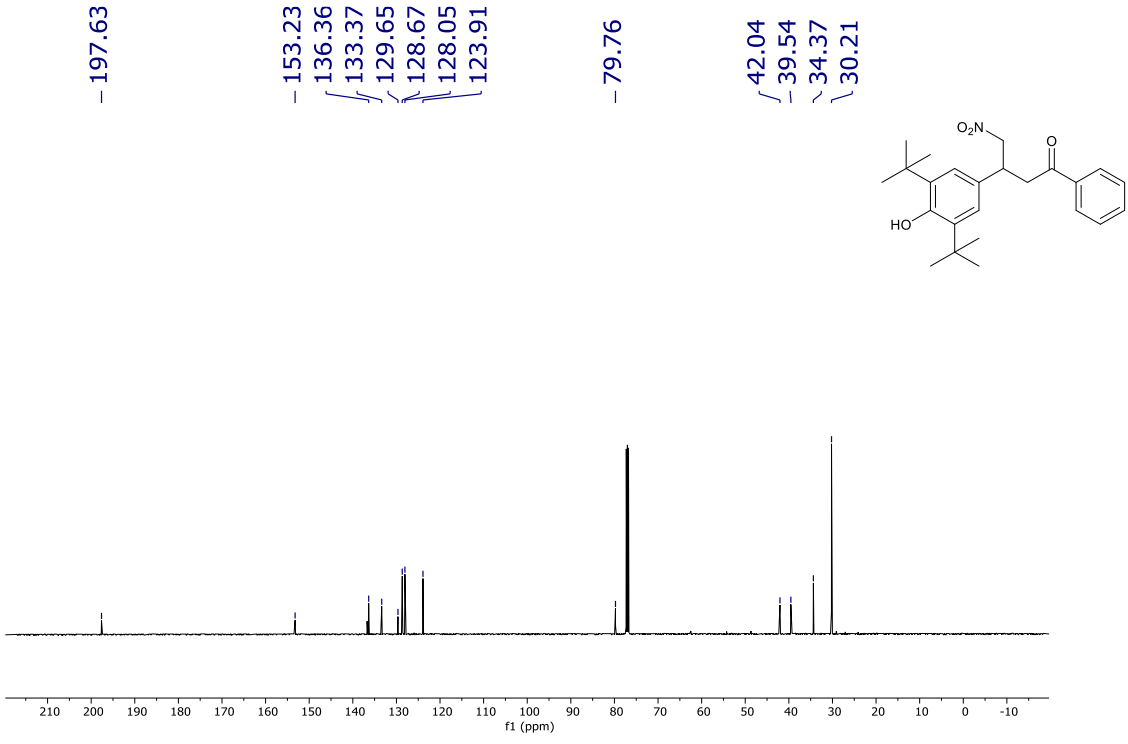


Figure 2.32: ^{13}C NMR spectra of compound **2.3** in $CDCl_3$.

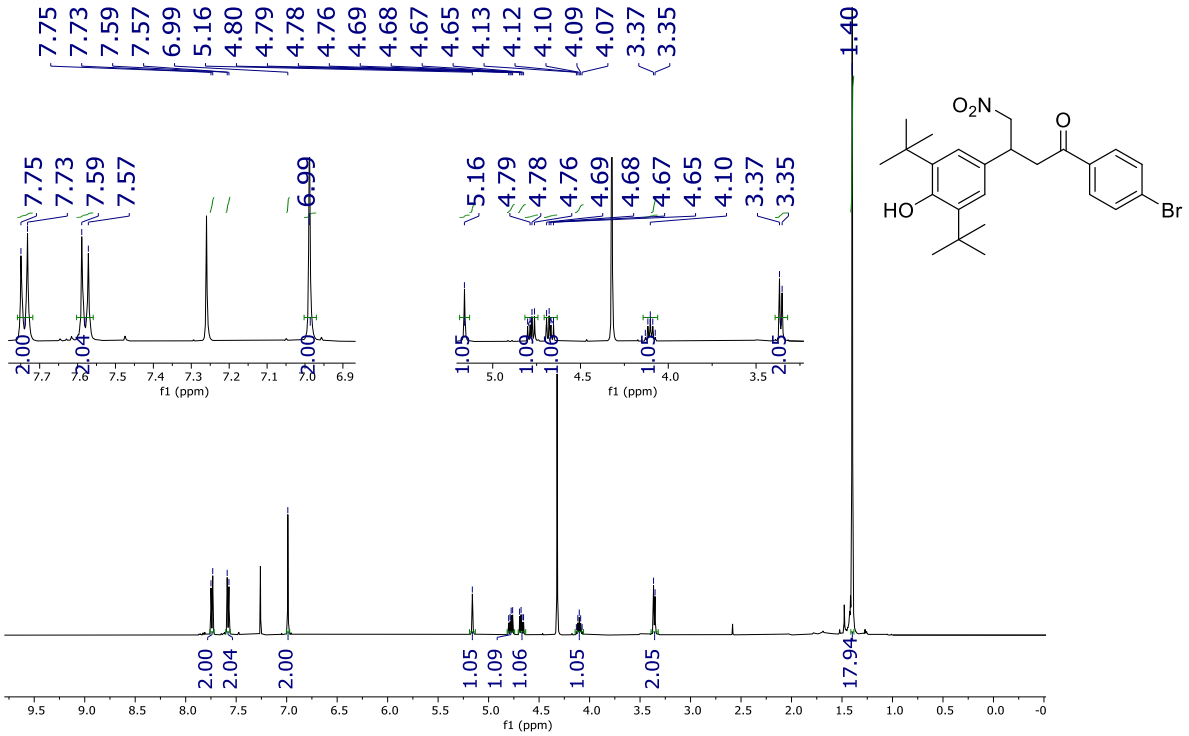


Figure 2.33: ^{1}H NMR spectra of compound **2.4** in $CDCl_3$.

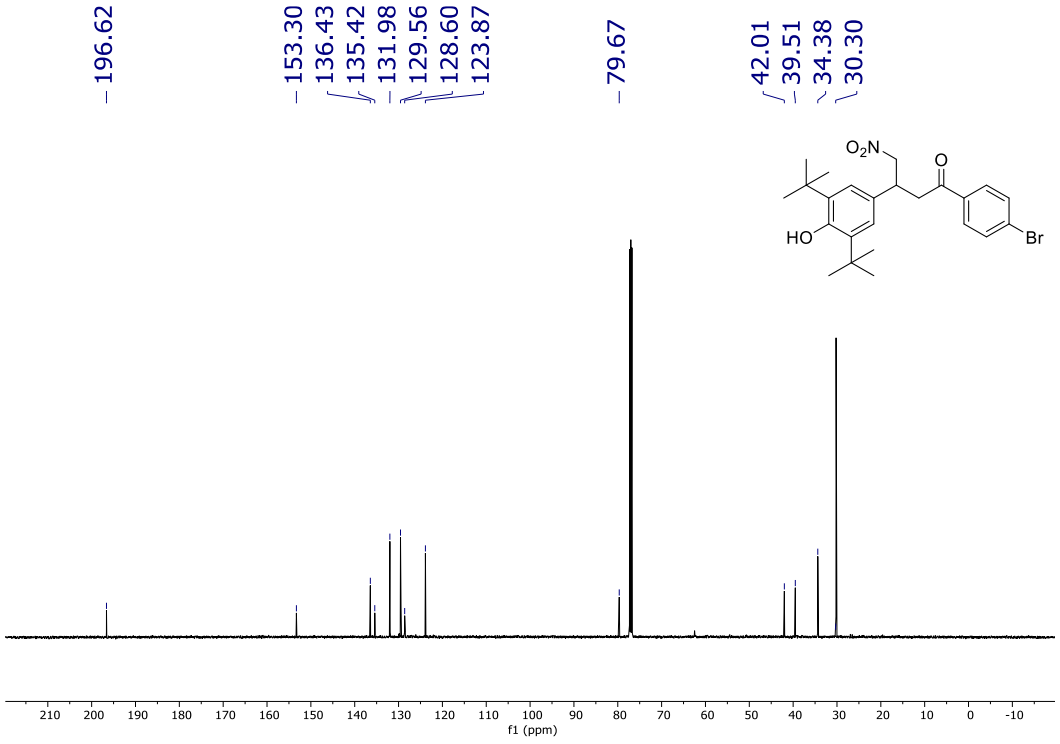


Figure 2.34: ^{13}C NMR spectra of compound **2.4** in $CDCl_3$.

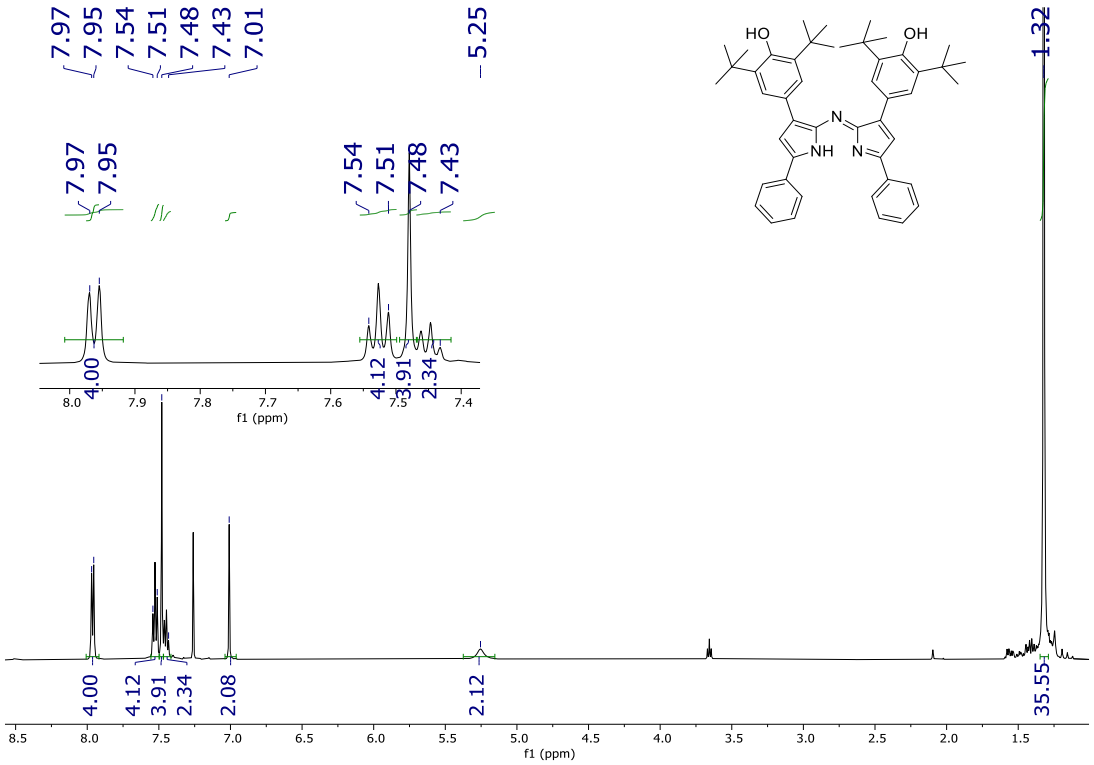


Figure 2.35: ^{1}H NMR spectra of compound **2.5** in $CDCl_3$.

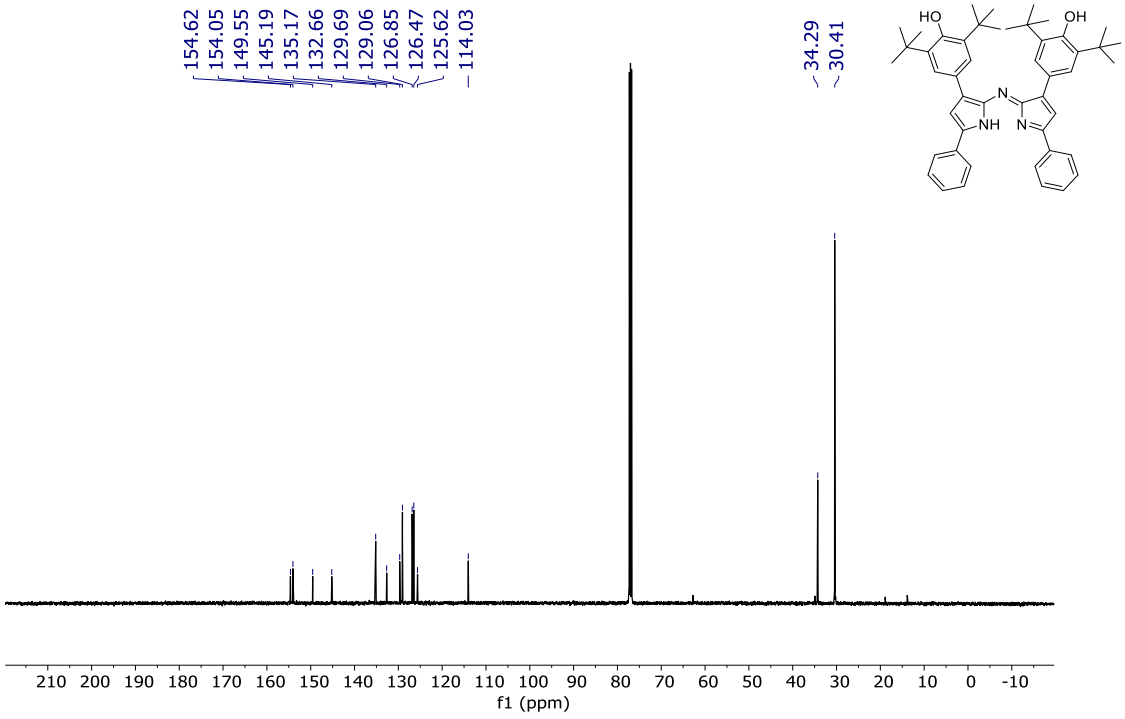


Figure 2.36: ^{13}C NMR spectra of compound **2.5** in $CDCl_3$.

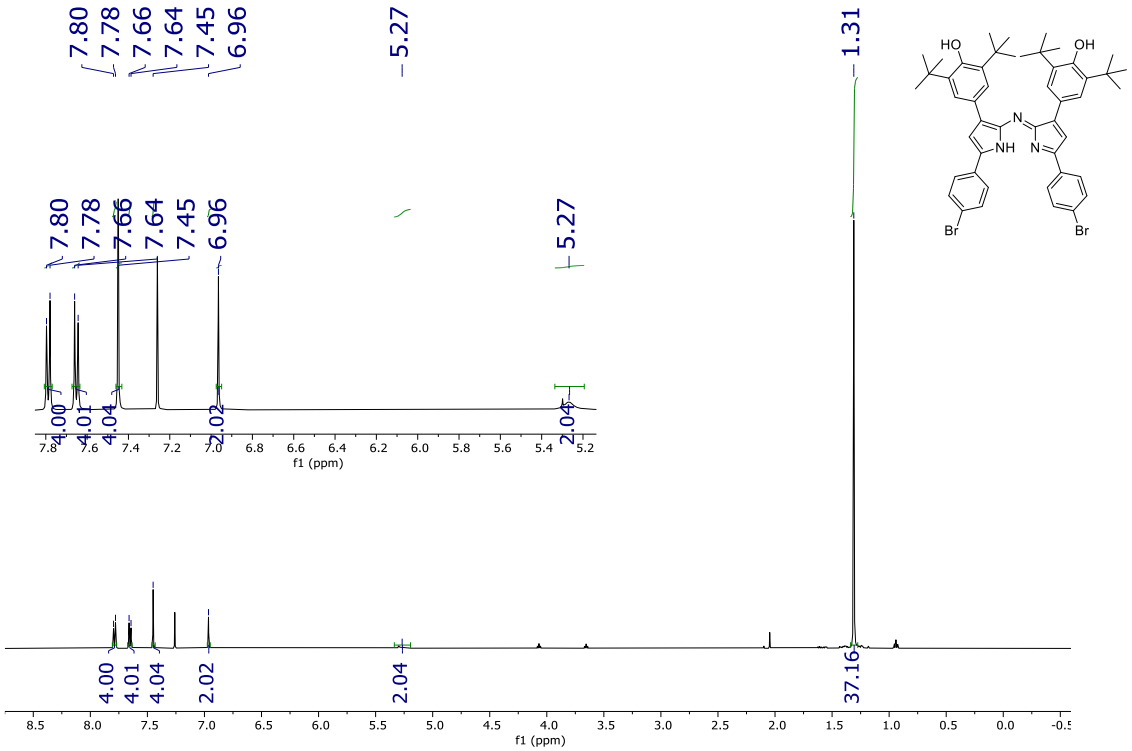


Figure 2.37: ^{1}H NMR spectra of compound **2.6** in $CDCl_3$.

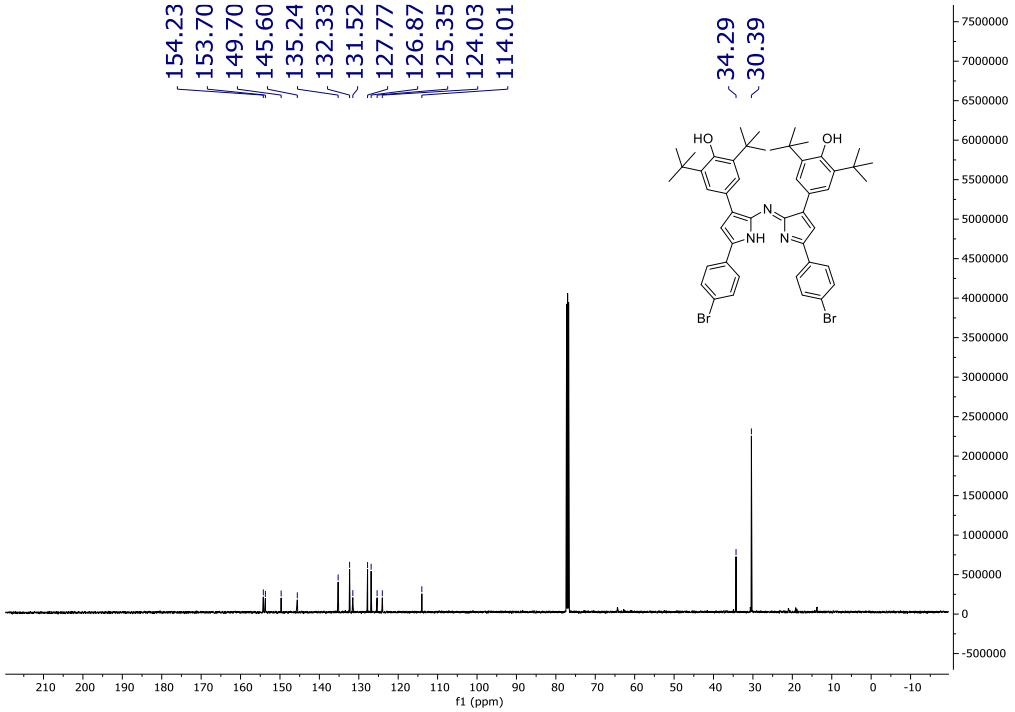


Figure 2.38: ^{13}C NMR spectra of compound **2.6** in $CDCl_3$.

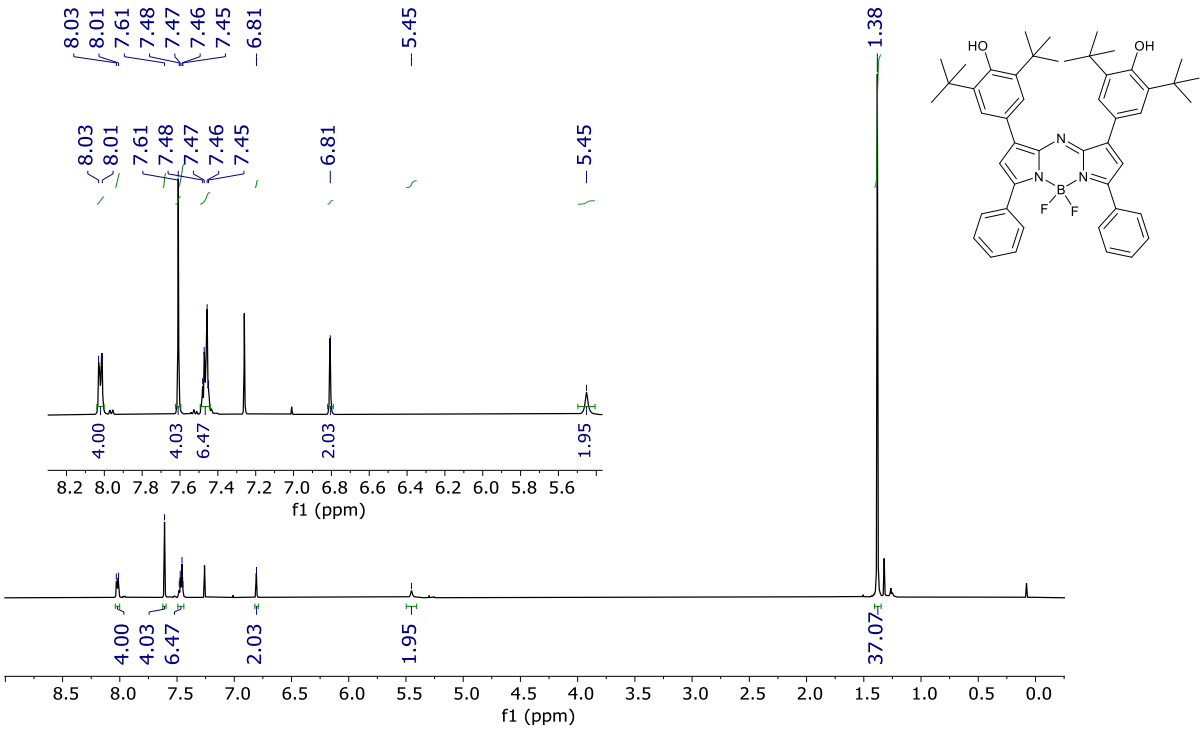


Figure 2.39: ^{1}H NMR spectra of compound **2.7** in $CDCl_3$.

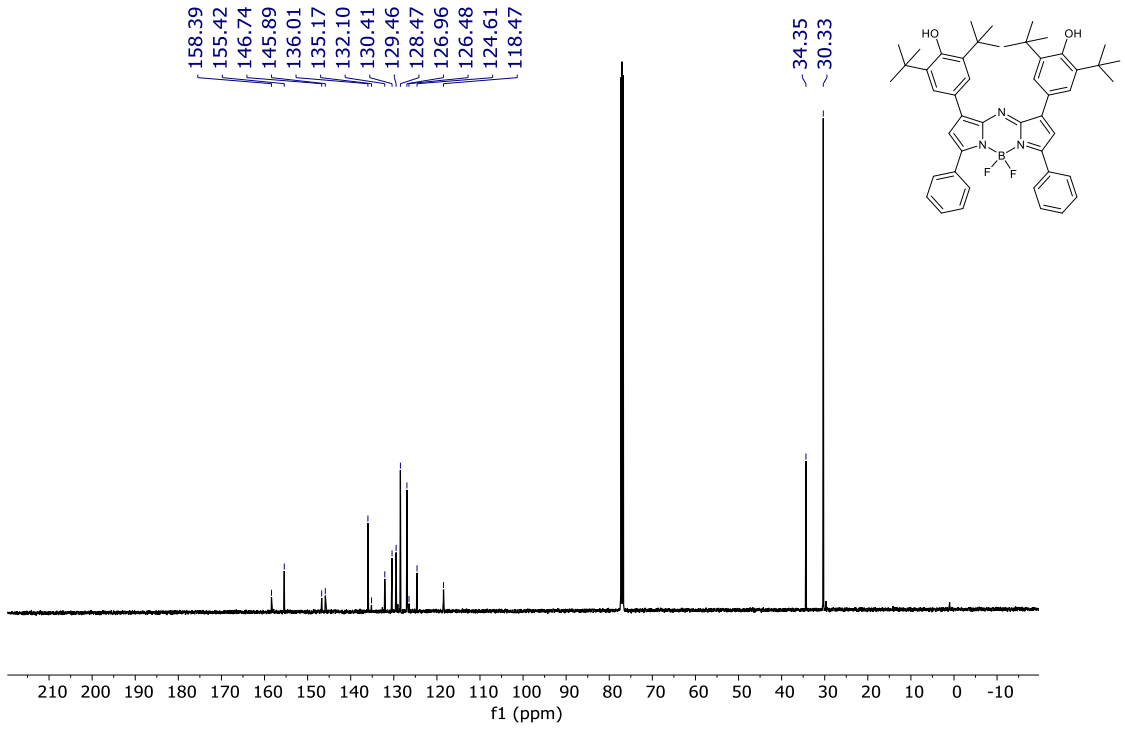


Figure 2.40: ^{13}C NMR spectra of compound **2.7** in $CDCl_3$.

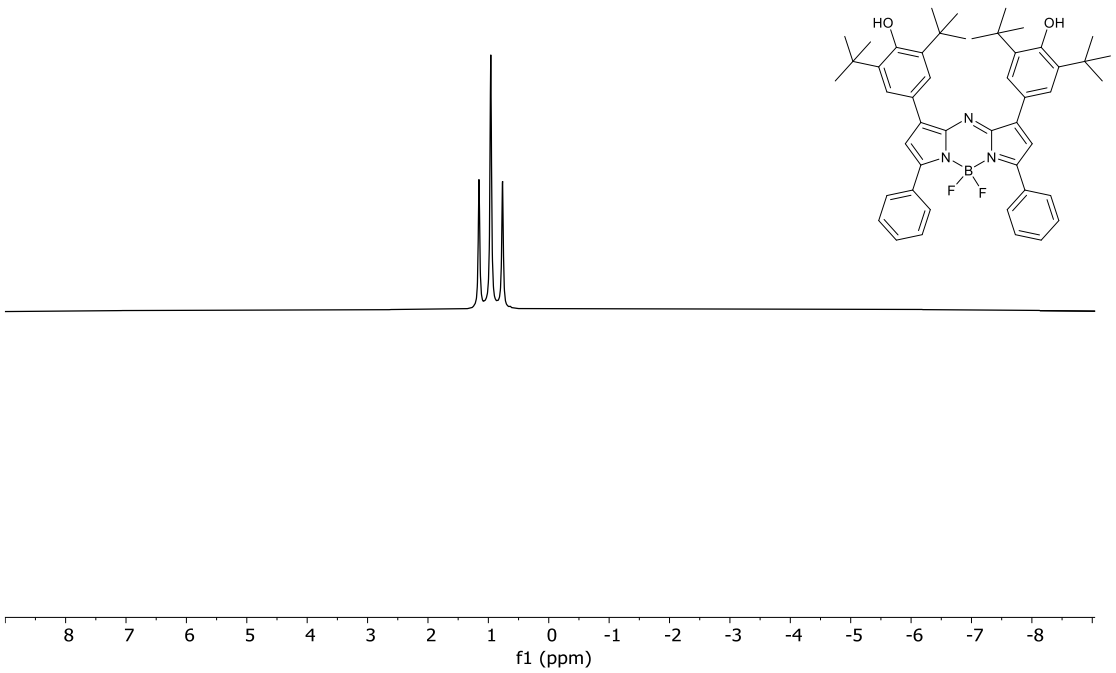


Figure 2.41: ^{11}B NMR of compound **2.7**.

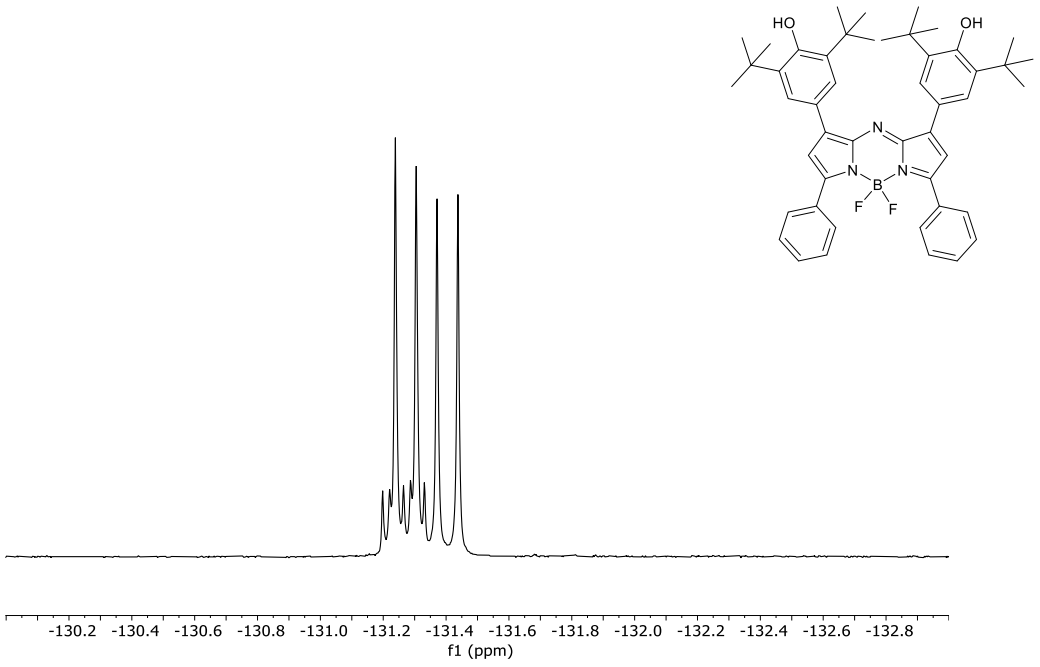


Figure 2.42: ^{19}F NMR of compound **2.7.**

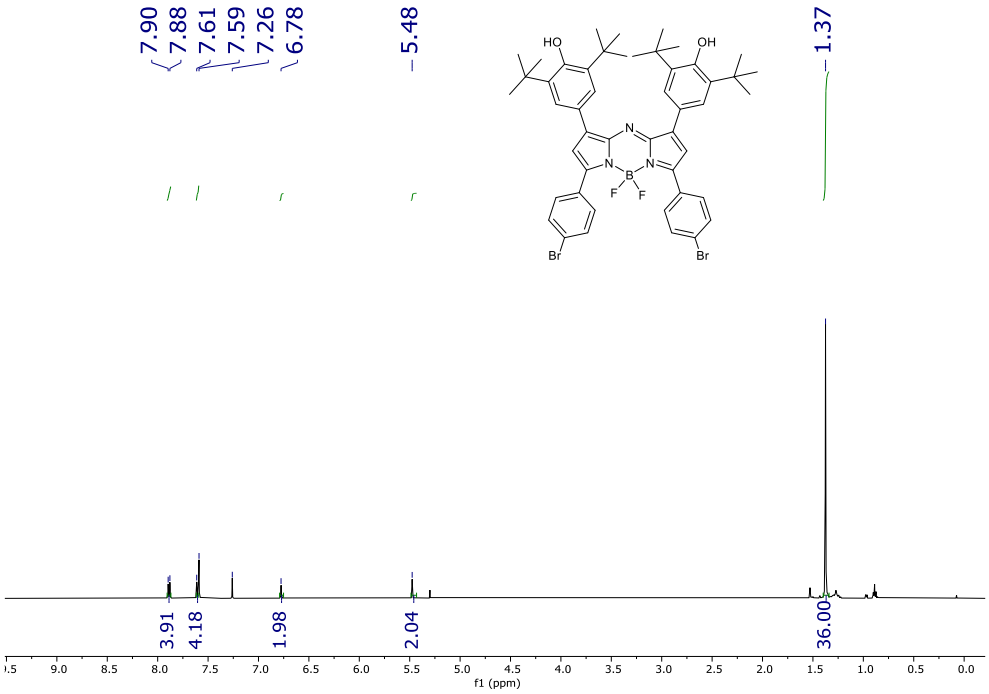


Figure 2.43: ^{1}H NMR spectra of compound **2.8** in $CDCl_3$.

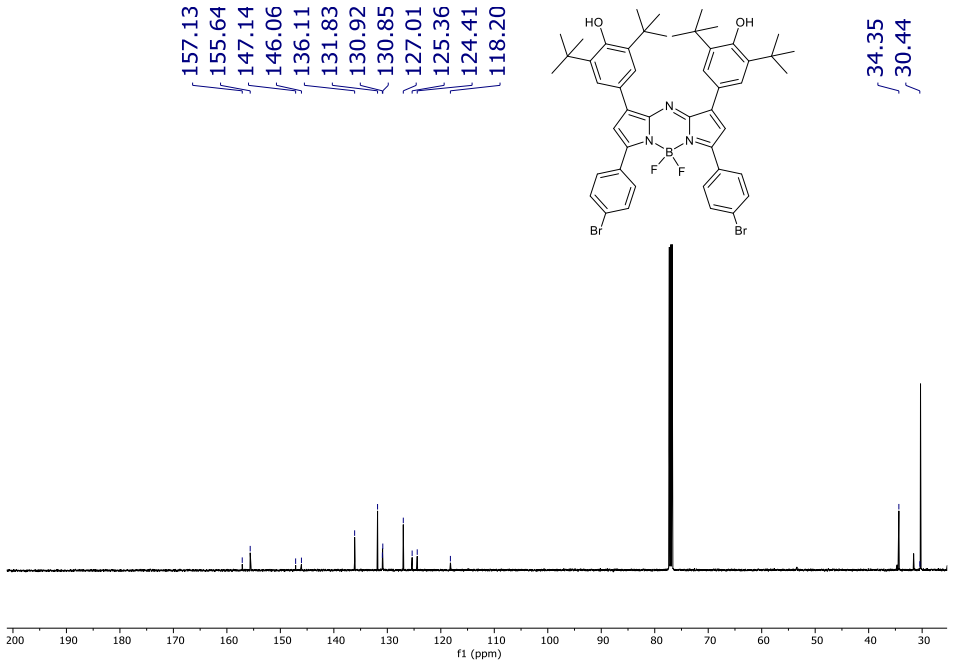


Figure 2.44: ^{13}C NMR spectra of compound **2.8** in $CDCl_3$.

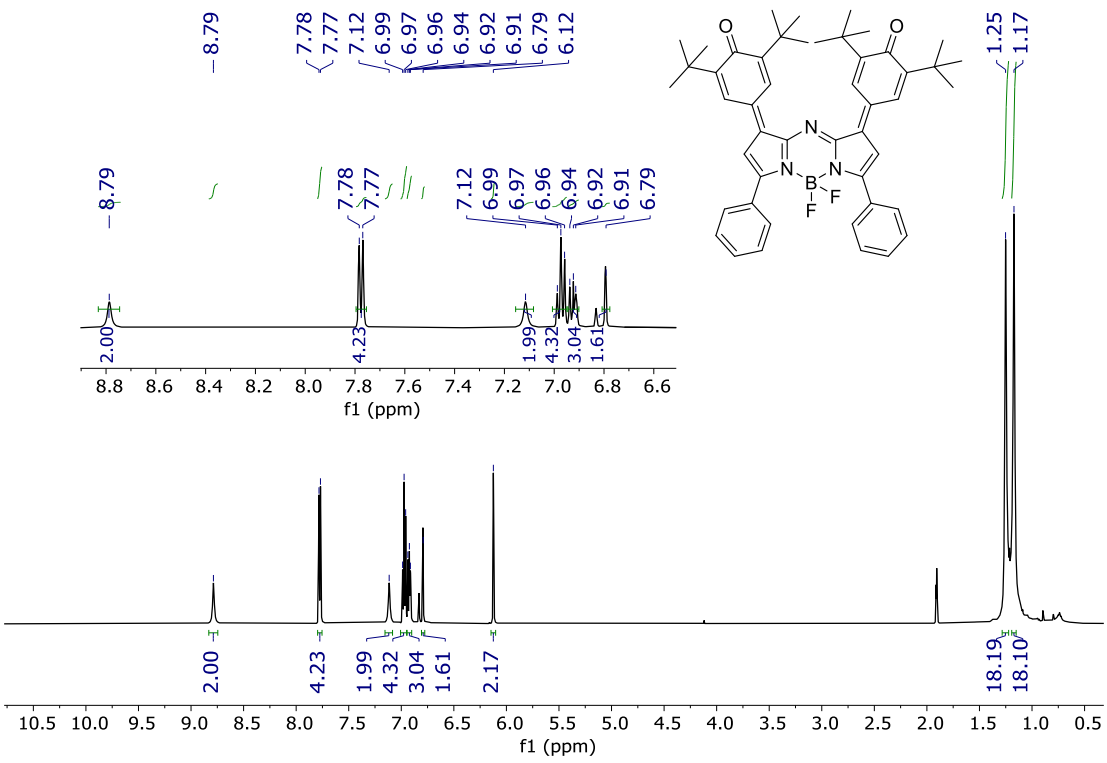


Figure 2.45: ^{1}H NMR spectra of compound **2.9** in $CDCl_3$.

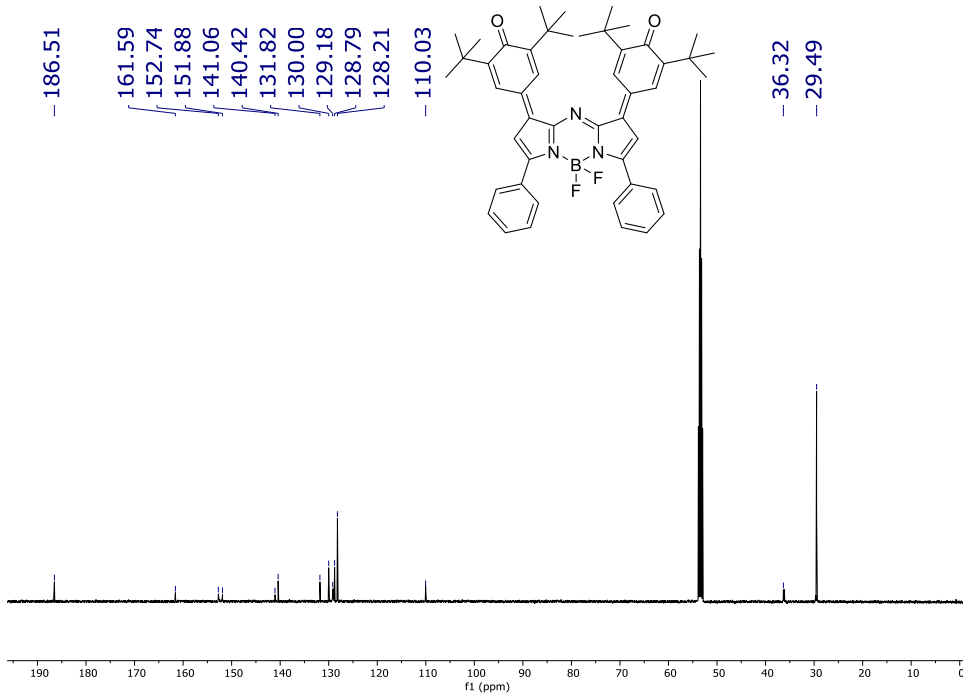


Figure 2.46: ^{13}C NMR spectra of compound **2.9** in $CDCl_3$.

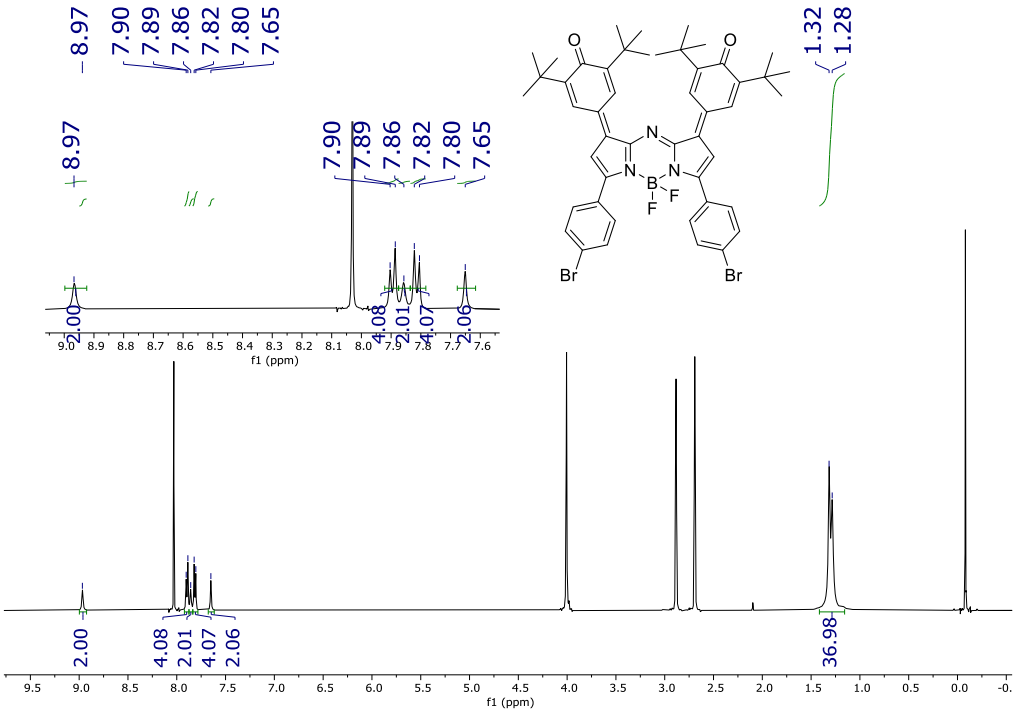


Figure 2.47: ^{1}H NMR spectra of compound **2.10** in $CDCl_3$.

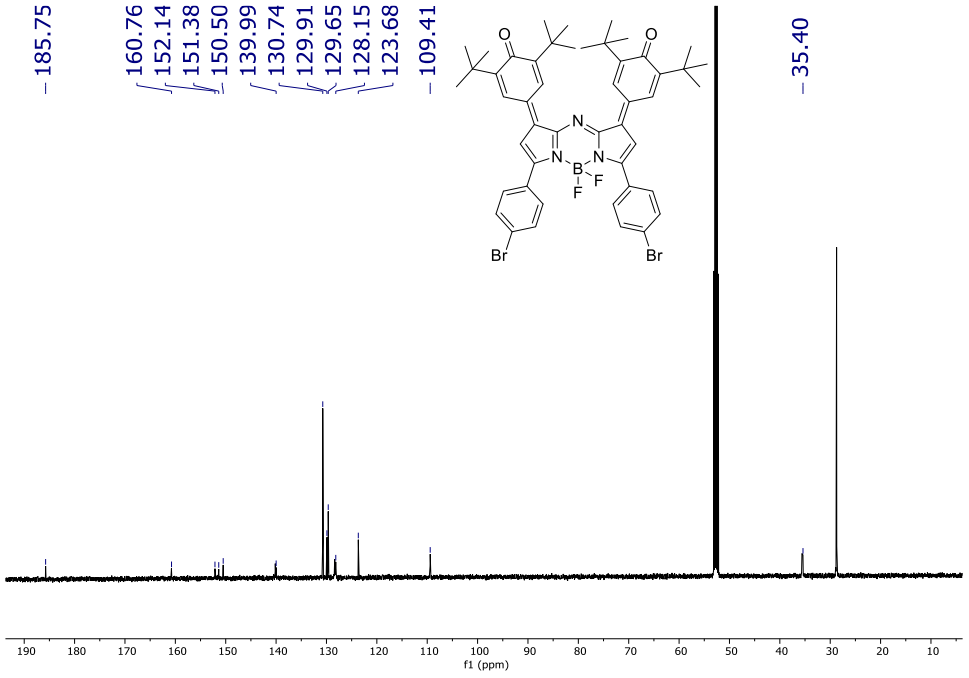


Figure 2.48: ^{13}C NMR spectra of compound **2.10** in $CDCl_3$.

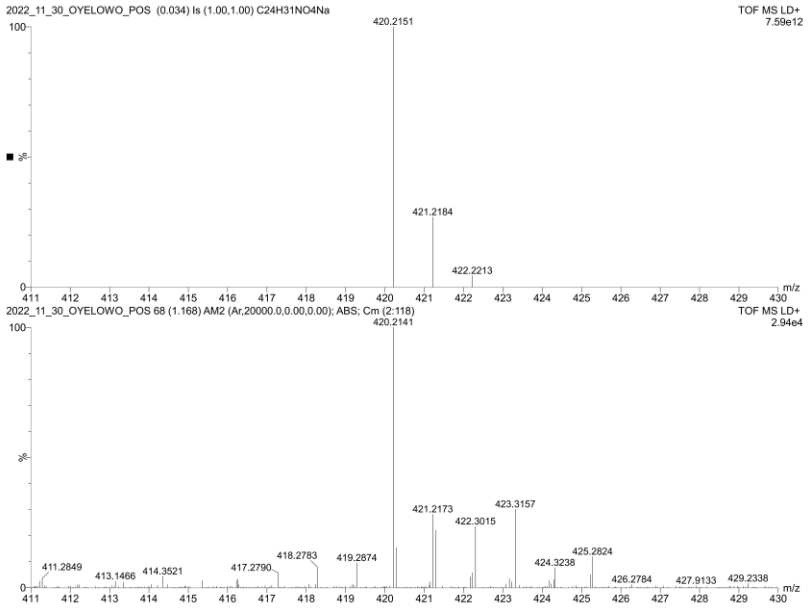


Figure 2.49: Mass Spectrum (MALDI) of Compound **2.3**.

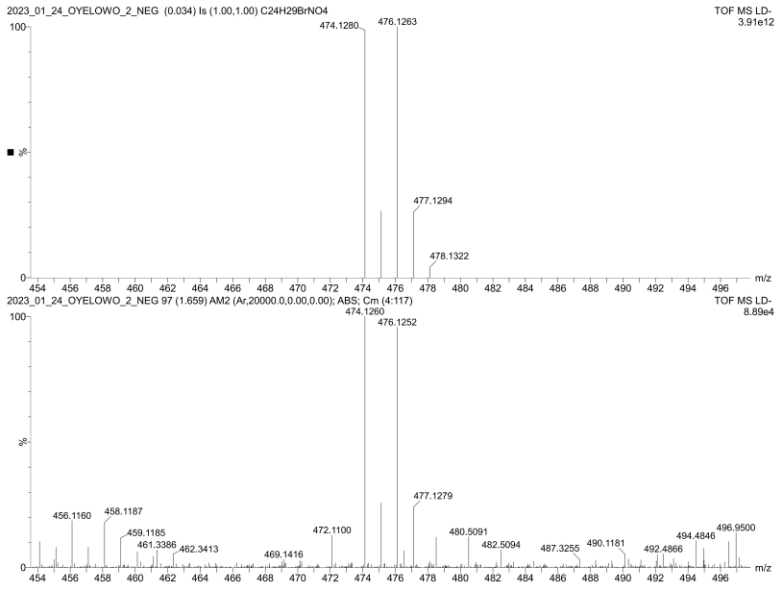


Figure 2.50: Mass Spectrum (MALDI) of Compound **2.4**.

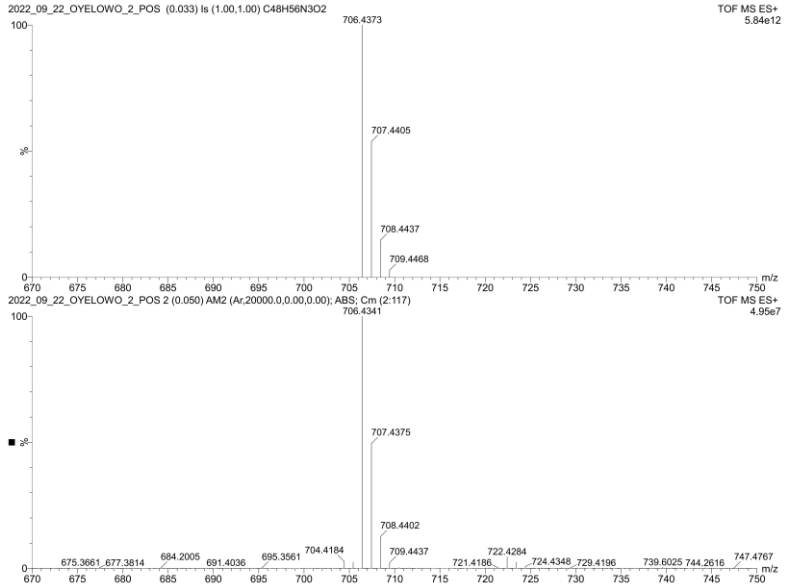


Figure 2.51: Mass Spectrum (MALDI) of Compound **2.5**

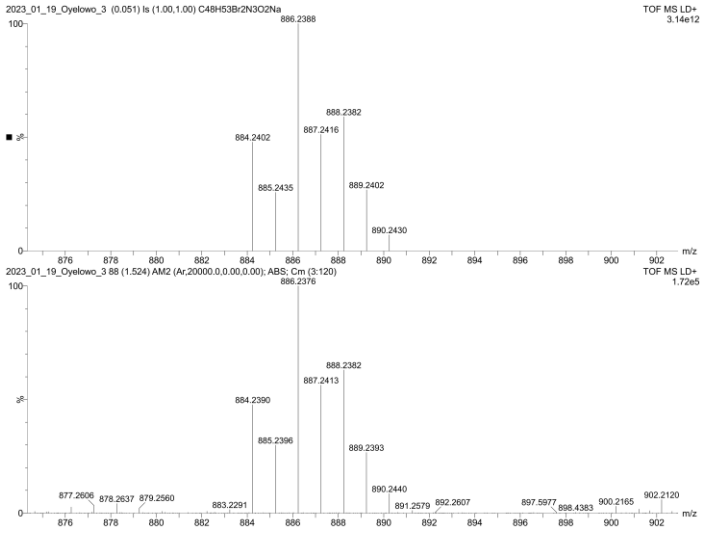


Figure 2.52: Mass Spectrum (MALDI) of Compound **2.6**

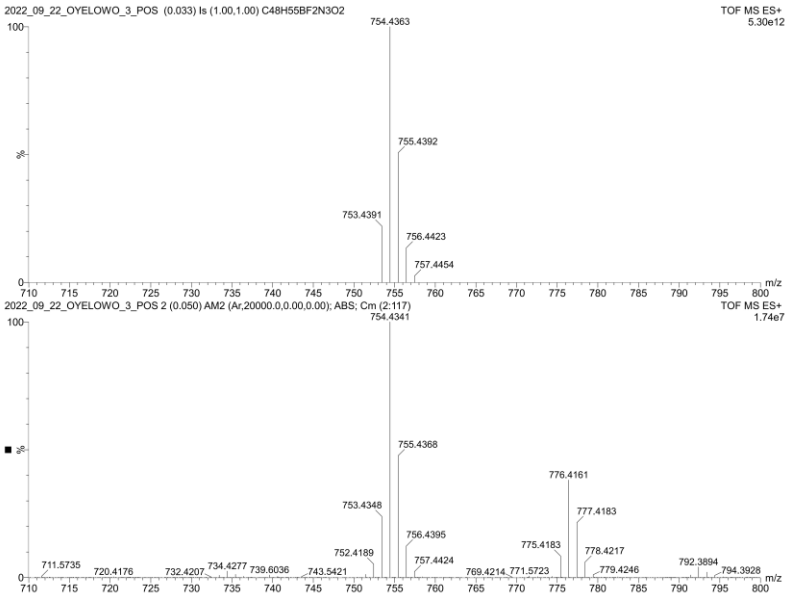


Figure 2.53: Mass Spectrum (MALDI) of Compound **2.7**

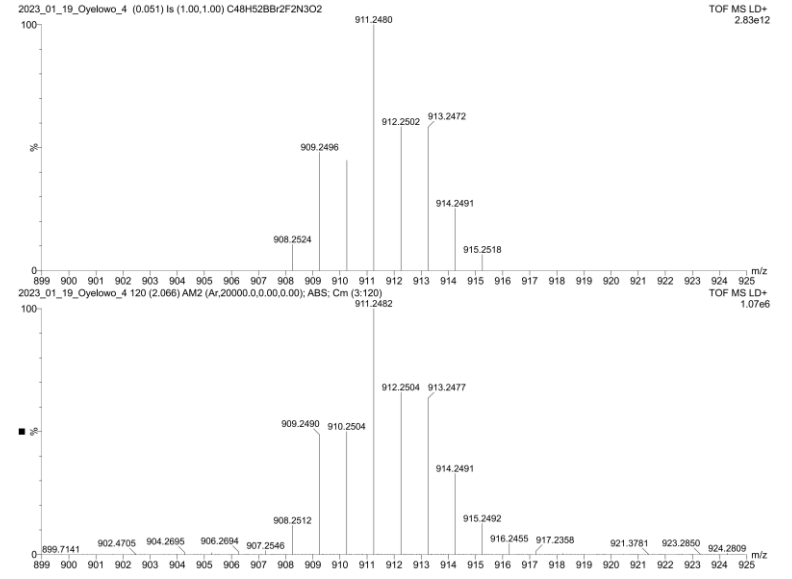


Figure 2.54: Mass Spectrum (MALDI) of Compound **2.8**

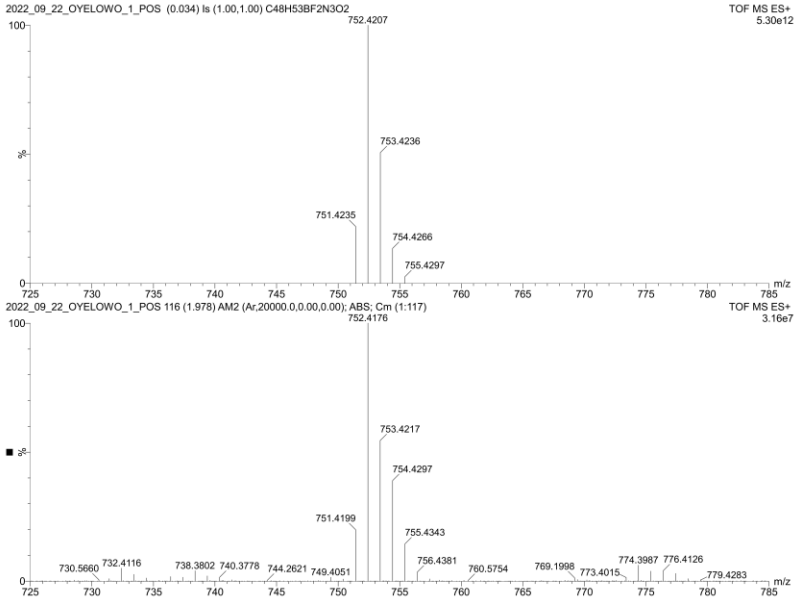


Figure 2.55: Mass Spectrum (MALDI) of Compound **2.9**

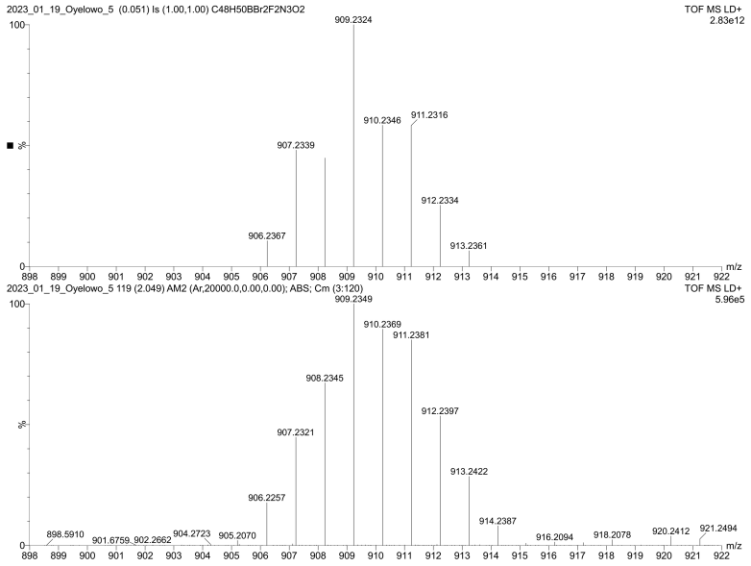


Figure 2.56: Mass Spectrum (MALDI) of Compound **2.10**.

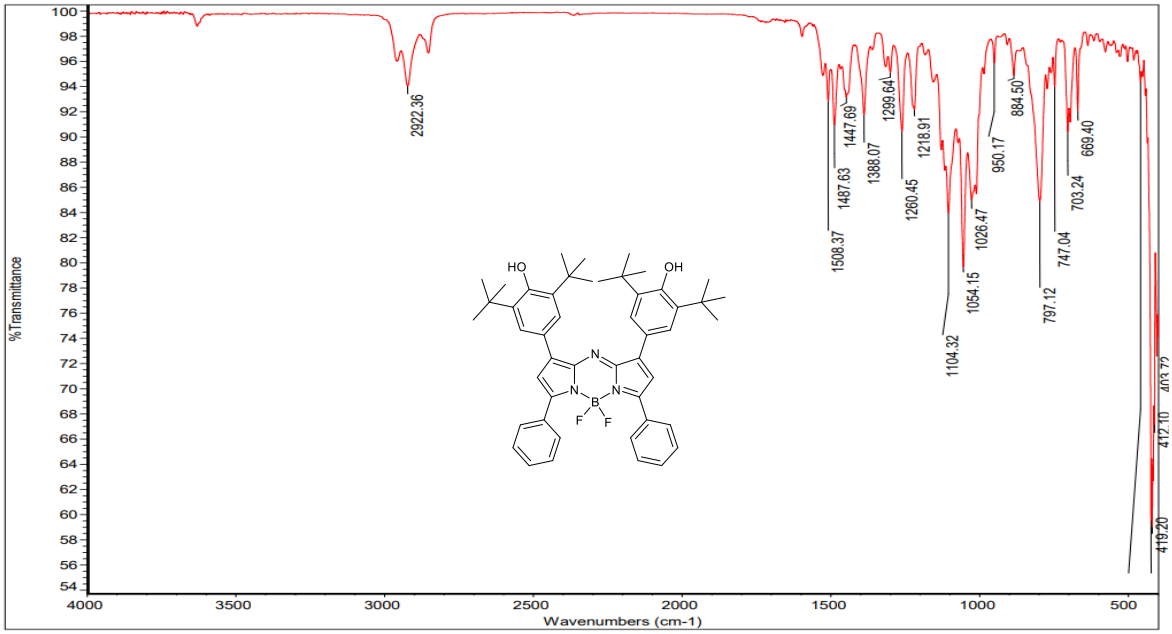


Figure 2.57: IR Spectrum of **2.7** in solid state.

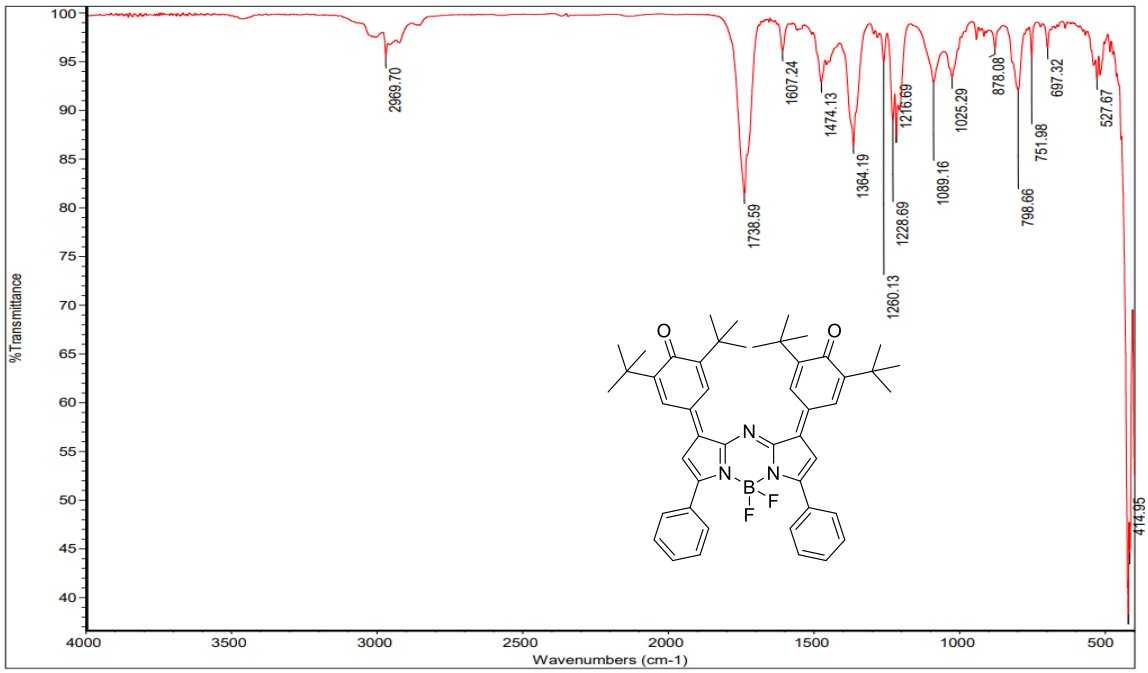


Figure 2.58: IR Spectrum of **2.9** in solid state.

Table 2.6a. Major TDDFT-Predicted Excited States of **2.7.**

Excited State	*Wavelength (nm)*	*Energy (Cm^{-1})*	*Oscillator Strength, f*	*% Contributions*
1	601	16626	0.6467	H→L (96%)
2	499	20031	0.2092	H-1→L (81%), H-2→L (13%)
3	493	20295	0.2277	H-2→L (80%), H-1→L (16%)
8	352	28437	0.1372	H-7→L (89%), H→L+1 (5%)
13	294	34066	0.1342	H→L+2 (74%), H→L+1(17%)
14	292	34191	0.5229	H→L+1 (65%), H→L+2 (19%), H→L+3 (8%)

Table 2.6b. Major TDDFT-Predicted Excited Staes of **$[2.12]^{2-}$.**

Excited State	*Wavelength (nm)*	*Energy (Cm^{-1})*	*Oscillator Strength, f*	*% Contributions*
1	915	10930	0.4979	H→L (106%)
2	642	15582	0.4929	H-1→L (99%)
5	484	20649	0.2040	H-2→L (92%)
19	314	31802	0.6968	H→L+7 (42%), H→L+5 (34%), H-8→L (6%)
22	309	32390	0.1172	H→L+9 (79%), H→L+6 (12%)
32	279	35866	0.2769	H-10→L (47%), H-2→L+3 (16%), H-2→L+1 (13%), H-12→L (10%)

Table 2.6c Major TDDFT-Predicted Excited States of **2.9(CS)**

Excited State	*Wavelength (nm)*	*Energy (Cm^{-1})*	*Oscillator Strength, f*	*% Contributions*
1	860	11626	0.3060	H→L (98%)
5	570	17558	0.4397	H→L+1 (77%), H-9→L (11%), H-1→L (9%)
11	439	22755	0.1261	H-6→L (94%)
13	385	25995	0.2273	H-3→L+1 (39%), H-9→L (32%), H-12→L (15%), H-2→L (6%)
14	382	26195	0.7080	H-11→L (60%), H-9→L (18%), H→L+1 (7%), H-12→L (6%)
16	374	26759	0.1144	H-3→L+1 (38%), H-9→L (28%), H-11→L (20%), H-2→L (5%), H-12→L (5%)

Table 2.6d Major TDDFT-Predicted Excited states of **2.9(OS)** using C2_wB97X_MO6

Excited State	*Wavelength (nm)*	*Energy (Cm^{-1})*	*Oscillator Strength, f*	*% Contributions*
3	837	11956	0.3325	H(A)→L(A) (47%), H(B)→L(B) (47%)
8	565	17714	0.4204	H(A)→L+1(A) (26%), H(B)→L+1(B) (26%), H-1(B)→L(B) (9%), H-1(A)→L(A) (9%)
16	450	22225	0.1158	H-1(B)→L+1(B) (40%), H-1(A)→L+1(A) (40%)
28	385	25968	0.7023	H-9(B)→L(B) (18%), H-9(A)→L(A) (17%), H-11(A)→L(A) (14%), H-11B→L(B) (13%), H-10(A)→L(A) (6%), H-10B→L(B) (5%)

Table 2.6e Major TDDFT-Predicted Excited Staes of **2.9(OS)** using C2_CAM_B3LYP

Excited State	*Wavelength (nm)*	*Energy (Cm^{-1})*	*Oscillator Strength, f*	*% Contributions*
3	837	11947	0.3371	H(A)→L(A) (46%), H(B)→L(B) (46%)
8	565	17686	0.4228	H(A)→L+1(A) (27%), H$\bar{1}$(B)→L+1(B) (27%), H-1(B)→L(B) (9%), H-1(A)→L(A) (9$\bar{1}$%), H-1(B)→L+1(B) (5%), H-1$\bar{1}$(A)→L+1(A) (5%)
16	450	22201	0.1207	H-1(A)→L+1(A) (41%), H-1$\bar{1}$(B)→L+1(B) (41%)
28	386	25928	0.6827	H-9(B)→L(B) (19%), H-9(A)→L(A) (1$\bar{1}$8%), H-11(A)→L(A) (13%), H-1$\bar{1}$B→L(B) (12%).

Table 2.6f. Major TDDFT-Predicted Excited Staes of **2.9(TS)**

Excited State	*Wavelength (nm)*	*Energy (Cm^{-1})*	*Oscillator Strength, f*	*% Contributions*
4	786	12719	0.3789	H(A)→L(A) (60%), H(B)→L(B) (34%)
10	534	18714	0.1714	H-8(B)→L(B) (73%), H(B)→L+2(B) (13%), H(A)→L(A) (6%)
14	489	20458	0.1555	H-5(B)→L(B) (39%), H-9(B)→L(B) (25%), H-7(B)→L(B) (23%), H-1(A)→L(A) (6%)
16	480	20845	0.1196	H-9(B)→L(B) (49%), H-5(B)→L(B) (21%), H-7(B)→L(B) (13%), H-1(A)→L(A) (6%)
17	478	20928	0.1701	H(B)→L+2(B) (45%), H-2(A)→L(A) (39%), H-8(B)→L(B) (10%)
24	403	24833	0.1328	H-8(B)→L+1(B) (36%), H-9(A)→L(A) (11%), H-9(B)→L+2(B) (10%), H-12(A)→L(A) (5%), H-4(A)→L(A) (5%)
57	305	32815	0.1319	H-9(B)→L+2(B) (43%), H(A)→L+3(A) (11%), H-12(A)→L(A) (10%), H-7(B)→L+2(B) (5%)
60	298	33574	0.1278	H-11(B)→L+1(B) (32%), H(A)→L+4(A) (17%), H(A)→L+3(A) (10%)

Table 2.6g. Major TDDFT-Predicted Excited Staes of **[2.11]**$^{-\cdot}$**.**

Excited State	*Wavelength (nm)*	*Energy (Cm^{-1})*	*Oscillator Strength, f*	*% Contributions*
3	870	11501	0.4085	H(A)→L(A) (72%), H(B)→L(B) (17.1%), H-1B→L+1B (7%)
8	568	17618	0.4047	H-1(A)→L(A) (61%), H(B)→L+1(B) (21%), H-1(B)→L(B) (9%), H-6(B)→L(B) (6%)
11	469	21341	0.1559	H-1(B)→L+1(B) (53%), H-2(A)→L(A) (34%), H-7(B)→L(B) (8%)
12	441	22667	0.1758	H-6(B)→L(B) (59%), H-7(B)→L+1(B) (10%), H(A)→L+5(A) (5%)
25	353	28319	0.1745	H(A)→L+5(A) (21%), H(A)→L+1(A) (20%), H-9(A)→L(A) (12%), H-11(A)→L(A) (10%), H(A)→L+3(A) (8%), H(B)→L+3(B) (5%)
27	351	28494	0.2526	H-8(A)→L(A) (17%), H-6(B)→L(B) (9%), H-11(A)→L(A) (9%), H(B)→L+3(B) (9%), H-12(B)→L(B) (8%), H(A)→L+5(A) (8%), H-9(A)→L(A) (5%)
41	319	31393	0.1183	H-7(B)→L+1(B) (41%), H(A)→L+6(A) (11%), H-9(A)→L(A) (11%), H-11(A)→L(A)

CHAPTER III: DESIGN OF STABLE DIRADICALOIDS BASED ON GROUP 13 DYES OF N_2O_2-BIS(PHENOLATE) AZA-DIPYRROMETHENE AND AZA-BODIPY

A version of this chapter was originally published by Morris Oyelowo, Towhidi Illius Jeaydi, Christopher J. Ziegler, and Victor N. Nemykin:

Oyelowo, M.; Jeaydi, T. I.; Ziegler, C. J.; Nemykin, V. N. Design of Stable Diradicals Based on Group 13 Dyes of N2O2-Bis(phenolate) Aza-Dipyrromethene and Aza-BODIPY. *Inorg Chem.* **2025**, *64*, 17946–17959. https://doi.org/10.1021/acs.inorgchem.5c03026

In this research article, I was responsible for designing and synthesizing all compounds studied. I performed characterization including variable temperature NMR, SQUID magnetometry, electrochemistry, spectroelectrochemistry, UV/Vis absorption and fluorescence emission. Towhidi Illius jeaydi carried out variable temperature EPR experiment. Dr. Christopher Ziegler facilitated the variable temperature EPR and helped in proofreading the manuscript. Dr. Viktor Nemykin helped with DFT and TDDFT calculations. He also facilitated editing of the manuscript.

3.1 Abstract

A series of strongly fluorescent N_2O_2-bis (phenolate) aza-dipyrromethene dyes incorporating boron (aza-BODIPY) **3.4a**, aluminum (Al-DIPY) **3.4b**, gallium (Ga-DIPY) **3.4c**, and indium (In-DIPY) **3.4d** were synthesized and characterized. These compounds were oxidized both chemically and electrochemically to give diradical molecules **3.5a** – **3.5d** with an open-shell singlet ground state and a thermally accessible triplet excited state. The ground state behavior of these diradical molecules was confirmed by a wide array of magnetic spectroscopies, including variable temperature ^{1}H NMR, EPR, and SQUID. X-ray crystallography confirmed the N_2O_2 coordination sphere in these systems.

DFT and TDDFT quantum chemical calculations were used to determine their electronic structures, natures of the excited states, diradical character (y_0), and spin density distributions for both open-shell singlet and triplet states. Spectroelectrochemical studies on the deprotonated dianions [**3.7a**]^{2} - [**3.7d**]$^{2-}$ showed the formation of mixed-valent radical anion species with intense absorption and broad inter-valence charge transfer bands in the near-infrared region. Upon further oxidation of the mixed-valent radical anion species, diradical molecules **3.5a** – **3.5d** were generated.

3.2 Introduction

In recent years, several localized and delocalized π-conjugated diradical molecules have been successfully synthesized based on different synthetic strategies to enhance the stability of these molecules.[14–23] The extension of π-conjugation and incorporation of diradicals into the Kekulé-type quinoidal resonance structures is one of the promising strategies for stabilizing these highly reactive species.[7,24–26] Generally, the Kekulé-based quinodimethane molecules can either be closed shell (diamagnetic), open-shell (paramagnetic), or a superposition of both.[24,27] For a better understanding of diradical behavior of Kekulé-type organic molecules, it's important to differentiate the open-shell diradical and closed-shell quinone singlet state both experimentally and theoretically.[21,23,28,29] Broadly, diradical molecules with an open-shell singlet ground states tend to display broad ^{1}H NMR signals at room temperature and EPR signals whose intensity increases with increasing temperature due to thermal population of the triplet excited state, while diamagnetic quinone molecules exhibit sharp ^{1}H NMR signals and are EPR silent at room temperature.[11,23,24,28–31] The magnetic ground state, diradical

character (y_0), and singlet-triplet energy gap of diradical materials are dependent on the number of aromatic sextet rings,[6,32] strain release,[6,33] and spatial distribution of frontier molecular orbitals.[6,34]

In this work, we successfully prepared, characterized, and carried out a detailed study on a series of 1,7-(4-(2,6-di-*tert*-butyl)phenol) functionalized N_2O_2-type aza-dipyrromethene complexes of boron **3.4a**, aluminum **3.4b**, gallium **3.4c**, and indium **3.4d** (Scheme 1). Inspired by our previous work on introducing stable aza-BODIPY diradicals,[35] we became interested in introducing diradicaloid to N_2O_2-bis(phenolate) aza-DIPY core structure, having ortho-functionalized phenolic group in the proximal positions and 1,7-(4-(2,6-di-*tert*-butyl)phenol) group in the distal positions (**3.5a – 3.5d**). Since boron chelates of bis(phenolate) dipyrromethenes were first reported by Burgess and co-workers,[36] other group 13 elements, including boron, have been chelated to both aza-dipyrromethene and dipyrromethene ligands to afford a wide array of compounds with interesting fluorescence and electronic properties.[48,49,54–63] Several transition metal complexes of the N_2O_2-type dipyrromethene and aza-dipyrromethene ligands have also been reported.[64–70] Nevertheless, to the best of our knowledge, the functionalities of diradicaloid systems of the heavier group 13 complexes of aza-dipyrromethene have not yet been reported. Although diradicaloids of BODIPY and aza-BODIPY have been reported by Wu's group and by us[35,71,72], no attention has been paid yet to introducing diradicaloids to complexes of the N_2O_2-type dipyrromethene and aza-dipyrromethene ligands. In this project, we show the synthesis of bisphenolate-aza-BODIPY **3.4a**, bisphenolate-aza-ALDIPY **3.4b**, bisphenolate-aza-GADIPY **3.4c**, bisphenolate-aza-

INDIPY **3.4d** dyes with good fluorescence quantum yields and present their corresponding oxidized diradicaloid derivatives **3.5a – 3.5d**. The ground states of all the oxidized diradical derivatives have closed-shell singlet ground state character, which is very close in energy to the open-shell singlet paramagnetic state, as well as a thermally accessible populated triplet excited state. The ground-state geometries and electronic structures of these diradical molecules were systematically investigated by variable-temperature (VT) proton nuclear magnetic resonance (^{1}H NMR) spectroscopy, electron paramagnetic resonance (EPR) spectroscopy, and superconducting quantum interference device (SQUID) measurements. These measurements were further elucidated by density functional theory (DFT) and time-dependent density functional theory (TDDFT) quantum chemical calculations. This study will lay the groundwork for an extensive investigation of this unexplored class of molecules and validate their magnetic, electronic, structural, and spectroscopic properties.

3.3 Results and Discussion

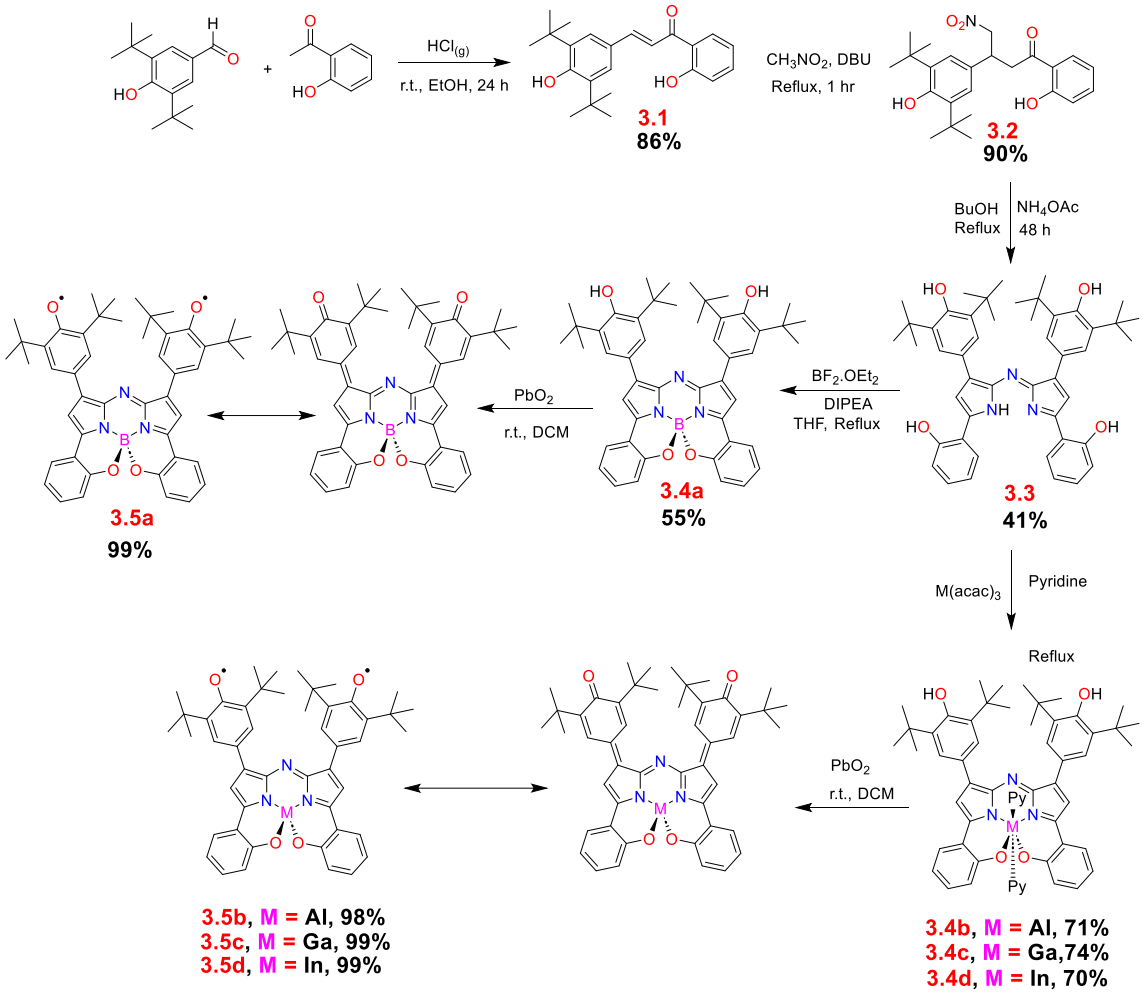
3.3.1. Synthesis and Characterization of Diradicaloids (3.5a - 3.5d) Based on N_2O_2-Bisphenolate-aza-BODIPY (3.4a), N_2O_2-Bisphenolate-aza-ALDIPY (3.4b), N_2O_2-Bisphenolate-aza-GADIPYs (3.4c), and N_2O_2-Bisphenolate -aza-INDIPY (3.4d).

The synthesis of target compounds follows well-established synthetic procedures depicted in Scheme 3.1. The first step involves aldol condensation of arylaldehydes and acetophenones to give chalcone **3.1**. Chalcone **3.1** undergoes 1,4-Michael addition of nitromethane to form compound **3.2** in excellent yield. The cyclization reaction of compound **3.2** with an excess of ammonium acetate in refluxing *n*-butanol afforded

compound **3.3** in moderate yield. To form bis(phenolate) aza-BODIPY **3.4a**, compound **3.3** was reacted with $BF_3.O(C_2H_5)_2$ in the presence of diisopropylethylamine (DIPEA) in refluxing THF as shown in Scheme 1. Compound **3.4a** was chemically oxidized by excess lead dioxide in DCM to form compound **3.5a.** To synthesize other group 13 derivatives, 1.5 equivalents of one of $Al(acac)_3$, $Ga(acac)_3$, or $In(acac)_3$ were added to compound **3.3** and then refluxed in pyridine to form corresponding bis(phenolate) aza-ALDIPY **3.4b**, aza-GADIPY **3.4c**, and aza-INDIPY **3.4d** compounds in excellent yield. The final diradical molecules of aza-ALDIPY **3.5b**, aza-GADIPY **3.5c**, and aza-INDIPY **3.5d** were obtained in excellent yield by chemical oxidation of bis(phenolate) aza-ALDIPY **3.4b**, aza-GADIPY **3.4c**, and aza-INDIPY **3.4d** using excess lead dioxide in DCM.

^{1}H NMR analysis of **3.4a**, **3.4b**, **3.4c**, and **3.4d** show up-field shifts of pyrrolic ^{1}H signal belonging to the 2- and 6-positions of the bis(phenolate) aza-DIPY **3.3**. For compounds **3.4b**, **3.4c,** and **3.4d**, we observed the appearance of pyridine signals in an approximate 2:1 ratio with respect to compound **3.3** (see appendix for Figures 3.25 – 3.32). Upon chemical oxidation, the pyridines ligands were unchelated from **3.4b** – **3.4c** abd this was confirmed by high resolution mass spec of all these samples. Bisphenolate-aza-BODIPY **3.4a** has purple coloration in both solution and solid state and is very stable to ambient conditions for months, while aza-ALDIPY **3.4b**, aza-GADIPY **3.4c,** and aza-INDIPY **3.4d** complexes are green in solution and solid state and very stable at room temperature for months in both solid state and solution. Complexes **3.5a**, **3.5b**, **3.5c,** and **3.5d** have

dark coloration in the solid state, but very dark green color in both DMSO and DCM solutions and are stable at room temperature for weeks in both solid state and solutions.



Scheme 3.1. The syntheses of compounds **3.4a – 3.4d** and **3.5a – 3.5d**.

3.3.2 Absorption and Emission Studies

The absorption and emission spectra of **3.4a – 3.4d** were studied in methanol (MeOH) and dimethyl sulfoxide (DMSO) solution, while the absorption spectra of **3.5a – 3.5d** were studied in DCM (Figure 3.1 and Table 3.1). The absorption spectra of **3.4a –**

3.4d in MeOH showed intense absorption maxima between 682-715 nm with molar absorption coefficients ranging between 50,000 and 99,000 M^{-1} cm^{-1}, see Table 3.1, and are typical for aza-BODIPYs and related metal-chelated dipyrromethenes. When absorption spectra of complexes **3.4a – 3.4d** were studied in DMSO, well-resolved vibronic progressions similar in shape and properties to spectra in MeOH were observed for the four complexes but are all red shifted with absorption maxima between 700-726 nm. The absorption maxima trend in both MeOH and DMSO is **3.4d** < **3.4b** < **3.4c** < **3.4a**. The red shift of the low-energy peak of **3.4a – 3.4d** in DMSO compared to MeOH (10-18nm, see Table 1) can be attributed to a stronger hydrogen bond formed between DMSO and -OH group in **3.4a – 3.4d**, which increases the partial negative charge on the oxygen atoms in -OH groups.

Upon chemical oxidation of **3.4a – 3.4d** by the excess of lead(IV) oxide in DCM, new red-shifted NIR absorption bands at about ~680 and 800 nm were observed for chemically oxidized **3.5a – 3.5d** diradicals. The red shift in absorption and reduction in intensity of the low-energy transition bands in **3.5a – 3.5d** as compared to the starting **3.4a – 3.4d** compounds is similar to what we observed earlier for aza-BODIPY diradical molecules.[35] The fluorescence spectra of dyes **3.4a – 3.4d** show intense emission between 730-750 nm in DMSO and 730-740 nm in MeOH. The emission spectrum of **3.dc** showed the largest bathochromic shift with good fluorescence quantum yield in DMSO. As expected, In-DIPY **3.4d** has a significantly lower fluorescence quantum yield because of the heavy-atom effect. In contrast, the fluorescent quantum yields for boron, aluminum, and gallium derivatives are very similar to each other. The emission

wavelength trend in DMSO is **3.4c** > **3.4a** > **3.4b** > **3.4d.** Regarding the Stokes shift in CH_3OH, the trend is **3.4c** > **3.4d** > **3.4b** > **3.4a**, and **3.4c** > **3.4b** > **3.4d** > **3.4a** in DMSO (Table 1). Similar to most aza-BODIPY dyes, the Stokes shifts in 4-7a are rather small (~0.05 eV). As we observed and reported in our previous work,[34] fluorescence in diradicaloids **3.5a – 3.5d** is completely quenched.

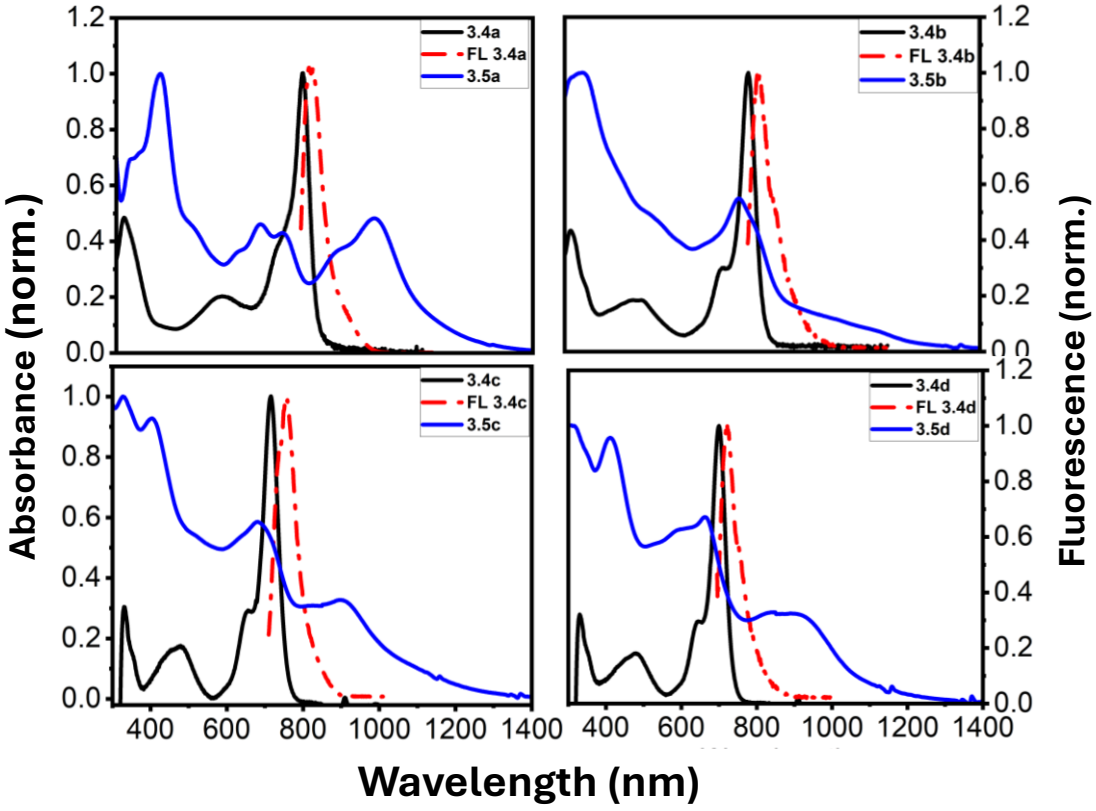


Figure 3.1: Normalized UV-vis-NIR absorption spectra (CH_3OH) of **3.4a – 3.4d** (black solid line), and emission spectra (CH_3OH) of **3.4a – 3.4d** (red dashed line). Also shown are the absorption spectra (CH_2Cl_2) of diradical molecules **3.5a – 3.5d** (blue solid line).

Table 3.1. Photophysical Properties of **3.4a – 3.4d** in MeOH and DMSO, **3.5a – 3.5d** in DCM at room

Compounds	$\lambda_{abs(max)}$ (nm)	λ_{em} (nm)	ε (M^{-1} cm^{-1})	Φ_f	Δ_{ss} (cm^{-1})
3.4a	716[a], 726[b]	731[a], 748[b]	50,534[a]	0.33[b]	287[a], 405[b]
3.4b	698[a], 711[b]	722[a], 744[b]	79,434[a]	0.31[b]	476[a], 624[b]
3.4c	700[a], 716[b]	728[a], 756[b]	99,010[a]	0.31[b]	549[a], 739[b]
3.4d	682[a], 700[b]	705[a], 722[b]	97,184[a]	0.16[b]	478[a], 435[b]
3.5a	633[c]	-	40,901[c]	-	-
3.5b	684[c]	-	30,516[c]	-	-
3.5c	681[c]	-	27,785[c]	-	-
3.5d	667[c]	-	39,578[c]	-	-

a) Using MeOH as a solvent for both absorption, emission, and molar absorptivity; [b)] Using DMSO as a solvent for both absorption, emission, and fluorescence quantum yield using 1,7-diphenyl-3,5-dimethoxyphenyl-aza-BODIPY as reference (Φ_f = 0.36 in chloroform); [c)] Using DCM as a solvent for absorption and molar absorptivity.

3.3.3 Electrochemical and Spectroelectrochemical Studies

Electrochemical studies were conducted in DCM for **3.4a** and DMF for **3.4b** - **3.4d**. The diradical derivatives **3.5a** - **3.5d** were investigated in DCM solution. The potential values of all compounds were measured by cyclic voltammetry (CV). Complexes **3.4b** - **3.4d** undergo several oxidation and reduction processes within accessible potential windows. Each complex exhibits several oxidation and reduction

processes, except compound **3.4a**, which has only one oxidation process in the solvent window. The first two oxidation processes are fully reversible for **3.4b** - **3.4d**. Compound **3.4a** exhibits one fully reversible oxidation process. Two of the four reduction processes are quasi-reversible in all complexes, while the remaining two are irreversible (Figure 3.2 and Table 3.2). Electrochemical characterization of diradical molecules **3.5a** - **3.5d** in DCM at room temperature reveals two reduction peaks, suggesting the diradical molecules can easily be reduced to stable dianions through a stepwise reduction process (Figure 3.3 and Table 3.2). In addition, one irreversible oxidation peak was also observed.

Table 3.2. Redox potentials (V) for the target compounds.[a]

Solvent	Compound	Ox_3	Ox_2	Ox_1	Red_1	Red_2	Red_3
DCM	**3.4a**	-	-	0.43	-0.98	-1.56	-1.77
DMF	**3.4b**	0.60	0.21	-0.13	-0.67	-1.33	-2.14
DMF	**3.4c**	0.61	0.24	-0.14	-1.23	-1.57	-2.25
DMF	**3.4d**	0.62	0.25	-0.12	-1.32	-1.86	-2.11
DCM	**3.5a**	-	-	0.65	-0.45	-0.95	-
DCM	**3.5b**	-	-	0.61	-0.80	-1.15	-
DCM	**3.5c**	-	-	0.62	-0.76	-	-
DCM	**3.5d**	-	-	0.63	-0.82	-1.08	-

[a] A 0.1 M tetra-n-butylammonium perchlorate (TBAP) was used as electrolyte in all cases. Half wave and peak potential values (volts) measured by cyclic voltammetry with

respect to Fc/Fc^+ as reference and corrected by 0.45 V to list potentials relative to SCE in DCM and 0.40 V relative to SCE in DMF.

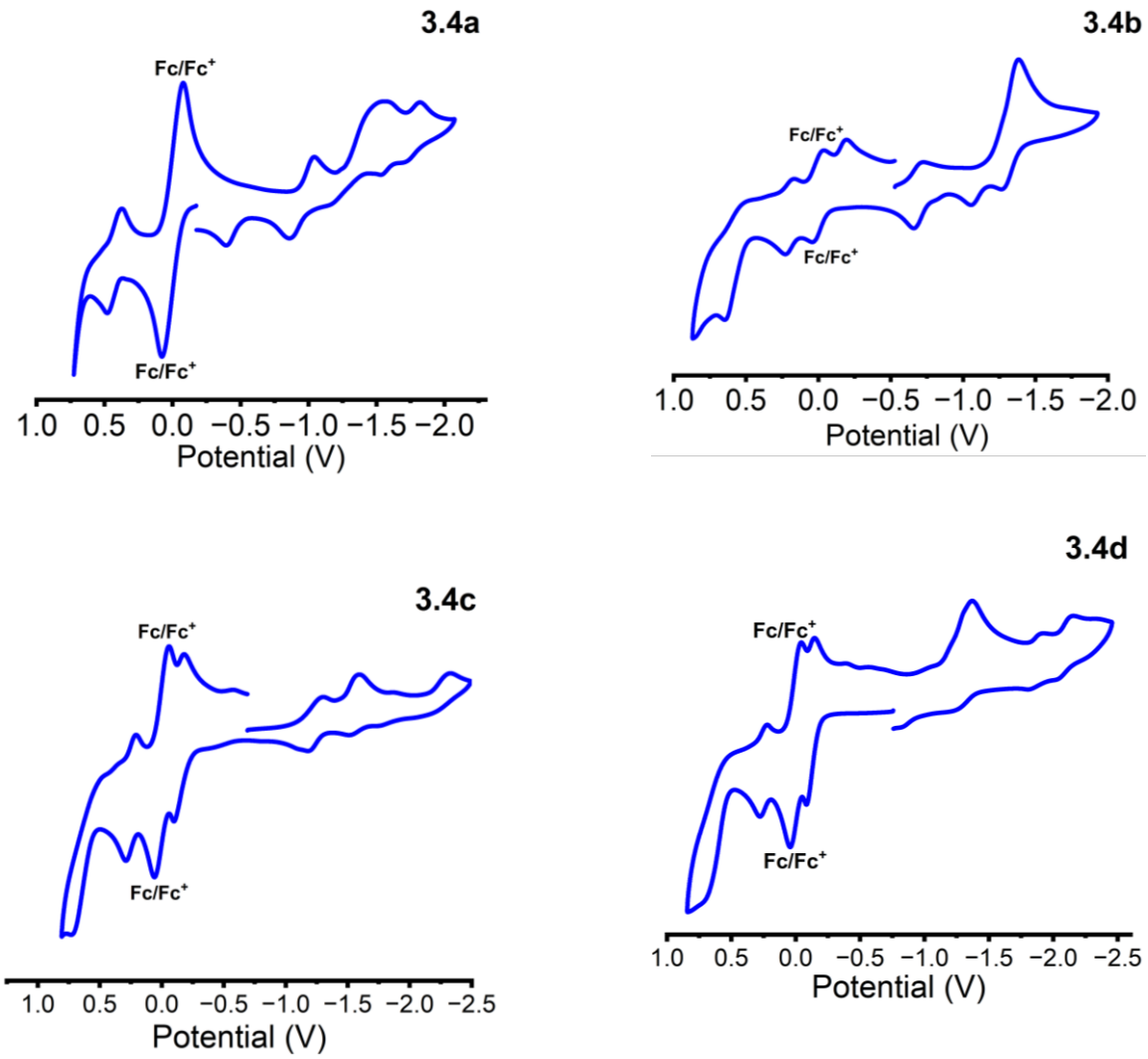


Figure 3.2: Cyclic voltammogram (blue curve) of **3.4a** in DCM and **3.4b – 3.4d** in DMF/0.1M TBAP system.

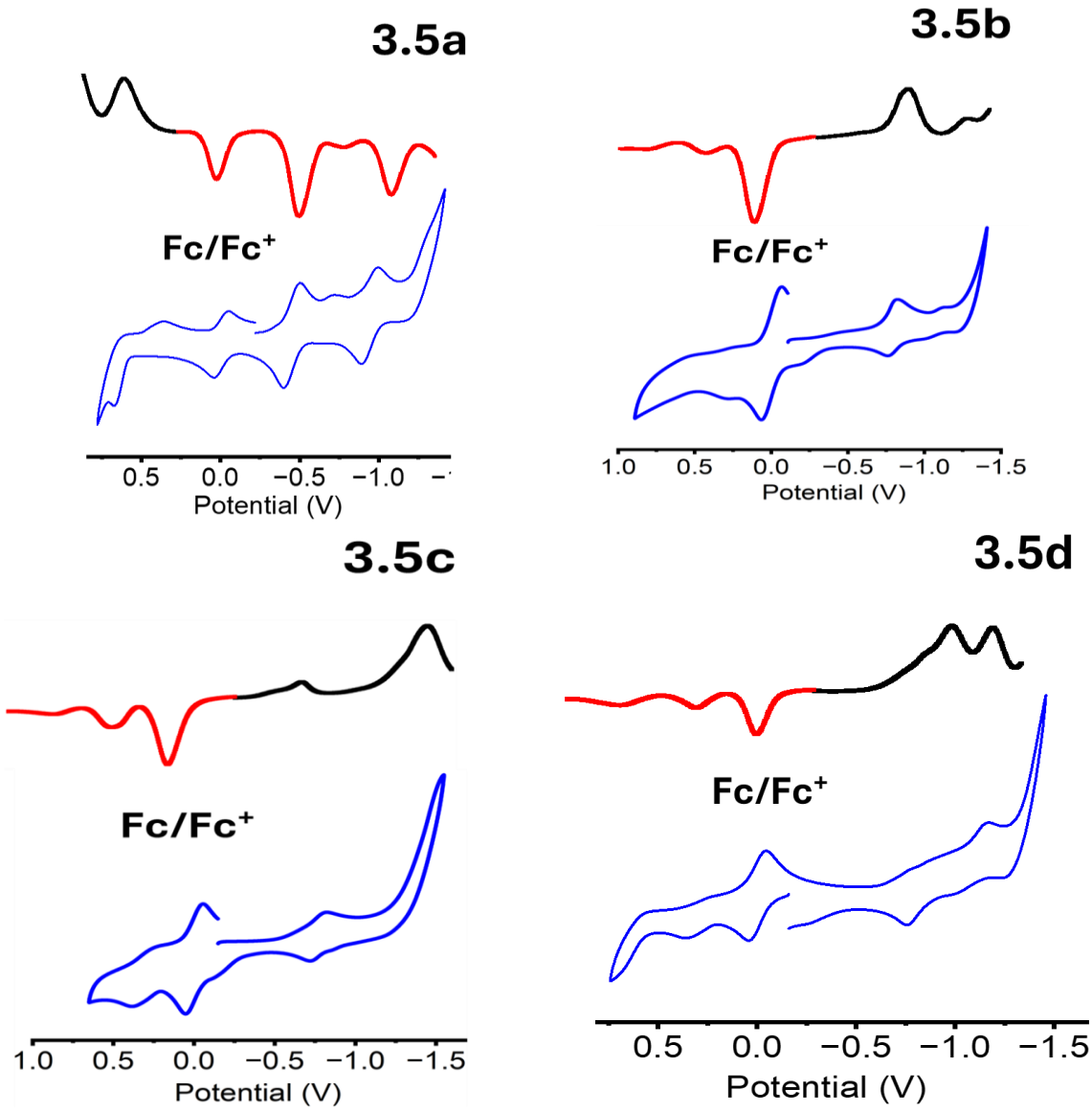
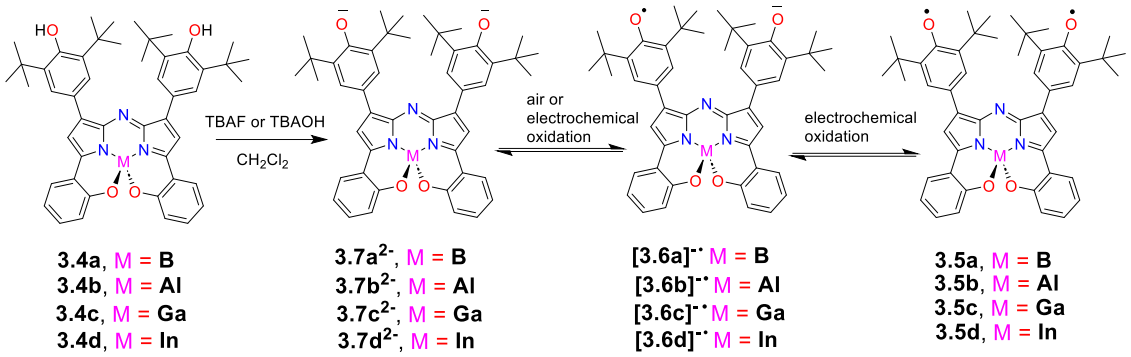


Figure 3.3: Cyclic voltammogram (blue curve), differential pulse voltammogram (red & black curve) of **3.4a – 3.4d** in DCM/0.1M TBAP system.



Scheme 3.2. Formation of dianions [**3.7a**]$^{2-}$ - [**3.7d**]$^{2-}$, mixed-valence radical anions [**3.6a**]$^{-\cdot}$ - [**3.6d**]$^{-\cdot}$, and diradicals **3.5a -3.5d**.

Spectroelectrochemical oxidation of **3.4a** - **3.4d** in THF led to the formation of **3.5b** - **3.5d** with the UV-vis-NIR spectra similar in shape and vibronic progression to those obtained from chemical oxidation using lead(IV) oxide (Figure 3.4). Deprotonation of compounds **3.4a** - **3.4d** were also studied. Solutions of **3.4a** - **3.4d** in THF were treated with tetra-*n*-butylammonium fluoride (TBAF) to obtain dianions [**3.7a**]$^{2-}$ - [**3.7d**]$^{2-}$**.** During the gradual titration of TBAF and TBAOH solutions in THF to solutions of **3.4a** - **3.4d** in THF, spectroscopic changes were observed with gradual decrease in the intensity λ_{max} of **3.4a** - **3.4d** and simultaneous rise of red shifted peaks at about ~950 nm indicating formation of dianions **3.7b**$^{2-}$ - **3.7d**$^{2-}$, and about ~800 nm for **3.7a**$^{2-}$ (Figure 3.5). Also, we noticed the formation of the additional band at about ~1120 nm during the titration of **3.4b** - **3.4d** solutions with TBAF, which we did not observe for **3.4a** (Figures 3.5). The appearance of this NIR band is reflective of the partial single-electron of the respective dianions by air, leading to the formation of mixed valent radical anions [**3.6b**]$^{-\cdot}$ - [**3.6d**]$^{-\cdot}$.

Observation of the NIR bands led us to conduct spectroelectrochemical oxidation on the dianion species [**3.7a**]$^{2-}$ - [**3.7d**]$^{2-}$ to get a better understanding of the redox behavior of these complexes. During the first oxidation process in [**3.7a**]$^{2-}$ under spectroelectrochemical conditions, we observed the appearance of the NIR band at ~1570 nm, along with the rise of a new NIR band at 979 nm, showing formation of mixed-valent radical anion [**3.6a**]$^{-\cdot}$ (Figure 3.6a). When the potential was raised further from 0.3 to 0.4V, the NIR bands attributed to mixed-valent radical anion [**3.6a**]$^{-\cdot}$ disappeared completely, and new absorption bands characteristic of diradical **3.5a** appear in the UV-Vis-NIR spectrum (Figure 3.6b), same bands were observed for **3.5b** - **3.5d** (Figure 3.7).

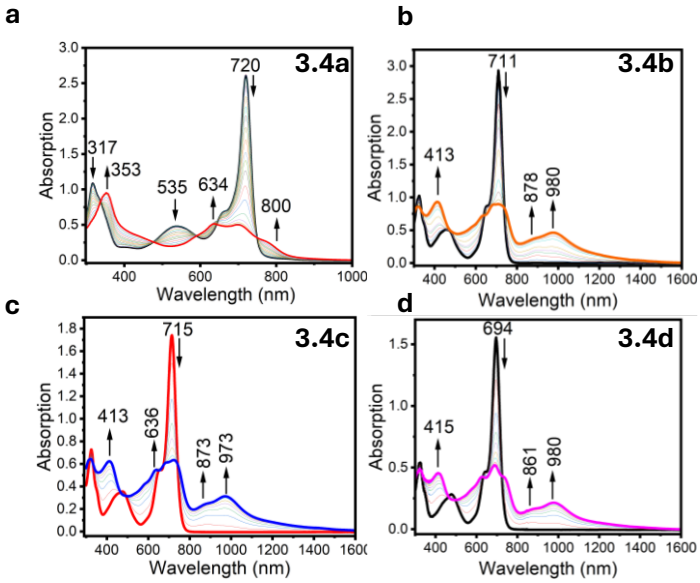


Figure 3.4: UV-vis-NIR spectroscopic changes of (a) **3.4a** to **3.5b**, (b) **3.4b** to **3.5b** (c) **3.4c** to **3.5c** and (d) **3.4d** to **3.5d** ($c \approx 4$ mM in THF, rt, 0.3 M TBAP (^{n}Bu$_4$N)[ClO$_4$] upon electrochemical oxidation in a spectroelectrochemical condition. Arrows show spectral changes with increasing positive potential.

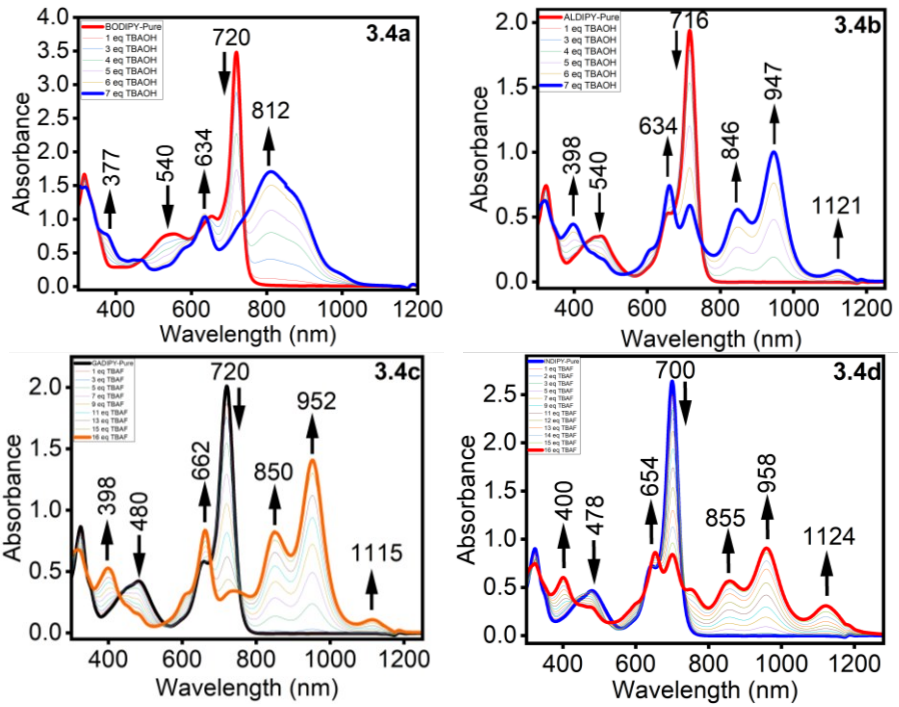


Figure 3.5: UV-vis-NIR spectroscopic changes of **3.4a – 3.4d** in THF upon titration with TBAOH (^{n}Bu$_4$NOH) for **3.4a** and TBAF (^{n}Bu$_4$NF) solution for **3.4b – 3.4d** to form dianion **[3.7a]$^{2-}$ - [3.7d]$^{2-}$**.

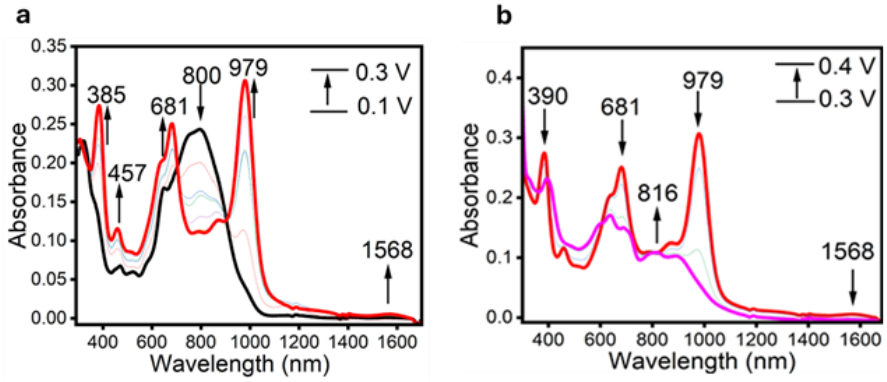


Figure 3.6: UV-vis-NIR spectroscopic changes observed upon gradual oxidation of the **3.7a^{2-}** to mixed valent **[3.6a]$^{-\cdot}$** (**a**) and **[3.6a]$^{-\cdot}$** to **3.5a** (**b**) the spectroelectrochemical experiment in THF/0.3 M (nBu$_4$N)[PF$_6$] system.

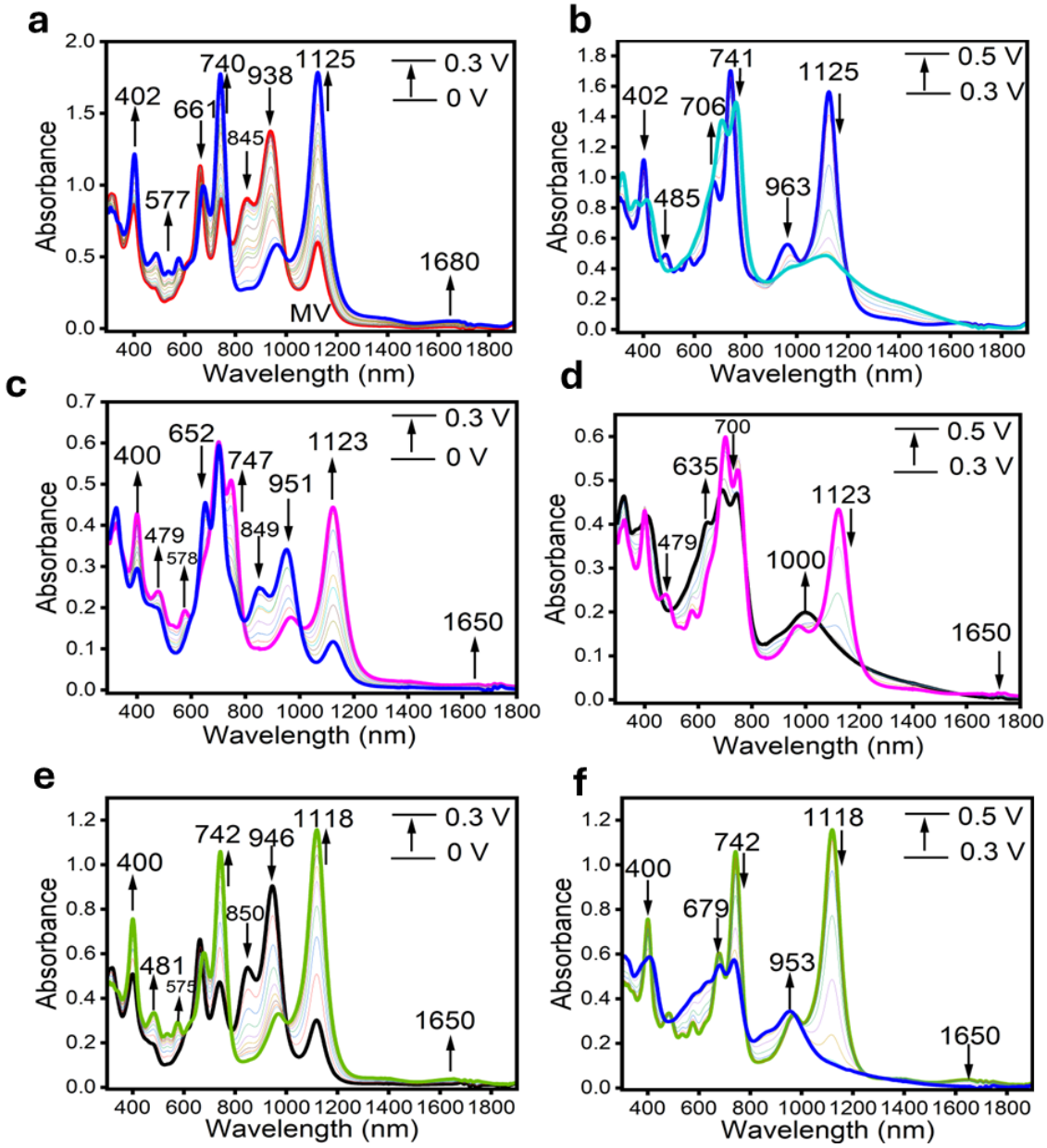


Figure 3.7: UV-vis-NIR absorption spectroscopic changes of [**3.7b**]$^{2-}$ to **[3.6b]**$^{-\cdot}$ (**a**), **[3.6b]**$^{-\cdot}$ to **3.5b** (**b**), [**3.7c**]$^{2-}$to **[3.6c]**$^{-\cdot}$ (**c**), **[3.6c]**$^{-\cdot}$ to **3.5c** (**d**), [**3.7d**]$^{2-}$ to **[3.6d]**$^{-\cdot}$ (**e**), and **[3.6d]**$^{-\cdot}$ to **3.5d** (**f**, THF, rt, 0.3 M (^{n}Bu$_4$N)[PF$_6$]) upon electrochemical oxidation in a spectroelectrochemical setup. Arrows indicate spectroscopic changes with increasing positive potential.

3.3.4 Magnetic Studies

3.3.4.1 Variable Temperature ^{1}H NMR

Variable temperature ^{1}H NMR spectra of **3.5a – 3.5d** were recorded in CD_2Cl_2 (Figures 3.8 – 3.11). The VT ^{1}H NMR of **3.5a – 3.5d** diradical molecules shows significantly broadened aromatic peaks at room temperature due to the thermal population of the triplet excited state and small singlet-triplet energy gap ($\Delta E_{S\text{-}T}$). Upon a gradual cooling to 220 K, the VT spectra of all diradical molecules display progressive sharpening of resonance peaks, and several new peaks appear. The narrowing of peaks at lower temperature indicates that **3.5a – 3.5d** are diradicaloids with a closed-shell singlet ground state and thermally accessible triplet state.

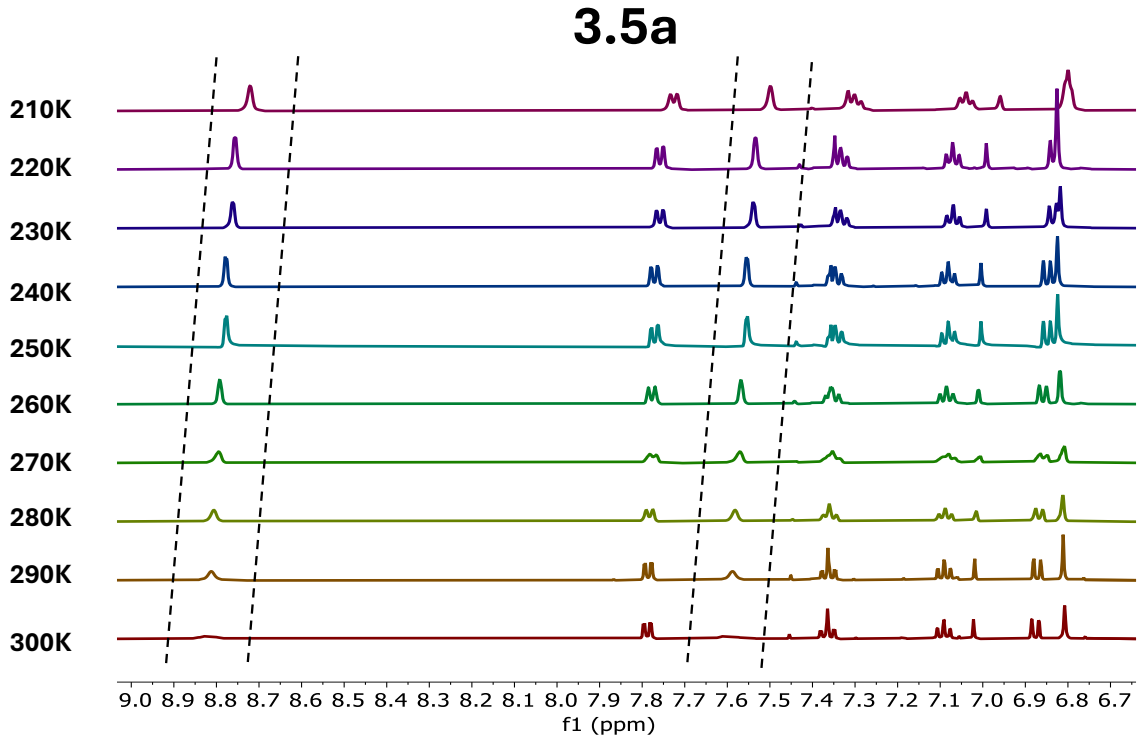


Figure 3.8: Variable temperature 1H NMR of **3.5a** in CD_2Cl_2

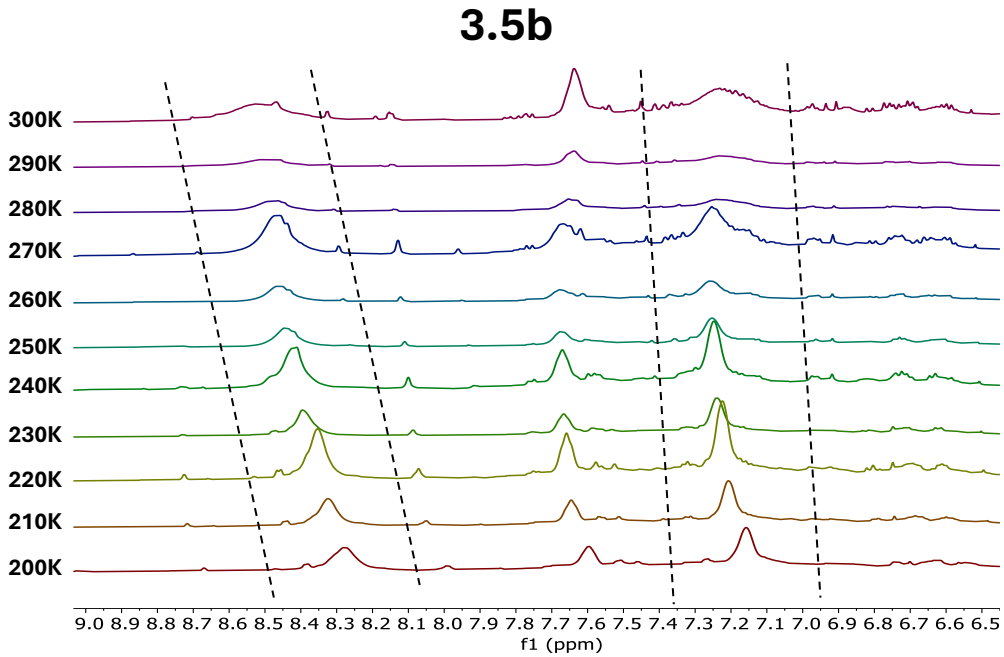


Figure 3.9: Variable temperature 1H NMR of **3.5b** in CD_2Cl_2

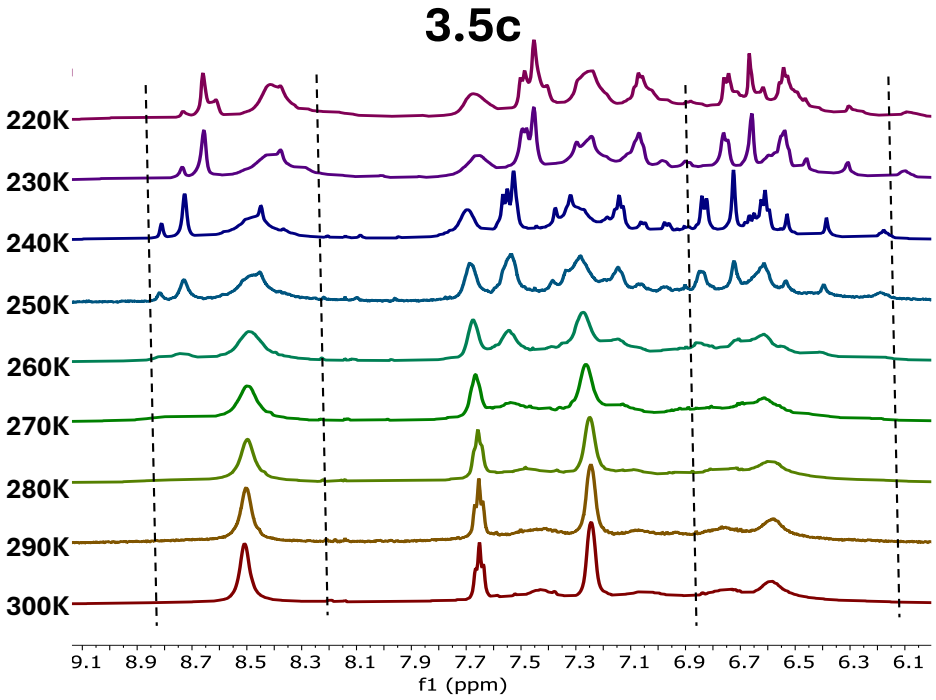


Figure 3.10: Variable temperature 1H NMR of **3.5c** in CD_2Cl_2

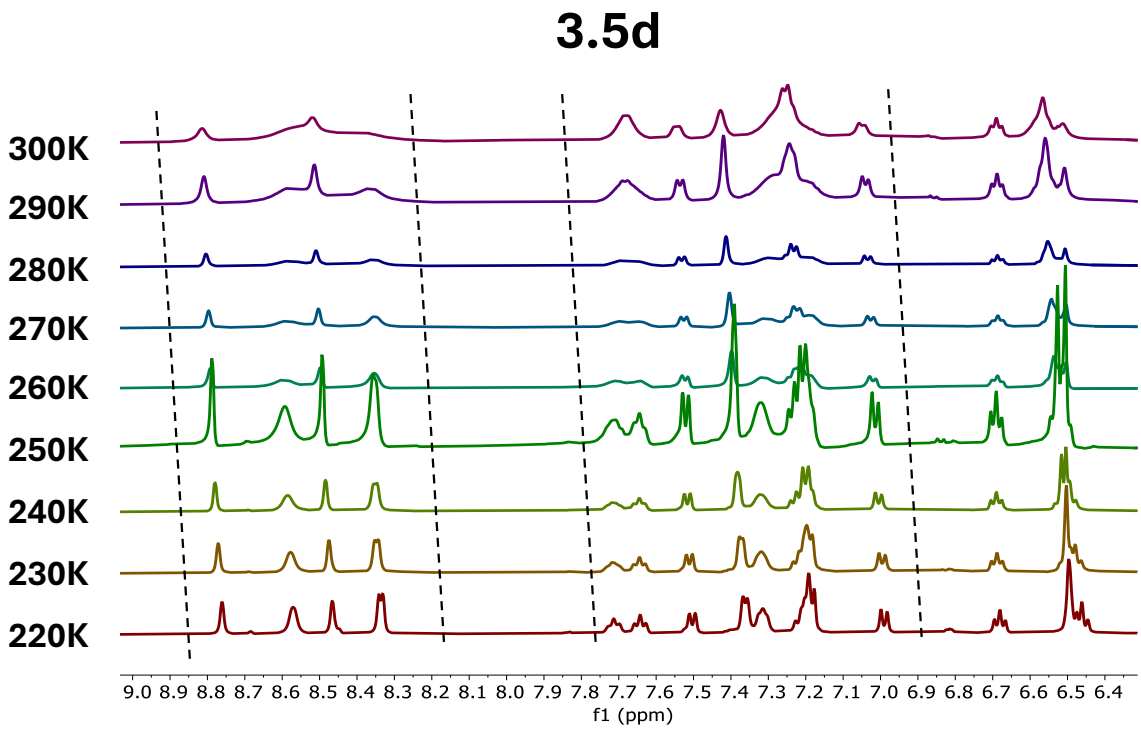


Figure 3.11: Variable temperature 1H NMR of **3.5d** in CD_2Cl_2

3.3.4.2 Variable Temperature EPR

Variable temperature EPR measurements were carried out on powders of all materials from 140 K to 260 K and show intense signals with g-factors of around 2 (Figure 3.12). The presence of the isotropic EPR signal in **3.5a – 3.5d** is indicative of the spin-density delocalization over the aza-DIPY core similar to that observed in the previously reported nickel(II) aza-DIPY platforms in radical state[69,70,73,74]. In general, the intensity of EPR signals increased as the temperature increased for **3.5c** and **3.5d**, indicating a closed-shell singlet ground state with a thermally accessible triplet excited state, and this pattern is consistent with variable temperature ^{1}H NMR spectra discussed earlier. In the case of **3.5a** and **3.5b**, the intensity of the signals are not consistent with increasing temperature and this can be ascribed to low concentration of thermally

accessible triplet excited state. The forbidden half-field transition $\Delta m_s = \pm 2$ was not detected in all diradical molecules **3.5a – 3.5d** due to the relatively low concentration of thermally populated excited state species as discussed earlier, but this was not surprising to us since this phenomenon has been observed for many diradical molecules with low or moderate diradical character[4,75,76]. Also, we tried running the VT EPR of **3.5a – 3.5d** in DCM and Toluene solutions, but no EPR signal was detected at room temperature and very weak inconsistent signals at lower temperature confirming closed-shell singlet ground state and low concentration of diradical character in this class of compounds and this observation was confirmed by our DFT calculations for diradical character discussed in DFT/TDDFT session.

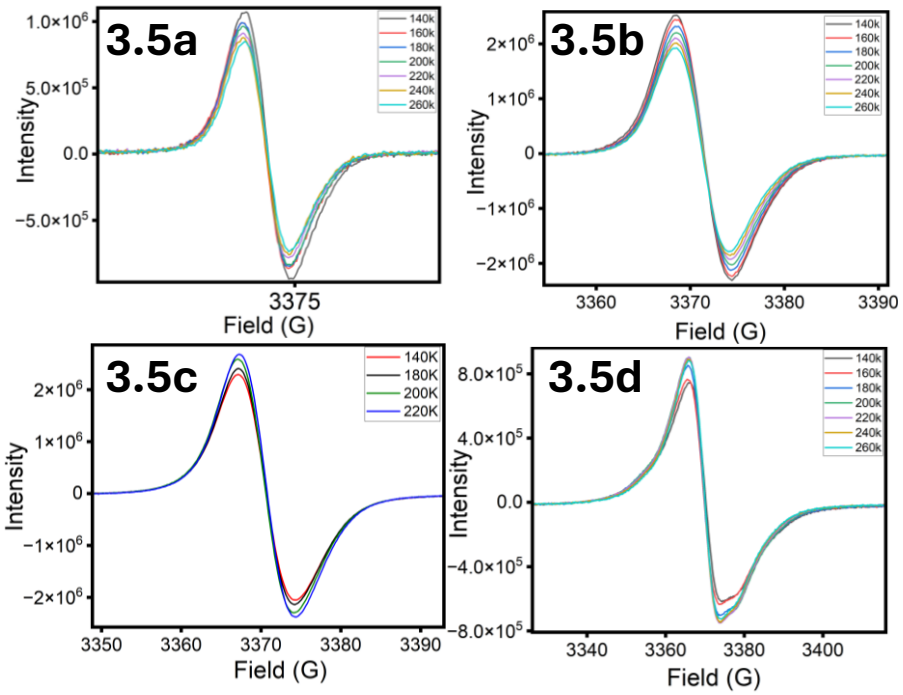


Figure 3.12: Variable temperature EPR spectra of **3.5a – 3.5d** with KBr in the solid state.

3.3.4.3 Variable Temperature SQUID Magnetometry

The singlet-triplet energy gap $\Delta E_{S\text{-}T}$ of **3.5a – 3.5d** was estimated from superconducting quantum interference device (SQUID) measurements performed on freshly prepared powder samples between 2 and 320 K. Through fitting the susceptibility data in this range, using the Bleaney-Bowers equations, the singlet-triplet energy gap ($\Delta E_{S\text{-}T}$) of **3.5a – 3.5d** was estimated to be about ~ -1.107 kcal mol^{-1} for all studied diradical samples. All diradical compounds display antiferromagnetic interactions, the $\chi_M T$ values increase linearly upon heating from 2 to 320 K (Figure 3.13), showing that the ground state of **3.5a – 3.5d** are dominated by closed-shell singlet ground state with an accessible singlet and triplet excited state, consistent with variable temperature ^{1}H NMR and EPR results.

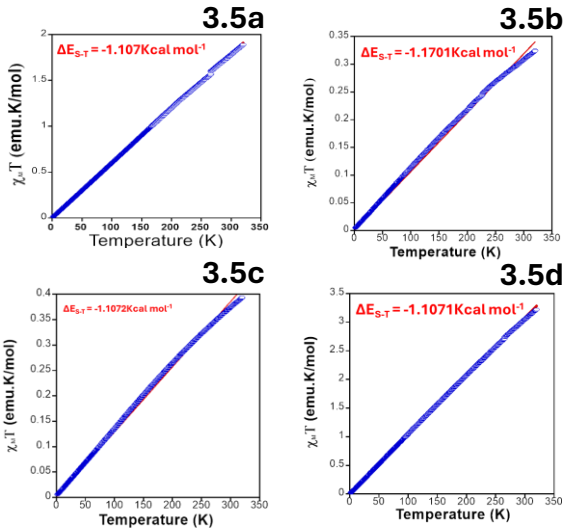


Figure 3.13: $\chi_M T$ vs T curve (blue line) in the SQUID measurement for the powder of **3.5a – 3.5d**. The fitting obtained by the Bleany-Bowers equation (red line).

3.3.5 X-Ray Crystallographic Studies

We grew the single crystals of compound **3.4a** by the slow diffusion of THF solution of **3.4a** with *n*-pentane. Single-crystal X-ray diffraction analysis of **3.4a** confirms the tetrahedral geometry of the boron center with bond angles along N3-B1-O2 (106°), N1-B1-O1 (106.77°), N3-B1-N1 (106.76°), and O1-B1-O2 (103.22°). The structure of aza-BODIPY is slightly twisted, and the two phenolic rings at 1,7-distal positions are bent from the aza-dipyrromethene ring with torsional angles of ~28.° and ~27° along C10-C12-C19-C20 and C11-C14-C25-C26 (Figure 3.14). The proximal phenolate rings are tilted away from the aza-DIPY core with dihedral angles of ~22° along C15-C16-C17-C31 and ~29° along C13-C9-C3-C4. The two phenolate oxygen atoms (O1 and O2) chelated to the boron ion are twisted in opposite directions, resulting in a tetrahedral geometry at the boron center.

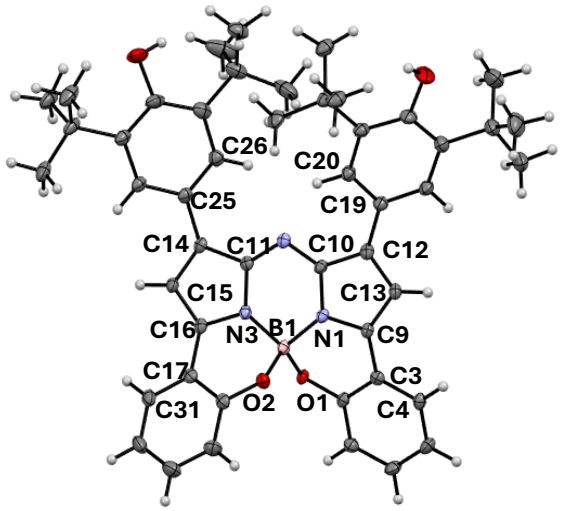


Figure 3.14: Molecular structure of **3.4a**. Ellipsoids are drawn to a 50% probability level.

Solid-state structures of two forms of **3.4c** were also determined by single-crystal X-ray diffraction analyses (Figures 3.15 and 3.16). The first structure of the single crystals of bis(phenolate) aza-GADIPY **3.4c** was grown by vapor diffusion of chloroform in a 1:1 pyridine:chloroform solution of **3.4c**. In this case (Figure 3.15), the Ga center has a pseudo octahedral coordination geometry, where the N_2O_2 of aza-dipyrromethene bidentate ligand forms the equatorial base of the coordination with bond lengths of 1.989 Å (N4-Ga1), 1.999 Å (N2-Ga1), 1.906 Å (O1-Ga1), and 1.903 Å (O2-Ga1). Two pyridine solvent molecules are chelated to the Ga ion at an axial position to complete the coordination sphere, as shown in Figure 3.15. The axially coordinated pyridine groups are linearly bound to the Ga center with a linear angle of 177.28° along the N5-Ga1-N6 axis and have bond lengths of 2.148 Å (N5-Ga1) and 2.237 Å (N6-Ga1), which are longer than all bi-chelating N_2O_2 bonds. Just like in the case of aza-BODIPY **3.4a**, the two phenolic rings at 1,7-distal positions are tilted away from the aza-dipyrromethene ring with torsional angles of 33.18° and 32.60° along C10-C9-C15-C16 and C11-C12-C37-C38. On the other hand, when we tried growing single crystals of **3.4c** by slow diffusion of *n*-pentane in THF solution of bis(phenolate) aza-GADIPY **3.4c**, the X-ray analysis shows that complex **3.4c** can behave as a dimer bridged by one of the two distal phenolate oxygen atoms of each ligand to form a four-membered Ga_2O_2 diamond motif with THF ligands bound axially to the Ga centers. The gallium ion also exhibits a pseudo-octahedral geometry and the phenolate's oxygen atoms chelated to gallium have bond lengths of 2.055 Å (O3-Ga1) and 1.881 Å (O2-Ga1), while the nitrogen atoms of the aza-DIPY core liganded to gallium ion have bond length of 1.955 Å (N3-Ga1) and

1.965 Å (N2-Ga1) as shown in Figure 3.4. The pseudo-octahedral coordination sphere of gallium ion was completed by the oxygen atom labelled O4 from the axially coordinated THF solvent molecule with bond length of 2.196 Å (O4-Ga1).

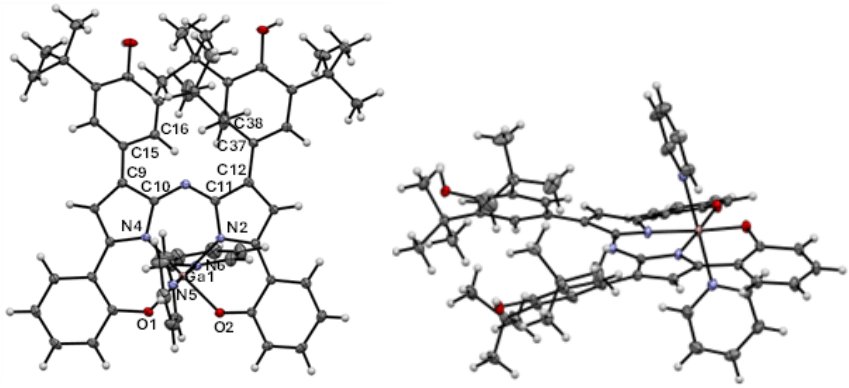


Figure 3.15: Molecular structure of **3.4c** with Pyridine. Ellipsoids are drawn to 50% probability level.

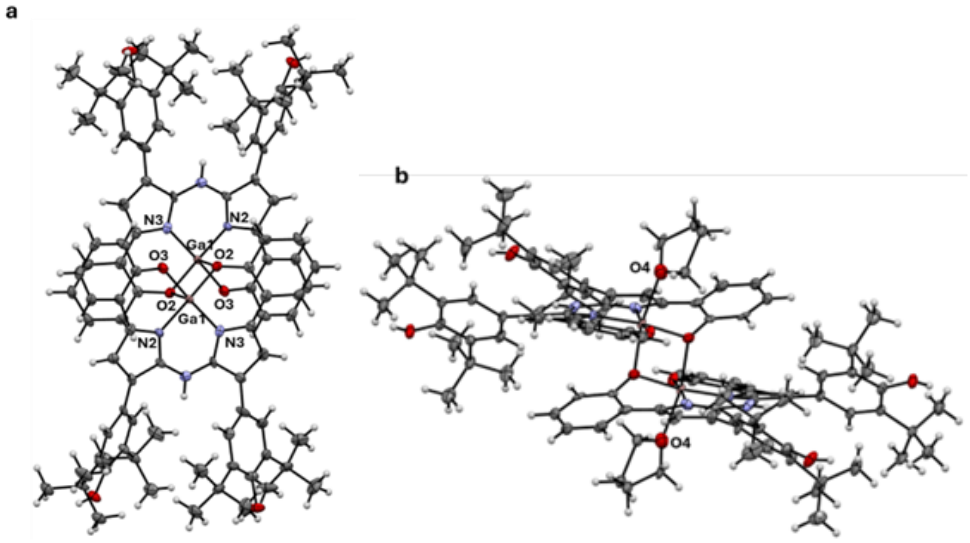


Figure 3.16: Molecular structure of **3.4c** dimer. Ellipsoids are drawn to 50% probability level. THF molecules are eliminated from view "**a**" for clarity.

3.3.6 DFT and TDDFT Calculations

We have carried out DFT and TDDFT quantum chemical calculations using M06 and TPSSh exchange correlation functionals for **3.4a** and [**3.7a**]$^{2-}$, as well as paramagnetic mixed valent radical anion [**3.6a**]$^{-\cdot}$ species. In addition, diradical compound **3.5a** was studied in three different spin states: (i) diamagnetic closed-shell singlet (CS), (ii) paramagnetic antiferromagnetically coupled open-shell singlet diradicaloid (OS), and (iii) paramagnetic open-shell triplet diradicaloid (TS). In the case of aza-BODIPY **3.4a** and its corresponding dianion [**3.7a**]$^{2-}$, only diamagnetic closed-shell singlet ground states were considered. Similarly, only the doublet ground state was considered for mixed valent species [**3.6a**]$^{-\cdot}$. Also, we calculated diradical character (y_0) for **3.5a – 3.5d** using the TPSSh exchange correlation functional using natural population analysis procedure (Table 3.3).

Independent of the exchange-correlation functionals used, the triplet excited state (TS) for **3.5a** was found to be ~2 to 4 kcal/mol above the open-shell singlet state (OS), which is, apparently, a slight overestimate of the experimental data. Both the closed-shell singlet state (CS) and the open-shell singlet diradical state (OS) in **3.5a** were found to have a gap of about ~0.7 kcal/mol. Using the occupation number of the lowest unoccupied natural orbital (LUNO) and the highest occupied natural orbital (HONO) from DFT calculations,[28,77,78] the diradical character, represented by y_0, has been evaluated for diradical compounds **3.5a – 3.5d**. These y_0 values are: **3.5a** (0.14), **3.5b** (0.13), **3.5c** (0.13), and **3.5d** (0.14). The calculated diradical characters for compounds**3.5a – 3.5d** are remarkably close, and this helps explain why there is not

much difference in the estimated singlet-triplet energy gap (ΔE_{S-T}) observed in the experimental SQUID data (Table 3.3). DFT predicted energy diagrams and the frontier molecular orbital compositions helped in understanding the HOMO-LUMO energy gap.

Table 3.3. The experimental singlet–triplet energy gap (ΔE_{S-T}) and calculated diradical character (y_0) using the TPSSh exchange correlation functional.

Compounds	ΔE_{S-T} (kcal mol^{-1})	Diradical character (y_0)
3.5a	-1.107	0.14
3.5b	-1.1071	0.13
3.5c	-1.1072	0.13
3.5d	-1.1071	0.14

Additionally, from quantum chemical calculations, spin density distributions are delocalized throughout the entire aza-BODIPY moiety in the open-shell singlet state (**OS**), which is similar to the aza-BODIPY diradicaloid systems reported earlier by us.[34] In the case of the open-shell triplet state (TS) of **3.5a**, the density distribution plot revealed effective spin delocalization over the distal phenoxy rings bearing the diradical species and aza-BODIPY core with little to no spin on the proximal phenoxy rings chelated to boron, as shown in Figure 3.17 and Table 3.4.

Figures 3.18 - 3.19 show TDDFT-predicted energy level, calculated and experimental UV-Vis-NIR electronic absorption spectra for **3.4a**, **[3.7a]$^{2-}$**, [**3.6a**]$^{\cdot-}$, **3.5a(CS)**, **3.5a(OS),** and **3.5a(TS)**.

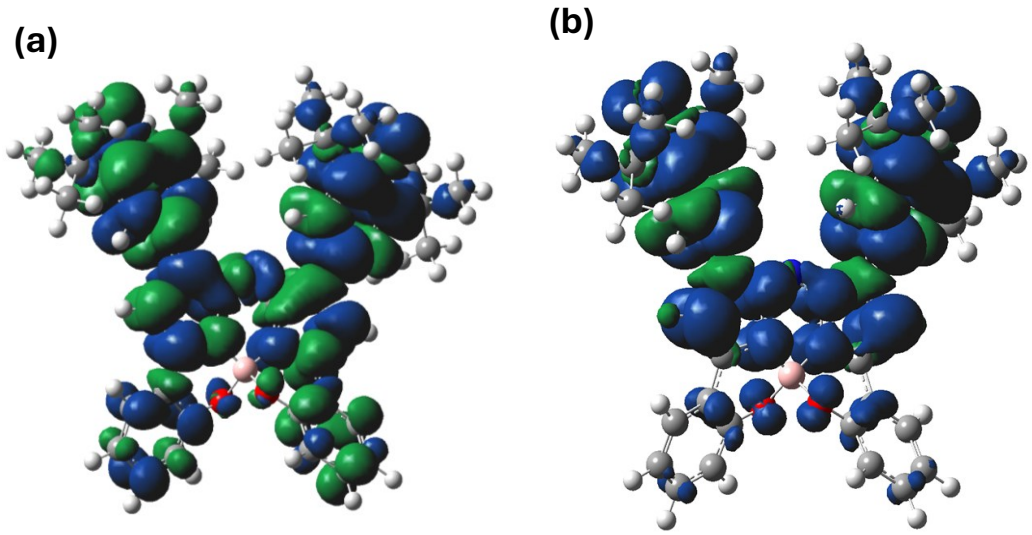


Figure 3.17: (a) Spin density distribution of open-shell singlet state **3.5a(OS)**. (b) Spin density distribution of open-shell triplet state **3.5a(TS)**.

Table 3.4. Spin Distribution in Open-Shell Singlet 4b(OS) and Open-shell Triplet 4b(TS) States

Compound	Exchange Function	Spin Density
3.5a(OS)	M06	
	O1	-0.208917
	O2	0.208917
	N3	0.066073
	N4	-0.066073
	O105	0.005875
	O106	-0.005875
3.5a(TS))	M06	
	O1	0.278348
	O2	0.278348
	N3	0.036424
	N4	0.036424
	O105	0.011460
	O106	0.011460

For aza-BODIPY **3.4a**, the lowest energy transition observed experimentally at 726 nm was predicted by TDDFT calculations at 730 nm (f = 0.75) due to pure HOMO→LUMO single-electron excitation, and this is usual for BODIPY and aza-BODIPY systems.[79] The HOMO→LUMO single-electron excitation has small phenol → aza-BODIPY core inter-ligand charge-transfer (ILCT) character. TDDFT quantum calculations also predicted two other excited state bands, one at about 551 nm (f = 0.53) resulting from HOMO-1→LUMO transition observed experimentally at 537 nm, and another major band predicted at 318 nm (f = 0.78) seen in the experimental absorption spectrum at 316 nm (Figure 3.19, see appendix for Table 3.5).

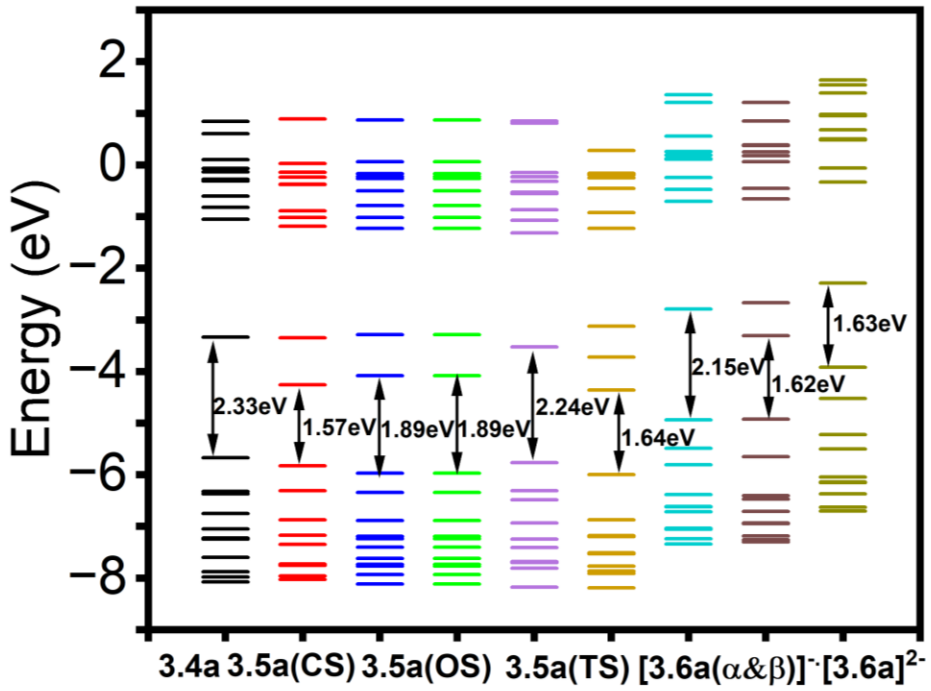


Figure 3.18: DFT-predicted energy diagram for the frontier MOs **3.4a, 3.5a(CS), 3.5a(OS)-α, 3.5a(OS)-β, 3.5a(TS)-α**, **3.5a(TS)-β, [3.6a]$^{\cdot-}$-α, [3.6a]$^{\cdot-}$-β** and **[3.7a]$^{2-}$.**

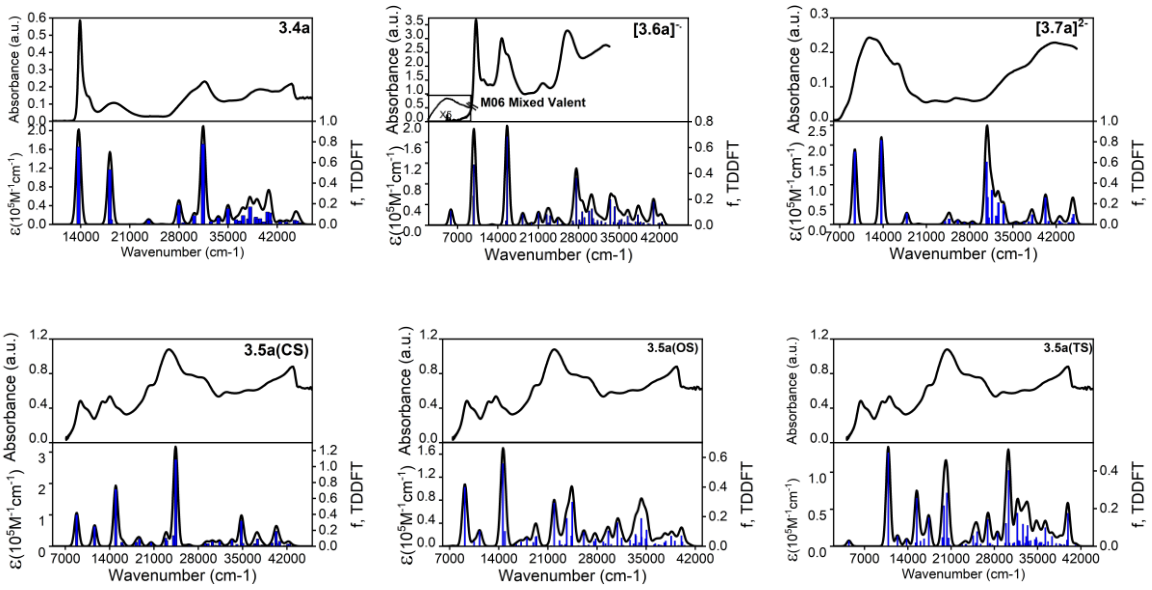


Figure 3.19: (a) Experimental versus TDDFT-predicted (M06 exchange-correlation functional) UV-vis spectra of **3.4a**, **[3.6a]**$^{-\cdot}$, **[3.7]**$^{2-}$, **3.5a(CS)**, **3.5a(OS)**, and **3.5a(TS)**.

Deprotonation of the aza-BODIPY **3.4a** to form dianion [**3.7a**]$^{2-}$ increases the donor ability of the distal phenoxide fragments and thus, it was not surprising to see that the ILCT process contributes more to the first and second excited states of [**3.7a**]$^{2-}$. TDDFT predicted spectrum of [**3.7a**]$^{2-}$ is dominated by the HOMO→LUMO, HOMO-1→LUMO, and HOMO→LUMO+1 single-electron transitions that have a significant phenolate → aza-BODIPY core ILCT character (Figures 3.19 & 3.21 and see appendix for Table 3.5). Single-electron oxidation of [**3.7a**]$^{2-}$ leads to the formation of the mixed-valent [**3.6a**]$^{-\cdot}$, species with characteristic intervalence charge transfer (IVCT) band observed at ~1650 nm. TDDFT calculations confirm that this first excited state has substantial IVCT character and was predicted at 1709 nm (f = 0.11) as shown in Figure 3.19, see appendix for Table 3.5. According to TDDFT quantum calculations, in the low-energy region, the absorption spectrum of [**3.6a**]$^{-\cdot}$ is dominated by the excited state 3

(1014 nm; f = 0.47) and excited state 8 (641 nm; f = 0.69). Both excited states have substantial ILCT (phenoxy → aza-BODIPY core) characters.

The experimental spectrum of **3.5a(OS)** shows a broad band at 887 nm predicted at 1091nm (f = 0.4) due to $HOMO_{\alpha,\beta} \rightarrow LUMO_{\alpha,\beta}$ transition having minor contributions from $HOMO - 1_{\alpha,\beta} \rightarrow LUMO_{\alpha,\beta}$, with vibronic satellite feature at 805 nm predicted at 887 nm (f = 0.1) resulting from $HUMO - 1_{\alpha,\beta} \rightarrow LUMO_{\alpha,\beta}$ transition; there are other prominent bands, one at 633 nm predicted at 687 nm (f = 0.56) arising from $HOMO_{\alpha,\beta} \rightarrow LUMO+1_{\alpha,\beta}$ with little contribution from $HOMO -1_{\alpha,\beta} \rightarrow LUMO_{\alpha,\beta}$ transitions, another band at 409 nm predicted at 457 nm (f = 0.29) with vibronic satellite at 351 nm predicted at 409 nm (f = 0.3) (Figures 3.19 - 3.20 & 3.22, see appendix for Table 3.5). TDDFT calculations for the open-shell triplet state **3.5a(TS**) predicted the highest oscillator strength (f = 0.5) at 924 nm due to $HOMO_{\alpha,\beta} \rightarrow LUMO_{\alpha,\beta}$ transition that can be assigned to the experimental UV-Vis/NIR absorption band at 887nm and another absorption shoulder band observed at about 351 nm was predicted at 330 nm (f = 0.4) arising from $HOMO_{\alpha} \rightarrow LUMO+1_{\alpha}$ (42%) transition with minor contribution from $HOMO_{\beta} \rightarrow LUMO+3_{\beta}$ (29%). The calculated HOMO/LUMO energy gap for the closed-shell **3.5a(CS)** is closer to the experimental HOMO/LUMO confirming the closed-shell singlet ground state of **3.5a**. The open-shell singlet state is near the closed-shell singlet state. The triplet state has the highest HOMO/LUMO energy gap confirming its excited state. Overall, TDDFT quantum calculations for **3.4a**, $\mathbf{[3.7a]^{2-}}$, $\mathbf{[3.6a]^{\cdot-}}$, **3.5a(CS)**, **3.5a(OS)**, and **3.5a(TS)** are in good agreement with the experimental data.

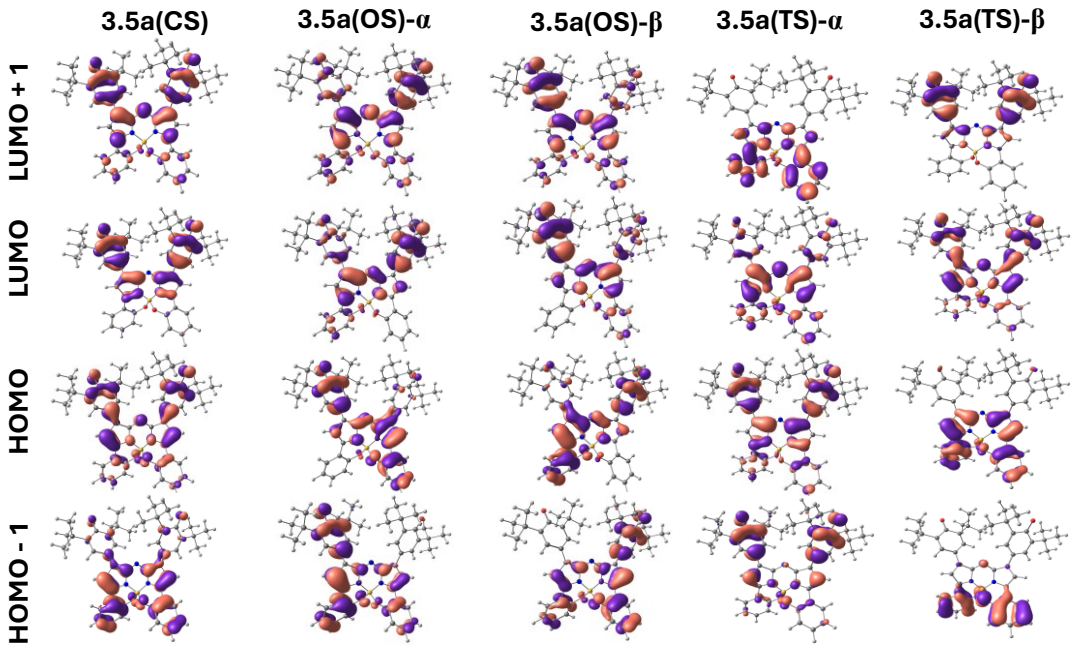


Figure 3.20: DFT-predicted frontier molecular orbitals for **3.5a(CS), 3.5a(OS),** and **3.5a(TS)**

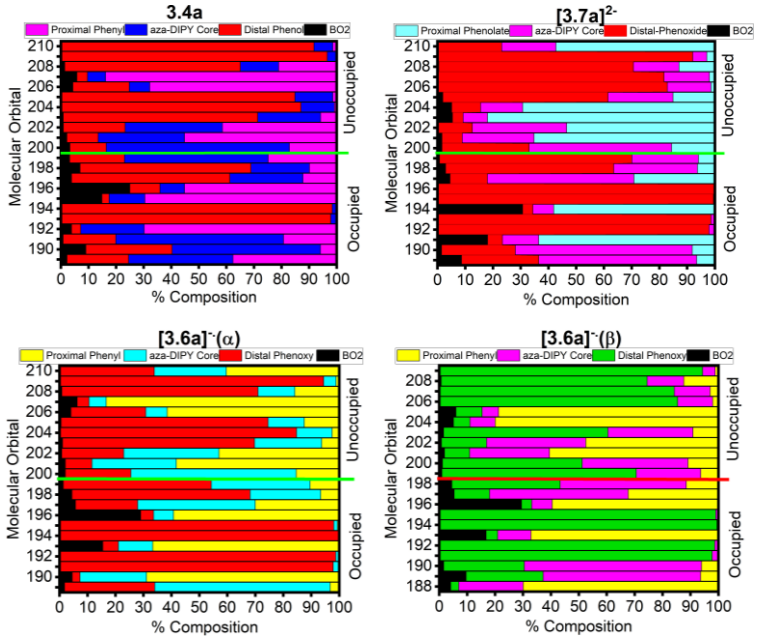


Figure 3.21: DFT-predicted compositions of frontier orbitals for **3.4a, [3.6a]$^{-}$(α)**, **[3.6a]$^{-}$(β)**, **[3.7a]$^{2-}$**. Abbreviation: "aza-DIPY" = aza-BODIPY

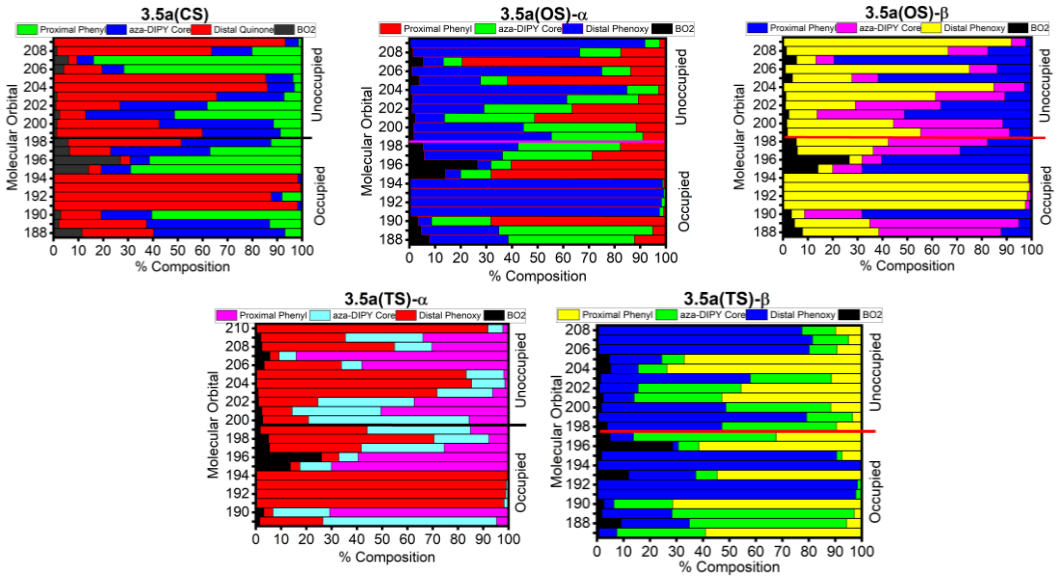


Figure 3.22: DFT-predicted compositions of frontier orbitals for **3.5a(CS), 3.5a(OS)-α**, **3.5a(OS)-β**, **3.5a(TS)-α**, and **3.5a(TS)-β** Abbreviation: "aza-DIPY" = aza-BODIPY

3.4 Conclusions

In summary, a series of strongly fluorescent dyes of boron, aluminum, gallium, and indium chelated to N_2O_2-bis(phenolate) aza-dipyrromethene functionalized with 1,7-(4-(2,6-di-*tert*-butyl)phenol) groups in the distal positions (**3.4a - 3.4d**) were synthesized and characterized. Upon oxidation with excess lead dioxide, diradical molecules **3.5a - 3.5d** were formed. Spectroelectrochemical studies confirm the formation of mixed valent radical anion species from oxidation of dianions $\mathbf{[3.7a]^{2-}}$ - $\mathbf{[3.7d]^{2-}}$, and magnetic spectroscopies, DFT, and TDDFT confirm the open-shell singlet diradical behavior of **3.5a - 3.5d**.

3.5 Experimental Section

3.5.1 General Materials and Methods

All solvents were purchased from commercial sources and purified using standard procedures. All glassware was rigorously dried overnight at 160 °C and cooled under vacuum prior to use. All reagents and starting materials were purchased from commercial vendors and used without further purification. Column chromatography was performed on silica gel (Dynamic Adsorbents, Inc, 63-200 μm). Deuterated solvents were purchased from Cambridge Isotope Laboratories and used as received.

Electrochemistry. Cyclic voltammetry measurements were made using a three-electrode system consisting of a glassy carbon or platinum working electrode, a platinum auxiliary electrode, and an Ag/AgCl wire pseudo-reference electrode. Ferrocene (Fc) was used as an internal standard for the studied compounds, and the reported potentials were corrected to the Fc/Fc^+ couple. For consistency, all potentials and figures in this work are reported vs the Fc/Fc^+ redox couple. All electrochemical experiments were conducted in either dichloromethane (DCM) or *N*,*N*-dimethylformamide (DMF) and 0.1M tetrabutylammonium perchlorate (TBAP) as electrolyte.

Spectroelectrochemistry. Spectroelectrochemical experiments were performed using a Jasco V-770 UV–vis–NIR spectrophotometer in tandem with a CH Instruments electrochemical analyzer, which was operated using the bulk electrolysis mode. The data were collected using a custom-made 1 mm cell, a platinum mesh working electrode, a platinum auxiliary electrode, and Ag/AgCl wire pseudo-reference electrode.

Spectroelectrochemical solutions consisted of 0.3 M solutions of TBAP in DCM and DMF.

NMR. NMR spectra were recorded on a 500 MHz Brucker III spectrometer. All chemical shifts (δ) are listed in parts per million (ppm) and are referenced to solvent. Spectra are referenced internally due to residual proton solvent resonances. Variable-temperature ^{1}H NMR spectra were collected in DCM-d_2, THF-d_8, or DMF-d_7 solutions in 10- or 20-degree increments.

Magnetometry. Magnetic studies were carried out using a 7-Tesla Quantum Design SQUID magnetometer at the applied magnetic fields H = 1000, 3000, and 5000 Oe and at temperature T = 2 – 320 K. The empty plastic capsule exhibited diamagnetism, and its magnetic moment was measured for correction. For both samples in powder form, primary correction for diamagnetism is implemented by point-by-point background subtraction, together with Pascal constants correction. KaleidaGraph software[78] was used for data analysis.

EPR. EPR spectra were recorded on a Bruker ELEXSYS E-500 instrument at the X-band frequency (9,82 GHz). DPPH (g = 2.0036) was used as the standard for field and frequency calibration.

Single Crystal X-ray Crystallographic Analysis. Crystalline samples were mounted on a 150 mm MiTeGen Dual-Thickness MicroMount using Paratone N oil (Hampton). X-ray diffraction experiments on **4a** and **6a** were conducted at 150 K. Diffraction data was collected using a Bruker Smart Apex II single crystal diffractometer with a TRIUMPH monochromated Mo Kα radiation (λ = 0.71073 Å) source with a crystal-to-detector

distance of 50 mm, using a series of θ and ω scans in 0.50° oscillations. The data was processed and corrected for Lorentz and polarization effects and an empirical absorption correction was applied, using the Bruker Apex II software suite. The structures were solved with ShelxS[79], and subsequent refinements were performed using the SHELXTL crystallographic software package of Bruker-AXS[80]. The coordinates and anisotropic displacement parameters for the non-hydrogen atoms were refined. Hydrogen atoms were placed in idealized geometric positions and linked to their respective carbon atoms using a riding model during refinement. Platon SQUEEZE algorithm[81] was used to remove the electron density associated with the DMF solvent molecule for the room-temperature dataset of **5a** because of the severe disorder of DMF molecule at this temperature. Diagrams were prepared using MERCURY[82].

Determination of Fluorescence Quantum Yield. All fluorescence spectra were corrected for apparatus response. Quartz cuvettes with an optical path of 1 cm were used. The sample concentrations were chosen to obtain a maximum absorbance between 0.3 and 1.0 for UV spectra and between 0.05 and 0.15 at excitation wavelength for quantum yield measurements. Relative quantum yields were obtained by comparing the areas under the corrected emission spectrum. All measurements were performed in chloroform and DCM at 298 K. methoxy-aza-BODIPY (Φ_F = 0.34 in $CHCl_3$, λ_{ex} = 650 nm) was used as a reference for all measurements. In all quantum yield determinations, correction for the solvent refractive index (η) was applied [$CHCl_3$: η = 1.4458, DCM: η = 1.442]. The following equation was used to calculate the quantum yield of the sample:

$\Phi_F(X) = \Phi_{ref}\ (Grad_X/Grad_{ref})\ (\eta_X^2/\eta_{ref}^2)$

Of which indices X and ref stand for the studied compounds (**3.4a**, **3.4b**, **3.4c** and **3.4d**) and the reference compound, respectively, Φ_F is the quantum yield, Grad is the gradient of the linear graph between the integrated fluorescence intensity versus absorbance at the excitation wavelength, and η is the refraction index of the solvent in which the measure is performed.

Computational Methods. All computations were performed using Gaussian 16 software[83] running under Windows or UNIX OS. Molecular orbital contributions were compiled from single-point calculations using the QMForge program[84]. In DFT calculations, the TPSSh[85,86] (10% of Hartree-Fock exchange) and M06[87] (27% of Hartree-Fock exchange) hybrid exchange correlation functionals. In all calculations, 6-311G(d) basis set was employed[88]. In the case of modeling compound **4b**, three spin states were considered. In the first one **3.5a(CS**), a molecule of **3.5a** was treated as a closed-shell singlet. In the case of **3.5a(OS)**, a molecule of **3.5a** was treated as an open-shell diradicaloid. Stable=opt keyword was used to ensure the correct diradicaloid character of the initial guess and the final wavefunction. In the case of **3.5a(TS)**, the triplet state was used in calculations. Frequencies were calculated for each geometry optimization to ensure the energy minimum. DFT calculations for **3.4a**, **3.5a(CS)**, **3.5a(OS)**, and **3.5a(TS)** converged to C_2 symmetry, which was used in the single-point and TDDFT calculations. In all TDDFT calculations, the lowest 40 excited states were calculated to cover experimentally observed transitions in the UV-visible region. Diradical character of all samples were calculated using TPSSh and NPA algorithm.

3.5.2 Synthesis of Chalcone 3.1

The chalcone was prepared as previously reported 3,5-di-tert-4-hydroxylbenzaldehyde (25 mmol, 5.86 g) and 2-hydroxyacetophenone (25 mmol, 3.40 g) were dissolved in 350 mL of absolute ethanol saturated with hydrogen chloride gas; the resultant solution was then stirred for two hours at room temperature and left overnight. Compound **3.1** was obtained upon dilution with water. Purification was carried out by recrystallization from ethanol (7.37g, 84% yield). HRMS-ESI$^-$ (m/z): $[M-H]^-$ calcd. for $[C_{23}H_{27}O_3]$, 351.1960; found, 351.1961.

3.5.3 Synthesis of Nitromethylated-Chalcone 3.2

The nitromethylated chalcone was prepared as previously reported. To a solution of compound **3.1** (8.22 mmol, 2.89g) in nitromethane (20 mL), 1,8-diazabicyclo[5.4.0]undec-7-ene (DBU) (8.22 mmol, 1.25 g) was added. This mixture was then refluxed for 1 hour. The resulting reddish-brown solution was cooled to room temperature and diluted with 2 mL 1% HCl and 30 mL of water. The product was extracted with chloroform, and the organic layer was dried over $MgSO_4$ and evaporated to dryness to give compound **3.2 (**3.0 g, 88% yield**).** HRMS-ESI$^-$ (m/z): $[M-H]^-$ calcd. for $[C_{24}H_{30}NO_5]$, 412.2124; found, 412.2132.

3.5.4 Synthesis of Bis(phenolate) aza-DIPY-H 3.3

A mixture of compound **3**.**2** (7.25 mmol, 3.0g) and ammonium acetate (50 equivalent) was refluxed in *n*-butanol (100 mL) for 48 h. After cooling to room temperature, the solvent was concentrated to 30 mL, and the precipitate was filtered off, washed with ethanol, and dried to yield compound **3.3** (0.4 g, 32% yield) as a dark brown

solid. ^{1}H NMR of compound **3.3** (500 MHz, 298 K, DMSO-d_6) δ (ppm) = 8.04 – 8.06 (d, J = 10Hz, 2H), 7.47(s, 2H), 7.41 (s, 4H), 7.33 - 7.36 (t, 2H), 7.11 – 7.13 (d, J = 10Hz, 2H), 6.99 – 7.02 (t, 2H), 1.91 (s, 3H), 1.23(s, 36H). ^{13}C NMR of **3.3** (500 MHz, 298 K, DMSO-d_6) δ (ppm) = 21.5, 30.7, 34.8, 114.5, 117.1, 117.5, 120.2, 125.31, 127.0, 129.2, 131.9, 137.9, 154.8, 158.2, 172.5. HRMS-MALDI^{+} (m/z): $[M+H]^{+}$ calcd. for $[C_{48}H_{56}N_3O_4]$, 738.4271; found, 738.4263. ^{1}H NMR and ^{13}C NMR spectra are shown in Figures 3.23 – 3.24.

3.5.5 Synthesis of Bis(phenolate) aza-BODIPY-H 3.4a

To a dry solution of THF, bis(phenolate) aza-DIPY-H compound **3.3** (0.068g, 0.092mmol) was added along with *N,N*-diisopropylethylamine (0.26mL, 1.5mmol). $BF_3.Et_2O$ (0.25mL, 2.0mmol) was added and the mixture was refluxed for 3 hours. After completion, the mixture evaporated to dryness. Column chromatography on silica gel eluting with methylene chloride gives bis(phenolate) aza-BODIPY-H compound **3.4a** (0.019g, 27% yield) as a purple powder. ^{1}H NMR of compound **3.4a** (500 MHz, 298 K, $CDCl_3$) δ (ppm) = 7.86 – 7.88 (d, J = 10Hz, 2H), 7.78 (s, 4H), 7.37 - 7.40 (t, 2H), 7.08 – 7.11 (t, 2H), 7.01 – 7.02 (d, J = 10Hz, 2H), 6.98 (s, 2H), 5.46 (s, 2H), 1.43 (s, 36H). ^{13}C NMR of compound **3.4a** (500 MHz, 298 K, $CDCl_3$) δ (ppm) = 29.5, 34.0, 67.7, 75.3, 102.5, 115.4, 120.6, 124.7, 128.2, 128.5, 131.0, 145.2, 145.7, 151.5. HRMS-ESI^{+} (m/z): $[M+Na]^{+}$ calcd. for $[C_{48}H_{52}BN_3O_4Na]$, 768.3957; found, 768.391. ^{1}H NMR and ^{13}C NMR spectra are shown in Figures 3.25 – 3.26. Mass Spectrum (Figure 3.35).

3.5.6 Synthesis of Bis(phenolate) aza-BODIPY Diradical 3.5a

Dry DCM was added to a mixture of bis(phenolate) aza-BODIPY-H compound **3.4a** (74.6 mg, 0.1 mmol) and lead (II) oxide (0.478 g, 2 mmol) under an argon atmosphere, and the reaction mixture was stirred at room temperature for half an hour. Once the reaction was finished, the solid lead (IV) oxide was filtered off. The filtrate was dried via rotary evaporator, and then the final product was obtained as a dark green solid (73.5 mg, 99%) without further purification. ^{1}H NMR of compound **3.5a** (500 MHz, 298 K, CD_2Cl_2) δ (ppm) = 8.77 (s, 2H), 7.73 - 7.74 (d, J = 10Hz, 2H), 7.54 (s, 2H), 7.30 – 7.33 (t, 2H), 7.02 – 7.05 (t, 2H), 6.97 (s, 1H), 6.81 – 6.83 (d, 2H), 5.78 (s, 1H), 1.32 – 1.36 (m, 36H). ^{13}C NMR of compound **3.5a** (500 MHz, 298 K, $CDCl_3$) δ (ppm) = 29.7, 35.0, 101.6, 118.6, 120.6, 121.1, 126.3, 128.2, 128.8, 132.7, 139.1, 139.9, 142.3, 145.5, 156.9, 162.6, 186.8. HRMS-ESI$^-$ (m/z): $[M]^+$ calcd. for $[C_{48}H_{50}BN_3O_4]$, 743.3903; found, 743.3861. ^{1}H NMR and ^{13}C NMR spectra are shown in Figures 3.33 – 3.34. Mass spec spectrum is shown in Figure 3.39.

3.5.7 Synthesis of Bis(phenolate) aza-ALDIPY 3.4b

Pyridine was added to a mixture of bis(phenolate) aza-DIPY-H compound **3.3** (0.108g g, 0.147 mmol) and aluminum acetylacetonate (72 mg, 0.2205 mmol), and the reaction mixture was refluxed overnight. Upon cooling to room temperature, hexanes (15 mL) were added to the mixture and cooled to 0 °C in ice bath. Once cold, resulting precipitate was collected over filter paper, washed with additional hexanes to afford compound **3.4b** (0.104 mg, 72%) as a green solid.

^{1}H NMR of compound **3.4b** (500 MHz, 298 K, DMSO-d_6) δ (ppm) = 8.57 – 8.58 (d, J = 5Hz, 2H), 7.77 – 7.80 (t, 2H), 7.65 – 7.67 (d, J = 10Hz, 2H), 7.37 – 7.40 (t, 4H), 7.30 (s, 4H), 7.07 – 7.10 (t, 2H), 7.01 (s, 2H), 6.80 (s, 2H), 6.68 – 6.69 (d, J = 10Hz, 2H), 6.53 – 6.56 (t, 2H), 1.23 (s, 36H). ^{13}C NMR of compound **3.4b** (500 MHz, 298 K, DMSO-d_6) δ (ppm) = 30.9, 34.8, 100.0, 113.6, 115.5, 120.0, 121.5, 124.4, 126.6, 136.6, 137.8, 144.3, 147.6, 150.1, 154.0, 156.3, 164.2. HRMS-ESI^{+} (m/z): $[M+Na]^{+}$ calcd. for $[C_{58}H_{60}AlN_5O_4Na]$, 940.4359; found, 940.3948. ^{1}H NMR and ^{13}C NMR spectra are shown in Figures 3.27 – 3.28. Mass spec spectrum is shown in Figure 3.36 .

3.5.8 Synthesis of Bis(phenolate) aza-ALDIPY Diradical 3.5B

Dry DCM was added to a mixture of bis(phenolate) aza-ALDIPY-H compound **3.4b** (91.8 mg, 0.1 mmol) and lead (II) oxide (0.478 g, 2 mmol) under a nitrogen atmosphere, and the reaction mixture was stirred at room temperature for half an hour with a color change from green to dark brown. The reaction was monitored via TLC. Once the reaction was finished, the solid lead (IV) oxide was filtered off. The filtrate was dried via rotary evaporator, and then the final product was obtained as a black solid (90 mg, 99%) without further purification. HRMS-MALDI^{-} (m/z): $[M]^{+}$ calcd. for $[C_{48}H_{50}AlN_3O_4]$, 759.3617; found, 759.3550. Mass spec spectrum is shown in Figure 3.40.

3.5.9 Synthesis of Bis(phenolate) aza-GADIPY 3.4c

Pyridine was added to a mixture of bis(phenolate) aza-DIPY-H compound **3.3** (0.1g g, 0.139 mmol) and gallium acetylacetonate (81 mg, 0.221 mmol), and the reaction mixture was refluxed overnight. Upon cooling to room temperature, hexanes (15 mL)

were added to the mixture and cooled to 0 °C in ice bath. Once cold, the resulting precipitate was collected over filter paper, washed with additional hexanes to afford compound **3.4c** (0.102 g, 76%) as a green solid. ^{1}H NMR of compound **3.4c** (500 MHz, 298 K, DMSO-d_6) δ (ppm) = 8.57 – 8.58 (d, J = 5Hz, 4H), 7.77 – 7.80 (t, 2H), 7.69 – 7.71 (d, J = 10Hz, 2H), 7.37 – 7.40 (t, 4H), 7.29 (s, 4H), 7.08 – 7.11 (m, 4H), 6.84 (s, 2H), 6.72 – 6.74 (d, J = 10Hz, 2H), 6.55 – 6.58 (t, 2H), 1.23 (s, 36H). ^{13}C NMR of compound **3.4c** (500 MHz, 298 K, DMSO-d_6) δ (ppm) = 30.9, 34.8, 113.7, 115.7, 118.6, 122.3, 124.4, 126.2, 126.7, 128.9, 131.6, 136.6, 137.8, 144.4, 146.9, 150.1, 154.2, 156.9, 166.1. HRMS-ESI^{+} (m/z): $[M+Na]^{+}$ calcd. for $[C_{58}H_{60}GaN_5O_4Na]$, 982.3799; found, 982.3349. ^{1}H NMR and ^{13}C NMR spectra are shown in Figures 3.29 – 3.30. Mass spec spectrum is shown in Figure 3.37

3.5.10 Synthesis of Bis(phenolate) aza-GADIPY Diradical 3.5c

Dry DCM was added to a mixture of bis(phenolate) aza-GADIPY-H compound **3.4c** (96.1 mg, 0.1 mmol) and lead (II) oxide (0.478 g, 2 mmol) under a nitrogen atmosphere, and the reaction mixture was stirred at room temperature for half an hour with a color change from green to dark brown solid. The reaction was monitored via TLC. Once the reaction was finished, the solid lead (IV) oxide was filtered off. The filtrate was dried via rotary evaporator, and then the final product was obtained as a black solid (92 mg, 99%) without further purification. HRMS-MALDI^{-} (m/z): $[M]^{+}$ calcd. for $[C_{48}H_{50}GaN_3O_4]$, 801.3057; found, 801.2983. Mass spectrum (Figure 3.41)

3.5.11 Synthesis of Bis(phenolate) aza-INDIPY 3.4d

Pyridine was added to a mixture of bis(phenolate) aza-DIPY-H compound **3.3** (0.108g g, 0.147 mmol) and indium acetylacetonate (91 mg, 0.221 mmol), and the reaction mixture was refluxed overnight. Upon cooling to room temperature, hexanes (15 mL) were added to the mixture and cooled to 0 °C in ice bath. The resulting precipitate was collected over filter paper, washed with additional hexanes to afford compound **3.4d** (0.140 g, 78%) as a dark green solid. ^{1}H NMR of compound **3.4d** (500 MHz, 298 K, DMSO-d_6) δ (ppm) = 8.57 – 8.58 (d, J = 5Hz, 4H), 7.77 – 7.80 (t, 4H), 7.69 – 7.71 (d, J = 10Hz, 2H), 7.37 – 7.39 (m, 5H), 7.29 (s, 4H), 7.22 (s, 2H), 7.09 – 7.12 (t, 2H), 6.82 (s, 2H), 6.76 – 6.78 (d, J = 10Hz, 2H), 6.57 – 6.60 (t, 2H), 1.20 (s, 36H). ^{13}C NMR of compound **3.4d** (500 MHz, 298 K, DMSO-d_6) δ (ppm) = 30.8, 34.7, 114.9, 115.7, 119.3, 124.4, 126.2, 127.0, 130.1, 131.3, 136.6, 137.5, 145.3, 146.4, 150.1, 154.3, 158.5, 167.5. HRMS-ESI$^+$ (m/z): $[M]^+$ calcd. for [$C_{58}H_{60}InN_5O_4$], 1005.3685; found, 1005.3300. ^{1}H NMR and ^{13}C NMR spectra are shown in Figures 3.31 – 3.32. Mass spec spectrum is shown in Figure 3.38.

3.5.12 Synthesis of Bis(phenolate) aza-INDIPY Diradical 3.5d

Dry DCM was added to a mixture of bis(phenolate) aza-INDIPY-H compound **3.4d** (0.1 g, 0.1 mmol) and lead (IV) oxide (0.717 g, 3 mmol) under a nitrogen atmosphere, and the reaction mixture was stirred at room temperature for half an hour with a color change from green to black-greenish. The reaction was monitored via TLC. Once the reaction was finished, the solid lead (II) oxide was filtered off.

The filtrate was dried via rotary evaporator, and then the final product was obtained as a black solid (95 mg, 99%) without further purification. HRMS-MALDI$^-$ (m/z): $[M]^+$ calcd. for $[C_{48}H_{50}InN_3O_4]$, 847.2841; found, 847.2789. Mass spec spectrum is shown in Figure 3.42.

References

(1) Wang, W.; Ge, L.; Xue, G.; Miao, F.; Chen, P.; Chen, H.; Lin, Y.; Ni, Y.; Xiong, J.; Hu, Y.; Wu, J.; Zheng, Y. Fine-Tuning the Diradical Character of Molecular Systems *via* the Heteroatom Effect. *Chem. Commun.* **2020**, *56*, 1405–1408. https://doi.org/10.1039/C9CC08538F.

(2) Wang, K.; Zhan, Q.; Han, B.; Quintero, S. M.; Huang, W.; Ji, Y.; Miao, F.; Chen, H.; Casado, J.; Zheng, Y. The Smallest Oligothiophene Diradicals by Asymmetric Substitution of Quinoidal Cores. *J Mater Chem C Mater* **2022**, *10* (35), 12724–12730. https://doi.org/10.1039/D2TC02433K.

(3) Miyazawa, Y.; Wang, Z.; Matsumoto, M.; Hatano, S.; Antol, I.; Kayahara, E.; Yamago, S.; Abe, M. 1,3-Diradicals Embedded in Curved Paraphenylene Units: Singlet versus Triplet State and In-Plane Aromaticity. *J. Am. Chem. Soc.* **2021**, *143*, 7426–7439. https://doi.org/10.1021/jacs.1c01329.

(4) Chen, Z.; Li, W.; Sabuj, M. A.; Li, Y.; Zhu, W.; Zeng, M.; Sarap, C. S.; Huda, M. M.; Qiao, X.; Peng, X.; Ma, D.; Ma, Y.; Rai, N.; Huang, F. Evolution of the Electronic Structure in Open-Shell Donor-Acceptor Organic Semiconductors. *Nat. Commun.* **2021**, *12*, 5889. https://doi.org/10.1038/s41467-021-26173-3.

(5) Zhou, J.; Zhu, W.; Zeng, M.; Yang, Q.; Li, P.; Lan, L.; Peng, J.; Li, Y.; Huang, F.; Cao, Y. Aromatic Inorganic Acid Radical. *Sci. China. Chem.* **2019**, *62*, 1656–1665. https://doi.org/10.1007/s11426-019-9641-2.

(6) Liu, Y.; Phan, H.; Herng, T. S.; Gopalakrishna, T. Y.; Ding, J.; Wu, J. Toward Benzobis(Thiadiazole)-based Diradicaloids. *Chem. Asian. J.* **2017**, *12* (17), 2177–2182. https://doi.org/10.1002/asia.201700732.

(7) Hu, X.; Chen, H.; Xue, G.; Zheng, Y. Correlation between the Strength of Conjugation and Spin–Spin Interactions in Stable Diradicaloids. *J Mater Chem C Mater* **2020**, *8* (31), 10749–10754. https://doi.org/10.1039/D0TC00868K.

(8) Wang, W.; Ge, L.; Xue, G.; Miao, F.; Chen, P.; Chen, H.; Lin, Y.; Ni, Y.; Xiong, J.; Hu, Y.; Wu, J.; Zheng, Y. Fine-Tuning the Diradical Character of Molecular Systems *via* the Heteroatom Effect. *Chemical Communications* **2020**, *56* (9), 1405–1408. https://doi.org/10.1039/C9CC08538F.

(9) Yang, K.; Zhang, X.; Harbuzaru, A.; Wang, L.; Wang, Y.; Koh, C.; Guo, H.; Shi, Y.; Chen, J.; Sun, H.; Feng, K.; Ruiz Delgado, M. C.; Woo, H. Y.; Ortiz, R. P.; Guo, X. Stable Organic Diradicals Based on Fused Quinoidal Oligothiophene Imides with High Electrical Conductivity. *J Am Chem Soc* **2020**, *142* (9), 4329–4340. https://doi.org/10.1021/jacs.9b12683.

(10) Gallagher, N.; Zhang, H.; Junghoefer, T.; Giangrisostomi, E.; Ovsyannikov, R.; Pink, M.; Rajca, S.; Casu, M. B.; Rajca, A. Thermally and Magnetically Robust Triplet Ground State Diradical. *J Am Chem Soc* **2019**, *141* (11), 4764–4774. https://doi.org/10.1021/jacs.9b00558.

(11) Hu, X.; Wang, W.; Wang, D.; Zheng, Y. The Electronic Applications of Stable Diradicaloids: Present and Future. *J Mater Chem C Mater* **2018**, *6* (42), 11232–11242. https://doi.org/10.1039/C8TC04484H.

(12) Lee, S.; Miao, F.; Phan, H.; Herng, T. S.; Ding, J.; Wu, J.; Kim, D. Radical and Diradical Formation in Naphthalene Diimides through Simple Chemical Oxidation. *ChemPhysChem* **2017**, *18* (6), 591–595. https://doi.org/10.1002/cphc.201700015.

(13) Zeng, W.; Wu, J. Push–Pull Type Quinoidal Perylene Showing Solvent Polarity Dependent Diradical Character and Negative Solvatochromism. *Mater Chem Front* **2019**, *3* (12), 2668–2672. https://doi.org/10.1039/C9QM00566H.

(14) Wang, Z.; Dai, Y.; Ding, L.; Dong, B.; Jiang, S.; Wang, J.; Pei, J. A Stable Triplet-Ground-State Conjugated Diradical Based on a Diindenopyrazine Skeleton. *Angewandte Chemie International Edition* **2021**, *60* (9), 4594–4598. https://doi.org/10.1002/anie.202012989.

(15) Ni, Y.; Gopalakrishna, T. Y.; Wu, S.; Wu, J. A Stable All-Thiophene-Based Core-Modified [38]Octaphyrin Diradicaloid: Conformation and Aromaticity Switch at Different Oxidation States. *Angewandte Chemie International Edition* **2020**, *59* (19), 7414–7418. https://doi.org/10.1002/anie.202000188.

(16) Ambhore, M. D.; Shukla, P.; Gonnade, R. G.; Anand, V. G. Tailoring Diradicaloid Properties of Expanded Isophlorinoids with Systematic Core-Modification. *Chemical Communications* **2022**, *58* (64), 8946–8949. https://doi.org/10.1039/D2CC02970G.

(17) Shimizu, A.; Kishi, R.; Nakano, M.; Shiomi, D.; Sato, K.; Takui, T.; Hisaki, I.; Miyata, M.; Tobe, Y. Indeno[2,1- *b*]Fluorene: A 20-π-Electron Hydrocarbon with Very Low-Energy Light Absorption. *Angewandte Chemie International Edition* **2013**, *52* (23), 6076–6079. https://doi.org/10.1002/anie.201302091.

(18) Ni, Y.; Gopalakrishna, T. Y.; Wu, S.; Wu, J. A Stable All-Thiophene-Based Core-Modified [38]Octaphyrin Diradicaloid: Conformation and Aromaticity Switch at Different Oxidation States. *Angewandte Chemie International Edition* **2020**, *59* (19), 7414–7418. https://doi.org/10.1002/anie.202000188.

(19) Y. Gopalakrishna, T.; Zeng, W.; Lu, X.; Wu, J. From Open-Shell Singlet Diradicaloids to Polyradicaloids. *Chemical Communications* **2018**, *54* (18), 2186–2199. https://doi.org/10.1039/C7CC09949E.

(20) Shimizu, A.; Morikoshi, T.; Sugisaki, K.; Shiomi, D.; Sato, K.; Takui, T.; Shintani, R. Synthesis and Isolation of a Kekulé Hydrocarbon with a Triplet Ground State. *Angewandte Chemie International Edition* **2022**, *61* (29). https://doi.org/10.1002/anie.202205729.

(21) Shimizu, A.; Morikoshi, T.; Sugisaki, K.; Shiomi, D.; Sato, K.; Takui, T.; Shintani, R. Synthesis and Isolation of a Kekulé Hydrocarbon with a Triplet Ground State. *Angewandte Chemie International Edition* **2022**, *61* (29). https://doi.org/10.1002/anie.202205729.

(22) Li, K.; Feng, Z.; Ruan, H.; Sun, Q.; Zhao, Y.; Wang, X. The Catenation of a Singlet Diradical Dication and Modulation of Diradical Character by Metal Coordination. *Chemical Communications* **2022**, *58* (44), 6457–6460. https://doi.org/10.1039/D2CC01539K.

(23) Abe, M. Diradicals. *Chem Rev* **2013**, *113* (9), 7011–7088. https://doi.org/10.1021/cr400056a.

(24) Rausch, R.; Röhr, M. I. S.; Schmidt, D.; Krummenacher, I.; Braunschweig, H.; Würthner, F. Tuning Phenoxyl-Substituted Diketopyrrolopyrroles from Quinoidal to Biradical Ground States through (Hetero-)Aromatic Linkers. *Chem Sci* **2021**, *12* (2), 793–802. https://doi.org/10.1039/d0sc05475e.

(25) Sun, Z.; Zeng, Z.; Wu, J. Zethrenes, Extended *p* -Quinodimethanes, and Periacenes with a Singlet Biradical Ground State. *Acc Chem Res* **2014**, *47* (8), 2582–2591. https://doi.org/10.1021/ar5001692.

(26) Privado, M.; Moles Quintero, S.; Barrejón, M.; de La Cruz, P.; P. M., J. B.; Casanova, D.; Langa, F.; Casado, J. Dibenzoquinone Cyclopentadithiophene Diradicaloids Show Optical Transitions of Different Spin States and Anomalous Near-Infrared Emission. *Angewandte Chemie International Edition* **2025**, *64* (2). https://doi.org/10.1002/anie.202413988.

(27) Casado, J. Para-Quinodimethanes: A Unified Review of the Quinoidal-Versus-Aromatic Competition and Its Implications. *Top Curr Chem* **2017**, *375* (4), 73. https://doi.org/10.1007/s41061-017-0163-2.

(28) Wu, J. *Diradicaloids*; Jenny Stanford Publishing: New York, 2022. https://doi.org/10.1201/9781003277248.

(29) Shen, L.; Gao, X.; Chang, Z.; Zhang, C.; Li, Y.; Lu, J.; Meng, Q.; Wu, Q. Sufficient Driving Force for Quinoidal Isoindigo-Based Diradicaloids with Tunable Diradical Characters. *Physical Chemistry Chemical Physics* **2024**, *26* (3), 2529–2538. https://doi.org/10.1039/D3CP05199D.

(30) Choppella, S.; Paramasivam, G.; Sambasivam, S.; Ravva, M. K. Understanding the Stability of π-Conjugated Diradicaloid Organic Molecules. *J Electron Mater* **2023**, *52* (3), 1681–1690. https://doi.org/10.1007/s11664-022-10082-2.

(31) Kodama, T.; Hirao, Y.; Kubo, T. Synthesis and Properties of a Through-Space Interacting Diradicaloid. *Precision Chemistry* **2023**, *1* (3), 183–191. https://doi.org/10.1021/prechem.3c00024.

(32) Wei, H.; Zhang, L.; Phan, H.; Huang, X.; Herng, T. S.; Zhou, J.; Zeng, W.; Ding, J.; Luo, S.; Wu, J.; Zeng, Z. A Stable *N* -Annulated Perylene-Bridged Bisphenoxyl Diradicaloid and the Corresponding Boron Trifluoride Complex. *Chemistry – A European Journal* **2017**, *23* (39), 9419–9424. https://doi.org/10.1002/chem.201701692.

(33) Zeng, Z.; Ishida, M.; Zafra, J. L.; Zhu, X.; Sung, Y. M.; Bao, N.; Webster, R. D.; Lee, B. S.; Li, R.-W.; Zeng, W.; Li, Y.; Chi, C.; Navarrete, J. T. L.; Ding, J.; Casado, J.; Kim, D.; Wu, J. Pushing Extended *p* -Quinodimethanes to the Limit: Stable Tetracyano-Oligo(*N* -Annulated Perylene)Quinodimethanes with Tunable Ground States. *J Am Chem Soc* **2013**, *135* (16), 6363–6371. https://doi.org/10.1021/ja402467y.

(34) Huang, R.; Phan, H.; Herng, T. S.; Hu, P.; Zeng, W.; Dong, S.; Das, S.; Shen, Y.; Ding, J.; Casanova, D.; Wu, J. Higher Order π-Conjugated Polycyclic Hydrocarbons with Open-Shell Singlet Ground State: Nonazethrene versus Nonacene. *J Am Chem Soc* **2016**, *138* (32), 10323–10330. https://doi.org/10.1021/jacs.6b06188.

(35) Oyelowo, M.; Schaffner, J. W.; Jeaydi, T. I.; Blank, D. A.; Ziegler, C. J.; Nemykin, V. N. Introducing of an Unexplored Aza-BODIPY Diradicaloids with 4-(2,6-

Ditert-Butyl)Phenoxyl Radicals Located in 1,7-Positions of the Aza-BODIPY Core. *Inorg Chem* **2024**. https://doi.org/10.1021/acs.inorgchem.4c04409.

(36) Kim, H.; Burghart, A.; Welch, M. B.; Reibenspies, J.; Burgess, K. Synthesis and Spectroscopic Properties of a New 4-Bora-3a,4a-Diaza-s-Indacene (BODIPY®) Dye. *Chemical Communications* **1999**, No. 18, 1889–1890. https://doi.org/10.1039/a905739k.

(37) Kovtun, Yu. P.; Yakubovskiy, V. P.; Shandura, M. P. Azadipyrromethene Dye with a Fully Chelated Boron Atom. *Chem Heterocycl Compd (N Y)* **2008**, *44* (10), 1298–1299. https://doi.org/10.1007/s10593-009-0179-9.

(38) Lim, H.; Seo, S.; Pascal, S.; Bellier, Q.; Rigaut, S.; Park, C.; Shin, H.; Maury, O.; Andraud, C.; Kim, E. NIR Electrofluorochromic Properties of Aza-Boron-Dipyrromethene Dyes. *Sci Rep* **2016**, *6* (1), 18867. https://doi.org/10.1038/srep18867.

(39) Shamova, L. I.; Zatsikha, Y. V.; Nemykin, V. N. Synthesis Pathways for the Preparation of the BODIPY Analogues: Aza-BODIPYs, BOPHYs and Some Other Pyrrole-Based Acyclic Chromophores. *Dalton Transactions* **2021**, *50* (5), 1569–1593. https://doi.org/10.1039/D0DT03964K.

(40) Li, H.; Wang, J.; Jiao, L.; Hao, E. BODIPY-Based Photocages: Rational Design and Their Biomedical Application. *Chemical Communications* **2024**, *60* (45), 5770–5789. https://doi.org/10.1039/D4CC01412J.

(41) Matarranz, B.; Fernández, G. BODIPY Dyes: Versatile Building Blocks to Construct Multiple Types of Self-Assembled Structures. *Chemical Physics Reviews* **2021**, *2* (4). https://doi.org/10.1063/5.0065873.

(42) Fan, G.; Yang, L.; Chen, Z. Water-Soluble BODIPY and Aza-BODIPY Dyes: Synthetic Progress and Applications. *Front Chem Sci Eng* **2014**, *8* (4), 405–417. https://doi.org/10.1007/s11705-014-1445-7.

(43) Loudet, A.; Bandichhor, R.; Wu, L.; Burgess, K. Functionalized BF2 Chelated Azadipyrromethene Dyes. *Tetrahedron* **2008**, *64* (17), 3642–3654. https://doi.org/10.1016/j.tet.2008.01.117.

(44) Loudet, A.; Bandichhor, R.; Burgess, K.; Palma, A.; McDonnell, S. O.; Hall, M. J.; O'Shea, D. F. *B* , *O* -Chelated Azadipyrromethenes as Near-IR Probes. *Org Lett* **2008**, *10* (21), 4771–4774. https://doi.org/10.1021/ol8018506.

(45) Hu, X.; Fang, Z.; Zhu, C.; Yang, Y.; Yang, Z.; Huang, W. Crucial Breakthrough of BODIPY-Based NIR-II Fluorescent Emitters for Advanced Biomedical Theranostics. *Adv Funct Mater* **2024**, *34* (36). https://doi.org/10.1002/adfm.202401325.

(46) Bumagina, N. A.; Antina, E. V. Review of Advances in Development of Fluorescent BODIPY Probes (Chemosensors and Chemodosimeters) for Cation Recognition. *Coord Chem Rev* **2024**, *505*, 215688. https://doi.org/10.1016/j.ccr.2024.215688.

(47) Kaur, M.; Janaagal, A.; Balsukuri, N.; Gupta, I. Evolution of Aza-BODIPY Dyes-A Hot Topic. *Coord Chem Rev* **2024**, *498*, 215428. https://doi.org/10.1016/j.ccr.2023.215428.

(48) Ballmann, G.; Rösch, B.; Harder, S. Stabilization of Heteroleptic Heavier Alkaline Earth Metal Complexes with an Encapsulating Dipyrromethene Ligand. *Eur J Inorg Chem* **2019**, *2019* (32), 3683–3689. https://doi.org/10.1002/ejic.201900743.

(49) Thoi, V. S.; Stork, J. R.; Magde, D.; Cohen, S. M. Luminescent Dipyrrinato Complexes of Trivalent Group 13 Metal Ions. *Inorg Chem* **2006**, *45* (26), 10688–10697. https://doi.org/10.1021/ic061581h.

(50) Jimenez, J. C.; Zhou, Z.; Rheingold, A. L.; Parker, S. M.; Sauvé, G. Tuning the Properties of Azadipyrromethene-Based Near-Infrared Dyes Using Intramolecular BO Chelation and Peripheral Substitutions. *Inorg Chem* **2021**, *60* (17), 13320–13331. https://doi.org/10.1021/acs.inorgchem.1c01597.

(51) Wang, Y.; Xiao, F.; Shao, T.; Jin, G. A Near-Infrared Azadipyrromethene Dye: Photophysical Properties under Different Acidity Conditions. *Inorg Chem Commun* **2020**, *116*, 107942. https://doi.org/10.1016/j.inoche.2020.107942.

(52) Pascal, S.; David, S.; Andraud, C.; Maury, O. Near-Infrared Dyes for Two-Photon Absorption in the Short-Wavelength Infrared: Strategies towards Optical Power Limiting. *Chem Soc Rev* **2021**, *50* (11), 6613–6658. https://doi.org/10.1039/D0CS01221A.

(53) Loudet, A.; Bandichhor, R.; Burgess, K.; Palma, A.; McDonnell, S. O.; Hall, M. J.; O'Shea, D. F. *B* , *O* -Chelated Azadipyrromethenes as Near-IR Probes. *Org Lett* **2008**, *10* (21), 4771–4774. https://doi.org/10.1021/ol8018506.

(54) Ikeda, C.; Ueda, S.; Nabeshima, T. Aluminium Complexes of N2O2-Type Dipyrrins: The First Hetero-Multinuclear Complexes of Metallo-Dipyrrins with High Fluorescence Quantum Yields. *Chemical Communications* **2009**, No. 18, 2544–2546. https://doi.org/10.1039/b820141b.

(55) Saikawa, M.; Daicho, M.; Nakamura, T.; Uchida, J.; Yamamura, M.; Nabeshima, T. Synthesis of a New Family of Ionophores Based on Aluminum-Dipyrrin Complexes

(ALDIPYs) and Their Strong Recognition of Alkaline Earth Ions. *Chemical Communications* **2016**, *52* (21), 4014–4017. https://doi.org/10.1039/c6cc00250a.

(56) Sumiyoshi, A.; Chiba, Y.; Matsuoka, R.; Noda, T.; Nabeshima, T. Efficient Luminescent Properties and Cation Recognition Ability of Heavy Group 13 Element Complexes of N2O2- and N2O4-Type Dipyrrins. *Dalton Transactions* **2019**, *48* (35), 13169–13175. https://doi.org/10.1039/c9dt02403d.

(57) Lane, A. M.; Luong, N. T. C.; Kelly, J. C.; Neal, M. J.; Jamrom, J.; Bloomfield, A. J.; Lummis, P. A.; Montgomery, T. D.; Chase, D. T. Synthetic Exploration of Bis(Phenolate) Aza-BODIPYs and Heavier Group 13 Chelates. *Molecules* **2022**, *27* (23). https://doi.org/10.3390/molecules27238256.

(58) Godard, A.; Galán, L. A.; Rouillon, J.; Al Shehimy, S.; Tajani, W.; Cave, C.; Malacea-Kabbara, R.; Rousselin, Y.; Le Gendre, P.; Fihey, A.; Bendellaa, M.; Busser, B.; Sancey, L.; Le Guennic, B.; Bucher, C.; Maury, O.; Goze, C.; Bodio, E. Al(III) and Ga(III) Bisphenolate Azadipyrromethene-Based "N2O2" Complexes as Efficient NIR-Fluorophores. *Inorg Chem* **2023**, *62* (13), 5067–5080. https://doi.org/10.1021/acs.inorgchem.2c03918.

(59) Zatsikha, Y. V.; Blesener, T. S.; Goff, P. C.; Healy, A. T.; Swedin, R. K.; Herbert, D. E.; Rohde, G. T.; Chanawanno, K.; Ziegler, C. J.; Belosludov, R. V.; Blank, D. A.; Nemykin, V. N. 1,7-Dipyrene-Containing Aza-BODIPYs: Are Pyrene Groups Effective as Ligands To Promote and Direct Complex Formation with Common Nanocarbon Materials? *The Journal of Physical Chemistry C* **2018**, *122* (49), 27893–27916. https://doi.org/10.1021/acs.jpcc.8b09504.

(60) Zatsikha, Y. V.; Shamova, L. I.; Blesener, T. S.; Kuzmin, I. A.; Germanov, Y. V.; Herbert, D. E.; Nemykin, V. N. Development of a Class of Easily Scalable, Electron-Deficient, Core-Extended Benzo-Fused Azadipyrromethene Derivatives ("MB-DIPY"). *J Org Chem* **2019**, *84* (22), 14540–14557. https://doi.org/10.1021/acs.joc.9b02074.

(61) Gao, H.; Liu, H.; Jiang, L.; Gai, L.; Shen, Z. A Near-Infrared Benzoquinone-Coupled BODIPY: Synthesis, Spectroscopic and Electrochemical Properties. *J Porphyr Phthalocyanines* **2019**, *23* (01n02), 76–83. https://doi.org/10.1142/S1088424619500044.

(62) Al-Imarah, E. M. A.; Derrick, P. J.; Partridge, A. New Wavelength-Tunable Aza-Dipyrromethene Dyes with Intense near-Infrared Absorption and Emission. *J Photochem Photobiol A Chem* **2017**, *337*, 82–90. https://doi.org/10.1016/j.jphotochem.2017.01.024.

(63) Gao, Y.; Pan, Y.; He, Y.; Chen, H.; Nemykin, V. N. A Fast-Response, Red Emission Aza-BODIPY-Hydrazone-Based Chemodosimeter for Selective Detection of HClO. *Sens Actuators B Chem* **2018**, *269*, 151–157. https://doi.org/10.1016/j.snb.2018.04.135.

(64) Yamamura, M.; Takizawa, H.; Gobo, Y.; Nabeshima, T. Stable Neutral Radicals of Planar N2O2-Type Dipyrrin Platinum Complexes: Hybrid Radicals of the Delocalized Organic π-Orbital and Platinum d-Orbital. *Dalton Transactions* **2016**, *45* (16), 6834–6838. https://doi.org/10.1039/c5dt05039a.

(65) Kochem, A.; Chiang, L.; Baptiste, B.; Philouze, C.; Leconte, N.; Jarjayes, O.; Storr, T.; Thomas, F. Ligand-Centered Redox Activity in Cobalt(II) and Nickel(II) Bis(Phenolate)-Dipyrrin Complexes. *Chemistry - A European Journal* **2012**, *18* (46), 14590–14593. https://doi.org/10.1002/chem.201202882.

(66) Curtis, C. J.; Astashkin, A. V.; Conradie, J.; Ghosh, A.; Tomat, E. Ligand-Centered Triplet Diradical Supported by a Binuclear Palladium(II) Dipyrrindione. *Inorg Chem* **2021**, *60* (16), 12457–12466. https://doi.org/10.1021/acs.inorgchem.1c01691.

(67) Cohen, S. M.; Halper, S. R. Dipyrromethene Complexes of Iron. *Inorganica Chim Acta* **2002**, *341*, 12–16. https://doi.org/10.1016/S0020-1693(02)01176-3.

(68) Shikha Singh, R.; Prasad Paitandi, R.; Kumar Gupta, R.; Shankar Pandey, D. Recent Developments in Metal Dipyrrin Complexes: Design, Synthesis, and Applications. *Coord Chem Rev* **2020**, *414*, 213269. https://doi.org/10.1016/j.ccr.2020.213269.

(69) Zatsikha, Y. V.; Shamova, L. I.; Shepit, M.; Berry, S. M.; Thomas, F.; Herbert, D. E.; van Lierop, J.; Nemykin, V. N. Radical Complexes of Nickel(II)/Copper(II) and Redox Non-innocent MB-DIPY Ligands: Unusual Stability and Strong Near-Infrared Absorption at λ_{max} ~1300 Nm. *Chemistry – A European Journal* **2022**, *28* (41). https://doi.org/10.1002/chem.202201181.

(70) Makarova, E. A.; Zatsikha, Y. V.; Newman, K. M. E.; Paidi, V. K.; Beletsky, V. A.; van Lierop, J.; Lukyanets, E. A.; Nemykin, V. N. Direct Synthesis of an Unprecedented Stable Radical of Nickel(II) 3,5-Bis(Dimedonyl)Azadiisoindomethene with Strong and Narrow Near-Infrared Absorption at λ ~ 1000 Nm. *Inorg Chem* **2017**, *56* (11), 6052–6055. https://doi.org/10.1021/acs.inorgchem.7b01140.

(71) Miao, F.; Phan, H.; Wu, J. A BODIPY-Bridged Bisphenoxyl Diradicaloid: Solvent-Dependent Diradical Character and Physical Properties. *Molecules* **2019**, *24* (8), 1446. https://doi.org/10.3390/molecules24081446.

(72) Ni, Y.; Lee, S.; Son, M.; Aratani, N.; Ishida, M.; Samanta, A.; Yamada, H.; Chang, Y.; Furuta, H.; Kim, D.; Wu, J. A Diradical Approach towards BODIPY-Based Dyes with Intense Near-Infrared Absorption around λ =1100 Nm. *Angewandte Chemie International Edition* **2016**, *55* (8), 2815–2819. https://doi.org/10.1002/anie.201511151.

(73) Jiang, Q.; Wang, L.; Wei, H.; Peng, Y.; Xu, G.; Li, Z.; Liu, P.; Hu, Z.; Niu, W.; Chen, Y.; Tang, H.; Zeng, W.; Li, G. A Kinetically Stabilized Dianthraceno[2,3- *a* :3′,2′- *h*]- *s* -Indacene: Stable Kekulé Diradical Polycyclic Hydrocarbon with Triplet Ground State. *Angewandte Chemie* **2025**, *137* (12). https://doi.org/10.1002/ange.202422994.

(74) Sun, Z.; Ye, Q.; Chi, C.; Wu, J. Low Band Gap Polycyclic Hydrocarbons: From Closed-Shell near Infrared Dyes and Semiconductors to Open-Shell Radicals. *Chem Soc Rev* **2012**, *41* (23), 7857. https://doi.org/10.1039/c2cs35211g.

(75) Nakano, M. Open-Shell-Character-Based Molecular Design Principles: Applications to Nonlinear Optics and Singlet Fission. *The Chemical Record* **2017**, *17* (1), 27–62. https://doi.org/10.1002/tcr.201600094.

(76) *Electron Paramagnetic Resonance*; Brustolon, M., Giamello, E., Eds.; Wiley, 2009. https://doi.org/10.1002/9780470432235.

(77) Shamova, L. I.; Zatsikha, Y. V.; Nemykin, V. N. Synthesis Pathways for the Preparation of the BODIPY Analogues: Aza-BODIPYs, BOPHYs and Some Other Pyrrole-Based Acyclic Chromophores. *Dalton Transactions* **2021**, *50* (5), 1569–1593. https://doi.org/10.1039/D0DT03964K.

(78) *KaleidaGraph, version 5.04*, 1986-2023; Synergy Software Inc.

(79) Sheldrick, G. M. A short history of *SHELX*. *Acta Crystallogr.* 2008, *A64*, 112-122.

(80) *Bruker-AXS APEX3 v2016.1-0*, Madison, Wisconsin, USA, 2016.

(81) Spek, A. L. Structure validation in chemical crystallography. *Acta Crystallogr.* 2009, *D65*, 148-155.

(82) Macrae, C. F.; Sovago, I.; Cottrell, S. J.; Galek, P. T. A.; McCabe, P.; Pidcock, E.; Platings, M.; Shields, G. P.; Stevens, J. S.; Towler, M.; Wood, P. A. Mercury 4.0: from visualization to analysis, design and prediction. *J. Appl. Crystallogr.* 2020, *53*, 226-235.

(83) Frisch, M. J.; Trucks, G. W.; Schlegel, H. B.; Scuseria, G. E.; Robb, M. A.; Cheeseman, J. R.; Scalmani, G.; Barone, V.; Petersson, G. A.; Nakatsuji, H.; Li, X.; Caricato, M.; Marenich, A. V.; Bloino, J.; Janesko, B. G.; Gomperts, R.; Mennucci, B.; Hratchian, H. P.; Ortiz, J. V.; Izmaylov, A. F.; Sonnenberg, J. L.; Williams-Young, D.; Ding, F.; Lipparini, F.; Egidi, F.; Goings, J.; Peng, B.; Petrone, A.; Henderson, T.; Ranasinghe, D.; Zakrzewski, V. G.; Gao, J.; Rega, N.; Zheng, G.; Liang, W.; Hada, M.; Ehara, M.; Toyota, K.; Fukuda, R.; Hasegawa, J.; Ishida, M.; Nakajima, T.; Honda, Y.; Kitao, O.; Nakai, H.; Vreven, T.; Throssell, K.; Montgomery, J. A., Jr.; Peralta, J. E.; Ogliaro, F.; Bearpark, M. J.; Heyd, J. J.; Brothers, E. N.; Kudin, K. N.; Staroverov, V. N.; Keith, T. A.; Kobayashi, R.; Normand, J.; Raghavachari, K.; Rendell, A. P.; Burant, J. C.; Iyengar, S. S.; Tomasi, J.; Cossi, M.; Millam, J. M.; Klene, M.; Adamo, C.; Cammi, R.; Ochterski, J. W.; Martin, R. L.; Morokuma, K.; Farkas, O.; Foresman, J. B.; Fox, D. J. *Gaussian 16, Revision B.01*; Gaussian, Inc.: Wallingford CT, 2016.

(84) Tenderholt, A. L. *QMForge, version 2.1*; Standord University: Stanford, CA, 2011. https://qmforge.net/.

(85) Tao, J. M.; Perdew, J. P.; Staroverov, V. N.; Scuseria, G. E. Climbing the density functional ladder: Nonempirical metageneralized gradient approximation designed for molecules and solids. *Phys. Rev. Lett.* 2003, *91*, 146401/1-146401/

(86) Staroverov, V. N.; Scuseria, G. N.; Tao, J.; Perdew, J. P.m Comparative assessment of new nonempirical density functional: Molecules and hydrogen-bonded complexes. *J. Chem. Phys.* 2003, *119*, 12129-12137.

(87) Zhao, Y.; Truhlar, D. G. The M06 Suite of density functionals for main group thermochemistry, thermochemical kinetics, noncovalent interactions, excited states, and transition elements: Two new functionals and systematic testing of four M06 functionals and twelve other functionals. *Theor. Chem. Acc.* 2008, *120*, 215-241.

(88) McLean, A. D.; Chandler, G. S. Contracted Gaussian Basis Sets for Molecular Calculations. I. Second Row Atoms, Z = 11−18. J. Chem. Phys. 1980, 72 (10), 5639−5648.

Appendix

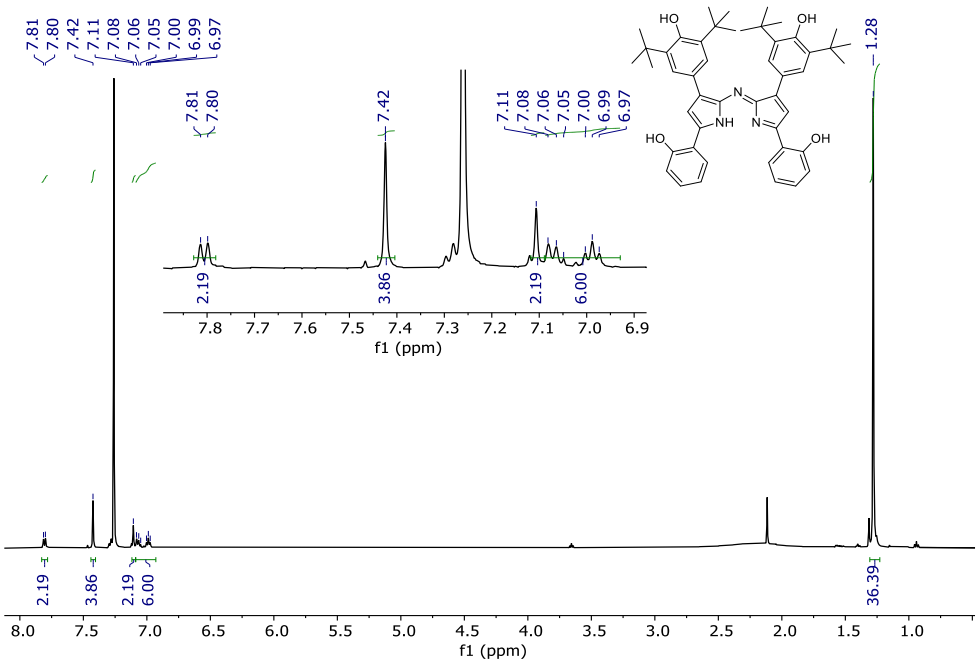


Figure 3.23: ^{1}H NMR spectrum of compound **3.3** in $CDCl_3$

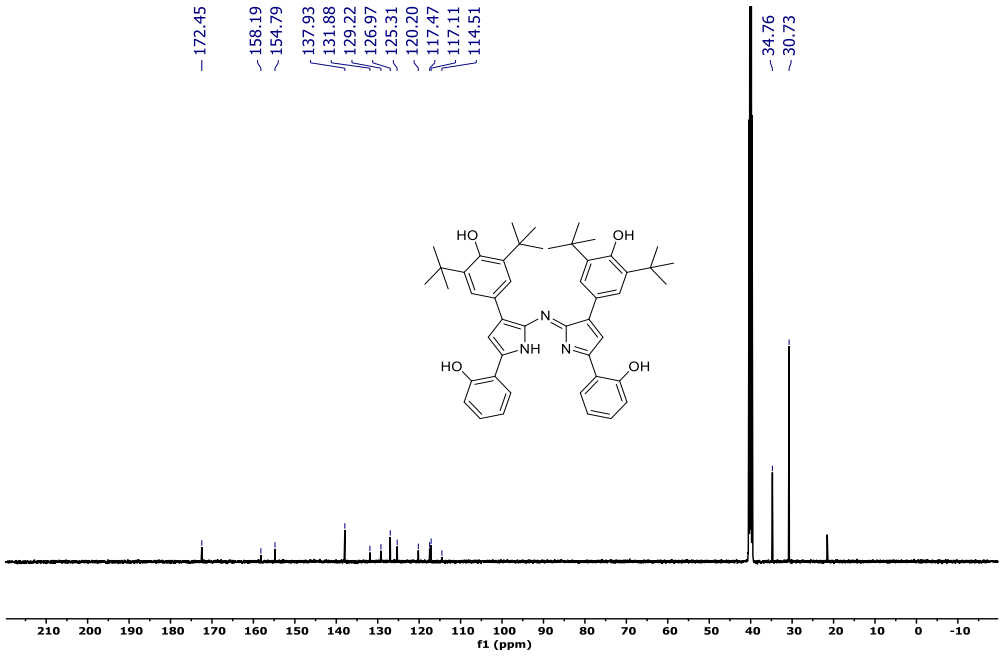


Figure 3.24: ^{13}C NMR spectrum of compound **3.3** in $CDCl_3$

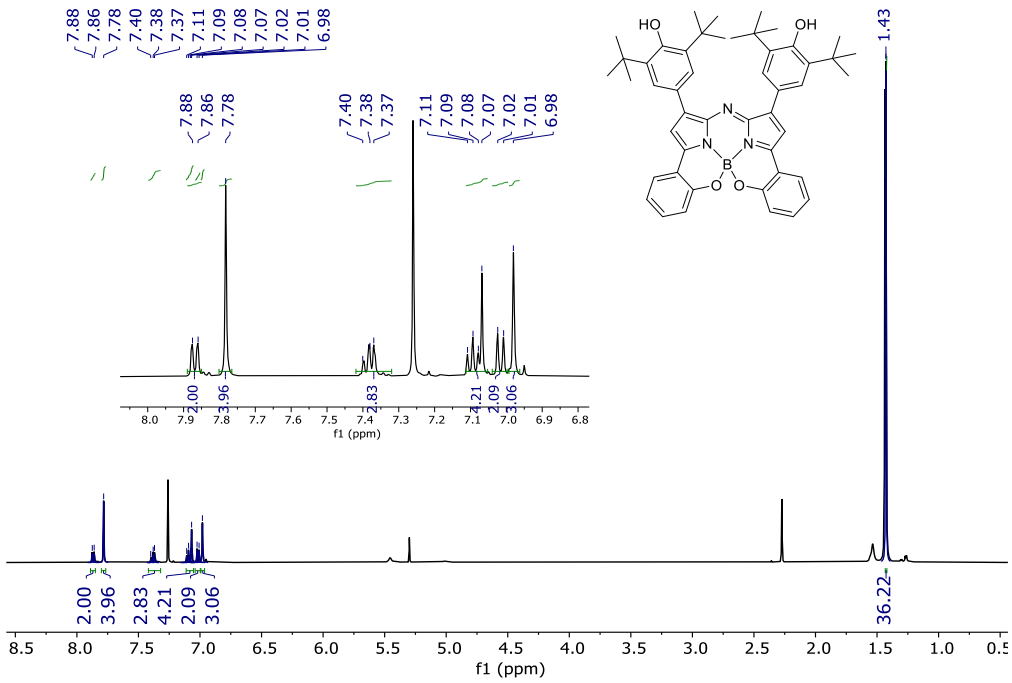


Figure 3.25: ^{1}H NMR spectrum of compound **3.4a** in $CDCl_3$

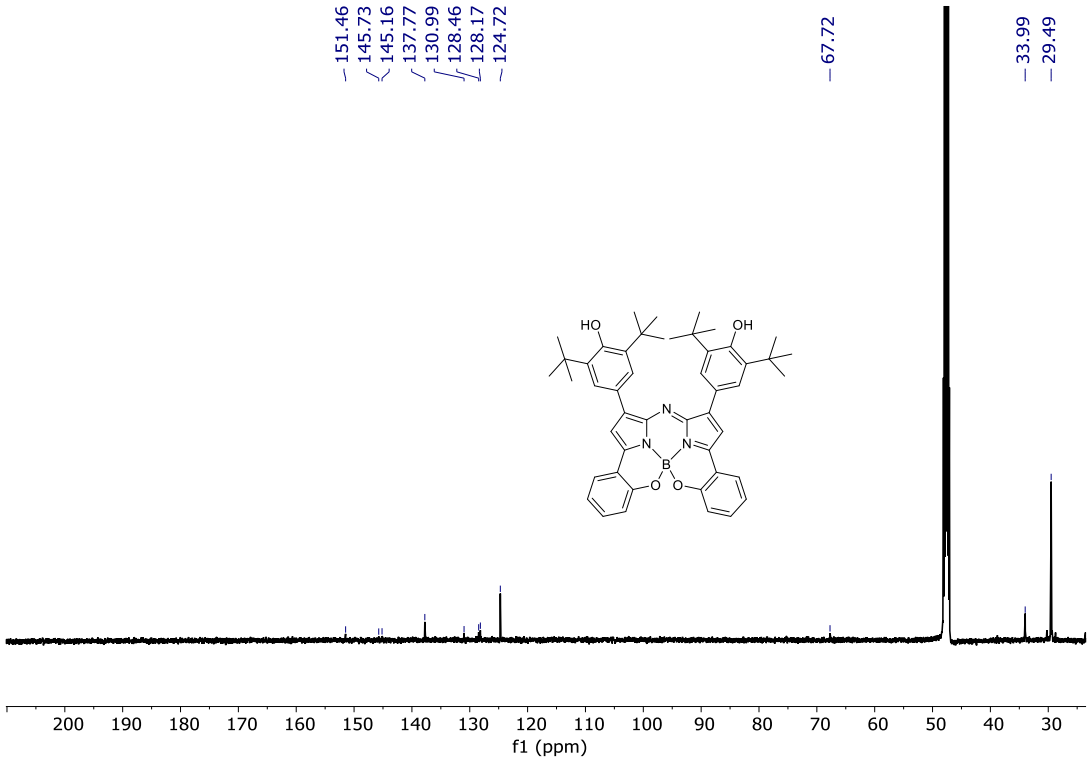


Figure 3.26: ^{13}C NMR spectrum of compound **3.4a** in $CDCl_3$

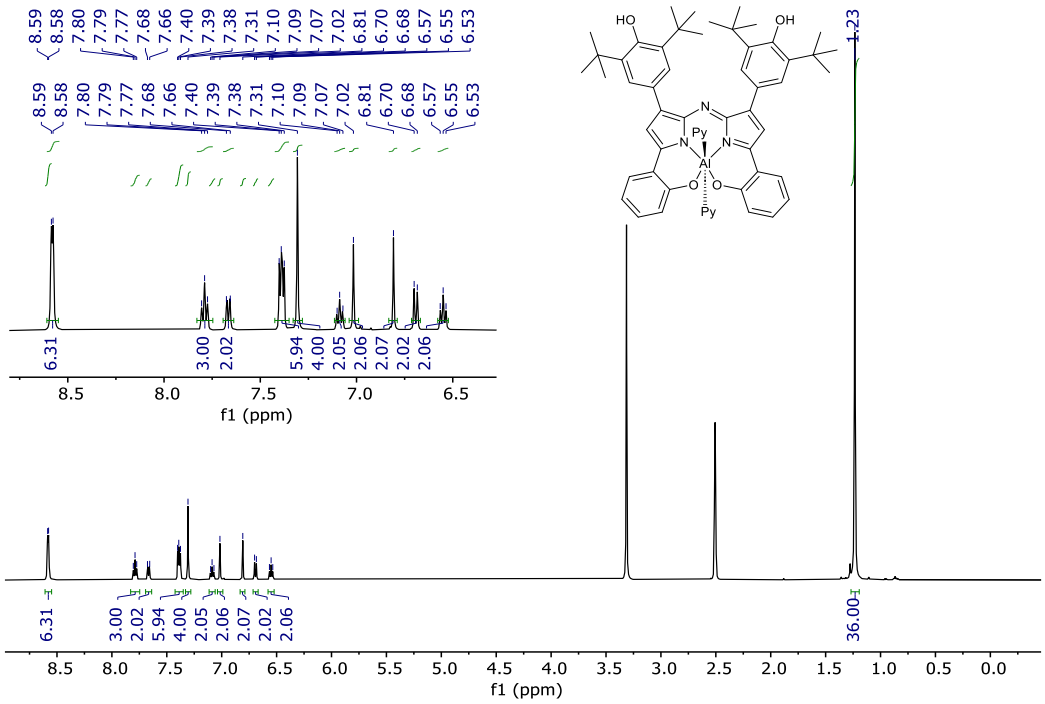


Figure 3.27: ^{1}H NMR spectrum of compound **3.4b** in DMSO-d_6

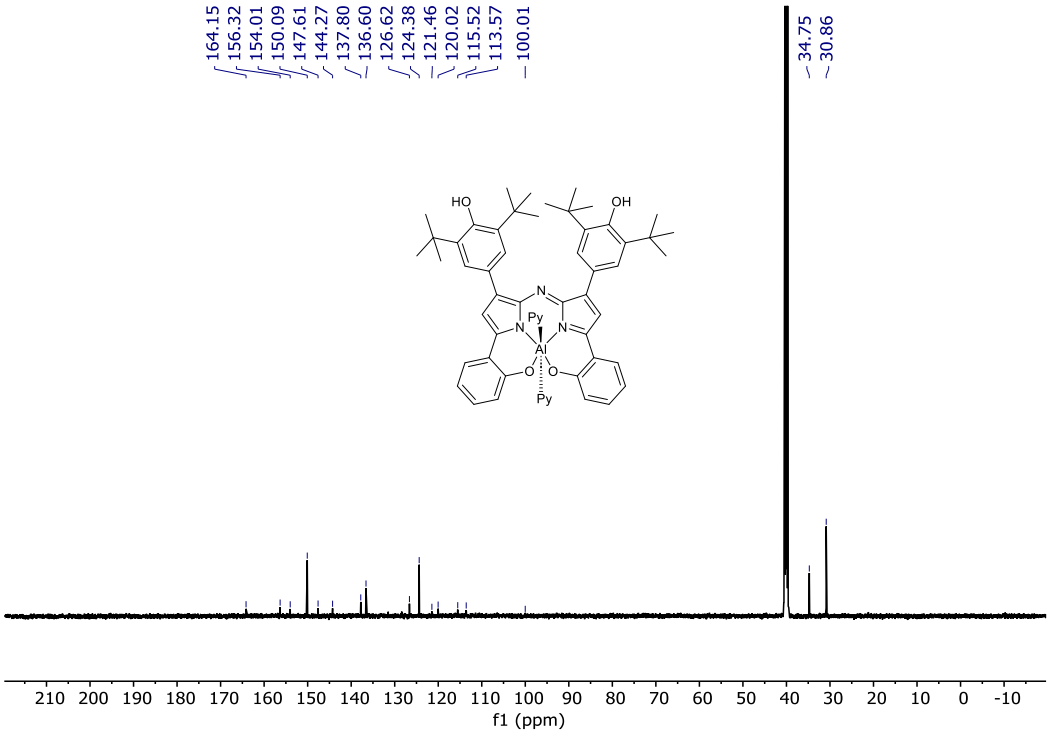


Figure 3.28: ^{13}C NMR spectrum of compound **3.4b** in DMSO-d_6

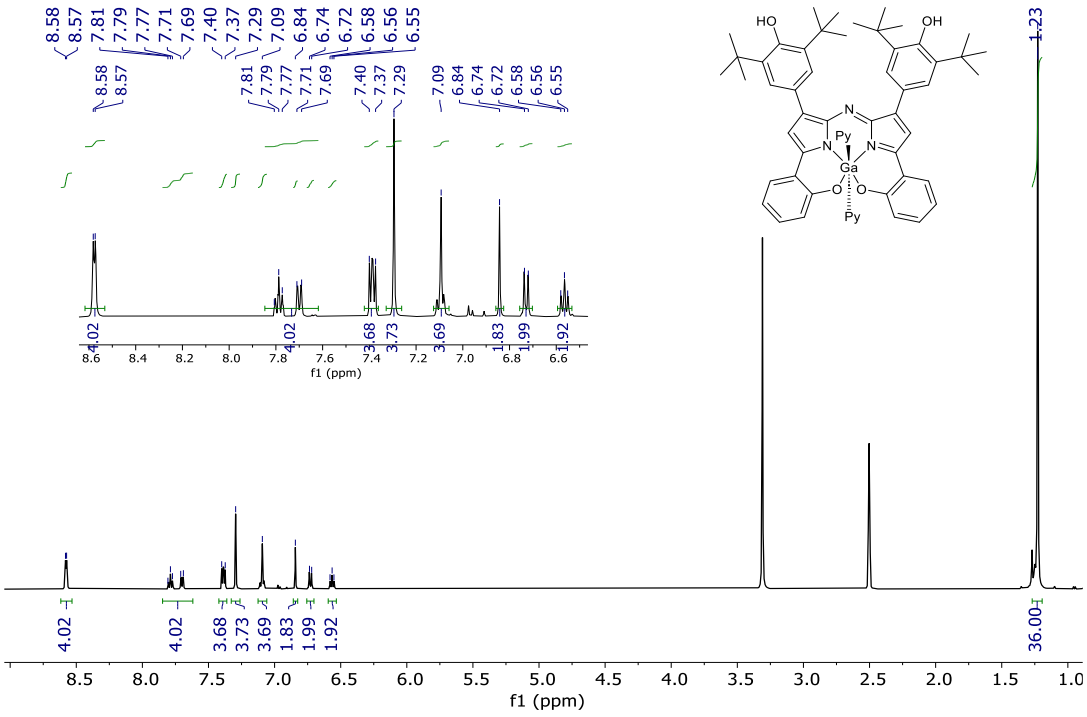


Figure 3.29: ^{1}H NMR spectrum of compound **3.4c** in DMSO-d$_6$

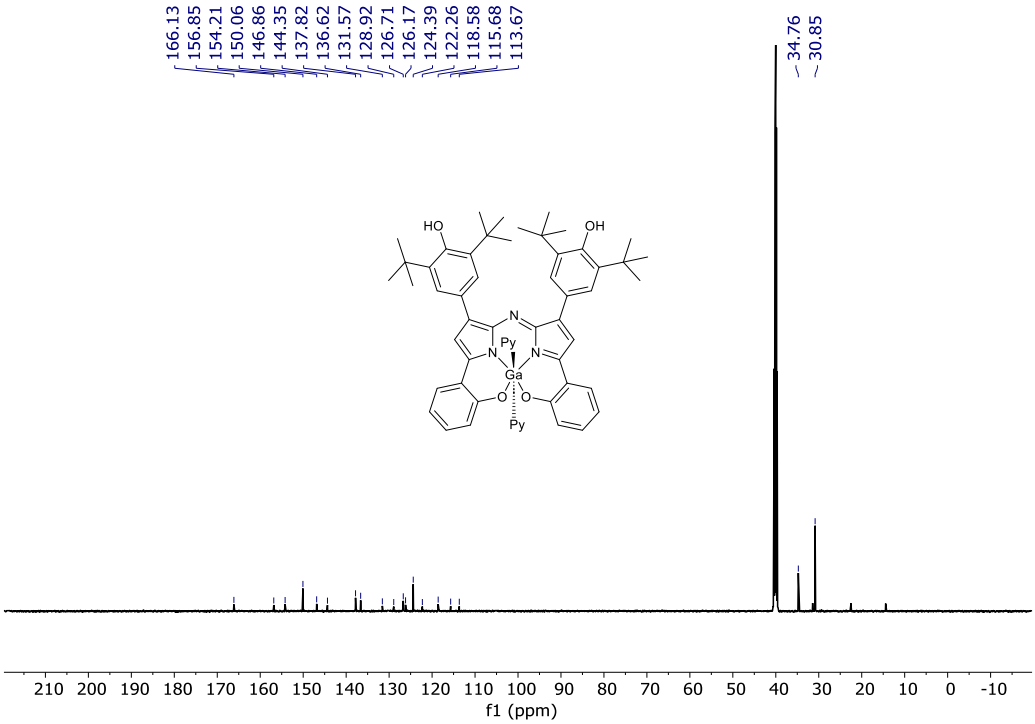


Figure 3.30: ^{13}C NMR spectrum of compound **3.4c** in DMSO-d$_6$

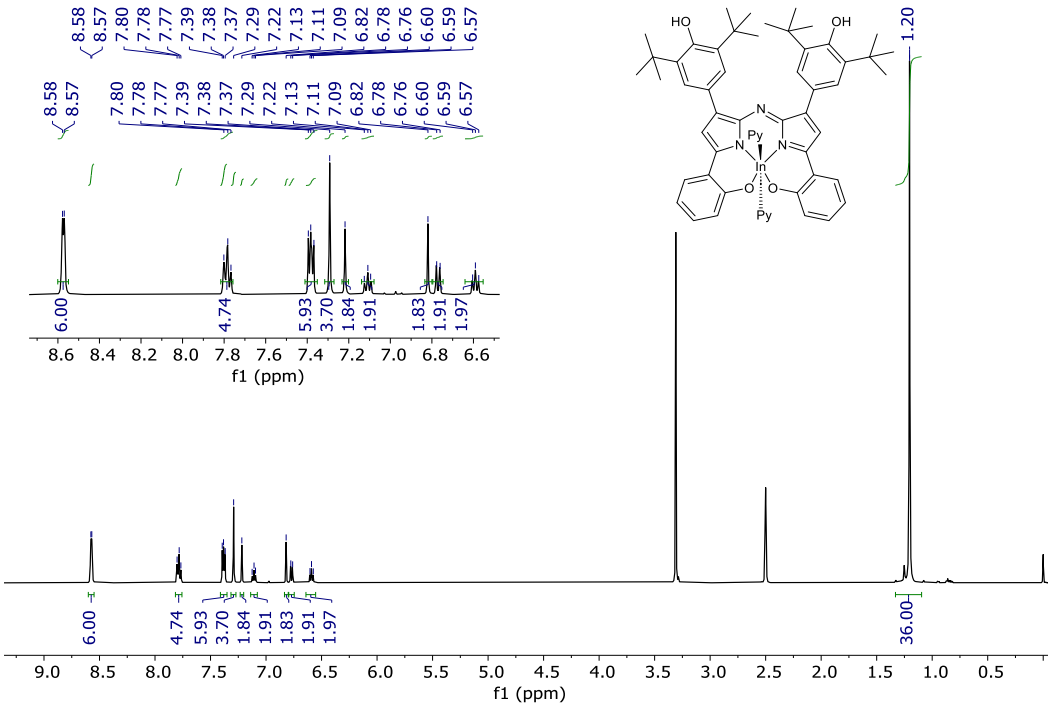


Figure 3.31: ^{1}H NMR spectrum of compound **3.4d** in DMSO-d_6

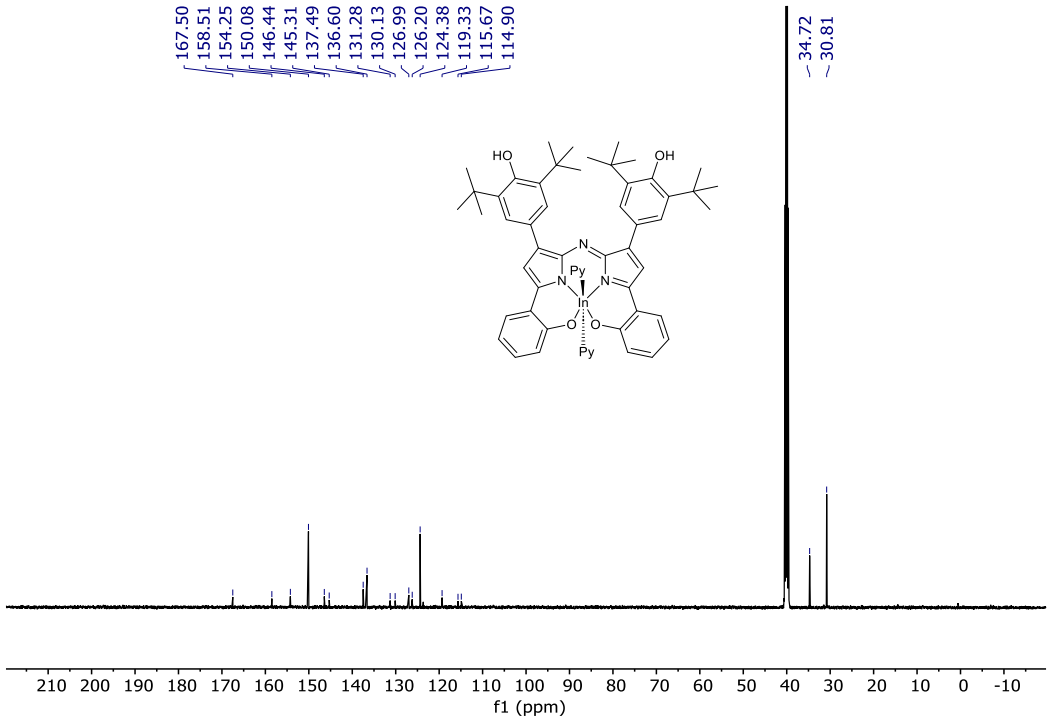


Figure 3.32: ^{13}C NMR spectrum of compound **3.4d** in DMSO-d_6

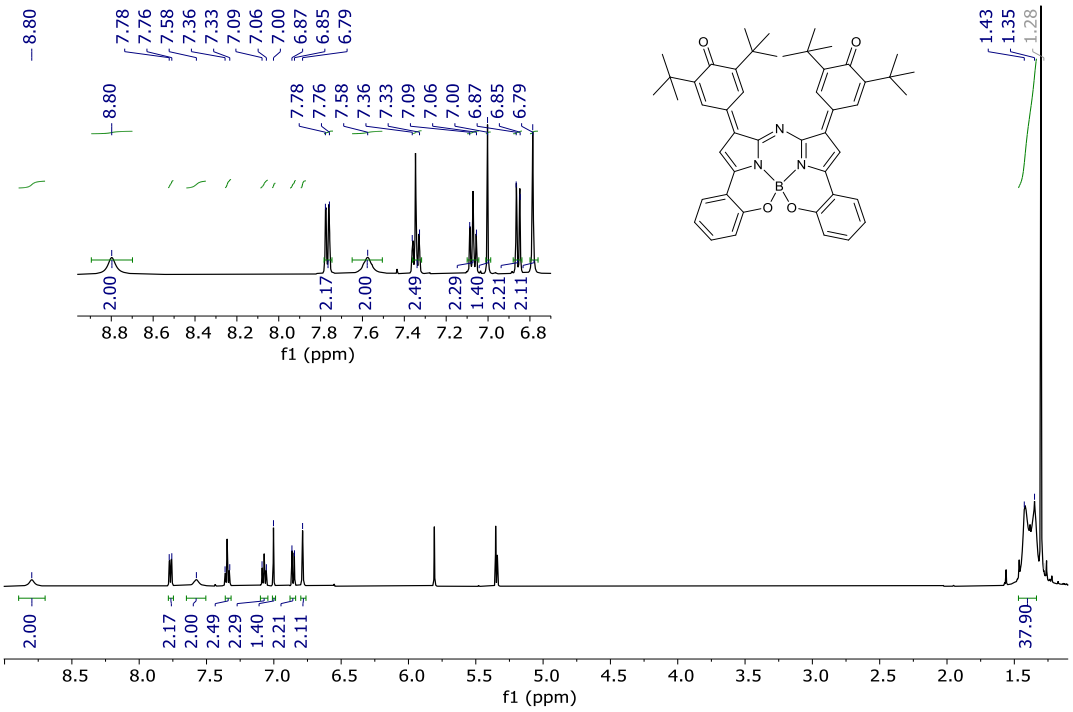


Figure 3.33: ^{1}H NMR spectrum of compound **3.5a** in CD_2Cl_2

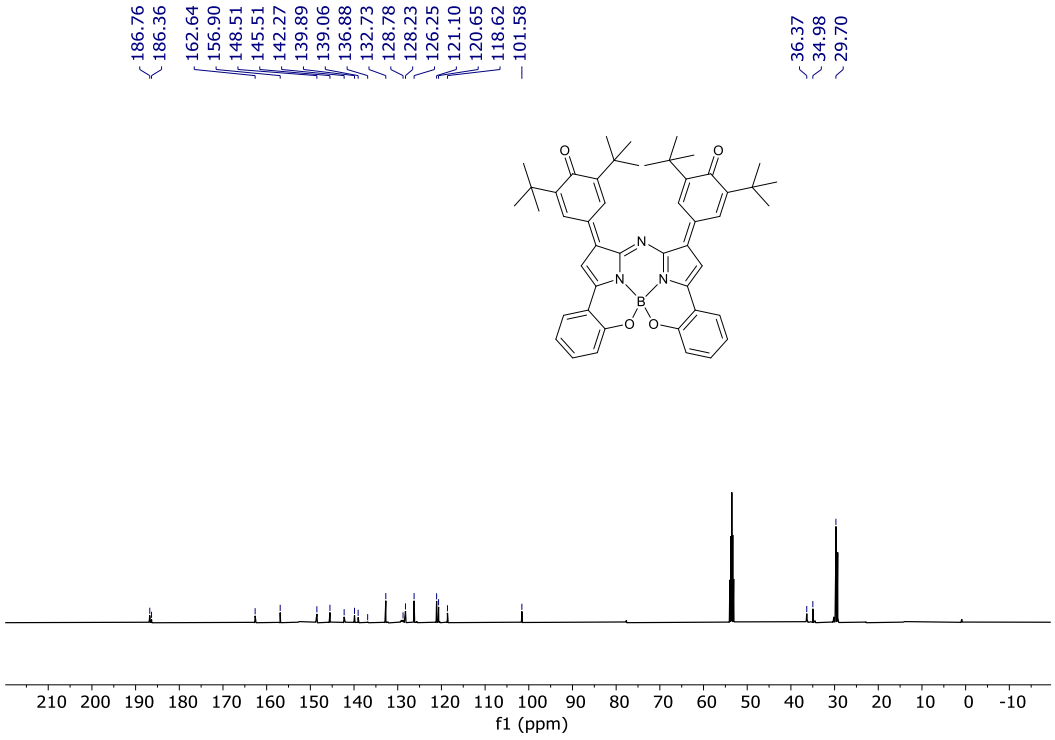


Figure 3.34: ^{13}C NMR spectrum of compound **3.5a** in CD_2Cl_2

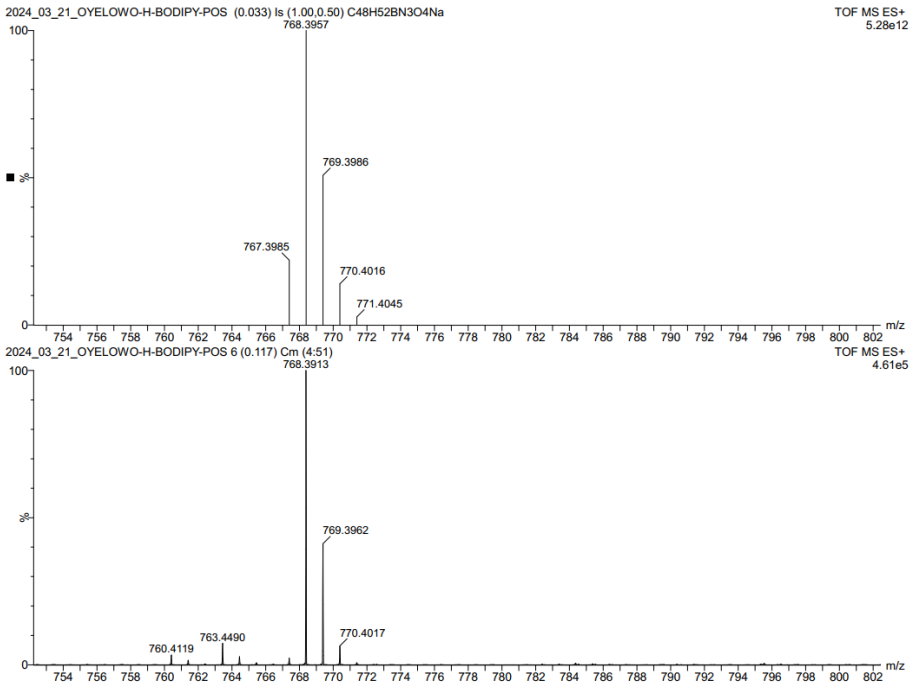


Figure 3.35: Mass spectrum of compound of compound **3.4a.**

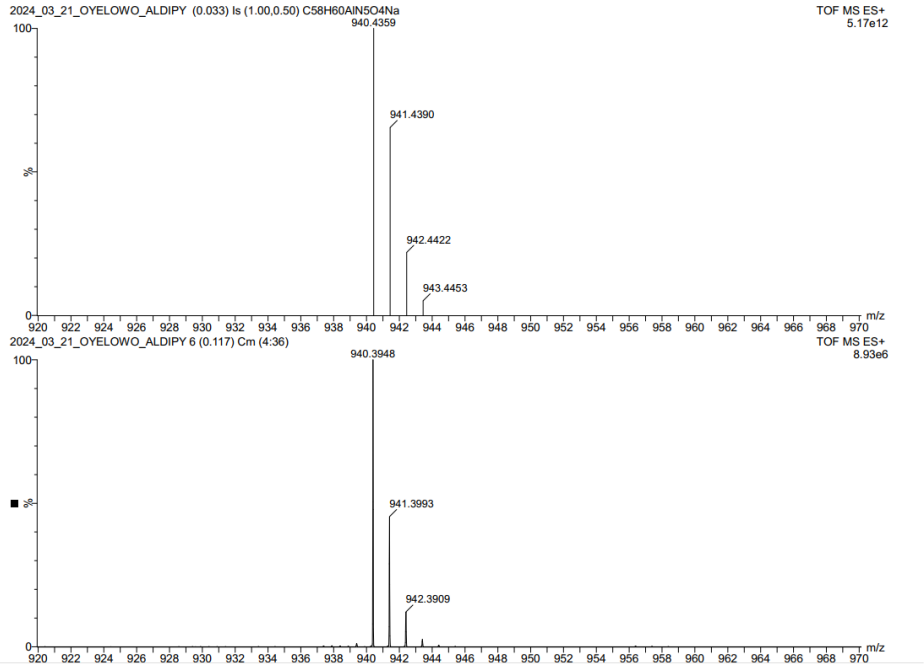


Figure 3.36 Mass spectrum of compound of compound **3.4b.**

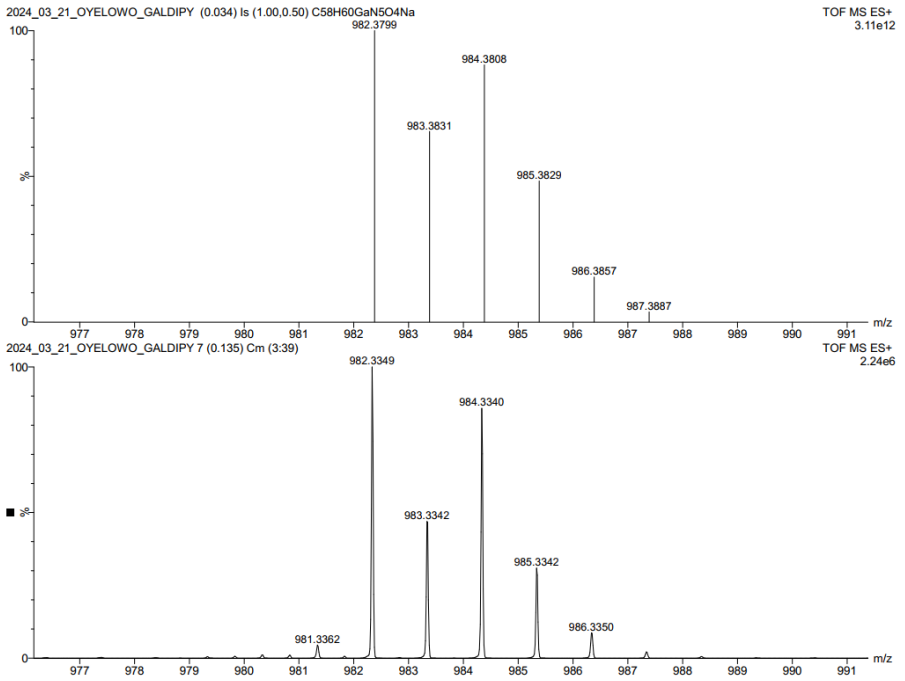


Figure 3.37: HRMS spectra of compound of compound **3.4c.**

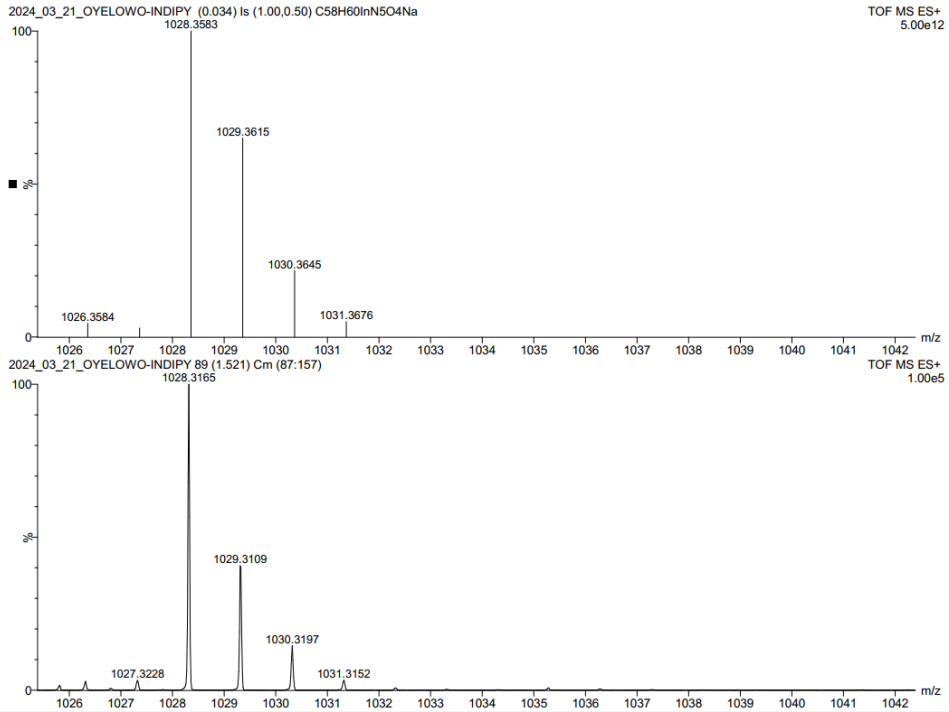


Figure 3.38: Mass spectrum of compound of compound **3.4d.**

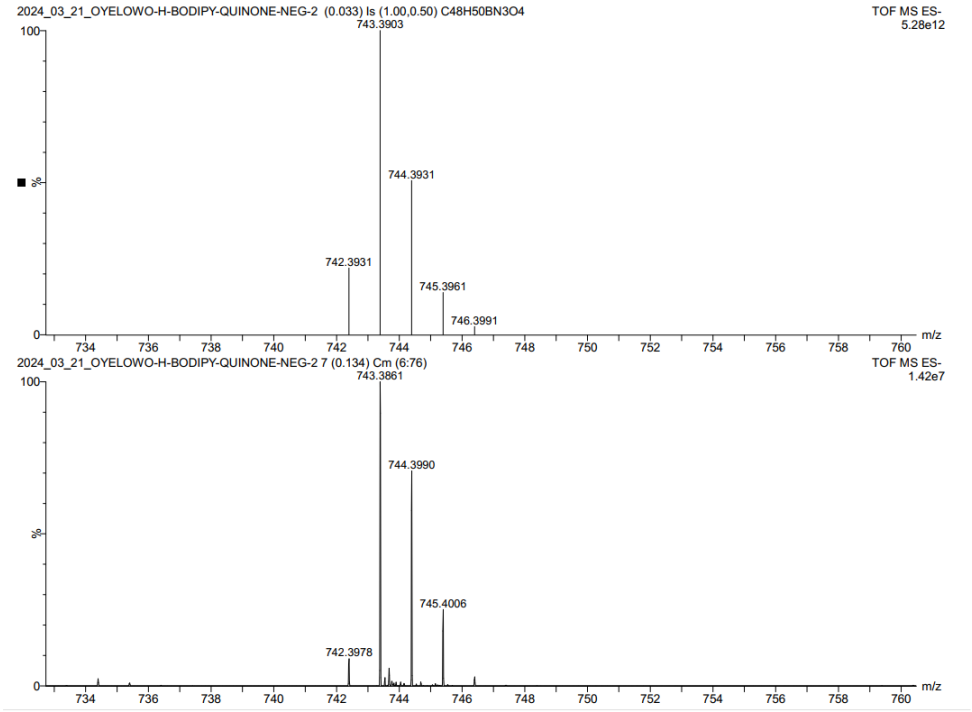


Figure 3.39: Mass spectrum of compound of compound **3.5a.**

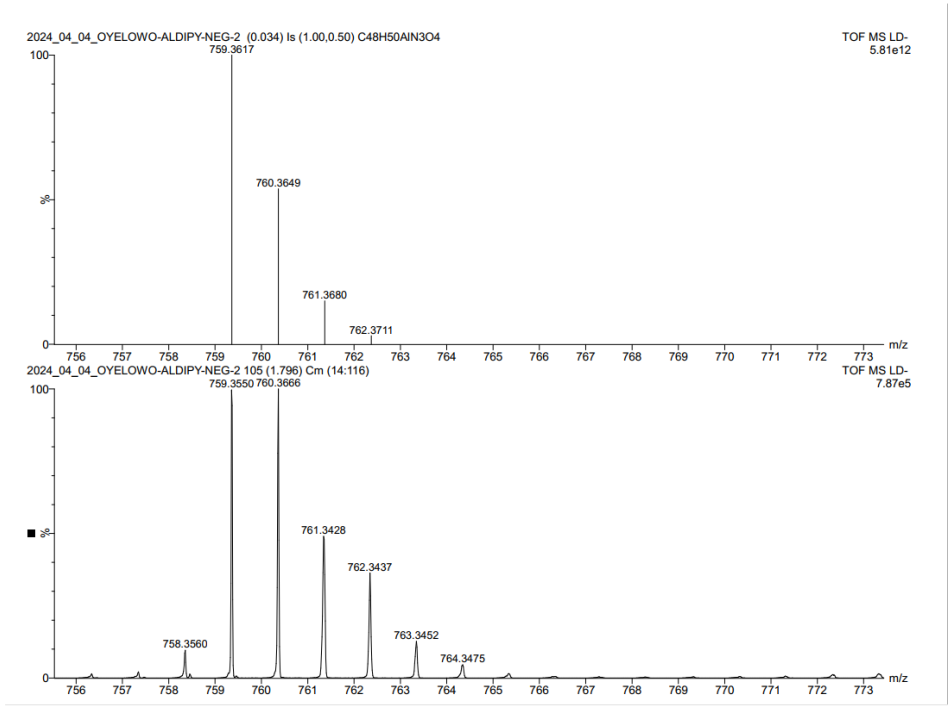


Figure 3.40: Mass spectrum of compound of compound **3.5b.**

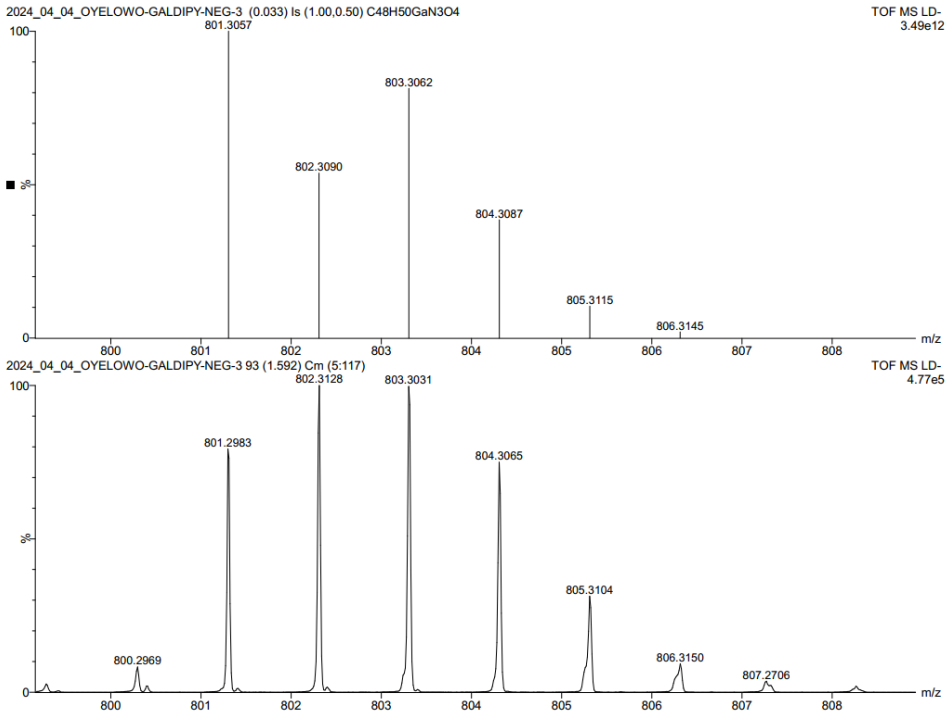


Figure 3.41: Mass spectrum of compound of compound **3.5c.**

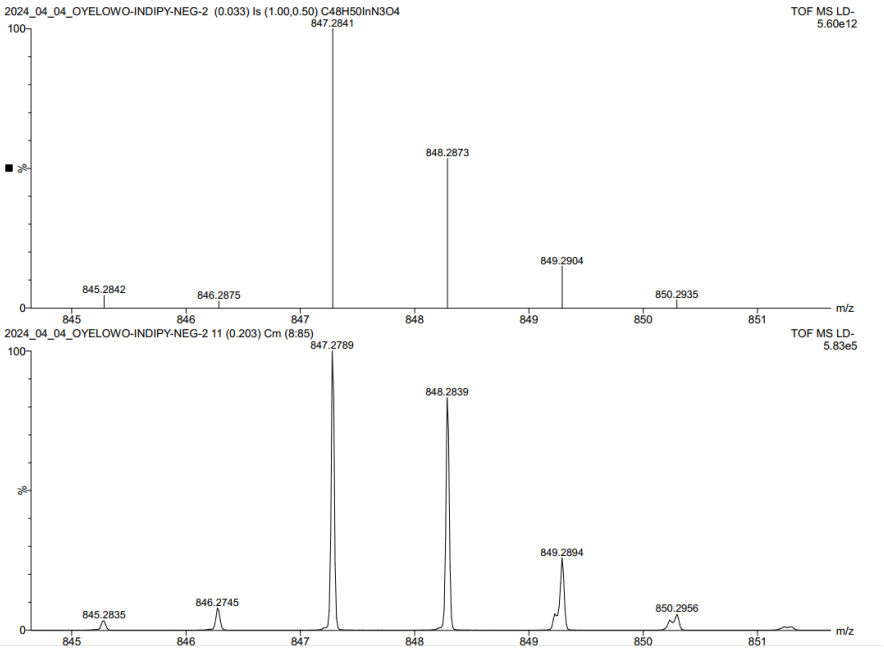


Figure 3.42: Mass spectrum of compound of compound **3.5d.**

Table 3.5a. Major TDDFT-Predicted Excited States of **3.4a.**

Excited State	*Wavelength (nm)*	*Energy (cm^{-1})*	*Oscillator Strength, f*	*% Contributions*
1	733	13636	0.6939	H→L (97%)
2	626	16042	0.4833	H-1→L (100%)
8	387	25819	0.1323	H-7→L (91%), H→L+1 (5%)
12	335	29878	0.7961	H→L+1 (78%), H-9→L (9%) H-7→L (6%)
17	299	33469	0.3074	H-2→L+1 (83%), H→L+3 (15%)
33	265	37804	0.2662	H-3→L+2 (44%), H-2→L+3 (38%), H-4→L+1 (11%)

Table 3.5b. Major TDDFT-Predicted Excited States of **3.5a(CS)**

Excited State	*Wavelength (nm)*	*Energy (cm^{-1})*	*Oscillator Strength, f*	*% Contributions*
1	1251	7988	0.3426	H→L (99%)
6	733	13650	0.5609	H→L+1 (83%), H-5→L (10%), H-1→L (5%)
7	638	15662	0.2099	H-5→L (89%), H→L+1 (7%)
15	466	21459	0.1595	H-10→L (69%), H-5→L+1
16	449	22277	0.9332	(28%)
18	429	23308	0.1690	H-9→L (69%), H-11→L (21%)
21	376	26569	0.1881	H-11→L (73%), H-9→L(11%)
40	302	33100	0.2824	H-8→L+1 (89%), H-10→L+1 (9%)
48	283	35301	0.1076	H-1→L+2 (57%), H-23→L (13%), H-25→L (13%), H→L+3 (69%). H→L+5 (58%), H-2→L+2 (69%), H-28→L (7%)

Table 3.5c. Major TDDFT-Predicted Excited States of **3.5a(OS)**

Excited State	*Wavelength (nm)*	*Energy (cm^{-1})*	*Oscillator Strength, f*	*% Contributions*
2	1295	7722	0.2779	H(B)→L(B) (39%), H(A)→L(A) (39%), H-1(B)→L(B) (9%), H-1(A)→L(A) (9%)
7	833	12006	0.1015	H(B)→ L+1(B) (42%), H(A) → L+1(A) (42%), H-1(B) → L(B) (6%), H-1(A) → L(A) (6%)
13	683	14640	0.1339	H-1(B) → L+1(B) (36%), H-1(A) → L+1(A) (36%), H(B) → L+1(B) (11%), H(A) → L+1(A) (11%)
18	603	16582	0.1033	H-1(B)→ L+1(B) (45%), H-1(A)→ L+1(A) (45%)
24	513	19492	0.1677	H-8(A) → L(A) (22%), H-8(B) → L(B) (22%), H-2(A) → L+1(A) (10%), H-2(B) → L+1(B) (10%), H-9(A)→ LUMO(A) (7%), H-9(B) → L(B) (7%), H-10(B)→ L(B) (7%), H-10(A) → L(A) (7%)
28	492	20340	0.1560	H-8(B) → L(B) (23%), H-8(A) → L(A) (23%), H-9(B) → L(B) (20%), H-9(A) → L(A) (20%)
33	458	21823	0.4347	H-10(B) → L(B) (21%), H-10(A) → L(A) (21%), H-9(B) → L(B) (13%), H-9(A) → L(A) (13%), H-11(B) → L(B) (5%), H-11(A) → L(A) (5%)
48	368	27167	0.2105	H-8(B)→ L+1(B) (26%), H-8(A)→ L+1(A) (26%), H-10(B)→ L+1(B) (8%) H-10(A)→ L+1(A) (8%)
53	338	29613	0.1078	H(B)→ L+3(B) (9%), H(A)→ L+3(A) (7%),H(B)→L+4(B)(7%), H(A)→L+4(A) (7%), H-15(A)→ L(A) (5%), H-15(B)→ L(B) (5%), H-19(A)→ L(A) (5%), H-19(B)→ L(B) (5%)
83	302	33138	0.2413	H-1(A)→L+2(A)(19%), H-1(B)→L+2(B) (19%), H-1(A)→ L+3(A) (8%),H-1(B)→ L+3(B) (8%)

Table 3.5d. Major TDDFT-Predicted Excited States of **3.5a(TS)**

Excited State	*Wavelength (nm)*	*Energy (cm^{-1})*	*Oscillator Strength, f*	*% Contributions*
5	873	10281	0.3618	H(A)→L(A) (74%), H(B)→L(B) (17%), H(B)→L+2(B) (7%)
8	745	13429	0.2265	H-1(A)→ L(A) (89%)
15	615	16267	0.2468	H(B)→L+2(B) (41%), H-2(A)→L(A) (39%), H-8(B)→L(B) (13%)
19	532	18786	0.1014	H-4(B)→L+1(B) (76%), H-9(B)→L(B) (12%), H-3(A)→L(A) (5%)
20	530	18872	0.2697	H-9(B)→L(B) (76%), H-4(B)→L+1(B) (7%), H-7(B) →L(B) (7%)
30	450	22210	0.2734	H-8(B) →L+1(B) (88%)
48	356	28123	0.2080	H(A)→L+1(A) (29%), H(B)→L+3(B) (26%), H-9(B)→L+2(B) (14%), H-2(A) →L+1(A) (8%), H-11(A)→L(A) (6%)
50	351	28454	0.2429	H-9(B)→L+2(B) (24%), H(A)→L+3(A) (18%), H-12(B) →L(B) (13%), H-11(A) →L(A) (11%), H-18(B)→ L(B) (5%), H(A) → L+1(A) (5%)
60	330	30261	0.1836	H-18(B)→L(B) (34%), H(A)→L+3(A) (26%), H-14(B) →L(B) (6%)

Table 3.5e. Major TDDFT-Predicted Excited States of [**3.6a**]$^{-\cdot}$

Excited State	*Wavelength (nm)*	*Energy (cm^{-1})*	*Oscillator Strength, f*	*% Contributions*
3	1036	9651	0.4877	H(A) →L(A) (83%), H(B) →L(B) (13%)
8	722	13847	0.6508	H-1(A) →L(A) (67%), H(B) →L+1(A) (25%)
10	592	16902	0.1013	H-1(B) → L+1(B) (51%), H-2(A) →L (44%)
19	483	20712	0.2907	H-8(B) → L(B) (75%), H-4(B) →L+1(B) (16%)
35	385	25974	0.1828	H-11(A) →L(A) (26%), H(B) → L+3(B) (20%), H-10(B)→L+1(B) (13%), H(A) → L+3(A) (11%), H-9(A) → L(A) (7%), H-1(A) → L+2(A) (5%)
40	360	27765	0.2833	H-12(B) → L(B) (46%), H(A) → L+3(A) (25%), H(B) → L+3(B) (11%), H-10(B) → L+1(B) (10%)
43	352	28396	0.1026	H-12(B) → L(B) (39%), H-10(B)→ L+1(B) (37%), H-11(A) → L(A) (6%)
45	342	29280	0.1	H(A)→ L+3(A) (24%), H-10(B)→ L+1(B) (18%), H-11(A)→ L(A) (16%), H-1(B)→ L+2(B) (11%), H-12(B) →L(B) (9%), H(B) → L+3(B) (6%)
55	312	32039	0.1	H(B) → L+5(B) (22%), H-2(A) →L+1(A) (18%), H-5(A) → L+2(A)

Table 3.5f. Major TDDFT-Predicted Excited States of **[3.7a]$^{2-}$**

Excited State	*Wavelength (nm)*	*Energy (cm^{-1})*	*Oscillator Strength, f*	*% Contributions*
1	1083	9234	0.6303	H→L (99%)
2	782	12781	0.7231	H-1→L (100%)
5	581	17199	0.1487	H-4→L (97%)
18	342	29267	0.2440	H-11→L (75%), H→L+5 (13%),H-4→L+1 (11%)
87	235	42532	0.1009	H-5→L+4 (82%), H-8→L+3 (10%)

CHAPTER IV: SYNTHESIS, SPIN DELOCALIZATION, AND CHARGE TRANSPORT PROPERTIES OF PHENOL-SUBSTITUTED AZA-DIPYRROMETHENE COMPLEXES OF COBALT, NICKEL, COPPER, ZINC AND THEIR OXIDIZED FORMS

A version of this chapter was originally published by Morris Oyelowo, Lexi Knight, Wei-Yuan Chen, Towhidi Illius Jeaydi, Geneviève Sauvé, Christopher J. Ziegler,Victor N. Nemykin:

Oyelowo, M.; Knight, L.; Chen, W.; Jeaydi, T.I.; Sauvé, G.; Ziegler, C.J.; Nemykin, V.N. Synthesis, Spin Delocalization, and Charge Transport Properties of Phenol-Substituted Aza-Dipyrromethene Complexes of Co, Ni, Cu and Zn and their Oxidized Forms. *Inorg Chem.* **2026,**

https://doi.org/10.1021/acs.inorgchem.6c01376

In this research article, I was responsible for designing and synthesizing all compounds studied. I performed characterization including variable temperature NMR, SQUID magnetometry, electrochemistry, spectroelectrochemistry, and UV/Vis absorption. Towhidi Illius jeaydi carried out variable temperature EPR experiment. Lexi Knight was responsible for charge transport experiment, and she assisted in writing the charge transport session of the manuscript. Dr. Christopher Ziegler facilitated the variable temperature EPR and helped in proofreading the manuscript. Dr. Geneviève Sauvé facilitated the charge transport experiment, and she proofread the manuscript before publication. Dr. Viktor Nemykin helped with DFT and TDDFT calculations. He also facilitated editing of the manuscript.

4.1 Abstract

We report the synthesis and characterization of homoleptic Co(II), Ni(II), Cu(II), and Zn(II) complexes of a phenol-substituted aza-dipyrromethene ligand. The complexes adopt distorted tetrahedral geometries, display ligand-centered redox activity and

panchromatic absorption. Chemical and electrochemical oxidation of the ML_2 complexes generate quinone/bis(diradicaloid) species exhibiting strong near-infrared absorption and antiferromagnetically coupled ligand-centered spins in the Zn(II) complex. Charge-transport measurements reveal modest electron mobilities and unusually high hole mobilities ($\approx 10^{-3}$ cm^2 V^{-1} s^{-1}) for the quinone/bis(diradicaloid) complexes making them potential hole transport materials. DFT and TD-DFT calculations confirm ligand-dominated frontier orbitals with metal-dependent electronic modulation. These results highlight aza-dipyrromethene metal complexes as promising platforms for redox-active and charge-transport materials.

4.2 Introduction

The design of transition metal complexes supported by redox-active ligands has emerged as an important strategy for accessing molecular systems with rich electronic structures and multifunctional properties like high molar absorptivity and chemical stability at room temperature.[1–8] In particular, ligands capable of undergoing redox transformations expand the electronic landscape beyond that of the central metal, enabling applications in areas such as catalysis, molecular magnetism, semiconductors, and organic electronics.[5–7,9–21] Dipyrromethene and aza-dipyrromethene belong to a class of monoanionic bidentate ligands with absorption and emission spectra properties in the visible and near infrared region.[26,28–31] This class of compounds have been widely explored because of the ease of tuning their optical, electronic and structural properties through chelation to either BF_2^+ (BODIPY and aza-BODIPY), group 13 elements (ALDIPYs, GADIPYs and INDIPYs) and transition metals.[32–46] Their tunability allows

the incorporation of substituents that further tailor redox behavior and solubility, making them promising candidates for the development of functional coordination complexes.[26,30,40–42,47–64]

Incorporation of redox-active substituents, such as phenolic groups, onto the dipyrromethene and aza-dipyrromethene core can provide additional opportunities to engineer electronic communication between ligand and metal centers. Phenolic substituents not only enhance the charge-transfer capacity of the ligand but can also stabilize radical states upon oxidation or deprotonation. Similar design principles have been extensively explored in porphyrinoid systems, where phenol- and quinone-derived substituents are known to promote ligand-centered radical formation and access quinonoidal electronic structures.[66-69] In such systems, the interplay between redox-active phenolic substituents and coordinated metal ions provides a powerful means of modulating spin delocalization, magnetic exchange coupling, and diradical character, with the identity of the metal often dictating the balance between ligand- and metal-centered redox processes.[69-70] These studies established an important conceptual framework for controlling open-shell electronic structures through metal–ligand cooperativity in conjugated tetrapyrrolic scaffolds,[69-70] motivating the extension of similar strategies to dipyrromethene and aza-dipyrromethene architectures. In parallel, the first-row transition metals such as Co(II), Ni(II), Cu(II), and Zn(II) offer rich coordination chemistry and accessible redox states that can be complementary to those of their ligands.[9,26,30,53,65]

Beyond redox tunability, an important design objective in functional chromophores is the achievement of panchromatic absorption, namely the ability to harvest light across a broad spectral window spanning the visible and near-infrared regions.[71] Porphyrinoid architectures have long served as important systems for panchromatic light harvesting owing to their intense and complementary absorption bands, which enable efficient photon capture and energy transfer across a wide spectral range.[71-73] These principles have inspired the development of subphthalocyanines, dipyrromethene- and aza-dipyrromethene-based chromophores, including BODIPY and aza-BODIPY derivatives, whose modular frameworks allow systematic tuning of absorption profiles through π-extension, donor–acceptor substitution, and metal coordination.[73-76] In particular, aza-dipyrromethene and other porphyrinoid systems are attractive because their low-energy electronic transitions can be readily shifted into the near-infrared region while maintaining high molar absorptivities, making them promising platforms for light-harvesting, photoredox, and optoelectronic applications.[77-82] Incorporating redox-active aza-dipyrromethene ligands into transition metal complexes provides an attractive avenue toward tuning both electronic structure and charge transport. Moreover, the ability to access radicaloid and multianionic states by controlled redox transformations opens further possibilities for coupling photophysical, electrochemical, and magnetic properties within a single molecular platform.

In this work, we report the synthesis and characterization of novel homoleptic complexes of Co(II), Ni(II), Cu(II), and Zn(II) supported by aza-dipyrromethene ligands bearing phenolic substituents at the 1,7-positions (**4.1a – 4.1d**). Chemical oxidation of the

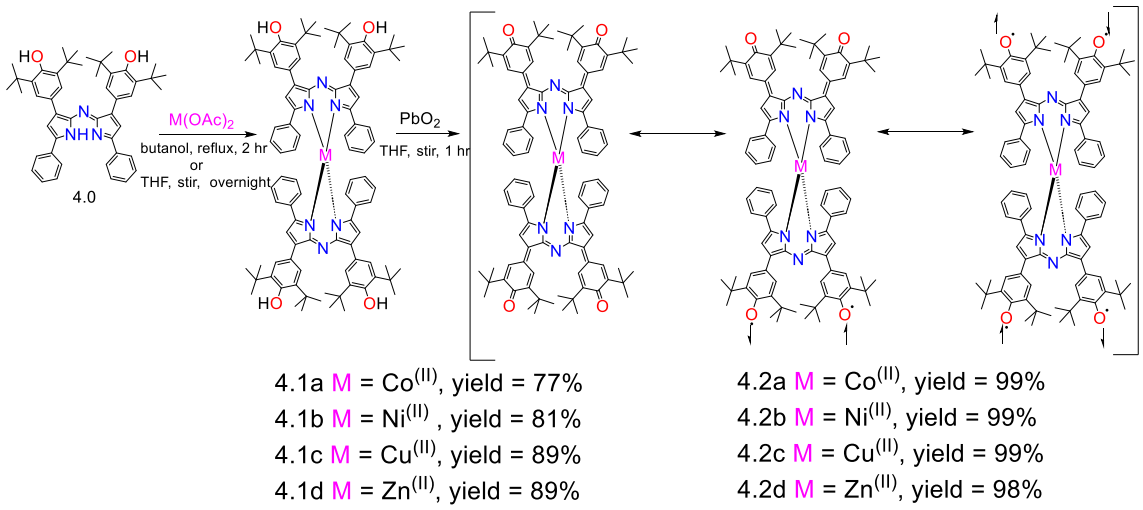
parent complexes (**4.1a – 4.1d**) yields quinone derivatives (**4.2a – 4.2d**), which exist in resonance with Kekulé-type bis(diradicaloid) forms, whose charge-transport properties were investigated to evaluate their potential as hole-transport materials and multifunctional spintronic components. The incorporation of redox-active phenolic substituents and transition-metal centers provides a strategy for modulating electronic communication and extending absorption across the visible and near-infrared regions, contributing to panchromatic light-harvesting behavior. The complexes adopt distorted tetrahedral geometries and display accessible redox activity arising primarily from the ligand centers. Additionally, electrochemical and spectroelectrochemical measurements were employed to map their redox profiles, while deprotonation with tetrabutylammonium fluoride allowed access to tetra-anionic species that undergo further oxidation under spectroelectrochemical conditions to generate quinone/bis(diradicaloid) resonance forms. Finally, DFT and TD-DFT calculations provide insight into the electronic structures and excited-state properties of complexes (**4.1a – 4.1d**).

4.3 Results and Discussion

4.3.1 Synthesis of Homoleptic Complexes of Co(II), Ni(II), Cu(II), and Zn(II) Supported by Aza-Dipyrromethene Ligand Bearing Phenolic Substituents at the 1,7-positions (4.1a – 4.1d) and their Oxidized Forms (4.2a – 4.2d).

Compound **4.0** (Z)-2,6-di-tert-butyl-4-(2-((3-(3,5-di-tert-butyl-4-hydroxyphenyl)-5-phenyl-1H-pyrrol-2-yl)imino)-5-phenyl-2H-pyrrol-3-yl)phenol was synthesized according to our previous work.[64] Refluxing compound **4.0** with $Co(OAc)_2.4H_2O$ and

$Ni(OAc)_2.4H_2O$ in butanol yielded homoleptic metal complexes **4.1a – 4.1b** in good yield as shown in Scheme 1.



Scheme 4.1. Synthetic scheme yielding homoleptic complexes **4.1a – 4.1d** and **4.2a – 4.2d.**

In each case, after cooling, the butanol solvent was evaporated, and the reaction mixture was washed with CH_2Cl_2 followed by filtration yielding complexes **4.1a – 4.1b** as brown powders in high yields. For the copper and zinc complexes **4.1c – 4.1d**, the reaction was changed from refluxing in butanol to stirring compound **4.0** with anhydrous $Cu(OAc)_2$ and $Zn(OAc)_2$ at room temperature in tetrahydrofuran (THF) to yield **4.1c – 4.1d** in excellent yield as blueish-brown solid. Complexes **4.1a – 4.1d** are insoluble in most organic solvents except THF. Upon dissolution in THF for few hours, complexes **4.1a – 4.1d** underwent deep blue coloration. Complexes **4.2a – 4.2d** were obtained in good yield (~100 %) by chemical oxidation of **4.1a – 4.1d** in THF using excess lead(IV) oxide. The identity of complexes **4.1a**, **4.1b**, **4.1d**, **4.2b** and **4.2d** were confirmed by

NMR spectroscopy. Mass spectrometry confirms 1:2 stoichiometry of ML_2 (M = Co, Ni, Cu, and Zn) for all complexes.

Closed-shell Zn(II) complex **4.1d** and its oxidized open-shell counterpart **4.2d** gave well resolved ^{1}H spectra ranging from 1 – 10 ppm. Cobalt and nickel complexes **4.1a – 4.1b** displayed considerable spectra shifts both negatively and positively ranging between about ≈ -4 – 60 ppm at room temperature (see appendix for Figures 4.22 – 4.23). The ^{1}H NMR spectra of Co(II) and Ni(II) complexes **4.1a – 4.1b** indicate that they are paramagnetic and adopt pseudo-tetrahedral geometries. Such behavior, while contrary to the square-planar geometry commonly expected for four-coordinate Ni(II) complexes, has been reported previously for Ni(II) systems bearing sterically demanding ligands like aza-dipyrromethene, where tetrahedral or distorted tetrahedral geometries are favored and result in paramagnetic ground states. [30] In general, ^{1}H NMR spectra of **4.1a** and **4.1b** correlate well with the spectra of previously reported paramagnetic ML_2 (M = Co or Ni; L = azadipyrromethene) compounds.[30]

4.3.2 Absorption and Emission Studies

UV/Vis/NIR studies for complexes **4.1a – 4.1d** and **4.2a – 4.2d** were performed in tetrahydrofuran (THF) solutions. Optical properties of all studied complexes are summarized in Table 4.1. The absorption spectra of complexes **4.1a – 4.1d** are all similar with distinct redshifted shoulder of the maximum absorption band (λ_{max}). The spectrum of copper complex **4.1c** was blue shifted by 17 nm compared to that of the zinc complex **4.1d**. The extinction coefficients of **4.1a – 4.1d** are all close to 1×10^5 $M^{-1}cm^{-1}$, showing strong panchromatic absorption properties of all complexes under study. Upon chemical

oxidation of **4.1a – 4.1d** with excess lead (IV) oxide in THF, new red-shifted NIR absorption bands at ~830-900 nm were observed for the complexes **4.2a – 4.2d** (Figure 4.1) confirming their panchromatic properties. Complexes **4.1a – 4.1d** and their quinone/bis(diradicaloid) counterparts **4.2a – 4.2d** were non-fluorescent in THF and other solvent explored.

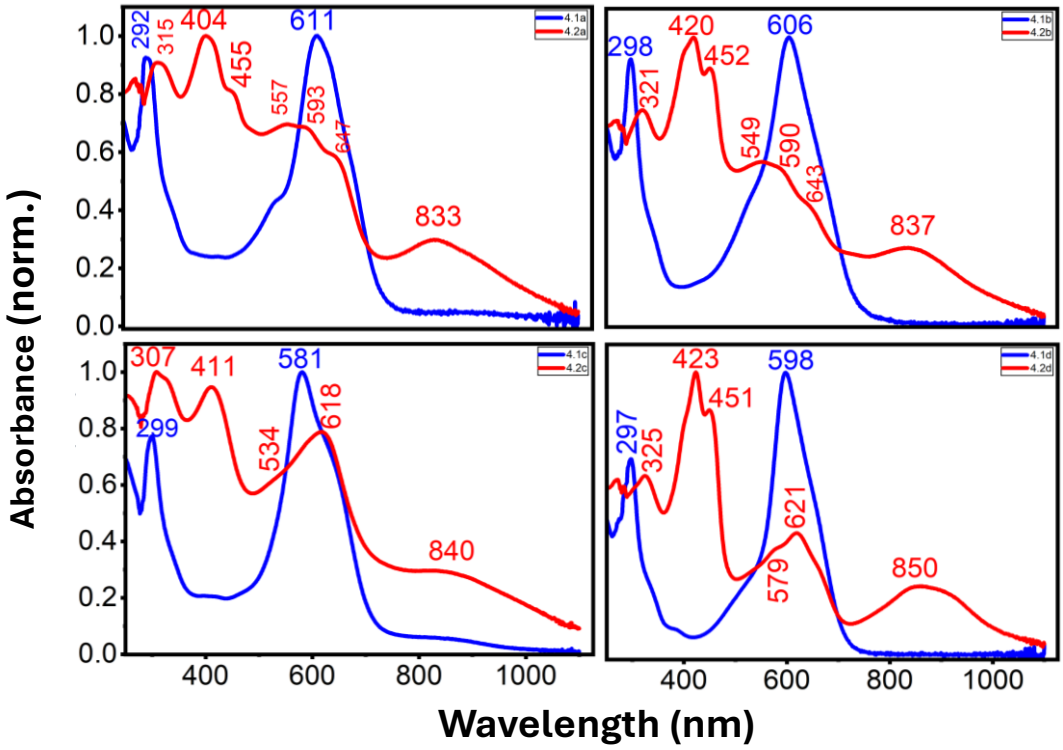


Figure 4.1: Normalized UV/vis/NIR absorption spectra (THF) of complexes **4.1a – 4.1d** (blue solid line), as well as the absorption spectra (THF) of bis(diradicaloid) complexes **4.2a – 4.2d** (red solid line).

Table 4.1: Summary of UV-Vis spectra of **4.1a – 4.1d** and **4.2a – 4.2d** in THF (sh = shoulder).

Compound	λ_{onset} (nm)	λ_{max}, nm ε (× 10^3 $M^{-1}cm^{-1}$)	E_{opt} (ev)
4.0		595(44)	
4.1a	789	667(sh), 611(136), 292(125)	1.57
4.1b	800	665(sh), 606(96), 298(82)	1.55
4.1c	786	634(sh), 581(68), 299(53)	1.58
4.1d	776	657(sh), 598(100), 297(69)	1.60
4.2a	1094	315(38), 404(42), 455(34), 557(29), 594(29), 647(25), 832(12)	1.13
4.2b	1091	321(38), 420(51), 452(45), 549(29), 590(28), 643(21), 837(14)	1.14
4.2c	1085	307(49), 411(46), 534(31), 618(39), 840(14)	1.14
4.2d	1083	325(36), 423(57), 451(49), 579(21), 621(24), 850(14)	1.14

4.3.3 Electrochemical and Spectroelectrochemical Studies

The electrochemical properties of the free ligand **4.0** and its homoleptic M(II) complexes **4.2a – 4.2d**, (where M = Co, Ni, Cu, and Zn) were investigated in DCM solution by cyclic voltammetry (CV) and differential pulse voltammetry (DPV) to probe the electron-donating and electron-accepting capabilities of the aza-dipyrromethene core, compound **4.0** and complexes **4.2a – 4.2d** (Figure 4.2 and Table 4.2). The redox

characteristics of aza-dipyrromethene complexes are typically dominated by the ligand's π-conjugated system.[26] All complexes studied exhibited multiple oxidation and reduction processes, supporting the conclusion that the redox activity is primarily ligand centered. The overall electrochemical window (the difference between the first oxidation and first reduction potential) indicates strong conjugation across the aza-dipyrromethene framework, which is largely preserved upon metal coordination.

Complexes **4.2a – 4.2d** display multiple oxidation waves, occurring at potentials positive of the Fc/Fc^+ couple, consistent with oxidation of the ligand core via stable quinone/radical intermediates. A key observation is the shift of the first oxidation potential, Ox_1 upon complexation compared to the free ligand **4.0**. All complexes show a negative shift in Ox_1 (easier to oxidize), indicating that the coordination of the metal ion destabilizes the ligand's highest occupied molecular orbital (HOMO) energy level. This destabilization follows the trend: **4.2a** < **4.2c** < **4.2b** < **4.2d**, with the Co(II) complex (**4.1a**) showing the largest negative shift (ΔE = 0.3 V). This trend reflects the relative effective nuclear charge and the extent of d-orbital mixing with the ligand's system, consistent with established literature for related aza-dipyrromethene complexes.[26,53] That being said, the first oxidation potentials in **4.2a – 4.2d** are not that different. The reduction potentials, which primarily involve the ligand's lowest unoccupied molecular orbital LUMO, also show consistency across the series. The first reduction potential, Red_1 occurs consistently in the narrow range of -0.81 to -0.89V for all complexes **4.2a – 4.2d**, which is almost identical to that of the free ligand **4.0** (-0.81V). This minimal variation confirms that the LUMO and subsequent unoccupied orbitals of the aza-

dipyrromethene core are largely unperturbed by the central metal ion, strongly supporting the assignment of these processes as π-system ligand-centered reductions. The presence of up to four distinct reduction waves in complexes **4.2a – 4.2d**, especially the highly negative ones, underscores the electron-accepting nature of the aza-dipyrromethene chromophore.

Electrochemical oxidation (0.7 V to 1 V) of complexes **4.1a, 4.1b,** and **4.1d** in spectroelectrochemistry setup in THF solution led to formation of complexes **4.2a**, **4.2b**, and **4.2d** with the UV-vis-NIR spectra similar in shape and properties to those obtained from chemical oxidation using lead (IV) oxide (Figure 4.3). The spectra changes observed in the spectroelectrochemical transformation of complexes **4.1a**, **4.1b**, and **4.1d** to complexes **4.2a**, **4.2b**, and **4.2d** confirm that the redox activities of these complexes are primarily ligand centered. Interestingly, unlike the other compounds complex **4.1c** slowly oxidizes to **4.2c** in THF solution.

Table 4.2. Electrochemical Complexes **4.2a – 4.2d**. Potentials are in volts vs Fc/Fc^{+} for dry DCM/0.1 M TBAP solutions.

Compound	M	Ox_3	Ox_2	Ox_1	Red_1	Red_2	Red_3	Red_4	E_{echem} (ev)
1	H		0.89	0.62	-0.81				
4.2a	Co(II)	0.94	0.73	0.32	-0.88	-1.00	-1.29	-1.47	1.03
4.2b	Ni(II)	0.99	0.76	0.35	-0.81	-0.95	-1.13	-1.22	1.01
4.2c	Cu(II)	1.16	0.78	0.33	-0.89	-1.10	-1.34	-1.63	1.01
4.2d	Zn(II)	1.07	0.69	0.44	-0.89	-1.02	-1.22	-1.35	0.99

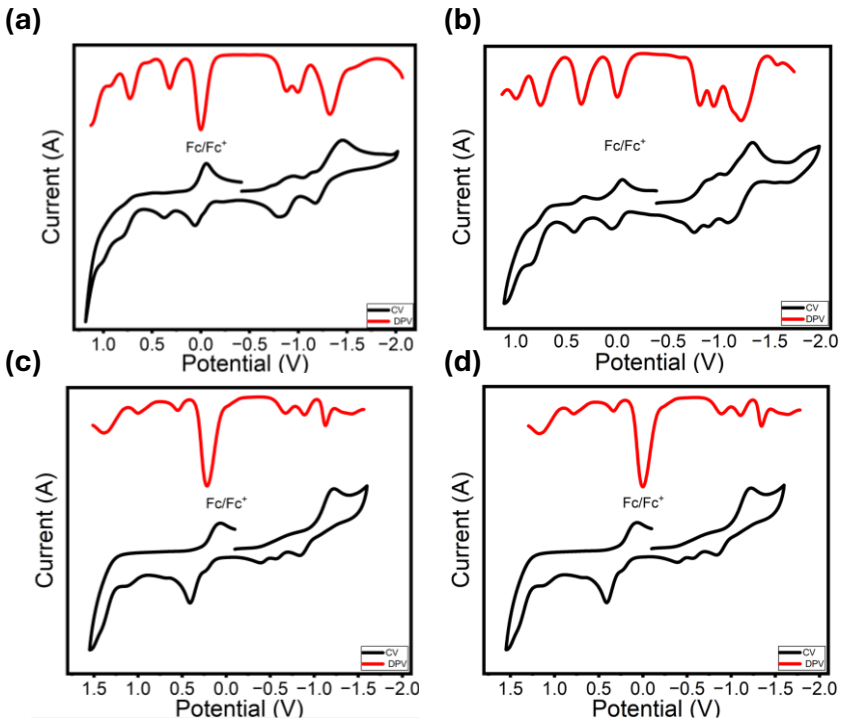


Figure 4.2: Cyclic voltammogram and differential pulse voltammogram of (a) Co(II) complex **4.2a,** (b) Ni(II) complex **4.2b,** (c) Cu(II) complex **4.2c,** (d) Zn(II) complex **4.2d** in DCM / 0.1 M TBAP as supporting electrolyte; scan rate of 50 mV/s for CV.

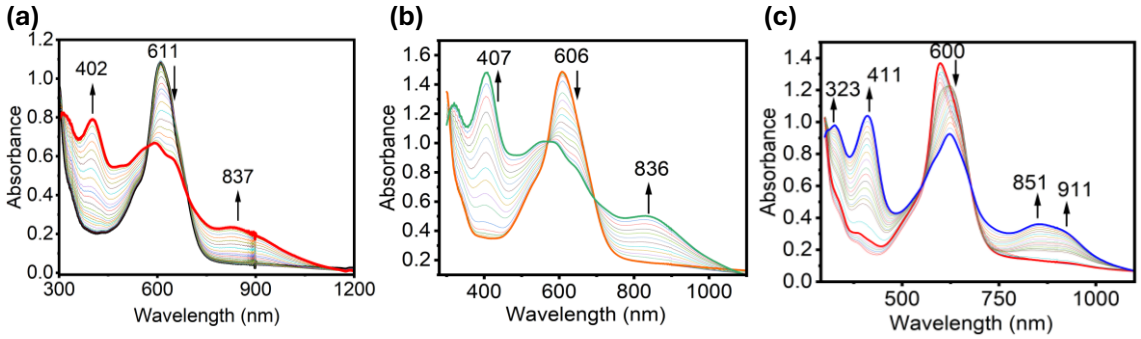
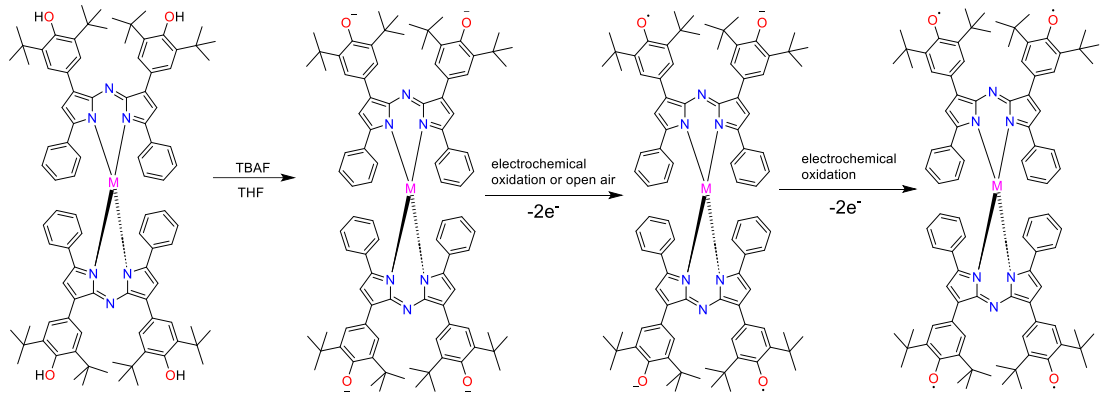


Figure 4.3: UV-vis-NIR absorption spectroscopic changes of **4.1a** to **4.2a** (a), **4.1b** to **4.2b** (b), **4.1d** to **4.2d** THF/0.3 M (NBu_4)[PF_6]) at room temperature upon oxidation.

Deprotonation of the **4.1a – 4.1d** to obtain tetra-anions [**4.4a**, **4.4b**, and **4.4d**]$^{4-}$ was conducted with tetra-*n*-butylammonium fluoride (TBAF) in THF solution. During the incremental addition of TBAF in THF to the solutions of complexes **4.1a**, **4.1b**, and **4.1d** in THF, spectral changes were observed with gradual decrease in the intensity λ_{max} of **4.1a**, **4.1b**, and **4.1d** and simultaneous rise of red shifted peaks at ~950 nm indicating formation of tetra-anions [**4.4a**, **4.4b**, and **4.4d**]$^{4-}$. Upon further addition of TBAF solution in open air, we observed formation of mixed valent species [**4.3a**, **4.3b**, and **4.3d**]$^{2.-}$ due to autooxidation by open air (Figures 4.4). We could not isolate tatra-anions of complex **4.1c** due to fast autooxidation in open air, so we decided to work it mixed valence species **[4.4c]**$^{2-.}$.

Spectroelectrochemical oxidation of tetra-anions [**4.4a**, **4.4b**, and **4.4d]**$^{4-}$ and mixed valent **[4.4c]**$^{2-.}$ were studied in THF solution. The first spectroelectrochemical/open air oxidation process of [**4.4a**, **4.4b**, and **4.4d**]$^{4-}$ led to an increase in the intensity of the NIR band observed at about ~1110 nm and ~1600 nm. The appearance of these red shifted bands at about ~1110 nm indicates the formation of mixed valent radical anion species [**4.3a**, **4.3b**, and **4.3d**]$^{2.-}$ and the one at ~1600 nm indicates the intervalence charge transfer (IVCT) process indicating delocalization of charged radical-anion species over the two aza-DIPY units. Also, we've seen similar IVCT band in our previous work on aza-BODIPY diradicaloids.[64] As the potential was increased, the NIR bands attributed to the mixed-valent radical anion [**4.3a – 4.3d**]$^{2.-}$ gradually decreased in intensity until they disappeared completely. Concurrently, new absorption bands appeared at approximately ~840 nm, whose spectral shapes and

vibronic progressions closely resemble those observed for **4.2a – 4.2d** from chemical oxidation of **4.1a – 4.1d** with lead (IV) oxide. (Figure 4.5).



Scheme 4.2. Formation of dianions (**4.4a – 4.4d**)$^{4-}$, mixed-valence radical anions [**4.3a – 4.3d**]$^{2-\bullet}$, and bis(diradicals) **4.2a – 4.2d**.

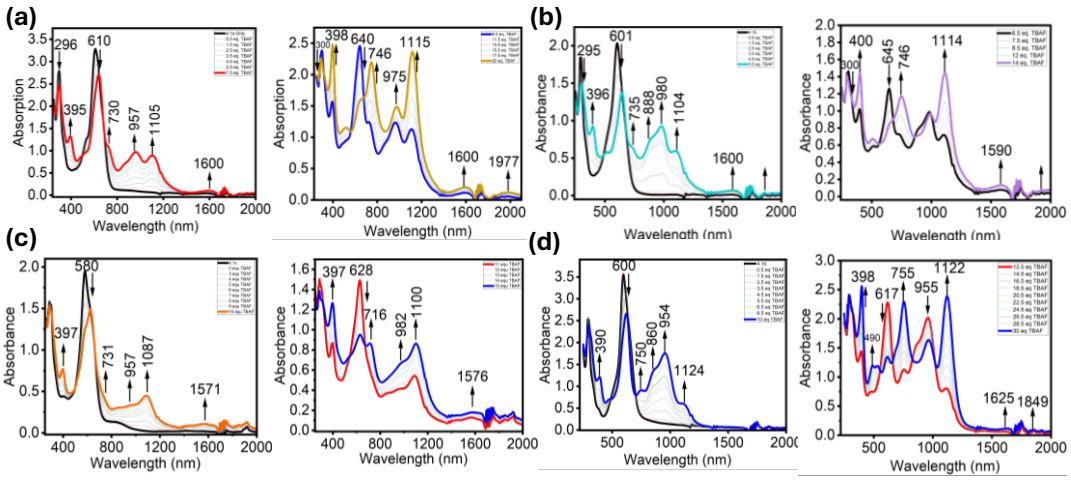


Figure 4.4: UV/vis/NIR absorption spectral changes during deprotonation and dehydrogenation of (a) Co(II) **4.1a**, (b) Ni(II) **4.1b**, (c) Cu(II) **4.1c**, and (d) Zn(II) **4.1d** in THF upon titration with TBAF (NBu_4)[F] solution.

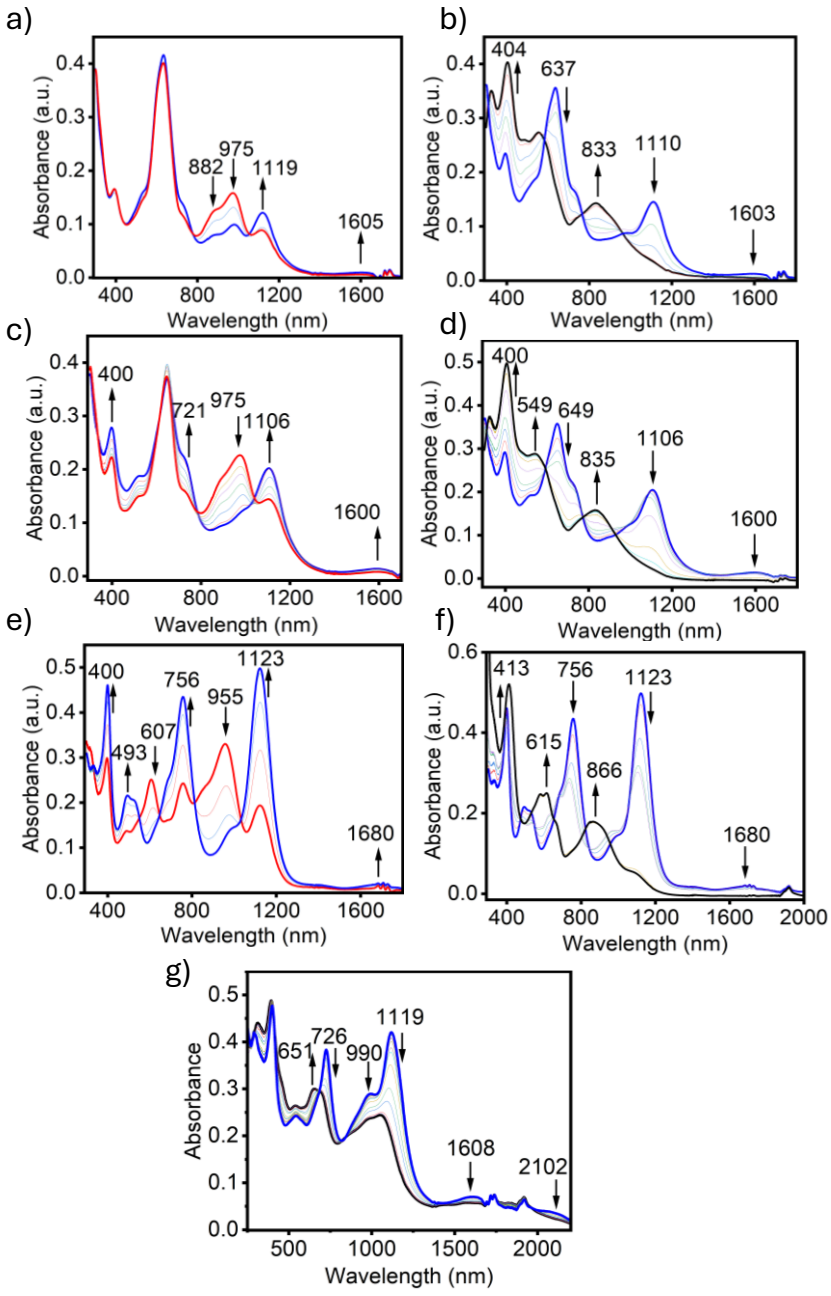


Figure 4.5: UV-vis-NIR absorption spectroscopic changes of **[4.4a]**$^{4-}$ to **[4.3a]**$^{2-\cdot}$ (a), **[4.3a]**$^{2-\cdot}$ to **4.2a** (b), **[4.4b]**$^{4-}$ to **[4.3b]**$^{2-\cdot}$ (c), **[4.3b]**$^{2-\cdot}$ to **4.2b** (d), **[4.4d]**$^{4-}$ to **[4.3d]**$^{2-\cdot}$ (e), and **[4.4d]**$^{2-\cdot}$ to **4.2d** (f), **[4.4c]**$^{2-\cdot}$ to **4.2c** (g). THF/0.3 M ($(NBu_4)[PF_6]$), room temperature, upon electrochemical oxidation in a spectroelectrochemical setup. Arrows indicate spectroscopic changes with increasing positive potential.

4.3.4 Magnetic Studies

4.3.4.1 Magnetic Studies of Co(II) complex 4.1a

The Co(II) d^7 complex **4.1a (**S = 3/2**)** in solid state at 4 K displays X-band EPR signals at **g** = (6.89, 1.37, 1.08) from the lowest Ms = ±3/2 doublet (Figure 8). At higher temperatures, a signal at g = 5.0 grows in intensity, from the excited Ms = ±1/2 doublet, indicative of a negative axial zero-field splitting (D < 0), as was previously observed for pseudo-tetrahedral Co(II) complexes.[30,83] The spectra are plotted as intensity times temperature to show the intensity gain of the Ms = ±1/2 signal relative to the Ms = ±3/2 signal. For higher temperatures, all signals are broader (Figure 4.6).

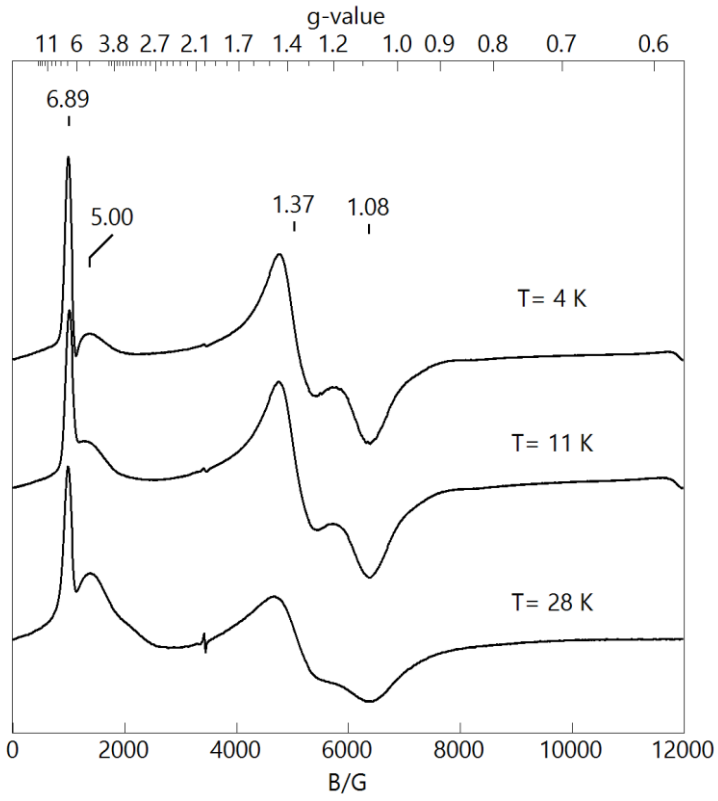


Figure 4.6: Variable temperature EPR spectra of complex **4.1a** in solid state.

4.3.4.1 Magnetic Studies of Ni(II) complex 4.2b

Despite its paramagnetic nature, the Ni(II) d^8 complex **4.1b** remains EPR silent at X-band over the temperature range 140–300 K. This observation is similar for what has been reported for other Ni(II) aza-dipyrromethene complexes and indicative of its triplet state.[30] Ni(II) complex **4.2b** gave an isotropic EPR signal at room temperature indicative of ligand centered organic radicals. Variable temperature EPR intensity of complex **4.2b** decreases with decreasing temperature. The product of the integrated EPR intensity and temperature (IT) increases with temperature (T). The singlet–triplet energy gaps ($\Delta E_{S\text{-}T}$) was extracted by fitting the data using the Bleaney–Bowers equation, yielding a value of -1.69 kcal/mol indicative of antiferromagnetic coupling between the ligand-centered unpaired electrons (Figure 4.7).

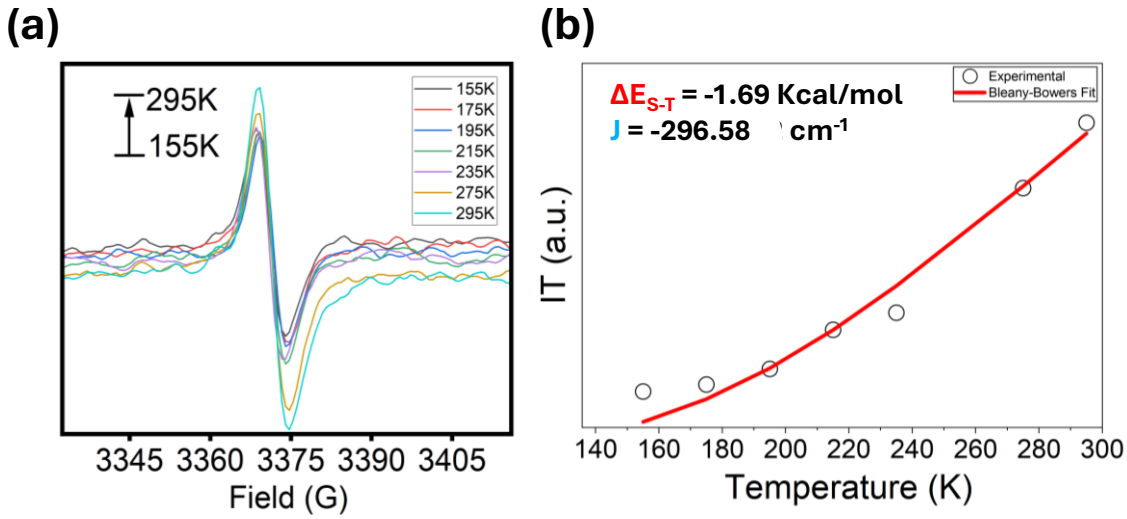


Figure 4.7: (a) Variable temperature EPR spectra of complex **4.2b** in solid state. (b) IT versus temperature plot of complex **4.2b** in solid state.

4.3.4.3 Magnetic Studies of Cu(II) complexes 4.1c and 4.2c

The $\chi_M T$ curves of complex **4.2c** is presented in Figure 4.8. At 300 K, the $\chi_M T$ is at 0.4 cm^3Kmol^{-1} close to the value expected for mononuclear Cu(II) center. At low temperature of 2 K, $\chi_M T$ is 0.2 cm^3Kmol^{-1} indicating the presence of other paramagnetic contributions from ligand centered bis (diradical) species. In THF solution, EPR spectra of both Cu(II) d^9 complexes **4.1c** and **4.2c** are axial at X-band and display two components (Figures 4.9 and 4.10). For complex **4.1c**, $g_\perp = 2.065$ for both major and minor components, while $g_\parallel = 2.24$ with A = 111 G for the major component, and $g_\parallel$ = 2.20 with A = 110 G for the minor component. In the case of complex **4.2c,** $g_\perp = 2.05$ for both components, while $g_\parallel = 2.17$ with A = 105 G for the major component, and $g_\parallel = 2.20$ with A = 103 G for the minor component. Powder EPR spectra of complex **4.1c** and **4.2c** appear axial at X-band: complex **2c** ($g_\perp = 2.05$, $g_\parallel = 2.20$ with A = 103 G); complex **3c** ($g_\perp = 2.06$ with unresolved $g_\parallel$) see Figures 4.9 – 4.10.

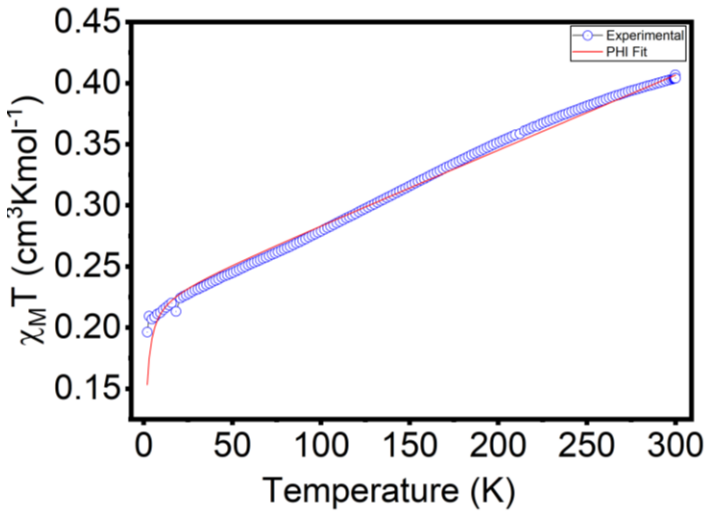


Figure 4.8: $\chi_M T$ versus temperature plot of complex **4.2c** at 1000 Oe.

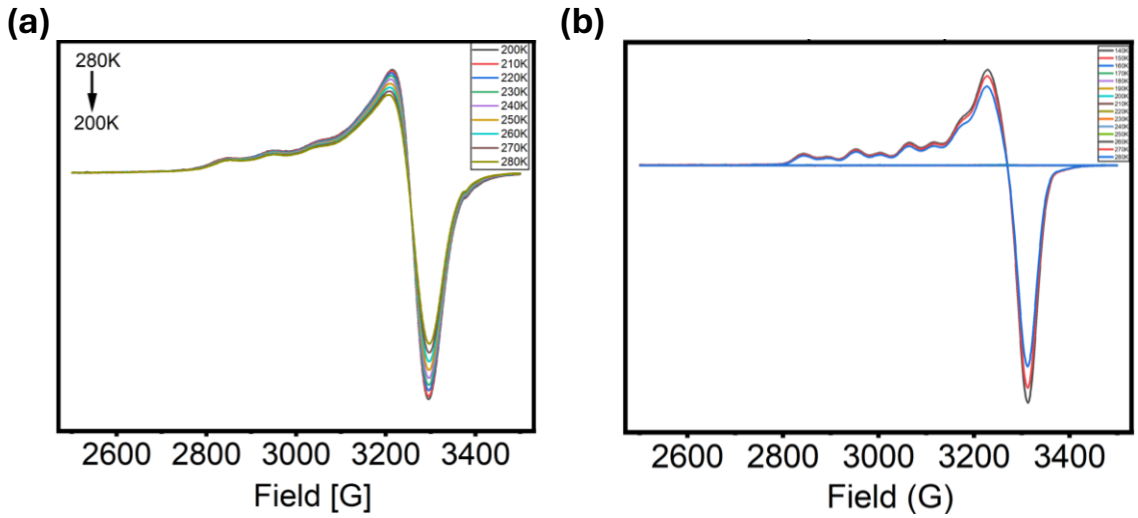


Figure 4.9: (a) Variable temperature EPR of complex **4.1c** in solid state at X-band. (b) Variable temperature EPR of complex **4.1c** in THF at X-band.

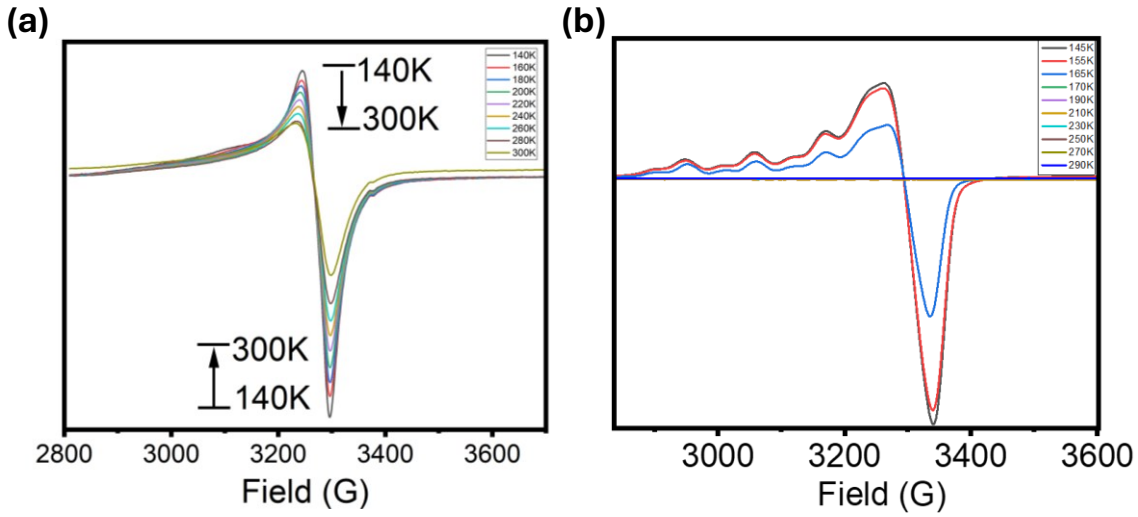


Figure 4.10: (a) Variable temperature EPR of complex **4.2c** in solid state at X-band. (b) Variable temperature EPR of complex **4.2c** in THF at X-band.

4.3.4.1 Magnetic Studies of Zn(II) Complex 4.2d

Closed-shell Zn(II) d^{10} metal functions primarily as structural linker that aids chelation and inter-ligand π-π interactions in both complexes **4.1d** and **4.2d**. We decide to explore the magnetic properties of complex **4.2d** knowing fully well that we are dealing with radicals centered on ligands only. The ground-state magnetic properties and electronic structures of complex **4.2d** were studied by variable temperature SQUID magnetometry and electron paramagnetic resonance. The temperature dependence of the product of magnetic susceptibility and temperature ($\chi_M T$) was measured on a powdered sample of complex **4.2d** at two different fields of 1000 Oe and 1 T to understand the magnetic properties of this complex. The plot of $\chi_M T$ versus temperature showed a linear increase from 0 to about 0.4 $cm^3 \cdot K \cdot mol^{-1}$ in both magnetic fields which is indicative of antiferromagnetic coupling between these ligands centered unpaired electrons (Figure 4.11). The Bleaney-Bowers fitting of the SQUID magnetic data at 1000 Oe and 1 Tesla from 2 K to 320 K reveals the singlet-triplet energy gap to be -0.34 Kcal/mol and -0.37 Kcal/mols (Figure 4.11) confirming its singlet ground state and thermally accessible triplet excited state. An isotropic EPR signals with g values of ~2.002 were seen for complex **4.2d** powder at room temperature, so we decided to carry out variable temperature EPR experiment on the powder of **4.2d**. Intensity of EPR signal decreased as temperature decreased from room temperature to 140K (Figure 4.12). The product of the integrated EPR intensity and temperature (IT) increases linearly with temperature (T). The singlet–triplet energy gaps (ΔE_{S-T}) was extracted by fitting the data using the Bleaney–Bowers equation, yielding a value of **-**0.33 kcal/mol very similar to variable

temperature SQUID data indicative of antiferromagnetic coupling between the unpaired electrons and ligand centered driven spin delocalization.

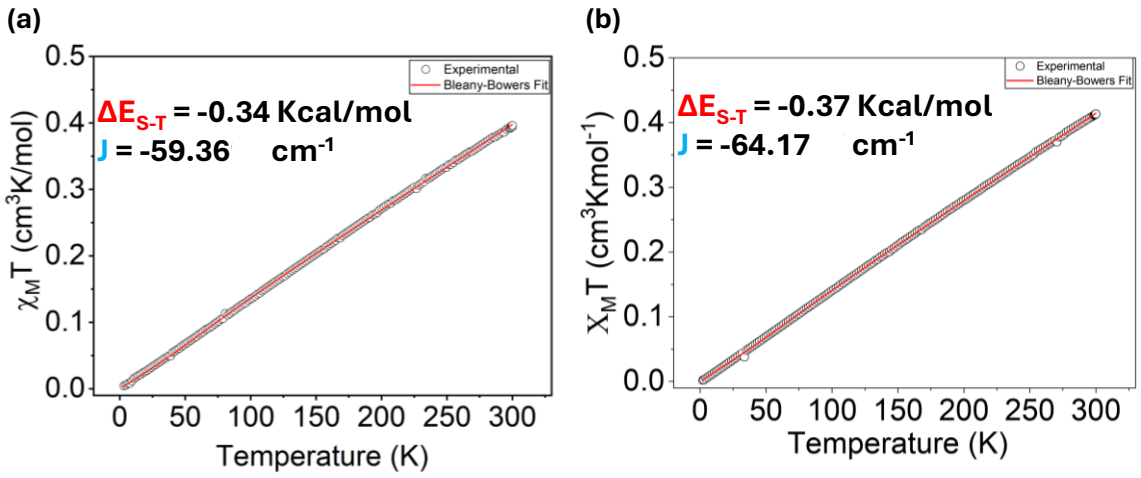


Figure 4.11: (a) χ_MT versus temperature plot of complex **4.2d** at 1000 Oe (b) χ_MT versus temperature plot of complex **4.2d** at 1 Tesla.

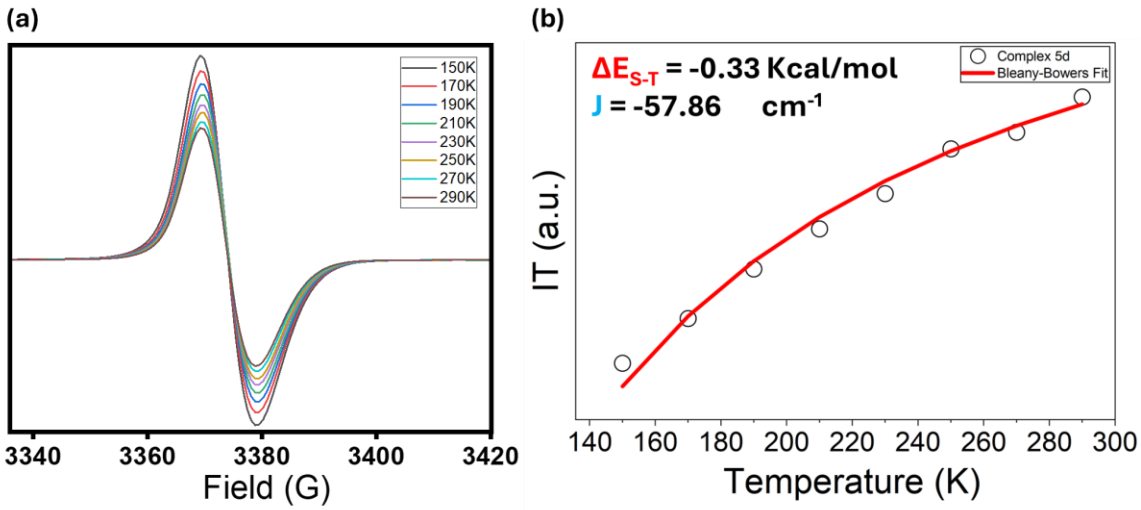


Figure 4.12: (a) Variable temperature EPR spectra of complex **4.2d** in solid state, (b) Bleany-Bowers fitting of IT vs Temperature curve of VT EPR of **4.2d** in solid state.

4.3.5 X-Ray Crystallographic Studies

Single crystals of the Zn(II) and Ni(II) complexes, **4.1d** and **4.1b**, respectively, were successfully obtained by slow diffusion of cyclohexane to THF solution of respective complexes. The structures of complexes **4.1d** and **4.1b** were determined by X-ray diffraction analysis, and are shown in Figure 4.13. Both complexes crystallize in the orthorhombic crystal system with the space group P_{nna}. The complexes exhibit the classic bis(aza-dipyrromethene) stoichiometry, M(aza-dipyrromethene)$_2$, where the central metal ion is coordinated by two bidentate aza-dipyrromethene ligands, resulting in a four-coordinate environment around the metal centers. Both the Zn(II) and Ni(II) complexes **4.1d** and **4.1b** adopt a distorted tetrahedral geometry, a common structural motif for homoleptic bis (aza-dipyrromethene) complexes,[30,50] particularly when the ligands are sterically bulky. A clear distinction is observed in the average M–N bond lengths: the Ni(II) complex **4.1b** exhibits significantly shorter Ni–N3 bond lengths compared to the Zn–N3 bonds in complex **4.1d** (~1.92 Å *vs* ~2.00 Å) see Table 4.3. This difference is primarily attributed to the smaller ionic radius of four-coordinate Ni(II) compared to Zn(II), and the stronger covalent character of the Ni–N bond. The shorter bond length in the Ni(II) complex results in greater structural rigidity and a slightly more constrained tetrahedral environment, consistent with the observed smaller N3–Ni1–N3 angle (~93.8°) compared to the Zn(II) analogue (~96.3°) see Tables 4.3 and 4.4. The Zn(II) complex **4.1d** has bond angles spanning ~95.2° to ~106.9°, while the Ni(II) complex **4.1b** exhibits a similar angular range from ~93.8° to ~106.1° (Table 4.4). These angles deviate significantly from the ideal 109.5° of a perfect tetrahedron due to the constraint imposed

by the small bite angle of the aza-dipyrromethene ligands. Specifically, the bond angles between the two coordinating nitrogen atoms within the same ligand (N1–M1–N1 and N3–M1–N3) are compressed to (~95°), while the angles between nitrogen atoms from different ligands (N1–M1–N3) are expanded (~106°) to compensate (Table 4.3).

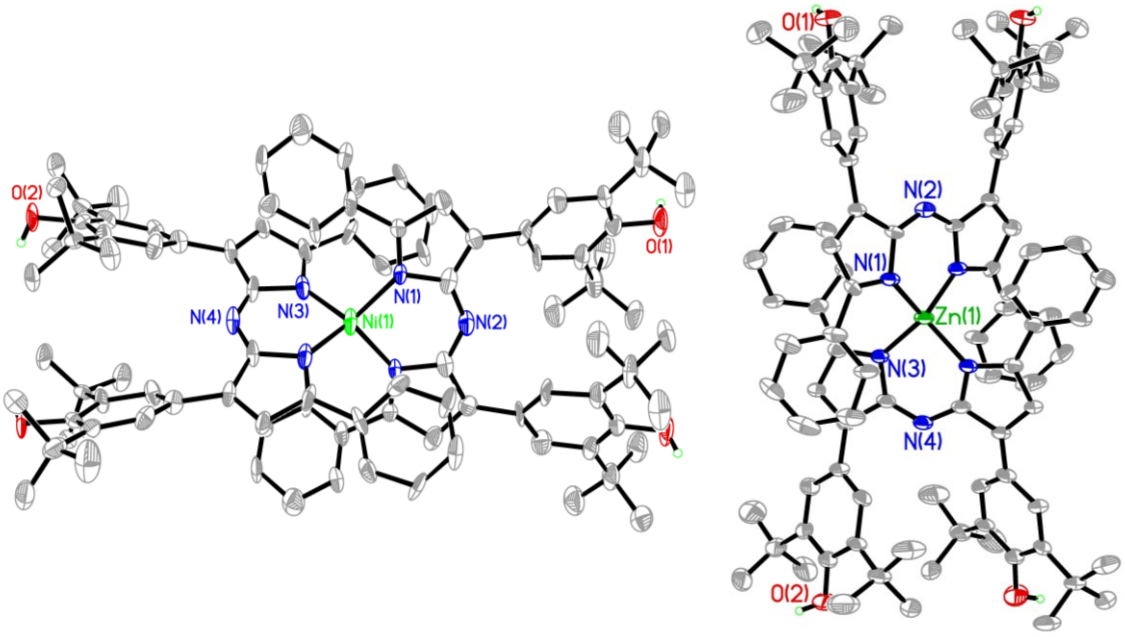


Figure 4.13: Molecular structure of **4.1b** (left) and **4.1d** (right). Thermal ellipsoids are drawn to 50% probability level. Hydrogen atoms except O-H groups are omitted for clarity.

Table 4.3: Selected bond length of Ni(II) **4.1b** and Zn(II) **4.1d** complexes

Bond Length	Ni(II) complex (**4.1b**)	Zn(II) complex (**4.1d**)
N1-M1	1.98(12) Å	1.98(5) Å
N3-M1	1.92(13) Å	2.00(5) Å

Table 4.4: Selected angles and torsion of Ni(II) **4.1b** and Zn(II) **4.1d** complexes

Angle	Ni(II) complex (**4.1b**)	Zn(II) complex (**4.1d**)
N1-M1-N1	95.6(8)°	95.2(3)°
N3-M1-N3	93.8(9)°	96.3(3)°
N1-M1-N3	106.1(5)°	106.9(2)°

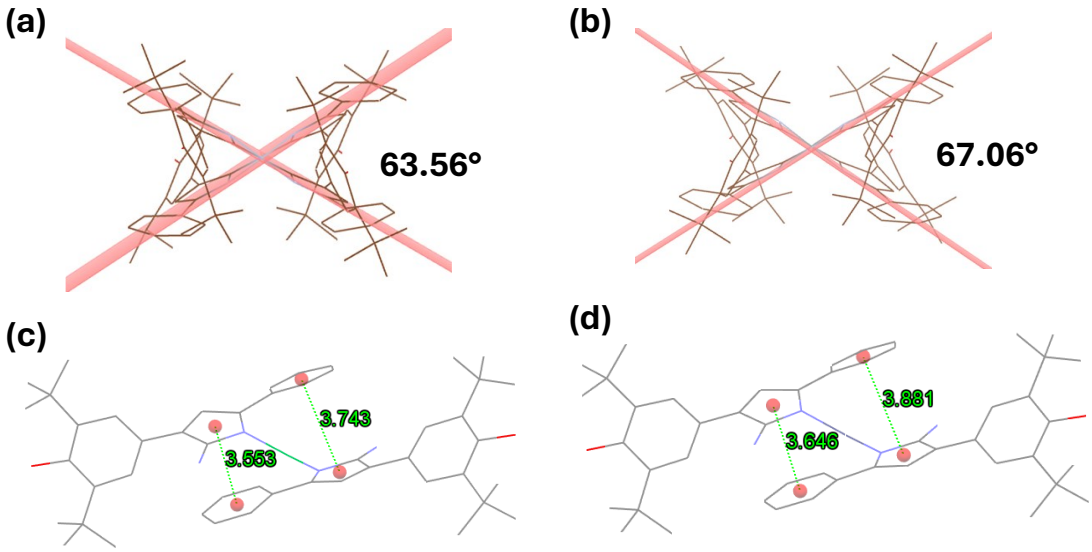


Figure 4.14: (a) dihedral angle between the two ligands in complex **4.1b**, and (b) dihedral angle between the two aza-dipyrromethene ligands in complex **4.1d** (c) intramolecular π–π stacking distances in **4.1b**. (d) intramolecular π–π stacking distances in **4.1b**.

Crucially, the aza-dipyrromethene ligands themselves are highly non-planar in these complexes, with significant torsion angles between the phenolic rings at 1,7-

positions, the phenyl rings at 3,5-positions and the pyrrole rings. For both complexes, the dihedral angle between the two ligands was 63.56° for **4.1b**, and 67.06° for **4.1d**. This non-planar twist is characteristic of the M(aza-dipyrromethene)$_2$ motif and is essential for minimizing steric repulsion between the substituents at proximal positions, which are close to the metal center. This non-planarity is important as it dictates the intermolecular packing efficiency and solid-state charge transport properties of the material. We observe that the proximal phenyl groups of one aza-dipyrromethene ligand align parallel to a pyrrole ring of the second one aza-dipyrromethene ligand. The distance between the centroids of the adjacent rings in complex **4.1b** varies between 3.553 Å and 3.743 Å, and 3.646 to 3.881 Å for complex **4.1d**, suggesting a possible slipped intramolecular phenyl-to-aza-DIPY π contact, but no intermolecular π – π interaction was observed in both complexes see Figure 4.14

4.3.6 Charge Transport Properties

The charge transport properties of complexes (**4.2a – 4.2d**) were estimated using the space charge-limiting current (SCLC) method. The electron mobility (μ_e) was evaluated using the ITO/ZnO/**4.2a-4.2d** complex/Ca/Al device configuration and the hole mobility (μ_h) was evaluated using the ITO/CuI/**4.2a-4.2d** complex/MoO_3/Ag device configuration. The complexes (**4.2a-4.2d**) were spin-coated from chloroform solutions, resulting in uniform films that could be tested. The films were not thermally annealed because annealing caused aggregation and non-uniform films. The μ_e and μ_h were extracted from the SCLC region, and the average of at least 3 devices are given in Table **5** and illustrated in Figure 4.15 – 4.17.

The average electron mobility (μ_e) for complexes (**4.2a-4.2d**) was relatively low, measuring approximately 10^{-6} $cm^2V^{-1}s^{-1}$, indicating that variations in the metal chelate did not significantly influence electron transport. In contrast, the hole mobility (μ_h) of these complexes was notably high, reaching approximately 10^{-3} $cm^2V^{-1}s^{-1}$. Similar to μ_e, modifications to the metal chelate had no discernible effect on hole mobility (μ_h). These hole mobility (μ_h) values are exceptionally high for non-planar molecules.[51] In the context of organic photovoltaics and photodetectors, these complexes are therefore great candidates as electron donors–hole transporting materials.

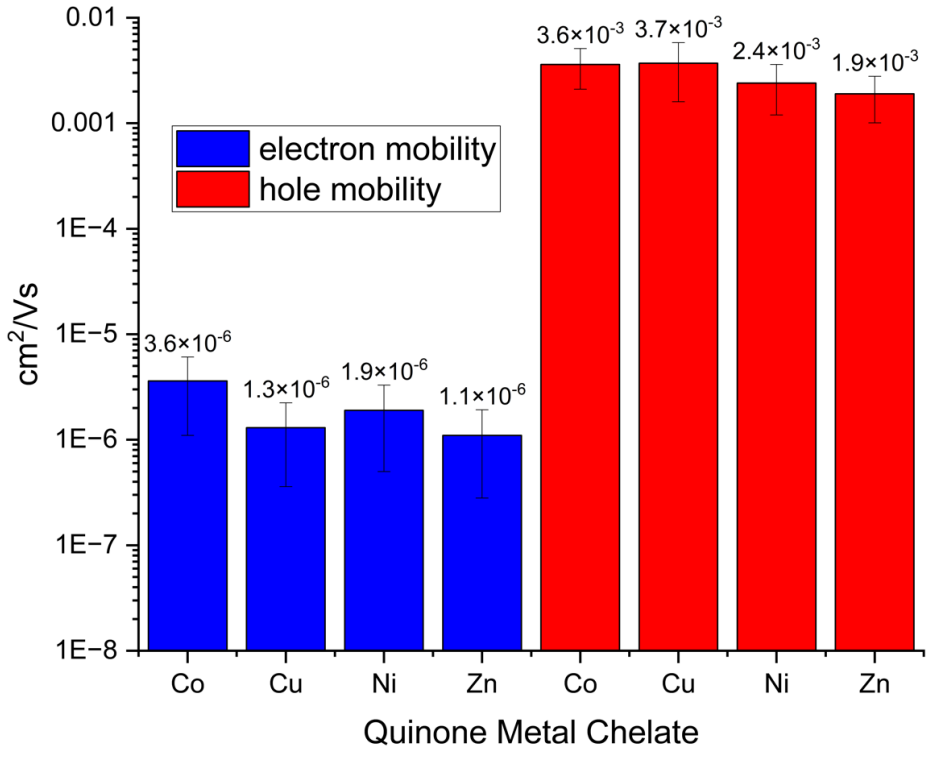


Figure 4.15: Electron and hole mobilities in diodes using the SCLC method.

Table 4.5: Summary of average electron and hole mobility in diodes using the SCLC method.

Compound	μ_e ($cm^2V^{-1}s^{-1}$)	μ_h ($cm^2V^{-1}s^{-1}$)
4.2a	$(4 \pm 3) \times 10^{-6}$	$(4 \pm 2) \times 10^{-3}$
4.2b	$(2 \pm 1) \times 10^{-6}$	$(2 \pm 1) \times 10^{-3}$
4.2c	$(1 \pm 0.9) \times 10^{-6}$	$(4 \pm 2) \times 10^{-3}$
4.2d	$(1 \pm 0.8) \times 10^{-6}$	$(2 \pm 0.9) \times 10^{-3}$

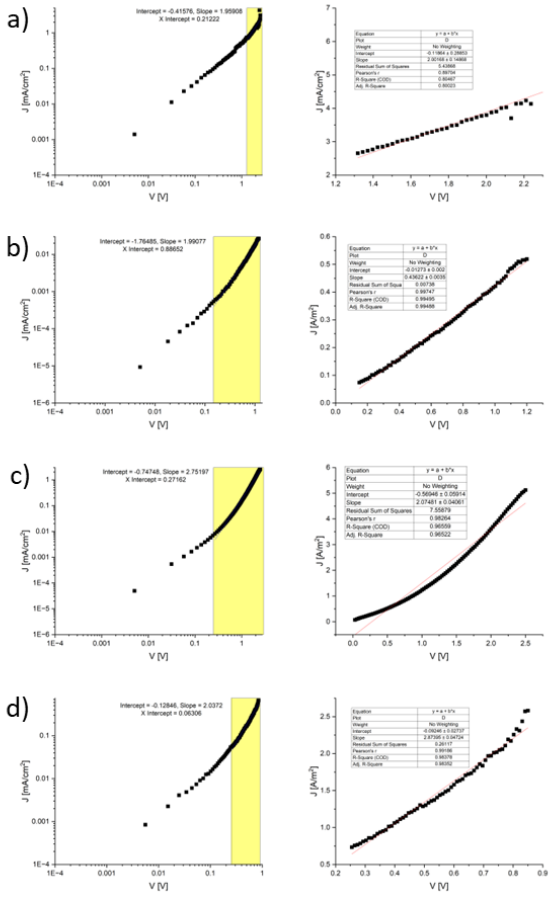


Figure 4.16: Electron mobility of (a) complex **4.2a**, (b) complex **4.2c,** (c) complex **4.2b**, and (d) complex **4.2d**: (left) plot of the double logarithm relationship between J and

absolute V. The data highlighted in yellow shows the SCLC region which fits to the Mott-Gurney law. (right) $J^{1/2}$ characteristics shown versus V for electron mobility.

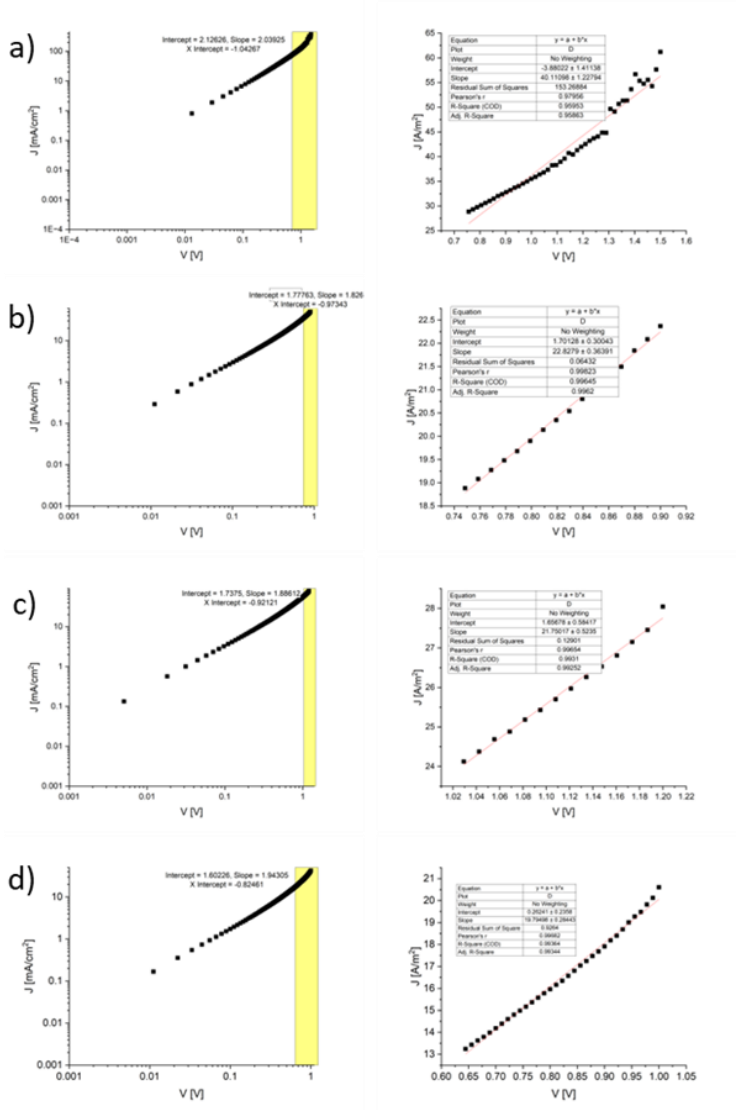


Figure 4.17: Hole mobility of (a) complex **4.2a**, (b) complex **4.2c,** (c) complex **4.2b**, and (d) complex **4.2d**: (left) plot of the double logarithm relationship between J and absolute V. The data highlighted in yellow shows the SCLC region which fits to the Mott-Gurney law. (right) $J^{1/2}$ characteristics shown versus V for electron mobility.

4.3.7 DFT and TDDFT Calculations

Density functional theory (DFT) calculations were carried out to obtain a detailed understanding of the opto-electronic properties of complexes **4.1a – 4.1d**. The TPSSh hybrid meta-GGA functional was employed together with the 6-311G(d) basis set for all light atoms and full-electron Wachter's basis set for transition-metal ions.[93] All molecular geometries were optimized without imposing symmetry constraints. For the closed-shell Zn(II) complex **4.1d**, geometry optimization was performed using the spin-restricted DFT, whereas the open-shell Co(II), Ni(II), and Cu(II) complexes (**4.1a – 4.1c**) were treated using the spin-unrestricted DFT approach. The spin multiplicities were defined as quartet for Co(d^7), triplet for Ni(d^8), doublet for Cu(d^9), and singlet for Zn(d^{10}) species. To ensure the identification of the most stable structures, multiple starting geometries were explored for each complex. The optimized structures reveal a distorted tetrahedral coordination geometry around the metal centers. Solvent effects were incorporated using a continuum solvation model, with tetrahydrofuran (THF) selected to approximate experimental conditions.

Time-dependent DFT (TDDFT) calculations were performed on the optimized structure of complex **4.1d** to simulate its electronic absorption spectrum and determine the corresponding vertical excitation energies. In addition, single-point energy calculations were carried out for all complexes to analyze the frontier molecular orbitals, providing insight into the nature of the electronic transitions. Mulliken population analysis was employed to examine charge distribution and metal–ligand electronic interactions.

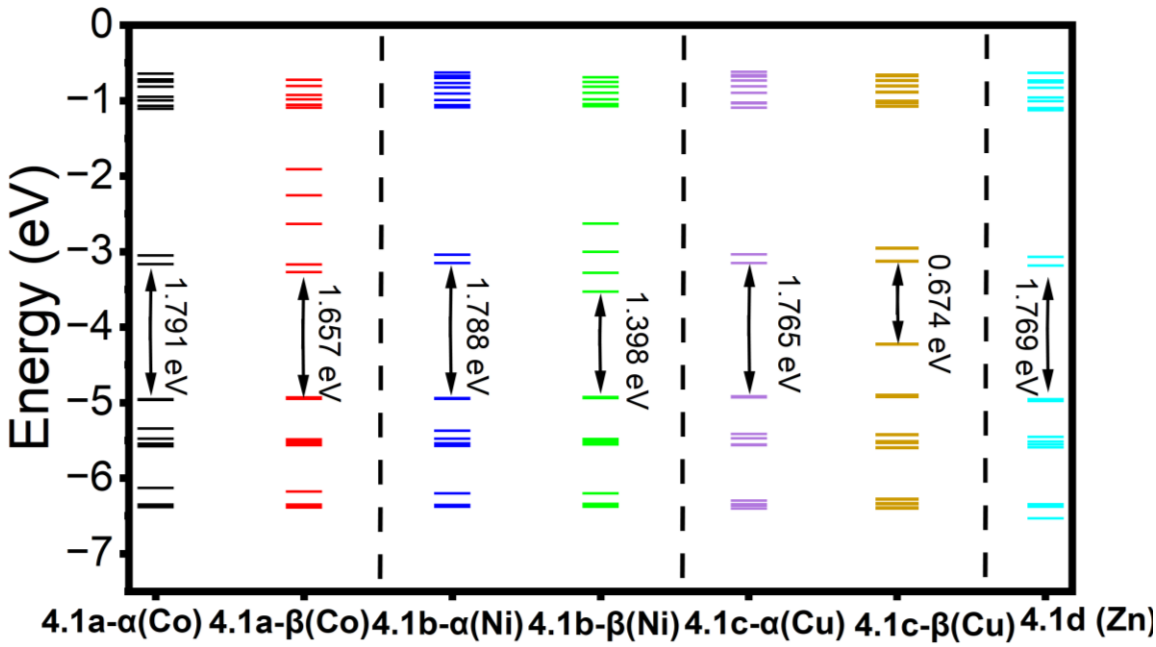


Figure 4.18: Calculated energy levels and HOMO-LUMO energy gaps of complexes **4.1a – 4.1d**.

The calculated molecular orbital energy levels are represented in Figure 4.18. The calculated HOMO-LUMO energy gaps of **4.1a – 4.1d** are slightly larger than the corresponding experimental optical gaps determined by UV-vis spectroscopy.

Percentage contributions from each of the aza-DIPY ligand to occupied and unoccupied frontier molecular orbitals is shown in Figures 4.19 – 4.20. DFT analysis reveals a clear dependence of frontier molecular orbital (FMO) composition on the electronic configuration of the metal center, and similar behavior was reported for some metalated subphthalocyanines (SubPcs).[82] The Zn(II) complex **4.1d** exhibits purely ligand-centered HOMO and LUMO, with no Zn metal contribution, consistent with its closed-shell d^{10} configuration, where metal d orbitals are energetically inaccessible for effective π-orbital mixing (Figure 4.19). Zn(II) therefore serves primarily as a structural

linker, enforcing ligand chelation without participating directly in the frontier electronic structure.

In contrast, the open-shell Co(II), Ni(II), and Cu(II) complexes show varying degrees of metal involvement due to partially occupied d orbitals (Figure 4.19). For Co(II) complex **4.1a**, the HOMO is dominated by one aza-DIPY ligand, while the LUMO is nearly equally distributed over both ligands in the α-spin state, with minimal metal contribution in both spin manifolds. However, Co(II) contributes significantly to deeper occupied and higher unoccupied orbitals, particularly in the β-spin manifold, with substantial contributions to LUMO+2, LUMO+3, and LUMO+4, indicating metal participation mainly beyond the lowest-energy frontier levels (Figure 4.20).

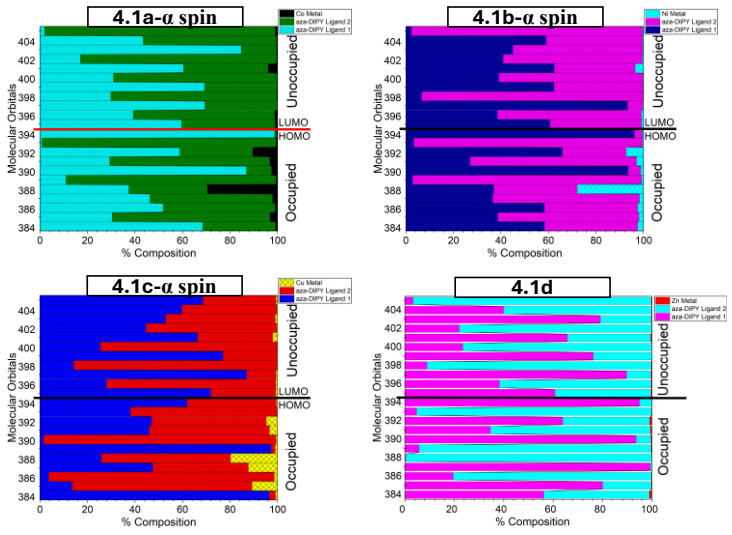


Figure 4.19: Calculated percentage contribution (α-spin only) of different segments of complexes **4.1a** (Co), **4.1b** (Ni), **4.1c** (Cu), and **4.1d** (Zn).

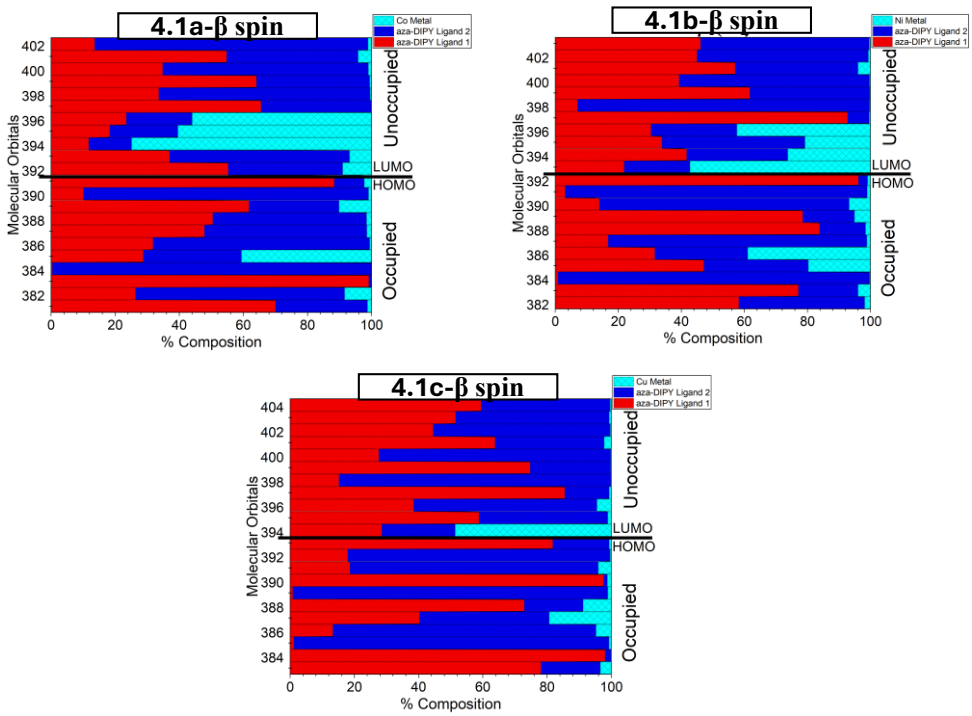


Figure 4.20: Calculated percentage contribution (β-spin only) of different segments of complexes **4.1a** (Co), **4.1b** (Ni), **4.1c** (Cu).

For Ni(II) complex **4.1b**, the α-spin HOMO and LUMO remain largely ligand-centered, whereas the β-spin LUMO exhibits strong metal character, with Ni(II) contributing predominantly to the LUMO and several higher unoccupied orbitals (Figure 4.20). Similarly, the Cu(II) complex **4.1c** shows negligible metal contribution to α-spin frontier molecular orbitals (Figure 4.19), while the β-spin LUMO displays pronounced Cu(II) involvement, reflecting the open-shell d^9 configuration (Figure 4.20). Overall, these results demonstrate that metal contributions to the molecular orbitals in complexes **4.1a – 4.1d** increase with open-shell character and are strongly spin-dependent, with the metal centers primarily influencing higher-lying acceptor orbitals rather than the HOMO–LUMO gap.

Time-dependent DFT calculations were carried out to elucidate the electronic transitions of Zn(II) complex **4.1d** and show good agreement with the experimental UV–Vis spectrum, reproducing the key features in the visible, near-infrared, and near-UV regions (Figure 4.21). A weak low-energy transition is predicted at 775 nm with a small oscillator strength (f = 0.022), dominated by HOMO–1 → LUMO (~48%) and HOMO → LUMO+1 (~30%) excitations. This transition is assigned to a ligand-to-ligand charge-transfer (LLCT) process and is consistent with the absence of a distinct near-IR absorption experimentally (Figure 4.21 and Table 4.6).

The intense experimental band at 598 nm, with a shoulder at 657 nm, is well reproduced by two strong calculated transitions at 643 nm (f = 0.745) and 658 nm (f = 0.536). The 658 nm transition arises primarily from HOMO → LUMO+1 (~42%) and HOMO → LUMO (~38%), while the 643 nm band is dominated by HOMO–1 → LUMO+1 (~58%) and HOMO–1 → LUMO (~22%) excitations. Both transitions exhibit pronounced LLCT character, reflecting strong electronic coupling between the two chelated aza-dipyrromethene ligands. Additional visible-region transitions at 595 nm (f = 0.419), 547 nm (f = 0.321), 531 nm (f = 0.181), and 517 nm (f = 0.295) originate mainly from π–π* excitations involving deeper occupied orbitals and contribute to the broad experimental absorption envelope (Figure 4.21 and Table 4.6).

In the near-UV region, TD-DFT predicts an intense transition at 325 nm with a large oscillator strength (f = 1.355), dominated by HOMO–1 → LUMO+3 (~41%) and HOMO–20 → LUMO+1 (~20%), corresponding to the experimental band at 297 nm. A weaker transition at 329 nm (f = 0.108), arising mainly from HOMO → LUMO+2 and

HOMO–1 → LUMO+3 excitations, accounts for the shoulder near 339 nm (Figure 4.21 and Table 4.6). TD-DFT calculation confirms that the low-energy absorptions are governed by LLCT transitions, while the high-energy bands originate from ligand-centered π–π* excitations, underscoring the role of inter-ligand electronic coupling in defining the optical properties of Zn(II) complex **4.1d**.

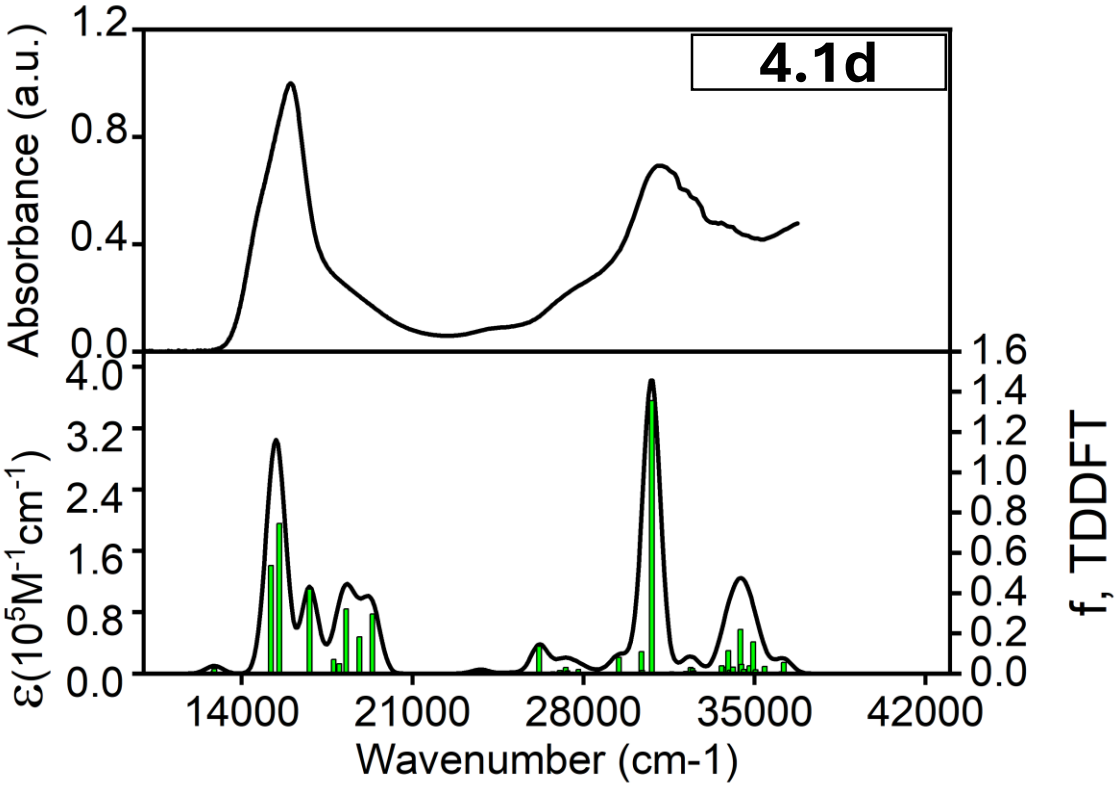


Figure 4.21: Experimental versus TDDFT-predicted (TPSSH exchange-correlation functional) UV-vis spectra of **4.1d.**

Table 4.6. Major TDDFT-predicted excited states contributions for complex **4.1d** using TPSSh exchange correlation functional

Excited State	*Wavelength (nm)*	*Energy (cm^{-1})*	*Oscillator Strength, f*	*% Composition*
2	776	12894	0.0222	H-1 → L (48%), H → L+1 (30%), H → L (17%), H-1 → L+1 (5%)
3	658	15199	0.5355	H → L+1 (42%), H→ L (38%), H-1 → L+1 (13%), H-4 → L (6%)
4	643	15546	0.7452	H-1→ L+1 (58%), H-1 → L (22%), H → L+1 (11%), H-5 → L (5%)
5	596	16783	0.4188	H-2 → L (100%)
10	547	18281	0.3210	H-3 → L+1 (99%)
11	531	18830	0.1814	H-4 → L+1 (81%), H-4 → L (7%), H-5 → L+1 (5%)
12	517	19357	0.2947	H-5 → L+1 (82%), H-5 → L (7%)
24	382	26188	0.1347	H-10 → L+1 (56%), H-11 → L (38%)
49	329	30368	0.1078	H → L+2 (41%), H-1 → L+3 (21%), H-18 → L+1 (10%), H-20 → L (7%)
53	325	30799	1.355	H-1 → L+3 (41%), H-20 → L+1 (20%), H → L+2 (8%), H-1 → L+2 (5%)
72	295	33929	0.1141	H-1 → L+10 (34%), H → L+13 (25%), H-1 → L+12 (21%), H-1 → L+11 (7%)
78	290	34424	0.2180	H-2 → L+4 (39%), H-4 → L+2 (31%), H-4 → L+3 (13%), H-24 → L+1 (7%)
86	286	34946	0.1566	H-5 → L+3 (74%), H-3 → L+4 (11%)

4.4 Conclusions

We have synthesized and characterized a series of homoleptic Co(II), Ni(II), Cu(II), and Zn(II) complexes **4.1a – 4.1d** supported by phenol-substituted aza-dipyrromethene ligands. All complexes adopt distorted tetrahedral geometries. Controlled oxidation of complexes **4.1a – 4.1d** both chemically and electrochemically enable access to quinone/bis(diradicaloid) complexes **4.2a – 4.2d** making these complexes good candidate for panchromatic absorption. Magnetic susceptibility and EPR studies reveal antiferromagnetically coupled, ligand-centered spins with small singlet–triplet gaps for Zn(II) and Ni(II) complexes **4.2d** and **4.2b**, highlighting these systems as promising molecular platforms for spin delocalization and spintronic applications. Charge-transport measurements indicate modest electron mobilities but notably high hole mobilities, underscoring the ability of these nonplanar complexes to support efficient charge transport. Density functional theory and TD-DFT calculations corroborate the experimental results, confirming ligand-dominated frontier orbitals with metal-dependent electronic modulation.

4.5 Experimental Section

4.5.1 General Materials and Methods

All solvents were purchased from commercial sources and purified using standard procedures. All glassware was rigorously dried overnight at 160 °C and cooled under vacuum prior to use. All reagents and starting materials were purchased from commercial vendors and used without further purification. Column chromatography was performed

on silica gel (Dynamic Adsorbents, Inc, 63-200 μm). Deuterated solvents were purchased from Cambridge Isotope Laboratories and used as received.

Space-charge-limited current (SCLC) method. The space-charge-limited current (SCLC) method was used to measure the charge-carrier mobility of the Zn(II) complexes in neat films. Mobility was calculated under the SCLC trap-free conditions using the Mott-Gurney law:

$$J = \frac{9\varepsilon_0\varepsilon_r u V^2}{8d^3} \qquad (1)$$

where J is the electric current density, ε_0 is the vacuum permittivity, ε_r is the relative permittivity of the material, μ is the charge-carrier mobility, V is the effective voltage, and d is the thickness of the zinc complex film. The equation was rearranged to:

$$u = \frac{8m^2d^3}{9\varepsilon_0\varepsilon_r} \qquad (2)$$

where m is the slope of a $J^{1/2}$ versus voltage plot in the SCLC region. To determine the SCLC region, data is plotted as J vs. V on a double logarithmic scale. Data with a higher slope (ideally 2) would be the SCLC region.

For electron mobility device fabrication, ITO-coated glass slides were cleaned using detergent water, DI water, acetone, and IPA under sonication for 15 min, respectively. Slides were then dried with a nitrogen gun and cleaned under UV ozone treatment (PSDP-UV8T) at 85 °C for 15 min. Devices had the structure: glass/ITO/ZnO/complex **4.2a-4.2d**/Ca/Al. The glass slides were purchased pre-coated with ITO. A zinc acetate solution was made by combining 0.46 g zinc acetate, 5.0 mL 2-methoxyethanol, and 0.15 mL ethanolamine into a 20 mL vial on a hot plate stirring at 45 °C overnight. An additional 5.0 mL 2-methoxyethanol were added and stirred at 45 °C for 10 min.

The ZnO was prepared by spin coating the zinc acetate solution at 4000 rpm for 1 min and annealed in air at 150 °C for 10 min. After deposition, the slides were cleaned using DI water, acetone, and IPA then dried with nitrogen. Each quinone complex was dissolved at 20 mg/mL in $CHCl_3$ inside the nitrogen glove box (Pure LabHE) at 55 °C for 1 h. Each solution was filtered through a 0.45 μm PTFE filter prior to spin-coating at 800 rpm for 40 s then 2000 rpm for 2 s inside the glovebox. Finally, 30 nm calcium and 100 nm aluminum were deposited under vacuum using an Angstrom Engineering Evovac Deposition System. Hole mobility measurements were completed using the device structure glass/ITO/CuI/active material/MoO_3/Ag. The copper iodide (CuI) layer was prepared using a 10 mg/mL solution of CuI in acetonitrile, spin coated at 4000 rpm for 30 s and annealed at 100 °C for 10 min inside the glove box. The active material was prepared in the same way as the electron mobility devices. In the Angstrom, 10 nm of MoO_3 and 80 nm of Ag were thermally deposited. Finally, dark current measurements were completed inside the glovebox using a Keithley 2400 source meter. All devices had a total effective area of 0.2 cm^2.

Electrochemistry. Cyclic voltammetry and differential pulse voltammetry measurements were made using a three-electrode system consisting of a glassy carbon or platinum working electrode, a platinum auxiliary electrode, and an Ag/AgCl wire pseudo-reference electrode. Ferrocene (Fc) was used as an internal standard for the studied compounds, and the reported potentials were corrected to the Fc/Fc^+ couple. For consistency, all potentials and figures in this work are reported vs the Fc/Fc^+ redox couple. All

electrochemical experiments were conducted in dichloromethane (CH_2Cl_2) and 0.1M tetrabutylammonium perchlorate (TBAP) as electrolyte.

Spectroelectrochemistry. Spectroelectrochemical experiments were performed using a Jasco V-770 UV–vis–NIR spectrophotometer in tandem with a CH Instruments electrochemical analyzer, which was operated using the bulk electrolysis mode. The data were collected using a custom-made 1 mm cell, a platinum mesh working electrode, a platinum auxiliary electrode, and Ag/AgCl wire pseudo-reference electrode. Spectroelectrochemical solutions consisted of 0.3 M solutions of (($^{n}Bu_4N$)[PF_6]) in THF.

NMR. NMR spectra were recorded on a 500 MHz Brucker III spectrometer. All chemical shifts (δ) are listed in parts per million (ppm) and are referenced to solvent. Spectra are referenced internally due to residual proton solvent resonances. ^{1}H and ^{13}C NMR spectra were collected in $CDCl_3$ or THF-d_8.

Magnetometry. Magnetic studies were carried out using a 7-Tesla Quantum Design SQUID magnetometer at the applied magnetic fields H = 1000 and 10,000 Oe and at temperature T = 2 – 300 K. The empty plastic capsule exhibited diamagnetism, and its magnetic moment was measured for correction. For both samples in powder form, primary correction for diamagnetism is implemented by point-by-point background subtraction, together with Pascal constants correction.

EPR. EPR spectra were recorded on a Bruker ELEXSYS E-500 instrument at the X-band frequency (9,82 GHz). DPPH (g = 2.0036) was used as the standard for field and frequency calibration.

Single Crystal X-ray Crystallographic Analysis. Crystalline samples were mounted on a 150 mm MiTeGen Dual-Thickness MicroMount using Paratone N oil (Hampton). X-ray diffraction experiments on **4.1b** and **4.1d** were conducted at 150 K. Diffraction data was collected using a Bruker Smart Apex II single crystal diffractometer with a TRIUMPH monochromated Mo Kα radiation (λ = 0.71073 Å) source with a crystal-to-detector distance of 50 mm, using a series of θ and ω scans in 0.50° oscillations. The data was processed and corrected for Lorentz and polarization effects and an empirical absorption correction was applied, using the Bruker Apex II software suite. The structures were solved with ShelxS[84], and subsequent refinements were performed using the SHELXTL crystallographic software package of Bruker-AXS[85]. The coordinates and anisotropic displacement parameters for the non-hydrogen atoms were refined. Hydrogen atoms were placed in idealized geometric positions and linked to their respective carbon atoms using a riding model during refinement. Platon SQUEEZE algorithm[86] was used to remove the electron density associated with the cyclohexane solvent molecule for the dataset of **4.1b** and **4.1d** because of the severe disorder of cyclohexane molecule at this temperature. Diagrams were prepared using MERCURY[87]. CCDC number for structure **4.1b** is 2532387, and for **4.1d** is 2532388.

Computational Methods. All computations were performed using Gaussian 16 software[88] running under Windows or UNIX OS. Molecular orbital contributions were compiled from single-point calculations using the QMForge program[89]. In DFT calculations, the TPSSh[90,91] (10% of Hartree-Fock exchange) hybrid exchange correlation

functionals. In all calculations, 6-311G(d) basis set was employed for light atoms,[92] and full-electron Wachter's basis set was used for the transition-metal centers.[93]

4.5.2 Synthesis of Bis[1,7-di-(2,6-di-tert-butylphenol)-3,5-di-phenylazadipyrromethene]cobalt (II), 4.1a

Compound **4.0** (0.141 g, 0.2 mmol) and ammonium acetate (0.200 g, 2.6 mmol) were added to a solution of cobalt(II)acetate tetrahydrate (0.061 g, 0.246 mmol) in *n*-butanol (10 mL). The mixture was stirred for 1 h at reflux, cooled to room temperature and the precipitate filtered and washed with excess CH_2Cl_2 as a purplish-brown powder (0.116 g, 77%). ^{1}H NMR of compound **2a** (500 MHz, 298 K, THF-d_8) δ (ppm) = 60.95 (s, 8H), 14.12 (s, 4H), 11.19 (s, 4H), 8.61 (s, 8H), 5.79 – 6.44 (m, 10H), 4.82 (s, 72H). HRMS-MALDI$^+$ (m/z): $[M]^+$ calcd. for $[C_{96}H_{108}N_6CoO_4]$, 1468.7797; found, 1468.7798. See Figures 4.22 for 1H NMR and 4.30 for mass spectrum.

4.5.3 Synthesis of Bis[1,7-di-(2,6-di-tert-butylphenol)-3,5-di-phenylazadipyrromethene]nickel (II), 4.1b

Compound **4.0** (0.141 g, 0.2 mmol) and nickel(II) acetate tetrahydrate (0.067 g, 0.271 mmol) in *n*-butanol (10 mL) stirred for 1 h at reflux, cooled to room temperature and the precipitate filtered and washed with excess CH_2Cl_2 as a purplish-brown powder (0.123 g, 81%). ^{1}H NMR of compound **2b** (500 MHz, 298 K, THF-d_8) δ (ppm) = 59.15 (s, 4H), 35.53 (s, 8H), 8.87 (s, 8H), 7.38 – 7.52 (m, 8H), 5.84 (s, 4H), -0.37 (s, 72H), -3.27 (s, 8H). HRMS-MALDI$^+$ (m/z): $[M]^+$ calcd. for $[C_{96}H_{108}N_6NiO_4]$, 1467.7819; found, 1467.7820. See Figures 4.23 for 1H NMR and 4.31 mass spectrum.

4.5.4 Synthesis of Bis[1,7-di-(2,6-di-tert-butylphenol)-3,5-di-phenylazadipyrromethene]copper (II), 4.1c

Compound **4.0** (0.141 g, 0.2 mmol) and copper(II) acetate monohydrate (0.043 g, 0.21 mmol) in THF (10 mL) was stirred overnight and the precipitate was filtered and washed with excess CH_2Cl_2 as a purplish-brown powder (0.132 g, 89%). HRMS-ESI$^+$ (m/z): $[M]^+$ calcd. for $[C_{96}H_{108}CuN_6O_4]$, 1471.7; found, 1471.7650. See Figure 4.32 mass spectrum.

4.5.5 Synthesis of Bis[1,7-di-(2,6-di-tert-butylphenol)-3,5-di-phenylazadipyrromethene]zinc (II), 4.1d

Compound **4.0** (0.141 g, 0.2 mmol) and zinc(II) acetate anhydrous (0.024 g, 0.11 mmol) in THF (10 mL) were stirred overnight and the precipitate was filtered and washed with excess CH_2Cl_2 as a purplish-brown powder (0.132 g, 89%). ^{1}H NMR of compound **4.1d** (500 MHz, 298 K, THF-d_8) δ (ppm) = 7.60 – 7.62 (d, J = 10Hz, 8H), 7.36 (s, 8H), 7.05 – 7.08 (t, 8H), 6.90 – 6.94 (t, 4H), 6.59 (s, 4H), 6.09 (s, 4H), 1.31 (s, 72H). ^{13}C NMR of compound **2d** (500 MHz, 298 K, $CDCl_3$) δ (ppm) = 30.0, 34.2, 40.4, 115.02, 126.3, 126.5, 127.3, 128.3, 134.0, 135.4, 147.7, 149.6, 154.1, 159.2. HRMS-MALDI$^+$ (m/z): $[M]^+$ calcd. for $[C_{96}H_{108}ZnN_6O_4]$, 1472.7510; found, 1472.7581. See Figures 4.24 – 4.25 for ^{1}H NMR and ^{13}C NMR spectra. See Figure 4.33 for mass spectrum.

4.5.6 Synthesis of Bis[1,7-di-(2,6-di-tert-butylcyclohexa-2,5-dien-1-one)-3,5-di phenylazadipyrromethene]cobalt(II), 4.2a.

Compound **4.1a** (0.146 g, 0.1 mmol) was stirred in dry THF for 24 h, then lead (IV) oxide (0.717 g, 3 mmol) was added under a nitrogen atmosphere, the reaction

mixture was stirred at room temperature overnight with an observed color change from deep blue to dark brown in THF solution. The reaction was monitored via TLC. Once the reaction was finished, the solid lead (IV) oxide was filtered off. The filtrate was dried via rotary evaporator, and then the final product was obtained as a black solid (95 mg, 99%) without further purification. HRMS-MALDI$^-$ (m/z): [M]$^-$ calcd. for [$C_{96}H_{104}N_6CoO_4$], 1468.7797; found, 1468.7798. see Figure 4.34 for mass spectrum.

4.5.7 Synthesis of Bis[1,7-di-(2,6-di-tert-butylcyclohexa-2,5-dien-1-one)-3,5-di-phenylazadipyrromethene]nickel (II), 4.2b

Compound **4.1b** (0.146 g, 0.1 mmol) was stirred in dry THF for 24 h, lead (IV) oxide (0.717 g, 3 mmol) was added under a nitrogen atmosphere, and the reaction mixture was stirred at room temperature overnight with an observed color change from deep blue to dark brown in THF solution. The reaction was monitored via TLC. Once the reaction was finished, the solid lead (II) oxide was filtered off. The filtrate was dried via rotary evaporator, and then the final product was obtained as a black solid (95 mg, 99%) without further purification. ^{1}H NMR of compound **3b** (500 MHz, 298 K, $CDCl_3$) δ (ppm) = 8.73 (s, 4H), 7.65 - 7.66 (d, J = 10Hz, 8H), 7.22 (s, 4H), 7.07 – 7.11 (t, 8H), 6.87 – 6.90 (t, 4H), 6.21 (s, 4H), 1.41 (s, 36H), 1.25 (s, 36H). ^{13}C NMR of compound **3b** (500 MHz, 298 K, $CDCl_3$) δ (ppm) = 25.5, 30.2, 32.8, 38.1, 106.0, 124.9, 125.5, 132.8, 135.7, 146.4, 151.8. HRMS-MALDI$^-$ (m/z): [M]$^-$ calcd. for [$C_{96}H_{104}N_6NiO_4$], 1464.7484; found, 1468.7482. See Figures 4.26 – 4.27 for ^{1}H NMR and ^{13}C NMR spectra. See Figure 4.35 for mass spectrum.

4.5.8 Synthesis of Bis[1,7-di-(2,6-di-tert-butylcyclohexa-2,5-dien-1-one)-3,5-di-phenylazadipyrromethene]copper (II), 4.2c

Compound **4.1c** (0.147 g, 0.1 mmol) was stirred in dry THF for 24 h, lead (IV) oxide (0.717 g, 3 mmol) was added under a nitrogen atmosphere, and the reaction mixture was stirred at room temperature overnight with an observed color change from deep blue to dark brown in THF solution. The reaction was monitored via TLC. Once the reaction was finished, the solid lead (II) oxide was filtered off. The filtrate was dried via rotary evaporator, and then the final product was obtained as a black solid (97 mg, 99%) without further purification. HRMS-MALDI$^-$ (m/z): $[M]^-$ calcd. for $[C_{96}H_{104}CuN_6O_4]$, 1468.7443; found, 1468.7460. See Figure 4.36 for mass spectrum.

4.5.9 Synthesis of Bis[1,7-di-(2,6-di-tert-butylcyclohexa-2,5-dien-1-one)-3,5-di-phenylazadipyrromethene]zinc (II), 4.2d

Compound **4.1d** (0.147 g, 0.1 mmol) was stirred in dry THF for 24 h and lead (IV) oxide (0.717 g, 3 mmol) was added under a nitrogen atmosphere, and the reaction mixture was stirred at room temperature overnight with a color change from deep blue to olive green in THF solution. The reaction was monitored via TLC. Once the reaction was finished, the solid lead (II) oxide was filtered off. The filtrate was dried via rotary evaporator, and then the final product was obtained as a black solid (98 mg, 99%) without further purification. ^{1}H NMR of compound **3d** (500 MHz, 298 K, $CDCl_3$) δ (ppm) = 8.73 (s, 4H), 7.65 - 7.66 (d, J = 10Hz, 8H), 7.22 (s, 4H), 7.07 – 7.11 (t, 8H), 6.87 – 6.90 (t, 4H), 6.21 (s, 4H), 1.41 (s, 36H), 1.25 (s, 36H). ^{13}C NMR of compound **3d** (500 MHz, 298 K, $CDCl_3$) δ (ppm) = 25.6, 29.2, 30.5, 68.0, 98.5, 126.9, 128.2, 130.2, 137.5,

140.3, 143.2, 149.8, 152.4, 158.0. HRMS-MALDI$^-$ (m/z): $[M]^-$ calcd. for $[C_{96}H_{104}N_6O_4Zn]$, 1470.7428; found, 1470.5388. See Figures 2.28 – 4.29 for ^1H NMR and ^{13}C NMR spectra. See Figure 4.37 for mass spectrum.

References

(1) Prasannan, D.; Zatsikha, Y. V.; Nemykin, V. N. Radical and Redox Forms of Pyridyl Appended MB-DIPYs. *Chem. Asian J.* **2025**, *20*, e00694 (1–11). https://doi.org/10.1002/asia.202500694.

(2) Li, W.; Gong, Q.; Zhao, Q.; Wu, Q.; Niu, C.; Jiao, L.; Hao, E. Synthesis, Photophysical and Redox Properties of Highly Stable Radicals of Nickel(II) Bis(2-Aminophenyl)-Azadipyrromethene. *Inorg.Chem.* **2025**, *64*, 9114–9123. https://doi.org/10.1021/acs.inorgchem.5c00662.

(3) Das, S.; Mondal, S.; Suthar, S.; Ray, R. K.; Mondal, K.; Raveendran, A. A.; Ahamed, S.; Maji, C.; Baidya, M.; Schwarz, B.; Chakraborty, D.; Ungur, L.; Mondal, K. C. Isolation and Characterization of Carbene-Supported Air Stable Co(II)-Radical Complexes with Bileptic Redox Non-Innocent Ligands: Stability, Bonding, Ring-Opening Copolymerization Studies and Photo-Catalytic Ring Cyclization Activity. *Dalton Trans.* **2025**, *54*, 11182–11192. https://doi.org/10.1039/D5DT00727E.

(4) Swatiputra, A. A.; Mukherjee, D.; Dinda, S.; Roy, S.; Pramanik, K.; Ganguly, S. Electron Transfer Catalysis Mediated by 3d Complexes of Redox Non-Innocent Ligands Possessing an Azo Function: A Perspective. *Dalton Trans.* **2023**, *52*, 15627–15646. https://doi.org/10.1039/D3DT02567E.

(5) Vagiakos, I.; Tsoureas, N.; Huang, T.; Christodoulou, S.; Maron, L.; Pickl, T.; Mink, J.; Halter, D. P. Monomeric M(II) (M = Fe, Co, Ni) Complexes Supported by Bulky Aryloxide Ligands Tethered to an Arene Functionality; Synthesis,

Electrochemistry and Study of the M(II)–Arene Interaction. *Dalton Trans.* **2025**, *54*, 8683–8694. https://doi.org/10.1039/D5DT00482A.

(6) Karmalkar, D. G.; Lim, H.; Sundararajan, M.; Lee, Y.-M.; Seo, M. S.; Bae, D. Y.; Lu, X.; Hedman, B.; Hodgson, K. O.; Kim, W.-S.; Lee, E.; Solomon, E. I.; Fukuzumi, S.; Nam, W. Synthesis, Structure, and Redox Reactivity of Ni Complexes Bearing a Redox and Acid–Base Non-Innocent Ligand with Ni II , Ni III , and Ni IV Formal Oxidation States. *J Am Chem. Soc.* **2025**, *147*, 3981–3993. https://doi.org/10.1021/jacs.4c11751.

(7) DeGayner, J. A.; Jeon, I.-R.; Harris, T. D. A Series of Tetraazalene Radical-Bridged M 2 (M = Cr III , Mn II , Fe II , Co II) Complexes with Strong Magnetic Exchange Coupling. *Chem. Sci.* **2015**, *6*, 6639–6648. https://doi.org/10.1039/C5SC02725J.

(8) Sarkar, S.; Tiwari, R. K.; Samanta, D.; Guchhait, T.; Sañudo, E. C.; Rajaraman, G.; Rath, S. P. Unusual Stabilisation of Remarkably Bent Tetra-Cationic Tetra-Radical Intermolecular Fe(III) μ-Oxo Tetranuclear Complexes. *Angew. Chem. Int. Ed.* **2024**, *63,* e202402344 (1-9). https://doi.org/10.1002/anie.202402344.

(9) Zou, M.; Waldie, K. M. Redox-Active Ligand Promoted Multielectron Reactivity at Earth-Abundant Transition Metal Complexes. *Inorg. Chem. Front*. **2024**, 11, 5795–5809. https://doi.org/10.1039/d4qi01265h.

(10) Nakada, A.; Matsumoto, T.; Chang, H. C. Redox-Active Ligands for Chemical, Electrochemical, and Photochemical Molecular Conversions. *Coord. Chem. Rev*. **2022**, 473, 214804. https://doi.org/10.1016/j.ccr.2022.214804.

(11) Queyriaux, N. Redox-Active Ligands in Electroassisted Catalytic H + and CO 2 Reductions: Benefits and Risks. *ACS Catal.* **2021**, *11*, 4024–4035. https://doi.org/10.1021/acscatal.1c00237.

(12) Ding, B.; Solomon, M. B.; Leong, C. F.; D'Alessandro, D. M. Redox-Active Ligands: Recent Advances towards Their Incorporation into Coordination Polymers and Metal-Organic Frameworks. *Coord. Chem. Rev.* **2021**, *439*, 213891. https://doi.org/10.1016/j.ccr.2021.213891.

(13) Ai, F.; Lu, Y.-C. Coordination Chemistry in Advanced Redox-Active Electrolyte Designs. *Nat. Rev. Mater.* **2025**, *10*, 929–946. https://doi.org/10.1038/s41578-025-00833-y.

(14) van der Vlugt, J. I. Radical-Type Reactivity and Catalysis by Single-Electron Transfer to or from Redox-Active Ligands. *Chem. Eur. J.* **2019**, *25*, 2651–2662. https://doi.org/10.1002/chem.201802606.

(15) Briand, G. G. Redox-Active Ligands – a Viable Route to Reactive Main Group Metal Compounds. *Dalton Trans.* **2023**, *52*, 17666–17678. https://doi.org/10.1039/D3DT03100D.

(16) Zhu, D.; Thapa, I.; Korobkov, I.; Gambarotta, S.; Budzelaar, P. H. M. Redox-Active Ligands and Organic Radical Chemistry. *Inorg. Chem.* **2011**, *50*, 9879–9887. https://doi.org/10.1021/ic2002145.

(17) Luca, O. R.; Crabtree, R. H. Redox-Active Ligands in Catalysis. *Chem. Soc. Rev.* **2013**, *42*, 1440–1459. https://doi.org/10.1039/C2CS35228A.

(18) Storr, T.; Mukherjee, R. Preface for the Forum on Applications of Metal Complexes with Ligand-Centered Radicals. *Inorg. Chem.* **2018**, *57*, 9577–9579. https://doi.org/10.1021/acs.inorgchem.8b02171.

(19) Tomson, N. C.; Labios, L. A.; Weyhermüller, T.; Figueroa, J. S.; Wieghardt, K. Redox Noninnocence of Nitrosoarene Ligands in Transition Metal Complexes. *Inorg. Chem.* **2011**, *50*, 5763–5776. https://doi.org/10.1021/ic2005979.

(20) Lohmeyer, L.; Werr, M.; Kaifer, E.; Himmel, H. Interplay and Competition Between Two Different Types of Redox-Active Ligands in Cobalt Complexes: How to Allocate the Electrons? *Chem. Eur. J.* **2022**, *28*, e202201789 (1–15). https://doi.org/10.1002/chem.202201789.

(21) Liu, L.; DeGayner, J. A.; Sun, L.; Zee, D. Z.; Harris, T. D. Reversible Redox Switching of Magnetic Order and Electrical Conductivity in a 2D Manganese Benzoquinoid Framework. *Chem. Sci.* **2019**, *10*, 4652–4661. https://doi.org/10.1039/C9SC00606K.

(22) Shamova, L. I.; Zatsikha, Y. V.; Nemykin, V. N. Synthesis Pathways for the Preparation of the BODIPY Analogues: Aza-BODIPYs, BOPHYs and Some Other Pyrrole-Based Acyclic Chromophores. *Dalton Trans.* **2021**, *50*, 1569–1593. https://doi.org/10.1039/D0DT03964K.

(23) Zatsikha, Y. V.; Shamova, L. I.; Shepit, M.; Berry, S. M.; Thomas, F.; Herbert, D. E.; van Lierop, J.; Nemykin, V. N. Radical Complexes of Nickel(II)/Copper(II) and Redox Non-innocent MB-DIPY Ligands: Unusual Stability and Strong Near-Infrared

Absorption at λ max ~1300 nm. *Chem. Eur. J.* **2022**, *28,* e202201181 (1–6). https://doi.org/10.1002/chem.202201181.

(24) Yang, R.; Guan, H.; Jin, J.; Zheng, T.; He, L.; Zhang, Y.; Tian, L.; Wang, J.; Li, X. A Review on the Synthetic Methods for the BODIPY Core. *Compounds* **2025**, *5*, 42, 1–17. https://doi.org/10.3390/compounds5040042.

(25) Sultan, S.; Crovetto, L.; Rios, R. Recent Advances in the Development of Enantiopure BODIPYs and Some Related Enantiomeric Compounds. *Chem. Commun.* **2025**, *61*, 1989–2010. https://doi.org/10.1039/D4CC05809G.

(26) Bessette, A.; Ferreira, J. G.; Giguère, M.; Bélanger, F.; Désilets, D.; Hanan, G. S. Azadipyrromethene Dye Derivatives in Coordination Chemistry: The Structure–Property Relationship in Homoleptic Metal(II) Complexes. *Inorg. Chem.* **2012**, *51*, 12132–12141. https://doi.org/10.1021/ic300872m.

(27) Moutet, J.; Philouze, C.; du Moulinet d'Hardemare, A.; Leconte, N.; Thomas, F. Ni(II) Complexes of the Redox-Active Bis(2-Aminophenyl)Dipyrrin: Structural, Spectroscopic, and Theoretical Characterization of Three Members of an Electron Transfer Series. *Inorg. Chem.* **2017**, *56*, 6380–6392. https://doi.org/10.1021/acs.inorgchem.7b00433.

(28) Bessette, A.; Ferreira, J. G.; Giguère, M.; Bélanger, F.; Désilets, D.; Hanan, G. S. Azadipyrromethene Dye Derivatives in Coordination Chemistry: The Structure–Property Relationship in Homoleptic Metal(II) Complexes. *Inorg. Chem.* **2012**, *51*, 12132–12141. https://doi.org/10.1021/ic300872m.

(29) Deligonul, N.; Gray, T. G. Azadipyrromethene Complexes of d 8 Metal Centers: Rhodium(I), Iridium(I), Palladium(II), and Platinum(II). *Inorg. Chem.* **2013**, *52*, 13048–13057. https://doi.org/10.1021/ic4017239.

(30) Palma, A.; Gallagher, J. F.; Müller-Bunz, H.; Wolowska, J.; McInnes, E. J. L.; O'Shea, D. F. Co(II), Ni(II), Cu(II) and Zn(II) Complexes of Tetraphenylazadipyrromethene. *Dalton Trans.* **2009**, 2, 273–279. https://doi.org/10.1039/B811764K.

(31) Schomberg-Sanchez, I. S.; Janusz, W. A.; Lemon, C. M. Beyond BODIPY: Dipyrrin Complexes of P-Block Elements. *J. Coord. Chem.* **2025**, *78*, 2449–2502. https://doi.org/10.1080/00958972.2025.2539945.

(32) Deligonul, N.; Gray, T. G. Azadipyrromethene Complexes of d^8 Metal Centers: Rhodium(I), Iridium(I), Palladium(II), and Platinum(II). *Inorg. Chem.* **2013**, *52*, 13048–13057. https://doi.org/10.1021/ic4017239.

(33) DiScipio, R.; Sauvé, G.; Crespo-Hernández, C. E. Photodynamics in Metal-Chelating Tetraphenylazadipyrromethene Complexes: Implications for Their Potential Use as Photovoltaic Materials. *J. Phys. Chemi C,* **2018**, *122*, 13579–13589. https://doi.org/10.1021/acs.jpcc.7b12657.

(34) Doğan, A.; Yılmaz, H.; Karatay, A.; Yıldız, E. A.; Sevinç, G.; Unver, H.; Boyacioglu, B.; Hayvali, M.; Elmali, A. Enhancing Near-Infrared Two-Photon Absorption of Aza-Boron-Dipyrromethene Compounds Through Intramolecular Charge Transfer Via Electron Donating Substitution. *ChemPlusChem* **2025**, *90*, e202500354 (1–13). https://doi.org/10.1002/cplu.202500354.

(35) Lecarme, L.; Kochem, A.; Chiang, L.; Moutet, J.; Berthiol, F.; Philouze, C.; Leconte, N.; Storr, T.; Thomas, F. Electronic Structure and Reactivity of One-Electron-Oxidized Copper(II) Bis(Phenolate)-Dipyrrin Complexes. *Inorg. Chem*. **2018**, 57, 9708–9719. https://doi.org/10.1021/acs.inorgchem.8b00044.

(36) Li, T.; Benduhn, J.; Li, Y.; Jaiser, F.; Spoltore, D.; Zeika, O.; Ma, Z.; Neher, D.; Vandewal, K.; Leo, K. Boron Dipyrromethene (BODIPY) with *Meso* -Perfluorinated Alkyl Substituents as near Infrared Donors in Organic Solar Cells. *J. Mater. Chem A* **2018**, *6*, 18583–18591. https://doi.org/10.1039/C8TA06261G.

(37) Yang, R.; Guan, H.; Jin, J.; Zheng, T.; He, L.; Zhang, Y.; Tian, L.; Wang, J.; Li, X. A Review on the Synthetic Methods for the BODIPY Core. *Compounds* **2025**, *5*, 42, 1–17. https://doi.org/10.3390/compounds5040042.

(38) Baudron, S. A. Dipyrrin Based Metal Complexes: Reactivity and Catalysis. *Dalton Trans.* **2020**, *49*, 6161–6175. https://doi.org/10.1039/D0DT00884B.

(39) Boens, N.; Verbelen, B.; Ortiz, M. J.; Jiao, L.; Dehaen, W. Synthesis of BODIPY Dyes through Postfunctionalization of the Boron Dipyrromethene Core. *Coord. Chem. Rev.* **2019**, *399*, 213024. https://doi.org/10.1016/j.ccr.2019.213024.

(40) Yadav, I. S.; Misra, R. Design, Synthesis and Functionalization of BODIPY Dyes: Applications in Dye-Sensitized Solar Cells (DSSCs) and Photodynamic Therapy (PDT). *J. Mater. Chem C,* **2023**, *11*, 8688–8723. https://doi.org/10.1039/D3TC00171G.

(41) Zatsikha, Y. V.; Shamova, L. I.; Blesener, T. S.; Kuzmin, I. A.; Germanov, Y. V.; Herbert, D. E.; Nemykin, V. N. Development of a Class of Easily Scalable, Electron-

Deficient, Core-Extended Benzo-Fused Azadipyrromethene Derivatives ("MB-DIPY") *J. Org. Chem.*, **2019**, *84*, 14540-14557. https://doi.org/10.1021/acs.joc.9b02074.

(42) Kovtun, O. M.; Zatsikha, Y. V.; Kovtun, Y. P. New Approaches to the Modification of Chemical Structure and Photophysical Properties of BODIPY Dyes. *Chem. Heterocycl. Compd.* **2023**, *59*, 357–367. https://doi.org/10.1007/s10593-023-03205-y.

(43) Ikeda, C.; Ueda, S.; Nabeshima, T. Aluminium Complexes of N2O2-Type Dipyrrins: The First Hetero-Multinuclear Complexes of Metallo-Dipyrrins with High Fluorescence Quantum Yields. *Chem. Commun.* **2009**, 18, 2544–2546. https://doi.org/10.1039/b820141b.

(44) Saikawa, M.; Daicho, M.; Nakamura, T.; Uchida, J.; Yamamura, M.; Nabeshima, T. Synthesis of a New Family of Ionophores Based on Aluminum-Dipyrrin Complexes (ALDIPYs) and Their Strong Recognition of Alkaline Earth Ions. *Chem. Commun.* **2016**, *52*, 4014–4017. https://doi.org/10.1039/c6cc00250a.

(45) Sumiyoshi, A.; Chiba, Y.; Matsuoka, R.; Noda, T.; Nabeshima, T. Efficient Luminescent Properties and Cation Recognition Ability of Heavy Group 13 Element Complexes of N_2O_2- and N_2O_4-Type Dipyrrins. *Dalton Trans.* **2019**, *48*, 13169–13175. https://doi.org/10.1039/c9dt02403d.

(46) Godard, A.; Galán, L. A.; Rouillon, J.; Al Shehimy, S.; Tajani, W.; Cave, C.; Malacea-Kabbara, R.; Rousselin, Y.; Le Gendre, P.; Fihey, A.; Bendellaa, M.; Busser, B.; Sancey, L.; Le Guennic, B.; Bucher, C.; Maury, O.; Goze, C.; Bodio, E. Al(III) and Ga(III) Bisphenolate Azadipyrromethene-Based "N_2O_2" Complexes as Efficient NIR-

Fluorophores. *Inorg. Chem.* **2023**, *62*, 5067–5080. https://doi.org/10.1021/acs.inorgchem.2c03918.

(47) Cariño, C.; Proust, A.; Guillemot, G.; K/Bidi, L.; Blanchard, S.; A. Gibson, E.; Izzet, G. Unveiling Photoinduced Electron Transfers in Photosensitized Polyoxometalates for Solar Energy Conversion. *Chem. Sci.* **2025**, *16*, 19493–19518. https://doi.org/10.1039/D5SC04351D.

(48) Loudet, A.; Burgess, K. BODIPY Dyes and Their Derivatives: Syntheses and Spectroscopic Properties. *Chem. Rev.* **2007**, *107*, 4891–4932. https://doi.org/10.1021/cr078381n.

(49) Ulrich, G.; Ziessel, R.; Harriman, A. The Chemistry of Fluorescent Bodipy Dyes: Versatility Unsurpassed. *Angew. Chem. Int. Ed.* **2008**, *47*, 1184–1201. https://doi.org/10.1002/anie.200702070.

(50) Kryjewski, M.; Wicher, B.; Tykarska, E.; Rębiś, T. Mesityl-Substituted Azadipyrromethene Zinc(II) and Cobalt(II) Complexes – Structural, Spectroscopic and Electrochemical Properties. *Polyhedron* **2023**, *241*, 116473. https://doi.org/10.1016/j.poly.2023.116473.

(51) Knight, L.; Jimenez, J. C.; Tran, Q.; Zhao, M.; Pugh, M. H.; Brancel, C. D.; Zhang, H.; Li, R.; Yuan, Y.; Li, Y.; Zhu, L.; Sauvé, G. Tuning the Charge Transport Properties of Non-Planar Zinc(II) Complexes of Azadipyrromethenes Using Solubilizing Groups. *Mater. Adv.* **2024**, *5*, 6145–6153. https://doi.org/10.1039/D4MA00313F.

(52) Akhüseyin, E.; Türkmen, O.; Küçüköz, B.; Yılmaz, H.; Karatay, A.; Sevinç, G.; Xu, K.; Hayvali, M.; Yaglioglu, H. G. Two Photon Absorption Properties of Four

Coordinated Transition Metal Complexes of Tetraarylazadipyrromethene Compounds. *Phys. Chem. Chem. Phys.* **2016**, *18*, 4451–4459. https://doi.org/10.1039/C5CP06410D.

(53) Senevirathna, W.; Sauvé, G. Introducing 3D Conjugated Acceptors with Intense Red Absorption: Homoleptic Metal(II) Complexes of Di(Phenylacetylene) Azadipyrromethene. *J. Mater. Chem C,* **2013**, *1*, 6684–6694. https://doi.org/10.1039/c3tc31377h.

(54) Su, J.; Zhu, L.; Dong, Z.; Liu, M.; Zhang, F.; Li, X.; Wang, S.; Chen, Z. Triphenylamine-Functionalized Aza-BODIPY Dyes: Synthesis, Characterization, and Their Application as Hole Transport Materials in Perovskite Solar Cells. *Org. Chem. Front.* **2024**, *11*, 7044–7052. https://doi.org/10.1039/D4QO01616E.

(55) Bodio, E.; Goze, C. Development of BODIPYS and Aza-BODIPYs for Molecular Imaging Applications: From the in Vitro to the in Vivo; *Advances in Inorganic Chemistry*. **2021**, 78, 65–107. https://doi.org/10.1016/bs.adioch.2021.06.002.

(56) Gao, H.; Liu, H.; Jiang, L.; Gai, L.; Shen, Z. A Near-Infrared Benzoquinone-Coupled BODIPY: Synthesis, Spectroscopic and Electrochemical Properties. *J Porphyrins Phthalocyanines* **2019**, *23*, 76–83. https://doi.org/10.1142/S1088424619500044.

(57) Ivaniuk, K.; Pidluzhna, A.; Stakhira, P.; Baryshnikov, G. V.; Kovtun, Y. P.; Hotra, Z.; Minaev, B. F.; Ågren, H. BODIPY-Core 1,7-Diphenyl-Substituted Derivatives for Photovoltaics and OLED Applications. *Dyes Pigments* **2020**, *175*, 108123. https://doi.org/10.1016/j.dyepig.2019.108123.

(58) Didukh, N. O.; Yakubovskyi, V. P.; Zatsikha, Y. V.; Rohde, G. T.; Nemykin, V. N.; Kovtun, Y. P. Flexible BODIPY Platform That Offers an Unexpected Regioselective Heterocyclization Reaction toward Preparation of 2-Pyridone[*a*]-Fused BODIPYs. *J. Org. Chem.* **2019**, *84*, 2133–2147. https://doi.org/10.1021/acs.joc.8b03119.

(59) Zatsikha, Y. V.; Swedin, R. K.; Healy, A. T.; Goff, P. C.; Didukh, N. O.; Blesener, T. S.; Kayser, M.; Kovtun, Y. P.; Blank, D. A.; Nemykin, V. N. Synthesis, Characterization, and Electron-Transfer Properties of Ferrocene–BODIPY–Fullerene Near-Infrared-Absorbing Triads: Are Catecholopyrrolidine-Linked Fullerenes a Good Architecture to Facilitate Electron-Transfer? *Chem. Eur. J.* **2019**, *25*, 8401–8414. https://doi.org/10.1002/chem.201901225.

(60) Oyelowo, M.; Jeaydi, T. I.; Ziegler, C. J.; Nemykin, V. N. Design of Stable Diradicals Based on Group 13 Dyes of N_2O_2 -Bis(Phenolate) Aza-Dipyrromethene and Aza-BODIPY. *Inorg. Chem.* **2025**, 64, 17946–17959. https://doi.org/10.1021/acs.inorgchem.5c03026.

(61) Cordeiro, P.; Menezes, V.; Ebersol, C.; Gomes, J. P. M.; Lião, L. M.; Braga, A. L.; Neto, J. S. S.; Nascimento, V. BODIPY Dyes: From Chalcogen-Based Synthesis to Emerging Applications and Sulfur Compound Detection. *Dyes Pigments* **2025**, *242*, 112985. https://doi.org/10.1016/j.dyepig.2025.112985.

(62) An, D.; Jiang, W.; Zhang, Z.; Wang, S.; Wang, W.; Miao, C.; Shao, J.; Dong, X. Aza-BODIPY Dye with D-π-A Architecture for 1064 nm Laser-Triggered Photothermal Theranostics. *Sens. Actuators B Chem.* **2025**, *442*, 138144. https://doi.org/10.1016/j.snb.2025.138144.

(63) Mastroeni, P. J.; Armstrong, C. B.; Black, D. J.; Strickland, A.; Hall, M.; Blundell, T.; Pridmore, N. E.; Pal, R.; Stachelek, P. Synthesis, Characterisation and Application of Red-Emitting BODIPY Dyes for Multiphoton Microscopy of Lipid Droplets. *Dyes Pigments* **2025**, *243*, 113045. https://doi.org/10.1016/j.dyepig.2025.113045.

(64) Oyelowo, M.; Schaffner, J. W.; Jeaydi, T. I.; Blank, D. A.; Ziegler, C. J.; Nemykin, V. N. Introducing of an Unexplored Aza-BODIPY Diradicaloids with 4-(2,6-Di *Tert* -Butyl)Phenoxyl Radicals Located in 1,7-Positions of the Aza-BODIPY Core. *Inorg Chem* **2024**, *63*, 24008–24021. https://doi.org/10.1021/acs.inorgchem.4c04409.

(65) Ali, I.; Afshan, G.; Singh, V. D.; Dutta, A.; Pandey, D. S. Efficacy of Redox-Active Cu(II) Dipyrrin Complexes toward Electrochemical Reduction of CO2. *Inorg. Chem.* **2025**, *64*, 5893–5903. https://doi.org/10.1021/acs.inorgchem.4c04204.

(66) Zhou, H.; Ishikawa, K.; Yoshimura, T.; Matera, K. M.; Fujii, H.; Sakaue, T.; Ikeda-Saito, M. Oxygen and One Reducing Equivalent Are Both Required for the Conversion of α-Hydroxyhemin to Verdoheme in Heme Oxygenase. *J. Biol. Chem.* **1996**, *271* (12), 6618–6624, DOI: 10.1074/jbc.271.12.6618.

(67) Naoda, K.; Shimizu, D.; Kim, J. O.; Furukawa, K.; Kim, D.; Osuka, A. Thienylquinonoidal Porphyrins and Hexaphyrins with Singlet Diradical Ground States. *Chem. – Eur. J.* **2017**, *23*, 8969–8979. DOI: 10.1002/chem.201701355.

(68) Hill, J. P.; Hewitt, I. J.; Anson, C. E.; Powell, A. K.; McCarty, A. L.; Karr, P. A.; Zandler, M. E.; D'Souza, F. Highly Nonplanar, Electron Deficient, N-Substituted *tetra*-Oxocyclohexadienylidene Porphyrinogens: Structural, Computational, and

Electrochemical Investigations. *J. Org. Chem.* **2004**, *69*, 5861–5869. DOI: 10.1021/jo049401d.

(69) Shimizu, D.; Osuka, A. Porphyrinoids as a platform of stable radicals. *Chem. Sci*. **2018**, 9, 1408-1423. DOI: 10.1039/C7SC05210C

(70) Cong, L.; Chahal, M. K.; Osterloh, R.; Sankar, M.; Kadish, K. M. Synthesis, Electrochemistry, and Reversible Interconversion among Perhalogenated Hydroxyphenyl Ni(II) Porphyrins, Porphodimethenes, and Porpho-5,15-Bis-Paraquinone Methide. *Inorg. Chem.* **2019**, *58*, 14361–14376. https://doi.org/10.1021/acs.inorgchem.9b01642.

(71) Labella, J.; Azizi, K.; Guldi, D. M.; Torres, T. Azaporphyrinoid-Based Photo- and Electroactive Architectures for Advanced Functional Materials. *Adv. Mater.* **2025**, *37*, 2514429. DOI: 10.1002/adma.202514429.

(72) Rothera, J. G.; Taing, H.; Cruz, M.; Dmitrienko, A.; Vukotic, V. N.; Ryno, S. M.; Risko, C.; Raj, A. M.; Skene, W. G.; Eichhorn, S. H. Panchromatic Absorption of Unsymmetrical Donor–Acceptor Dyes Based on a Meta-Conjugated 1,3,5-Heteroaryltriazine Core. *Chem. Eur. J.* **2025**, *31*, e202403860. DOI: 10.1002/chem.202403860.

(73) Labella, J.; Laforga-Martín, J. B.; Torres, T. Porphyrinic Acceptors for Fullerene-Free Molecular Photovoltaics. *CCS Chem.* **2024**, *6*, 124–146. DOI: 10.31635/ccschem.023.202303395.

(74) Li, Y.; Wang, J.; Zhang, X.; Wang, H.; Gao, X.; Li, C.; Wang, Z. Triphenylamine-Functionalized Aza-BODIPY Dyes: Synthesis, Characterization, and

Their Application as Hole Transport Materials in Perovskite Solar Cells. *Org. Chem. Front.* **2024**, *11*, 7044–7052. DOI: 10.1039/D4QO01616E.

(75) Song, X.; Xu, Y.; Tao, X.; Gao, X.; Wu, Y.; Yu, R.; He, Y.; Tao, Y. BODIPY Cored A–D–A′–D–A Type Nonfused-Ring Electron Acceptor for Efficient Polymer Solar Cells. *Macromol. Rapid Commun.* **2022**, *43* (6), 2100828. https://doi.org/10.1002/marc.202100828

(76) Kubo, Y.; Watanabe, K.; Nishiyabu, R.; Hata, R.; Murakami, A.; Shoda, T.; Ota, H. Near-Infrared Absorbing Boron-Dibenzopyrromethenes That Serve as Light-Harvesting Sensitizers for Polymeric Solar Cells. *Org. Lett.* **2011**, *13* (17), 4574–4577. https://doi.org/10.1021/ol201770g.

(77) Wang, C.; Daddario, C.; Pejić, S.; Sauvé, G. Synthesis and Properties of Azadipyrromethene-Based Complexes with Nitrile Substitution. *Eur. J. Org. Chem.* **2020**, *2020*, 714–722. https://doi.org/10.1002/ejoc.201901736.

(78) Lu, C.; Wang, C.; Jimenez, J. C.; Rheingold, A. L.; Sauvé, G. Large Non-Planar Conjugated Molecule with Strong Intermolecular Interactions Achieved with Homoleptic Zn(II) Complex of Di(5-Quinolylethynyl)-Tetraphenylazadipyrromethene. *ACS Omega* **2020**, *5*, 31467–31472. https://doi.org/10.1021/acsomega.0c05169.

(79) Patil, Y. Emerging BODIPY-Based NonFullerene Acceptors: Innovations for Organic Solar Cells. *Chem. Eur. J.* **2025**, *31*, e02963 (1–12). https://doi.org/10.1002/chem.202502963.

(80) Zhao, M.; Jimenez, J. C.; Wang, C.; Rui, G.; Ma, T.; Lu, C.; Rheingold, A. L.; Li, R.; Zhu, L.; Sauvé, G. Monofluorination of Naphthyls Promotes the Cofacial π–π

Stacking and Increases the Electron Mobility of Non-Planar Zinc(II) Complexes of Di(Naphthylethynyl)Azadipyrromethene. *The J. Phys. Chem. C* **2022**, *126*, 6543–6555. https://doi.org/10.1021/acs.jpcc.1c09734.

(81) Wang, C.; Wei, P.; Ngai, J. H. L.; Rheingold, A. L.; Gray, T. G.; Li, Y.; Pentzer, E.; Li, R.; Zhu, L.; Sauvé, G. A Zinc(II) Complex of Di(Naphthylethynyl)Azadipyrromethene with Low Synthetic Complexity Leads to OPV with High Industrial Accessibility. *J. Mater. Chem. A* **2019**, *7*, 24614–24625. https://doi.org/10.1039/C9TA08654D.

(82) Labella, J.; Labrador-Santiago, J.; Holgado, D.; Torres, T. Effects of Removing Boron from Subphthalocyanines: A Theoretical Perspective. *Dalton Trans.* **2025**, *54*, 5355–5366. https://doi.org/10.1039/D4DT03173C.

(83) Guggenberger, L. J.; Prewitt, C. T.; Meakin, P.; Trofimenko, S.; Jesson, J. P. Crystal Structure and Single-Crystal Electron Paramagnetic Resonance Data for Bis[Dihydrobis(1-Pyrazolyl)Borato]Cobalt(II). *Inorg. Chem.* **1973**, *12*, 508–515. https://doi.org/10.1021/ic50121a002.

(84) Sheldrick, G. M. A short history of *SHELX*. *Acta Crystallogr.* **2008**, *A64*, 112-122. DOI: 10.1107/S0108767307043930.

(85) *Bruker-AXS APEX3 v2016.1-0*, Madison, Wisconsin, USA, **2016**.

(86) Spek, A. L. Structure validation in chemical crystallography. *Acta Crystallogr.* **2009**, *D65*, 148-155. DOI: 10.1107/S090744490804362X.

(87) Macrae, C. F.; Sovago, I.; Cottrell, S. J.; Galek, P. T. A.; McCabe, P.; Pidcock, E.; Platings, M.; Shields, G. P.; Stevens, J. S.; Towler, M.; Wood, P. A. Mercury 4.0:

from visualization to analysis, design and prediction. *J. Appl. Crystallogr.* **2020**, *53*, 226-235. DOI: 10.1107/S1600576719014092.

(88) Frisch, M. J.; Trucks, G. W.; Schlegel, H. B.; Scuseria, G. E.; Robb, M. A.; Cheeseman, J. R.; Scalmani, G.; Barone, V.; Petersson, G. A.; Nakatsuji, H.; Li, X.; Caricato, M.; Marenich, A. V.; Bloino, J.; Janesko, B. G.; Gomperts, R.; Mennucci, B.; Hratchian, H. P.; Ortiz, J. V.; Izmaylov, A. F.; Sonnenberg, J. L.; Williams-Young, D.; Ding, F.; Lipparini, F.; Egidi, F.; Goings, J.; Peng, B.; Petrone, A.; Henderson, T.; Ranasinghe, D.; Zakrzewski, V. G.; Gao, J.; Rega, N.; Zheng, G.; Liang, W.; Hada, M.; Ehara, M.; Toyota, K.; Fukuda, R.; Hasegawa, J.; Ishida, M.; Nakajima, T.; Honda, Y.; Kitao, O.; Nakai, H.; Vreven, T.; Throssell, K.; Montgomery, J. A., Jr.; Peralta, J. E.; Ogliaro, F.; Bearpark, M. J.; Heyd, J. J.; Brothers, E. N.; Kudin, K. N.; Staroverov, V. N.; Keith, T. A.; Kobayashi, R.; Normand, J.; Raghavachari, K.; Rendell, A. P.; Burant, J. C.; Iyengar, S. S.; Tomasi, J.; Cossi, M.; Millam, J. M.; Klene, M.; Adamo, C.; Cammi, R.; Ochterski, J. W.; Martin, R. L.; Morokuma, K.; Farkas, O.; Foresman, J. B.; Fox, D. J. *Gaussian 16, Revision B.01*; Gaussian, Inc.: Wallingford CT, **2016**.

(89) Tenderholt, A. L. *QMForge, version 2.1*; Standord University: Stanford, CA, **2011**. https://qmforge.net/.

(90) Tao, J. M.; Perdew, J. P.; Staroverov, V. N.; Scuseria, G. E. Climbing the density functional ladder: Nonempirical metageneralized gradient approximation designed for molecules and solids. *Phys. Rev. Lett.* **2003**, *91*, 146401(1−4). https://doi.org/10.1103/PhysRevLett.91.146401

(91) Staroverov, V. N.; Scuseria, G. N.; Tao, J.; Perdew, J. P.m Comparative assessment of new nonempirical density functional: Molecules and hydrogen-bonded complexes. *J. Chem. Phys.* **2003**, *119*, 12129-12137. https://doi.org/10.1063/1.1626543.

(92) McLean, A. D.; Chandler, G. S. Contracted Gaussian Basis Sets for Molecular Calculations. I. Second Row Atoms, Z = 11−18. *J. Chem. Phys*. **1980**, 72, 5639−5648. https://doi.org/10.1063/1.438980

(93) Wachters, A. J. H. Gaussian Basis Set for Molecular Wavefunctions Containing Third-Row Atoms. *J. Chem. Phys.* **1970**, *52*, 1033–1036. DOI: 10.1063/1.1673095.

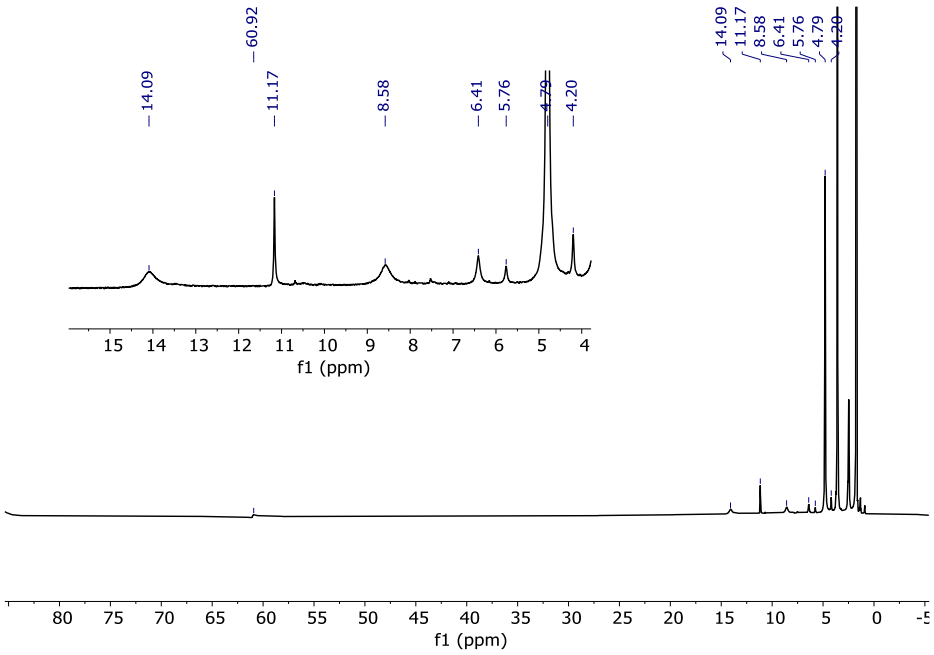


Figure 4.22: ^{1}H NMR of compound **4.1a** in THF-d_8.

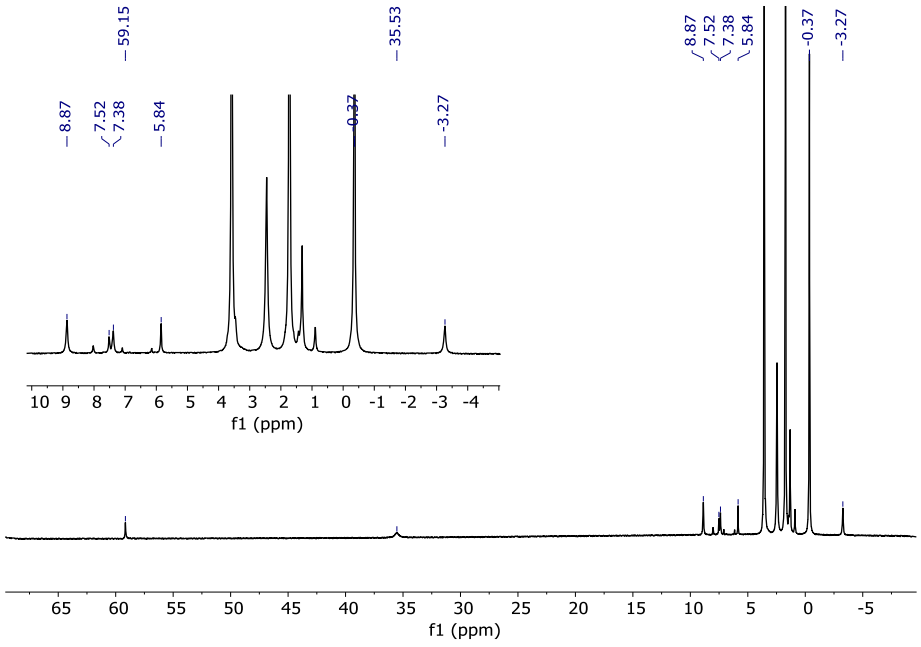


Figure 4.23: ^{1}H NMR of compound **4.1b** in THF-d_8.

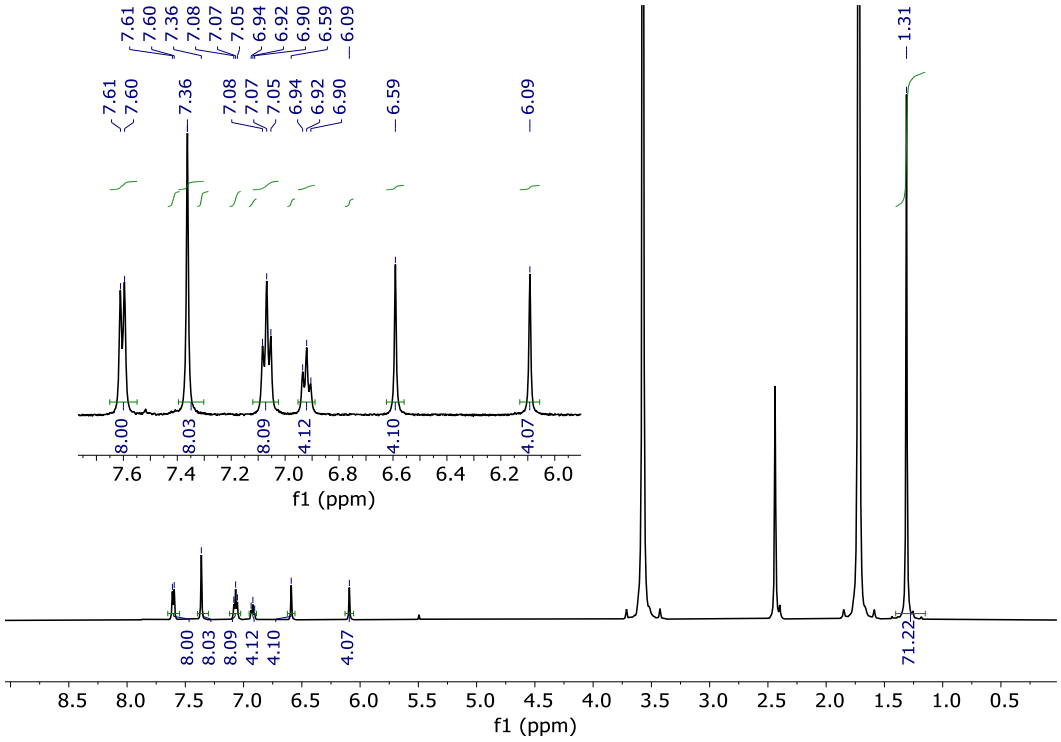


Figure 4.24: ^{1}H NMR of compound **4.1d** in THF-d_8.

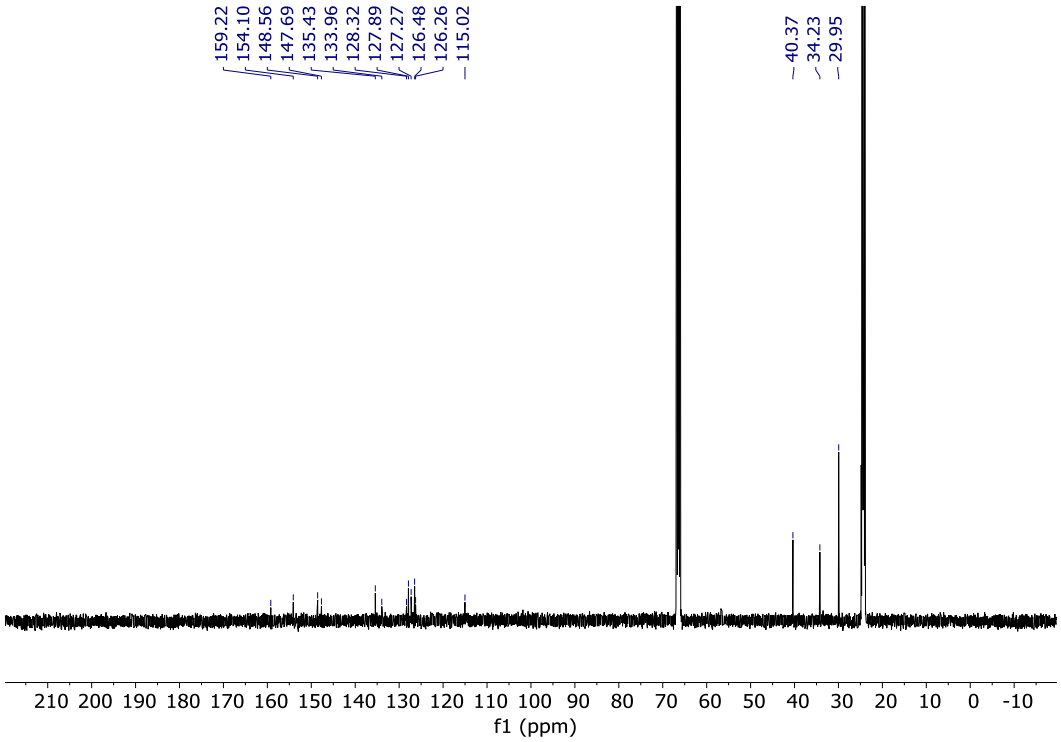


Figure 4.25: ^{13}C NMR of compound **4.1d** in THF-d_8.

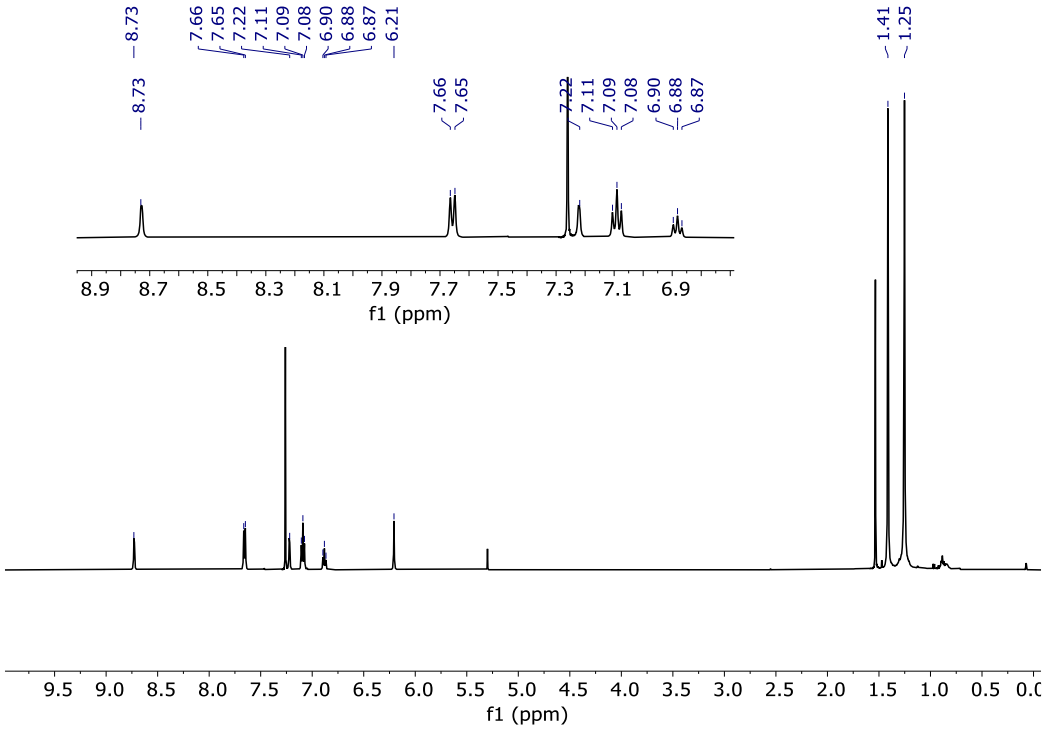


Figure 4.26: ^{1}H NMR of compound **4.2b** in $CDCl_3$.

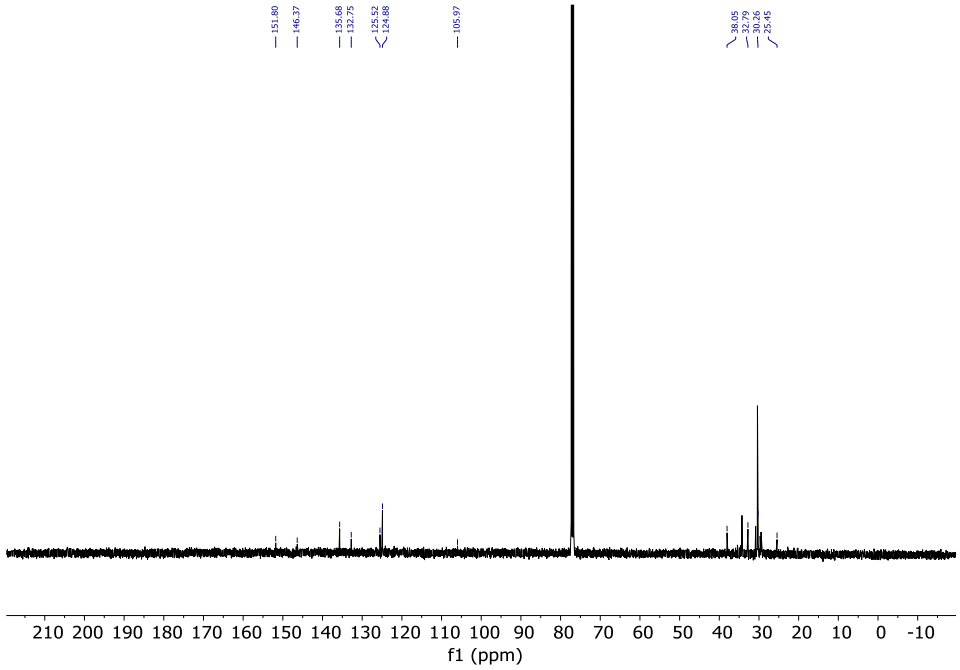


Figure 4.27: ^{13}C NMR of compound **4.2b** in Chloroform-$CDCl_3$.

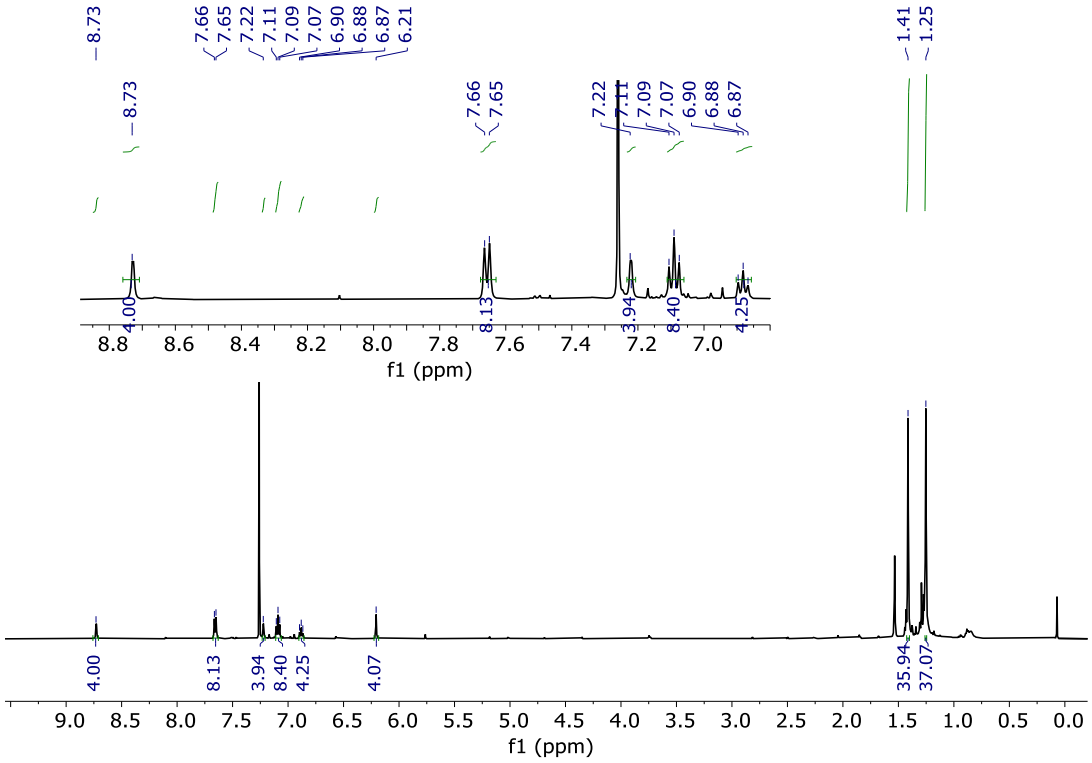


Figure 4.28: ^{1}H NMR of compound **4.2d** in $CDCl_3$.

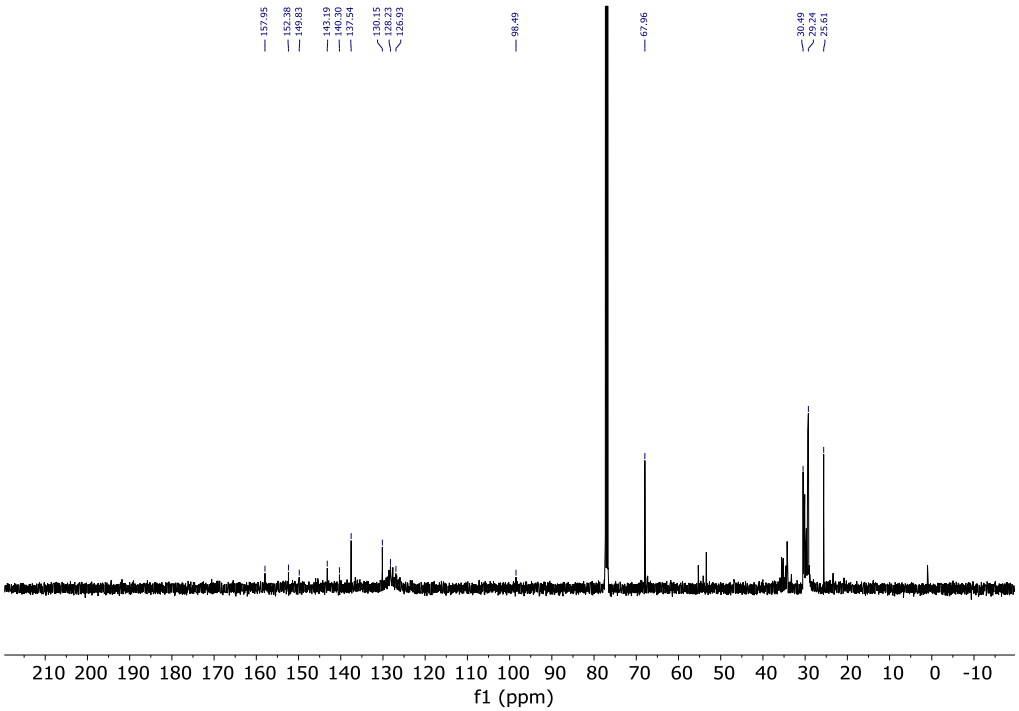


Figure 4.29: ^{13}C NMR of compound **4.2b** in Chloroform-$CDCl_3$.

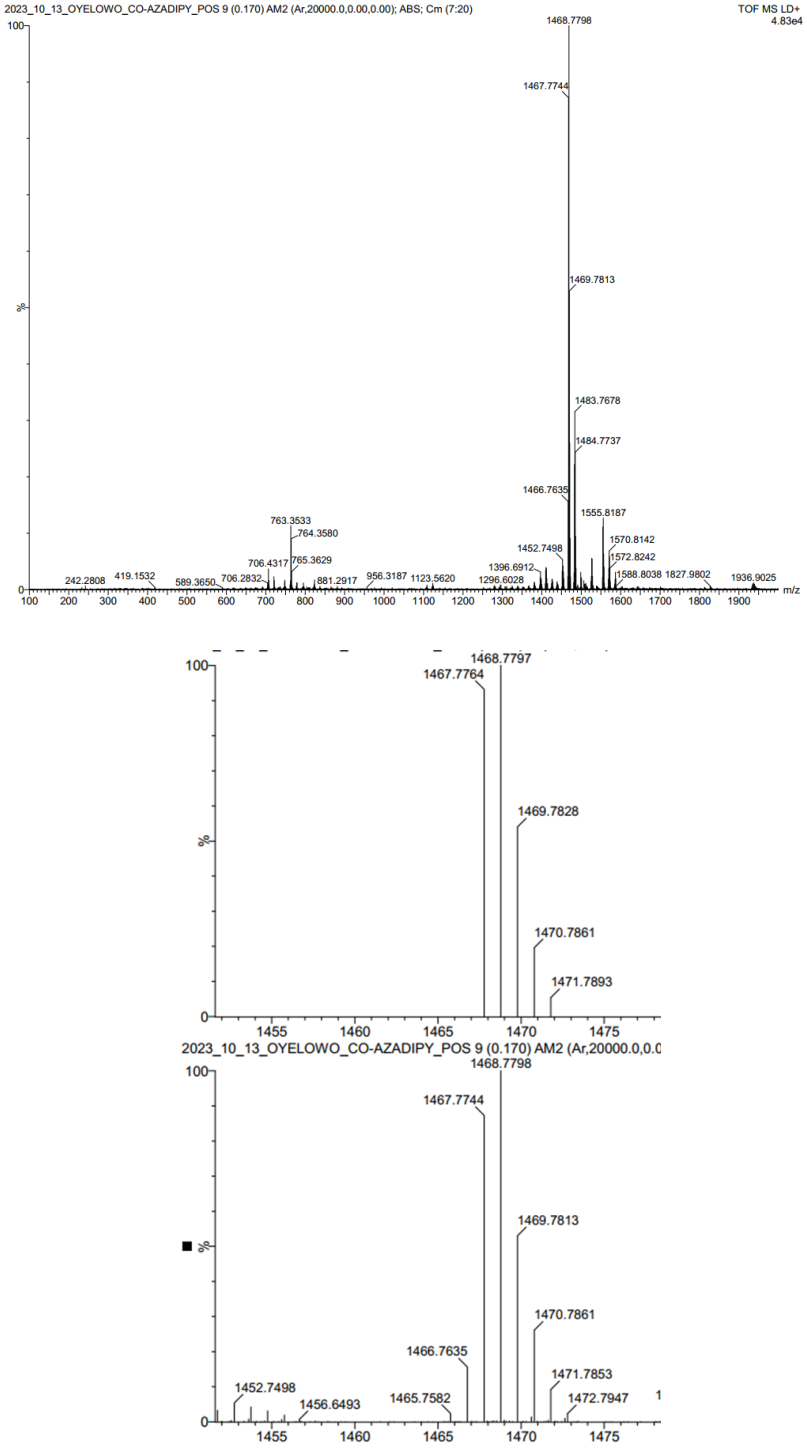


Figure 4.30: **Mass spectrum of complex 4.1a (MALDI).**

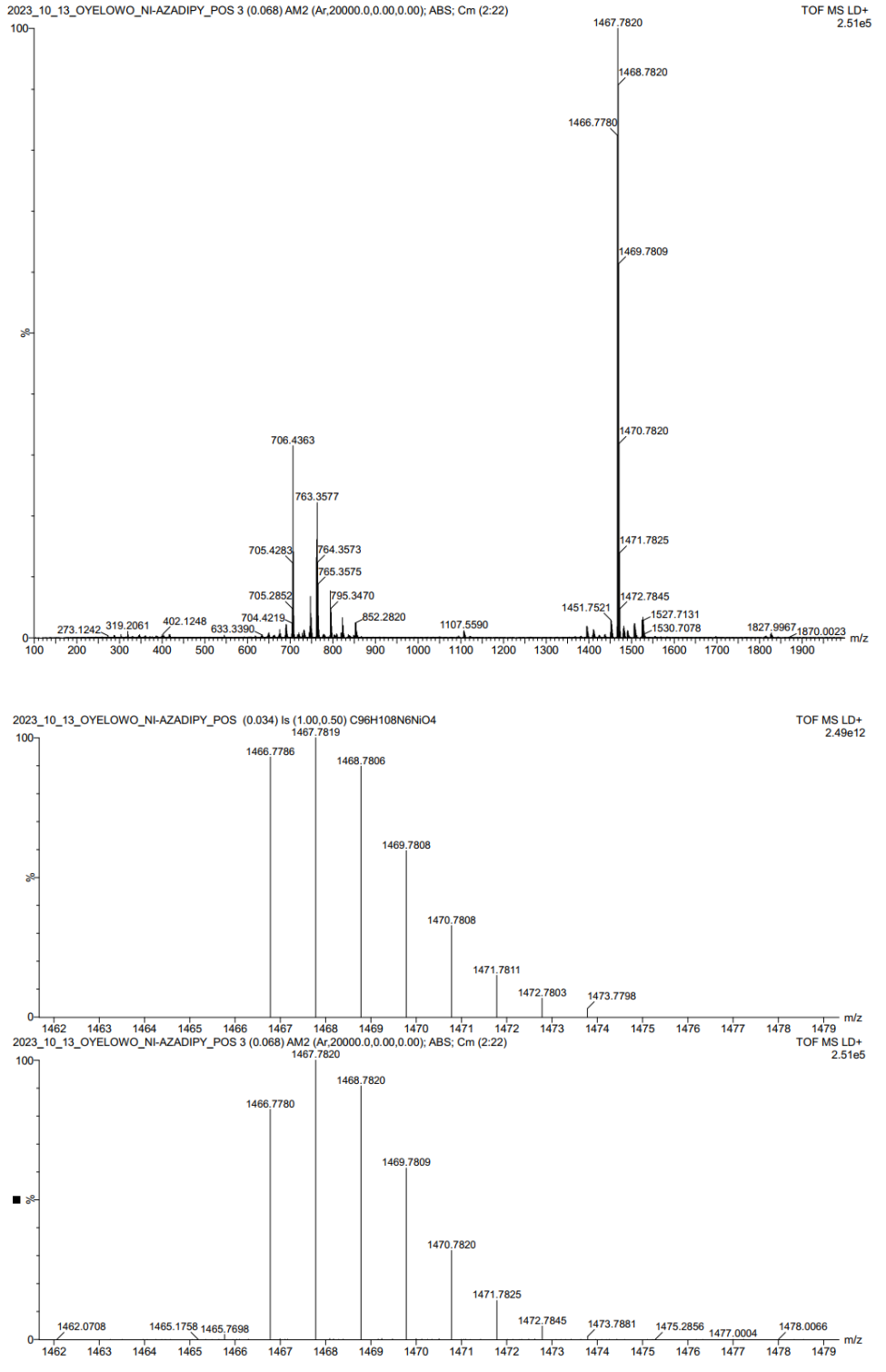


Figure 4.31: **Mass spectrum of complex 4.1b (MALDI).**

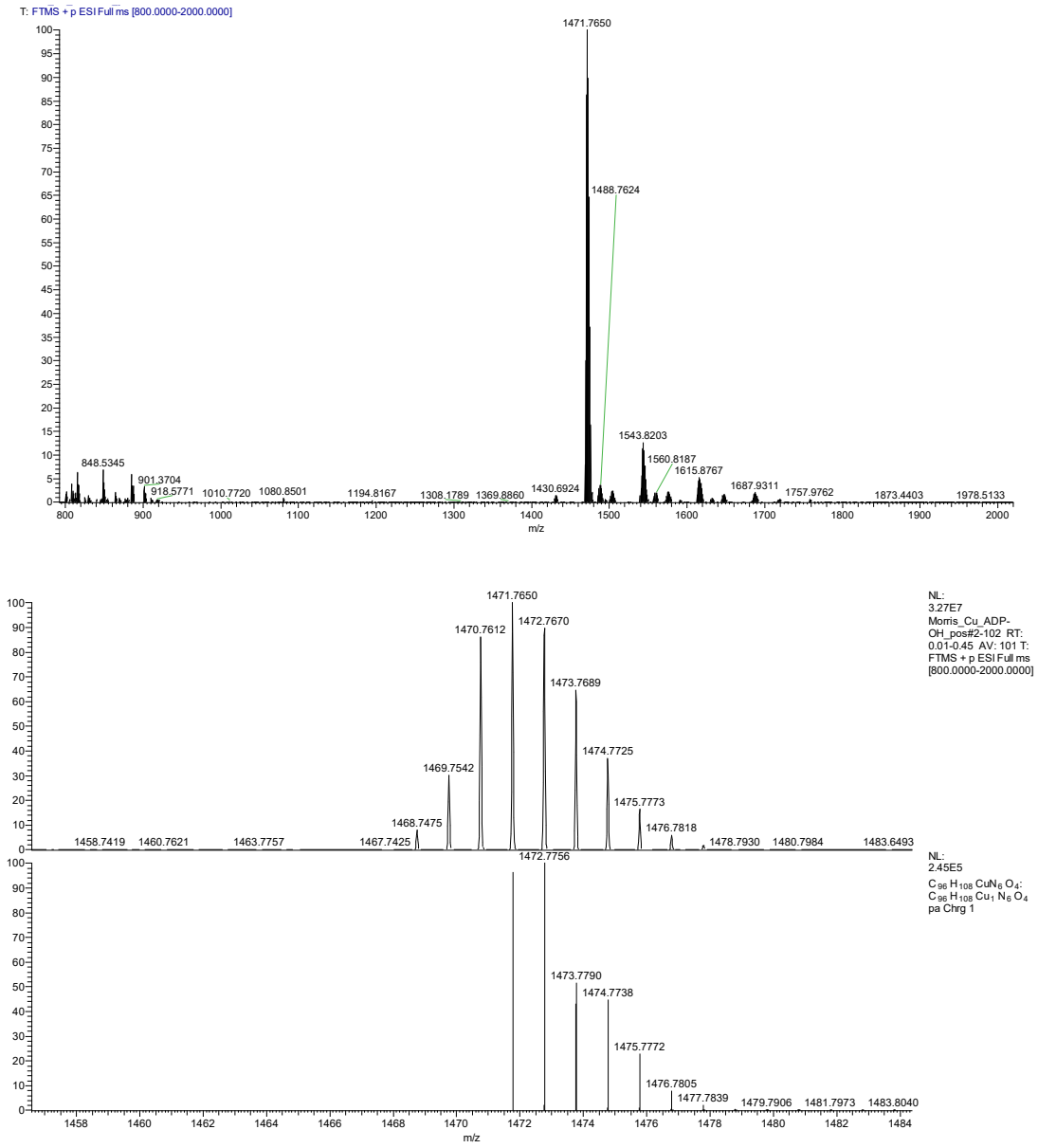


Figure 4.32: **Mass spectrum of complex 4.1c (ESI).**

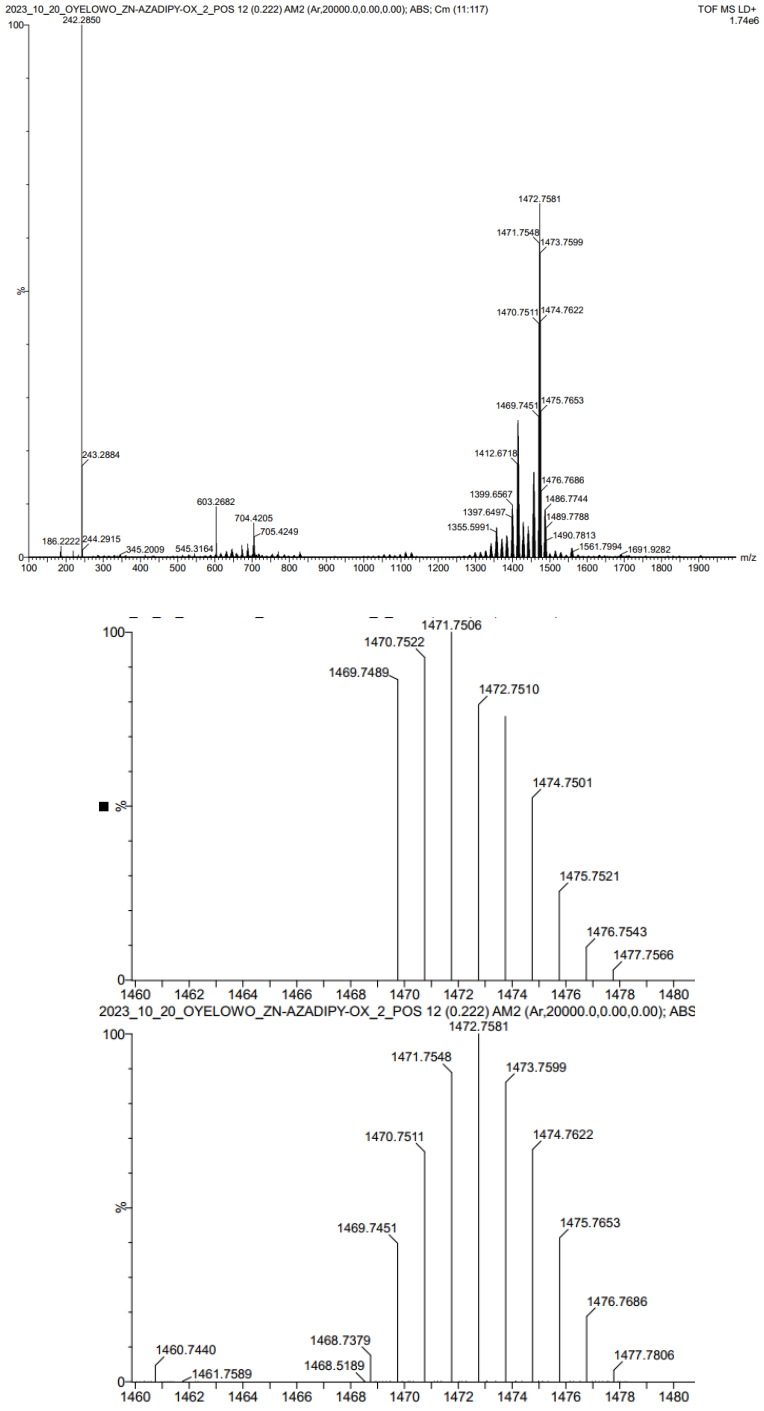


Figure 4.33: **Mass spectrum of complex 4.1d (MALDI).**

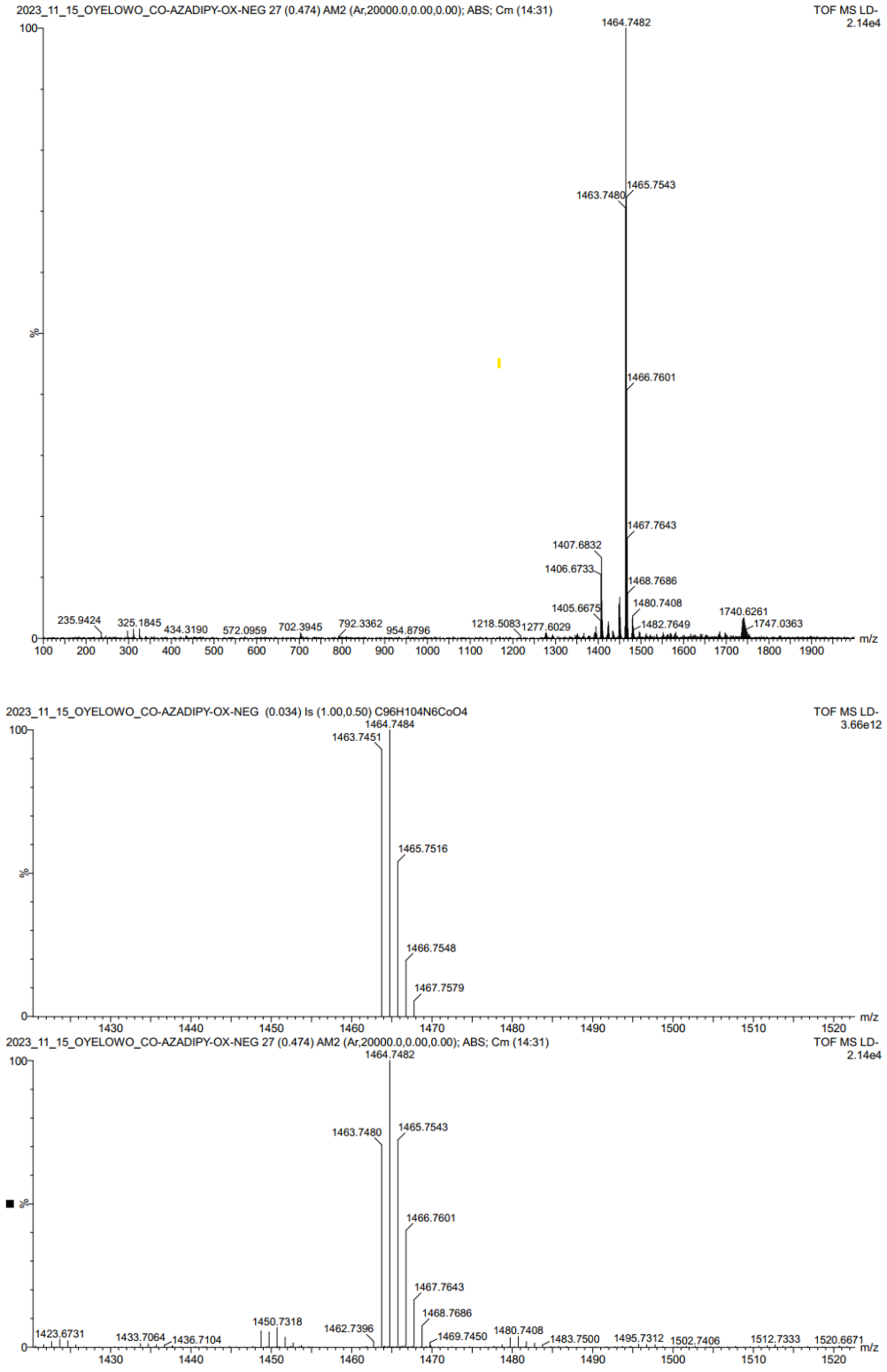


Figure 4.34: **Mass spectrum of complex 4.2a (MALDI).**

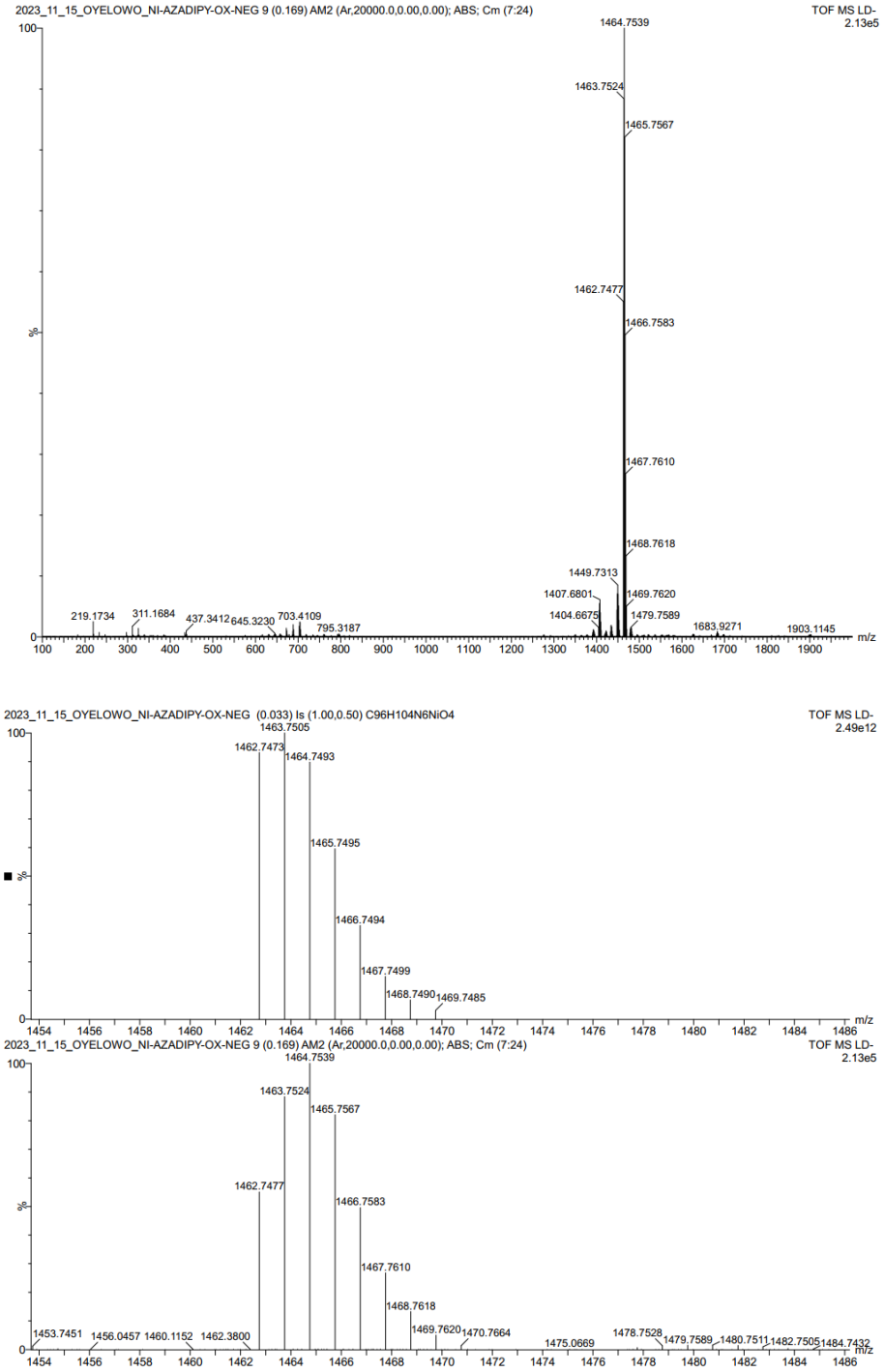


Figure 4.35: **Mass spectrum of complex 4.2b (MALDI).**

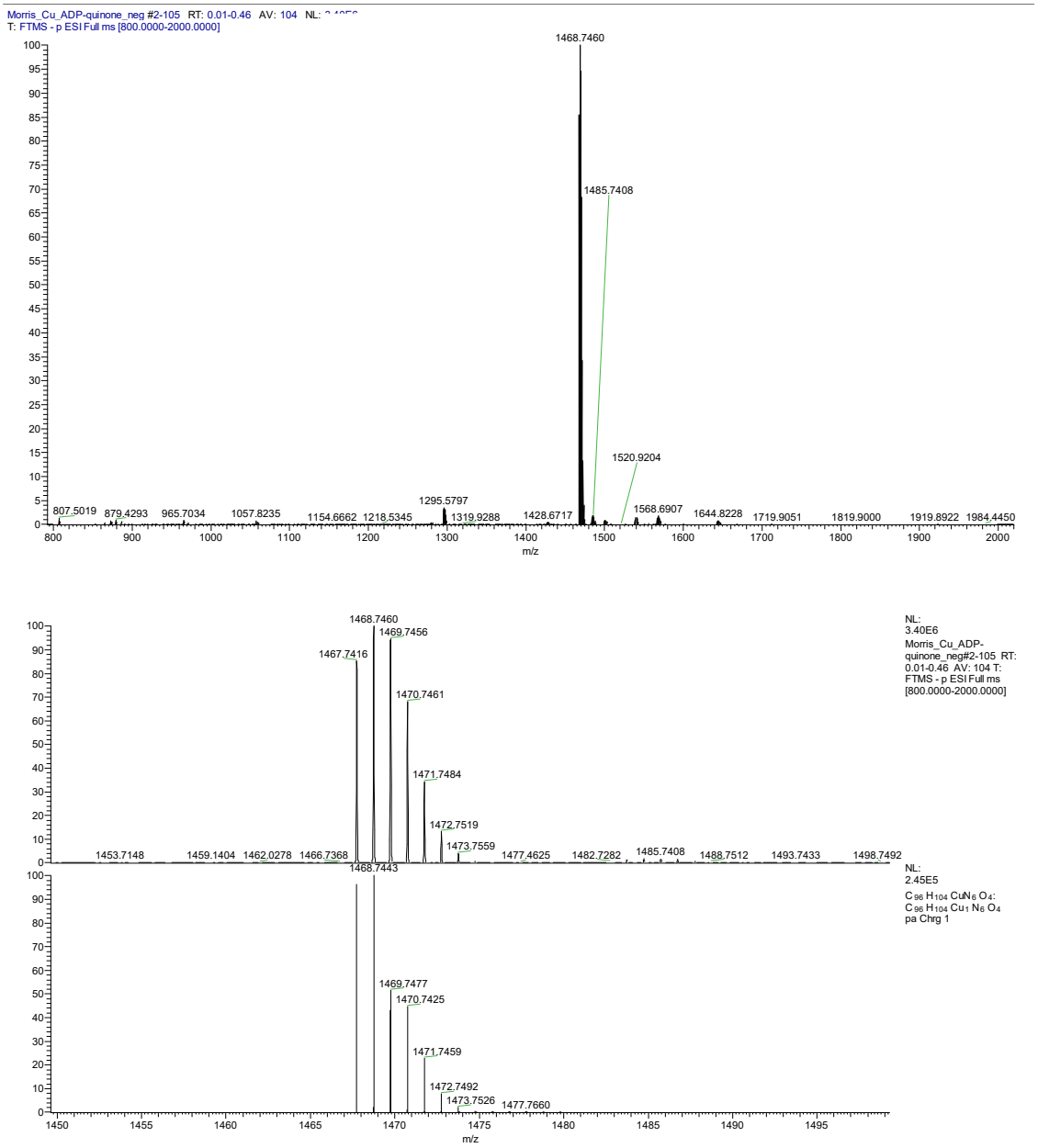


Figure 4.36: **Mass spectrum of complex 4.2c (ESI).**

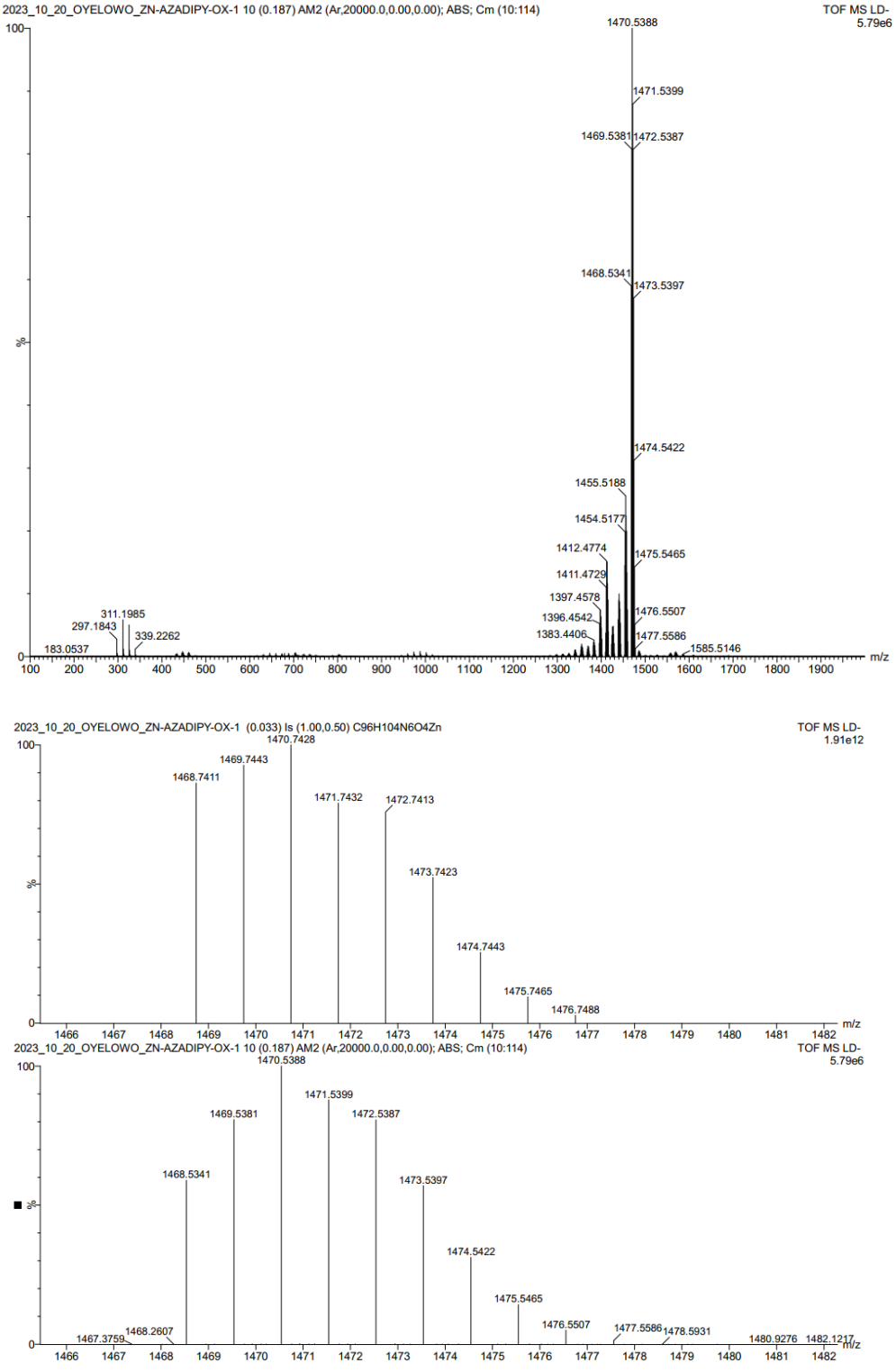


Figure 4.37: **Mass spectrum of complex 4.2d (MALDI).**

CHAPTER V: TRYING TO CRACK THE SHELL: INVESTIGATING THE MAGNETIC PROPERTIES AND ELECTRONIC STRUCTURES OF REDOX-ACTIVE ESTER-SUBSTITUTED BODIPY-BENZOQUINONE DIRADICALOID

A version of this chapter has been accepted for publication by Morris Oyelowo, Andrii Hotynchan, Wei-Yuan Chen, Towhidi Illius Jeaydi, Yuriy P. Kovtun, Christopher J. Ziegler,[c] and Victor N. Nemykin:

In this research article, I performed characterization including variable temperature NMR, SQUID magnetometry, electrochemistry, spectroelectrochemistry, FT-IR, UV/Vis absorption and fluorescence emission. I also grew the crystals used for X-ray diffractions. Andrii Hotynchan synthesized all compounds studied and helped in writing a part of the introduction session. Towhidi Illius jeaydi carried out variable temperature EPR experiment only. Dr. Christopher Ziegler facilitated the variable temperature EPR and helped in proofreading the manuscript. Dr. Yuriy P. Kovtun designed the compounds under study and proofread the manuscript. Dr. Viktor Nemykin helped with DFT and TDDFT calculations. He also assisted in editing and proofreading the manuscript.

5.1 ABSTRACT

BODIPY dyes with extended conjugation and redox-active substituents are promising chromophores for accessing open-shell electronic structures relevant to molecular electronics and spintronics. We report the synthesis of a BODIPY **5.3**, which bears ester substituents at the 2,6-positions and is coupled to a benzoquinone unit through an ethanediylidene linker. The hydroxyphenyl precursor, **5.2**, was obtained via Knoevenagel condensation and oxidized chemically or electrochemically to yield the benzoquinone-BODIPY **5.3** conjugate. Magnetic properties of **5.3** were probed by EPR spectroscopy, VT ^{1}H NMR spectroscopy, and DFT/TDDFT calculations. The

benzoquinone-BODIPY **5.3** exhibited a predominantly closed-shell singlet ground state, with the open-shell singlet and triplet states being higher in energy, consistent with the absence of a room-temperature EPR signal in solution. Electrochemistry and spectroelectrochemistry revealed stepwise oxidation from the dianionic precursor $\mathbf{[5.5]^{2-}}$ to a mixed-valence anion-radical $\mathbf{[5.4]^{\cdot-}}$, featuring a broad IVCT band at 1980 nm (TDDFT-predicted at 1790 nm), before full conversion to BODIPY **5.3**. These results demonstrate fine-tuning of diradical character and charge-transfer behavior in BODIPY chromophores through conjugation and redox modulation. We also discovered the formation of an unexpected blue-colored BODIPY dimer **5.6** upon treatment of compound **5.3** with methanol. In this dimer, two BODIPY units are connected by a single sp^3-sp^3 carbon bond located at the carbon atoms directly attached to the α-position of the BODIPY core.

5.2 INTRODUCTION

Borondipyrromethene and aza-borondipyrromethene (BODIPY and aza-BODIPY, respectively) dyes represent a versatile class of chromophores with exceptional photophysical and electrochemical properties,[1–25] making them attractive scaffolds for applications ranging from fluorescence imaging[5,9,26,27] and photodynamic therapy[4,28,29] to organic electronics and molecular spintronics.[13,30,31] Their structural tunability,[32,33] high molar absorptivity,[34,35] and remarkable chemical stability[36,37] have positioned BODIPY derivatives at the forefront of functional dye chemistry.[2,28,38,39] Among the many strategies to modulate their properties, extending π-conjugation,[40,41] functionalization at the 2,6-positions of the dipyrrin core,[42–44] and covalent coupling with redox-active

moieties[45,46] have emerged as particularly powerful approaches. Such modifications can not only shift optical absorption profiles into the visible and near-infrared regions, but also engender novel ground state electronic structures, including monoradical, diradical, and multiradical character, which are of fundamental and technological significance.[46–51] The design and stabilization of organic diradicals and diradicaloids have recently attracted considerable attention due to their unusual magnetic and electronic properties.[52–61] Systems with appreciable diradical character can display low-energy electronic transitions,[52,62] enhanced nonlinear optical responses,[50] unique spin-polarization phenomena,[63] and even potential utility as organic spin carriers.[53,58,64–73] In BODIPY chemistry, the introduction of electron-withdrawing substituents at the 2,6-positions and extension of conjugation *via* vinylene or styryl linkers have been shown to favorably tune the energy gap between frontier molecular orbitals,[43,74,75] thereby increasing the possibility of diradical contributions in the ground state. Moreover, covalent integration of BODIPY cores with redox-active units, such as hydroxyphenyl or benzoquinone groups, provides a platform to interrogate the interplay between redox chemistry, conjugation, and magnetic ground states.[14,49,51]

In the series of oxidized BODIPYs shown below (Figure 1), despite their formal similarities, the compounds belong to distinctly different chromophoric systems. Compound **5.1**[76] is a typical polyene, characterized by a broad, low-intensity absorption band centered at approximately 450 nm.[76]

The introduction of substituents that induce a diradical character leads either to a distinct EPR signal as observed in compound **5.2**,[14] and its analogues or to a solvent-dependent

response. For instance, in compound **5.3**,[49] the signal is negligible in nonpolar solvents but becomes detectable in DMF.[49] Despite the structural divergence between compounds **5.2** and **5.3**, they share a highly specific absorption profile: a sharp, intense band between 350 - 450 nm and a broader, less intense NIR band (700–950 nm) featuring two distinct maxima. These shared features suggest a common 'optical signature' for this class of structures. In the paper describing the structure of **5.4**,[74] there is no mention of radical states and EPR investigations, but the absorption spectrum very clearly demonstrates the same optical signature,[74] which is probably a strong argument in favor of the existence of a diradicaloid form. That is why the search for the diradicaloid state and a more thorough physicochemical study of analogues of compound **5.4** was one of the main prerequisites of our work.

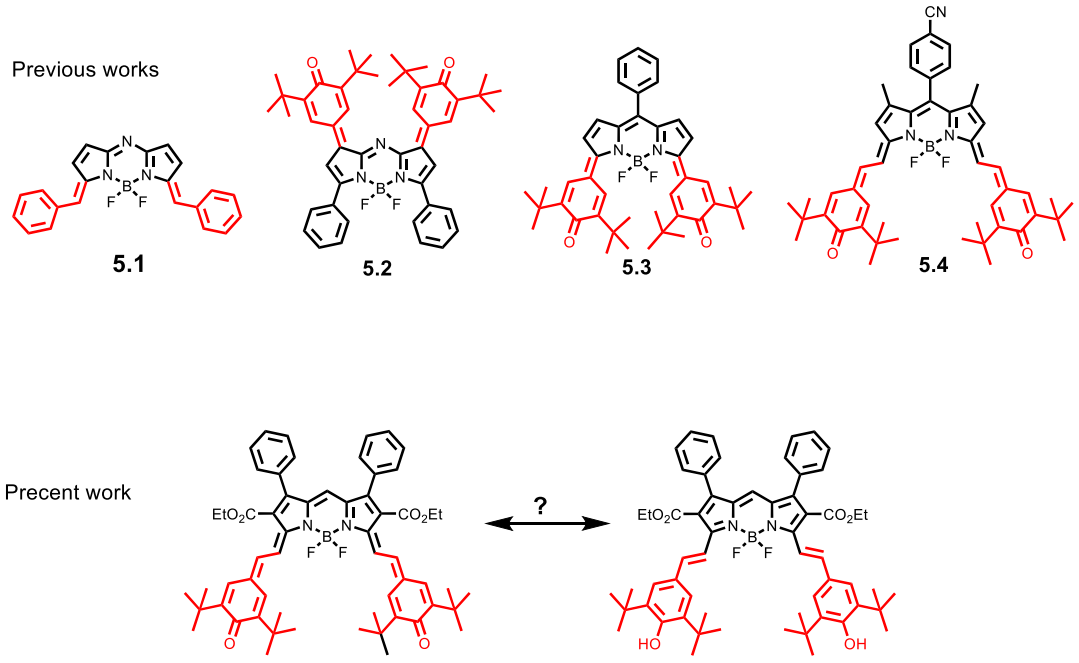
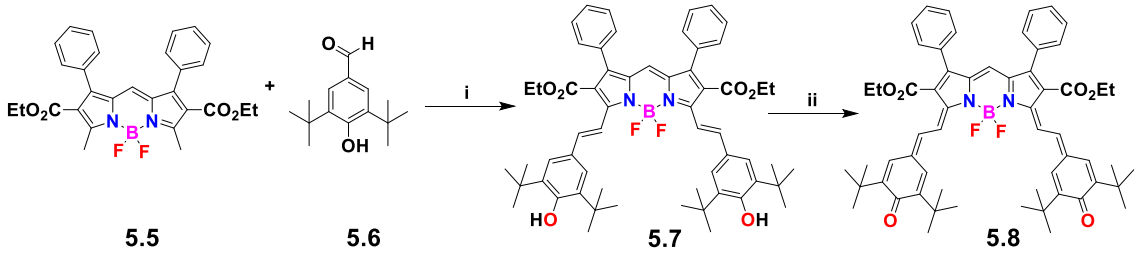


Figure 5.1: Representative examples of BODIPYs and aza-BODIPYs related to this work.

In this context, we hypothesized that BODIPY dyes bearing ester substituents at the 2,6-positions and coupled to benzoquinone groups through an ethanediylidene linker would exhibit enhanced diradical character. The electron-withdrawing ester groups are expected to stabilize charge-separated resonance structures, while the quinone methide fragment provides extended conjugation between the BODIPY core and appended redox-active units. Such a design should lower the HOMO–LUMO energy gap, thereby stabilizing open-shell singlet ground states. Importantly, the quinone methide moiety serves as both an electron acceptor and a redox switch, enabling systematic exploration of the electronic structure across different oxidation states.

5.3 Results and Discussion

5.3.1 Synthesis and characterization of BODIPYs 5.7 and 5.8



Scheme 5.1. Synthetic pathways to BODIPY **5.8**. Reagents and conditions: (i) acetic acid, piperidine, toluene, reflux 48 hours (ii) DDQ, DCM, RT, 15 min.

BODIPY **5.7** was prepared according to the previously reported method46,50 as shown in Scheme **5.**1. Knoevenagel condensation of BODIPY **5.5** with 3,5-di-tert-butyl-4-hydroxybenzaldehyde **5.6** and a catalytic amount of piperidine and acetic acid in refluxing toluene afforded BODIPY **5.7**. We prepared its benzoquinone derivative

BODIPY **5.8** in excellent yield by chemically oxidizing BODIPY **5.7** with DDQ in DCM. Chemical structures of BODIPYs **5.7** and **5.8** were confirmed by ^{1}H and ^{13}C NMR spectroscopy, as well as high-resolution mass spectrometry.

5.3.2 Photophysical Studies

The UV-Vis-NIR absorption spectra of BODIPYs **5.7** and **5.8** were studied in DCM (Figure 5.2 and Table 5.1). The absorption spectrum of BODIPY **5.7** shows four bands at 678, 468, 396, and 331 nm. The maximum absorption band at 678 nm has a blue-shifted shoulder at 624 nm. In contrast, benzoquinone-coupled BODIPY **5.8** is characterized by a broad absorption in the UV-Vis-NIR spectra range, having maxima at 916, 802, and 456 nm with well-resolved vibronic progression, which is significantly redshifted compared to BODIPY **5.7**. The emission spectra of both BODIPYs **5.7** and **5.8** are studied in DCM (Figure 5.2 and Table 5.1). BODIPY **5.7** exhibits intense fluorescence at 712 nm with a large Stokes shift of 704 cm^{-1}. Fluorescence was completely quenched in benzoquinone BODIPY **5.8**.

The absorption spectrum of dimer **5.9** is consistent with its mono(4-hydroxytyril)substituted BODIPY structure. It is clear that the non-conjugated quinomethide fragment practically does not affect the color. In addition, this compound is an intense fluorophore (Figure 5.2, Table 5.1).

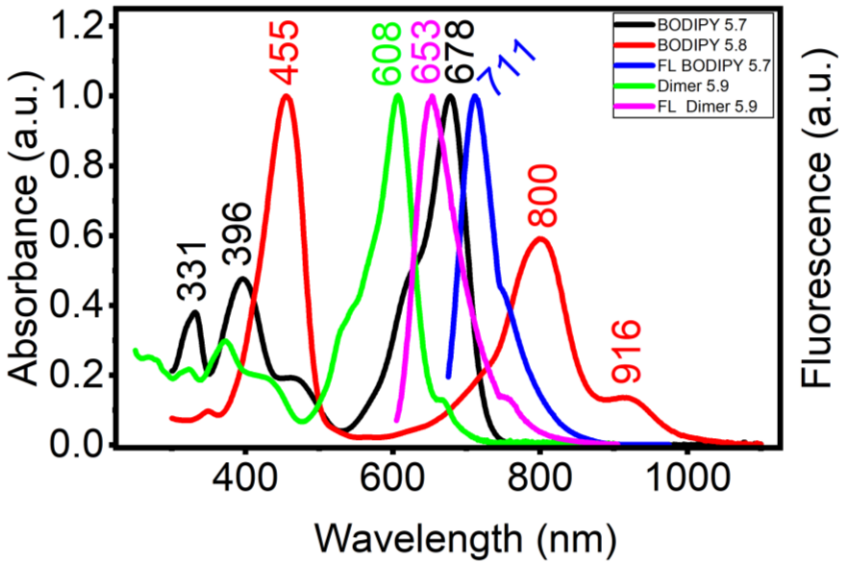


Figure 5.2: Normalized UV-Vis-NIR absorption (black) and emission (blue) spectra of BODIPY **5.7**, UV-Vis-NIR absorption (green) and emission (Magenta) spectra of Dimer **5.9**, and absorption spectrum (red) of BODIPY **5.8** in DCM.

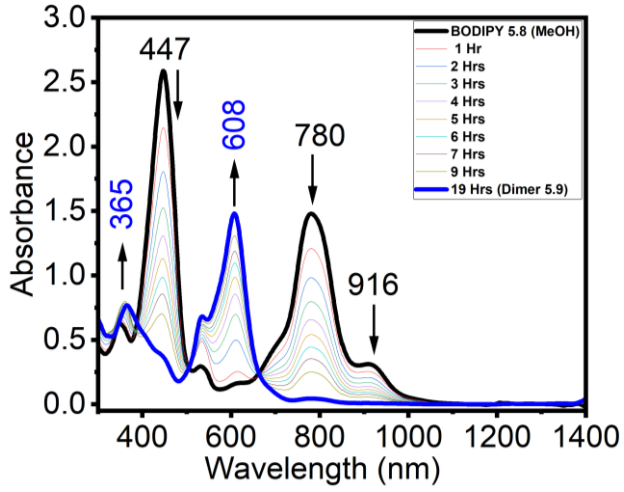


Figure 5.3: Changes in the UV-Vis-NIR absorption spectra of BODIPY **5.8** in the methanol/DCM system resulting to formation of dimer **5.9** at room temperature .

Table 5.1: Photophysical properties of BODIPYs **5.7, 5.8** and **5.9** in DCM at room temperature.

Compound	λ_{abs}, nm ($\varepsilon \times 10^4$, $M^{-1}cm^{-1}$)	$\lambda_{em,}$ (nm)	Φ_f	Δ_{ss} (cm^{-1})
5.7	678(5.8), 468(1.1), 396(2.8), 331(2.2)	711	0.61	704
5.8	916(1.2), 800(5.2), 455(8.9)	-	-	-
5.9	608(8.5), 428(1.6), 365(2.5)	653	0.1	1133

5.3.3 Electrochemical and Spectroelectrochemical studies

Electrochemical studies were carried out for all samples in dry DCM (Figure 5.4). The potential values of all compounds were measured by cyclic voltammetry (CV). BODIPY **5.7** exhibits multiple reduction and oxidation processes. The reduction waves were observed at -1.08, -1.34, and -1.6 V, with each representing a one-electron reduction process. Reversible oxidation waves are seen at +0.44 and +0.79 V, with each representing one-electron oxidation processes. Both oxidation waves are for oxidation of the phenoxy-OH groups to benzoquinone groups, and we ascribed the reduction waves to reduction of the electro deficient BODIPY core. Peak at -0.5 V is reflective of the box reaction at the first reduction potential. BODIPY **5.8** displays two one-electron reversible reduction peaks at -0.56 and -0.94 V, indicating that the benzoquinonemethide molecule easily undergoes reduction processes to form mixed valent radical-anion species and stable dianions (Scheme 5.2). In addition, one partially reversible oxidation peak was also observed at 0.70 V.

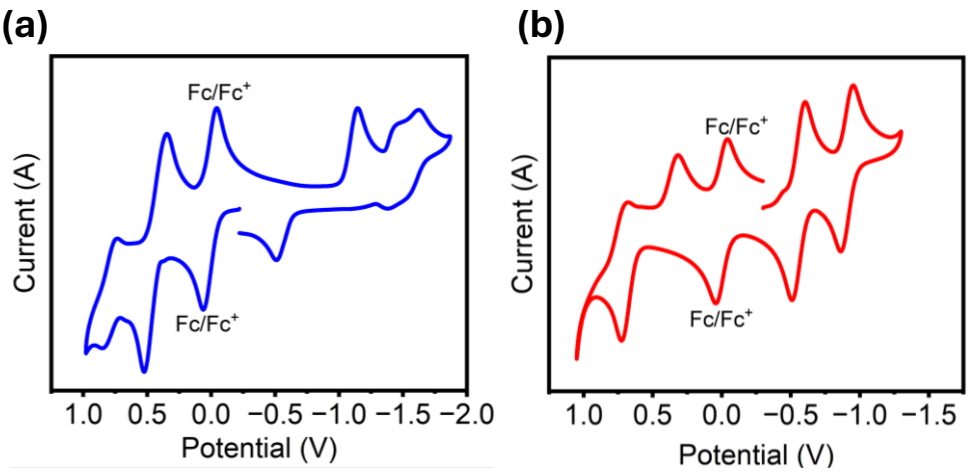
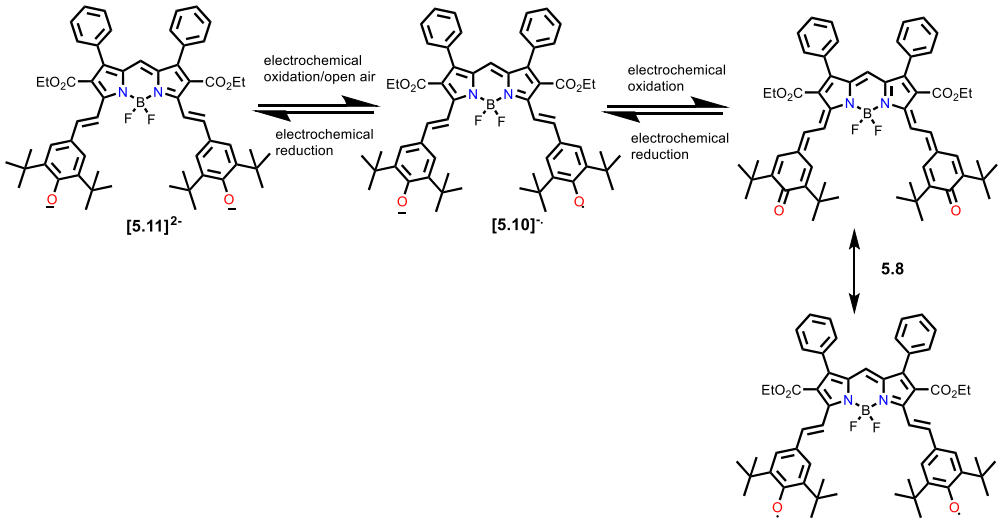


Figure 5.4: Cyclic voltammogram of BODIPY **5.7** (blue curve, left) and BODIPY **5.8** (red curve, right) in DCM/0.1M TBAP system.



Scheme 5.2: Formation of dianion **[5.11]**$^{2-}$ and mixed-valent radical-anion **[5.10]**$^{-\cdot}$ from benzoquinonemethide BODIPY **5.8**.

Deprotonation of BODIPY **5.7** was easily carried out at room temperature by treating its solution in DCM with tetra-*n*-butylammonium fluoride (TBAF) to obtain dianions **[5.11]**$^{2-}$. Spectrum change was observed upon stepwise addition of TBAF solution in DCM to the solution of BODIPY **5.7**, with the intense peak of starting BODIPY **5.7** at 678 nm gradually disappearing with a concomitant appearance of a new broad peak at 807 nm, indicating the formation of dianion species (Figure 5.5). The appearance of a broad, red-shifted absorption peak at 807 nm in the dianion species is attributed to strong intramolecular charge transfer from the electron-rich phenoxide groups to the electron-deficient BODIPY core, mediated by the conjugated styryl linker.

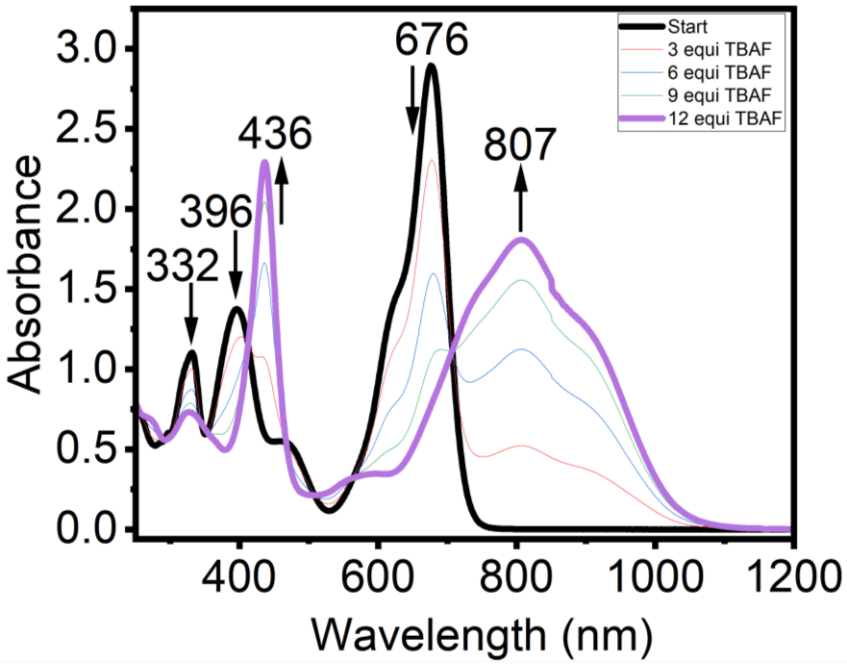


Figure 5.5: UV-vis-NIR spectral changes observed for BODIPY **5.7** in DCM upon titration with TBAF solution to form dianion **[5.11]**$^{2-}$.

To better understand the spectroscopic properties of the peak observed at 807 nm for the dianion species, spectroelectrochemical studies were carried out on the deprotonated **[5.11]**$^{2-}$ solution at room temperature. During electrochemical oxidation using a spectroelectrochemical setup, the characteristic absorption peak of the dianion species at 807 nm gradually diminishes, accompanied by the emergence of new absorption bands at 978 and ~1980 nm, indicative of the formation of a mixed-valence radical-anion species **[5.10]**$^{\bullet-}$, similar to those reported by us for aza-BODIPYs.[41,42] Band deconvolution analysis of the IVCT region (Figure 5.7) gives H_{ab} values of 175 (if DFT-predicted O---O distance is used) or 224 cm^{-1} (if =C---C= methyne to methyne carbons distance is used; we prefer to use two distances at the quinoidal fragments as the total spin density in this chromophore is strongly delocalized). Our analysis is indicative of the mixed-valence Class II system in Robin–Day classification.56 As the applied oxidation potential is increased from 0.1 V to 0.2 V, the 807 nm peak disappears entirely, leaving a prominent absorption band at 978 nm and a broad band centered at 1980 nm (Figure 7). The broad absorption feature at 1980 nm is attributed to an intervalence charge transfer (IVCT) process, consistent with the presence of mixed-valent character. When the oxidation potential was further increased from 0.2 V to 0.3 V, the signature absorption bands of mixed valent species at 978 and 1980 nm disappeared completely, and a new absorption spectrum with bands at 802 and 456 nm was observed, having similar vibronic progression and spectrum properties similar to the absorption spectrum observed earlier for chemically oxidized benzoquinone BODIPY **5.8** (see Figure 7). The dianion is stable in solution at room temperature, but with prolonged exposure to air it auto-oxidate.

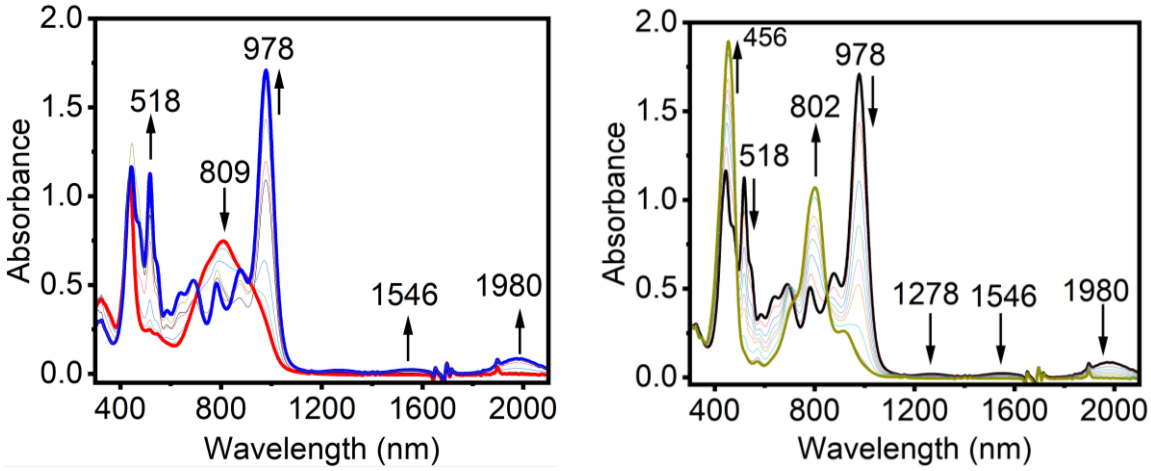


Figure 5.6: UV-vis-NIR spectral changes observed upon gradual oxidation of the **[5.11]**$^{2-}$ to **[5.10]**$^{-\cdot}$ (left) and **[5.10]**$^{-\cdot}$ to **5.8** (right) the spectroelectrochemical experiment in DCM/0.3 M TBAP system.

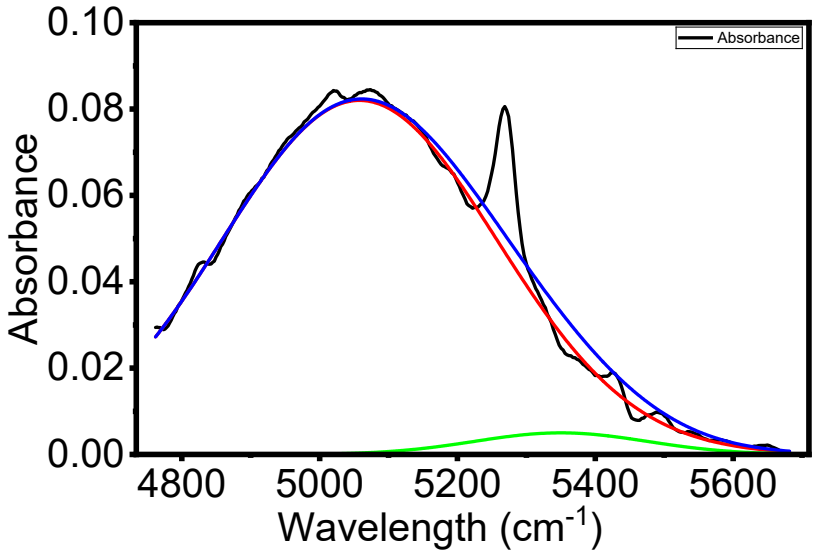


Figure 5.7**:** IVCT region band deconvolution analysis of mixed valent radical anion **[5.10]**$^{-\cdot}$

5.3.4 Magnetic Studies

5.3.4.1 Variable-Temperature (VT) ^{1}H NMR and EPR Spectroscopic Studies

BODIPY **5.8** was designed based on the hypothesis that introducing ester groups at the 2,6-positions of the BODIPY core, in conjunction with a styryl bridge coupling the phenoxy substituents to the core, would enhance the diradical character of this compound by extending the π-conjugation. Variable-temperature (VT) ^{1}H NMR spectra of BODIPY **5.8** were recorded in DCM-d_2. At room temperature, the aromatic and styryl proton signals appeared significantly broadened. Upon gradual cooling to 220 K, these signals sharpened progressively, resulting in improved resolution of the resonance peaks (Figure 8). Based on this behavior, we initially attributed the spectral broadening to thermal population of a triplet excited state and a potentially small singlet–triplet energy gap. Notably, EPR spectroscopy of BODIPY **5.8** revealed no detectable signal in DCM solution at room temperature and only a very weak signal in the solid state. The lack of the EPR signal in solution at room temperature could be indicative of the very small diradical character of **5.8**, and DFT calculations using TPSSh exchange correlation functional suggested that the molecule possesses less than 1% of diradical character. These findings indicate that the ester substituents at the 2,6-positions of the BODIPY core exert minimal influence on the diradical character of BODIPY **5.8**, contrary to our initial hypothesis, and the broadening of the ^{1}H NMR spectra is highly likely to reflect hindered rotation of the styryl fragments in **5.8**.

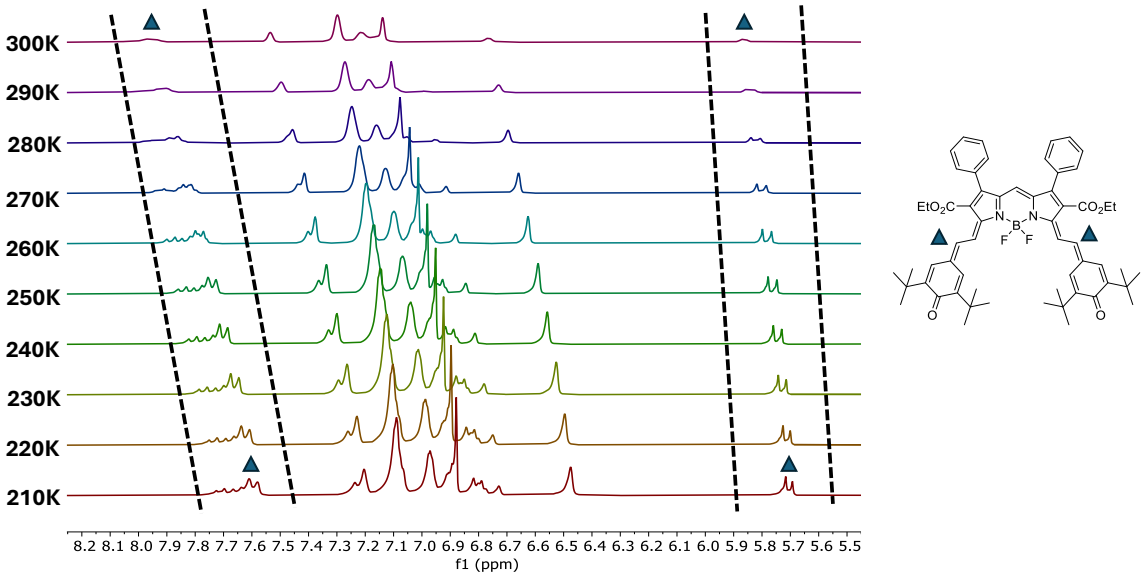


Figure 5.8: Variable temperature ^{1}H NMR spectra of styryl and aromatic region for BODIPY **5.8** (500 MHz, DCM-d_2).

5.3.5 X-Ray Diffraction Experiments and Related studies

When crystals of BODIPY **5.8** were intended to be obtained *via* slow diffusion of methanol into a chloroform solution of the compound, single-crystal X-ray diffraction analysis revealed the formation of a dimeric BODIPY **5.9**, in which two units are covalently linked through the α-carbon positions, effectively connecting one benzoquinone unit to another moiety (Scheme 5.2 and Figure 3). This dimer can be viewed as a two-electron, two-proton reduction product in which one of the two quinone groups in each monomer is reduced to the phenol. Single-crystal X-ray diffraction analysis of the dimer revealed that the quinone methide of two BODIPY units is covalently linked through the α-carbon positions, forming a C–C bond at C103 and C44 that connects the BODIPY cores of the dimer. The bond length of this newly formed interunit linkage was determined to be 1.583(5) Å, which is significantly elongated

relative to a typical C–C single bond (~1.54 Å), suggesting reduced bond order and/or steric and electronic effects.

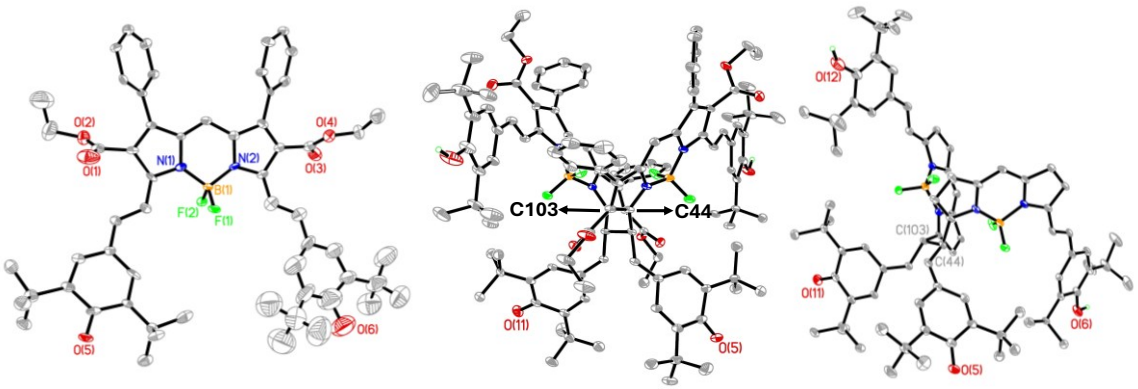
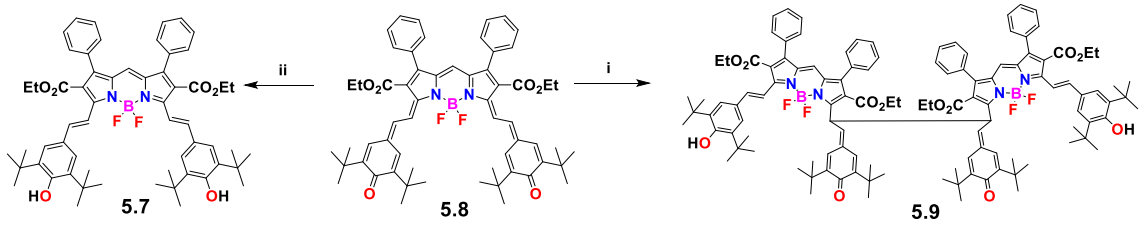


Figure 5.9: X-ray crystallographic structure of BODIPY **5.3** (left), BODIPY **5.9** (center), and side view of BODIPY **5.9** (right) excluding distal phenyl groups. All hydrogen atoms except phenolic hydrogens are omitted for clarity.

Notably, each BODIPY unit in the dimer contains a single benzoquinone substituent, rather than two, consistent with the observed coupling mode. Furthermore, the ethanediylidene linkages connecting the BODIPY cores to the quinone methide groups exhibit saturation of the original C=C double bond, resulting in C–C single bonds with measured bond lengths of 1.506(5) and 1.514(5) Å. These values are consistent with standard single bond distances, indicating loss of π-character upon dimer formation. The quinone methide moieties within the dimer display clear bond length alternation, characteristic of a quinoidal structure, further supporting the assignment of localized double and single bonds within the ring system. C=O bond distances are also indicative of their carbonyl character (1.23-1.25 Å). In contrast to the quinoidal fragments in **5.9**, the phenolic fragments are fully conjugated with the BODIPY system and have typical

delocalized benzene fragment bond distances (~1.4 Å). Phenolic C-OH bond distances (~1.37 Å) are also characteristic of the carbon-oxygen single bond (Figure 3). To the best of our knowledge, formation of the dimeric BODIPYs of this type has never been reported. Finally, we should note that BODIPY **5.9** crystallizes as a racemic mixture in a centrosymmetric space group. We were able to grow single crystals suitable for X-ray diffraction for monomeric BODIPY **5.8** by slow diffusion of hexane into a dichloromethane solution of the compound. Bond length analysis of the quinone methide subunits reveals that the C33–O5 1.236(11) Å exhibits a characteristic carbonyl double-bond character. Furthermore, the pronounced bond length alternation within the two quinone methide rings confirms a dominant closed-shell quinoidal electronic configuration (Figure 3). The styryl fragments in **5.8** are nearly co-planar with the BODIPY core, highlighting expected extended □-conjugation in this chromophore. In contrast, the phenyl groups are rotated by ~45° and two ester groups are rotated by ~60° away from the BODIPY core.



Scheme 5.3: Synthetic pathways to dimer **5.9**. Reagents and conditions: (i) DCM-MeOH, RT, 24 h; (ii) Zn, HOAc, RT, 5 min.

Motivated by the observation of a dimeric structure from an X-ray diffraction experiment, we sought to deliberately access BODIPY dimer **5.9**. To achieve this,

bisquinonemethide **5.8** was dissolved in a mixture of methanol: DCM (1:1 v/v, because the solubility of compound **5.8** in pure methanol is low), and the reaction mixture was left for a day at room temperature. After completion of the reaction (control by TLC and absorption spectra), product **5.9** was chromatographed on silica gel using a mixture of MTBE: hexane (2:3 v/v) as eluent. BODIPY **5.9** was sufficiently stable to allow full characterization, including NMR spectroscopy and mass spectrometry. For a more complete understanding of the essence of the process, several more experiments were conducted. In particular, the above reaction was repeated under argon and oxygen. In both cases, the same result was obtained. Moreover, the replacement of methanol with other alcohols (ethanol, propanol, and isopropanol) led to the same dimer **5.9**. The reaction does not proceed with *tert*-butanol. We speculate that during the reaction, primary and secondary alcohols get oxidized by the quinone fragments of BODIPY **5.8**, while such oxidation is not possible for the tertiary alcohols. At room temperature, the reaction proceeds cleanly. However, when heated, in all cases, additional red-colored by-products appear in the reaction mixture that we could not isolate and fully characterize because of their low stability. Thus, it became clear that we were observing a very specific chemical reaction: partial reduction of quinonemethide **5.8** with alcohols (methanol is the best choice), accompanied by dimerization. We could not find close analogies to such a process of reductive dimerization in the literature. A curious feature of this case is that dimer **5.9** was originally obtained in a routine crystal growing process for the X-ray experiment using methanol, which unexpectedly turned out to be a reagent. Therefore, it was interesting to test other reducing agents for this purpose. It turned out

that sodium borohydride in alcohols caused complete discoloration of the BODIPY **5.8**, which is certainly due to the hydrogenation of the base core of BODIPY. Instead, zinc in acetic acid at room temperature almost quantitatively reduced quinonemethide **5.8** to the original bis(hydroxytyryl) dye **5.7**. Finally, sodium dithionite in aqueous methanol yielded a mixture of dimer **5.9** and BODIPY **5.8**.

5.3.6 Quantum chemical calculations

For a clearer understanding of the structural, electronic, and magnetic behavior of BODIPYs **5.7** and **5.8**, quantum chemical calculations have been performed. Geometry optimization, single-point calculations, and TDDFT calculations of BODIPY **5.7** and its corresponding dianion **[5.11]**$^{2-}$ were conducted using restricted closed-shell formalism, and a doublet state was used for the mixed-valent species **[5.10]**$^{\cdot-}$ using unrestricted open-shell calculations. We also optimized structures and calculated electronic structures, excited states, diradical character, and spin density distributions of BODIPY **5.3** in three different spin states using the TPSSh exchange correlation functional. The three spin states considered are: (i) closed-shell singlet **5.8(CS)**; (ii) diradical open-shell singlet state **5.8(OS)**; (iii) diradical open-shell triplet state **5.3(TS)**. Our calculations indicate that the ground state of BODIPY **5.8** is predominantly characterized by a closed-shell quinoidal structure in agreement with X-ray analysis and EPR spectra. The open-shell singlet diradical character, evaluated from the occupation numbers of the highest occupied natural orbital (HONO) and the lowest unoccupied natural orbital (LUNO), was found to be minimal ($y_0 < 1\%$). The substantial singlet–triplet energy gap ($\Delta E_{S-T} = -5.82$ kcal/mol) aligns with the experimentally observed EPR silence of BODIPY **5.8** in DCM

solution at room temperature. The spin-density distribution plot showed spin delocalization over the benzoquinone moieties, styryl linkers, and BODIPY core in both the open-shell singlet and triplet states (Figure 5.10).

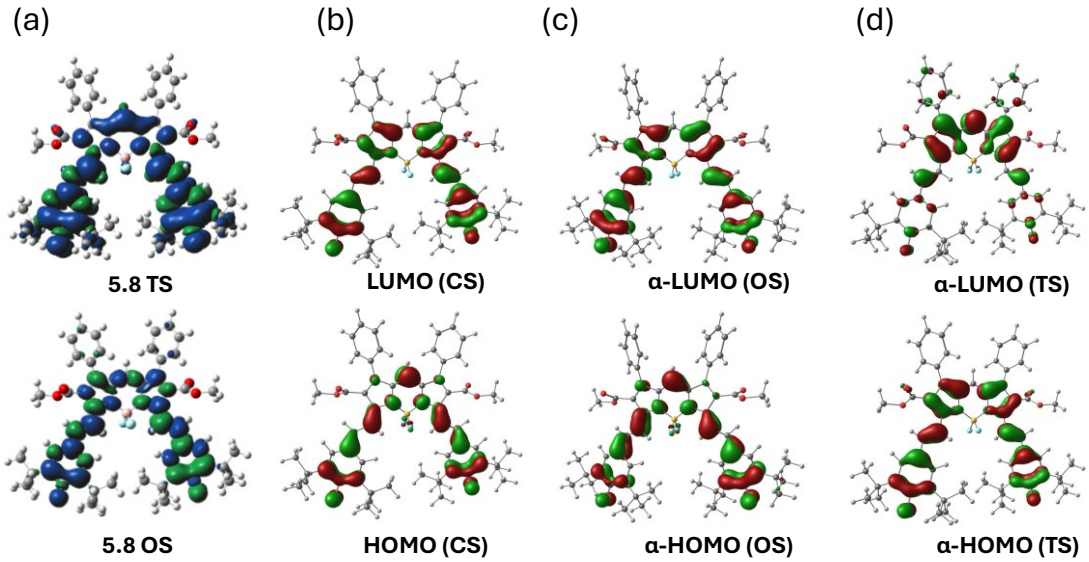


Figure 5.10: (a) Spin density distribution of open-shell singlet state **5.8(OS)** and open-shell triplet state **5.8 (TS)**. Blue and green surfaces indicate α and β spin densities. (b) Highest occupied and lowest unoccupied molecular orbitals of BODIPY **5.3** in closed-shell singlet state **5.8 (CS)**. (c) broken symmetry orbitals α-HOMO and α-LUMO of BODIPY **5.8** in open-shell singlet state **5.8 (OS)**. (c) α-HOMO and α-LUMO of BODIPY **5.8** in open-shell triplet state **5.8 (TS)**.

We have calculated vertical electronic transitions for BODIPY **5.7**, dianion **[5.11]**$^{2-}$, mixed-valent species **[5.10]**$^{-}$, and BODIPY **5.8** in its three different configurations (CS, OS, and TS) using time-dependent density functional theory (TDDFT). The absorption spectrum of BODIPY **5.7** displays the maximum absorption

band at 678 nm, predicted at 746 nm (f = 1.077) due to the HOMO→LUMO single-electron transition corresponding to $S_0 \rightarrow S_1$. Two other major bands are predicted at 560 nm (f = 0.574) and 409 nm (f = 1.006), corresponding to the HOMO-1→LUMO and the HOMO→LUMO+1 transitions (Figures 5.12 – 5.13, see appendix for Table 5.2). For dianion **[5.11]**$^{2-}$, three main bands are predicted at 1077 nm (f = 1.005), experimentally observed at 809 nm, 737 nm (f = 0.571) and 524 nm (f = 1.368) seen on experimental absorption spectrum at 438 nm, these bands are assigned to the HOMO→LUMO, HOMO-1→LUMO, and HOMO→LUMO+2 electronic transitions (Figures 5.11 – 5.13, and see appendix for Table 5.2). To elucidate the electronic transitions responsible for the spectral features of the mixed-valence intermediate **[5.10]**$^{-\cdot}$, time-dependent DFT (TDDFT) calculations were performed and compared with the spectroelectrochemically recorded absorption spectrum. The calculated transitions show excellent agreement with experiment, both in energy and relative intensity. A broad, low-energy absorption band predicted at 1790 nm (f = 0.1716) corresponds to the experimentally observed intervalence charge-transfer (IVCT) band at 1980 nm. Orbital analysis indicates that this transition is primarily composed of the HOMO(β) → LUMO(β) (87%) with a minor contribution from the HOMO(α) → LUMO(α) (13%), consistent with charge delocalization between the BODIPY core and benzoquinone acceptor. At higher energy, TDDFT predicts a strong absorption at 988 nm (f = 0.9134), in excellent agreement with the experimental band at 978 nm. This transition is dominated by the HOMO(α) → LUMO(α) (87%), with a minor contribution from the HOMO(β) → LUMO(β) (12%),

further reflecting charge-transfer excitations mediated by the styryl linker. In the visible region, two intense bands are reproduced with high fidelity.

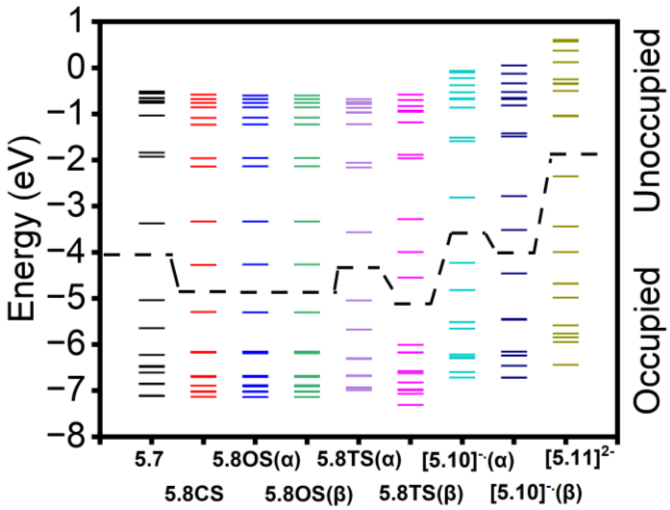


Figure 5.11: Calculated energy levels and HOMO-LUMO energy gaps of **5.7**, **[5.11]$^{2-}$**, **[5.10]$^{-\cdot}$**, **5.8 (CS)**, **5.8 (OS)**, and **5.8 (TS)**.

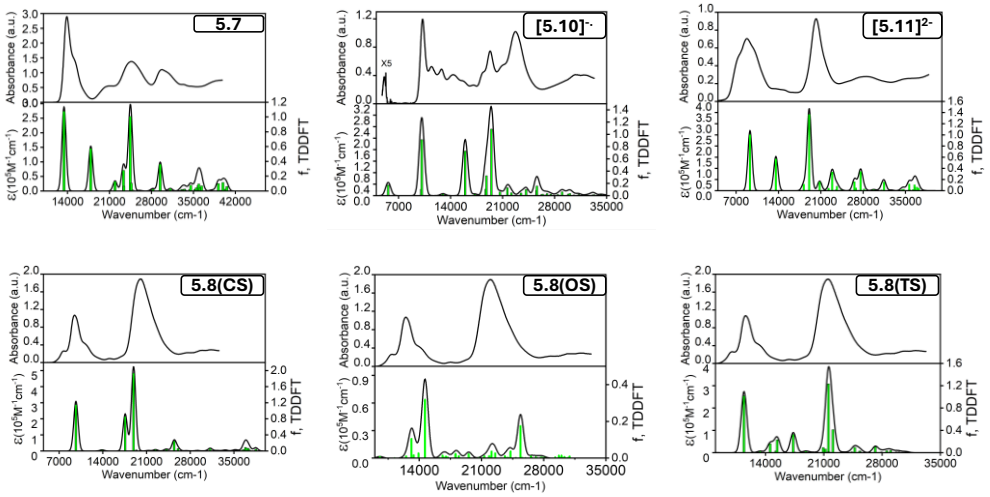


Figure 5.12. (a) Experimental versus TDDFT-predicted (TPSSH exchange-correlation functional) UV-vis spectra of **5.7**, **[5.11]$^{2-}$**, **[5.10]$^{-\cdot}$**, **5.8 (CS)**, **5.8 (OS)**, and **5.8 (TS)**.

A transition calculated at 627 nm (f = 0.7273) matches the experimental absorption at 694 nm and is primarily assigned to the HOMO–1(α) → LUMO(α) (54%), while another band at 531 nm (f = 0.3237) corresponds to the observed peak at 518 nm, dominated by the HOMO-4(β) → LUMO(β) (58%). Together, these transitions reflect contributions from deeper-lying occupied orbitals into the benzoquinone-centered LUMO, highlighting the delocalized electronic communication across the conjugated framework. Overall, the close correspondence between experimental and TDDFT-predicted spectra provides strong support for the proposed mixed-valence character of the intermediate. The assignment of the low-energy IVCT band underscores the critical role of the styryl linker in enabling electronic coupling between BODIPY and benzoquinone fragments, thereby facilitating the intervalence charge transfer process (Figures 5.12 – 5.13, and see appendix for Table 5.2).

TDDFT calculations for the BODIPY **5.8** molecule reveal distinct absorption features for the closed-shell singlet (CS), open-shell singlet (OS), and open-shell triplet (TS) states, which can be compared with the experimental UV-Vis-NIR spectrum (Figures 10, S13-S17, Table S1). For the **5.8 (CS)**, three major bands are predicted: 1033 nm (f = 1.151, the HOMO → LUMO) transition, corresponding qualitatively to the experimental peak at 802 nm and its shoulder at 942 nm; 569 nm (f = 0.8579, the HOMO-4 → LUMO) transition; and 529 nm (f = 1.938) with mixed character (the HOMO-4 → LUMO 37%, HOMO → LUMO+1 34%, and HOMO-1 → LUMO 25%) transitions, corresponding to the experimental strong band at 496 nm (Figure 8 and Table S1). The **5.8 (OS)** state shows a major band at 683 nm (f = 0.3182, multiple

contributions) with a weaker shoulder at 762 nm (f = 0.1051, the HOMO-11(β) → LUMO+6(β)) and a higher-energy band at 394 nm (f = 0.1748, mixed α/β contributions), indicating minor low-energy features consistent with shoulders in the experimental spectrum.

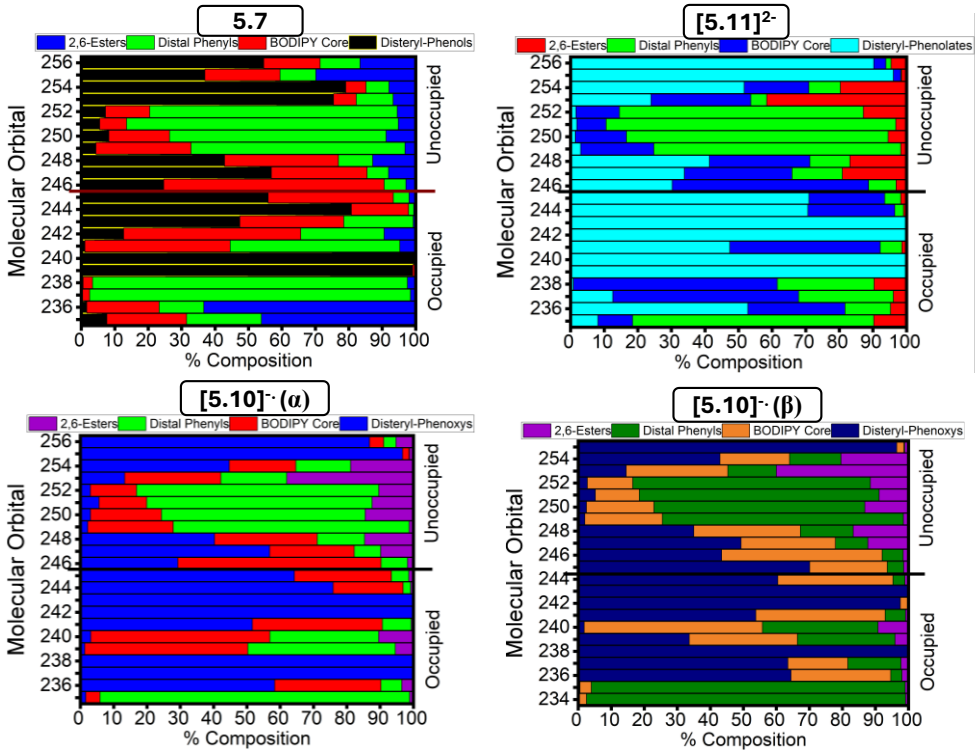


Figure 5.13: DFT-predicted percentage compositions of frontier orbitals for **5.7**, [**5.11**]$^{2-}$, [**5.10**]$^{-\cdot}$.

For the **5.8(TS)**, several spin-allowed but singlet-forbidden transitions are predicted, including 876 nm (f = 1.02, the HOMO(α) → LUMO(α) 53% and HOMO(β) → LUMO(β) 46%), 687 nm (f = 0.158, the H-4(β) → L(β) 79%), 649 nm (f = 0.231, the H-1(α) → L(α) 34% and H(β) → L+1(β) 31%), 577 nm (f = 0.328, the H-9(β) → LUMO(β) 44% and H(α) → L+1(α) 21%), 452 nm (f = 0.413, the H-6(α) → L(α) 45%, H(α) → L+1(α) 20%, and H-4(β) → L+2(β) 12%), and 368 nm (f = 0.104, H-1(α) → L+2(α) 54%,

H-13(α) → L(α) 10%, and H-12(β) → L+1(β) 10%) (Figures 5.12 & 5.14, see appendix for Table 5.2). Overall, the TDDFT calculation of the **5.8(CS)** spectrum captures the main experimental absorption features, while the **5.8(OS)** predicted spectrum accounts for minor low-energy shoulders, and the **5.8(TS)** provides insight into triplet-state contributions, illustrating a comprehensive picture of the molecule's electronic excitations.

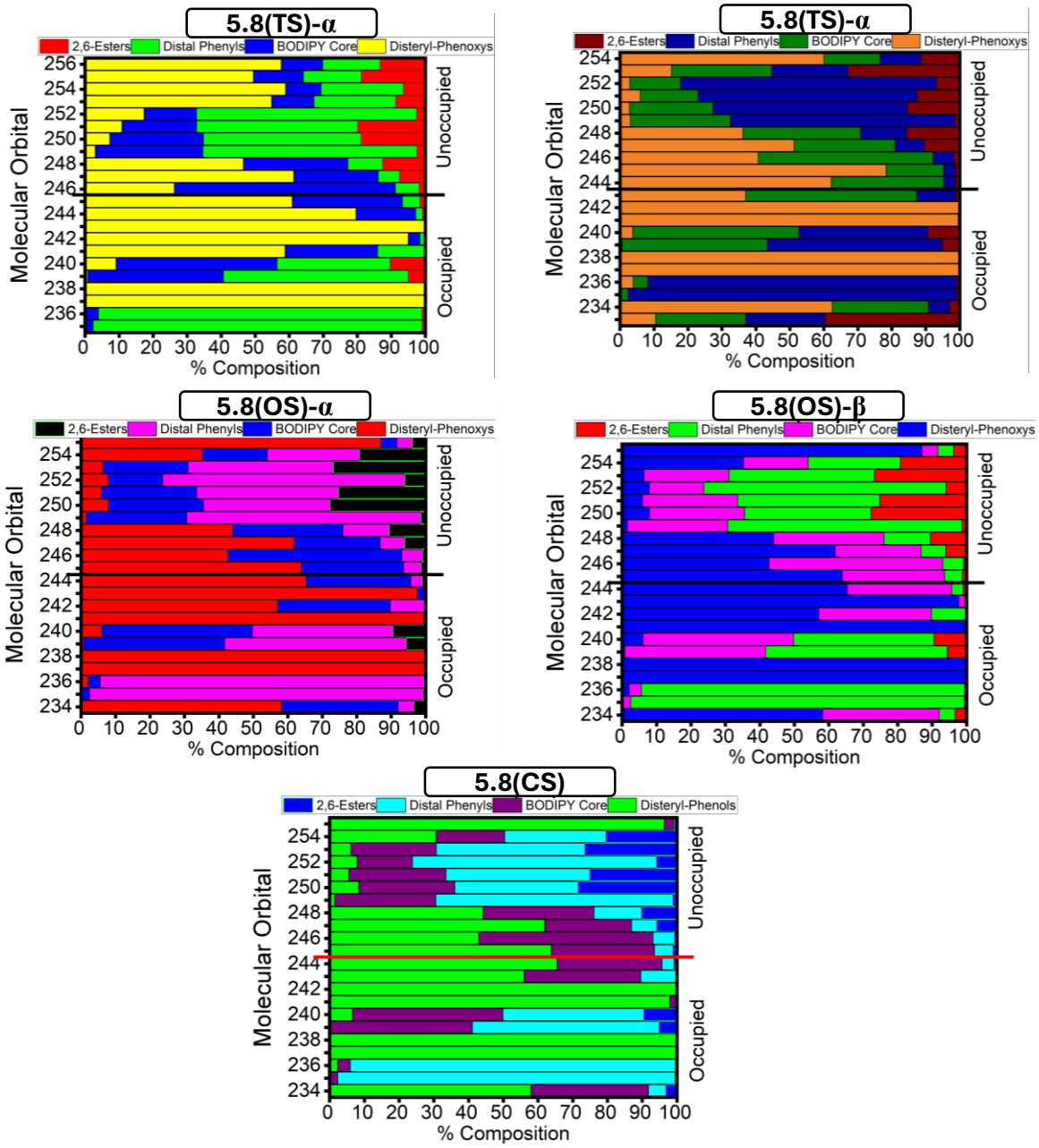


Figure 5.14: DFT-predicted percentage compositions of frontier orbitals for **5.8 (CS)**, **5.8 (OS)**, **5.8 (TS)**.

5.4 CONCLUSIONS

In this work, we synthesized and characterized a benzoquinone-BODIPY conjugate bearing ester groups at the 2,6-positions and linked through a styryl bridge. Experimental and computational studies established a closed-shell singlet ground state with a nearly isoenergetic open-shell singlet. DFT/TDDFT analyses reveal close to zero diradical character. Electrochemistry and spectroelectrochemistry confirmed the stepwise formation of mixed-valence intermediates, featuring a broad IVCT band at 1980 nm. To test this hypothesis, we synthesized a hydroxyphenyl-coupled BODIPY **5.7** via Knoevenagel condensation, which, upon chemical oxidation, yielded the corresponding benzoquinone-coupled BODIPY **5.8** (Scheme 1). The benzoquinone groups allowed us to explore a continuum of electronic and magnetic behaviors across neutral, anionic, and dianionic states. The ground state electronic and magnetic properties of these systems were examined using a combination of experimental and computational tools. VT EPR and VT ^{1}H NMR spectroscopy were employed to probe the presence of paramagnetic species and to assess the singlet–triplet energy gap. DFT and TDDFT calculations were used to evaluate diradical character, spin density distributions, and excited-state properties, providing molecular-level insight into the electronic structure and ground-state magnetic behavior.

In addition, electrochemical and spectroelectrochemical studies were carried out to elucidate the redox properties of the BODIPYs **5.7** and **5.8**. The starting hydroxyphenyl coupled BODIPY **7** was deprotonated to afford the corresponding dianion $\mathbf{[5.11]^{2-}}$, which, upon controlled electrochemical oxidation, in a spectroelectrochemical setup generated

mixed-valence anion-radical species **[5.10]**$^{\bullet-}$. At higher potentials, complete oxidation of the mixed-valent species yielded the benzoquinone-coupled BODIPY **5.8**, allowing us to directly correlate redox transformations with changes in electronic structure. The spectroelectrochemical data, combined with theoretical results, provide evidence for the possibility of diradical character and tunable ground state magnetism as a function of conjugation and redox state. In this work, we establish a framework for understanding how conjugation extension and redox-active substituents can be leveraged to modulate the ground state electronic and magnetic properties of BODIPY diradicaloid.

5.5 Experimental

5.5.1 General Materials and Methods

All solvents were purchased from commercial sources and purified using standard procedures. All glassware was rigorously dried overnight at 160 °C and cooled under vacuum prior to use. All reagents and starting materials were purchased from commercial vendors and used without further purification. Column chromatography was performed on silica gel (Dynamic Adsorbents, Inc, 63-200 μm). Deuterated solvents were purchased from Cambridge Isotope Laboratories and used as received.

Electrochemistry. Cyclic voltammetry measurements were made using a three-electrode system consisting of a glassy carbon or platinum working electrode, a platinum auxiliary electrode, and an Ag/AgCl wire pseudo-reference electrode. Ferrocene (Fc) was used as an internal standard for the studied compounds, and the reported potentials were corrected to the Fc/Fc^+ couple. For consistency, all potentials and figures in this work are reported vs the Fc/Fc^+ redox couple. All electrochemical experiments were conducted in

dichloromethane (DCM) and 0.1M tetrabutylammonium perchlorate (TBAP) as electrolyte.

Spectroelectrochemistry. Spectroelectrochemical experiments were performed using a Jasco V-770 UV–vis–NIR spectrophotometer in tandem with a CH Instruments electrochemical analyzer, which was operated using the bulk electrolysis mode. The data were collected using a custom-made 1 mm cell, a platinum mesh working electrode, a platinum auxiliary electrode, and Ag/AgCl wire pseudo-reference electrode. Spectroelectrochemical solutions consisted of 0.3 M solutions of TBAP in DCM.

NMR. NMR spectra were recorded on a 500 MHz Brucker III spectrometer. All chemical shifts (δ) are listed in parts per million (ppm) and are referenced to solvent. Spectra are referenced internally due to residual proton solvent resonances. Variable-temperature ^{1}H NMR spectra were collected in DCM-d_2

EPR. EPR spectra were recorded on a Bruker ELEXSYS E-500 instrument at the X-band frequency (9,82 GHz). DPPH (g = 2.0036) was used as the standard for field and frequency calibration.

Determination of Fluorescence Quantum Yield. All fluorescence spectra were corrected for apparatus response. Quartz cuvettes with an optical path of 1 cm were used. The sample concentrations were chosen to obtain a maximum absorbance between 0.1 and 0.2 for UV spectra and between 0.05 and 0.15 at the excitation wavelength for quantum yield measurements. Relative quantum yields were obtained by comparing the areas under the corrected emission spectrum. All measurements were performed in DCM at 298 K. Rhodamine 6G (Φ_F = 0.95 in CH_2Cl_2, λ_{ex} = 520 nm) was used as a reference for

all measurements. In all quantum yield determinations, correction for the solvent refractive index (η) was applied [DCM: η = 1.442]. The following equation was used to calculate the quantum yield of the sample:

$$\Phi_F(X) = \Phi_{ref}\,(Grad_X/Grad_{ref})\,(\eta_X^2/\eta_{ref}^2)$$

Of which indices X and ref stand for the studied BODIPYs **5.7** and **5.9,** and the reference compound, respectively, Φ_F is the quantum yield, Grad is the gradient of the linear graph between the integrated fluorescence intensity versus absorbance at the excitation wavelength, and η is the refraction index of the solvent in which the measurement is performed.

Computational Methods. All computations were performed using Gaussian 16 software[57] running under Windows or UNIX OS. Molecular orbital contributions were compiled from single-point calculations using QMForge program[79]. In DFT calculations, the TPSSh[80] (10% of Hartree-Fock exchange) hybrid exchange correlation functionals. In all calculations, 6-311G(d) basis set was employed[81]. In the case of modeling BODIPY **5.8**, three spin states were considered. In the first one, **5.8(CS**), a molecule of BODIPY **5.8** was treated as a closed-shell singlet. In the case of **5.8(OS)**, a molecule of BODIPY **5.8** was treated as an open-shell diradicaloid. Stable=opt keyword was used to ensure the correct diradicaloid character of the initial guess and the final wavefunction. In the case of **5.8(TS)**, the triplet state was used in calculations. Frequencies were calculated for each geometry optimization to ensure the energy minimum. DFT calculations for BODIPY **5.7**, **5.8(CS)**, **5.8(OS)**, and **5.8(TS)** converged to C_2 symmetry, which was used in the

single-point and TDDFT calculations. In all TDDFT calculations, the lowest 40 excited states were calculated to cover experimentally observed transitions in the UV-visible region. Diradical character (y_0) of BODIPY **5.8** was further probed using TPSSh exchange-correlation functionals and the Natural Population Analysis (NPA) algorithm.[80]

Single Crystal X-ray Crystallographic Analysis. Crystalline samples were mounted on a 150 mm MiTeGen Dual-Thickness MicroMount using Paratone N oil (Hampton). X-ray diffraction experiments on BODIPYs **5.8** and **5.9** were conducted at 150 K. Diffraction data was collected using a Bruker Smart Apex II single crystal diffractometer with a TRIUMPH monochromated Mo Kα radiation (λ = 0.71073 Å) source with a crystal-to-detector distance of 50 mm, using a series of θ and ω scans in 0.50° oscillations. The data was processed and corrected for Lorentz and polarization effects, and an empirical absorption correction was applied, using the Bruker Apex II software suite. The structures were solved with ShelxS[82], and subsequent refinements were performed using the SHELXTL[82] crystallographic software package of Bruker-AXS[83]. The coordinates and anisotropic displacement parameters for the non-hydrogen atoms were refined. Hydrogen atoms were placed in idealized geometric positions and linked to their respective carbon atoms using a riding model during refinement. Platon SQUEEZE algorithm[84] was used to remove the electron density associated with the cyclohexane solvent molecule for the dataset of **5.8** and **5.9** because of the severe disorder of the cyclohexane molecule at this temperature. Diagrams were prepared using MERCURY[85]. CCDC number for **5.8** is 2552354, and for **5.9** is 2552355.

5.5.2 Synthesis of Diethyl 3,7-bis((E)-3,5-di-tert-butyl-4-hydroxystyryl)-5,5-difluoro-1,9-diphenyl-5H-4l4,5l4-dipyrrolo[1,2-c:2',1'-f][1,3,2]diazaborinine-2,8-dicarboxylate, BODIPY 5.7.

The mixture of BODIPY **5.5** (1.032 g, 2 mmol), 3,5-di-*tert*-butyl-4-hydroxybenzaldehyde (0.983 g, 4.2 mol) **5.6**, acetic acid (0.105 g, 1.75 mmol, 0.1 ml) and piperidine (0.043 g, 0.507 mmol, 0.05 ml) in toluene (10 ml) was refluxed for 2 days. After cooling to room temperature, the solution was washed with water (2x5 mL), dried over Na_2SO_4 and evaporated to dryness. The residue was purified by column chromatography on silica using CH_2Cl_2 as eluent, yielding 0.948 g (50%) **5.7** as green solid. ^{1}H NMR of BODIPY **5.7** (500 MHz, 298 K, $CDCl_3$) δ (ppm) = 7.68 (s, 4H), 7.46(s, 4H), 7.38 - 7.41 (m, 6H), 7.32 – 7.34 (m, 4H), 6.85 (s, 1H), 4.16 – 4.20 (q, 4H), 1.49 (s, 36H), 1.06 – 1.09 (t, 6H). ^{13}C NMR of BODIPY **5.7** (500 MHz, 298 K, $CDCl_3$) δ (ppm) = 13.8, 30.3, 34.4, 61.0, 115.1, 125.2, 128.3, 128.7, 129.6, 132.0, 134.8, 136.3, 141.8, 145.1, 153.2, 155.8, 165.5. HRMS-ESI$^+$ (m/z): $[M+H]^+$ calcd. for $[C_{59}H_{67}BF_2N_2O_6]$, 949.5133; found, 949.5133. For both ^{1}H NMR and ^{13}C NMR spectra (Figures 5.15 – 5.16) . Mass Spectrum (Figure 5.20).

5.5.3 Synthesis of Diethyl (3E,7E)-3,7-bis(2-(3,5-di-tert-butyl-4-oxocyclohexa-2,5-dien-1-ylidene)ethylidene)-5,5-difluoro-1,9-diphenyl-5,7-dihydro-3H-4l4,5l4-dipyrrolo[1,2-c:2',1'-f][1,3,2]diazaborinine-2,8-dicarboxylate, 5.8.

DDQ (0.095 g, 0.42 mmol) was added to the mixture of **5.7** (0.2 g, 0.21 mmol) in 10 ml of DCM. The solution was stirred at room temperature for 15 min, then it was washed with water (2x10 mL), dried over Na_2SO_4, and evaporated to dryness. The crude

product was purified by column chromatography on silica using DCM as eluent, yielding 0.190 g (95%) BODIPY **5.8** as a yellowish solid. ^{1}H NMR of BODIPY **5.8** (500 MHz, 220 K, CD_2Cl_2) δ (ppm) = 7.55 – 7.58 (d, 2H), 7.17 – 7.20 (m, 2H), 7.03 - 7.05 (m, 6H), 6.84 (s, 4H), 6.75 – 6.78 (d, 2H), 3.87 – 3.91 (q, 4H), 0.86 – 0.94 (d, 36H), 0.74 – 0.77 (t, 6H). ^{13}C NMR of BODIPY **5.8** (500 MHz, 298 K, CD_2Cl_2) δ (ppm) = 13.8, 29.8, 35.5, 35.9, 62.3, 85.2, 124.5, 128.9, 150.1, 182.8. HRMS-ESI^{+} (m/z): $[M+H]^{+}$ calcd. for $[C_{59}H_{65}BF_2N_2O_6]$, 947.4977; found, 947.4987. For both ^{1}H NMR and ^{13}C NMR spectra see appendix for Figures 5.17 – 5.18 . For mass spectrum, see appendix for Figure 5.21.

5.5.4 Synthesis of diethyl 3-((E)-3,5-di-tert-butyl-4-hydroxystyryl)-7-(3-(7-((E)-3,5-di-tert-butyl-4-hydroxystyryl)-2,8-bis(ethoxycarbonyl)-5,5-difluoro-1,9-diphenyl-5H-5l4,6l4-dipyrrolo[1,2-c:2',1'-f][1,3,2]diazaborinin-3-yl)-1,4-bis(3,5-di-tert-butyl-4-oxocyclohexa-2,5-dien-1-ylidene)butan-2-yl)-5,5-difluoro-1,9-diphenyl-5H-4l4,5l4-dipyrrolo[1,2-c:2',1'-f][1,3,2]diazaborinine-2,8-dicarboxylate, 5.9

Compound **5.8** (100 mg, 0.1 mmol) was dissolved in the mixture of methanol (50 ml) and dichloromethane (50 ml) and left for a day. After the completion of the reaction, the solvents were removed under reduced pressure. The crude dye **5.9** was subjected to preparative chromatography on silica gel with a mixture of MTBE: hexane (2:3 v/v) as eluent, affording compound **5.9** as a dark blue solid (60 mg, 60%). ^{1}H NMR of BODIPY **5.9** (500 MHz, 220 K, $CDCl_3$) δ (ppm) = 7.51 – 7.54 (d, 2H), 7.38 – 7.43 (m, 16H), 7.33 (s, 2H), 7.01 – 7.15 (m, 4H), 6.89 (s, 2H), 5.69 (s, 2H), 5.10 (s, 2H), 4.13 – 4.21 (m, 8H), 3.42 – 3.45 (D, 4H), 1.46 – 1.46 (m, 36H), 1.22 – 1.24 (m, 36H), 1.00 – 1.07 (m, 12H). ^{13}C NMR of BODIPY **5.9** (500 MHz, 298 K, $CDCl_3$) δ (ppm) = 12.7, 29.3, 33.4, 52.4,

56.4, 57.3, 60.2, 80.7, 84.6, 113.5, 123.5, 124.2, 124.5, 125.7, 127.0, 127.2, 127.3, 127.5, 128.5, 128.6, 130.4, 131.1, 133.8, 134.1, 135.4, 142.9, 146.0, 152.0, 154.7, 155.2, 164.0, 173.3. HRMS-ESI$^+$ (m/z): $[M]^+$ calcd. for $[C_{118}H_{132}B_2F_4N_4O_{12}]$, found, 1894.4041. For both ^{1}H NMR spectrum see appendix for Figure 5.19. For mass spectrum, see appendix for Figure 5.22.

5.5.5 Reduction of dye 5.8 to BODIPY 5.7

Compound **5.8** (100 mg, 0.1 mmol) was suspended in acetic acid (10 ml), and zinc powder (10 mg, 0.15 mmol) was added under stirring. After the completion of the reaction, zinc was removed by filtration, and water (10 ml) was poured into the mixture. The resulting precipitate was filtered off, yielding BODIPY **5.7** as green powder (95 mg, 95%).

References

(1) Shamova, L. I.; Zatsikha, Y. V.; Nemykin, V. N. Synthesis Pathways for the Preparation of the BODIPY Analogues: Aza-BODIPYs, BOPHYs and Some Other Pyrrole-Based Acyclic Chromophores. *Dalton Trans* **2021**, *50*, 1569–1593. https://doi.org/10.1039/D0DT03964K.

(2) Yadav, I. S.; Misra, R. Design, Synthesis and Functionalization of BODIPY Dyes: Applications in Dye-Sensitized Solar Cells (DSSCs) and Photodynamic Therapy (PDT). *J. Mater. Chem. C Mater.* **2023**, *11*, 8688–8723. https://doi.org/10.1039/D3TC00171G.

(3) Gong, Q.; Shao, J.; Li, W.; Guo, X.; Ling, S.; Wu, Y.; Wei, Y.; Xu, X.; Jiang, X.; Jiao, L.; Hao, E. Fully Conjugated Thiophene-Fused Oligo-BODIPYs: A Class of Intensely Near-Infrared Absorbing, Arc-Shaped Materials with up to 31 Linearly-Fused Rings. *J. Am. Chem. Soc.* **2025**, *147*, 21041–21052. https://doi.org/10.1021/jacs.5c05873.

(4) An, D.; Jiang, W.; Zhang, Z.; Wang, S.; Wang, W.; Miao, C.; Shao, J.; Dong, X. Aza-BODIPY Dye with D-π-A Architecture for 1064 nm Laser-Triggered Photothermal Theranostics. *Sens. Actuators B Chem.* **2025**, *442*, 138144. https://doi.org/10.1016/j.snb.2025.138144.

(5) Kim, Y.; Kim, Y. Strategic Acetylation of BODIPY Dyes: Tuning Excited-State Geometry for the Design of Fluorogenic Sensing Probes. *Org. Lett.* **2025**, *27*, 6710–6715. https://doi.org/10.1021/acs.orglett.5c01822.

(6) Kim, H.; Burghart, A.; Welch, M. B.; Reibenspies, J.; Burgess, K. Synthesis and Spectroscopic Properties of a New 4-Bora-3a,4a-Diaza-s-Indacene (BODIPY) Dye. *Chem. Commun.* **1999**, *1999*, 1889-1890.

(7) Lim, H.; Seo, S.; Pascal, S.; Bellier, Q.; Rigaut, S.; Park, C.; Shin, H.; Maury, O.; Andraud, C.; Kim, E. NIR Electrofluorochromic Properties of Aza-Boron-Dipyrromethene Dyes. *Sci. Rep.* **2016**, *6*, 18867. https://doi.org/10.1038/srep18867.

(8) Cordeiro, P.; Menezes, V.; Ebersol, C.; Gomes, J. P. M.; Lião, L. M.; Braga, A. L.; Neto, J. S. S.; Nascimento, V. BODIPY Dyes: From Chalcogen-Based Synthesis to Emerging Applications and Sulfur Compound Detection. *Dyes Pigm.* **2025**, *242*, 112985. https://doi.org/10.1016/j.dyepig.2025.112985.

(9) Mastroeni, P. J.; Armstrong, C. B.; Black, D. J.; Strickland, A.; Hall, M.; Blundell, T.; Pridmore, N. E.; Pal, R.; Stachelek, P. Synthesis, Characterisation and Application of Red-Emitting BODIPY Dyes for Multiphoton Microscopy of Lipid Droplets. *Dyes Pigm.* **2025**, *243*, 113045. https://doi.org/10.1016/j.dyepig.2025.113045.

(10) Zhu, Y.; Zhu, Z.; Wang, S.; Peng, Q.; Abdurahman, A. Stable Luminescent Diradicals: The Emergence and Potential Applications. *Angew. Chem. Int. Ed.* **2025**, *64*, e202423470. https://doi.org/10.1002/anie.202423470.

(11) Su, J.; Zhu, L.; Dong, Z.; Liu, M.; Zhang, F.; Li, X.; Wang, S.; Chen, Z. Triphenylamine-Functionalized Aza-BODIPY Dyes: Synthesis, Characterization, and Their Application as Hole Transport Materials in Perovskite Solar Cells. *Org. Chem. Front.* **2024**, *11*, 7044–7052. https://doi.org/10.1039/D4QO01616E.

(12) Żubertowski, J.; Rapp, M.; Dolicher, J.; Rubiś, B.; Dembska, A. Investigation of Simple BODIPY Dyes as G-Quadruplex Recognizing Ligands. *RSC Adv.* **2025**, *15*, 5220–5231. https://doi.org/10.1039/D4RA08464K.

(13) Schad, C.; Ray, C.; Díaz-Norambuena, C.; Serrano-Buitrago, S.; Moreno, F.; Maroto, B. L.; García-Moreno, I.; Muñoz-Úbeda, M.; López-Montero, I.; Bañuelos, J.; Moya, S. de la. Water-Soluble BODIPY Dyes: A Novel Approach for Their Sustainable Chemistry and Applied Photonics. *Chem. Sci.* **2025**, *16*, 8030–8039. https://doi.org/10.1039/D5SC01295C.

(14) Oyelowo, M.; Schaffner, J. W.; Jeaydi, T. I.; Blank, D. A.; Ziegler, C. J.; Nemykin, V. N. Introducing of an Unexplored Aza-BODIPY Diradicaloids with 4-(2,6-Di *Tert* -Butyl)Phenoxyl Radicals Located in 1,7-Positions of the Aza-BODIPY Core. *Inorg. Chem.* **2024**, *63*, 24008–24021. https://doi.org/10.1021/acs.inorgchem.4c04409.

(15) Zou, Y.; Li, Z.; Ma, H.; Xu, X.; Yang, C.; Huang, Y.; Zhang, H. Phenolic Deprotonation Triggered NIR Emission and Large Stokes Shifts of BODIPY Dyes. *J. Mater. Chem. C Mater.* **2025**, *13*, 12944–12955. https://doi.org/10.1039/D5TC00937E.

(16) Boens, N.; Verbelen, B.; Dehaen, W. Postfunctionalization of the BODIPY Core: Synthesis and Spectroscopy. *Eur. J. Org. Chem.* **2015**, *2015*, 6577–6595. https://doi.org/10.1002/ejoc.201500682.

(17) Boens, N.; Verbelen, B.; Ortiz, M. J.; Jiao, L.; Dehaen, W. Synthesis of BODIPY Dyes through Postfunctionalization of the Boron Dipyrromethene Core. *Coord. Chem. Rev.* **2019**, *399*, 213024. https://doi.org/10.1016/j.ccr.2019.213024.

(18) Sheng, W.; Cui, J.; Ruan, Z.; Yan, L.; Wu, Q.; Yu, C.; Wei, Y.; Hao, E.; Jiao, L. [*A*]-Phenanthrene-Fused BF $_2$ Azadipyrromethene (AzaBODIPY) Dyes as Bright Near-Infrared Fluorophores. *J. Org. Chem.* **2017**, *82*, 10341–10349. https://doi.org/10.1021/acs.joc.7b01803.

(19) Sheng, W.; Zheng, Y. Q.; Wu, Q.; Wu, Y.; Yu, C.; Jiao, L.; Hao, E.; Wang, J. Y.; Pei, J. Synthesis, Properties, and Semiconducting Characteristics of BF2 Complexes of β,β-Bisphenanthrene-Fused Azadipyrromethenes. *Org. Lett.* **2017**, *19*, 2893–2896. https://doi.org/10.1021/acs.orglett.7b01133.

(20) Gayathri, T.; Rao, R. S.; Gupta, V.; Singh, S. P. Panchromatic Aza-Bodipy Based π-Conjugates. *New J. Chem.* **2021**, *45*, 7792–7798. https://doi.org/10.1039/d1nj00847a.

(21) Bialas, D.; Kirchner, E.; Röhr, M. I. S.; Würthner, F. Perspectives in Dye Chemistry: A Rational Approach toward Functional Materials by Understanding the Aggregate State. *J. Am. Chem. Soc*. **2021**, *143*, 4500−4518. https://doi.org/10.1021/jacs.0c13245.

(22) Wang, Y.; Xiao, F.; Shao, T.; Jin, G. A Near-Infrared Azadipyrromethene Dye: Photophysical Properties under Different Acidity Conditions. *Inorg. Chem. Commun.* **2020**, *116*, 107942. https://doi.org/10.1016/j.inoche.2020.107942.

(23) Glembockyte, V.; Cosa, G. Redox-Based Photostabilizing Agents in Fluorescence Imaging: The Hidden Role of Intersystem Crossing in Geminate Radical Ion Pairs. *J. Am. Chem. Soc.* **2017**, *139*, 13227–13233. https://doi.org/10.1021/jacs.7b08134.

(24) Didukh, N. O.; Yakubovskyi, V. P.; Zatsikha, Y. V.; Nemykin, V. N.; Kovtun, Y. P. Meso-Nitromethyl-Substituted BODIPYs – A New Type of Water Switchable

Fluorogenic Dyes Useful for Further Core Modifications. *Dyes Pigm.* **2018**, *149*, 774–782. https://doi.org/10.1016/j.dyepig.2017.11.037.

(25) Langhals, H. Color Chemistry. Synthesis, Properties and Applications of Organic Dyes and Pigments. 3rd Revised Edition. By Heinrich Zollinger. *Angew. Chem. Int. Ed.* **2004**, *43*, 5291–5292. https://doi.org/10.1002/anie.200385122.

(26) Tang, Q.; Si, W.; Huang, C.; Ding, K.; Huang, W.; Chen, P.; Zhang, Q.; Dong, X. An Aza-BODIPY Photosensitizer for Photoacoustic and Photothermal Imaging Guided Dual Modal Cancer Phototherapy. *J. Mater. Chem. B* **2017**, *5*, 1566–1573. https://doi.org/10.1039/c6tb02979e.

(27) Pliquett, J.; Dubois, A.; Racoeur, C.; Mabrouk, N.; Amor, S.; Lescure, R.; Bettaïeb, A.; Collin, B.; Bernhard, C.; Denat, F.; Bellaye, P. S.; Paul, C.; Bodio, E.; Goze, C. A Promising Family of Fluorescent Water-Soluble Aza-BODIPY Dyes for in Vivo Molecular Imaging. *Bioconjug. Chem.* **2019**, *30*, 1061–1066. https://doi.org/10.1021/acs.bioconjchem.8b00795.

(28) Yadav, I. S.; Misra, R. Design, Synthesis and Functionalization of BODIPY Dyes: Applications in Dye-Sensitized Solar Cells (DSSCs) and Photodynamic Therapy (PDT). *J. Mater. Chem. C Mater.* **2023**, *11*, 8688–8723. https://doi.org/10.1039/D3TC00171G.

(29) Zhang, Y.; Cui, Z.; Širůček, J.; Jacquemin, D.; Le Guennic, B.; Sun, X.; Jiang, X.-D.; Qin, G. Embedding Oxygen Heterocycles into BODIPY to Enhance Intersystem Crossing for Photodynamic Therapy. *J. Mater. Chem. B* **2025**, *13*, 8833–8843. https://doi.org/10.1039/D5TB00427F.

(30) Ivaniuk, K.; Pidluzhna, A.; Stakhira, P.; Baryshnikov, G. V.; Kovtun, Y. P.; Hotra, Z.; Minaev, B. F.; Ågren, H. BODIPY-Core 1,7-Diphenyl-Substituted Derivatives for Photovoltaics and OLED Applications. *Dyes Pigm.* **2020**, *175*, 108123. https://doi.org/10.1016/j.dyepig.2019.108123.

(31) Bertran, A.; Ciuti, S.; Panariti, D.; Rogers, C. J.; Wang, H.; Zhao, J.; Timmel, C. R.; Gobbo, M.; Barbon, A.; Di Valentin, M.; Bowen, A. M. I $_2$ BODIPY as a New Photoswitchable Spin Label for Light-Induced Pulsed EPR Dipolar Spectroscopy Exploiting Magnetophotoselection. *Phys. Chem. Chem. Phys.* **2024**, *26*, 28398–28405. https://doi.org/10.1039/D4CP02297A.

(32) Kaur, M.; Janaagal, A.; Balsukuri, N.; Gupta, I. Evolution of Aza-BODIPY Dyes-A Hot Topic. *Coord. Chem. Rev.* **2024**, *498*, 215428. https://doi.org/10.1016/j.ccr.2023.215428.

(33) Zhang, D.; Liu, L.; Zhang, X.; Lu, J.; Jiang, X.-D. Rational Design of Photofunctional Dyes BODIPYs/Aza-BODIPYs and Applications for Photocatalysis, Photoelectric Conversion and Thermochromic Materials. *Resour. Chem. Mater.* **2024**, *3*, 103–122. https://doi.org/10.1016/j.recm.2024.01.001.

(34) Wang, Y.; Zhang, D.; Xiong, K.; Shang, R.; Jiang, X.-D. Near-Infrared Absorbing (>700 Nm) Aza-BODIPYs by Freezing the Rotation of the Aryl Groups. *Chin. Chem. Lett.* **2022**, *33*, 115–122. https://doi.org/10.1016/j.cclet.2021.06.083.

(35) Rappitsch, T.; M. Borisov, S. Carbazole- and Fluorene-Fused Aza-BODIPYs: NIR Fluorophores with High Brightness and Photostability. *Chem. - Eur. J.* **2021**, *27*, 10685–10692. https://doi.org/10.1002/chem.202100965.

(36) Duran-Sampedro, G.; Agarrabeitia, A. R.; Garcia-Moreno, I.; Costela, A.; Bañuelos, J.; Arbeloa, T.; López Arbeloa, I.; Chiara, J. L.; Ortiz, M. J. Chlorinated BODIPYs: Surprisingly Efficient and Highly Photostable Laser Dyes. *Eur. J. Org. Chem.* **2012**, *2012*, 6335–6350. https://doi.org/10.1002/ejoc.201200946.

(37) Wang, M.; Vicente, M. G. H.; Mason, D.; Bobadova-Parvanova, P. Stability of a Series of BODIPYs in Acidic Conditions: An Experimental and Computational Study into the Role of the Substituents at Boron. *ACS Omega* **2018**, *3*, 5502–5510. https://doi.org/10.1021/acsomega.8b00404.

(38) Rohand, T.; Qin, W.; Boens, N.; Dehaen, W. Palladium-Catalyzed Coupling Reactions for the Functionalization of BODIPY Dyes with Fluorescence Spanning the Visible Spectrum. *Eur. J. Org. Chem.* **2006**, *20*, 4658–4663. https://doi.org/10.1002/ejoc.200600531.

(39) Loudet, A.; Bandichhor, R.; Wu, L.; Burgess, K. Functionalized BF2 Chelated Azadipyrromethene Dyes. *Tetrahedron* **2008**, *64,* 3642–3654. https://doi.org/10.1016/j.tet.2008.01.117.

(40) Patra, A.; Patalag, L. J.; Jones, P. G.; Werz, D. B. Extended Benzene-Fused Oligo-BODIPYs: In Three Steps to a Series of Large, Arc-Shaped, Near-Infrared Dyes. *Angew. Chem. Int. Ed.* **2021**, *60*, 747–752. https://doi.org/10.1002/anie.202012335.

(41) Labella, J.; Durán-Sampedro, G.; Krishna, S.; Martínez-Díaz, M. V.; Guldi, D. M.; Torres, T. Anthracene-Fused Oligo-BODIPYs: A New Class of Π-Extended NIR-Absorbing Materials. *Angew. Chem. Int. Ed.* **2023**, *62*, e202214543. https://doi.org/10.1002/anie.202214543.

(42) Shandura, M. P.; Yakubovskyi, V. P.; Kovtun, Y. P. (4,4-Difluoro-4-bora-3a,4a,-diaza-s-indacen-3-yl)Acetaldehyde: Synthesis and Chemical Properties. *J. Heterocycl. Chem.* **2009**, *46*, 1386–1391. https://doi.org/10.1002/jhet.263.

(43) Kovtun, O. M.; Zatsikha, Y. V.; Kovtun, Y. P. New Approaches to the Modification of Chemical Structure and Photophysical Properties of BODIPY Dyes. *Chem. Heterocycl. Compd.* **2023**, *59*, 357–367. https://doi.org/10.1007/s10593-023-03205-y.

(44) Zatsikha, Y. V.; Swedin, R. K.; Healy, A. T.; Goff, P. C.; Didukh, N. O.; Blesener, T. S.; Kayser, M.; Kovtun, Y. P.; Blank, D. A.; Nemykin, V. N. Synthesis, Characterization, and Electron-Transfer Properties of Ferrocene–BODIPY–Fullerene Near-Infrared-Absorbing Triads: Are Catecholopyrrolidine-Linked Fullerenes a Good Architecture to Facilitate Electron-Transfer? *Chem. - Eur. J.* **2019**, *25*, 8401–8414. https://doi.org/10.1002/chem.201901225.

(45) Thompson, B. L.; Kieffer, I. A.; Heiden, Z. M. Utilization of BODIPY-Based Redox Events to Manipulate the Lewis Acidity of Fluorescent Boranes. *Chem. Commun.* **2022**, *58*, 2646–2649. https://doi.org/10.1039/D1CC06400B.

(46) Benniston, A. C.; Copley, G.; Elliott, K. J.; Harrington, R. W.; Clegg, W. Redox-Controlled Fluorescence Modulation in a BODIPY-Quinone Dyad. *Eur. J. Org. Chem.* **2008**, *2008*, 2705–2713. https://doi.org/10.1002/ejoc.200800191.

(47) Wei, H.; Feng, R.; Fang, Y.; Wang, L.; Chen, C.; Zhang, L.; Cui, H.; Wang, X. The Diradical-Dication Strategy for BODIPY- and Porphyrin-Based Dyes with Near-

Infrared Absorption Maxima from 1070 to 2040 Nm. *Chem. - Eur. J.* **2018**, *24*, 19341–19347. https://doi.org/10.1002/chem.201804449.

(48) Pachpatil, P. K.; Kanojia, S. V.; Ghosh, A.; Majumdar, A. G.; Wadawale, A.; Mohapatra, M.; Patro, B. S.; Ghanty, T. K.; Goswami, D. Stable, Triplet Ground State BODIPY-TEMPO Diradical as a Selective Turn on Fluorescence Sensor for Intracellular Labile Iron Pool. *Sens. Actuators B Chem.* **2022**, *370*, 132474. https://doi.org/10.1016/j.snb.2022.132474.

(49) Miao, F.; Phan, H.; Wu, J. A BODIPY-Bridged Bisphenoxyl Diradicaloid: Solvent-Dependent Diradical Character and Physical Properties. *Molecules* **2019**, *24*, 1446. https://doi.org/10.3390/molecules24081446.

(50) Ni, Y.; Lee, S.; Son, M.; Aratani, N.; Ishida, M.; Samanta, A.; Yamada, H.; Chang, Y.; Furuta, H.; Kim, D.; Wu, J. A Diradical Approach towards BODIPY-Based Dyes with Intense Near-Infrared Absorption around λ =1100 Nm. *Angew. Chem. Int. Ed.* **2016**, *55*, 2815–2819. https://doi.org/10.1002/anie.201511151.

(51) Oyelowo, M.; Jeaydi, T. I.; Ziegler, C. J.; Nemykin, V. N. Design of Stable Diradicals Based on Group 13 Dyes of N_2O_2-Bis(Phenolate) Aza-Dipyrromethene and Aza-BODIPY. *Inorg. Chem.* **2025**, *64*, 17946−17959. https://doi.org/10.1021/acs.inorgchem.5c03026.

(52) Wu, J. *Diradicaloids*; Jenny Stanford Publishing: New York, **2022**, (1−638). https://doi.org/10.1201/9781003277248.

(53) Hu, X.; Wang, W.; Wang, D.; Zheng, Y. The Electronic Applications of Stable Diradicaloids: Present and Future. *J. Mater. Chem. C Mater.* **2018**, *6*, 11232–11242. https://doi.org/10.1039/C8TC04484H.

(54) Liu, Y.; Phan, H.; Herng, T. S.; Gopalakrishna, T. Y.; Ding, J.; Wu, J. Toward Benzobis(Thiadiazole)-based Diradicaloids. *Chem. Asian J.* **2017**, *12*, 2177–2182. https://doi.org/10.1002/asia.201700732.

(55) Vidal, E.; Warren, G. I.; Barker, J. E.; Haley, M. M. The Interplay of Antiaromaticity and Diradical Character in Diarenoindacenes and Diindenoarenes. *Chem. Sci.* **2025**, *16*, 19026–19047. https://doi.org/10.1039/D5SC05050B.

(56) Barker, J. E.; Dressler, J. J.; Cárdenas Valdivia, A.; Kishi, R.; Strand, E. T.; Zakharov, L. N.; Macmillan, S. N.; Gómez-García, C. J.; Nakano, M.; Casado, J.; Haley, M. M. Molecule Isomerism Modulates the Diradical Properties of Stable Singlet Diradicaloids. *J. Am. Chem. Soc.* **2020**, *142*, 1548–1555. https://doi.org/10.1021/jacs.9b11898.

(57) Huang, R.; Phan, H.; Herng, T. S.; Hu, P.; Zeng, W.; Dong, S.; Das, S.; Shen, Y.; Ding, J.; Casanova, D.; Wu, J. Higher Order π-Conjugated Polycyclic Hydrocarbons with Open-Shell Singlet Ground State: Nonazethrene versus Nonacene. *J. Am. Chem. Soc.* **2016**, *138*, 10323–10330. https://doi.org/10.1021/jacs.6b06188.

(58) Lee, S.; Miao, F.; Phan, H.; Herng, T. S.; Ding, J.; Wu, J.; Kim, D. Radical and Diradical Formation in Naphthalene Diimides through Simple Chemical Oxidation. *ChemPhysChem* **2017**, *18*, 591–595. https://doi.org/10.1002/cphc.201700015.

(59) Wang, Z.; Dai, Y.; Ding, L.; Dong, B.; Jiang, S.; Wang, J.; Pei, J. A Stable Triplet-Ground-State Conjugated Diradical Based on a Diindenopyrazine Skeleton. *Angew. Chem. Int. Ed.* **2021**, *60*, 4594–4598. https://doi.org/10.1002/anie.202012989.

(60) Kodama, T.; Hirao, Y.; Kubo, T. Synthesis and Properties of a Through-Space Interacting Diradicaloid. *Precision Chemistry* **2023**, *1*, 183–191. https://doi.org/10.1021/prechem.3c00024.

(61) Nakano, M. Open-Shell-Character-Based Molecular Design Principles: Applications to Nonlinear Optics and Singlet Fission. *The Chemical Record* **2017**, *17*, 27–62. https://doi.org/10.1002/tcr.201600094.

(62) Ramos-Cordoba, E.; Salvador, P. Diradical Character from the Local Spin Analysis. *Physical Chemistry Chemical Physics* **2014**, *16*, 9565. https://doi.org/10.1039/c4cp00939h.

(63) Nguyen, K. A.; Pachter, R. Density Functional Theory Calculations of Spin Polarization for Diradicals in Single-Molecule Junctions. *ACS Omega* **2026**, *11*, 15786–15794. https://doi.org/10.1021/acsomega.5c07837.

(64) Yeo, H.; Debnath, S.; Krishnan, B. P.; Boudouris, B. W. Radical Polymers in Optoelectronic and Spintronic Applications. *RSC Applied Polymers* **2024**, *2*, 7–25. https://doi.org/10.1039/D3LP00213F.

(65) Gao, S.; Li, F. Neutral Stable Nitrogen-Centered Radicals: Structure, Properties, and Recent Functional Application Progress. *Adv. Funct. Mater.* **2023**, *33*, 2304291. https://doi.org/10.1002/adfm.202304291.

(66) Chen, Z. X.; Li, Y.; Huang, F. Persistent and Stable Organic Radicals: Design, Synthesis, and Applications. *Chem* **2021**, *7*, 288–332. https://doi.org/10.1016/j.chempr.2020.09.024.

(67) Hu, P.; Lee, S.; Herng, T. S.; Aratani, N.; Gonçalves, T. P.; Qi, Q.; Shi, X.; Yamada, H.; Huang, K.-W.; Ding, J.; Kim, D.; Wu, J. Toward Tetraradicaloid: The Effect of Fusion Mode on Radical Character and Chemical Reactivity. *J. Am. Chem. Soc.* **2016**, *138*, 1065–1077. https://doi.org/10.1021/jacs.5b12532.

(68) Sugiura, S.; Kubo, T.; Haketa, Y.; Hori, Y.; Shigeta, Y.; Sakai, H.; Hasobe, T.; Maeda, H. Deprotonation-Induced and Ion-Pairing-Modulated Diradical Properties of Partially Conjugated Pyrrole–Quinone Conjunction. *J. Am. Chem. Soc.* **2023**, *145*, 8122–8129. https://doi.org/10.1021/jacs.3c01025.

(69) Palit, D. K.; Pal, H.; Mukherjee, T.; Mittal, J. P. Triplet Excited States and Semiquinone Radicals of 1,4-Disubstituted Anthraquinones. *J. Photochem. Photobiol. A Chem.* **1990**, *52*, 375–390. https://doi.org/10.1016/1010-6030(90)85017-Q.

(70) Intorp, S. N.; Hodecker, M.; Müller, M.; Tverskoy, O.; Rosenkranz, M.; Dmitrieva, E.; Popov, A. A.; Rominger, F.; Freudenberg, J.; Dreuw, A.; Bunz, U. H. F. Quinoidal Azaacenes: 99 % Diradical Character. *Angew. Chem. Int. Ed.* **2020**, *59*, 12396–12401. https://doi.org/10.1002/anie.201915977.

(71) Petakova, V.; Nedyalkova, M.; Stoycheva, J.; Tadjer, A.; Romanova, J. The Interplay between Diradical Character and Stability in Organic Molecules. *Symmetry.* **2021**, *13*, 1448. https://doi.org/10.3390/sym13081448.

(72) Zeng, W.; Wu, J. Push–Pull Type Quinoidal Perylene Showing Solvent Polarity Dependent Diradical Character and Negative Solvatochromism. *Mater. Chem. Front.* **2019**, *3*, 2668–2672. https://doi.org/10.1039/C9QM00566H.

(73) Casado, J. Para-Quinodimethanes: A Unified Review of the Quinoidal-Versus-Aromatic Competition and Its Implications. *Top. Curr. Chem.* **2017**, *375*, 73. https://doi.org/10.1007/s41061-017-0163-2.

(74) Gao, H.; Liu, H.; Jiang, L.; Gai, L.; Shen, Z. A Near-Infrared Benzoquinone-Coupled BODIPY: Synthesis, Spectroscopic and Electrochemical Properties. *J. Porphyr. Phthalocyanines* **2019**, *23*, 76–83. https://doi.org/10.1142/S1088424619500044.

(75) Yakubovskyi, V. P.; Didukh, N. O.; Zatsikha, Y. V.; Kovtun, Y. P. A New Approach to the Synthesis of *Meso* -CN-Substituted BODIPYs. *ChemistrySelect* **2016**, *1*, 1462–1466. https://doi.org/10.1002/slct.201600246.

(76) Díaz-Moscoso, A.; Emond, E.; Hughes, D. L.; Tizzard, G. J.; Coles, S. J.; Cammidge, A. N. Synthesis of a Class of Core-Modified Aza-BODIPY Derivatives. *J. Org. Chem.* **2014**, *79*, 8932–8936. https://doi.org/10.1021/jo501863t.

(77) Parthey, M.; Kaupp, M. Quantum-Chemical Insights into Mixed-Valence Systems: Within and beyond the Robin–Day Scheme. *Chem. Soc. Rev.* **2014**, *43*, 5067–5088. https://doi.org/10.1039/C3CS60481K.

(78) Frisch, M. J.; Trucks, G. W.; Schlegel, H. B.; Scuseria, G. E.; Robb, M. A.; Cheeseman, J. R.; Scalmani, G.; Barone, V.; Petersson, G. A.; Nakatsuji, H.; Li, X.; Caricato, M.; Marenich, A. V.; Bloino, J.; Janesko, B. G.; Gomperts, R.; Mennucci, B.; Hratchian, H. P.; Ortiz, J. V.; Izmaylov, A. F.; Sonnenberg, J. L.; Williams-Young, D.;

Ding, F.; Lipparini, F.; Egidi, F.; Goings, J.; Peng, B.; Petrone, A.; Henderson, T.; Ranasinghe, D.; Zakrzewski, V. G.; Gao, J.; Rega, N.; Zheng, G.; Liang, W.; Hada, M.; Ehara, M.; Toyota, K.; Fukuda, R.; Hasegawa, J.; Ishida, M.; Nakajima, T.; Honda, Y.; Kitao, O.; Nakai, H.; Vreven, T.; Throssell, K.; Montgomery, J. A., Jr.; Peralta, J. E.; Ogliaro, F.; Bearpark, M. J.; Heyd, J. J.; Brothers, E. N.; Kudin, K. N.; Staroverov, V. N.; Keith, T. A.; Kobayashi, R.; Normand, J.; Raghavachari, K.; Rendell, A. P.; Burant, J. C.; Iyengar, S. S.; Tomasi, J.; Cossi, M.; Millam, J. M.; Klene, M.; Adamo, C.; Cammi, R.; Ochterski, J. W.; Martin, R. L.; Morokuma, K.; Farkas, O.; Foresman, J. B.; Fox, D. J. *Gaussian 16, Revision B.01*; Gaussian, Inc.: Wallingford CT, **2016**.

(79) Tenderholt, A. L. *QMForge, version 2.1*; Standord University: Stanford, CA, **2011**. https://qmforge.net/.

(80) Tao, J. M.; Perdew, J. P.; Staroverov, V. N.; Scuseria, G. E. Climbing the density functional ladder: Nonempirical metageneralized gradient approximation designed for molecules and solids. *Phys. Rev. Lett.* **2003**, *91*, 146401(1−4). https://doi.org/10.1103/PhysRevLett.91.146401

(81) McLean, A. D.; Chandler, G. S. Contracted Gaussian Basis Sets for Molecular Calculations. I. Second Row Atoms, Z = 11−18. *J. Chem. Phys*. **1980**, *72*, 5639−5648. https://doi.org/10.1063/1.438980

(82) Sheldrick, G. M. A short history of *SHELX*. *Acta Crystallogr.* **2008**, *A64*, 112-122. DOI: 10.1107/S0108767307043930

(83) *Bruker-AXS APEX3 v2016.1-0*, Madison, Wisconsin, USA, **2016**.

(84) Spek, A. L. Structure validation in chemical crystallography. *Acta Crystallogr.* **2009**, *D65*, 148-155. DOI: 10.1107/S090744490804362X

(85) Macrae, C. F.; Sovago, I.; Cottrell, S. J.; Galek, P. T. A.; McCabe, P.; Pidcock, E.; Platings, M.; Shields, G. P.; Stevens, J. S.; Towler, M.; Wood, P. A. Mercury 4.0: from visualization to analysis, design and prediction. *J. Appl. Crystallogr.* **2020**, *53*, 226-235. DOI: 10.1107/S1600576719014092.

Appendix

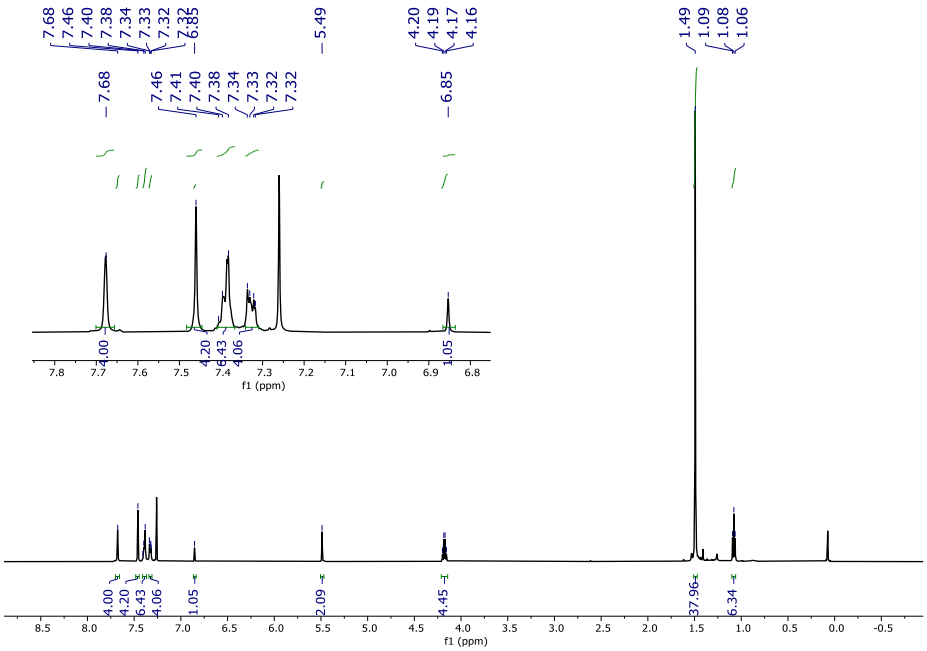


Figure 5.15**:** ^{1}H NMR of BODIPY **5.7** in $CDCl_3$ at 298 K.

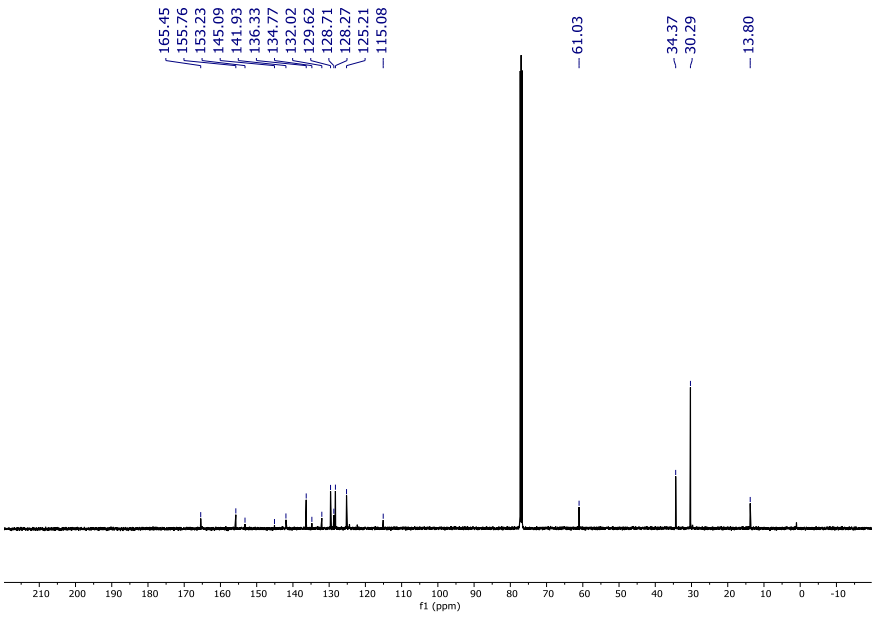


Figure 5.16: ^{13}C NMR of BODIPY **5.7** in $CDCl_3$ at 298 K.

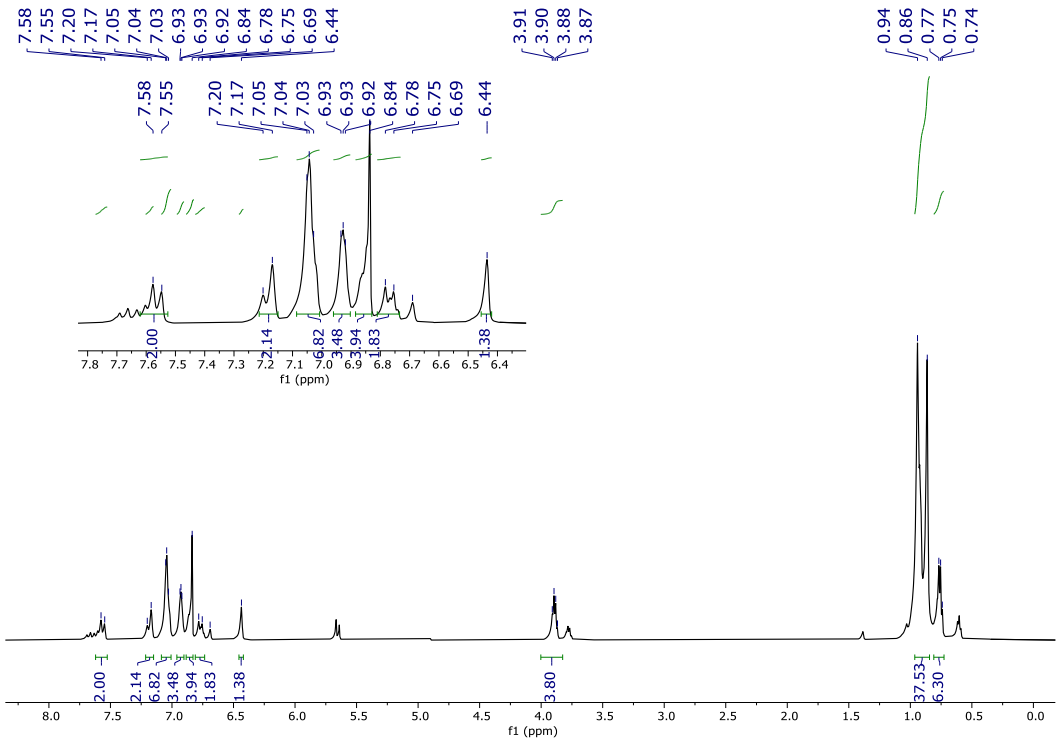


Figure 5.17: ^{1}H NMR of BODIPY **5.8** in CD_2Cl_2 at 220 K

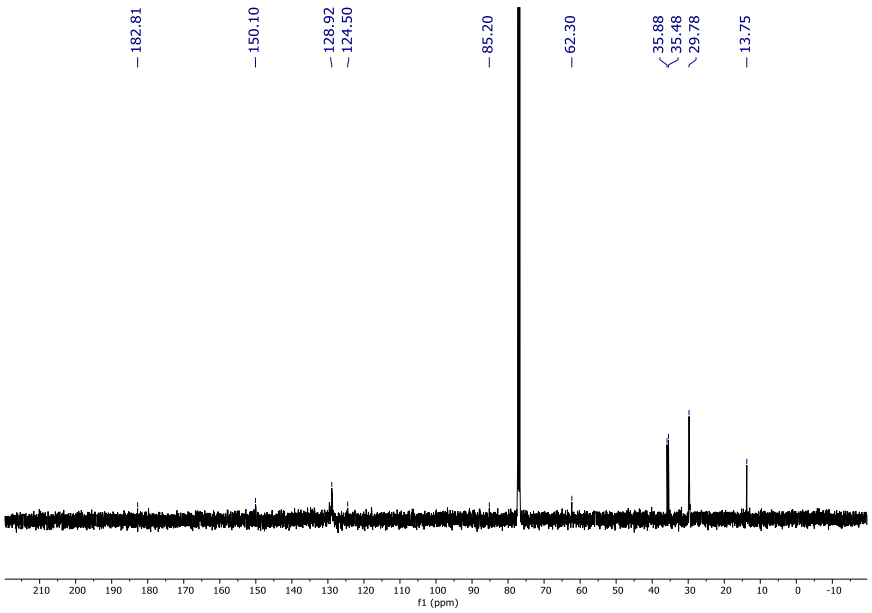


Figure 5.18: ^{13}C NMR of BODIPY **5.8** in $CDCl_3$ at 298 K

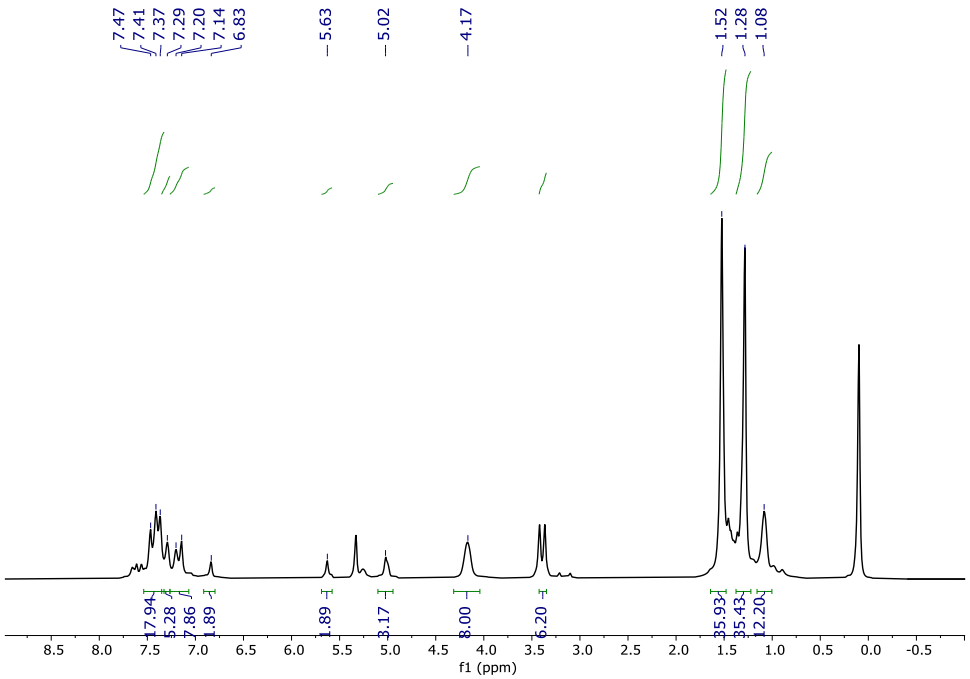


Figure 5.19: ^{1}H NMR of BODIPY **5.9** in CD_2Cl_2 at 220 K

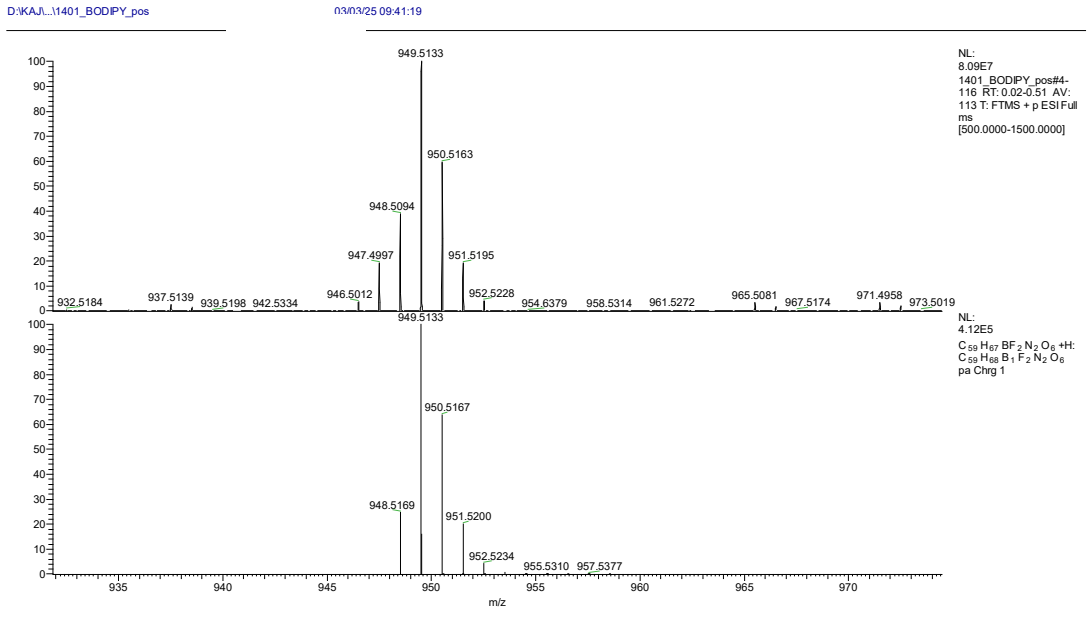


Figure 5.20: Mass spectrum of BODIPY **5.7** (ESI)

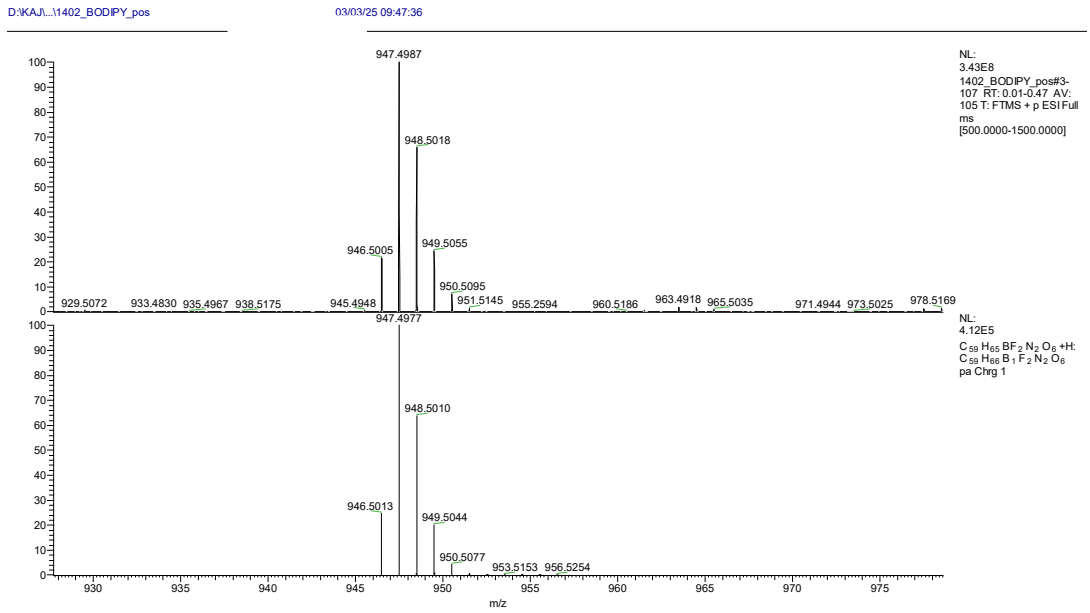


Figure 5.21: Mass spectrum of BODIPY **5.8** (ESI)

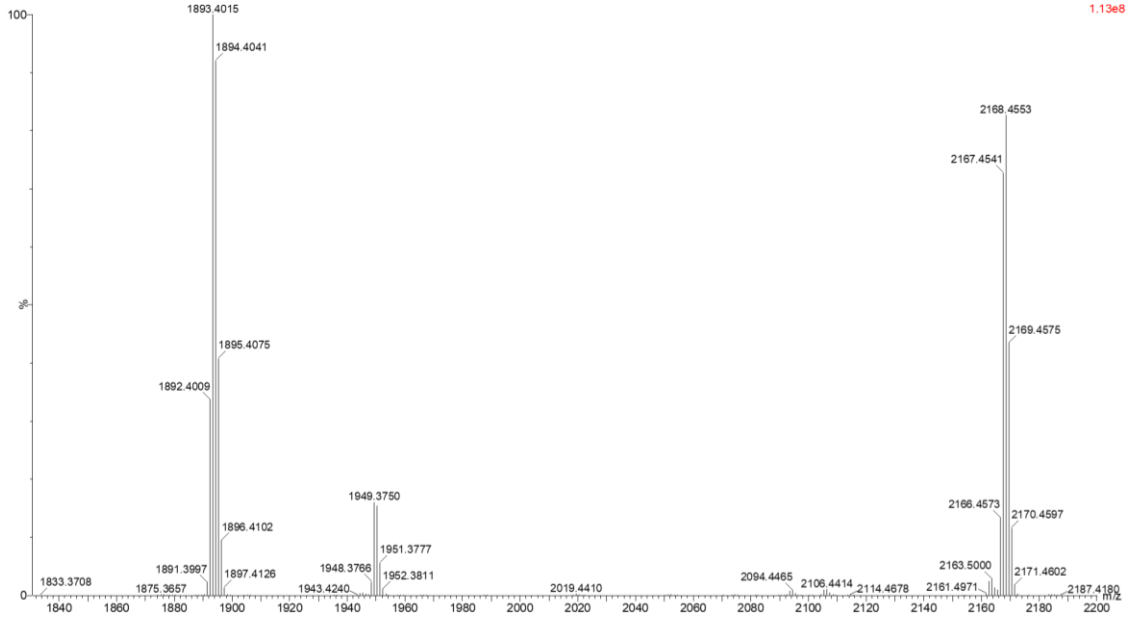


Figure 5.22: Mass Spectrum of BODIPY **5.9** (ESI).

Table 5.2a. Major TDDFT-Predicted Excited States of BODIPY **5.7**

Excited State	*Wavelength (nm)*	*Energy (cm^{-1})*	*Oscillator Strength, f*	*% Contributions*
1	746	13409	1.077	H→L (100%)
2	560	17872	0.5740	H-1→ L (97%)
3	456	21921	0.1289	H-2→L (84%), H-3→L (11%)
4	429	23337	0.2782	H-4→L (97%)
6	409	24464	1.006	H→L+1 (86%), H-5→L (8%)
8	406	24632	0.1034	H-5→L (92%), H→L+1 (8%)
15	340	29454	0.3619	H-1→L+2 (80%), H-11→L (12%), H→L+3 (7%)
57	251	39916	0.1133	H-1→L+9 (80%), H-1→L+8 (8%)

Table 5.2b. Major TDDFT-Predicted Excited States of BODIPY **5.8(CS)**

Excited State	*Wavelength (nm)*	*Energy (cm^{-1})*	*Oscillator Strength, f*	*% Contributions*
1	1033	9685	1.151	H→L (100%)
5	569	17574	0.8579	H-4→L (62%), H→L+1 (24%), H-1→L(14%)
7	529	18912	1.938	H-4→L (37%), H→L+1 (34%), H-1→L(25%)
19	393	25421	0.2461	H-5→L+1 (63%), H→L+3 (33%)

Table 5.2c. Major TDDFT-Predicted Excited States of BODIPY **5.8(TS)**

Excited State	*Wavelength (nm)*	*Energy (cm^{-1})*	*Oscillator Strength, f*	*% Contributions*
4	876	11421	1.020	H(A) →L(A) (53%), H(B) →L(B) (46%)
7	687	14566	0.1576	H-4(B) →L(B) (79%), H(B) →L+1(B)
12	649	15414	0.2311	H-1(A) →L(A) (34%), H(B) →L+1(B) (31%), H-9(B) →L(B) (15%), H-4(B) →L(B) (15%)
13	577	17328	0.3278	H-9(B) →L(B) (44%), H(A) →L+1(A) (21%), H-1(A) →L(A) (17%), H-7(B) →L(B) (9%)
31	452	22107	0.4129	H-6(A) →L(A) (45%), H(A) →L+1(A) (20%), H-4(B) →L+2(B) (12%), H-9(B) →L(B) (8%)
49	368	27182	0.1040	H-1(A)→L+2(A) (54%), H-13(A)→L(A) (10%), H-12(B)→L+1(B) (10%), H-9(B)→L+2(B) (7%), H-11(A)→L(A) (6%)

Table 5.2d. Major TDDFT-Predicted Excited States of BODIPY **5.8(OS)**

Excited State	*Wavelength (nm)*	*Energy (cm^{-1})*	*Oscillator Strength, f*	*% Contributions*
2	1304	7669	0.422	H-49(B)→L+1(B) (6%), H-45(A)→L(A) (6%), H-13(B)→L+9(B) (6%), H-5(B)→L+6(B) (6%), H-48(B)→L(B) (5%), H-12(B)→L+4(B) (5%), H-12(B)→L+8(B) (5%)
7	762	13118	0.1051	H-11(B)→L+6(B) (5%)
11	683	14643	0.3182	H-57(A)→L(A) (49%), H-29(B)→L+1(B) (22%), H-47(B)→L(B) (15%), H-61(A)→L(A) (15%), H-12(B)→L+5(B) (15%), H-61(B)→L(B) (14%), H-45(A)→L(A) (12%), H-5(A)→L+6(A) (11%), H-13(A)→L+6(A) (10%), H-3(B)→L+10(B) (10%), H-62(A)→L(A) (10%), H-1(A)→L+10(A) (10%), H-10(A)→L+6(A) (10%), H-49(A)→L+1(A) (10%), H-38(A)→L+1(A) (9%), H-13(A)→L+9(A) (8%), H-12(B)→L+6(B) (8%), H-1(B)→L+10(B) (8%), H-57(B)→L(B) (8%), H-14(A)→L+8(A) (8%), H-14(B)→L+3(B) (7%), H-56(A)→L(A) (7%), H-11(A)→L+4(A) (7%), H-37(B)→L+1(B) (7%), H-13(A)→L+3(A) (7%), H-58(A)→L(A) (7%), H-11(A)→L+6(A) (7%), H-60(A)→L(A) (6%), H-5(B)→L+8(B) (6%), H-5(B)→L+6(B) (6%), H-59(A)→L(A) (6%), H-10(B)→L+5(B) (6%)
44	394	25392	0.1748	H-5(B)→L+1(B) (27%), H-5(A)→L+1(A) (27%), H(B)→L+3(B) (18%), H(A)→L+3(A) (17%)

Table 5.2e. Major TDDFT-Predicted Excited States of Mixed Valent Radical Anion **[5.10]**$^{-\cdot}$

Excited State	*Wavelength (nm)*	*Energy (cm^{-1})*	*Oscillator Strength, f*	*% Contributions*
1	1790	5586	0.1716	H(B)→L(B) (87%), 12.8% H(A)→L(A) (13%)
2	996	10043	0.1024	H(B)→L+1(B) (69%), H-1(A)→L(A) (29%)
3	988	10125	0.9134	H(A)→L(A) (87%), H(B)→L(B) (12%)
7	627	15956	0.7273	H-1(A)→L(A) (54%), H(B)→L+1(B) (16%), H(A)→L+1(A) (16%), H-3(B)→L(B) (11%)
9	534	18723	0.1047	H-6(B)→L(B) (73%), H-4(B)→L(B) (13%)
11	531	18829	0.3237	H-4(B) →L(B) (58%), H-6(B)→L(B) (19%), H(A)→L+1(A) (10%)
21	462	21645	0.1280	H(B)→L+3(B) (61%), H-1(A)→L+2(A) (13%), H(A)→L+1(A) (9%)
25	414	24166	0.1001	H-1(A)→L+2(A) (26%), H-11(B)→L(B) (23%), H(B)→L+3(B) (19%), H-8(B)→L+1(B) (7%), H-5(B)→L+1(B) (7%), H-6(A)→L(A) (6%)
33	390	25616	0.1558	H-11(B)→L(B) (47%), H-8(B)→L+1(B) (12%), H-7(B)→L+1(B) (8%), H-6(A)→L(A) (7%), H-5(B)→L+1(B) (5%)

Table 5.2f. Major TDDFT-Predicted Excited States of Dianion **[5.11]$^{2-}$**

Excited State	*Wavelength (nm)*	*Energy (cm^{-1})*	*Oscillator Strength, f*	*% Contributions*
1	1077	9284	1.005	H→L (100%)
2	737	13563	0.5713	H-1→L (94%), H→L+2 (5%)
5	550	18180	0.1164	H→L+1 (81%), H→L+2 (9%), H-4→L (9%)
6	524	19073	1.368	H→L+2 (82%), H→L+1 (9%), H-1→L(5%)
7	480	20805	0.1604	H-4→L (69%), H-1→L+2 (19%), H→L+1 (6%)
9	437	22875	0.3361	H-1→L+1 (55%), H→L+3 (25%), H-1→L+2 (7%)
17	377	26541	0.1614	H-8→L (89%), H-9→L (7%)
21	363	27566	0.3462	H→L+7 (74%), H-9→L (15%), H-8→L (6%)
35	318	31444	0.1569	H→L+10 (78%), H-1→L+7 (19%)
53	281	35606	0.1195	H-1→L+9 (61%), H-4→L+4 (16%), H-6→L+2 (12%), H-5→L+2 (8%)
59	274	36476	0.1060	H-7→L+1 (79%), H-4→L+6 (10%), H-16→L(8%)

CHAPTER VI: CONCLUSIONS AND OUTLOOK

6.1 Conclusion

This dissertation has demonstrated that aza-BODIPY and aza-dipyrromethene frameworks provide versatile and highly tunable platforms for the development of stable open-shell molecular systems with attractive photophysical, magnetic, electrochemical, and charge-transport properties. Through systematic molecular design, synthesis, and comprehensive experimental and computational investigations, clear relationships between molecular structure, electronic configuration, magnetic spin-state behavior, and functional properties have been established.

The first part of this work introduced the first aza-BODIPY diradicaloids bearing 4-(2,6-di-tert-butyl)phenoxyl radicals at the 1,7-positions of the aza-BODIPY core. These compounds exhibited predominantly closed-shell singlet ground states with thermally accessible open-shell singlet and triplet states. Variable-temperature NMR, EPR spectroscopy, SQUID magnetometry, transient absorption spectroscopy, and DFT calculations revealed solvent-dependent diradical character, small singlet–triplet energy gaps, and ultrafast excited-state deactivation pathways associated with their open-shell nature. These results established aza-BODIPY chromophores as promising scaffolds for stable diradicaloid design.

Building upon this foundation, Chapter III focuses on design, synthesis and characterization of a series of strongly fluorescent Group 13 N_2O_2-bisphenolate aza-dipyrromethene complexes incorporating boron, aluminum, gallium, and Indium. Oxidation of these systems generated stable diradical species exhibiting strong near-infrared absorption, accessible mixed-valence states, and tunable magnetic properties.

Computational and experimental investigations demonstrated that the identity of the central Group 13 element plays a critical role in controlling spin delocalization, photophysical behavior, and redox activity. These studies established the first comprehensive family of Group 13 aza-dipyrromethene diradicaloids and provided valuable insights into metal-dependent tuning of open-shell electronic structures.

The work was further expanded to first-row transition-metal complexes of cobalt, nickel, copper, and zinc supported by phenol-substituted aza-dipyrromethene ligands. Controlled oxidation generated quinone/bis(diradicaloid) species with panchromatic absorption, ligand-centered spin delocalization, and accessible magnetic states. Importantly, charge-transport studies revealed unusually high hole mobilities relative to electron mobilities, highlighting the potential of these materials as hole-transport and molecular electronic materials.

In Chapter 5, highly conjugated ester substituted BODIPY systems were developed to achieve broad visible-to-near-infrared absorption and enhanced electronic communication through controlled redox transformations. Spectroelectrochemical, magnetic, and computational studies established the formation of stable mixed-valence (radical-anion), dianionic, and diradicaloid states possessing intense low-energy optical transitions profiles. These results further demonstrated that redox-state control provides an effective strategy for tuning optical and electronic properties over a broad spectral range.

6.2 Future Outlook

The results presented in this dissertation establish aza-BODIPY, BODIPY and aza-dipyrromethene frameworks as highly versatile platforms for the development of stable open-shell molecular systems with tunable optical, electronic, magnetic, and charge-transport properties. While significant progress has been made toward understanding the relationships between molecular structure, redox activity, and diradical character, numerous opportunities remain for expanding the scope and functionality of these materials.

One particularly promising direction involves the incorporation of donor–acceptor architectures into aza-BODIPY diradicaloid systems. During the course of this work, a new donor–acceptor aza-BODIPY diradicaloid containing triphenylamine donor units and an aza-BODIPY acceptor core was successfully synthesized and characterized. The introduction of strong electron-donating triphenylamine groups is expected to enhance intramolecular charge transfer, increase electronic communication across the π-conjugated framework, and provide additional pathways for tuning the diradical character and spin-state energetics of the molecule.

Future investigations will focus on understanding the electronic and magnetic consequences of this donor–acceptor design. Detailed spectroscopic and computational studies will be performed to examine the extent of spin delocalization throughout the molecular framework and to determine how donor–acceptor interactions influence the distribution of unpaired electron density. Variable-temperature NMR spectroscopy, EPR spectroscopy, SQUID magnetometry, and quantum chemical calculations will be

employed to establish the magnetic ground state and quantify singlet–triplet energy gaps. Particular attention will be directed toward identifying strategies for stabilizing open-shell singlet states while maintaining strong electronic communication between donor and acceptor fragments.

In addition to magnetic studies, future work will investigate the charge-transport properties of these donor–acceptor diradicaloids. The coexistence of diradical character and efficient charge-transfer pathways may provide a unique opportunity to develop materials that combine spin functionality with high carrier mobility. Thin-film characterization and device-based measurements will be used to evaluate electron and hole transport, with the ultimate goal of identifying structure–property relationships that govern charge transport in open-shell molecular systems.

More broadly, future efforts will continue to explore new molecular architectures capable of integrating optical absorption, spin delocalization, redox activity, and charge transport within a single framework. Such advances will contribute to the development of next-generation materials for molecular spintronics, organic electronics, photovoltaics, and quantum information technologies.

VITA

Tayo Morris Oyelowo was born and raised in Igbope, a small town in the southwestern region of Nigeria. He earned his Bachelor of Science degree in Chemistry from the University of Abuja, Nigeria, where he graduated as the Overall Best Graduating Student and Valedictorian of the 2015/2016 graduating class.

Following his undergraduate studies, he pursued a Master of Science degree in Organic Chemistry at the University of Ibadan, Nigeria. His master's research focused on the organic geochemical characterization of crude oil samples from the Niger Delta region of Nigeria. During this period, he developed a strong interest in research and advanced chemical characterization techniques, which motivated him to pursue a career in scientific research.

In 2021, Morris began his doctoral studies in Chemistry at the University of Tennessee, Knoxville. Prior to joining the University of Tennessee, he received multiple offers for graduate study from several institutions in the United States, including the University of Alabama, Tuscaloosa, Florida International University, and the University of South Florida. He ultimately chose the University of Tennessee, Knoxville, where he joined the research group of Dr. Viktor N. Nemykin at the end of 2021.

His doctoral research focused on the synthesis, characterization, and electronic properties of aza-BODIPY and aza-dipyrromethene complexes of Group 13 and first-row transition metals. His work contributed to the development of novel open-shell molecular systems with applications in molecular magnetism, spintronics, optoelectronics, and organic electronics. During his graduate studies, he authored and co-authored several peer-

reviewed publications, presented his research at regional, national, and international scientific conferences, and mentored undergraduate researchers in the laboratory.

Beyond research, Morris served as an active member of the scientific community, graduate student senate, and was recognized with several academic honors, fellowships, and travel awards. He remains passionate about advancing molecular materials chemistry and fostering the next generation of scientists.

In his free time, Morris enjoys reading current events, following financial markets, analyzing stocks, and watching soccer.